

Faculty of Science & Engineering
School of Earth & Planetary Sciences

Meteoroid Orbital Analysis: Connecting Meteorites and
Asteroids

Patrick M. Shober

0000-0003-4766-2098

This thesis is presented for the Degree of
Doctor of Philosophy
of
Curtin University

September 2021

Declaration

To the best of my knowledge and belief this thesis contains no material previously published by any other person except where due acknowledgement has been made.

This thesis contains no material which has been accepted for the award of any other degree or diploma in any university.

Signature:

Date:

“We make our world significant by the courage of our questions and by the depth of our answers.”

— Carl Sagan

Acknowledgements

The work presented in this thesis was supported by a Curtin International Post-graduate Research Scholarship. This research was also funded by the Australian Research Council as part of the Australian Laureate Fellowship scheme and carried out at the School of Earth and Planetary Sciences. Support and resources were also provided by the Pawsey Supercomputing Centre with funding from the Australian Government and the Government of Western Australia.

I would like to gratefully acknowledge the guidance and support I have received throughout my research and thank all those without whom this thesis would not have been possible. In particular:

- **Prof. Phil Bland** — At first, I believed you might have made a mistake taking me as your PhD student. Like, here is this 22-year-old geologist coming to do a PhD project on orbital mechanics, what? Apparently, you had a better judgement than I did. At first, I worked tirelessly because I believed I was unqualified and unable to live up to expectations. However, at some point, I started to work hard not because I was afraid of failing, but because I was relentlessly curious about where the research was taking me. Thank you for giving me the freedom to dive into a completely new topic and let curiosity guide the research outcomes. Thank you so much for helping me, teaching me, and encouraging me to be better.
- **My associate supervisors Prof. Gretchen Benedix and Dr. Eleanor Sansom** — Thank you so much for helping me with everything. From sort-

ing out requirements for Curtin stuff, complaining about said requirements, talking about my research, helping me when I first moved here. You have both been there for me so much during the last 3.5 years. Thank you.

- **Prof. Ralph Harvey** — I don't even know where to start, because you have done so much for me. You have been my mentor, my teacher, and my friend. I could not possibly be here finishing my PhD without you. You have always been there when I needed help or advice. Whether it be about my research, my life, or memes, I can always rely on you. Thank you so much for everything.
- **DFN Team** — Thank you Hadrien, Ellie, Tront, Seamus, Martin C, Martin T, Rob, Ben and everyone else involved with the DFN. Your support and encouragement throughout the previous few years has been critical to the success of my PhD.
- **Prof. Steven Hauck & Prof. James Van Orman** — As an undergraduate, the way you taught and spoke about your work made me want to study planetary science as well. I was only 19 trying to figure out my path and what I wanted to study, and anytime I needed advice or was freaking out about my engineering classes you both would take time to talk to me. You both gave me my first opportunity to do planetary science research. Eventually, leading me to switch my major to geology. I would not be finishing my PhD in planetary science without you, thank you.
- **Deborah Waters** — You have continued to be a mentor and friend long after my internship at NASA Glenn ended. Thank you so much for the support and inspiration during the past few years.
- **Eric Schmuhl** — As a coach and mentor, you positively shaped my life and continue to shape the lives of many others like me. In the most challenging times of my self-doubt, you always believed in me before I was able to believe in myself. Thank you for everything you have done for me. I would not have gotten this far without you.

- **Matt Barber** — Matty, moving across the planet is not an easy thing to do. Though, you had this innate ability to make people feel at home. I always loved listening to your stories of the old days and our hour-long sessions turning into three. Thanks Matt for being a good coach and friend. Rest in peace.
- **Other planetary PhD students** — Thank you to all the other PhD students that have been around during my time at Curtin. You guys made living in Perth and doing my research the awesome experience it was. Lots of beverages went into making this thesis, thank you for sharing a few with me.
- **My family & friends** — Thank you to my parents, my sisters, my extended family, and all my friends here in Australia or back home. At the end of the day, you are what is most important. Thank you so much for always supporting me and at least pretending to think what I am doing is cool.
- **Kristen** — I cannot imagine where I would be without you. You have always believed in me and been there for me. It has been complicated and challenging living so far away from each other. Things have been far from perfect. However, I could never have started and certainly never had finished a PhD without you. My path has certainly always been my own, but you were right there with me every step of the way. Thank you for being you and being there for me despite how hard it has been.
- **Bailey** — As things got crazy because of COVID-19 and I could not visit home or my family, you were my family. It seems silly, but it's true. Thank you for taking me back from the world every so often, because sometimes the world sucks and you just need to play with your dog.

Abstract

Every day, debris in near-Earth space impacts the atmosphere, annually adding up to $\sim 40,000$ tonnes of material. A vast majority of this material is tiny (sub-millimetre). However, some can be kilograms in size and produce meteorites on the ground. These meteorites can tell us a plethora of information about small bodies and the solar system's origin and evolution. Nevertheless, for nearly all of the $> 60,000$ meteorites in the world's collections, we do not have any information about where they came from.

Fireball observation networks over the previous half-century have attempted to solve this problem. Although, these networks recovered only a handful of meteorites after decades of observations. The number has drastically increased in the previous ten years as equipment has become more affordable and automation of the data reduction has improved. The Desert Fireball Network (DFN) is now the largest single photographic fireball network in the world, covering over 2.5 million km^2 of the Australian outback. The observational data collected since becoming fully operational in 2015 has given us the clearest picture yet of meteorites' source populations.

In this thesis, the impact data from the DFN was used to understand the meteoroid population in near-Earth space. Analysis of fireball data provided insights into the temporarily captured object ('minimoon') population and the close encounters of meteoroids with the Earth. Two fireball events were studied in detail. One of which had a $>90\%$ probability of being generated by an object gravitationally captured by the Earth prior to impact. Objects temporarily captured by

the Earth are perfect for testing future in-situ resource utilisation and impact mitigation technologies. Thus, any characterisation of this population is extremely valuable.

The other fireball event analysed was extremely long (~ 90 sec) and travelled over 1300 km through the atmosphere before returning to interplanetary space. Grazing fireball events push our atmospheric modelling efforts to the brink, providing a good test of our fireball triangulation methodologies. Furthermore, the close encounter was peculiar because the object gained energy as a result. This gravitational slingshot transferred the meteoroid from an asteroidal orbit to one resembling cometary debris. Based on this observation, a model was subsequently built to determine if significant mixing could occur between the Jupiter-family comet and asteroidal debris populations. The model simulated meteoroid close encounters with the Earth, based on data collected by the DFN. The results provided clear evidence of a positive net-flux onto comet-like orbits due to close encounters with the Earth. This flux of material between traditionally separate populations has significant implications.

Meteorites originating from comets has been debated for the previous century. However, even with over 60,000 samples to examine, there has never been a distinctly cometary meteorite. Thus, either we do not know what cometary meteorites should look like, or they do not exist in our collections. This question was finally answered by analysing the physical strength and dynamic stability of sporadic material on Jupiter-family comet-like orbits ($2 < T_J < 3$) observed by the DFN. Using Bayesian inference, we found that a majority of all meteoroids on cometary orbits in the centimetre to metre size-range originate in the main-belt. The results clearly demonstrated that mechanisms to diffuse debris out from the main-belt onto cometary orbits, as shown in our close encounter model, can significantly affect the meteoroid population. Additionally, Jupiter-family comet debris has very short physical lifetimes, less than the decoherence lifetimes of meteor showers (< 1000 yrs). Therefore, the likelihood of meteorites originating from comets is extremely low.

Contents

Acknowledgements	vii
Abstract	xi
Contents	xiii
List of Coauthored Publications	xxi
List of Figures	xxv
List of Abbreviations	xlvii
List of Symbols	li
1 Introduction	1
1.1 Background	1
1.1.1 Meteorites	2
1.1.2 Telescopic Observations	3
1.1.3 Fireball Observation Networks	3
1.2 Aims and Objectives	7
1.3 Thesis Structure	8
Bibliography	11

2 Identification of a Minimoon Fireball	17
2.1 Introduction	18
2.2 Event DN160822_03 Observations	22
Event Detection	22
Astrometric calibration	25
Triangulation	25
2.3 Methods	25
Summary of Definitions and Abbreviations	25
Orbital Integrator	27
Atmosphere Model	27
Integration Method	28
2.4 Results and Discussion	29
Calculating Probabilities	29
Capture Probability	32
Capture Mechanisms	33
Orbital Evolution	34
Pre-capture Orbit	36
Comparison to Models	36
Annual Variations	38
Comparison to Clark et al. (2016)	40
2.5 Conclusions	41
2.6 Acknowledgements	43
2.7 Summary of Definitions and Abbreviations	43
Bibliography	45
3 Where Did They Come From, Where Did They Go: Grazing Fireballs	53
3.1 Introduction	54

3.1.1	Reports of Grazing Fireballs	54
3.1.2	Small Inner Solar System Bodies	57
3.1.3	The Desert Fireball Network	58
3.2	DFN Observations	59
3.3	Methods	60
3.3.1	Triangulation	60
3.3.2	Mass Determination	63
3.3.3	Orbital Integration	63
	Initialization	64
	Integration	64
3.4	Results and Discussion	65
3.4.1	Atmospheric Trajectory	65
3.4.2	Short-term Simulations	68
	Close Encounters with Earth	74
3.4.3	Long-Term Simulations	74
3.4.4	Analysis of Other Grazing Meteors/Fireballs	78
	Other Grazing DFN Events	80
3.4.5	Implications and Further Research	80
3.5	Conclusions	81
3.6	Acknowledgements	81
	Bibliography	83
4	Using atmospheric impact data to model meteoroid close encounters	91
4.1	Introduction	92
4.1.1	Jupiter Family Comets	93
4.1.2	Meteors and Fireballs	94
4.1.3	Meteorite Falls	95

4.1.4	Addressing the Problem	95
4.2	Methods	97
4.2.1	Desert Fireball Network Data	97
4.2.2	Addressing Observational Biases	97
4.2.3	Creating the Close Encounter Dataset	102
4.3	Results and Discussion	104
4.3.1	Orbital Changes	104
4.3.2	Cumulative Size-Frequency Distributions	109
4.3.3	Impact Frequency	113
4.3.4	Additional Results	114
4.4	Future Work	114
4.5	Conclusions	115
4.6	Data availability	117
4.7	Close Encounter Flux Tables	117
	Bibliography	121
5	The main asteroid belt: the primary source of debris on comet-like orbits	129
5.1	Introduction	130
5.2	Materials and Methods	133
5.2.1	Experimental Design	133
5.2.1.1	Trajectory Analysis & Orbit Determination	133
5.2.1.2	Addressing Observational Biases	134
5.2.1.3	Data Selection	135
5.2.2	Dynamic Analysis	136
5.2.3	Physical Analysis	136
5.2.4	Statistical Analysis	139
5.3	Results	140

5.3.1	Orbital characteristics of sporadic JFC-like meteoroids . . .	140
5.3.2	Physical characteristics of sporadic JFC-like meteoroids . . .	141
5.3.2.1	Meteorite production from JFC-like meteoroids . .	143
5.4	Discussion	146
5.4.1	Meteoroids beyond the 2:1 resonance	147
5.4.2	Statistical Significance	148
5.4.3	Why are there no sporadic cometary meteoroids?	149
5.4.3.1	Alternative explanations	149
5.4.3.2	Short physical-lifetimes	150
5.4.4	Meteorites from Jupiter-family comets	151
5.4.5	Limitations	151
5.5	Summary	152
5.6	Acknowledgments	152
	Bibliography	155
	6 Thesis Conclusions and Future Work	165
	Appendices	171
	Bibliography	329

Coauthored Publications

Multiple coauthored manuscripts were published and are included in the main-body of the thesis. Reprints may be found in Appendix 6 along with statements of authorship. The coauthored publications are listed below along with a justification for their inclusion:

Coauthored Paper 1 – *Determining fireball fates using the α - β criterion.* Eleanor K. Sansom, Maria Gritsevich, Hadrien A. R. Devillepoix, Trent Jansen-Sturgeon, **Patrick M. Shober**, Phil A. Bland, Martin C. Towner, Martin Cupák, Robert M. Howie, Benjamin A. D. Hartig. *The Astrophysical Journal* (2019), Volume 885, Issue 2, p. 115-122.

Reason for inclusion– I helped with the processing of the fireball data included in the study and with the manual picking of the fireball trajectories. I also assisted with the editing and revision of the final manuscript.

Coauthored Paper 2 – *A Global Fireball Observatory.* H.A.R. Devillepoix, M. Cupák, P.A. Bland, E.K. Sansom, M.C. Towner, R.M. Howie, B.A.D. Hartig, T. Jansen-Sturgeon, **P.M. Shober**, S.L. Anderson, G.K. Benedix, D. Busan, R. Sayers, P. Jenniskens, J. Albers, C.D.K. Herd, P.J.A. Hill, P.G. Brown, Z. Krzeminski, G.R. Osinski, H. Chennaoui Aoudjehane, Z. Benkhaldoun, A. Jabiri, M. Guennoun, A. Barka, H. Darhmaoui, L. Daly, G.S. Collins, S. McMullan, M.D. Suttle, T. Ireland, G. Bonning, L. Baeza, T.Y. Alrefay, J. Horner, T.D. Swindle,

C.W. Hergenrother, M.D. Fries, A. Tomkins, A. Langendam, T. Rushmer, C. O'Neill, D. Janches, J.L. Hormaechea, C. Shaw, J.S. Young, M. Alexander, A.D. Mardon, J.R. Tate. *Planetary and Space Science* (2020), Volume 191, p. 105036.

Reason for inclusion— I contributed to the reduction of the fireball observations collected, analysis of fireball orbits, maintenance of the Australian node of the Global Fireball Observatory and the revisions of the manuscript.

Coauthored Paper 3 — *Machine learning for semi-automated meteorite recovery*. Seamus Anderson, Martin Towner, Phil Bland, Christopher Haikings, William Volante, Eleanor Sansom, Hadrien Devillepoix, **Patrick Shober**, Benjamin Hartig, Martin Cupak, Trent Jansen-Sturgeon, Robert Howie, Gretchen Benedix, Geoff Deacon. *Meteoritics & Planetary Science* (2020), Volume 55, Issue 11 p. 2461-2471.

Reason for inclusion— As a coauthor I helped with processing the fireball observations collected used to predict the fall locations of the meteorites. I also assisted with the analysis of fireball trajectories and the revisions of the manuscript.

Coauthored Paper 4 — *The Silicate-Sulfuric Acid Process: Mineral Processing for In Situ Resource Utilization (ISRU)*. Seamus Anderson, Eleanor Sansom, **Patrick Shober**, Benjamin Hartig, Hadrien Devillepoix, Martin Towner. *Acta Astronautica* (2021), Volume 188, p. 57-63.

Reason for inclusion— As a coauthor I helped with the discussion of the proposed ISRU technique. I also helped revise the manuscript.

Coauthored Paper 5 — *Taurid meteoroid stream 628: a reservoir of large impactors*. Hadrien Devillepoix, Peter Jenniskens, Phil Bland, Eleanor Sansom, Martin Towner, **Patrick Shober**, Martin Cupak, Robert Howie, Benjamin Hartig, Seamus Anderson, Trent Jansen-Sturgeon, Jim Albers. *The Planetary Science Journal* (2021), Volume 55, Issue 11 p. 2461-2471.

Reason for inclusion— As a coauthor I assisted with processing the fireball observations. More importantly, I helped analyse the orbital simulations of the Taurid fireballs detected and aid the discussion of the results in the manuscript.

List of Figures

- 1.1 Diagram demonstrating the process of observing fireballs with photographic all-sky networks and the recovery of subsequent meteorites. First meteoroids are ejected from their parent body through various mechanisms (part A), and then spend time orbiting the Sun until they cross the Earth’s path (part B). Upon impact with the Earth, the meteoroid’s surface undergoes extreme heating and begins to give off light as a fireball (part C). As the meteoroid passes through the atmosphere, it eventually slows down enough to stop emitting visible light and continues to fall during the ‘dark flight’ (part D). Large enough meteoroids eventually may reach the ground as intact meteorites (part E). 4
- 2.1 Map of camera observations for event DN160822_03 in Southern Australia by the DFN. The orange arrow indicates the ground-track of the fireball’s luminous trajectory. This path is extremely small due to the nearly vertical slope of the trajectory ($\approx 86.6^\circ$). Six camera observations were collected during the 5.32 sec duration. . . 24

-
- 2.2 Cross-track residuals to the straight line trajectory fit (SLLS) of the event DN160822_03. The dots correspond to the perpendicular distance between the observed lines-of-sight and the predicted straight line trajectory. The error bars represent the 1σ formal astrometric uncertainties, however, these uncertainties are likely overestimated due to not well-constrained point-picking uncertainties (nominally 0.5 pixel error). The observation range from each DFN station is given in the legend as [highest point - lowest point]. 26
- 2.3 Comparison of the v_0 distribution generated by the EKS and the DTF methods using either (a) the full trajectory or (b) the top of the trajectory (observations >65 km altitude). Given the large amount of data collected for event DN160822_03, 506 data points, the v_0 is more dependent than usual on the choice of triangulation and velocity determination methods. When only the top of the observed atmospheric trajectory is used, the models' assumptions affect the results less and the v_0 distributions converge. 30
- 2.4 Particle orbits within the Sun-Earth-Particle synodic reference frame centered on the Earth's center of mass and co-rotating with the Earth so that the direction of the sun is always at(-1AU, 0) in the x-y plane in this figure (not shown). The colors are indicative of the particles' spatial density, yellow being the most dense and black/purple being the least. The axes are in units of lunar distances (LD). There appears to be a clear preference of entry into the Earth-Moon system through either the L1 or L2 Lagrange points (represented by red points), as shown by the prevalence of trajectories in the directions of the co-linear Lagrange points. 31

-
- 2.5 Gravitational capture locations in synodic reference frame with L1 and L2 points marked by red crosses. The Sun-Earth synodic frame is centered on the Earth's center of mass and co-rotates with the Earth so that the direction of the sun in this case is always at $(-1\text{AU}, 0)$ in the x-y plane. The figures above show 3 distinct capture regions: L1 capture, L2 capture and close lunar-encounter capture. The tail-like feature near the L2 point is caused by a large group of particles that were captured fairly quickly into the integration so they did not scatter as much. 37
- 2.6 TCs that get within 3 Hill radii of the Moon (3H) produced by the SLLS and DTF. Each point represents one particle within 3H and the y-axis indicates the geocentric semi-major axis (LD) for that particle at that time. Most of the TCs in the simulations have close encounters with the Moon multiple times. The probability of an encounter increases once a month, due to the geometry of this specific event. This indicates that the Moon was likely critically important for the geocentric orbital evolution of the meteoroid and the impact of the meteoroid with the Earth. 38
- 2.7 Geocentric semi-major axis vs eccentricity and inclination for the temporarily captured particles. The color bar is indicative of gravitational capture duration during the simulation. Yellow corresponding to a longer capture duration and black corresponding to a shorter capture duration. Particles that were captured the longest tended to have lower eccentricity, lower semi-major axis and lower inclinations. This is generally true because the particles that had more close encounters with the Moon tended to be less dynamically stable. Also, particles that were not able to transition from the initially highly eccentric detected orbit to lower eccentricities typically had lower capture durations. 39

- 2.8 Total capture duration vs velocity during capture for TC particles. The relatively large annual variation in probable capture velocity results from the eccentricity of the Earth, as the Earth moves closer or further from the Sun during the year the capture velocity also varies. This annual variation in the probable capture velocity thus produces annual variations in the Lagrange point capture location and the source NEO group (Fig. b and Fig. c). Probably due to the geometry of the event (high eccentricity, low inclination, apogee $\approx 1LD$), there also exists vertical bands of close lunar-encounter captures that occur every lunar month (Fig. a) 42
- 3.1 Long exposure images of event DN170707_01. The event lasted over 90 seconds and spanned four 30 second exposures (A, B, C, D). The fireball was first observed at 85 km altitude, reached as low as 58 km, and then was visible until 86 km before escaping the Earth's atmosphere. The initial velocity was 16.1 km s^{-1} , and the exit velocity after passing through the atmosphere was about 14.6 km s^{-1} . The images are all oriented so that the fireball travels from left to right (west to east). 61
- 3.2 Fragmentation event captured for event DN170707_01 near the closest approach of its trajectory. The image shows two distinct paths offset from each other. The brighter path on the right side of the image belonging to the primary piece, whereas on the left the trail of a smaller fainter fragment can be seen. The decrease in velocity due to the observed fragmentation was not significant relative to the velocity scatter, and thus was not included during the trajectory fit. Additionally, only one camera observed the fragment due to cloud coverage and geometry, and therefore a trajectory for the fragment was unable to be determined. No other fragmentation events were detected along the path. 61

-
- 3.3 Light curve based on video from observatory DFNSMALL34-Kybo in the Nullarbor Plain in Western Australia during the fragmentation of event DN170707_01. The fragmentation occurs about 25 sec into this exposure (enclosed by dashed vertical lines), forming one detectable fragment. The y-axis is brightness in arbitrary units due to the photometry data lacking calibration. The ram pressure on the meteoroid just prior to the fragmentation was ~ 0.08 MPa. The line-of-sight was briefly obstructed by a telephone pole, reducing the brightness. 62
- 3.4 Height variation as a function of time determined by the straight-line least-squares (SLLS) and the Dynamic Trajectory Fit (DTF) methods. The pointwise heights represent the points that minimizing all the angular distances between the simultaneous lines-of-sight (given > 2), the respective observatory, and the point itself. The DTF fits much better to the pointwise than the SLLS due to its incorporation of gravity, drag, and ablation. This non-straight line fit produces a much more useful model to understand these grazing fireball events. The shape of the trajectory is somewhat misleading, as the trajectory would be concave with respect to a global, inertial reference frame instead of convex, as shown here. The three distinct gaps in the trajectory are due to latency between observation periods (Howie et al., 2017a). This lapse in observations occurs once every thirty seconds and is only typically noticeable for the longest fireball trajectories observed by the DFN. Towards the end of the trajectory, the largest lapse in observations was also due to the cloud coverage at the time 65

-
- 3.5 The velocity of the DN170707_01 meteoroid event as determined using both the Dynamic Trajectory Fit model (red) and a pointwise triangulation fit (blue). The DTF method fits the line-of-sight observations directly to the dynamic equations of motion that describe the motion of fireballs. Pointwise scattered instantaneous speeds correspond to the center-difference between adjacent data points seen by > 2 observatories. These points in 3D space are calculated by minimizing all the angular distances between the simultaneous lines-of-sight, the respective observatory, and the point itself. 66
- 3.6 Triangulated luminous atmospheric trajectory for event DN170707_01, as seen over Western Australia and South Australia. The triangulation method used involves fitting the line-of-sight observations directly to the meteoroid's dynamic equations of motion, thereby dropping any straight-line assumptions (Jansen-Sturgeon et al., 2019b). The event lasted 90 seconds, initially hitting the atmosphere at 4.6° and covering over 1300 km through the atmosphere. The white rays indicate the line-of-sight measurements from each DFN observatory, whereas the black path marks the triangulated trajectory based on the observations of the fireball. . . 66
- 3.7 Mass estimation based on DTF triangulation fit to the DFN's observations. The fragmentation event was taken into account, as seen by the sudden mass loss experienced at ~ 40 sec into the luminous phase. Each line represents a different density estimate for the object, given the DTF ballistic parameter. 68
- 3.8 The meteoroid's orbit before and after the grazing encounter with the Earth. The meteoroid originated from an Apollo-type asteroidal orbit and was inserted into a JFC orbit. Once in this JFC orbit, the object's path rapidly becomes less certain due to multiple close-encounters with Jupiter. 69

3.9 Semi-major axis vs. eccentricity during ± 100 years of integrations involving 10,000 test particles. Particle density over time is indicated by opacity. A majority of the particles remain close together after the grazing encounter, with a small number of particles being scattered by Jupiter very quickly. The significant mean-motion resonances are also plotted as vertical dotted lines. The object came from an eccentric orbit between the 4:1 and 3:1 mean motion resonances. After the grazing encounter with the Earth, the object gained energy and was transferred onto a JFC orbit near the 2:1 resonance with Jupiter. In this orbit, the future of the meteoroid is strongly influenced by the gas giant. Over time, the meteoroid will tend to follow the aphelion and perihelion lines for Jupiter. 70

3.10 Specific relative angular momentum of the meteoroid ± 12 hours relative to the grazing event. The meteoroid gains energy after its encounter with the Earth despite losing some energy during the atmospheric passage. At time = 0, the discontinuity is due to the exclusion of the time when the meteoroid was passing through the atmosphere. The ‘instant’ drop in energy here corresponds to the energy lost due to atmospheric drag. The object continues to gain angular momentum briefly after leaving the atmosphere before losing some energy as it travels away from the Earth. This net gain in angular momentum effectively increased the semi-major axis and eccentricity of the body. 71

3.11 After grazing Earth’s atmosphere, the meteoroid will complete 1.5 orbits around the Sun before likely having its first close encounter with Jupiter. Both plots provide the distance from Jupiter in terms of Jupiter Hill Radii (JHR). Of the 5,000 particles in this integration, nearly 40% come within 1 JHR and 80% are within 3 JHR. The mean approach is about 0.7 JHR. Consequently, the orbit of the meteoroid is highly uncertain after this point, approximately 7.52 years after its grazing encounter with the Earth (January-March 2025). . 72

3.12 Due to the grazing encounter with the Earth, the meteoroid from event DN170707.01 was sent into a Jupiter intersecting orbit. On this new trajectory, the object will likely experience many close encounters with Jupiter over its lifetime. In these density plots, the blue and orange particles represent the meteoroid before and after the grazing encounter, respectively. The darker coloration is indicative of a higher particle density. The many possible close encounters with Jupiter manifest as discrete “jumps” in the semi-major axis, eccentricity, or inclination. Over time the orbits tend to spread out due to numerous close encounters with Jupiter. Thus, the orbit of the meteoroid becomes less clear over a relatively short period of time. 75

-
- 3.13 Plot of distance relative to the Earth over time. These 2 simulations were conducted with 5,000 particles and lasted 20 years (forward and backward). The time on the x-axis is relative to the event epoch. The probability of an encounter with the Earth for the 20 years before and after the fireball observation is extremely low. There is a 2.4% probability of coming within 3 Hill radii and a 0.7% probability having a 1 Hill radii encounter with the Earth within 20 years before the grazing encounter. Meanwhile, there is a 1.4% and a 0.5% probability of the meteoroid encountering the Earth again within one and three Hill radii in the next 20 years respectively. There is 1.1% that the object will approach within 3 Hill radii in July 2023. 76
- 3.14 Plot showing the change in the orbital classification of the 1,000 particles in the forward integration of event DN170707_01 for 500 kyrs. The lines separating the labels in the legend group classifications together that are mutually exclusive (e.g. particles cannot be simultaneously hyperbolic and heliocentric). Over time, the likelihood that the meteoroid will have a close enough encounter to eject it from the Solar System increases. By the end of the simulation, 60.1% of the particles are ejected, 27.3% are still on JFC orbits, and 12.6% have remained in the Solar System but have either gone onto long-period cometary or asteroid-like orbits. Many of the particles ($\sim 20\%$) evolve onto Centaur and then trans-Neptunian orbits due to close-encounters with Jupiter. 77

-
- 3.15 Tisserand's parameter variation of 1,000 particles integrated for 500 *kyrs* post-grazing event for DN170707.01. Particles that are ejected from the Solar System are removed. The meteoroid is likely to stay in a JFC orbit for an amount of time normal for a 'natural' JFC object. The colouration in the plot is indicative of density - darker in areas of higher particle density and lighter in areas of lower particle density. 78
- 3.16 Semi-major axis vs eccentricity for the particles that are still gravitationally bound to the Sun after the forward integration of 1,000 particles for 500 *kyrs*. The lines of equal perihelion and aphelion are plotted for Jupiter and Neptune in black, and in gray for Saturn and Uranus. Most of the remaining heliocentric particles (68.4%) are in JFC-like orbits (blue) according to their Tisserand's parameter. However, a considerable number of particles (29.1%) are considered "asteroidal", according to their Tisserand's parameter with respect to Jupiter (red). Only a very small number of these are in the inner Solar System. A vast majority appear to be former JFC particles that have completely decoupled from Jupiter and have drifted onto Centaur and trans-Neptunian orbits due to planetary perturbations over time. The Centaur and trans-Neptunian particles can have either JFC or asteroidal like Tisserand's parameters ($T_J > 2$), as shown by the colourisation in this plot. Also, about 2.5% of the particles are categorized as "long-period comets" despite their low semi-major axis because they are orbiting in retrograde orbits. . . . 79
- 4.1 Tisserand's parameters (T_J) of the DFN events used in this study along with the time of day in which each fireball was observed. The red line represents the median T_J value. 98

-
- 4.2 Solar longitude distribution for DFN events used to generate artificial close encounter population. There is a noticeable decrease in events detected during the summer months as the duration of the night is shortest. 99
- 4.3 Change in semi-major axis (a), eccentricity (e), and inclination (inc) for every particle in our simulation as a function of the minimum orbital intersection distance (MOID) in Lunar Distances (LD). The color bar indicates the number of objects each particle represents annually. 105
- 4.4 Percentage change in the particles' semi-major axis (a) varying according to the minimum orbital intersection distance (MOID). The red points indicate the median change. The largest change in orbital energy is logically experienced by objects with the closest encounters. 106
- 4.5 4.5a and 4.5b show the semi-major axis vs. eccentricity and inclination respectively for all the test particles in the model (2.3 million particles) before and after having a close encounter with the Earth. The grouping of black particles tend to get dispersed along lines of equal aphelion/perihelion after having a close encounter (grey particles). There is typically minimal change in the inclination, however, as $a \sim 1$ the changes in inclination becomes more significant. 107
- 4.6 Close encounter simulation particles energy change in terms of Tisserand's parameter (T_J). The T_J value before and after encountering the Earth are the x and y axis respectively. Region A denotes contains particles that were transferred from a asteroid-like orbit to a JFC-like one, whereas region B contains particles that underwent the reverse transfer. 108

-
- 4.7 Cumulative size frequency distribution of annual close encounters < 1.5 LD redirected from asteroidal to JFC-like orbits. Horizontal lines are indicative of uncertainty in the diameter. This sub-population only represents $\sim 0.1\%$ of the close encounters given the maximum MOID. The slopes of branches A and B are -1.21 ± 0.01 and -7.22 ± 1.30 respectively. Compared to the entire close encounter flux, the B branch is steeper and the A branch is shallower. There are proportionally more higher mass meteoroids. 110
- 4.8 Semi-major axis vs. eccentricity for particles that were transferred from asteroidal like orbits ($T_J > 3$) to JFC-like orbits ($2 < T_J < 3$). As shown by the particles lying on or past the perihelion of Jupiter, close encounters transfer objects onto orbits indistinguishable at times from native JFCs. 111
- 4.9 Semi-major axis vs. eccentricity for particles in model that were transferred onto Aten-type orbits as a result of the close encounter with the Earth. Meteoroids with similar orbits to the Earth ($a \sim 1 - 2$ au), are the most likely to undergo this process. 115
- 5.1 Backward integrations -10 kyrs of two particles generated within the triangulated trajectory uncertainties of event DN200104_01 where q is perihelion, a is semi-major axis, i is inclination, ω is argument of perihelion, and Ω is longitude of ascending node. On the left, a particle on a chaotic unstable orbit typical of a comet with numerous Jupiter close encounters. On the right, another particle provides an example of a stable orbit following a predictable path with no close encounters with Jupiter. This specific fireball event lasted over 5 sec and was recorded by 4 DFN stations, providing an excellent trajectory fit with very minimal uncertainties. Thus, this demonstrates the difficulty associated with backward propagation of meteoroids coming from orbits on the edge of two source regions (JFC and main-belt in this case). 137

- 5.2 Triangulated semi-major axis vs. eccentricity for 50 non-shower JFC-like fireballs observed by the DFN that have predicted initial masses greater than 10 g. Error bars denote the formal 1σ orbital uncertainties associated with each meteoroid, and coloration is indicative of the orbital stability determined through numerical integrations -10 kyrs. The vertical red lines indicate the major MMRs with the dashed gray lines marking the maximum libration in semi-major axis (Tancredi, 2014). Most of the events originate from stable orbits near the MMRs. The densogram (<http://www.star.bris.ac.uk/~protect/unhbox/voidb@x\protect\penalty\@M\{}mbt/stilts/sun256/layer-densogram.html>) at the bottom of the plot represents the semi-major axis density for near-Earth ($q < 1.3$ au) JFCs within according to the NASA HORIZONS system (<http://ssd.jpl.nasa.gov/horizons.cgi>). . 142
- 5.3 Sporadic JFC-like fireballs observed by the DFN with a minimum initial mass of 10 g. The end heights of meteors can be used to ascertain the physical-nature of meteoroids using the PE criterion (Ceplecha and McCrosky, 1976). The PE values for the 50 fireballs examined are overwhelmingly stronger than the traditional comet types (Types IIIa and IIIb). The error bars associated with each meteoroid's semi-major axis and PE value are due to triangulation uncertainties. 144
- 5.4 Distribution of non-shower JFC fireballs with enough deceleration to determine $\alpha - \beta$ values (at least $\sim 20\%$ deceleration). γ is the trajectory slope relative to the horizontal. If a macroscopic event is considered to have a final mass of ≥ 50 g, assuming $\rho_m = [2240, 3500]$ kg m $^{-3}$ (carbonaceous and ordinary chondrite respectively) and $c_{dA} = 1.5$, meteorite dropping events can easily be identified given the range of possible shape change coefficients (μ). 145

List of Tables

2.1	Locations and observation details for DFN observatories that detected event DN160822.03. Start and end times are given relative to the event start/end (first event to detect fireball has relative start time of 0.00) * Line of sight distance to start of trajectory † Relative to 12:17:10.826 UTC on 22 August 2016	22
2.2	Atmospheric trajectory of event DN160822.03	23
2.3	Summary of 5 year recursion results for event DN160822.03 in which over 16,000 valid particles were integrated, 10,000 for each run and 80,000 in total. TCs represent any captured particles, TCOs are captured and have orbited the Earth at least once, TCFs are captured and have not yet completed 1 orbit of the Earth, Sputniks are particles that originate from the Earth, SC represents particles that are still captured after 5 years, and TC 3LH is for TCs that go within 3 lunar Hill radii. The %TCO, %TCF, and %TC values are calculated after removing Sputniks. In all of the integrations initialized from the SLLS, the Sputniks account for > 90% of the particles. Due to the highly irregular orbit originating from the Earth, Sputnik particles are assumed to be invalid. There are no unbound particles that go within 3 lunar Hill radii recorded in the simulations, suggesting that the capture was facilitated by a close encounter with the Moon.	35

-
- 3.1 Observations and triangulated trajectory for event DN170707_01, recorded over Western Australia and South Australia on July 7th, 2017. Mass range determined by varying density between $2800 - 7300 \text{ kg m}^{-3}$ and includes formal uncertainties. Timing uncertainty is nominally $10^{-4} - 10^{-5} \text{ s}$, considerably less than other sources of uncertainty for the trajectory (Howie et al., 2017b). 59
- 3.2 Heliocentric orbital elements for the meteoroid associated with event DN170707_01 just before and after its grazing encounter with the Earth. The uncertainties of the orbital elements were determined by a short Monte Carlo simulation consisting of 5,000 particles randomly generated within triangulation errors and numerically integrated forward and backward relative to the grazing event. The immediate effect of the encounter on the orbit is apparent; the semi-major axis, eccentricity, and argument of perihelion of the meteoroid were all significantly increased. The grazing encounter changed the orbit of the meteoroid from an Apollo-type NEO to a JFC orbit. The resulting orbit is comparatively unstable due to its aphelion being very similar to the semi-major axis of Jupiter, increasing the chance of a close encounter with the gas giant. 73
- 3.3 Summary of six of the ten previous Earth-grazing meteors within scientific literature in which the meteoroid survived the passage through the atmosphere. Information omitted in the table was not included in the corresponding study. 80
- 4.1 Close encounter object flux table. Columns represent the T_J value before, and the rows represent the T_J value after the close encounter. 118
- 4.2 Close encounter mass flux table (kg). Columns represent the T_J value before, and the rows represent the T_J value after the close encounter. 119

- 4.3 Close encounter mass error flux table (kg). Columns represent the T_J value before, and the rows represent the T_J value after the close encounter. 120
- 5.1 Traditional PE classifications based on the atmospheric density at terminal height (Ceplecha and McCrosky, 1976). 143

List of Abbreviations

AU	Astronomical Unit
CSD	Cumulative Size-frequency Distribution
Dec	Declination
Deg	Degree
DFN	Desert Fireball Network
DSLR	Digital Single-Lens Reflex camera
DTF	Dynamic Trajectory Fit
ECEF	Earth Centred, Earth Fixed reference frame
ECI	Earth Centred Inertial reference frame
EKF	Extended Kalman Filter
EKS	Extended Kalman Smoother
GFO	Global Fireball Observatory
IAS15	Implicit integrator with Adaptive time Stepping, 15th order
JHR	Jupiter Hill Radius
JFC	Jupiter-Family Comet
LD	Lunar Distance
LPC	Long Period Comet
LSST	Large Synoptic Survey Telescope
MB	Main-Belt
MBO	Main-Belt Object
MBC	Main-Belt Comet
MCMC	Markov-Chain Monte-Carlo

MMR	Mean Motion Resonance
MOID	Minimum Orbital Intersection Distance
MOP	Method of Planes
MPI	Message Passing Interface
NASA	National Aeronautics and Space Administration
NEA	Near-Earth Asteroid
NEO	Near-Earth Object
NES	Natural Earth Satellite
NIC	Nearly Isotropic Comet
RA	Right Ascension
SC	Still Captured
SD	Scattered Disk
SFD	Size-Frequency Distribution
LLS	Straight Line Least Squares
SOI	Sphere of Influence
SSTC	Space Science & Technology Centre
TC	Temporarily Captured
TCF	Temporarily Captured Flyby
TCO	Temporarily Captured Orbiter
UB	Unbound
USG	United States Government
UT	Universal Time
UTC	Coordinated Universal Time
WHFast	Wisdom-Holman fast symplectic integrator

List of Symbols

A	shape coefficient	-
A_G	effective cross-sectional area of Earth due to gravitational focusing	km ²
A_{NG}	cross-sectional area of Earth	km ²
α	ballistic coefficient	-
α	hyperparameters of the prior distribution	-
a	semi-major axis	au
β	mass-loss parameter	-
γ	trajectory slope relative to the horizontal	°
c_d	drag coefficient	-
°	degree symbol	-
c	observation vector	-
D_J	similarity criterion described in Jopek (1993)	-
e	eccentricity	-
H_F	enhancement factor due to gravitational focusing	-
i	inclination	°
ι_T	total terrestrial impact flux at top of atmosphere	year ⁻¹
m_∞	initial mass of the meteoroid	g
μ	shape change coefficient	-
N_{HF}	gravitational enhancement scaling factor	-
ν_6	prominent secular resonance with Saturn	-
Ω	longitude of the ascending node	°

ω	argument of periapsis	°
r_{\oplus}	radius of the earth	km
ρ_E	density of the atmosphere at the end the luminous trajectory	kg/m ³
ρ_h	atmospheric density at fragmentation height	MPa
ρ_m	meteoroid density	kg/m ³
PE	criterion used to estimate meteoroid strengths (Ceplecha and McCrosky, 1976)	-
p_v	geometric albedo	-
Q	aphelion distance	au
q	perihelion distance	au
σ	standard deviation	-
T_J	Tisserand's parameter relative to Jupiter	-
v_0	top of luminous trajectory velocity	m/s
V_{∞}	initial velocity of the meteoroid	m/s
V_{esc}	escape velocity on Earth's surface	m/s
V_i	meteoroid velocity prior to Earth encounter	m/s
v_h	meteoroid velocity at fragmentation height	m/s
Z_R	local entry angle measured from the zenith	°

CHAPTER 1

Introduction

1.1 Background

One of the primary goals of planetary science research is to better understand small planetary bodies, like asteroids and comets. Generally, comets originated further out from the Sun in the protoplanetary disk and have retained their volatile components. In contrast, asteroids formed much closer to the Sun and have usually undergone some degree of thermal alteration, giving them a rocky composition. These elusive objects tend to be kilometres or less in scale and have varying compositions and orbital characteristics. Most asteroids exist in the main asteroid belt, an area between Jupiter and Mars. However, some of these primordial leftovers from the early solar system have evolved onto orbits near the Earth (Binzel et al., 2015). These aptly called ‘near-Earth objects’ (NEOs) are of great concern for the international community. They pose a significant impact threat to humanity as well as provide an abundance of primitive material near the Earth that could be utilised for scientific or economic purposes (Mazanek et al., 2015; Mathias et al., 2017). Therefore, research of NEOs has been significant over the previous couple of decades. There are primarily two ways this research is typically done: directly observing asteroids with large telescopes or examining the debris

from the asteroids that impact the Earth and survive as meteorites.

1.1.1 Meteorites

Across human history, we have associated some special importance with curious alien rocks that come from the sky (Burke, 1991; Rehren et al., 2013; Heineman and Brady, 1929). However, it was not until the late 18th and early 19th century that it was recognised that meteorites originated from space (Chladni, 1794; Lauretta and McSween, 2006). Since this time extensive scientific analysis has been performed on meteorites. We have gained key insights into the formation and evolution of our solar system.

Nevertheless, it took some time for people to conclude that they came from asteroids. Meteorites are small pieces of rock that were ejected from an asteroid and survived the journey to the Earth intact. Geologists can similarly decipher the history of meteorites to methodologies used on terrestrial samples. For example, by examining the mineralogy, the chemical composition, the petrographic features, and the isotope composition we can learn a lot about the parent body from which a meteorite originated (Hutchison, 2006). There are over 60,000 meteorite samples in the world's collections, and from this massive amount of material, we can build a detailed history of our solar system.

They have also split the meteorites into types based on their composition, degree of alteration, level of shock, etc. (Hutchison, 2006; Lauretta and McSween, 2006). Principally they can be divided into three types: stones, stoney-irons, and iron meteorites. The different classifications of meteorites each tell us something different about small bodies in our solar system.

However, compared to the terrestrial geologist, a meteoriticist is unable to go into the field (to an asteroid) and collect samples. Instead, they rely on the serendipity of the Earth crossing the path of debris ejected from an asteroid. Thus, for nearly all of the meteorites found on Earth, we do not know which object was the parent body or even where they originated in the solar system.

1.1.2 Telescopic Observations

Conversely, another method to gain insights about small bodies in our solar system is by directly observing them using telescopes. The first minor planets and asteroids were not discovered until the early 19th century (Forbes, 1971). At the beginning of the 20th century, less than one thousand asteroids had been discovered. Today, we have identified and confirmed the observations of over one million small bodies in our solar system¹.

From the main-belt, asteroids evolve over time onto Earth-crossing orbits. Debris from these asteroids, called ‘meteoroids’, evolve similarly and sometimes impact the Earth and survive as meteorites. These objects are critically important to understand as they are the leftovers from the solar system’s formation. Their composition and dynamics show us how we got to the current layout of planets we see today. Additionally, impacts from NEOs pose a significant threat to life on Earth. Also, they contain an abundance of resources that could be utilised in the future as humanity ventures out from our pale blue dot.

Similar to meteorite analysis, observational astronomers also categorise and split asteroids into different types. However, to discriminate between different groups, they classify asteroids based on their spectral properties (Reddy et al., 2015). The spectra give some sense of the physical properties and composition of each asteroid. Nevertheless, due to the spectra being a function of more than just the composition, we still mostly do not know how the asteroid types correspond to the defined meteorite classifications (Borovička et al., 2015). We have come up with two distinct ways to study the same population of objects within planetary science.

1.1.3 Fireball Observation Networks

There are a few methods to identify the parent bodies of the meteorite types we observe on Earth.

The first way is to physically send sample-return missions to many asteroids

¹<https://minorplanetcenter.net//mpc/summary>

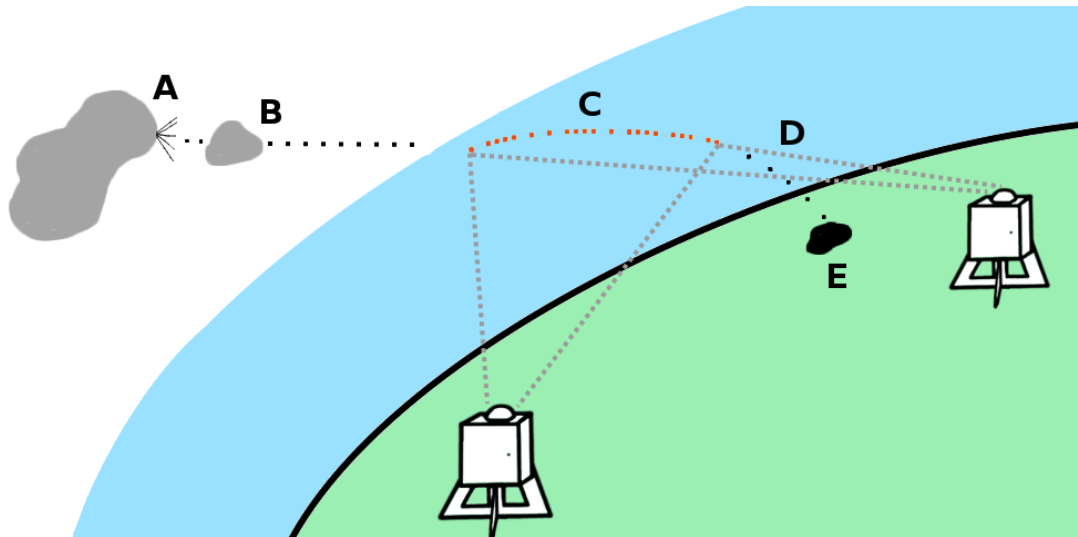


Figure 1.1: Diagram demonstrating the process of observing fireballs with photographic all-sky networks and the recovery of subsequent meteorites. First meteoroids are ejected from their parent body through various mechanisms (part A), and then spend time orbiting the Sun until they cross the Earth’s path (part B). Upon impact with the Earth, the meteoroid’s surface undergoes extreme heating and begins to give off light as a fireball (part C). As the meteoroid passes through the atmosphere, it eventually slows down enough to stop emitting visible light and continues to fall during the ‘dark flight’ (part D). Large enough meteoroids eventually may reach the ground as intact meteorites (part E).

and comets to calibrate the spectral observations with the returned samples. This is a very effective and definitive way to solve this overt gap in knowledge in planetary science, yet it is costly and a very slow process. There have only been two successful sample-return missions from an asteroid, with one more currently in-progress (Fujiwara et al., 2006; Watanabe et al., 2017; Lauretta et al., 2017).

Another way to connect the results from telescopic surveys to the meteoritic analysis is fireball observation networks (Ceplecha and Rajchl, 1965; Ceplecha et al., 1998; Bland et al., 2012; Borovička et al., 2015; Devillepoix et al., 2020). Fireball observation networks continuously observe the entirety of the night-sky until a piece of asteroidal debris impacts the atmosphere forming a very bright meteor (brighter than stellar magnitude -4), also known as a ‘fireball’. An overwhelming majority of meteoroids that impact the atmosphere completely disintegrate; however, fireballs can often produce meteorites on the ground. Fireball observations can be used to predict the fall locations of the meteorites in addition with the pre-impact orbital characteristics (Ceplecha et al., 1998; Shober et al.,

2019, 2020b; Devillepoix et al., 2020). This methodology is easier and significantly cheaper in comparison to sample-return missions. Fireball orbital data is thus crucial for our understanding of the relationship between asteroids and meteorites.

The first sizeable photographic fireball network was started in 1963 in Czechoslovakia and later joined by collaborators in Germany (Ceplecha and Rajchl, 1965; Ceplecha et al., 1973). This network is still active and known as the European Fireball Network (EFN) (Oberst et al., 1998). Other networks were also built in North America, such as the Prairie Network in the US (1963-1975) and the Meteorite Observation and Recovery Project (MORP) in Canada (1971-1985) (McCrosky and Boeschenstein, 1965; Halliday et al., 1978). Since, there have been several, usually smaller, photographic networks set up for fireball detections (Babadzhanov et al., 2009; Trigo-Rodríguez et al., 2005; Wiśniewski et al., 2017; Devillepoix et al., 2020). Additionally, there are many amateur and professional video meteor networks set up around the world (Brown et al., 2010; Molau and Rendtel, 2009).

The largest photographic fireball network in the world is the Desert Fireball Network (DFN) in Australia (2005-Present) (Bland, 2004; Bland et al., 2012; Howie et al., 2017). The DFN has a coverage area of over 2.5 million km², about one-third of the continent. This massive network of digital fireball cameras aims to optimise the process of finding meteorite falls with orbital data. Currently, there are only about ~ 40 meteorite falls² with precisely measured atmospheric trajectories from which an orbit can be determined Granvik and Brown (2018). These observations, combined with dynamic analyses of the meteoroid orbits, have provided a great deal of invaluable information about the asteroid population.

A great deal of information can also be obtained from just the observations of fireballs and determination of the pre-encounter orbits. Even without a meteorite recovery, the fireball data collected by the DFN provides a plethora of knowledge about the physical and dynamic properties of debris in the solar system.

Using the observations of the passage through the atmosphere, fireball networks can determine a best-fit trajectory for the object (Sansom et al., 2015).

²<https://www.meteoriteorbits.info/>

The progenitor meteoroid's pre-atmospheric orbit can be obtained from this fitted trajectory (Ceplecha et al., 1998; Jansen-Sturgeon et al., 2019). However, when going through this data reduction, the observations and models' relevant uncertainties must be propagated appropriately. Therefore, the orbits extracted from fireball data have associated uncertainties. These uncertainties must be accurate and sufficiently small to attain accurate statistics. The maximum uncertainty allowable is dependent on the desired regression time, i.e., greater uncertainty is tolerable if the numerical simulations are only integrating backwards in time a minimal amount. For example, to perform meaningful source region analysis of fireball data the initial velocity errors at the top of the atmosphere should be below 100 m s^{-1} (Granvik and Brown, 2018).

Formal uncertainties accompany orbital data generated by the DFN. Analysis of fireball orbital data is normally done by conducting a Monte Carlo simulation. Test particles are sampled from within the formal orbital uncertainties and then are numerically integrated backwards in time to statistically analyse the orbital evolution of the original meteoroid (Borovička et al., 2015). This analysis can provide critical insights into the object's history and where it came from within the solar system.

The physical nature of meteoroid can also be inferred from the observed ablation characteristics. The traditional metric to characterise the strengths of meteoroids is the PE criterion, which is principally dependent on the end height of the fireball (Ceplecha and McCrosky, 1976; Ceplecha et al., 1998). The equation for the PE criterion is as follows:

$$PE = \log(\rho_E) - 0.42 \log(m_\infty) + 1.49 \log(V_\infty) - 1.29 \log(\cos Z_R) \quad (1.1)$$

where ρ_E is the density of the atmosphere at the end the luminous trajectory, m_∞ is the initial mass of the meteoroid in grams, V_∞ is the initial velocity of the meteoroid in km/s, and Z_R is the local entry angle measured from the zenith. This metric has been used for decades to understand the strength of meteoroids (Ceplecha, 1994; Brown et al., 2013; Borovička et al., 2015; Brown et al., 2016).

Recently, a new metric has been proposed a better alternative, the α - β criterion

(Gritsevich and Stulov, 2006; Gritsevich, 2007; Lyytinen and Gritsevich, 2016). The ballistic coefficient (α) and the mass-loss parameter (β) offer an alternative approach to characterising strength based on physical parameters and with fewer assumptions (Moreno-Ibáñez et al., 2020). These values have also been shown to be extremely useful to predict whether a meteorite was produced from a fireball event (Sansom et al., 2019).

The observations of the DFN provide the clearest opportunity yet to understand the meteoroid population in near-Earth space better. The dynamic and physical evolution of meteoroids is complicated and mostly unconstrained. The massive fireball dataset collected by the DFN can be utilised to unravel the mysteries about centimetre to metre debris as a whole along with the sub-populations contained within it.

In this thesis, the DFN dataset is used to better understand sub-populations such as the temporarily captured population (Chapter 2) and the close encounter population (Chapter 3 and Chapter 4). The dynamic results from these studies combined with analysis of the fireballs' atmospheric ablation characteristics helped us gain substantial insights into the entire source population of meteorites (Chapter 5).

1.2 Aims and Objectives

This thesis's primary goal is to analyse the massive fireball dataset collected by the Desert Fireball Network and determine what we can learn about the source population for meteorites. This information is critical for the planetary science community who study meteorites and the asteroids from which they originate. The goals of the thesis can be summarised as follows:

1. Characterise the dynamics of meteoroids in near-Earth space.
2. Characterise the physical nature of meteoroids impacting the Earth.
3. Make conclusions about the orbital history of meteorites based on the dynamic and physical analysis of the DFN dataset.

1.3 Thesis Structure

This doctoral thesis has been prepared in a thesis by publication format, consisting of four peer-reviewed first author published manuscripts. Three coauthored published manuscripts are additionally included in the appendix. Each manuscript includes contribution statements from coauthors. The thesis is arranged as follows:

CHAPTER 2: IDENTIFICATION OF A MINIMOON FIREBALL (Shober et al., 2019) — Reviews in detail the study of the temporarily captured object population and details a thorough analysis of a fireball observed by the DFN in 2016. The fireball event was very likely ($> 90\%$ probability) produced by a meteoroid captured gravitationally by the Earth before impacting the atmosphere. This population of objects is significant. It consists of the easiest objects to visit in the solar system (lowest Δ -v), which could help test future technologies related to in-situ resource utilisation or asteroid impact mitigation. The numerical simulations performed help us understand the dynamics of this sub-population.

CHAPTER 3: WHERE DID THEY COME FROM, WHERE DID THEY GO: GRAZING FIREBALLS (Shober et al., 2020b) — Details the analysis of a grazing fireball that travelled over 1300 km through the atmosphere above Australia in 2017. The approximately half-meter meteoroid transited the atmosphere for 90 sec and penetrated as deep as 58.5 km before returning back to interplanetary space. The object originated from an Apollo-type NEO orbit and exited onto a JFC-like orbit due to the extreme close encounter with the Earth. The analysis also reviews orbital changes recorded during other grazing fireball events and discusses the implications of close terrestrial encounters on the inner solar system's meteoroid population.

CHAPTER 4: USING ATMOSPHERIC IMPACT DATA TO MODEL METEOROID CLOSE ENCOUNTERS (Shober et al., 2020a) — This work built off the analysis in Chapter 3, taking advantage the entirety of the DFN's orbital dataset to model the population of meteoroid close encounters. Large kilometre-

scale bodies regularly have close encounters with the Earth and are telescopically observed. However, metre-scale objects or smaller have extremely close encounters with the Earth all the time but are too faint to be detected by telescope surveys. This study used the massive fireball dataset of the DFN to characterise the close encounter populations of centimetre to metre-scale objects and infer what effect these encounters have on the entire near-Earth meteoroid population.

CHAPTER 5: THE MAIN ASTEROID BELT: THE PRIMARY SOURCE OF DEBRIS ON COMET-LIKE ORBITS (Shober et al., 2021) — This chapter presents a thorough analysis of the physical and dynamic characteristics of sporadic meteoroids on comet-like orbits. Based on the work in Chapter 4, there is at least one effective mechanism to transfer material from the main-belt to orbits similar to those of cometary debris. However, based on the telescopic observations of JFCs, small JFCs (below kilometre size) have been predicted to have very short physical lifetimes. This prediction has been confirmed by the analysis performed within this chapter, demonstrating that main-belt material is dominant on JFC-like orbits within the size-range that commonly produces meteorites on Earth. Thus, the presence of cometary meteorites in the world's collections is extremely unlikely.

CHAPTER 6: THESIS CONCLUSIONS AND FUTURE WORK — This chapter summarises the principal findings of the thesis. The results of each manuscript and the novel contributions made to planetary science are discussed. Additionally, several possible avenues of continued research are proposed.

Bibliography

- P. Babadzhanov, G. Kokhirova, J. Borovička, and P. Spurný. Photographic observations of fireballs in tajikistan. *Solar System Research*, 43(4):353–363, 2009.
- R. P. Binzel, V. Reddy, and T. Dunn. The near-earth object population: Connections to comets, main-belt asteroids, and meteorites. *Asteroids IV*, 1:243, 2015.
- P. Bland, P. Spurný, A. Bevan, K. Howard, M. Towner, G. Benedix, R. Greenwood, L. Shrbený, I. Franchi, G. Deacon, et al. The australian desert fireball network: a new era for planetary science. *Australian Journal of Earth Sciences*, 59(2):177–187, 2012.
- P. A. Bland. The desert fireball network. *Astronomy & Geophysics*, 45(5):5–20, 2004.
- J. Borovička, P. Spurný, and P. Brown. Small near-earth asteroids as a source of meteorites. *Asteroids IV*, 257, 2015.
- P. Brown, R. Weryk, S. Kohut, W. Edwards, and Z. Krzeminski. Development of an all-sky video meteor network in southern ontario, canada the asgard system. *WGN, Journal of the International Meteor Organization*, 38:25–30, 2010.
- P. Brown, V. Marchenko, D. E. Moser, R. Weryk, and W. Cooke. Meteorites from meteor showers: A case study of the taurids. *Meteoritics & Planetary Science*, 48(2):270–288, 2013.

- P. Brown, P. Wiegert, D. Clark, and E. Tagliaferri. Orbital and physical characteristics of meter-scale impactors from airburst observations. *Icarus*, 266:96–111, 2016.
- J. G. Burke. *Cosmic debris: Meteorites in history*. Univ of California Press, 1991.
- Z. Ceplecha. Impacts of meteoroids larger than 1 m into the earth’s atmosphere. *Astronomy and Astrophysics*, 286:967–970, 1994.
- Z. Ceplecha and R. McCrosky. Fireball end heights: A diagnostic for the structure of meteoric material. *Journal of Geophysical Research*, 81(35):6257–6275, 1976.
- Z. Ceplecha and J. Rajchl. Programme of fireball photography in czechoslovakia. *Bulletin of the Astronomical Institutes of Czechoslovakia*, 16:15, 1965.
- Z. Ceplecha, M. Jezkova, J. Bocek, T. Kirsten, and J. Kiko. Data on three significant fireballs photographed within the european network in 1971. *Bulletin of the Astronomical Institutes of Czechoslovakia*, 24:13, 1973.
- Z. Ceplecha, J. Borovička, W. G. Elford, D. O. ReVelle, R. L. Hawkes, V. Porubčan, and M. Šimek. Meteor phenomena and bodies. *Space Science Reviews*, 84(3-4):327–471, 1998.
- E. F. F. Chladni. *Über den Ursprung der von Pallas gefundenen und anderer ihr ähnlicher Eisenmassen und über einige damit in Verbindung stehende Naturerscheinungen*. bey Johann Friedrich Hartknoch, 1794.
- H. A. R. Devillepoix, M. Cupák, P. A. Bland, E. K. Sansom, M. C. Towner, R. M. Howie, B. A. D. Hartig, T. Jansen-Sturgeon, P. M. Shober, S. L. Anderson, G. K. Benedix, D. Busan, R. Sayers, P. Jenniskens, J. Albers, C. D. K. Herd, P. J. A. Hill, P. G. Brown, Z. Krzeminski, G. R. Osinski, H. C. Aoudjehane, Z. Benkhaldoun, A. Jabiri, M. Guennoun, A. Barka, H. Darhmaoui, L. Daly, G. S. Collins, S. McMullan, M. D. Suttle, T. Ireland, G. Bonning, L. Baeza, T. Y. Arefay, J. Horner, T. D. Swindle, C. W. Hergenrother, M. D. Fries, A. Tomkins, A. Langendam, T. Rushmer, C. O’Neill, D. Janches, J. L. Hormaechea, C. Shaw, J. S. Young, M. Alexander, A. D. Mardon, and J. R. Tate.

- A Global Fireball Observatory. *Planetary and Space Science*, 191:105036, Oct. 2020. doi: 10.1016/j.pss.2020.105036.
- H. A. R. Devillepoix, M. Cupák, P. A. Bland, E. K. Sansom, M. C. Towner, R. M. Howie, B. A. D. Hartig, T. Jansen-Sturgeon, P. M. Shober, S. L. Anderson, G. K. Benedix, D. Busan, R. Sayers, P. Jenniskens, J. Albers, C. D. K. Herd, P. Carlson, P. J. A. Hill, P. G. Brown, Z. Krzeminski, G. R. Osinski, H. C. Aoudjehane, T. Shisseh, Z. Benkhaldoun, A. Jabiri, M. Guennoun, A. Barka, H. Darhmaoui, L. Daly, G. S. Collins, S. McMullan, M. D. Suttle, C. Shaw, J. S. Young, M. Alexander, A. D. Mardon, T. Ireland, G. Bonning, L. Baeza, T. Y. Alrefay, J. Horner, T. D. Swindle, C. W. Hergenrother, M. D. Fries, A. Tomkins, A. Langendam, T. A. Rushmer, C. O'Neill, D. Janches, and J. L. Hormaechea. A global fireball observatory, 2020.
- E. G. Forbes. Gauss and the discovery of ceres. *Journal for the History of Astronomy*, 2(3):195–199, 1971. doi: 10.1177/002182867100200305. URL <https://doi.org/10.1177/002182867100200305>.
- A. Fujiwara, J. Kawaguchi, D. Yeomans, M. Abe, T. Mukai, T. Okada, J. Saito, H. Yano, M. Yoshikawa, D. Scheeres, et al. The rubble-pile asteroid itokawa as observed by hayabusa. *Science*, 312(5778):1330–1334, 2006.
- M. Granvik and P. Brown. Identification of meteorite source regions in the solar system. *Icarus*, 311:271–287, 2018.
- M. Gritsevich and V. Stulov. Extra-atmospheric masses of the canadian network bolides. *Solar System Research*, 40(6):477–484, 2006.
- M. I. Gritsevich. Approximation of the observed motion of bolides by the analytical solution of the equations of meteor physics. *Solar System Research*, 41(6):509–514, Dec. 2007. doi: 10.1134/S003809460706007X.
- I. Halliday, A. Blackwell, and A. Griffin. The innisfree meteorite and the canadian camera network. *Journal of the Royal Astronomical Society of Canada*, 72: 15–39, 1978.

- R. E. S. Heineman and L. F. Brady. The winona meteorite. *American Journal of Science*, (108):477–486, 1929.
- R. M. Howie, J. Paxman, P. A. Bland, M. C. Towner, M. Cupak, E. K. Sansom, and H. A. Devillepoix. How to build a continental scale fireball camera network. *Experimental Astronomy*, 43(3):237–266, 2017.
- R. Hutchison. *Meteorites: A petrologic, chemical and isotopic synthesis*, volume 2. Cambridge University Press, 2006.
- T. Jansen-Sturgeon, E. K. Sansom, H. A. R. Devillepoix, P. A. Bland, M. C. Towner, R. M. Howie, and B. A. D. Hartig. A dynamic trajectory fit to multi-sensor fireball observations, 2019.
- D. Lauretta, S. Balram-Knutson, E. Beshore, W. V. Boynton, C. D. d’Aubigny, D. DellaGiustina, H. Enos, D. Golish, C. Hergenrother, E. Howell, et al. Osiris-rex: sample return from asteroid (101955) bennu. *Space Science Reviews*, 212(1-2):925–984, 2017.
- D. S. Lauretta and H. Y. McSween. *Meteorites and the early solar system II*. University of Arizona Press, 2006.
- E. Lyytinen and M. Gritsevich. Implications of the atmospheric density profile in the processing of fireball observations. *Planetary and Space Science*, 120:35–42, 2016.
- D. L. Mathias, L. F. Wheeler, and J. L. Dotson. A probabilistic asteroid impact risk model: assessment of sub-300 m impacts. *Icarus*, 289:106–119, 2017.
- D. D. Mazanek, R. G. Merrill, J. R. Brophy, and R. P. Mueller. Asteroid redirect mission concept: a bold approach for utilizing space resources. *Acta Astronautica*, 117:163–171, 2015.
- R. E. McCrosky and H. Boeschenstein. The prairie meteorite network. *Optical Engineering*, 3(4):304127, 1965.

- S. Molau and J. Rendtel. A comprehensive list of meteor showers obtained from 10 years of observations with the imo video meteor network. *WGN, Journal of the International Meteor Organization*, 37:98–121, 2009.
- M. Moreno-Ibáñez, M. Gritsevich, J. M. Trigo-Rodríguez, and E. A. Silber. Physically based alternative to the pe criterion for meteoroids. *Monthly Notices of the Royal Astronomical Society*, 494(1):316–324, 2020.
- J. Oberst, S. Molau, D. Heinlein, C. Gritzner, M. Schindler, P. Spurny, Z. Ceplecha, J. Rendtel, and H. Betlem. The “european fireball network”: current status and future prospects. *Meteoritics & Planetary Science*, 33(1):49–56, 1998.
- V. Reddy, T. L. Dunn, C. A. Thomas, N. A. Moskovitz, and T. H. Burbine. Mineralogy and surface composition of asteroids. *Asteroids IV*, (2867), 2015.
- T. Rehren, T. Belgya, A. Jambon, G. Káli, Z. Kasztovszky, Z. Kis, I. Kovács, B. Maróti, M. Martinón-Torres, G. Miniaci, et al. 5,000 years old egyptian iron beads made from hammered meteoritic iron. *Journal of Archaeological Science*, 40(12):4785–4792, 2013.
- E. K. Sansom, P. Bland, J. Paxman, and M. Towner. A novel approach to fireball modeling: The observable and the calculated. *Meteoritics & Planetary Science*, 50(8):1423–1435, 2015.
- E. K. Sansom, M. Gritsevich, H. A. Devillepoix, T. Jansen-Sturgeon, P. Shober, P. A. Bland, M. C. Towner, M. Cupák, R. M. Howie, and B. A. Hartig. Determining fireball fates using the α - β criterion. *The Astrophysical Journal*, 885(2):115, 2019.
- P. M. Shober, T. Jansen-Sturgeon, E. Sansom, H. Devillepoix, P. Bland, M. Cupák, M. C. Towner, R. M. Howie, and B. A. Hartig. Identification of a minimoon fireball. *The Astronomical Journal*, 158(5):183, 2019.
- P. M. Shober, T. Jansen-Sturgeon, P. Bland, H. Devillepoix, E. Sansom, M. Towner, M. Cupák, R. Howie, and B. Hartig. Using atmospheric impact

- data to model meteoroid close encounters. *Monthly Notices of the Royal Astronomical Society*, 498(4):5240–5250, 2020a.
- P. M. Shober, T. Jansen-Sturgeon, E. K. Sansom, H. A. Devillepoix, M. C. Towner, P. A. Bland, M. Cupák, R. M. Howie, and B. A. Hartig. Where did they come from, where did they go: Grazing fireballs. *The Astronomical Journal*, 159(5):191, 2020b.
- P. M. Shober, E. K. Sansom, P. A. Bland, H. A. Devillepoix, M. C. Towner, M. Cupák, R. M. Howie, B. A. Hartig, and S. L. Anderson. The main asteroid belt: the primary source of debris on comet-like orbits. *The Planetary Science Journal*, 2(3):98, 2021.
- J. Trigo-Rodríguez, A. Castro-Tirado, J. Llorca, J. Fabregat, V. Martínez, V. Reglero, M. Jelínek, P. Kubánek, T. Mateo, and A. de Ugarte Postigo. The development of the spanish fireball network using a new all-sky ccd system. In *Modern Meteor Science An Interdisciplinary View*, pages 553–567. Springer, 2005.
- S.-i. Watanabe, Y. Tsuda, M. Yoshikawa, S. Tanaka, T. Saiki, and S. Nakazawa. Hayabusa2 mission overview. *Space Science Reviews*, 208(1-4):3–16, 2017.
- M. Wiśniewski, P. Żoładek, A. Olech, Z. Tyminski, M. Maciejewski, K. Fietkiewicz, R. Rudawska, M. Gozdalski, M. Gawroński, T. Suchodolski, et al. Current status of polish fireball network. *Planetary and Space Science*, 143:12–20, 2017.

CHAPTER 2

Identification of a Minimoon Fireball

Patrick M. Shober^a, Trent Jansen-Sturgeon^a, Eleanor K. Sansom^a, Hadrien A.R. Devillepoix^a, Phil A. Bland^a, Martin Cupák^a, Martin C. Towner^a, Robert M. Howie^a, Benjamin A.D. Hartig^a

^aSpace Science and Technology Centre (SSTC), School of Earth and Planetary Sciences, Curtin University, GPO Box U1987, Perth, Western Australia 6845, Australia

This article is published in The Astronomical Journal, accepted 27 August 2019, published 14 October 2019

Abstract

Objects gravitationally captured by the Earth-Moon system are commonly called temporarily captured orbiters (TCOs), natural Earth satellites, or minimoons. TCOs are a crucially important subpopulation of near-Earth objects to understand because they are the easiest targets for future sample-return, redirection, or asteroid mining missions. Only one TCO has ever been observed telescopically, 2006 RH₁₂₀, and it orbited the Earth for about 11 months (Kwiatkowski et al., 2009). Additionally, only one TCO fireball has ever been observed prior to this study (Clark et al., 2016). We present our observations of an extremely slow fireball (codename DN160822.03) with an initial velocity of around 11.0 km s⁻¹ that was detected by 6 of the high-resolution digital fireball observatories located in the South Australian region of the Desert Fireball Network (DFN). Due to the inherent dynamics of the system, the probability of the meteoroid being temporarily captured before impact is extremely sensitive to its' initial velocity. We examine the sensitivity of the fireball's orbital history to the chosen triangulation method. We use the numerical integrator REBOUND to assess particle histories and assess the statistical origin of DN160822.03. From our integrations we have found that the most probable capture time, velocity, semi-major axis, NEO group, and capture mechanism vary annually for this event. Most particles show that there is an increased capture probability during Earth's aphelion and perihelion. In the future, events like these may be detected ahead of time using telescopes like the LSST, and the pre-atmospheric trajectory can be verified.

2.1 Introduction

Occasionally when an object gets close to the Earth-Moon system, it is captured by the Earth's gravity. These objects are commonly called temporarily captured orbiters (TCOs), natural Earth satellites or "minimoons" (Granvik et al., 2012). The first mention of TCOs was by Chant (1913) and then Denning (1916) in a description of a extraordinarily long fireball that was witnessed over North America.

Since the event lasted so long, according to witnesses, the source was speculated to be orbiting the Earth before entering the atmosphere. Besides this brief hypothesis, the study of TCOs was mostly left unexplored for the rest of the 20th century. During the space race, when artificial satellites began to be launched into orbit, there was speculation on whether or not natural Earth satellites would exist side-by-side with the artificial satellites (Baker, 1958).

For the last half-century, there have been many studies of captured objects by the large gas giants in the solar system, particularly Jupiter (Heppenheimer and Porco, 1977; Pollack et al., 1979; Kary and Dones, 1996; Nesvorný et al., 2003, 2007). There have also been several papers discussing the capture mechanisms and dynamics in the circular restricted three-body problem (CRTBP) and whether or not individual planets are even capable of sustaining a TCO population. Originally the models were simple and showed that only the large gas giants were capable of capturing satellites (Yegorov, 1959). Eventually, Bailey (1972) extended this methodology to any planet in the solar system. He showed that TCOs are possible for any planet when considering each in the limiting framework of the elliptic restricted three-body problem, instead of assuming circular orbits.

Following this study, Cline (1979) was the first to explore the viability of a lunar assisted capture as a way to check for viable ballistic trajectories to the outer solar system's planets. Since then, there have been a handful of studies interested in the feasibility of Moon-assisted captures along with using moons for decreasing the delta- V required for space missions to outer solar system objects (Tsui, 2000, 2002; Lynam et al., 2011; Gong and Li, 2015; Luo and Topputo, 2017).

While studying the capture dynamics of Jupiter, several papers found that the capture duration was highly unpredictable (Murison, 1989; Brunini, 1996; Kary and Dones, 1996). This unpredictability was due to the fractal nature of the orbital phase space from which the objects originate. Furthermore, Murison (1989) stated that temporarily captured objects may have to have some chaotic origin, being on the boundary of two adjacent sinks (i.e., they can either evolve towards a heliocentric orbit or a planetocentric orbit). Thus, small perturbations in the initial conditions can radically change the evolutionary behavior of objects, i.e.,

whether or not it is captured and for how long the object is captured. Astakhov et al. (2003) also showed that whether an orbit displayed prograde or retrograde behavior was intrinsically tied to the initial energy along with the size and distribution of regular satellites in the Hill sphere. This chaotic nature associated with the dynamics of natural satellites will make it much more difficult to predict where the meteoroid observed by the Desert Fireball Network (DFN) originated from in the solar system.

It was not until 2006 that the first Earth TCO was observed. Asteroid 2006 RH₁₂₀ orbited the Earth from July 2006 to July 2007 before escaping the Earth-moon system (Kwiatkowski et al., 2009). This asteroid is still the only observed TCO, but this will undoubtedly change once the Large Synoptic Survey Telescope (LSST) starts making regular survey observations in 2022 (Ivezić et al., 2008; Fedorets et al., 2015). Granvik et al. (2012) was the first to model TCOs that considered capture probability as a function of orbital element space for the NEO population. The model also calculated the size-frequency distribution and orbital distribution for TCOs. Fedorets et al. (2017) expanded on this work by focusing on objects that approached the Earth and were captured but escaped before they could complete one orbit, also known as ‘temporarily captured flybys’ (TCFs). Based upon these models, they predict that the largest object in orbit around the Earth at any given time is about 1 m in diameter and that these objects are typically captured through the Earth’s co-linear L1 and L2 regions. Additionally, they predicted that 0.1% of all meteors were previously TCOs before they impacted the Earth. Given this information, we expect to find about 1 TCO within the DFN’s dataset.

Clark et al. (2016) searched for fireballs that were natural satellites of the Earth before they impacted the atmosphere. They found one fireball detected by the European Fireball Network that had a 92-98% chance of being captured by Earth before detection according to their model. Although, the capture duration for this meteoroid varied from 48 days up to over 5 years. Clark et al. (2016) also looked at data from the Prairie Network in the US along with data collected by US Government sensors. None of the low-speed objects could be confidently

said to be captured before impact due to the unknown or high uncertainty in the pre-atmospheric velocity for the measurements. To date, the event recorded by the EFN and described by Clark et al. (2016) is the only fireball observed with a very high probability of originating from a TCO orbit.

Granvik et al. (2012) assumed the orbit-density distribution is independent of the size-frequency distribution for their TCO model. While this is accurate for more substantial objects, it is unlikely true for smaller NEOs. The DFN and other fireball networks like it are particularly ideal for characterizing this portion of the meteoroid population. Using TCO fireball data collected from these types of networks, we can ascertain how likely the Granvik model is accurate for smaller size ranges.

Generating an accurate orbital model for TCOs and TCFs is vital because these bodies are the most accessible in the solar system. They are the ideal targets for future sample-return, in-situ resource utilization (ISRU), and asteroid impact mitigation technology testing (Chodas, 2014; Brelsford et al., 2016). Additionally, since the average TCO orbits multiple times before escaping, this allows for multiple observations within a small time frame. These observations of TCOs can be used to understand the smallest members of the NEO population (Bolin et al., 2014). TCOs have the potential to have far-reaching effects on our understanding of asteroids and the history of the solar system along with many other future space-based technology applications. Thus, if we can better predict the orbital paths of these bodies based on observations and models, finding TCOs and TCFs will become easier.

The Desert Fireball Network (DFN) is a continental scale facility that observes fireballs in our atmosphere, calculates their pre-entry orbit, and determines where any possible meteorite material may land (Howie et al., 2017a). There are currently 1300+ fully triangulated events detected by the DFN. Previous models of the natural Earth satellite population (Granvik et al., 2012; Fedorets et al., 2017), predicted that about 0.1% of all meteors impacting the Earth should have been temporarily captured prior to impact. Based on these models, assuming the orbit-density distribution is independent of the size-frequency distribution, there

should be one or two events in the DFN dataset that were captured objects before impacting the atmosphere.

The questions to be addressed within this study include:

1. Is the number of TCOs in the DFN dataset consistent with previous models?
2. How would such meteoroids get captured by the Earth-Moon system and is this different than expected from past models?
3. How long might any TCOs have been captured before they hit the Earth?
4. How much does the presence of the Moon affect the capturability?

2.2 Event DN160822_03 Observations

Within the orbital dataset of the DFN, one event was indeed flagged as a possible TCO: DN160822_03. Here we will detail the event from initial observations to triangulation and will discuss in the following sections its' nature as a TCO.

Event Detection

observatory	range (km) *	start time (sec) [†]	end time (sec) [†]
Moolawatana	117	0.10	5.32
Wertaloonna	117	0.20	5.12
Fowlers Gap	157	0.00	5.06
Weekeroo	203	0.20	2.66
Wilpoorinna	221	0.50	4.96
Etadunna	270	1.10	4.16

Table 2.1: Locations and observation details for DFN observatories that detected event DN160822_03. Start and end times are given relative to the event start/end (first event to detect fireball has relative start time of 0.00)

* Line of sight distance to start of trajectory

[†] Relative to 12:17:10.826 UTC on 22 August 2016

DN160822_03 was observed by six of the DFN's high-resolution fireball cameras in South Australia just before 11 PM local time on August 22, 2016 (Figure 2.1).

All but one of the cameras were able to image nearly the entire trajectory (Table 1). The event lasted over five seconds and had a nearly vertical atmospheric trajectory ($\sim 87^\circ$). This high-angle impact argues against an artificial origin and pre-atmospheric trajectory integrations eliminate the possibility of standard satellite debris. Although, however unlikely, this does not eliminate the possibility of debris from Apollo or other past lunar/interplanetary missions. Table 2 summarizes the atmospheric trajectory, mass, and velocities determined for event DN160822_03.

The camera systems used to observe the event are described fully in Howie et al. (2017a). The absolute timing for the event was recorded using a de-Bruijn sequence that is encoded into the fireball image by using a liquid crystal shutter in addition to the built-in shutter (Howie et al., 2017b). The liquid crystal is synchronized with a Global Navigation Satellite System (GNSS) module using a microcontroller, which produces absolute times accurate to ± 0.4 ms.

	Beginning	Terminal
Time (isot)	2016-08-22T12:17:10.826	2016-08-22T12:17:16.146
Height (km)	74.1	24.1
Mass (kg)	11.8	0.3
Latitude (deg)	-30.53009	-30.53960
Longitude (deg)	140.38927	140.36020
SLLS tops Velocity (km s^{-1})	10.95 ± 0.07	3.90 ± 0.18
DTF tops Velocity (km s^{-1})	11.07 ± 0.14	3.77 ± 0.07
RA (deg)	-63.06557 ± 0.00831	
Dec. (deg)	-29.35007 ± 0.00726	
Slope (deg)	86.55081 ± 0.00725	
Duration (sec)	5.32	
Best Convergence Angle (deg)	87.8	
Number of Observations	6	
Number of Datapoints	506	

Table 2.2: Atmospheric trajectory of event DN160822_03

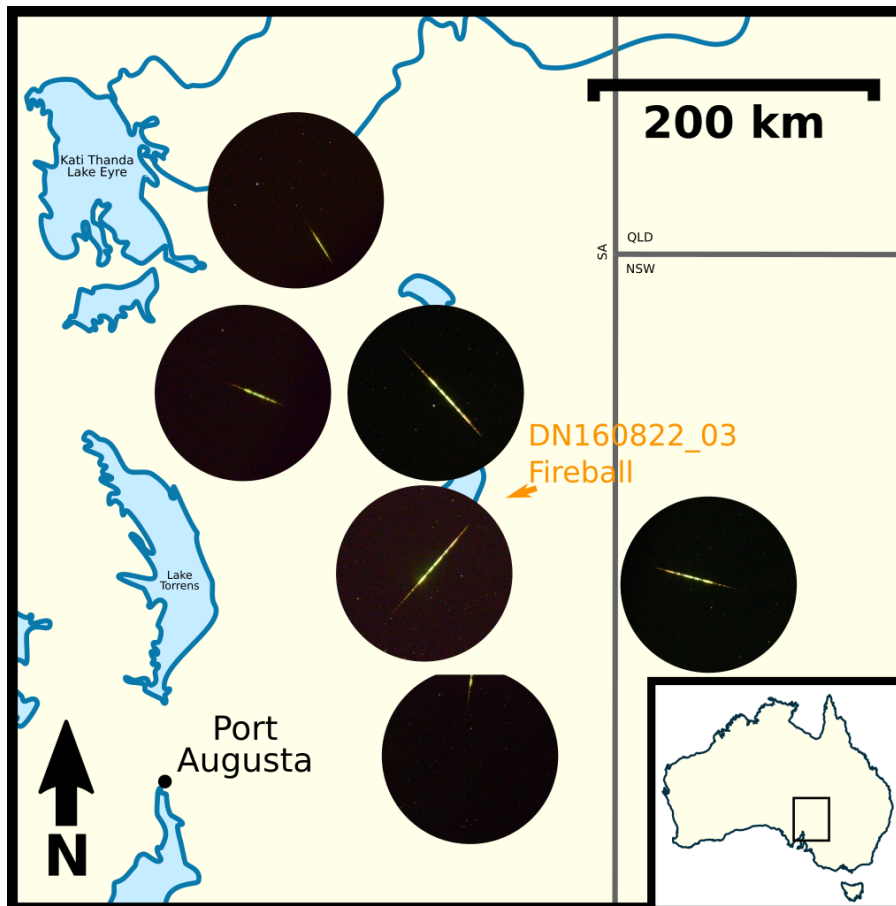


Figure 2.1: Map of camera observations for event DN160822_03 in Southern Australia by the DFN. The orange arrow indicates the ground-track of the fireball's luminous trajectory. This path is extremely small due to the nearly vertical slope of the trajectory ($\approx 86.6^\circ$). Six camera observations were collected during the 5.32 sec duration.

Astrometric calibration Astrometric calibration is performed using background stars, as described by Devillepoix et al. (2018). This results in astrometric measurements that are generally accurate (1σ) down to $\simeq 1.5$ minutes of arc (as shown by the errors-bars in Fig. 2.2), limited by astrometric noise in this case.

Triangulation During the analysis of the event detected by the DFN, two separate triangulation methods were used. We did this to check the sensitivity of the orbital history for this meteoroid to the triangulation method based on the work of previous studies (Vida et al., 2018). Our primary method is a straight line least squares (SLLS) algorithm, modified from (Borovicka, 1990), with an Extended Kalman Smoother (EKS) for velocity determination (Sansom et al., 2015). Additionally, the Dynamic Trajectory Fit (DTF) of Jansen-Sturgeon, et al. (in prep.) was utilised alongside the traditional triangulation methods for comparison. The SLLS algorithm determines the straight-line trajectory by minimizing the angular distance between it and the observed lines-of-sight from every camera. The DTF algorithm is similar, however, it fits the observation rays to a trajectory based on meteor equations of motion, therefore dropping the straight-line assumption. One might say the SLLS is a purely geometric and simplifying fit, while the DTF is more based in reality. However, the initial velocity at the top of the luminous path (v_0) errors produced when using this DTF method cannot account for model error. The SLLS with an EKS velocity analysis can include this factor, therefore producing more reliable errors. Moreover, the event in question has a nearly vertical slope (87.8°), and the luminous path deviates negligibly from linear (Fig. 2.2). Thus, the backward integrations initiated after using the SLLS method in this paper are more statistically robust than those produced by the DTF method. We use both methods to demonstrate the highly sensitive pre-atmospheric orbit of event DN160822_03 to the calculated v_0 .

2.3 Methods

Summary of Definitions and Abbreviations Within this study we followed the notation of Granvik et al. (2012) and Fedorets et al. (2017) for consistency

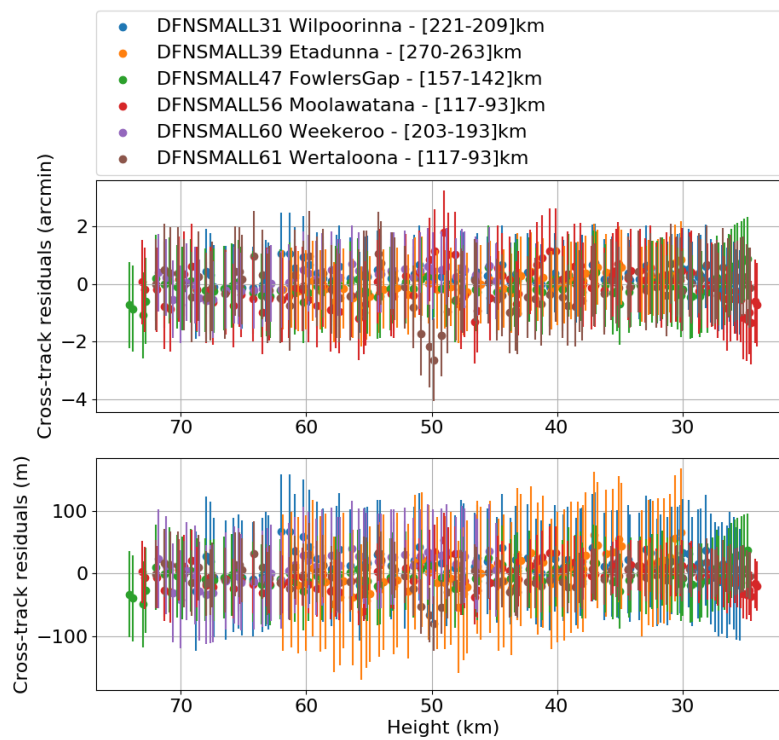


Figure 2.2: Cross-track residuals to the straight line trajectory fit (SLLS) of the event DN160822_03. The dots correspond to the perpendicular distance between the observed lines-of-sight and the predicted straight line trajectory. The error bars represent the 1σ formal astrometric uncertainties, however, these uncertainties are likely overestimated due to not well-constrained point-picking uncertainties (nominally 0.5 pixel error). The observation range from each DFN station is given in the legend as [highest point - lowest point].

(see Section 2.6 for a full list of symbols). Consistent with Granvik et al. (2012) and Kary and Dones (1996), to be considered TC the particle has to be within at least 3 Hill radii of the Earth and have a planetocentric Keplerian energy $E < 0$. Additionally, to be classified as a TCO, the particle must have orbited the Earth at least once. Unlike previous studies (Granvik et al., 2012; Fedorets et al., 2017; Clark et al., 2016), instead of determining TCO membership by measuring the change in ecliptic longitudinal angle in the synodic frame, the TCO membership was determined by measuring the proportion of an orbital period each particle was captured. This reduces some of the ambiguity between TCFs and TCOs as demonstrated by Urrutxua and Bombardelli (2017).

Orbital Integrator Simulations in this paper made use of the publicly available REBOUND code ¹. REBOUND’s 15th order IAS15 integrator was used for this study because of its resolution of close-encounters, its adaptive time-step, and the ability to incorporate non-gravitational forces along with other perturbations like the non-sphericity of the Earth (Rein and Liu, 2012; Rein and Spiegel, 2015). The IAS15 integrator is based on the RADAU-15 developed in Everhart (1985) used by Clark et al. (2016) to model a captured-object impact detected by the European Fireball Network. IAS15 improves upon the RADAU-15 by suppressing the systematic error generated by the algorithm to well-below machine precision, implementing an adaptive time step, and adding the ability to include non-conservative forces easily while ensuring that the round-off errors are symmetric and at machine-precision (Rein and Spiegel, 2015).

Atmosphere Model REBOUNDx’s ² publicly available additional forces were used as a way to add other forces to our model. We split up the regression model into two scripts: one that integrates back through the top of the atmosphere, and one that integrates back until the particles are out of the Earth-Moon system. The first integration code uses the whfast integrator provided by REBOUND

¹<http://github.com/hannorein/REBOUND>

²<https://github.com/dtamayo/REBOUNDx>

along with the NRLMSISE-00 model 2001 ³ to take into account atmospheric drag that took place before the meteoroid started to ablate significantly in the upper atmosphere (Rein and Spiegel, 2015). The model produces a multivariate normal distribution of 10,000 particles given by our triangulation of the event. The particles vary in shape factor from a sphere to a brick (1.21-1.55) and are either chondritic or metallic in density (3500 kg m^{-3} or 7500 kg m^{-3}) Gritsevich (2009); Consolmagno et al. (2008). These particles are then integrated backward in time until all the particles are above 200 km. At this point, the simulation is handed-off to the next integration script.

Integration Method The long term integration script takes the distribution of particles from the results of the atmosphere script and generates particles from this distribution to be integrated out of the Earth-Moon system. The Sun, Moon, and Jupiter are directly added to the simulation from the JPL Horizons solar system data ⁴ and ephemeris computation service. Only these bodies were added to reduce the computational load and because they are the primary gravitational perturbers. REBOUNDx was used to incorporate orbital variations due to the Earth’s oblateness, and J2 and J4 gravitational harmonic coefficients were applied to the particles. We additionally accounted for radiation pressure using the REBOUNDx module. The model automatically adjusts the time-steps based on the non-linearity at that point in time. The integration itself is also split up into thousands of sections in order to save the appropriate outputs at regular time intervals. At the end of each integration section, the algorithm checks and records the particle’s positions, orbital elements, and capture status, along with many other metrics.

In total, eight distinct orbit recursions were run. We varied the triangulation method, the meteoroid density, and the segment of the trajectory used to generate the orbits from the observations. In Table 3, we varied the density between ‘high’ and ‘low’, corresponding to metallic (7500 kg m^{-3}) and chondritic (3500 kg m^{-3}) densities respectively (Consolmagno et al., 2008). Half of the orbital integrations

³ported to python based off of Dominik Brodowski 20100516 version at <http://www.brodo.de/english/pub/nrlmsis/>

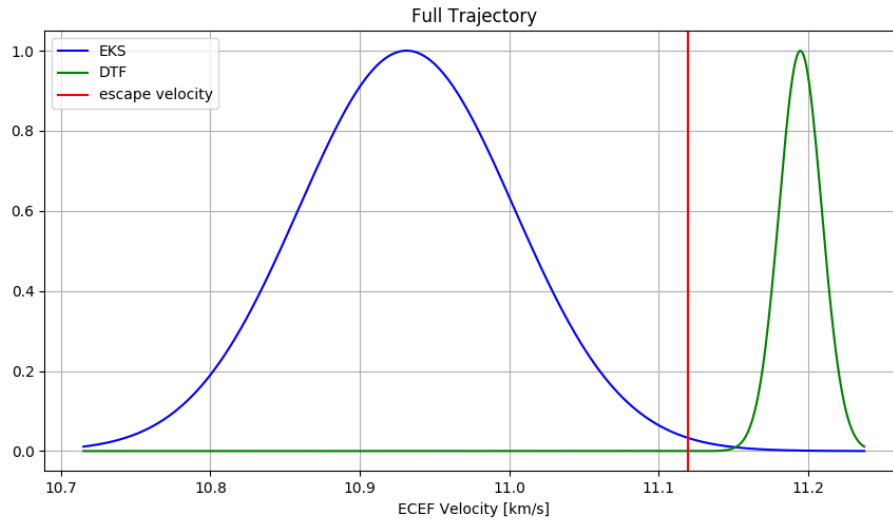
⁴<https://ssd.jpl.nasa.gov/>

were performed from triangulations using only the upper portion of the observed atmospheric trajectories. This ‘top of trajectory’ (denoted ‘tops’ in Table 3) is defined by all observations triangulated above 65 km altitude. This was done to reduce the dependency on the chosen triangulation model where high sample rates can observe variations due to additional physical effects occurring lower in the atmosphere (i.e., gravity, atmosphere). (Figure 2.3). If a similar event occurred where the sampling rate was lower, varying the triangulation method could lead to an erroneous analysis of the results as the models will likely converge on full trajectory solutions.

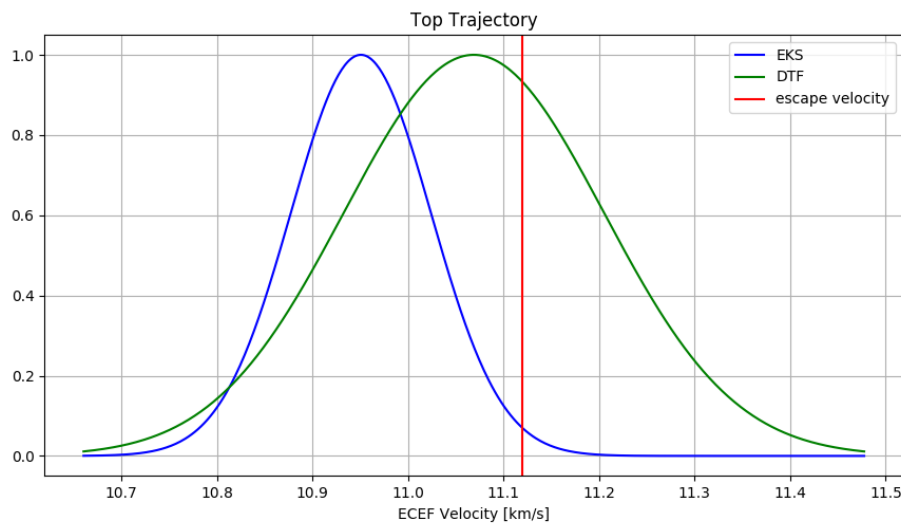
By reducing the amount of data, the uncertainties increase and the mean TCO probabilities converge. Therefore, any study that states that a TCO fireball was observed based on atmospheric observations by photographic networks should be accepted with a degree of skepticism. Events like these, that come from inherently chaotic dynamics, cannot have their orbital histories definitively known. Usually, the triangulation and velocity determination methods do not vary the results significantly. Although, event DN160822_03 is long-lasting, has a significantly large observational dataset (506 points, Table 2), and most importantly it is on the boundary of being geocentric and heliocentric. It is significantly more prone to model selection biases because slight variations in the starting conditions for this event drastically change the calculated orbital history. The particles were integrated back five years, enabling comparison with Clark et al. (2016).

2.4 Results and Discussion

Calculating Probabilities The capture probabilities listed in Table 3 were calculated in a very similar way to Clark et al. (2016). If a particle was deemed to be gravitationally captured while integrating backward, it was classified as a TCF until completing one orbit around the Earth and then it was reclassified as a TCO. The total number of TCs was determined by taking the sum of the TCO and TCF particles. If a particle appears to originate from the Earth (i.e., impacts the Earth in the backward integration), it would be removed from the TC, TCO, and TCF counts and classified as a ‘Sputnik’. Additionally, particles



(a) Full trajectory



(b) Top of trajectory

Figure 2.3: Comparison of the v_0 distribution generated by the EKS and the DTF methods using either (a) the full trajectory or (b) the top of the trajectory (observations >65 km altitude). Given the large amount of data collected for event DN160822_03, 506 data points, the v_0 is more dependent than usual on the choice of triangulation and velocity determination methods. When only the top of the observed atmospheric trajectory is used, the models' assumptions affect the results less and the v_0 distributions converge.

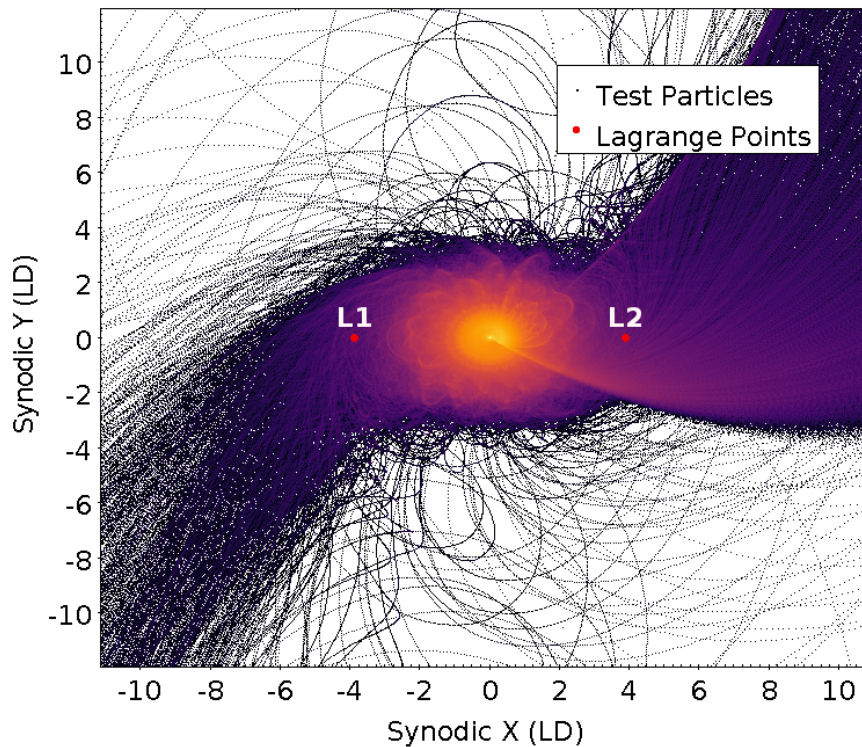


Figure 2.4: Particle orbits within the Sun-Earth-Particle synodic reference frame centered on the Earth's center of mass and co-rotating with the Earth so that the direction of the sun is always at $(-1\text{AU}, 0)$ in the x - y plane in this figure (not shown). The colors are indicative of the particles' spatial density, yellow being the most dense and black/purple being the least. The axes are in units of lunar distances (LD). There appears to be a clear preference of entry into the Earth-Moon system through either the L1 or L2 Lagrange points (represented by red points), as shown by the prevalence of trajectories in the directions of the co-linear Lagrange points.

that were captured but never escaped from the Earth-Moon system within the 5 year integration time were labeled as still captured (SC). If the particles were never captured by the Earth-Moon, then they were marked as unbound (UB). Furthermore, if the particles passed within 3 or 1 lunar Hill spheres of the Moon, they were recorded as 3H or 1H respectively.

Based on the pre-atmospheric orbit of event DN160822_03, the probability that the meteoroid originated from typical artificial satellite debris is unlikely. However, due to the lack of spectral data, the possibility of originating from some previous lunar or interplanetary mission can not be eliminated. Subsequently, we have assumed based on the orbital characteristics that the event has a sufficiently small likelihood of coming from an artificial source. Thus, when calculating the capture probabilities, the Sputniks were removed from consideration due to their unlikelihood, producing the following general equation:

$$Probability_{min} = \frac{Subset}{TotalParticles - Sputniks} \quad (2.1a)$$

$$Probability_{max} = \frac{Subset}{TotalParticles - Sputniks - SC} \quad (2.1b)$$

where the subsets are either SCs, TCs, TCOs, or TCFs. The SCs were considered invalid when calculating the TCF, TCO, and TC minimum percentages and included when calculating the maximum percentages. This is done because they could either eventually evolve into Sputniks or they could just have TCO dynamic lifetimes longer than the five year integration period. The 80,000 particles that describe this one event were integrated in groups of 1,000 for computational purposes, and the results of each run were very consistent with each other. The %SC was calculated using equation 2.1a.

Capture Probability Considering the large amount of data collected, the model choice affects the TC probability results more significantly when using the entire trajectory to determine v_0 . In order to reduce this dependency of the model choice, the integrations were also performed using just the top of the observed atmospheric trajectory (> 65 km altitude). This reduces the effect of the assump-

tions you make when choosing a model. Predictably, the two models' results tend to converge more when only the top is used (Fig. 2.3).

During the integrations using the top of the trajectory, the particles generated from the SLLS still are nearly all either gravitationally captured or seem to originate from the Earth. On the other hand, about 30-60% of the particles generated by the DTF method are TCs. The DTF produces non-conclusive probabilities for this event considering the v_0 distribution of the DTF is nearly centered (within 0.38σ) on the escape velocity for the Earth at the corresponding altitude (Fig. 2.3). In other words, the mean initial velocity (at the beginning of observations) predicted by the DTF method is very similar to the escape velocity. Therefore, the TCO probability for this event determined by the integrations initiated from DTF triangulation is predictably around 50%.

Given the results from the integrations (Table 3) using our most statistically robust triangulation method (SLLS with EKS), there is a >95% probability that the meteoroid observed was captured by the Earth-Moon system before atmospheric entry (i.e., only <5% chance it was heliocentric). Although, the pre-atmospheric path is impossible to exactly model due to the intrinsically chaotic nature of the system (as seen in Fig. 2.4), and small variations in how the initial state of the fireball is determined has the potential to affect the resulting capture probability seriously. Especially considering that event DN160822_03 probably had a close encounter with the Moon, producing chaotic scattering; the system is highly unpredictable.

Capture Mechanisms As exhibited in Table 3, the captured particles have a significantly higher amount of close encounters with the Moon compared to unbound particles. This implies that the Moon likely played a significant role in the meteoroid's eventual impact with the Earth. Considering nearly all of the particles generated from the SLLS/EKS are still captured at the end of the integration, this may imply that the meteoroid was an extremely long-lived TCO like those described in Granvik et al. (2012). Granvik et al. (2012) found that the longest-lived TCO particles in their simulations were those that had multiple close encounters with the Moon, which lowered the apogee of the orbit below 1 LD. As

seen in Fig. 2.6, the temporarily captured particles within our simulations for the most extended times do indeed have numerous close encounters with the Moon throughout the integration. The presence of the Moon more often contributes to the length of the capture rather than the actual capture itself.

In Fig. 2.5, the capture distribution is clearly multi-modal. Most of the TCs are captured through the first or second Lagrange points, with the remaining TCs captured through a close encounter with the Moon. The capture location probabilities for the L1, L2, and lunar captures are 23.8%, 67.1%, and 9.1% respectively. The specific Lagrange point capture locations depend on the Jacobi value for that given particle; in other words, the spread of Lagrange capture locations is due to the variations in the orbital energy of the particles. These capture mechanisms are easily seen in Fig. 2.5. The capture locations also do not significantly change when the triangulation method is changed, however the proportion of the captures at each location does because of differences in the v_0 estimate in each model.

Orbital Evolution As shown in Fig. 2.7, there appear to be some trends over time for the geocentric orbital elements of captured particles. In Fig. 2.7a, the captured particles that are integrated until they become heliocentric tend to approach higher semi-major axis and eccentricity values asymptotically. In Fig. 2.7b, TCs that are retrograde and do not have a low semi-major axis encounter the Moon more often, causing them to be less dynamically stable and have shorter capture durations. The longest-lived particles have an apogee value lower than 1 LD, thus reducing the number of close encounters with the Moon. This is consistent with the longest-lived TCOs in the simulations done by Granvik et al. (2012) in which particles with the longest dynamical lifetimes tended to have multiple close encounters with the Moon that resulted in an orbit completely interior to the lunar orbit. Within this study, as shown in Fig. 2.7, TCOs with low apogee values that had capture durations shorter than the integration period tended to evolve from highly eccentric retrograde orbits with larger semi-major axis values. This evolution from a retrograde, eccentric orbit to an orbit internal to the Moon was most likely due to a series of fortunate lunar close encounters like those described in Granvik et al. (2012).

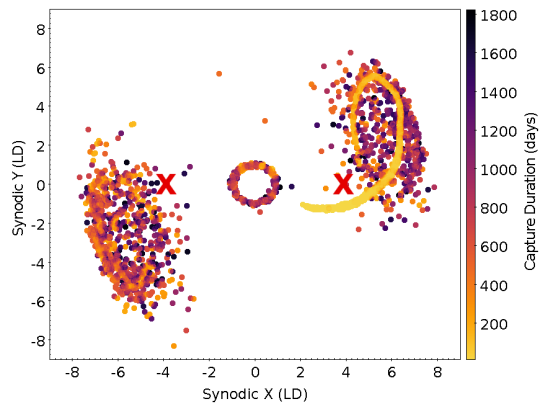
Triang. Method	Density	# Sputniks	%SC	% TCO	% TCF	% TC 3LH	% TC
SLLS full	low	9728	98.1	93.3 – 99.9	0.1 – 6.2	92.9	99.5 – 100.0
SLLS full	high	9711	96.4	97.0 – 99.9	0.1 – 2.9	96.6	100.0
SLLS tops	low	9060	95.3	88.5 – 99.5	0.4 – 8.5	87.8	97.0 – 99.9
SLLS tops	high	9173	95.5	90.6 – 99.6	0.3 – 6.8	90.0	97.4 – 99.9
DTF tops	low	2974	36.5	23.3 – 51.3	8.4 – 13.3	22.5	36.6 – 59.7
DTF tops	high	2879	35.6	22.7 – 50.2	8.5 – 13.2	21.9	35.9 – 58.7

Table 2.3: Summary of 5 year recursion results for event DN160822_03 in which over 16,000 valid particles were integrated, 10,000 for each run and 80,000 in total. TCs represent any captured particles, TCOs are captured and have orbited the Earth at least once, TCFs are captured and have not yet completed 1 orbit of the Earth, Sputniks are particles that originate from the Earth, SC represents particles that are still captured after 5 years, and TC 3LH is for TCs that go within 3 lunar Hill radii. The %TCO, %TCF, and %TC values are calculated after removing Sputniks. In all of the integrations initialized from the SLLS, the Sputniks account for > 90% of the particles. Due to the highly irregular orbit originating from the Earth, Sputnik particles are assumed to be invalid. There are no unbound particles that go within 3 lunar Hill radii recorded in the simulations, suggesting that the capture was facilitated by a close encounter with the Moon.

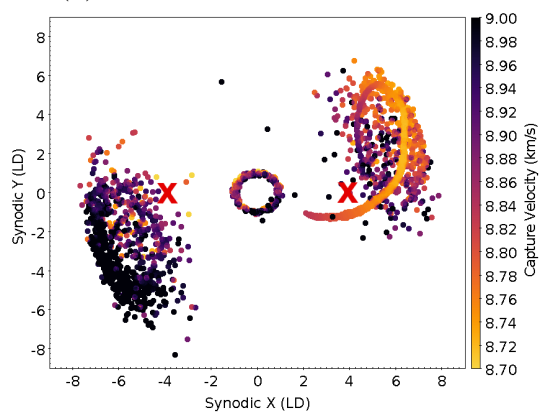
Pre-capture Orbit By studying the trajectories of the simulated particles before encountering the Earth-Moon system, we find the event DN160822_03 most likely to belong to the Apollo NEO group. Event DN160822_03 produced particles that were 88.4% Apollos, 6.2% Amors, 2.9% Atiras, and 2.5% Atens. Although, due to the chaotic nature of the event, the heliocentric orbit is impossible to determine accurately without more data, preferably pre-atmospheric observations (Murison, 1989; Astakhov et al., 2003).

Comparison to Models Finding this single TCO in the DFN dataset is consistent with the model of (Granvik et al., 2012; Fedorets et al., 2017), although not statistically robust as numbers are small. We found the most probable capture locations were concentrated at the Earth’s aphelion and perihelion, as described in both Granvik et al. (2012) and Fedorets et al. (2017). Although, as shown in Fig. 2.8, the particles captured in proximity to the L1 and L2 points clearly display an annual variation in the probable magnitude of the capture velocity. Also, unlike general models of the entire TCO population, particles were captured through close encounters with the Moon (Fig. 2.4a) and had only slightly lower capture durations compared to the Lagrange point captures.

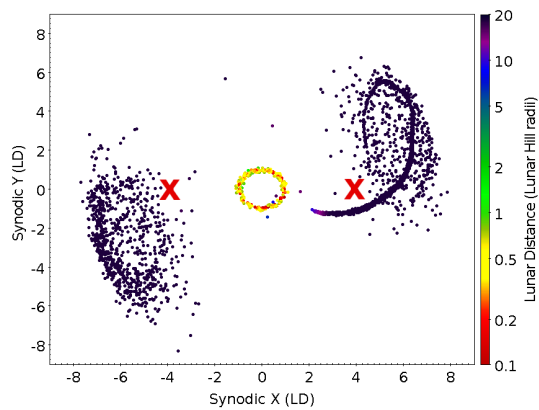
Moreover, these close lunar encounter captures varied according to the lunar month for this event. This is seen in Fig. 2.8a, where the yellow/red points representing captures close to the Moon seem to make vertical stripes every 28 days. This lunar cycle is also seen in Fig. 2.6, where the amount of lunar encounters seems to spike every month. Although, this cycle of close lunar encounters every lunar month is most likely specific to the geometry of this event. Due to the low geocentric inclination and very high geocentric eccentricity, the particles generated are consistently capable of making numerous close encounters with the Moon. The presence of a lunar influence was also identified by Clark et al. (2016), where the lunar encounters tended to occur directly before the impact with the Earth. Implying the Moon is highly influential on whether or not TCOs dynamically evolve into an Earth-impacting orbit.



(a) Variation in capture duration.



(b) Variation in capture velocity.



(c) Variation in lunar distance.

Figure 2.5: Gravitational capture locations in synodic reference frame with L1 and L2 points marked by red crosses. The Sun-Earth synodic frame is centered on the Earth's center of mass and co-rotates with the Earth so that the direction of the sun in this case is always at $(-1\text{AU}, 0)$ in the x-y plane. The figures above show 3 distinct capture regions: L1 capture, L2 capture and close lunar-encounter capture. The tail-like feature near the L2 point is caused by a large group of particles that were captured fairly quickly into the integration so they did not scatter as much.

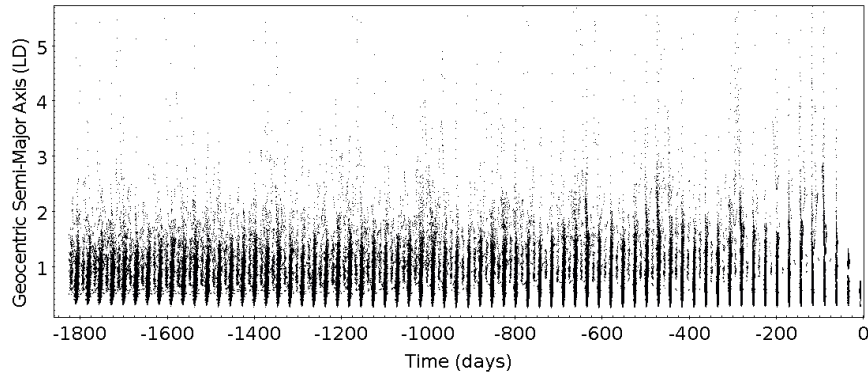
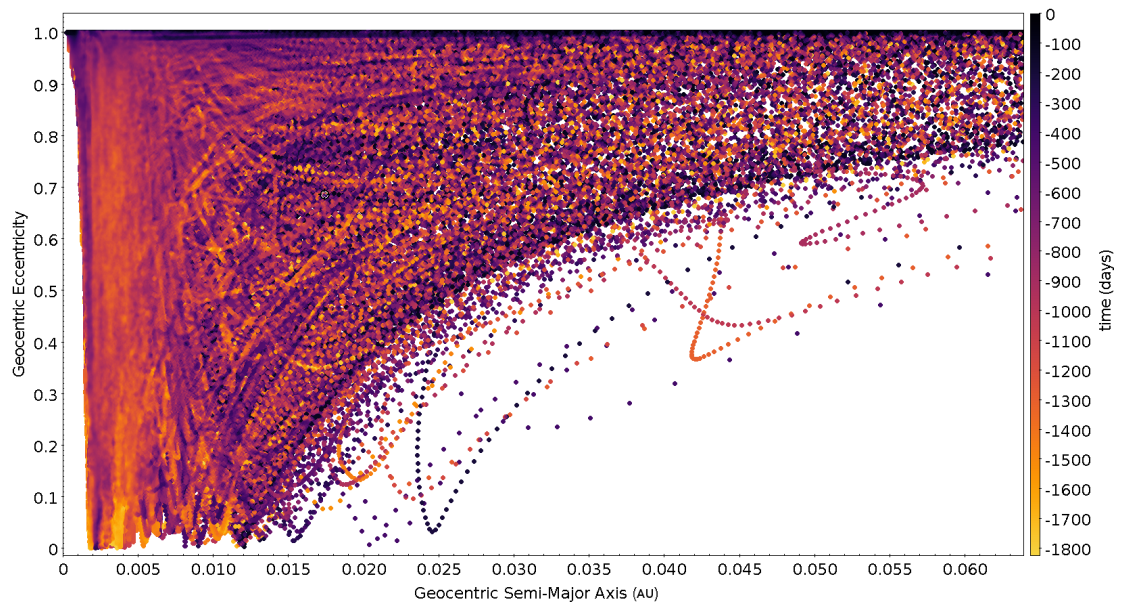
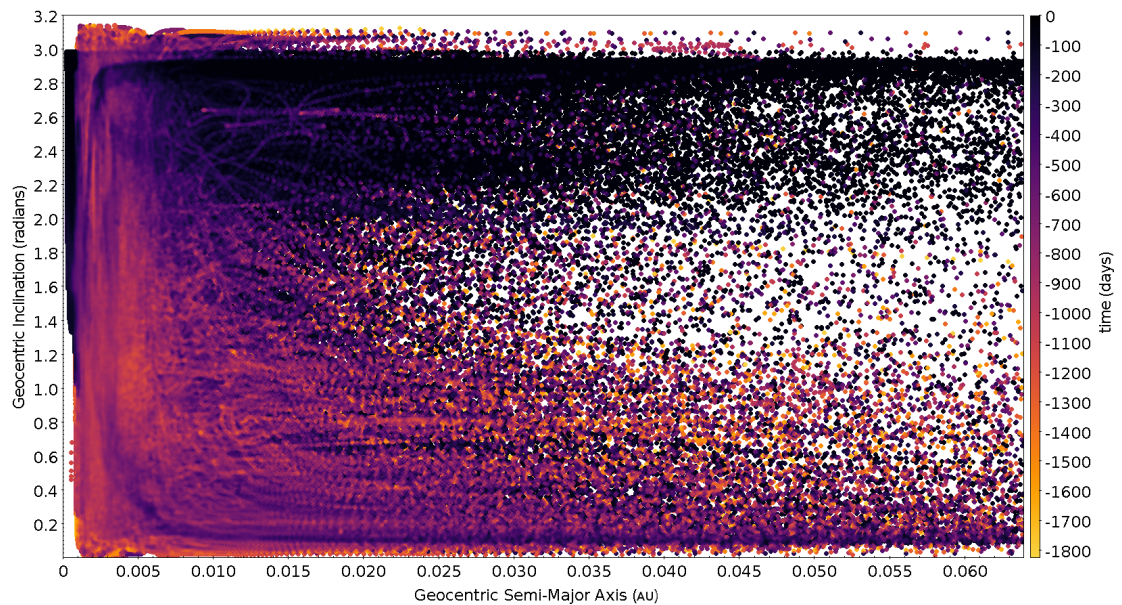


Figure 2.6: TCs that get within 3 Hill radii of the Moon (3H) produced by the SLLS and DTF. Each point represents one particle within 3H and the y-axis indicates the geocentric semi-major axis (LD) for that particle at that time. Most of the TCs in the simulations have close encounters with the Moon multiple times. The probability of an encounter increases once a month, due to the geometry of this specific event. This indicates that the Moon was likely critically important for the geocentric orbital evolution of the meteoroid and the impact of the meteoroid with the Earth.

Annual Variations There is a relatively large annual variation in the expected capture velocity and capture semi-major axis, varying over 300 ms^{-1} and 0.15 AU respectively for this particular event. This large annual variation in this event is due to the fact that the Earth does not have a perfectly circular orbit around the Sun. This eccentricity causes the L1 and L2 Lagrange points in the simplified circular restricted three-body problem to “wobble” in and out throughout the year by about 3.4%. As a result, the capture characteristics also “wobble” throughout the year. This implies that the source region for TCs also varies annually with Atiras and Atens more likely to be gravitationally captured during perihelion (January) and Amors and Apollos more likely to be gravitationally captured during aphelion (July) (Fig. 2.8d). Atira and Aten orbits are more likely to be gravitationally captured during perihelion because the L1 and L2 points are closer to the Earth and faster objects relative to the Earth are capable of being captured, i.e., objects with orbits interior to that of the Earth. Conversely, the Amor and Apollos are more likely during aphelion because they orbit relatively more slowly and have orbits more outward from the Earth. As shown in Fig. 2.8d, interestingly the faster and slower lunar captures consistently come from Apollo and Aten type orbits respectively. Additionally, this annual variation in probable capture



(a) Semi-major axis vs Eccentricity



(b) Semi-major axis vs Inclination

Figure 2.7: Geocentric semi-major axis vs eccentricity and inclination for the temporarily captured particles. The color bar is indicative of gravitational capture duration during the simulation. Yellow corresponding to a longer capture duration and black corresponding to a shorter capture duration. Particles that were captured the longest tended to have lower eccentricity, lower semi-major axis and lower inclinations. This is generally true because the particles that had more close encounters with the Moon tended to be less dynamically stable. Also, particles that were not able to transition from the initially highly eccentric detected orbit to lower eccentricities typically had lower capture durations.

velocity also implies that the capture mechanism by L1 and L2 varies annually, as in Fig. 2.8c. The most probable gravitational capture time for this event is either during aphelion or perihelion, consistent with Granvik et al. (2012) and Fedorets et al. (2017).

Comparison to Clark et al. (2016) In the study by Clark et al. (2016), they detected an 8.1-second fireball over the Czech portion of the European Fireball Network (EFN) with two high-resolution digital camera observatories. Given their observations, they determined that the detected event had a 92-98% chance of being captured by the Earth before impact detection. The DFN event described here was about 5.3 seconds in duration and was detected by six high-resolution digital camera stations in South Australia (Fig. 2.1). Despite a large amount of data collected of our event (6 cameras with > 500 data points), the results varied significantly between model choices. Previous studies have demonstrated the sensitivity initial orbits can have to the choice of initial velocity method (Vida et al., 2018). This is especially true for shallow events that penetrate deeper into the atmosphere where v_0 variations are more sensitive to model choice. The capture probabilities given for the EFN event are valid for the triangulation method that they used, but similar to our event, the use of a different triangulation method on their data may likewise find a reasonably high variation in the TC probability. Given that the event described in Clark et al. (2016) was longer and shallower than the one described here, the v_0 variation due to model choice may cause more discrepancy in their v_0 estimates if fitting to the entire trajectory. Despite this, the Clark et al. (2016) event has fewer observations, decreasing the sensitivity of model choice. This is because the v_0 distributions for multiple models have a higher chance of overlapping and possibly not causing as large of an issue with the discrepancy between models.

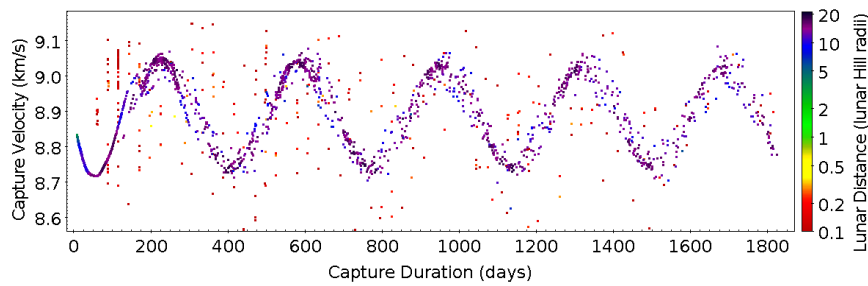
If an object likely has a geocentric orbit, we further need to prove it is of natural origin and not from a human-made object. The event observed by the EFN recorded spectral data of the fireball and was able to conclude the object was conclusively natural. The event described here, on the other hand, may still have originated from an artificial source; however, this is very improbable given the

pre-atmospheric orbit of the event.

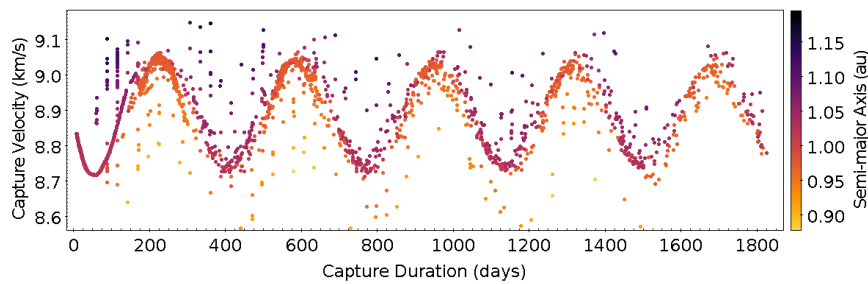
In the future, the best way to confirm TC impact events would be by collecting more data prior to atmospheric entry using telescopes; which may come to fruition with the beginning of observations in 2022 by the LSST (Ivezić et al., 2008; Fedorets et al., 2015). In addition, if TCs can be detected far enough in advance, future sample return missions could target these objects as the delta- V for the mission could be extremely low relative to other asteroid sample return missions.

2.5 Conclusions

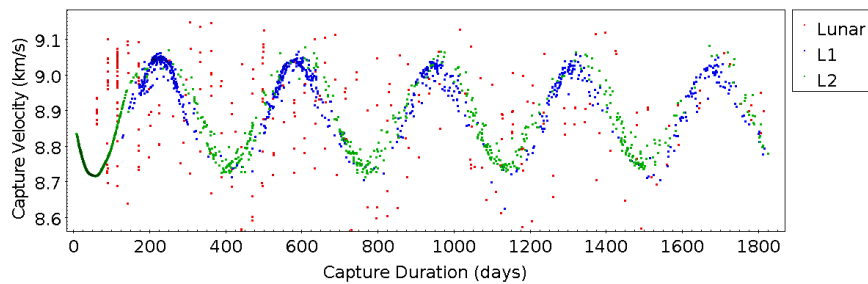
Based on our analysis, the event DN160822.03 detected by the Desert Fireball Network has a high pre-impact capture probability, as large as $> 95\%$ captured with our most statistically robust model. We find that the probable capture time, capture velocity, capture semi-major axis, capture NEO group, and capture mechanism all vary annually, with most captures occurring during Earth's aphelion or perihelion. This has been noted to some extent previously (Granvik et al., 2012; Fedorets et al., 2017), but most of the annual probability variations associated with the Earth's eccentricity found for this particular event have not been described before. We also discover that the probability of capture occurring as a result of a close lunar encounter varies according to the lunar month for this event. Although, this is probably due to the specific geometry of this event (i.e., low inclination, high eccentricity, geocentric apogee $\approx 1LD$). Despite the large amount of data collected by our six cameras of the event, we can not say for certain what the pre-atmospheric orbit was due to the highly unpredictable nature of the system, and the chaotic scattering that occurs with every close encounter with the Moon and the Earth. We caution future analysis of possible TCO events to explore the effects of small variations in the initial conditions and various triangulation methodologies. Despite these uncertainties and chaotic elements, we can determine the probable origins of this event statistically to be 88.4% Apollos, 6.2% Amors, 2.9% Atiras, and 2.5% Atens. In a couple of years, more fireball events like this may be able to confirmed by additional telescopic observations like those from the LSST.



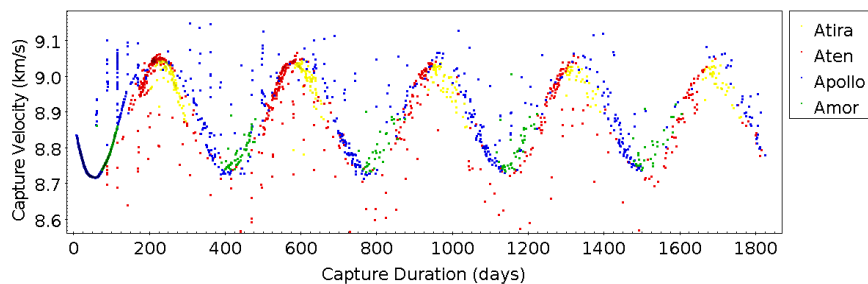
(a) Variation in lunar distance.



(b) Variation in heliocentric semi-major axis.



(c) Variation in capture mechanism.



(d) Variation in NEO type.

Figure 2.8: Total capture duration vs velocity during capture for TC particles. The relatively large annual variation in probable capture velocity results from the eccentricity of the Earth, as the Earth moves closer or further from the Sun during the year the capture velocity also varies. This annual variation in the probable capture velocity thus produces annual variations in the Lagrange point capture location and the source NEO group (Fig. b and Fig. c). Probably due to the geometry of the event (high eccentricity, low inclination, apogee $\approx 1LD$), there also exists vertical bands of close lunar-encounter captures that occur every lunar month (Fig. a)

2.6 Acknowledgements

This work was funded by the Australian Research Council as part of the Australian Discovery Project scheme.

This research made use of Astropy, a community-developed core Python package for Astronomy (Robitaille et al., 2013). Simulations in this paper made use of the REBOUND code which can be downloaded freely at <http://github.com/hannorein/REBOUND>.

2.7 Summary of Definitions and Abbreviations

Within this study we followed the notation of Granvik et al. (2012) and Fedorets et al. (2017) for consistency.

- SLLS - Straight Line Least Squares triangulation method with extended Kalman filter for velocity and error determination
- DTF - Dynamic Trajectory Fit triangulation and dynamic modelling method
- TC - Temporarily-Captured. The sum of the total TCOs and TCFs
- TCF - Temporarily-Captured Flyby. TC that has not orbited the Earth once
- TCO - Temporarily-Captured Orbiter. TC that has orbited the Earth at least once
- Sputnik - Particle in integration that originates from the Earth
- NES - Natural Earth Satellite
- NEO - Near Earth Object
- UB - Unbound (i.e., not gravitationally captured by the Earth)
- 1H - Came within 1 lunar Hill Spheres of the Moon
- 3H - Came within 3 lunar Hill Spheres of the Moon

- SC - Particles that are still captured by the end of the integration
- LD - Distance from Earth to the Moon

Bibliography

- S. A. Astakhov, A. D. Burbanks, S. Wiggins, and D. Farrelly. Chaos-assisted capture of irregular moons. *Nature*, 423:264–267, May 2003. doi: 10.1038/nature01622.
- J. M. Bailey. Studies on Planetary Sattelites. Satellite Capture in the Three-Body Elliptical Problem. *The Astronomical Journal*, 77:177, Mar. 1972. doi: 10.1086/111263.
- J. Baker, Robert M. L. Ephemeral Natural Satellites of the Earth. *Science*, 128: 1211–1213, Nov. 1958. doi: 10.1126/science.128.3333.1211.
- B. Bolin, R. Jedicke, M. Granvik, P. Brown, E. Howell, M. C. Nolan, P. Jenniskens, M. Chyba, G. Patterson, and R. Wainscoat. Detecting Earth’s temporarily-captured natural satellites-Minimoons. *Icarus*, 241:280–297, Oct. 2014. doi: 10.1016/j.icarus.2014.05.026.
- J. Borovicka. The comparison of two methods of determining meteor trajectories from photographs. *Bulletin of the Astronomical Institutes of Czechoslovakia*, 41:391–396, 1990.
- S. Brelsford, M. Chyba, T. Haberkorn, and G. Patterson. Rendezvous missions to temporarily captured near Earth asteroids. *Planetary and Space Science*, 123: 4–15, Apr. 2016. doi: 10.1016/j.pss.2015.12.013.
- A. Brunini. On the Satellite Capture Problem Capture and stability regions for planetary satellites. *Celestial Mechanics and Dynamical Astronomy*, 64:79–92, Mar. 1996. doi: 10.1007/BF00051607.

- C. A. Chant. An Extraordinary Meteoric Display. *Journal of the Royal Astronomical Society of Canada*, 7:145, June 1913.
- P. Chodas. Finding and characterizing candidate targets for the Asteroid Redirect Mission (ARM). In K. Muinonen, A. Penttilä, M. Granvik, A. Virkki, G. Fedorets, O. Wilkman, and T. Kohout, editors, *Asteroids, Comets, Meteors 2014*, page 94, July 2014.
- D. Clark, P. Spurný, P. Wiegert, P. G. Brown, J. Borovicka, E. Tagliaferri, and L. Shrubeny. Impact detections of temporarily captured natural satellites. In *AAS/Division for Planetary Sciences Meeting Abstracts #48*, AAS/Division for Planetary Sciences Meeting Abstracts, page 311.06, Oct. 2016.
- J. K. Cline. Satellite Aided Capture. *Celestial Mechanics*, 19:405–415, May 1979. doi: 10.1007/BF01231017.
- G. Consolmagno, D. Britt, and R. Macke. The significance of meteorite density and porosity. *Chemie der Erde-Geochemistry*, 68(1):1–29, 2008.
- W. F. Denning. Great Meteoric Stream of February 9th, 1913. *Journal of the Royal Astronomical Society of Canada*, 10:294, Aug. 1916.
- H. A. R. Devillepoix, E. K. Sansom, P. A. Bland, M. C. Towner, M. Cupák, R. M. Howie, T. Jansen-Sturgeon, M. A. Cox, B. A. D. Hartig, G. K. Benedix, and J. P. Paxman. The Dingle Dell meteorite: A Halloween treat from the Main Belt. *Meteoritics and Planetary Science*, 53:2212–2227, Oct. 2018. doi: 10.1111/maps.13142.
- E. Everhart. An efficient integrator that uses Gauss-Radau spacings. In A. Carusi and G. B. Valsecchi, editors, *IAU Colloq. 83: Dynamics of Comets: Their Origin and Evolution*, volume 115, page 185, Jan. 1985.
- G. Fedorets, M. Granvik, L. Jones, and R. Jedicke. Discovering asteroids temporarily captured by the Earth with LSST. In *IAU General Assembly*, volume 29, page 2257052, Aug. 2015.

- G. Fedorets, M. Granvik, and R. Jedicke. Orbit and size distributions for asteroids temporarily captured by the Earth-Moon system. *Icarus*, 285:83–94, Mar. 2017. doi: 10.1016/j.icarus.2016.12.022.
- S. Gong and J. Li. Planetary capture and escape in the planar four-body problem. *Astrophysics and Space Science*, 357:155, June 2015. doi: 10.1007/s10509-015-2376-6.
- M. Granvik, J. Vaubaillon, and R. Jedicke. The population of natural Earth satellites. *Icarus*, 218:262–277, Mar. 2012. doi: 10.1016/j.icarus.2011.12.003.
- M. Gritsevich. Determination of parameters of meteor bodies based on flight observational data. *Advances in Space Research*, 44(3):323–334, 2009.
- T. A. Heppenheimer and C. Porco. New Contributions to the Problem of Capture. *Icarus*, 30:385–401, Feb. 1977. doi: 10.1016/0019-1035(77)90173-7.
- R. M. Howie, J. Paxman, P. A. Bland, M. C. Towner, M. Cupak, E. K. Sansom, and H. A. Devillepoix. How to build a continental scale fireball camera network. *Experimental Astronomy*, 43(3):237–266, 2017a.
- R. M. Howie, J. Paxman, P. A. Bland, M. C. Towner, E. K. Sansom, and H. A. Devillepoix. Submillisecond fireball timing using de bruijn timecodes. *Meteoritics & Planetary Science*, 52(8):1669–1682, 2017b.
- Ž. Ivezić, S. M. Kahn, J. A. Tyson, B. Abel, E. Acosta, R. Allsman, D. Alonso, Y. AlSayyad, S. F. Anderson, J. Andrew, J. R. P. Angel, G. Z. Angeli, R. Ansari, P. Antilogus, C. Araujo, R. Armstrong, K. T. Arndt, P. Astier, É. Aubourg, N. Auza, T. S. Axelrod, D. J. Bard, J. D. Barr, A. Barrau, J. G. Bartlett, A. E. Bauer, B. J. Bauman, S. Baumont, A. C. Becker, J. Becla, C. Beldica, S. Bellavia, F. B. Bianco, R. Biswas, G. Blanc, J. Blazek, R. D. Blandford, J. S. Bloom, J. Bogart, T. W. Bond, A. W. Borgland, K. Borne, J. F. Bosch, D. Boutigny, C. A. Brackett, A. Bradshaw, W. Nielsen Brandt, M. E. Brown, J. S. Bullock, P. Burchat, D. L. Burke, G. Cagnoli, D. Calabrese, S. Callahan, A. L. Callen, S. Chandrasekharan, G. Charles-Emerson, S. Chesley, E. C.

Cheu, H.-F. Chiang, J. Chiang, C. Chirino, D. Chow, D. R. Ciardi, C. F. Claver, J. Cohen-Tanugi, J. J. Cockrum, R. Coles, A. J. Connolly, K. H. Cook, A. Cooray, K. R. Covey, C. Cribbs, W. Cui, R. Cutri, P. N. Daly, S. F. Daniel, F. Daruich, G. Daubard, G. Daues, W. Dawson, F. Delgado, A. Dellapenna, R. de Peyster, M. de Val-Borro, S. W. Digel, P. Doherty, R. Dubois, G. P. Dubois-Felsmann, J. Durech, F. Economou, M. Eracleous, H. Ferguson, E. Figueroa, M. Fisher-Levine, W. Focke, M. D. Foss, J. Frank, M. D. Freemon, E. Gangler, E. Gawiser, J. C. Geary, P. Gee, M. Geha, C. J. B. Gessner, R. R. Gibson, D. K. Gilmore, T. Glanzman, W. Glick, T. Goldina, D. A. Goldstein, I. Goodenow, M. L. Graham, W. J. Gressler, P. Gris, L. P. Guy, A. Guyonnet, G. Haller, R. Harris, P. A. Hascall, J. Haupt, F. Hernandez, S. Herrmann, E. Hileman, J. Hoblitt, J. A. Hodgson, C. Hogan, D. Huang, M. E. Huffer, P. Ingraham, W. R. Innes, S. H. Jacoby, B. Jain, F. Jammes, J. Jee, T. Jenness, G. Jernigan, D. Jevremović, K. Johns, A. S. Johnson, M. W. G. Johnson, R. L. Jones, C. Juramy-Gilles, M. Jurić, J. S. Kalirai, N. J. Kallivayalil, B. Kalmbach, J. P. Kantor, P. Karst, M. M. Kasliwal, H. Kelly, R. Kessler, V. Kinison, D. Kirkby, L. Knox, I. V. Kotov, V. L. Krabbendam, K. S. Krughoff, P. Kubánek, J. Kuczewski, S. Kulkarni, J. Ku, N. R. Kurita, C. S. Lage, R. Lambert, T. Lange, J. B. Langton, L. Le Guillou, D. Levine, M. Liang, K.-T. Lim, C. J. Lintott, K. E. Long, M. Lopez, P. J. Lotz, R. H. Lupton, N. B. Lust, L. A. MacArthur, A. Mahabal, R. Mandelbaum, D. S. Marsh, P. J. Marshall, S. Marshall, M. May, R. McKercher, M. McQueen, J. Meyers, M. Migliore, M. Miller, D. J. Mills, C. Miraval, J. Moeyens, D. G. Monet, M. Moniez, S. Monkewitz, C. Montgomery, F. Mueller, G. P. Muller, F. Muñoz Arancibia, D. R. Neill, S. P. Newbry, J.-Y. Nief, A. Nomerotski, M. Nordby, P. O'Connor, J. Oliver, S. S. Olivier, K. Olsen, W. O'Mullane, S. Ortiz, S. Osier, R. E. Owen, R. Pain, P. E. Palecek, J. K. Parejko, J. B. Parsons, N. M. Pease, J. M. Peterson, J. R. Peterson, D. L. Petravick, M. E. Libby Petrick, C. E. Petry, F. Pierfederici, S. Pietrowicz, R. Pike, P. A. Pinto, R. Plante, S. Plate, P. A. Price, M. Prouza, V. Radeka, J. Rajagopal, A. P. Rasmussen, N. Regnault, K. A. Reil, D. J. Reiss, M. A. Reuter, S. T. Ridgway, V. J. Riot, S. Ritz, S. Robinson, W. Roby,

- A. Roodman, W. Rosing, C. Roucelle, M. R. Rumore, S. Russo, A. Saha, B. Sas-solas, T. L. Schalk, P. Schellart, R. H. Schindler, S. Schmidt, D. P. Schneider, M. D. Schneider, W. Schoening, G. Schumacher, M. E. Schwamb, J. Sebag, B. Selvy, G. H. Sembroski, L. G. Seppala, A. Serio, E. Serrano, R. A. Shaw, I. Shipsey, J. Sick, N. Silvestri, C. T. Slater, J. A. Smith, R. C. Smith, S. Sobhani, C. Soldahl, L. Storrie-Lombardi, E. Stover, M. A. Strauss, R. A. Street, C. W. Stubbs, I. S. Sullivan, D. Sweeney, J. D. Swinbank, A. Szalay, P. Takacs, S. A. Tether, J. J. Thaler, J. G. Thayer, S. Thomas, V. Thukral, J. Tice, D. E. Trilling, M. Turri, R. Van Berg, D. Vanden Berk, K. Vetter, F. Virieux, T. Vucina, W. Wahl, L. Walkowicz, B. Walsh, C. W. Walter, D. L. Wang, S.-Y. Wang, M. Warner, O. Wiecha, B. Willman, S. E. Winters, D. Wittman, S. C. Wolff, W. M. Wood-Vasey, X. Wu, B. Xin, P. Yoachim, H. Zhan, and for the LSST Collaboration. LSST: from Science Drivers to Reference Design and Anticipated Data Products. *ArXiv e-prints*, art. arXiv:0805.2366, May 2008.
- D. M. Kary and L. Dones. Capture Statistics of Short-Period Comets: Implications for Comet D /Shoemaker-Levy 9. *Icarus*, 121:207–224, June 1996. doi: 10.1006/icar.1996.0082.
- T. Kwiatkowski, A. Kryszczyńska, M. Polińska, D. Buckley, D. O’Donoghue, P. Charles, L. Crause, S. Crawford, Y. Hashimoto, A. Kniazev, et al. Photometry of 2006 rh120: an asteroid temporary captured into a geocentric orbit. *Astronomy & Astrophysics*, 495(3):967–974, 2009.
- Z. F. Luo and F. Topputo. Capability of satellite-aided ballistic capture. *Communications in Nonlinear Science and Numerical Simulations*, 48:211–223, July 2017. doi: 10.1016/j.cnsns.2016.12.021.
- A. E. Lynam, K. W. Kloster, and J. M. Longuski. Multiple-satellite-aided capture trajectories at Jupiter using the Laplace resonance. *Celestial Mechanics and Dynamical Astronomy*, 109:59–84, Jan. 2011. doi: 10.1007/s10569-010-9307-1.
- M. A. Murison. The fractal dynamics of satellite capture in the circular restricted three-body problem. *The Astronomical Journal*, 98:2346–2359, Dec. 1989. doi: 10.1086/115303.

- D. Nesvorný, J. L. A. Alvarelos, L. Dones, and H. F. Levison. Orbital and Collisional Evolution of the Irregular Satellites. *The Astronomical Journal*, 126: 398–429, July 2003. doi: 10.1086/375461.
- D. Nesvorný, D. Vokrouhlický, and A. Morbidelli. Capture of Irregular Satellites during Planetary Encounters. *The Astronomical Journal*, 133:1962–1976, May 2007. doi: 10.1086/512850.
- J. B. Pollack, J. A. Burns, and M. E. Tauber. Gas drag in primordial circumplanetary envelopes: A mechanism for satellite capture. *Icarus*, 37:587–611, Mar. 1979. doi: 10.1016/0019-1035(79)90016-2.
- H. Rein and S. F. Liu. REBOUND: an open-source multi-purpose N-body code for collisional dynamics. *Astronomy and Astrophysics*, 537:A128, Jan. 2012. doi: 10.1051/0004-6361/201118085.
- H. Rein and D. S. Spiegel. IAS15: a fast, adaptive, high-order integrator for gravitational dynamics, accurate to machine precision over a billion orbits. *Monthly Notices of the Royal Astronomical Society*, 446(2):1424–1437, Jan. 2015. doi: 10.1093/mnras/stu2164.
- T. P. Robitaille, E. J. Tollerud, P. Greenfield, M. Droettboom, E. Bray, T. Aldcroft, M. Davis, A. Ginsburg, A. M. Price-Whelan, W. E. Kerzendorf, et al. Astropy: A community python package for astronomy. *Astronomy & Astrophysics*, 558:A33, 2013.
- E. K. Sansom, P. Bland, J. Paxman, and M. Towner. A novel approach to fireball modeling: The observable and the calculated. *Meteoritics & Planetary Science*, 50(8):1423–1435, 2015.
- K. H. Tsui. Asteroid-Planet-Sun Interaction in the Presence of a Planetary Satellite. *Icarus*, 148:139–146, Nov. 2000. doi: 10.1006/icar.2000.6475.
- K. H. Tsui. Satellite capture in a four-body system. *Planetary and Space Science*, 50:269–276, Mar. 2002. doi: 10.1016/S0032-0633(01)00131-3.

-
- H. Urrutxua and C. Bombardelli. A look at the capture mechanisms of the “temporarily captured asteroids” of the earth,”. In *26th International Symposium on Space Flight Dynamics, number ISSFD-2017*, volume 74, pages 1–7, 2017.
- D. Vida, P. G. Brown, and M. Campbell-Brown. Modelling the measurement accuracy of pre-atmosphere velocities of meteoroids. *Monthly Notices of the Royal Astronomical Society*, 479(4):4307–4319, 07 2018. ISSN 0035-8711. doi: 10.1093/mnras/sty1841. URL <https://doi.org/10.1093/mnras/sty1841>.
- V. A. Yegorov. The capture problem in the three-body restricted orbital problem. *Artificial Earth Satellites*, 3:17, Jan. 1959.

CHAPTER 3

Where Did They Come From, Where Did They Go: Grazing Fireballs

Patrick M. Shober^a, Trent Jansen-Sturgeon^a, Eleanor K. Sansom^a, Hadrien A.R. Devillepoix^a, Martin Cupák^a, Phil A. Bland^a, Martin C. Towner^a, Robert M. Howie^a, Benjamin A.D. Hartig^a

^aSpace Science and Technology Centre (SSTC), School of Earth and Planetary Sciences, Curtin University, GPO Box U1987, Perth, Western Australia 6845, Australia

This article is published in The Astronomical Journal, accepted 14 March 2020, published 7 April 2020

Abstract

For centuries extremely-long grazing fireball displays have fascinated observers and inspired people to ponder about their origins. The Desert Fireball Network (DFN) is the largest single fireball network in the world, covering about one third of Australian skies. This expansive size has enabled us to capture a majority of the atmospheric trajectory of a spectacular grazing event that lasted over 90 seconds, penetrated as deep as ~ 58.5 km, and traveled over 1,300 km through the atmosphere before exiting back into interplanetary space. Based on our triangulation and dynamic analyses of the event, we have estimated the initial mass to be at least 60 kg, which would correspond to a 30 cm object given a chondritic density (3500 kg m^{-3}). However, this initial mass estimate is likely a lower bound, considering the minimal deceleration observed in the luminous phase. The most intriguing quality of this close encounter is that the meteoroid originated from an Apollo-type orbit and was inserted into a Jupiter-family comet (JFC) orbit due to the net energy gained during the close encounter with the Earth. Based on numerical simulations, the meteoroid will likely spend ~ 200 kyrs on a JFC orbit and have numerous encounters with Jupiter, the first of which will occur in January-March 2025. Eventually the meteoroid will likely be ejected from the Solar System or be flung into a trans-Neptunian orbit.

3.1 Introduction

3.1.1 Reports of Grazing Fireballs

People have reported witnessing brilliantly long-lasting and bright meteor processions for at least hundreds of years. The 1783 ‘Great Meteor’ was estimated to have traveled > 1600 km through the atmosphere over western Europe (Cavallo, 1784). The ‘Great Comet of 1860’, which was most likely an Earth-grazing fireball over the eastern United States, was accounted for in a painting by American landscape artist Frederic Church entitled ‘The Meteor of 1860’ and by American poet Walt Whitman in his poem ‘Year of Meteors’ (Olson et al., 2010). Additionally,

the ‘1913 Great Meteor Procession’ reported sightings across Canada, the north-eastern United States, Bermuda, and many ships in the Atlantic as far south as Brazil. The event was initially hypothesized to have been formed by a natural Earth satellite that had a grazing encounter with the atmosphere (Chant, 1913; Denning, 1916).

A grazing event is considered to be when a meteoroid impacts the atmosphere at an extremely low-angle relative to the horizon, and there are generally three possible outcomes. It can either escape back to interplanetary space after passing through the atmosphere, fully ablate, or slow down enough to fall to the Earth. The first scientifically observed and triangulated grazing event was not until 1972 over Canada and the northwestern United States (Ceplecha, 1979, 1994). The 1972 fireball lasted ~ 100 sec, covering over 1500 km, and reached a minimum height of 58 km. Ceplecha (1979) estimated the mass to be between $10^5 - 10^6$ kg with the most likely diameter of about 5 m. The original analysis done by Rawcliffe et al. (1974) and Jacchia (1974) is known to contain mistakes, and the values given should not be relied upon (Ceplecha, 1979).

Since the 1972 fireball, there have been several atmospheric grazing events reported within scientific literature:

- In 1990, Borovicka and Ceplecha (1992) published analysis of the first Earth-grazing fireball observed by a photographic fireball network in which the meteoroid was estimated to be 44 kg with the closest approach of 98 km detected by two Czech stations of the European Fireball Network.
- In October of 1992, a bright fireball endured for over 700 km over the eastern United States before dropping a meteorite in Peekskill, New York (Brown et al., 1994; Beech et al., 1995; Ceplecka et al., 1996).
- In 1996 a fireball was observed to hit the western United States and only briefly escape for one orbit before allegedly impacting the Earth (Revelle et al., 1997).
- On March 29, 2006, a ~ 40 sec grazing fireball was observed over Japan (Abe et al., 2006). The meteoroid traveled over 700 km through the atmosphere

and reached a minimum height of 71.4 km. It appeared to come from a JFC-like orbit and the spectra collected was consistent with a chondritic composition.

- On August 7, 2007, a grazing fireball was observed by the European Fireball Network originating from a Aten-type orbit (Spurný et al., 2008).
- In June 2012, the first grazing meteoroid associated with a meteor shower in the scientific literature was recorded by 13 stations with a 98 km minimum altitude over Spain and Portugal and belonged to the daytime ζ -Perseid shower (Madiedo et al., 2016).
- In 2003, another grazing meteor, mass loss $\approx 5 \times 10^{-3}$ g, was detected over Ukraine before exiting back into interplanetary space (Kozak and Watanabe, 2017).
- In December 2014, a 1200 km long grazing event occurred over Algeria, Spain, and Portugal and lasted approximately 60 seconds, reaching a minimum height of 75 km (Moreno et al., 2016).
- On March 31, 2014, a ~ 34 sec fireball over Germany and Austria originating from an Apollo-type orbit was observed. The meteoroid was estimated to have an initial mass of about 200 kg, but no material is believed to have exited back into interplanetary space (Oberst et al., 2014). Many meteorites may have survived to the ground, however, the uncertainty on the fall ellipse is very large due to the extremely shallow entry angle.

For some of these grazing meteoroids mentioned above, the object was able to survive its passage through the atmosphere. The rock then re-entered interplanetary space on an altered orbit, sending material from one part of the inner Solar System to another. This could be significant since various parts of the inner Solar System are thought to be dynamically and physically distinct from one another.

3.1.2 Small Inner Solar System Bodies

The classical view of the Solar System says that the Sun formed with a debris disk around it that was originally compositionally heterogeneous within bands of constant radial distance from the Sun. The ‘snow line’ denoted the boundary between the planetesimals in which water ice and other volatiles would be retained and the bodies which were unable to hold ice, thus remaining dry. This classically separated the small bodies within the Solar System into two main groups: comets and asteroids respectively.

Although, we have seen that this classical ideology does not usually fit our observations of the small bodies within the Solar System. The Solar System is complicated and dynamic. In the last 4.5 billion years, small bodies have been jumbled around and altered. The layout and distribution of the Solar System is much more complicated than the idealized stratified one we tend to imagine.

Within the inner Solar System there are short-period comets, main-belt objects (MBOs), and near-Earth objects (NEOs). Traditionally, the MBOs were considered asteroidal and inner Solar System in origin, and NEOs primarily evolved from the MBO space after entering an orbital resonance (Bottke Jr et al., 2002; Granvik et al., 2018). However, with the identifications of Main-Belt Comets (MBCs) (Hsieh and Jewitt, 2006) and dry asteroidal material in the Kuiper Belt (Meech et al., 2016), we have realized that the material in the Solar System is more mixed than previously believed (Fernández and Sosa, 2015). Additionally, the starkly drawn lines between asteroidal and cometary material have since faded with the identification of active asteroids, extinct comets, and mixing between populations (Fernández et al., 2001, 2002, 2005; Kim et al., 2014; Jewitt, 2012). In reality, the physical properties of small bodies in the Solar System most likely exist in a spectrum from primitive volatile-rich (“comet-like”) to dry volatile-poor (“asteroid-like”). We are still trying to determine the most probable mechanism by which this mixing could have occurred, but several models such as the ‘Nice Model’ and the ‘Grand Tack’ have begun to elucidate some of these mysteries (Walsh et al., 2011; Tsiganis et al., 2005).

Jupiter family comets (JFCs) are a class of short-period comets, believed to have

evolved from scattered disk and Kuiper belt orbits (Fernández, 1980; Levison and Duncan, 1997; Duncan and Levison, 1997; Binzel et al., 2004). JFCs are primitive and contain a large amount of hydrated minerals and volatile ices (Kelley and Wooden, 2009; Jenniskens et al., 2012). They are also characterized by their orbits being strongly linked to the orbit of Jupiter, typically defined by their Tisserand’s parameter to be $2 < T_J < 3$ (Carusi and Valsecchi, 1987; Levison and Duncan, 1994). JFCs usually have multiple low-velocity encounters with the gas-giant over their lifetime (Levison and Duncan, 1997; Duncan and Levison, 1997; Duncan et al., 2004). These encounters with Jupiter make the orbits of JFCs more unpredictable compared to other small bodies, where the median dynamic lifetime of a JFC ~ 325 kyr (Duncan et al., 2004). However, as described by Fernández and Sosa (2015), JFCs that display cometary features frequently encounter Jupiter at distances of ≤ 0.1 AU making them highly unstable compared to a small subset of near-Earth “asteroidal” JFCs which typically exist on more stable orbits comparatively. A tiny fraction of JFCs are also thought to decouple from Jupiter and become Encke-like comets through either non-gravitational perturbations or close planetary encounters (Steel and Asher, 1996; Levison et al., 2006).

3.1.3 The Desert Fireball Network

Since 2003, the Desert Fireball Network (DFN) has been operating observatories across south-western Australia to capture images of fireball events (Bland, 2004). The network has since grown from 4 observatories by 2007 to over 50 observatories in Western Australia and South Australia by 2015 (Bland et al., 2012; Howie et al., 2017a). No other fireball camera network in the world is this expansive. Furthermore, we have expanded this effort worldwide with the start of Global Fireball Observatory (GFO) collaboration (Devillepoix et al., in prep.) with coverage area expected to increase to 2% of the Earth’s entire surface. This coverage area makes the GFO particularly well suited to characterize grazing meteoroids and other more rare fireball events (Shober et al., 2019).

Table 3.1: Observations and triangulated trajectory for event DN170707.01, recorded over Western Australia and South Australia on July 7th, 2017. Mass range determined by varying density between $2800 - 7300 \text{ kg m}^{-3}$ and includes formal uncertainties. Timing uncertainty is nominally $10^{-4} - 10^{-5}$ s, considerably less than other sources of uncertainty for the trajectory (Howie et al., 2017b).

	Entry Conditions	Exit Conditions
Time (UTC) after 2017-07-07	12:33:45.900	12:35:16.050
Height (km)	85.66 ± 0.03	86.04 ± 0.02
Mass range (depending on density; kg)	14-92	9-62
Latitude (deg)	-28.6933 ± 0.0003	-28.4144 ± 0.0002
Longitude (deg)	122.7161 ± 0.0010	136.3318 ± 0.0002
Velocity (km s^{-1})	15.71 ± 0.13	14.24 ± 0.10
Slope (deg)	4.6	7.8
Duration (sec)		90.15
Minimum Height (km)		58.5
Best Convergence Angle (deg)		45.9
Number of Observations (with timing)		13
Number of Observations (without timing)		7
Number of Datapoints		2541

3.2 DFN Observations

On July 7th, 2017, a 90 second extremely shallow fireball was observed to graze the atmosphere above Western Australia and South Australia, entering the atmosphere at a slope of $\sim 4.6^\circ$ (Fig. 3.1). Ten DFN observatories made observations of the fireball as it traveled over 1300 km through the atmosphere. The luminous phase started at about 85 km and penetrated as deep as 58 km before ceasing to be visibly ablating at 86 km. This event is only equaled by the ‘Great Daylight Fireball of 1972’, which reached a similar depth and lasted ~ 9 seconds longer than our witnessed event (Cepelcha, 1979). However, unlike the 1972 event, the DFN was able to photographically image a majority of the the atmospheric trajectory of the fireball (including the beginning and the end), with observations from many of our fireball observatories spread across Western Australia and South Australia. Thus, providing us with a substantial amount of data to accurately fit a trajectory to our observations (2541 astrometric datapoints). A summary of the observations made of event DN170707.01 and the fitted trajectory are provided in Table 3.1. The number of observations refers to the number of 30-second expo-

tures. Whereas, ‘without timing’ denotes when observations of the fireball were collected, however, either the angular velocity of the meteoroid was too slow or the fireball was too bright to distinguish the encoded de Bruijn sequence (Howie et al., 2017b). Unfortunately, due to the DFN’s viewing geometry at the beginning of the observed luminous trajectory, the initial observation convergence angle is only a few degrees. Therefore, the uncertainty associated with the initial velocity is higher than usual, however, still sufficient to determine what part of the Solar System the meteoroid originated.

At the meteoroid’s closest approach, a fragmentation event occurred in which a smaller piece of the primary object broke off (Fig. 3.2). DFN observatories captured the fragmentation event on video, and an uncalibrated light curve was able to be extracted (Fig. 3.3). There are no other instances of fragmentation observed during the trajectory. This fragmentation event was taken into account when triangulating the path of the primary and determining the mass of the meteoroid.

3.3 Methods

3.3.1 Triangulation

In the past, fireball and meteor observation networks estimated the trajectories they witnessed using a simplified straight-line-fit approach (Cep-lecha, 1987; Borovicka, 1990). These simplified straight-line fit techniques are sufficient enough to obtain meaningful results when the trajectory is shorter than 100 km. However, recent studies have shown that more satisfactory results can be obtained with the use of more rigorous methodologies (Sansom et al., 2015, 2019; Jansen-Sturgeon et al., 2019a). This is particularly true for a grazing fireball where the meteoroid is traveling hundreds to thousands of kilometers through the atmosphere. In previous grazing fireball studies, this non-linearity was accounted for in several different ways. Cep-lecha (1979) was the first to recognize that a grazing trajectory should fit a hyperbola when neglecting the atmosphere, but is otherwise slightly more curved due to the atmospheric drag experienced. Thus, Cep-lecha (1979)

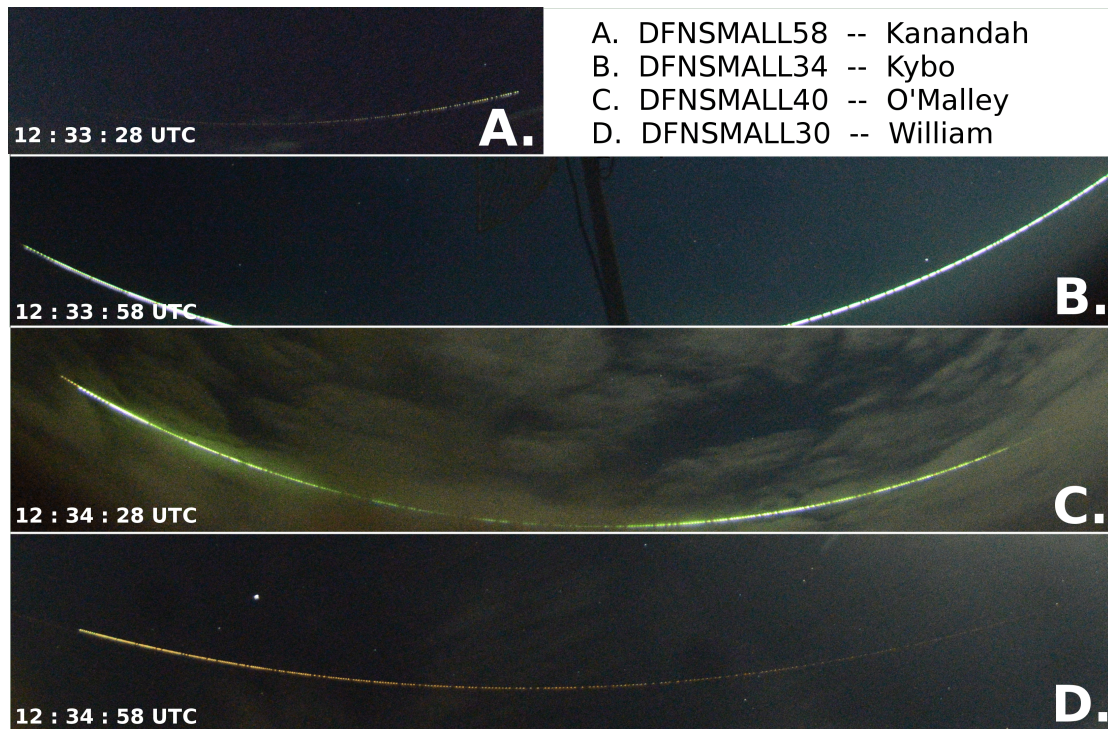


Figure 3.1: Long exposure images of event DN170707_01. The event lasted over 90 seconds and spanned four 30 second exposures (A, B, C, D). The fireball was first observed at 85 km altitude, reached as low as 58 km, and then was visible until 86 km before escaping the Earth's atmosphere. The initial velocity was 16.1 km s^{-1} , and the exit velocity after passing through the atmosphere was about 14.6 km s^{-1} . The images are all oriented so that the fireball travels from left to right (west to east).

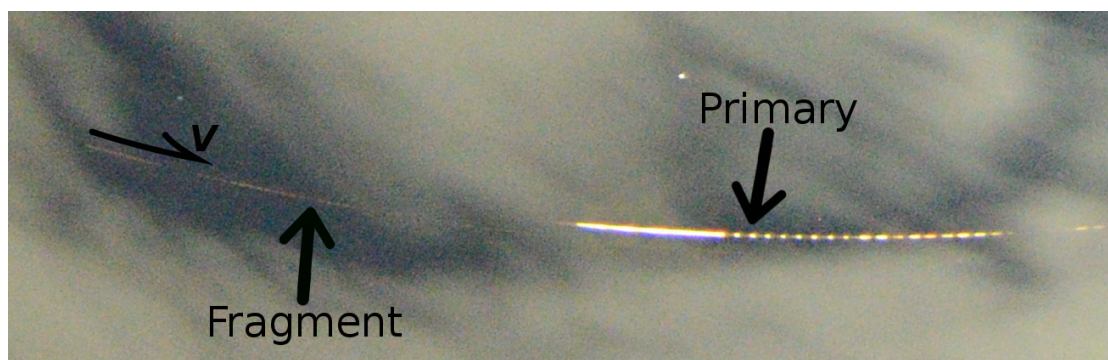


Figure 3.2: Fragmentation event captured for event DN170707_01 near the closest approach of its trajectory. The image shows two distinct paths offset from each other. The brighter path on the right side of the image belonging to the primary piece, whereas on the left the trail of a smaller fainter fragment can be seen. The decrease in velocity due to the observed fragmentation was not significant relative to the velocity scatter, and thus was not included during the trajectory fit. Additionally, only one camera observed the fragment due to cloud coverage and geometry, and therefore a trajectory for the fragment was unable to be determined. No other fragmentation events were detected along the path.

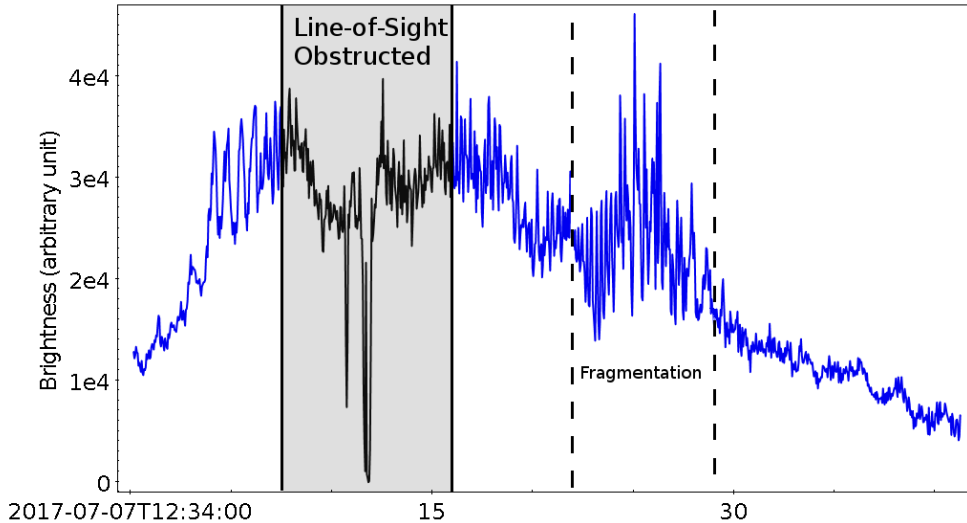


Figure 3.3: Light curve based on video from observatory DFNSMALL34-Kybo in the Nullarbor Plain in Western Australia during the fragmentation of event DN170707_01. The fragmentation occurs about 25 sec into this exposure (enclosed by dashed vertical lines), forming one detectable fragment. The y-axis is brightness in arbitrary units due to the photometry data lacking calibration. The ram pressure on the meteoroid just prior to the fragmentation was ~ 0.08 MPa. The line-of-sight was briefly obstructed by a telephone pole, reducing the brightness.

fit osculating circles to the trajectory of the 1972 grazing daylight fireball to account for this added curvature with reasonable accuracy. Borovicka and Ceplecha (1992) utilized the fact that one of the observation stations was nearly directly below the fireball (passed nearly through zenith) and saw the entire trajectory. They took their observations and performed a least-squares fit to an osculating circle at the point of pericenter, neglecting drag in this case based on fireball type. Similar methodologies using osculating circular trajectory fits have been utilized by other studies as well (Abe et al., 2006). Kozak and Watanabe (2017) triangulated a small, fast grazing, high-altitude meteor detected by video observatories in Ukraine by assuming minimal drag and fitting the observations to a hyperbolic orbit in the geocentric frame. Meanwhile, Madiedo et al. (2016) determined the atmospheric trajectory of a meteor belonging to the Daytime ζ -Perseid shower by using a segmented method-of-planes approach adapted from Ceplecha (1987).

For standard DFN events, we implement a modified straight-line least-squares (SLLS) method with an Extended Kalman Smoother (EKS) for velocity determination (Sansom et al., 2015). We then numerically determine the meteoroid's orbit

by including all relevant perturbations. Numerical methods are a slightly more accurate way to handle the orbit determination, especially for meteoroids that were slow or closely approached the Moon (Clark and Wiegert, 2011; Dmitriev et al., 2015; Jansen-Sturgeon et al., 2019a). For longer and/or shallower fireball events, where the meteoroid trajectory can have noticeable curvature, the SLLS method cannot account for the non-linear motion. Within this study, we implemented a Dynamic Trajectory Fit (DTF) triangulation method that fits the observation rays directly to the equations of motion for fireballs (Jansen-Sturgeon et al., 2019b). This non-straight-line approach to the event triangulation represents the physical system more veraciously. Consequently, the DTF method produces a much better fit to the observations compared to the SLLS for both positions and velocities (Fig. 3.4 & Fig. 3.5). We then use this trajectory (Fig. 3.6), to numerically estimate the pre- and post-grazing orbits. Although, currently the DTF method does not provide adequate formal velocity errors, thus a EKS was utilized to determine the velocity uncertainties for this study.

3.3.2 Mass Determination

During the DTF procedure, the meteoroid’s ballistic parameter and ablation coefficient are determined alongside its dynamic parameters, based directly on the line-of-sight observations. By assuming the meteoroid’s shape and density, a mass estimation can be deduced from the meteoroid’s fitted ballistic parameter.

3.3.3 Orbital Integration

After triangulating the grazing event, we initialized several orbital integrations using the publicly available REBOUND code¹ (Rein and Liu, 2012). We utilized the 15th order non-symplectic IAS15 integrator for our simulations of the event (Rein and Spiegel, 2015). This integrator is based upon the RADAU-15 integrator developed by Everhart (1985). It improves upon its predecessor by minimizing the systematic error generated by the algorithm to well-below machine precision, implementing an adaptive time-step, and adding the ability to include in non-

¹<http://github.com/hannorein/REBOUND>

conservative forces easily while ensuring that the round-off errors are symmetric and at machine-precision.

Initialization From the trajectory determined by the DTF method, the pre- and post-atmospheric state vectors for the meteoroid can be used to initialize orbital simulations. These simulations contain N number of particles within the meteoroid state's uncertainties produced by the triangulation. Currently, the DTF methodology does not provide formal uncertainties as model errors are not accounted for (Jansen-Sturgeon et al., 2019b). Subsequently, for this event, we determined the velocity uncertainties using the EKS method in conjunction with the DTF trajectory fit. Additionally, we assume a Gaussian distribution for the errors, although this may not be strictly true. However, the results from the integration should not deviate significantly due to this assumption. The particles' positions are generated from the initial and final latitude, longitude, and height determined from the DTF triangulation. The speed of the particles and their right ascension and declination are given in the Earth-centered Earth-fixed (ECEF) frame and then converted to the Earth-centered inertial (ECI) frame in order to generate the particles in the simulations.

Integration Initial simulations were run within ± 100 years of the grazing event in order to accurately characterize the short-term evolution of the meteoroid. The number of outputs recorded was increased so that any close encounters with Jupiter or the Earth would be well resolved. Afterward, a series of long-term integrations were done in a similar manner. The primary goal of these more extended integrations was to determine what were the lasting effects of the meteoroid's grazing encounter with the Earth. Does it stay on a JFC orbit as long as any typical JFC, and where does it evolve to after? Each integration recorded the positions, velocities, and osculating orbital elements for the meteoroid particles for a total period of 500,000 years forward relative to the event epoch. Close encounters with other planets were also considered and inspected, particularly with Jupiter.

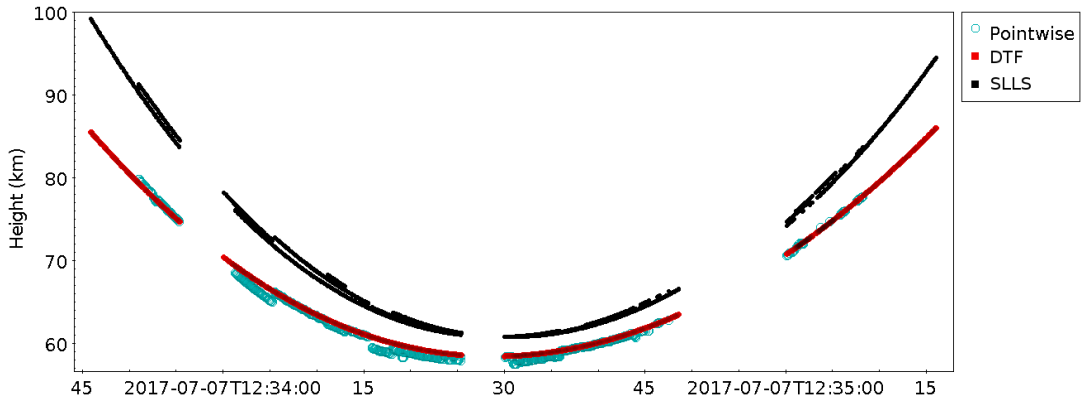


Figure 3.4: Height variation as a function of time determined by the straight-line least-squares (SLLS) and the Dynamic Trajectory Fit (DTF) methods. The pointwise heights represent the points that minimizing all the angular distances between the simultaneous lines-of-sight (given > 2), the respective observatory, and the point itself. The DTF fits much better to the pointwise than the SLLS due to its incorporation of gravity, drag, and ablation. This non-straight line fit produces a much more useful model to understand these grazing fireball events. The shape of the trajectory is somewhat misleading, as the trajectory would be concave with respect to a global, inertial reference frame instead of convex, as shown here. The three distinct gaps in the trajectory are due to latency between observation periods (Howie et al., 2017a). This lapse in observations occurs once every thirty seconds and is only typically noticeable for the longest fireball trajectories observed by the DFN. Towards the end of the trajectory, the largest lapse in observations was also due to the cloud coverage at the time

3.4 Results and Discussion

3.4.1 Atmospheric Trajectory

As seen in Fig. 3.4, the DTF methods fit the pointwise observations much better than the SLLS method for an event that is thousands of kilometers in length. The pointwise heights are given by minimizing the angular distance between the lines-of-sight when at least two observations are made. If a center-difference is taken between all these points, a velocity scatter can be generated (Fig. 3.5). The velocity scatter for event DN170707_01 is very large in some circumstances considering the low convergence angles especially for the beginning of the trajectory. A majority of the fireball's trajectory was north of the DFN observatories (Fig. 3.6). Thus reducing the accuracy of each measurement. However, since we gathered over 2500 datapoints from ten DFN observatories, a reasonably good trajectory

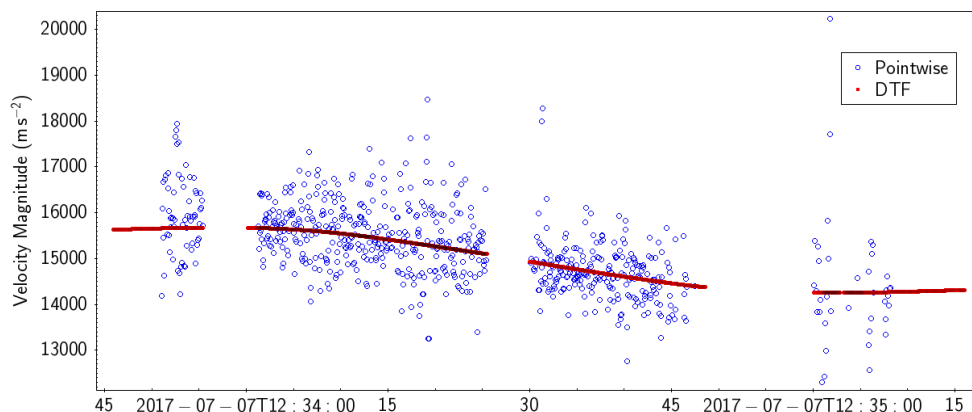


Figure 3.5: The velocity of the DN170707_01 meteoroid event as determined using both the Dynamic Trajectory Fit model (red) and a pointwise triangulation fit (blue). The DTF method fits the line-of-sight observations directly to the dynamic equations of motion that describe the motion of fireballs. Pointwise scattered instantaneous speeds correspond to the center-difference between adjacent data points seen by > 2 observatories. These points in 3D space are calculated by minimizing all the angular distances between the simultaneous lines-of-sight, the respective observatory, and the point itself.

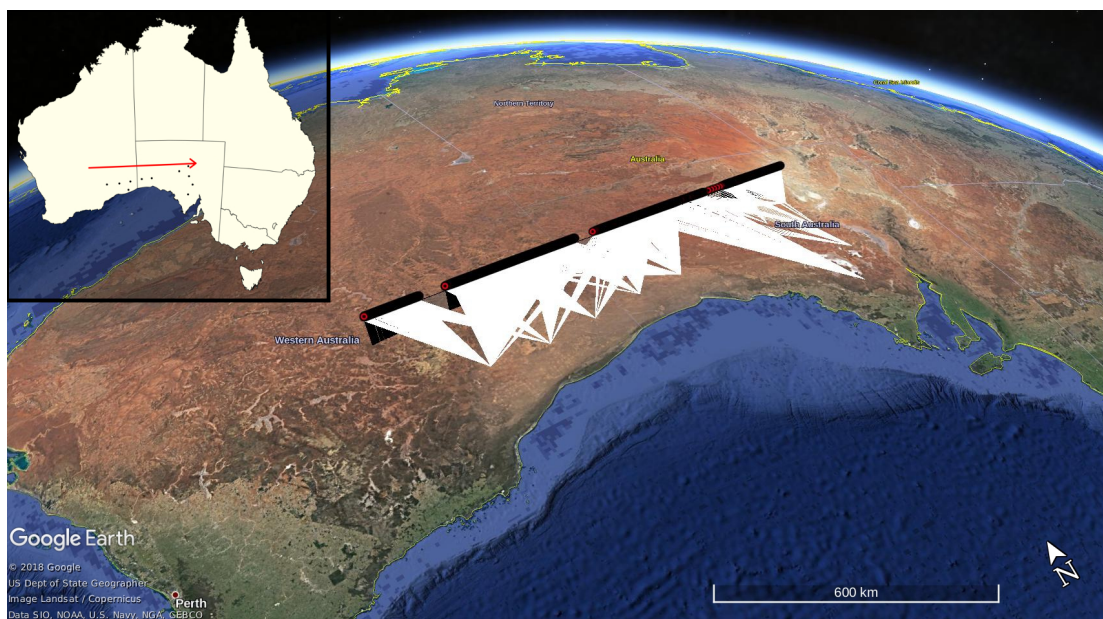


Figure 3.6: Triangulated luminous atmospheric trajectory for event DN170707_01, as seen over Western Australia and South Australia. The triangulation method used involves fitting the line-of-sight observations directly to the meteoroid's dynamic equations of motion, thereby dropping any straight-line assumptions (Jansen-Sturgeon et al., 2019b). The event lasted 90 seconds, initially hitting the atmosphere at 4.6° and covering over 1300 km through the atmosphere. The white rays indicate the line-of-sight measurements from each DFN observatory, whereas the black path marks the triangulated trajectory based on the observations of the fireball.

was able to be extracted. There are also three distinct gaps in the observations of event DN170707_01 primarily due to the latency between the 30-sec observation periods. These lapses in observations are typically only noticeable for the longest enduring fireballs observed by the DFN. The longest gap, towards the end of the trajectory, is compounded by the poor visibility for the DFN observatories in that area of the network due to the cloud coverage at the time.

During the DTF procedure, the ballistic parameter was determined throughout the trajectory based directly on the line-of-sight measurements, and hinges on the deceleration profile of the observed meteoroid. The meteoroid's mass was estimated by assuming its shape and density, as seen in Fig. 3.7. For instance, assuming a spheroid of chondritic density (3500 kg m^{-3}), the DN170707_01 meteoroid was estimated to have a 60 kg initial mass and a 40 kg outbound mass. A majority of the mass loss is predicted to have occurred during the fragmentation observed near the closest approach of the object. However, as minimal deceleration was observed during the luminous atmospheric encounter (Fig. 3.5), this mass estimate would be more accurately viewed as a lower bound.

The loading ram pressure for the meteoroid at the time of fragmentation was also calculated using the following equation:

$$p = \rho_h v_h^2 \quad (3.1)$$

where ρ_h is the atmospheric density at the height h of the fragmentation and v_h is the speed of the meteoroid at that instant. For event DN170707_01, we determined the fragmentation height based on the time of fragmentation observed in the light-curve from video observations. We estimated the meteoroid to have fragmented at $58.49 \pm 0.01 \text{ km}$, just before the minimum height reached, with a velocity of $15.5 \pm 0.1 \text{ km s}^{-1}$. We then used the NRLMSISE-00 global atmospheric model to determine the density of the atmosphere at the fragmentation height (Picone et al., 2002). The ram pressure experienced by the meteoroid just before fragmentation was calculated to be $0.084 \pm 0.01 \text{ MPa}$. This very low-value is consistent with the results of Popova et al. (2011), in which it was found that bulk strengths determined by initial fragmentation are consistently much lower

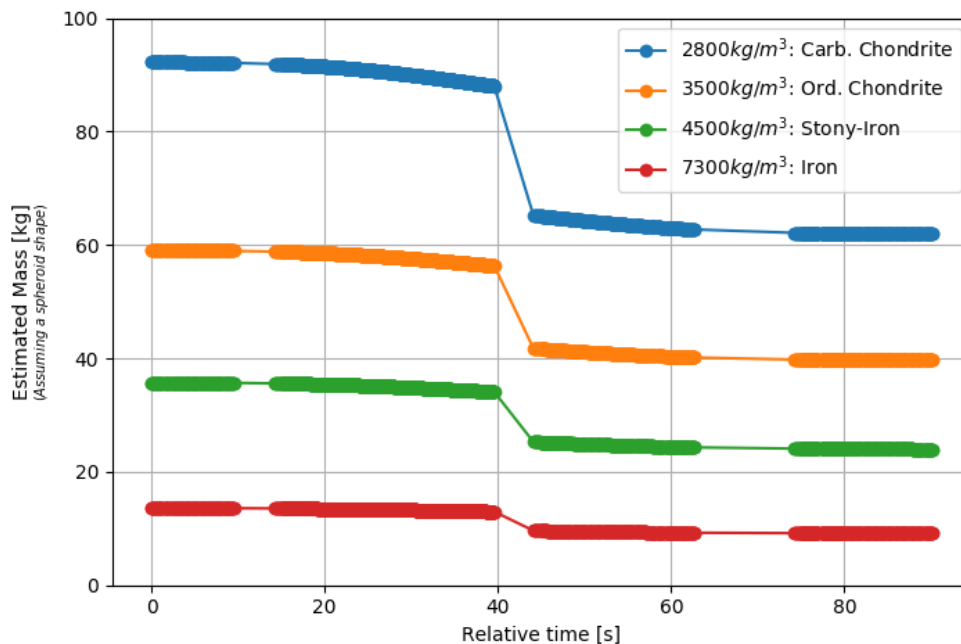


Figure 3.7: Mass estimation based on DTF triangulation fit to the DFN’s observations. The fragmentation event was taken into account, as seen by the sudden mass loss experienced at ~ 40 sec into the luminous phase. Each line represents a different density estimate for the object, given the DTF ballistic parameter.

than the strengths of recovered meteorites. Thus, this value likely reflects macro-scale fractures in the object and not the intrinsic material strength. For example, the Dingle Dell ordinary chondrite meteorite recovered by the DFN in 2016 also experienced similar low-pressure fragmentations (0.03 – 0.11 MPa) early in its brightflight, despite having a recovered bulk density of 3450 kg m^{-3} (Devillepoix et al., 2018).

3.4.2 Short-term Simulations

As shown in Table 3.2, the meteoroid that skipped off the atmosphere over Western Australia and South Australia in July 2017 originally came from an orbit in the inner main-belt, between the 4:1 and the 3:1 mean-motion resonances with Jupiter (Fig. 3.9). It most likely evolved into an Earth-crossing orbit after passing through either the 3:1 or the ν_6 complex, which are the two most significant entry routes into the NEO region (Bottke Jr et al., 2002; Granvik et al., 2018). As a result of

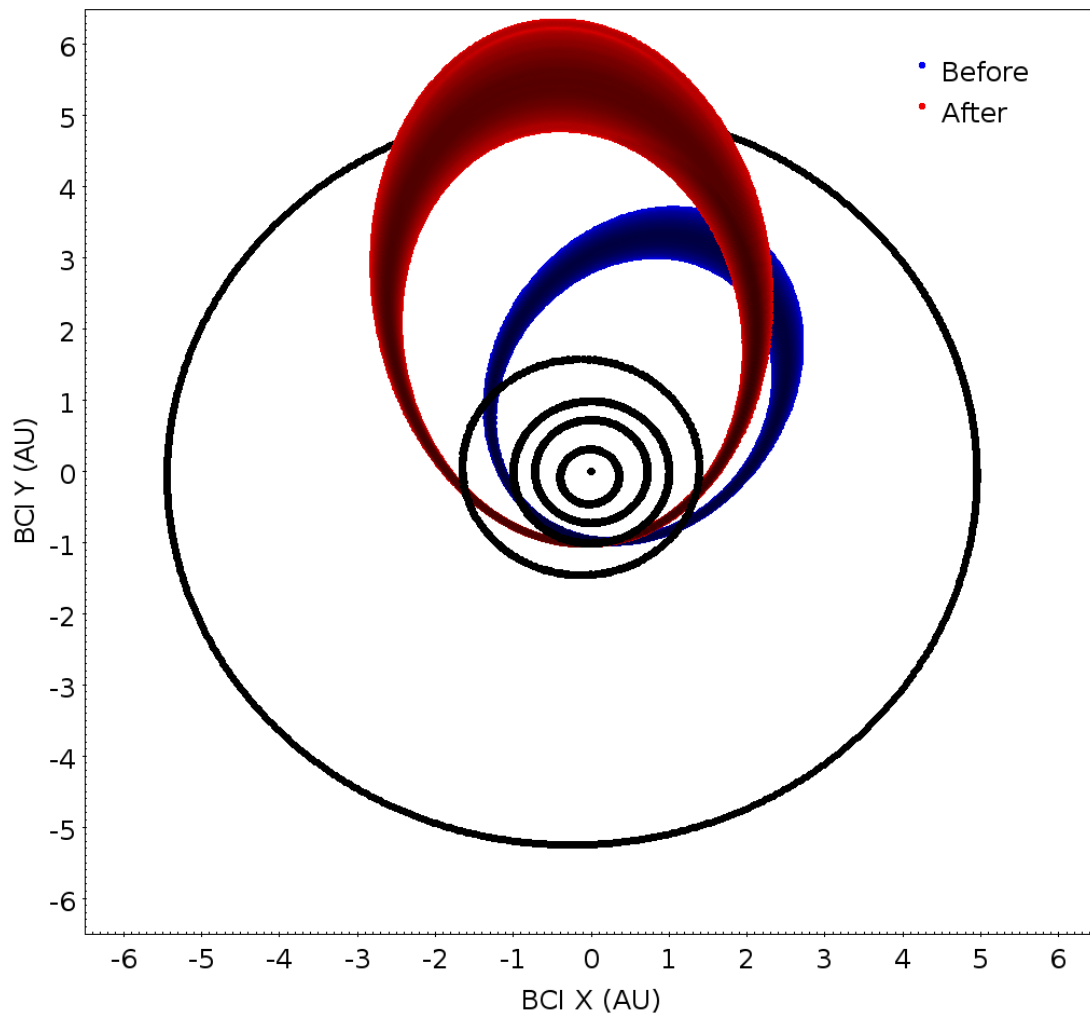


Figure 3.8: The meteoroid's orbit before and after the grazing encounter with the Earth. The meteoroid originated from an Apollo-type asteroidal orbit and was inserted into a JFC orbit. Once in this JFC orbit, the object's path rapidly becomes less certain due to multiple close-encounters with Jupiter.

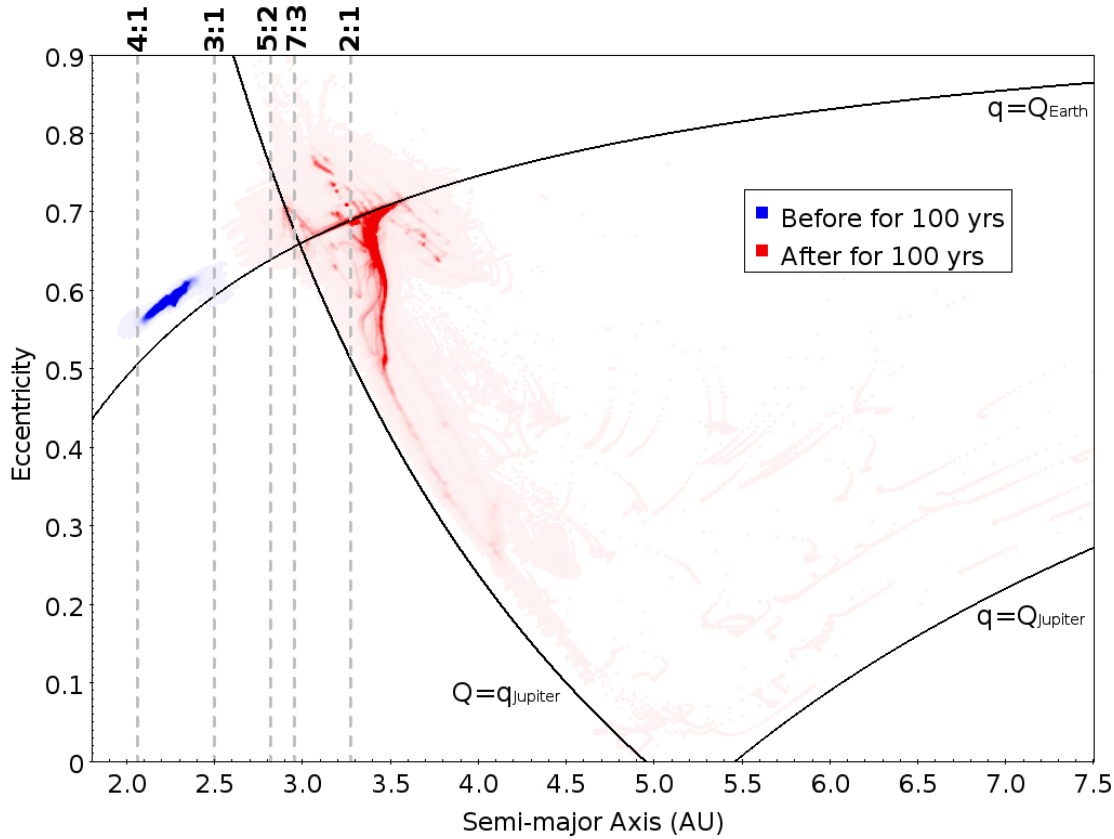


Figure 3.9: Semi-major axis vs. eccentricity during ± 100 years of integrations involving 10,000 test particles. Particle density over time is indicated by opacity. A majority of the particles remain close together after the grazing encounter, with a small number of particles being scattered by Jupiter very quickly. The significant mean-motion resonances are also plotted as vertical dotted lines. The object came from an eccentric orbit between the 4:1 and 3:1 mean motion resonances. After the grazing encounter with the Earth, the object gained energy and was transferred onto a JFC orbit near the 2:1 resonance with Jupiter. In this orbit, the future of the meteoroid is strongly influenced by the gas giant. Over time, the meteoroid will tend to follow the aphelion and perihelion lines for Jupiter.

the grazing encounter with the Earth, the meteoroid was flung into an orbit with a higher energy (Fig. 3.8). The geometry of the encounter enabled the meteoroid to gain angular momentum around the Sun (Fig. 3.10). As a result, the semi-major axis and eccentricity both increased due to the increase in energy, and the object was inserted into a JFC orbit. Hereon, the object's future is strongly governed by its interactions with the gas-giant. Fig. 3.9 shows the evolution of the orbital elements for the meteoroid ± 100 years relative to the grazing encounter.

With an post-encounter aphelion near Jupiter's orbit, the meteoroid is likely to have multiple close-encounters with the planet in the future. Thus, the object

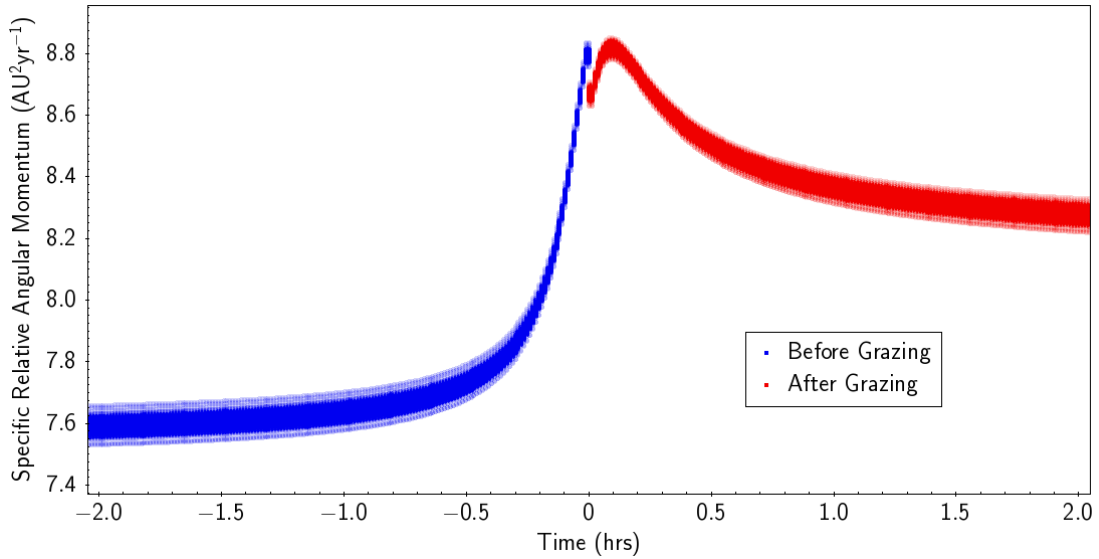
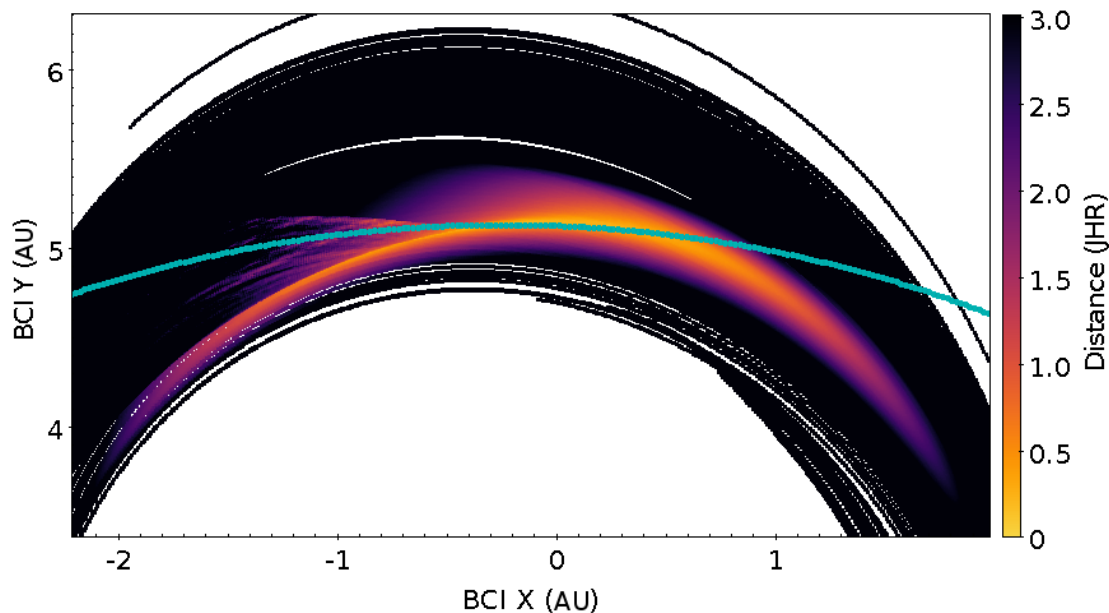


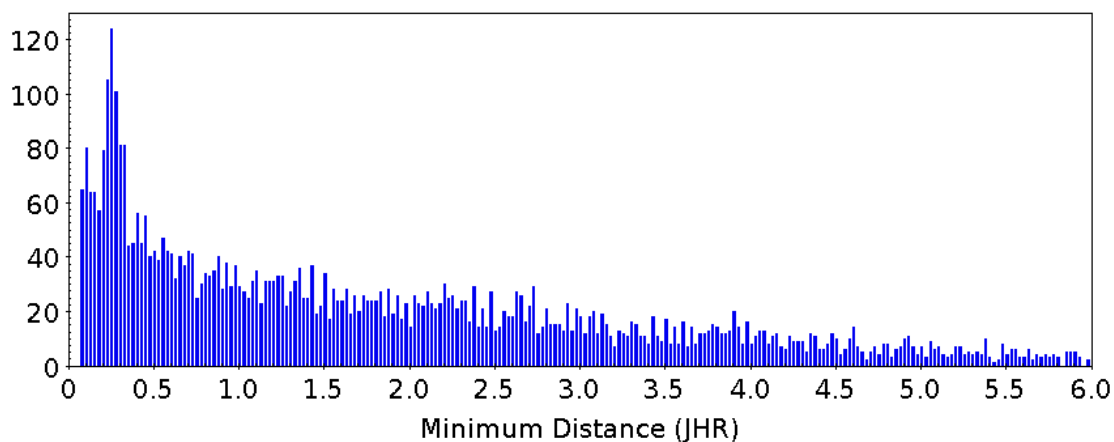
Figure 3.10: Specific relative angular momentum of the meteoroid ± 12 hours relative to the grazing event. The meteoroid gains energy after its encounter with the Earth despite losing some energy during the atmospheric passage. At time = 0, the discontinuity is due to the exclusion of the time when the meteoroid was passing through the atmosphere. The ‘instant’ drop in energy here corresponds to the energy lost due to atmospheric drag. The object continues to gain angular momentum briefly after leaving the atmosphere before losing some energy as it travels away from the Earth. This net gain in angular momentum effectively increased the semi-major axis and eccentricity of the body.

is unpredictable on relatively short timescales compared to other small bodies in the Solar System. This is to be expected for an object on a JFC-like orbit that originated from the trans-Neptunian region (Fernández and Sosa, 2015). As seen in Fig. 3.9, the object will tend to decrease in eccentricity and slightly increase in semi-major axis over time. This will occur slowly for a majority of particles over about 10-100 kyrs, as Jupiter perturbs them. If the orbit of the meteoroid evolves into an orbit with a similar semi-major axis to Jupiter, the close encounters with the gas giant will begin to increase the eccentricity of the meteoroid again and throw the body towards the outer Solar System. The meteoroid is also nearly centered on the 2:1 mean motion resonance (Fig. 3.9), however, this resonance is not as destabilizing as the other prominent resonances on such short timescales (Morbidelli et al., 2002).

The first of these close-encounters will most likely occur between January and March, 2025 (~ 7.52 years after encountering the Earth) in which the meteoroid



(a) Close encounter of meteoroid with Jupiter (blue path).



(b) Histogram of the minimum distances between the particles and Jupiter.

Figure 3.11: After grazing Earth's atmosphere, the meteoroid will complete 1.5 orbits around the Sun before likely having its first close encounter with Jupiter. Both plots provide the distance from Jupiter in terms of Jupiter Hill Radii (JHR). Of the 5,000 particles in this integration, nearly 40% come within 1 JHR and 80% are within 3 JHR. The mean approach is about 0.7 JHR. Consequently, the orbit of the meteoroid is highly uncertain after this point, approximately 7.52 years after its grazing encounter with the Earth (January-March 2025).

	Before	After
a (AU)	2.23 ± 0.06	3.26 ± 0.12
e	0.59 ± 0.01	0.69 ± 0.01
i (deg)	2.79 ± 0.04	3.30 ± 0.04
Ω (deg)	286.46 ± 6.03	285.29 ± 0.01
ω (deg)	316.43 ± 3.56	350.91 ± 0.29
q (AU)	0.9104 ± 0.0003	1.007 ± 0.0004
Q (AU)	3.458 ± 0.114	5.36 ± 0.2300
T_J	3.41 ± 0.05	2.75 ± 0.05

Table 3.2: Heliocentric orbital elements for the meteoroid associated with event DN170707_01 just before and after its grazing encounter with the Earth. The uncertainties of the orbital elements were determined by a short Monte Carlo simulation consisting of 5,000 particles randomly generated within triangulation errors and numerically integrated forward and backward relative to the grazing event. The immediate effect of the encounter on the orbit is apparent; the semi-major axis, eccentricity, and argument of perihelion of the meteoroid were all significantly increased. The grazing encounter changed the orbit of the meteoroid from an Apollo-type NEO to a JFC orbit. The resulting orbit is comparatively unstable due to its aphelion being very similar to the semi-major axis of Jupiter, increasing the chance of a close encounter with the gas giant.

will very likely come within 3 Jupiter Hill radii (JHR) of the planet. A series of short-term highly resolved integrations were performed with 5,000 test particles to analyze this first close encounter with Jupiter. As shown in Fig. 3.11a, the meteoroid is likely to get close to Jupiter (blue path), just 1.5 orbits after our observations of the fireball. Fig. 3.11b shows the minimum distances reached by every particle in the integration, many of which (40%) approaching within 1 JHR with the mean approach of all particles being 0.7 JHR. After this close encounter, the test particles disperse relatively quickly, and precisely predicting the future orbit of the meteoroid becomes unrealistic.

As seen in Fig. 3.12, the well-constrained orbit prior to the close encounter with Jupiter rapidly spreads out in the orbital space. Following the likely meteoroid-Jupiter close encounter of 2025, the orbit of the meteoroid can only be treated statistically. The density plots in Fig. 3.12 show the evolution of the semi-major axis, eccentricity, and inclination of 10,000 test particles forward in time only 100 years. Most of the particles stay together, indicated by the darker portions of the plot. However, as seen by the multiple jumps in values over time, the

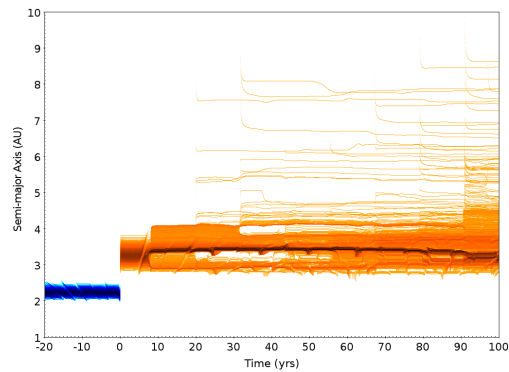
meteoroid is likely to have a plethora of close encounters with Jupiter over its lifetime in a JFC orbit, and every one of these encounters obscures the future of the object.

Close Encounters with Earth In order to determine the likelihood of future or previous close encounters with the Earth, two simulations with 5,000 particles were integrated both backward and forward 20 years relative to the event (Fig. 3.13). During these simulations, outputs were collected at a higher frequency in order to accurately characterize all possible close encounters. The probability that there was an encounter with the Earth within three and one Hill radii within 20 years prior to the grazing event was 2.4% and 0.7%, respectively. Additionally, the probability that a future close encounter with the Earth will occur within the preceding 20 years after the grazing event is 1.4% and 0.5%, respectively. Therefore, the probability of having the opportunity to telescopically observe this object as it re-approaches the Earth is very slim. The most likely time for this to occur is in mid-July 2023, but there is still only a 1.1% chance that it will get within 3 Hill radii of the planet.

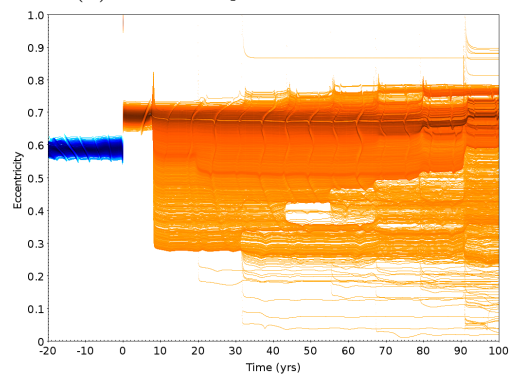
3.4.3 Long-Term Simulations

Further analysis using substantially longer integrations of test particles was performed in order to statistically characterize the meteoroid's future. The longest of these simulations was a forward integration of 1,000 test particles for 500 kyrs. Over the course of the 500 kyr forward integration, most of the particles (60.1%) are eventually ejected from the Solar System, as expected (Fig. 3.14). The vast majority of the particles that remain in the Solar System (heliocentric orbits) stay in JFC orbits (as defined by the Tisserand's parameter) for the entire integration (Fig. 3.15).

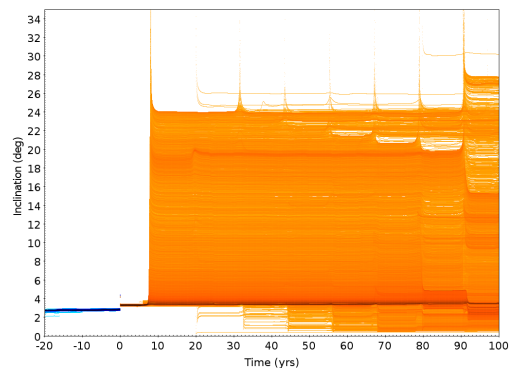
As seen in Fig. 3.14, there is an exponential decay in the number of particles in heliocentric and JFC orbits. The average dynamical lifetime for the particles in JFC orbits is approximately 200 kyrs, which is shorter than the ~ 325 kyrs dynamical lifetime estimate for JFCs (Duncan et al., 2004; Levison and Duncan, 1997).



(a) Semi-major axis variation



(b) Eccentricity variation



(c) Inclination variation

Figure 3.12: Due to the grazing encounter with the Earth, the meteoroid from event DN170707_01 was sent into a Jupiter intersecting orbit. On this new trajectory, the object will likely experience many close encounters with Jupiter over its lifetime. In these density plots, the blue and orange particles represent the meteoroid before and after the grazing encounter, respectively. The darker coloration is indicative of a higher particle density. The many possible close encounters with Jupiter manifest as discrete “jumps” in the semi-major axis, eccentricity, or inclination. Over time the orbits tend to spread out due to numerous close encounters with Jupiter. Thus, the orbit of the meteoroid becomes less clear over a relatively short period of time.

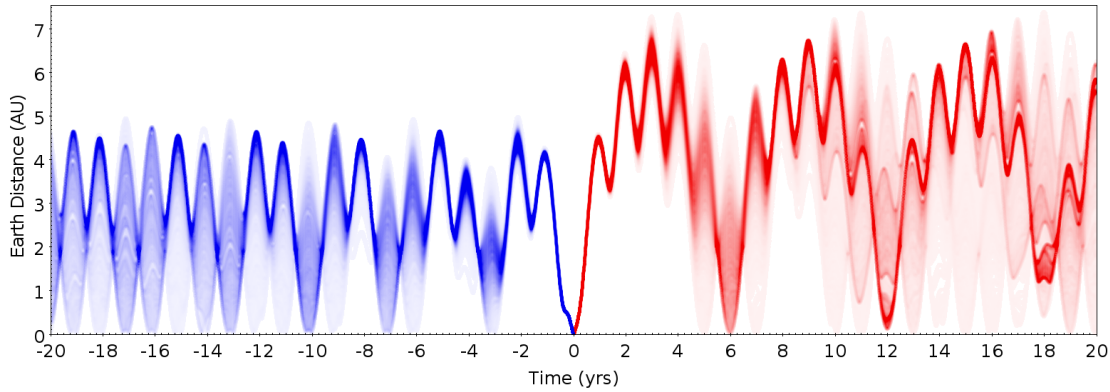


Figure 3.13: Plot of distance relative to the Earth over time. These 2 simulations were conducted with 5,000 particles and lasted 20 years (forward and backward). The time on the x-axis is relative to the event epoch. The probability of an encounter with the Earth for the 20 years before and after the fireball observation is extremely low. There is a 2.4% probability of coming within 3 Hill radii and a 0.7% probability having a 1 Hill radii encounter with the Earth within 20 years before the grazing encounter. Meanwhile, there is a 1.4% and a 0.5% probability of the meteoroid encountering the Earth again within one and three Hill radii in the next 20 years respectively. There is 1.1% that the object will approach within 3 Hill radii in July 2023.

This is likely due to the initial post-grazing orbit, which has an aphelion very near the orbit of Jupiter. However, bodies in JFC orbits that display cometary features are more likely to have multiple ≤ 0.1 AU encounters with Jupiter, reducing the orbital stability compared to asteroidal interlopers within the population (Fernández and Sosa, 2015). Therefore, the JFC-orbit dynamical lifetime for the meteoroid is indistinguishable from a JFC from a more “traditional” source region. In Fig. 3.14, the JFC, asteroidal, and LPC categories are solely determined by the particles’ Tisserand’s parameter. Whereas, the Centaur and trans-Neptunian objects are defined as having orbits between Jupiter and Neptune, and beyond the orbit of Neptune, respectively. This classification does lend itself to including some Centaurs and trans-Neptunian objects when counting the number of JFCs.

A smaller fraction (31.6%) of the test particles evolve onto asteroidal or long-period cometary orbits as defined by their Tisserand’s parameter values (Fig. 3.16). The majority of asteroidal particles are determined to be in the outer Solar System. These are particles that originated from JFC space that were decoupled from Jupiter over time due to planetary perturbations and are now on Centaur or trans-Neptunian orbits. This portrays a similar mechanism alluded to in the

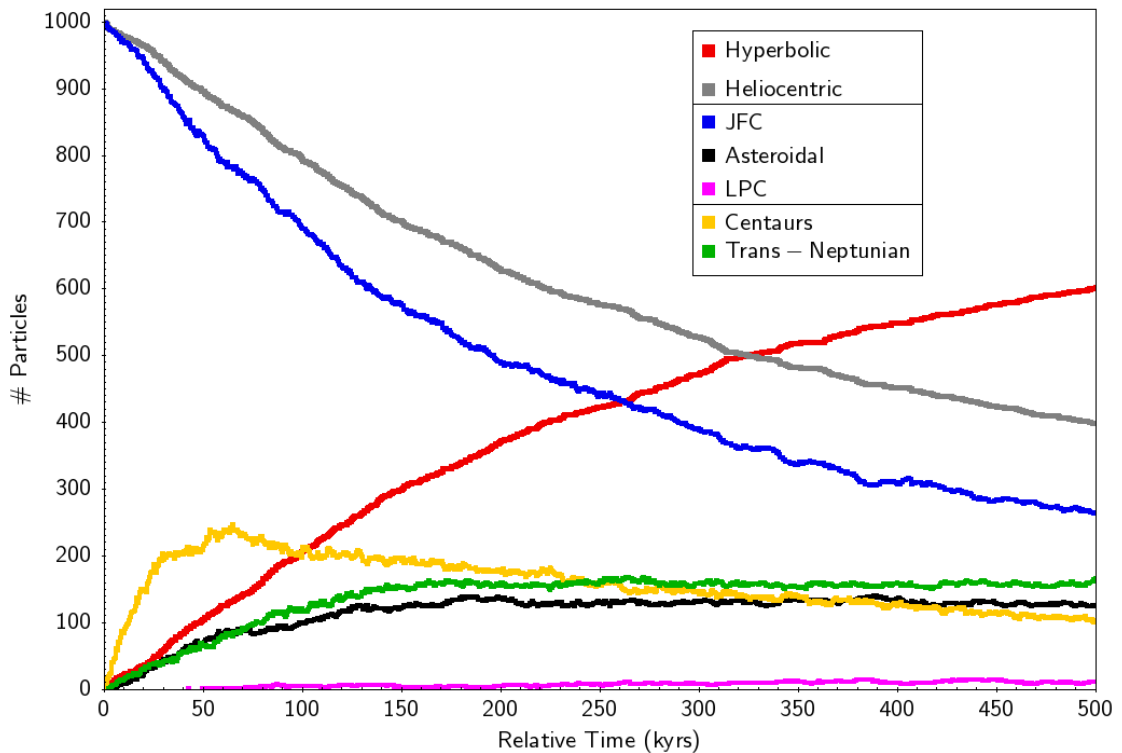


Figure 3.14: Plot showing the change in the orbital classification of the 1,000 particles in the forward integration of event DN170707_01 for 500 kyr. The lines separating the labels in the legend group classifications together that are mutually exclusive (e.g. particles cannot be simultaneously hyperbolic and heliocentric). Over time, the likelihood that the meteoroid will have a close enough encounter to eject it from the Solar System increases. By the end of the simulation, 60.1% of the particles are ejected, 27.3% are still on JFC orbits, and 12.6% have remained in the Solar System but have either gone onto long-period cometary or asteroid-like orbits. Many of the particles ($\sim 20\%$) evolve onto Centaur and then trans-Neptunian orbits due to close-encounters with Jupiter.

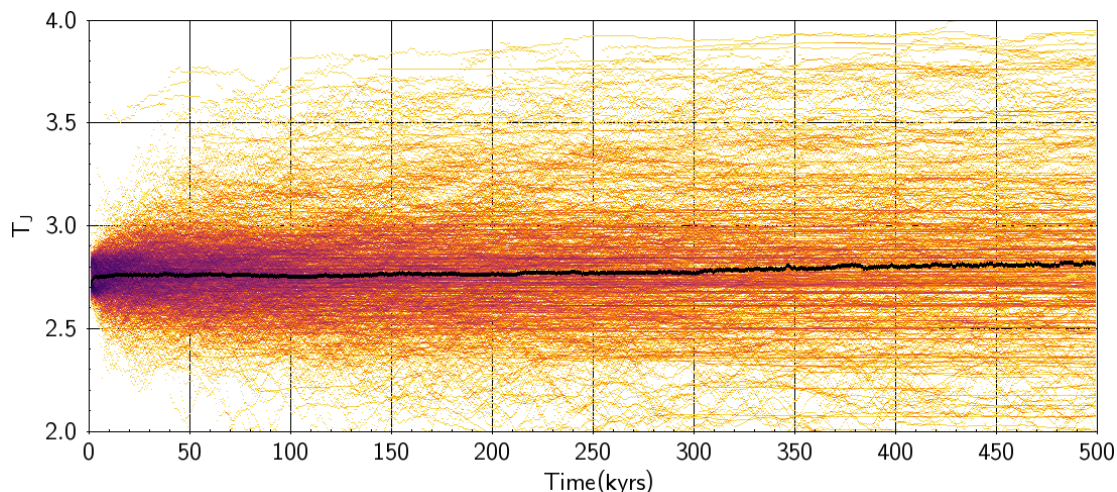


Figure 3.15: Tisserand’s parameter variation of 1,000 particles integrated for 500 *kyrs* post-grazing event for DN170707_01. Particles that are ejected from the Solar System are removed. The meteoroid is likely to stay in a JFC orbit for an amount of time normal for a ‘natural’ JFC object. The colouration in the plot is indicative of density - darker in areas of higher particle density and lighter in areas of lower particle density.

concluding statements in Meech et al. (2004), where they estimate there should be ~ 20 objects of kilometer-size from the main-belt being scattered by Jupiter every million years in today’s Solar System. The object discussed in this study differs in that it was gravitationally scattered by the Earth and then by Jupiter, resulting in the possible transfer of volatile-depleted inner Solar System material to the outer Solar System.

3.4.4 Analysis of Other Grazing Meteors/Fireballs

Within the current scientific literature, there have been in total ten grazing fireballs observed. However, in only six of these cases did the meteoroid survive the atmospheric passage and return to interplanetary space (Table 3.3). These grazing events demonstrate the orbital changes experienced by meteoroids that come very close to Earth. In most of these occurrences, the objects experience a significant change to their orbits. Although, this does not necessarily change them enough to be orbitally reclassified. For the first photographically observed grazing fireball, in October of 1990, a $10^5 - 10^6$ kg meteoroid in a higher inclination Apollo-type orbit with a JFC-like Tisserand’s parameter was inserted into a lower-energy orbit with

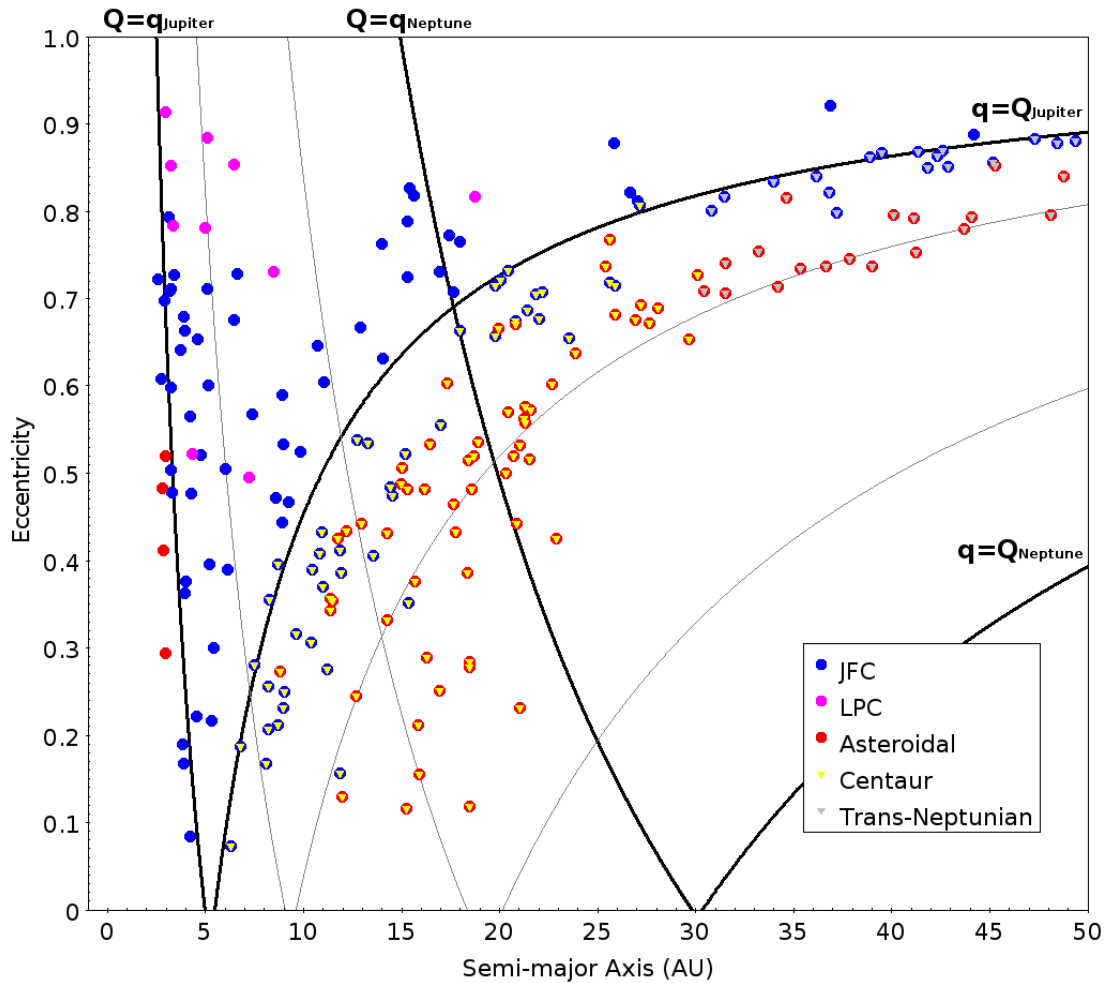


Figure 3.16: Semi-major axis vs eccentricity for the particles that are still gravitationally bound to the Sun after the forward integration of 1,000 particles for 500 kyrs. The lines of equal perihelion and aphelion are plotted for Jupiter and Neptune in black, and in gray for Saturn and Uranus. Most of the remaining heliocentric particles (68.4%) are in JFC-like orbits (blue) according to their Tisserand’s parameter. However, a considerable number of particles (29.1%) are considered “asteroidal”, according to their Tisserand’s parameter with respect to Jupiter (red). Only a very small number of these are in the inner Solar System. A vast majority appear to be former JFC particles that have completely decoupled from Jupiter and have drifted onto Centaur and trans-Neptunian orbits due to planetary perturbations over time. The Centaur and trans-Neptunian particles can have either JFC or asteroidal like Tisserand’s parameters ($T_J > 2$), as shown by the colourisation in this plot. Also, about 2.5% of the particles are categorized as “long-period comets” despite their low semi-major axis because they are orbiting in retrograde orbits.

Table 3.3: Summary of six of the ten previous Earth-grazing meteors within scientific literature in which the meteoroid survived the passage through the atmosphere. Information omitted in the table was not included in the corresponding study.

Event Date	Event Location	Detection Method	Initial Mass	Orbit Before	Orbit After	T_J Before	T_J After	Reference
Aug. 10, 1972	Western US and Canada	satellite infrared radiometer	$10^5 - 10^6$ kg	Amor	Apollo	4.14	4.52	Ceplecha (1979)
Oct. 13, 1990	Czechoslovakia and Poland	photographic	~44 kg	Apollo	Apollo	2.27	3.07	Borovicka (1990)
Sept. 23, 2003	Ukraine	video		Apollo	Apollo	0.66	0.79	Kozak and Watanabe (2017)
Mar. 29, 2006	Japan	video, photographic, telescope	~100kg	JFC		2.85		Abe et al. (2006)
June 10, 2012	Spain	video	1.5 - 115 kg	Daytime ζ -Perseid	Daytime ζ -Perseid	3.31	4.04	Madiedo et al. (2016)
Dec. 24, 2014	Spain	video		Apollo		5.3		Moreno et al. (2016)

a $T_J > 3$. Thus, not only has a meteoroid with a more asteroid-like T_J become more cometary due to close encounters, but the reverse has also been observed. It has been shown that using the Tisserand's parameter is a better metric to classify small Solar System bodies compared to the traditional arbitrary classification based on the orbital period (Carusi and Valsecchi, 1987; Levison and Duncan, 1997). Nevertheless, as shown in this study, small meter-sized objects occasionally experience close encounters with the Earth and have a sufficient orbital energy change to be reclassified even under this scheme.

Other Grazing DFN Events If we consider a fireball event to be grazing simply when the initial slope of the trajectory is $< 5^\circ$ and travelled > 100 km through the atmosphere, in the four years since the DFN has been fully operational, we have observed $\sim 1.2\%$ of the DFN dataset to be grazing events. Indicating that although somewhat uncommon, grazing events are not extremely rare. However, in most of the events detected, the meteoroid either does not survive the atmospheric passage or loses enough velocity to be incapable of re-entering interplanetary space.

3.4.5 Implications and Further Research

Grazing fireballs indicate that meter-scale NEOs are occasionally inserted into categorically new orbits due to close encounters with the Earth, or indeed other planets. How effective this mechanism is for mixing material in the inner Solar System for small objects is still to be determined. Current work is being done to produce an artificial dataset of close encounters undetected by telescopes based upon the entire orbital dataset of the DFN (Shober et al., in prep.). This analysis will be extremely valuable to conclusively determine how significant this process is

for small objects in the inner Solar System. If it is non-negligible, what populations in the near-Earth space may be more or less contaminated by genetically unrelated material, how significant are the orbit alterations, and what may this imply about where meteorites come from?

3.5 Conclusions

On July 7th, 2017, the Desert Fireball Network observed a > 1300 km long grazing fireball by ten of its high-resolution digital fireball observatories. The meteoroid transited the atmosphere for over 90 seconds and reached a minimum height of 58.5 km before returning to interplanetary space. This fireball is only matched by the notorious ‘Great Daylight Fireball of 1972’, which penetrated to a very similar depth in the atmosphere but lasted ~ 9 seconds longer. As a result of the grazing encounter with the Earth, the meteoroid observed by the DFN underwent a natural slingshot maneuver in which it was transferred from an asteroidal Apollo-type orbit to a JFC orbit. Additionally, numerical integration of the object forward 500 kyrs indicated that it will most likely stay in a JFC orbit for ~ 200 kyrs – indistinguishable from any other JFC. Considering there are likely many small objects that go telescopically undetected that have close encounters with the Earth, there may be a non-negligible amount of meter-sized objects in modified orbits within the inner Solar System.

3.6 Acknowledgements

This work was funded by the Australian Research Council as part of the Australian Discovery Project scheme (DP170102529). SSTC authors acknowledge institutional support from Curtin University.

This research made use of Astropy, a community-developed core Python package for Astronomy (Robitaille et al., 2013). Simulations in this paper made use of the REBOUND code which can be downloaded freely at <http://github.com/hannorein/REBOUND> (Rein and Liu, 2012).

The authors would also like to thank David Clark for his assistance in creating

animations of event DN170707_01 and searching telescope surveys for images of the meteoroid before and after DFN observations. Additionally, we would like to thank Prof. Jürgen Oberst for being being extremely helpful and providing additional information about the grazing fireball observed over central-Europe in 2014.

Bibliography

- S. Abe, J. Borovicka, P. Spurný, P. Koten, Z. Ceplecha, T. Tamagawa, et al. Earth-grazing fireball on march 29, 2006. In *European Planetary Science Congress 2006*, page 486, 2006.
- M. Beech, P. Brown, R. Hawkes, Z. Ceplecha, K. Mossman, and G. Wetherill. The fall of the peekskill meteorite: Video observations, atmospheric path, fragmentation record and orbit. *Earth, Moon, and Planets*, 68(1):189–197, 1995.
- R. P. Binzel, A. S. Rivkin, J. S. Stuart, A. W. Harris, S. J. Bus, and T. H. Burbine. Observed spectral properties of near-earth objects: results for population distribution, source regions, and space weathering processes. *Icarus*, 170(2):259–294, 2004.
- P. Bland, P. Spurný, A. Bevan, K. Howard, M. Towner, G. Benedix, R. Greenwood, L. Shrubbery, I. Franchi, G. Deacon, et al. The australian desert fireball network: a new era for planetary science. *Australian Journal of Earth Sciences*, 59(2):177–187, 2012.
- P. A. Bland. The desert fireball network. *Astronomy & Geophysics*, 45(5):5–20, 2004.
- J. Borovicka. The comparison of two methods of determining meteor trajectories from photographs. *Bulletin of the Astronomical Institutes of Czechoslovakia*, 41:391–396, 1990.
- J. Borovicka and Z. Ceplecha. Earth-grazing fireball of october 13, 1990. *Astronomy and Astrophysics*, 257:323–328, 1992.

- W. F. Bottke Jr, A. Morbidelli, R. Jedicke, J.-M. Petit, H. F. Levison, P. Michel, and T. S. Metcalfe. Debaised orbital and absolute magnitude distribution of the near-earth objects. *Icarus*, 156(2):399–433, 2002.
- P. Brown, Z. Ceplecha, R. Hawkes, G. Wetherill, M. Beech, and K. Mossman. The orbit and atmospheric trajectory of the peekskill meteorite from video records. *Nature*, 367(6464):624, 1994.
- A. Carusi and G. Valsecchi. Dynamical evolution of short-period comets. *Publications of the Astronomical Institute of the Czechoslovak Academy of Sciences*, 67:21–28, 1987.
- T. Cavallo. Ix. description of a meteor, observed aug. 18, 1783. *Philosophical Transactions of the Royal Society of London*, 74:108–111, 1784.
- Z. Ceplecha. Earth-grazing fireballs/the daylight fireball of aug. 10, 1972. *Bulletin of the Astronomical Institutes of Czechoslovakia*, 30:349–356, 1979.
- Z. Ceplecha. Geometric, dynamic, orbital and photometric data on meteoroids from photographic fireball networks. *Bulletin of the Astronomical Institutes of Czechoslovakia*, 38:222–234, 1987.
- Z. Ceplecha. Earth-grazing daylight fireball of august 10, 1972. *Astronomy and Astrophysics*, 283:287–288, 1994.
- Z. Ceplecha, P. Brown, R. Hawkes, G. Wetherill, M. Beech, and K. Mossman. Video observations, atmospheric path, orbit and fragmentation record of the fall of the peekskill meteorite. *Earth, Moon, and Planets*, 72(1-3):395–404, 1996.
- C. A. Chant. An Extraordinary Meteoric Display. *Journal of the Royal Astronomical Society of Canada*, 7:145, June 1913.
- D. L. Clark and P. A. Wiegert. A numerical comparison with the ceplecha analytical meteoroid orbit determination method. *Meteoritics & Planetary Science*, 46(8):1217–1225, 2011. doi: 10.1111/j.1945-5100.2011.01226.x. URL <https://onlinelibrary.wiley.com/doi/abs/10.1111/j.1945-5100.2011.01226.x>.

- W. F. Denning. Great Meteoric Stream of February 9th, 1913. *Journal of the Royal Astronomical Society of Canada*, 10:294, Aug. 1916.
- H. A. Devillepoix, E. K. Sansom, P. A. Bland, M. C. Towner, M. Cupák, R. M. Howie, T. Jansen-Sturgeon, M. A. Cox, B. A. Hartig, G. K. Benedix, et al. The dingle dell meteorite: A halloween treat from the main belt. *Meteoritics & Planetary Science*, 53(10):2212–2227, 2018.
- V. Dmitriev, V. Lupovka, and M. Gritsevich. Orbit determination based on meteor observations using numerical integration of equations of motion. *Planetary and Space Science*, 117:223–235, 2015.
- M. Duncan, H. Levison, and L. Dones. Dynamical evolution of ecliptic comets. *Comets II*, 193:204, 2004.
- M. J. Duncan and H. F. Levison. A disk of scattered icy objects and the origin of jupiter-family comets. *Science*, 276(5319):1670–1672, 1997.
- E. Everhart. An efficient integrator that uses Gauss-Radau spacings. In A. Carusi and G. B. Valsecchi, editors, *IAU Colloq. 83: Dynamics of Comets: Their Origin and Evolution*, volume 115, page 185, Jan. 1985.
- J. A. Fernández. On the existence of a comet belt beyond neptune. *Monthly Notices of the Royal Astronomical Society*, 192(3):481–491, 1980.
- J. A. Fernández and A. Sosa. Jupiter family comets in near-earth orbits: Are some of them interlopers from the asteroid belt? *Planetary and Space Science*, 118:14–24, 2015.
- J. A. Fernández, T. Gallardo, and A. Brunini. Are there many inactive jupiter-family comets among the near-earth asteroid population? *Icarus*, 159(2):358–368, 2002.
- Y. R. Fernández, D. C. Jewitt, and S. S. Sheppard. Low albedos among extinct comet candidates. *The Astrophysical Journal Letters*, 553(2):L197, 2001.
- Y. R. Fernández, D. C. Jewitt, and S. S. Sheppard. Albedos of asteroids in comet-like orbits. *The Astronomical Journal*, 130(1):308, 2005.

- M. Granvik, A. Morbidelli, R. Jedicke, B. Bolin, W. F. Bottke, E. Beshore, D. Vokrouhlický, D. Nesvorný, and P. Michel. Debaised orbit and absolute-magnitude distributions for near-earth objects. *Icarus*, 312:181–207, 2018.
- R. M. Howie, J. Paxman, P. A. Bland, M. C. Towner, M. Cupak, E. K. Sansom, and H. A. Devillepoix. How to build a continental scale fireball camera network. *Experimental Astronomy*, 43(3):237–266, 2017a.
- R. M. Howie, J. Paxman, P. A. Bland, M. C. Towner, E. K. Sansom, and H. A. Devillepoix. Submillisecond fireball timing using de bruijn timecodes. *Meteoritics & Planetary Science*, 52(8):1669–1682, 2017b.
- H. H. Hsieh and D. Jewitt. A population of comets in the main asteroid belt. *Science*, 312(5773):561–563, 2006.
- L. G. Jacchia. A meteorite that missed the earth. *Sky and Telescope*, 48, 1974.
- T. Jansen-Sturgeon, E. K. Sansom, and P. A. Bland. Comparing analytical and numerical approaches to meteoroid orbit determination using hayabusa telemetry. *Meteoritics & Planetary Science*, 54(9):2149–2162, 2019a. doi: 10.1111/maps.13376. URL <https://onlinelibrary.wiley.com/doi/abs/10.1111/maps.13376>.
- T. Jansen-Sturgeon, E. K. Sansom, H. A. R. Devillepoix, P. A. Bland, M. C. Towner, R. M. Howie, and B. A. D. Hartig. A dynamic trajectory fit to multi-sensor fireball observations, 2019b.
- P. Jenniskens, M. D. Fries, Q.-Z. Yin, M. Zolensky, A. N. Krot, S. A. Sandford, D. Sears, R. Beauford, D. S. Ebel, J. M. Friedrich, et al. Radar-enabled recovery of the sutter’s mill meteorite, a carbonaceous chondrite regolith breccia. *Science*, 338(6114):1583–1587, 2012.
- D. Jewitt. The active asteroids. *The Astronomical Journal*, 143(3):66, 2012.
- M. S. Kelley and D. H. Wooden. The composition of dust in jupiter-family comets inferred from infrared spectroscopy. *Planetary and Space Science*, 57(10):1133–1145, 2009.

- Y. Kim, M. Ishiguro, and F. Usui. Physical properties of asteroids in comet-like orbits in infrared asteroid survey catalogs. *The Astrophysical Journal*, 789(2):151, 2014.
- P. M. Kozak and J. Watanabe. Upward-moving low-light meteor – I. Observation results. *Monthly Notices of the Royal Astronomical Society*, 467(1):793–801, 01 2017. ISSN 0035-8711. doi: 10.1093/mnras/stx008. URL <https://doi.org/10.1093/mnras/stx008>.
- H. F. Levison and M. J. Duncan. The long-term dynamical behavior of short-period comets. *Icarus*, 108(1):18–36, 1994.
- H. F. Levison and M. J. Duncan. From the kuiper belt to jupiter-family comets: The spatial distribution of ecliptic comets. *Icarus*, 127(1):13–32, 1997.
- H. F. Levison, D. Terrell, P. A. Wiegert, L. Dones, and M. J. Duncan. On the origin of the unusual orbit of comet 2p/encke. *Icarus*, 182(1):161–168, 2006.
- J. M. Madiedo, F. Espartero, A. J. Castro-Tirado, S. Pastor, and J. A. de los Reyes. An earth-grazing fireball from the daytime ζ -perseid shower observed over spain on 2012 june 10. *Monthly Notices of the Royal Astronomical Society*, 460(1):917–922, 2016.
- K. Meech, O. Hainaut, and B. Marsden. Comet nucleus size distributions from hst and keck telescopes. *Icarus*, 170(2):463–491, 2004.
- K. J. Meech, B. Yang, J. Kleyna, O. R. Hainaut, S. Berdyugina, J. V. Keane, M. Micheli, A. Morbidelli, and R. J. Wainscoat. Inner solar system material discovered in the oort cloud. *Science Advances*, 2(4):e1600038, 2016.
- A. Morbidelli, W. Bottke, C. Froeschlé, P. Michel, et al. Origin and evolution of near-earth objects. *Asteroids iii*, 409, 2002.
- A. Moreno, J. Madiedo, J. Zamorano, R. Goncalves, F. Esparteros, J. Trigo-Rodríguez, J. Ortiz, J. Lacruz, J. Aceituno, E. De Guindos, et al. Preliminary spectroscopic and dynamical analysis of an earth-grazer fireball observed on

- december 24, 2014. In *Lunar and Planetary Science Conference*, volume 47, page 1088, 2016.
- J. Oberst, D. Heinlein, M. Gritsevich, E. Lyytinen, J. Flohrer, A. Margonis, V. Lupovka, V. Dmitriev, F. Schweidler, J. Peltoniemi, et al. The extraordinary grazing fireball over central europe on march 31, 2014. In *Proceedings of the European Planetary Science Congress 2014. EPSC Abstracts*, volume 9, 2014.
- D. W. Olson, M. S. Olson, R. L. Doescher, and A. G. Pope. Literary mystery: Walt whitman’s” year of meteors”. *Sky and telescope*, 120(1):28–33, 2010.
- J. M. Picone, A. E. Hedin, D. P. Drob, and A. C. Aikin. Nrlmsise-00 empirical model of the atmosphere: Statistical comparisons and scientific issues. *Journal of Geophysical Research: Space Physics*, 107(A12):SIA 15–1–SIA 15–16, 2002. doi: 10.1029/2002JA009430. URL <https://agupubs.onlinelibrary.wiley.com/doi/abs/10.1029/2002JA009430>.
- O. Popova, J. Borovička, W. K. Hartmann, P. Spurný, E. Gnos, I. Nemtchinov, and J. M. Trigo-Rodríguez. Very low strengths of interplanetary meteoroids and small asteroids. *Meteoritics & Planetary Science*, 46(10):1525–1550, 2011.
- R. Rawcliffe, C. Bartky, F. Li, E. Gordon, and D. Carta. Meteor of august 10, 1972. *Nature*, 247(5441):449, 1974.
- H. Rein and S. F. Liu. REBOUND: an open-source multi-purpose N-body code for collisional dynamics. *Astronomy and Astrophysics*, 537:A128, Jan. 2012. doi: 10.1051/0004-6361/201118085.
- H. Rein and D. S. Spiegel. IAS15: a fast, adaptive, high-order integrator for gravitational dynamics, accurate to machine precision over a billion orbits. *Monthly Notices of the Royal Astronomical Society*, 446(2):1424–1437, Jan. 2015. doi: 10.1093/mnras/stu2164.
- D. O. Revelle, R. W. Whitaker, and W. T. Armstrong. Infrasonic observations of bolides on October 4, 1996. In F. A. Allahdadi, E. K. Casani, and T. D.

- Maclay, editors, *Small Spacecraft, Space Environments, and Instrumentation Technologies*, volume 3116 of *Proceedings Volume 3116, Small Spacecraft, Space Environments, and Instrumentation Technologies*, pages 156–167, Oct. 1997. doi: 10.1117/12.293343.
- T. P. Robitaille, E. J. Tollerud, P. Greenfield, M. Droettboom, E. Bray, T. Aldcroft, M. Davis, A. Ginsburg, A. M. Price-Whelan, W. E. Kerzendorf, et al. Astropy: A community python package for astronomy. *Astronomy & Astrophysics*, 558:A33, 2013.
- E. K. Sansom, P. Bland, J. Paxman, and M. Towner. A novel approach to fireball modeling: The observable and the calculated. *Meteoritics & Planetary Science*, 50(8):1423–1435, 2015.
- E. K. Sansom, T. Jansen-Sturgeon, M. G. Rutten, H. A. Devillepoix, P. A. Bland, R. M. Howie, M. A. Cox, M. C. Towner, M. Cupák, and B. A. Hartig. 3d meteoroid trajectories. *Icarus*, 321:388–406, 2019.
- P. M. Shober, T. Jansen-Sturgeon, E. Sansom, H. Devillepoix, P. Bland, M. Cupák, M. C. Towner, R. M. Howie, and B. A. Hartig. Identification of a minimoon fireball. *The Astronomical Journal*, 158(5):183, 2019.
- P. Spurný, J. Borovicka, Z. Ceplecha, and L. Shrbený. Precise multi-instrument data on 45 fireballs recorded over central europe in the period 2006-2008. In *Asteroids, Comets, Meteors 2008*, volume 1405, 2008.
- D. Steel and D. Asher. On the origin of comet encke. *Monthly Notices of the Royal Astronomical Society*, 281(3):937–944, 1996.
- K. Tsiganis, R. Gomes, A. Morbidelli, and H. Levison. Origin of the orbital architecture of the giant planets of the solar system. *Nature*, 435(7041):459, 2005.
- K. J. Walsh, A. Morbidelli, S. N. Raymond, D. P. O’Brien, and A. M. Mandell. A low mass for mars from jupiter’s early gas-driven migration. *Nature*, 475(7355):206, 2011.

CHAPTER 4

Using atmospheric impact data to model meteoroid close encounters

Patrick M. Shober^a, Trent Jansen-Sturgeon^a, Eleanor K. Sansom^a, Hadrien A.R. Devillepoix^a, Martin Cupák^a, Phil A. Bland^a, Martin C. Towner^a, Robert M. Howie^a, Benjamin A.D. Hartig^a

^aSpace Science and Technology Centre (SSTC), School of Earth and Planetary Sciences, Curtin University, GPO Box U1987, Perth, Western Australia 6845, Australia

This article is published in The Monthly Notices of the Royal Astronomical Society, accepted 17 August 2020, published 27 August 2020

Abstract

Based on telescopic observations of Jupiter-family comets (JFCs), there is predicted to be a paucity of objects at sub-kilometre sizes. However, several bright fireballs and some meteorites have been tenuously linked to the JFC population, showing metre-scale objects do exist in this region. In 2017, the Desert Fireball Network (DFN) observed a grazing fireball that redirected a meteoroid from an Apollo-type orbit to a JFC-like orbit. Using orbital data collected by the DFN, in this study, we have generated an artificial dataset of close terrestrial encounters that come within 1.5 lunar distances (LD) of the Earth in the size-range of 0.01 – 100 kg. This range of objects is typically too small for telescopic surveys to detect, so using atmospheric impact flux data from fireball observations is currently one of the only ways to characterise these close encounters. Based on this model, we predict that within the considered size-range 2.5×10^8 objects (0.1% of the total flux) from asteroidal orbits ($T_J > 3$) are annually sent onto JFC-like orbits ($2 < T_J < 3$), with a steady-state population of about 8×10^{13} objects. Close encounters with the Earth provide another way to transfer material to the JFC region. Additionally, using our model, we found that approximately 1.96×10^7 objects are sent onto Aten-type orbits and $\sim 10^4$ objects are ejected from the Solar System annually via a close encounter with the Earth.

4.1 Introduction

The diffusion of material out from the main-belt (MB) onto comet-like orbits has been discussed briefly in previous studies (Fernández et al., 2002, 2014; Hsieh and Haghighipour, 2016; Shober et al., 2020). This mixing potentially can send many durable meteoroids from the MB onto comet-like orbits. Without a clear understanding of this process, meteoroids may be misidentified, leading to inaccurate conclusions about the comet population.

The possibility of already having cometary meteorites in the world’s collections has been a topic of discussion for decades (Campins and Swindle, 1998; Gounelle et al.,

2008). Jupiter Family Comets (JFCs) are the most likely source region to supply cometary meteorites to the Earth, as the contribution from the nearly isotropic comet (NIC) population is negligible in comparison. However, whether JFCs are capable of producing genetically cometary material on Earth is dependent on the physical lifetimes of JFCs, the dynamic efficiency of JFCs evolving onto Earth-intersecting orbits, and the ability of the meteoroids to eventually survive the atmospheric passage intact as meteorites.

4.1.1 Jupiter Family Comets

Dynamical studies have shown that the scattered disk (SD) and the Kuiper Belt are the two primary sources for modern JFCs (Levison and Duncan, 1997; Duncan and Levison, 1997). The SD is the most dominant as the Kuiper Belt is slower at producing JFCs. The SD is cold, likely very primitive and volatile-rich, with larger eccentricities than the classical Kuiper Belt (Gomes et al., 2008). Other sources from within the MB have also been proposed to partially supply material to the JFCs (Fernández et al., 2002; Kim et al., 2014; Fernández and Sosa, 2015; Hsieh et al., 2020). This can occur as a result of outward diffusion from the MB via mean-motion resonances (MMR), primarily the 2:1 MMR (3.27 au). Other outer-MB resonances such as the 9:4 and 11:5 MMRs have been suggested to be able to produce a modest amount of objects on JFC-like orbits (Fernández et al., 2014; Fernández and Sosa, 2015; Hsieh et al., 2020). Studies have additionally found that terrestrial planets (particularly Earth and Venus) may play an important role by perturbing MB objects onto JFC-like orbits (Fernández et al., 2002; Hsieh et al., 2020).

Two primary factors are responsible for the observed JFC size distribution: the size distribution for the source regions of the JFCs and the physical evolution that bodies on JFC orbits underwent. Several studies have attempted to characterize the JFC cumulative size-frequency distribution (CSD) (Meech et al., 2004; Fernández et al., 2013). The CSDs determined in these studies, based on telescopic observations, predict a break in the slope for sub-kilometre bodies. This break is due to the obvious sampling bias against telescopically observing these

objects. However, Meech et al. (2004) argued that despite this sampling bias, there should still be more discovered sub-kilometre JFC objects according to their model. The most likely explanation for this paucity of sub-kilometre objects is the short physical lifetimes associated with these objects. While the average dynamical lifetime for JFCs is typically 10^5 years, there is ample evidence that the physical lifetimes are $\sim 10^3$ years for JFCs in the inner solar system (Kresák, 1981; Kresák and Kresáková, 1990; Levison and Duncan, 1997; Fernández et al., 1999; Hughes, 2003; Di Sisto et al., 2009; Sosa et al., 2012).

4.1.2 Meteors and Fireballs

On the other end of the spectrum, ground-based meteor and fireball observation networks are able to characterise the smallest subset of objects on JFC-like orbits. There are several meteor showers observed to originate from JFCs (e.g., Draconids and Andromedids). These showers tend to have larger meteoroids than long-period comets (LPCs) ($\sim 100 \mu\text{m}$) and lower impact speeds ($11 - 35 \text{ km s}^{-1}$) (Jenniskens and Jenniskens, 2006). In the study of the zodiacal cloud by Nesvorný et al. (2010), they concluded that particles from JFCs should represent 85% of the total terrestrial mass influx. This result provides an explanation for the abundance of micrometeorites with primitive carbonaceous compositions found in Antarctica. Though, as the meteoroid sizes increase to centimetre and metre scales, the story becomes uncertain.

Despite the predicted paucity of sub-kilometre objects based on CSDs of the JFC population, there have been many bright fireballs observed to originate from JFC-like orbits. These meteoroids can be centimetres to metres in scale. However, the delivery mechanism and composition of these objects is still unclear. For example, Madiedo et al. (2014) reported observing a bright fireball originating from a JFC orbit with mass of $40 \pm 5 \text{ kg}$. The meteoroid penetrated as deep as 68 km altitude and had a maximum luminosity of -13 ± 0.5 absolute magnitude. However, the object could not be associated with any known JFCs. If the object was genetically JFC material ($T_J = 2.3 \pm 0.2$), given its low perihelion distance, the meteoroid is predicted to have an extremely short physical lifetime. The physical

lifetimes for kilometre-size JFCs is typically on the order of 10^3 years, however, metre-sized fragments are estimated to only persist for a few revolutions (≤ 10 yrs) (Beech and Nikolova, 2001). Therefore, either it did not originate from the Jupiter family comet population or there is a mechanism capable of extending the physical lifetimes of JFC material in this size-range. Brown et al. (2016) also analysed 59 fireballs caused by meteoroids ≥ 1 m in diameter, and found 10 – 15% have a possibly cometary origin, but only about half of these were observed to be weaker than average based on ablation behavior. Additionally, in Flynn et al. (2018), they compared the connection between T_J and PE criterion for 600 fireball observations showing that fireballs with JFC-like T_J values display a similar spectrum of PE values to those of meteoroids from asteroidal orbits ($T_J > 3$). The catastrophic breakup or splitting of the parent body is currently the most favoured explanation to produce large fragments from a comet, as no other mechanism is capable of producing debris in this size-range (Jenniskens, 2004; Jenniskens and Lyytinen, 2005).

4.1.3 Meteorite Falls

There have been a handful of meteorite falls associated with JFC-like orbits. Nearly all of these have likely origins in the MB, given they all have $T_J \sim 3$. Granvik and Brown (2018) re-calculated the source region probabilities for 25 meteorite falls and found only one meteorite, Ejby, to have its most likely source be the JFCs. Curiously, Ejby and Košice, the two meteorites with the highest likelihoods of originating from the JFC source region, are both H-chondrites. Meanwhile, two CM-chondrites (Maribo and Sutter’s Mill) both have non-negligible chances of coming from the JFC population, but are most likely sourced from the MB via the 3 : 1 resonance.

4.1.4 Addressing the Problem

Telescopic observations of JFCs display a paucity at sub-kilometre scales. When observing dust-sized objects, primitive CM-chondritic material is abundant and associated with JFCs (Nesvorný et al., 2010). Nevertheless, fireball networks re-

port metre-scale objects on JFC orbits impacting the Earth. If asteroidal material from the MB is regularly transferred to the JFC population, given the extremely short physical lifetimes expected for cometary meteoroids, the fireballs from non-shower JFC-like orbits may be highly contaminated by asteroidal material.

Objects that are > 100 m in diameter regularly come close to the Earth¹. However, these bodies are also much easier to identify telescopically. Thus, there is certainly a much larger group of smaller objects that are not seen by telescopes that pass very close to the Earth. This smaller-size subset encompasses the size-range of objects that typically generate meteorites. In a previous study, Shober et al. (2020) described a grazing fireball event that transferred a meteoroid from an Apollo-type orbit to a JFC-like orbit. Since there are many objects like this that go unnoticed by telescope surveys, there is likely a non-negligible amount of small objects that are quickly inserted into dynamically distinct orbits. Additionally, objects tend to evolve along the lines of equal perihelion or aphelion. Therefore, the probability of re-observing these gravitationally scattered objects may be worth consideration. Close encounters with the Earth could provide an additional way to transfer material from the MB to JFC-like orbits (Fernández and Sosa, 2015; Hsieh et al., 2020).

Objectives for this study:

- Simulate the close encounter population with the Earth based on the DFN dataset.
- Identify how the orbits have changed as a result of the close encounters with the Earth.
- Characterise the sub-population of objects redirected onto JFC-like orbits ($2 < T_J < 3$) from asteroid-like orbits ($T_J > 3$).
- Estimate the impact frequency of objects redirected from asteroid-like ($T_J > 3$) to JFC-like orbits ($2 < T_J < 3$); i.e., determine whether this population impacts the Earth frequently enough to be observed by fireball networks.

¹<https://cneos.jpl.nasa.gov/ca/>

4.2 Methods

4.2.1 Desert Fireball Network Data

The DFN is part of the Global Fireball Observatory (GFO), a multi-institutional collaboration of partner fireball networks around the Earth. The DFN, the largest single fireball network in the world, covers about one-third of Australian skies every night using automated high-resolution digital fireball observatories (Bland et al., 2012; Howie et al., 2017a). The DFN collects massive amounts of all-sky imagery that is automatically processed, producing a highly accurate orbital dataset of fireballs (Howie et al., 2017b; Sansom et al., 2015; Jansen-Sturgeon et al., 2019; Towner et al., 2020; Sansom et al., 2019b,a).

4.2.2 Addressing Observational Biases

In this study, we will be producing an artificial dataset of close encounters with the Earth of centimetre to metre-sized objects using data collected by the DFN. The flux of objects observed by the DFN for the previous four years was employed to construct a model of the close encounter population. However, in order to adequately estimate this population, we must first address the intrinsic observational biases of the DFN. Biases are listed below along with how each were considered in this study:

1. Observations are optimised for the size-range specific to meteorite dropping events.
 - The DFN was designed to observe meteorite-dropping fireball events (fireball limiting magnitude ~ 0.5) (Howie et al., 2017a). Thus our dataset represents a subset of larger objects compared to other meteor networks. However, in this study, we are interested in the close encounters of centimetre to metre-sized objects, so this bias is what makes the DFN dataset a good way of understanding these encounters.
2. The DFN exclusively observes at night; i.e. the antihelion direction.

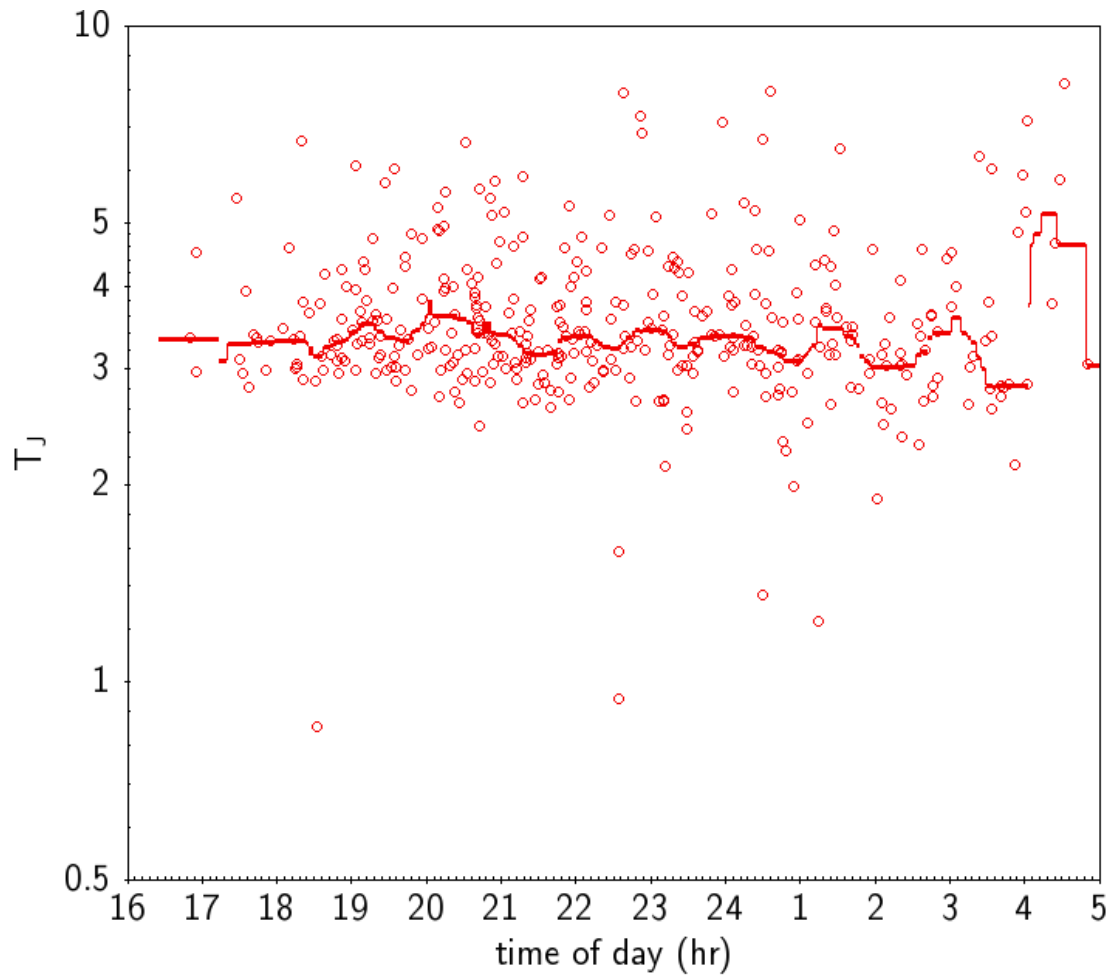


Figure 4.1: Tisserand's parameters (T_J) of the DFN events used in this study along with the time of day in which each fireball was observed. The red line represents the median T_J value.

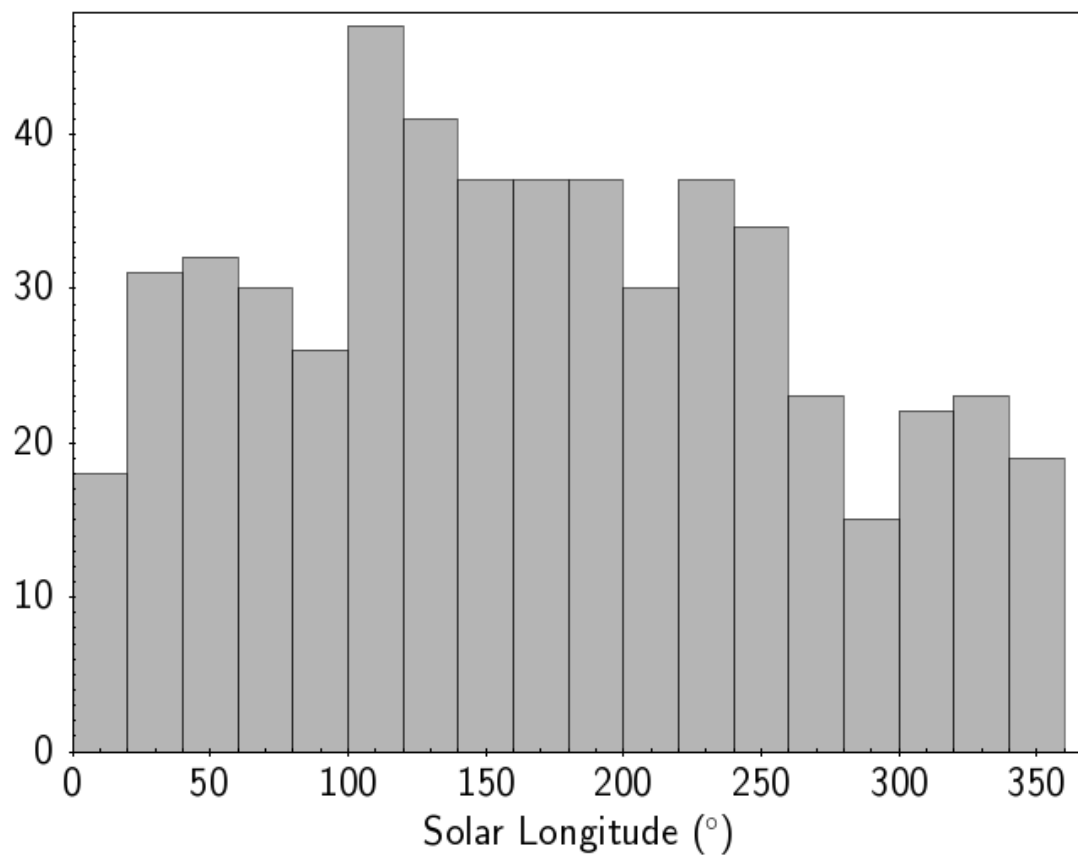


Figure 4.2: Solar longitude distribution for DFN events used to generate artificial close encounter population. There is a noticeable decrease in events detected during the summer months as the duration of the night is shortest.

- We anticipate that this bias will have a negligible effect on the observed population of objects, as it is primarily due to small changes in the orbital geometry at impact (Halliday and Griffin, 1982). As seen in Fig. 4.1, the median Tisserand's parameter does not vary significantly over the course of the night. There is a single aberration, but this is due to low-statistics in this subset only around 4 am.
3. The DFN fireball dataset contains some meteor showers in addition to sporadic events.
 - The methodology used explicitly assumes there are meteoroids in similar nearby orbits. This assumption for the sporadic meteoroids may be an oversimplification. However, given we have the largest self-consistent fireball dataset in the world (most of which are sporadic), this should reduce the bias as much as possible.
 4. The DFN observations vary annually with the seasons.
 - Seasonal weather variation can also have a significant effect on observations, notably cloud cover. However, given the continental-scale and dry climate of Australia, the DFN's four years of observations are negligibly affected. As seen in Fig. 4.2, even though the weather is more inclement during the winter months, there is no effect on the observations. There are, in fact, more observations during the winter, due to the longer nights. The amount of observable hours due to changes in daytime length varies about $\pm 25\%$ for DFN stations annually. This significantly decreases the total number of events observed during the summer; however, $\sim 91\%$ of the events used in this study are sporadic. Thus, since the vast majority of the events are not affected by seasonal biases, we have decided to ignore it. This will cause only a minor underestimate in the summer shower contribution to the close encounter flux.
 5. The sensitivity of the DFN cameras varies due to whether the Moon is above or below the horizon.

- The DFN cameras have lower sensitivity when the Moon is above the horizon and higher sensitivity when it is below. The minimum-size cutoff in this study (0.01 kg) should eliminate these monthly variations as we typically observe masses down to $\sim 1\text{-}2\text{g}$ on moonlit nights. However, there is expected to be a slight underestimate for objects that are tens of grams in mass.
6. Observed meteor velocities vary nightly due to changes in the viewing orientation relative to the Earth's motion around the Sun.
 - This bias should not affect observations on an annual level.
 7. The lower end of the observed size-range varies with impact speed.
 - As noted by Vida et al. (2018), the minimum size object observed by meteor networks decreases as the velocity increases. Nevertheless, this observational bias can be mitigated by setting a minimum size limit when building the artificial dataset in this study (0.01 kg). This mass limit was chosen as it is the limiting mass observed by the DFN. Events in the dataset with nominal masses less than this are likely inaccurate.
 8. Due to gravitational focusing, the Earth is hit by a higher proportion of slower objects.
 - When objects approach the Earth at slower relative velocities, they tend to be more gravitationally focused towards the Earth; slightly increasing the ratio of slow impactors observed. Neglecting to account for gravitational focusing would lead to a slight overestimate of the proportion of slow close encounters. In this study, we used the formulation for the enhancement factor by Öpik (1951) to account for the gravitational focusing. The enhancement factor is thus defined as:

$$H_F = \frac{A_G}{A_{NG}} = \left(1 + \frac{V_{esc}^2}{V_i^2} \right) \quad (4.1)$$

where A_G is the effective cross-sectional area of the Earth due to gravitational focusing, and A_{NG} is the physical cross-section of the Earth.

This ratio can be estimated using the escape velocity at the surface of the Earth (V_{esc}) and the initial velocity of the meteoroid before the encounter (V_i). This enhancement factor was used to normalise the artificial close encounter flux generated, producing better relative abundances of certain kinds of encounters (i.e., not overestimating the number of slow-approachers).

4.2.3 Creating the Close Encounter Dataset

The DFN is designed to observe and triangulate fireballs over Australia. Using the data collected over the last four years, assuming that the flux is reasonably representative of the global flux, we can extrapolate outward and try to characterise the close encounter flux for this size range. The events used to generate our model were limited to those with a predicted pre-atmospheric mass ranging from 0.01 – 100 kg. This size range was chosen to limit bias at small sizes, and it is the most well-measured range within the DFN dataset. This results in a set of 581 fireball events with which to initiate our model. Of these events, 50 ($\sim 9\%$) are associated with established and non-established showers.

For each event, the predicted state of the meteoroid at the beginning of the luminous phase was integrated back until it was at least three lunar distances (LD) away from the Earth. This procedure was chosen in order to primarily limit the close encounters to a minimum orbital intersection distance (MOID) of within about 1.5 LD, as the orbits will be decreasingly affected with larger MOID values. For the orbital integrations, we used the IAS15 integrator described in Rein and Spiegel (2015) including perturbations from all the planets in the Solar System as well as the Moon. At this point, a cloud of 4000 particles were generated uniformly by varying the position relative to the actual prediction of the meteoroid by ± 1.0 LD in each Cartesian direction in the heliocentric frame, without varying the velocity. A Hill radius for the Earth is ~ 3.89 LD, however we decided to integrate slightly less to save on computation time. We justified this decision by finding that, for all DFN events, the Tisserand's parameter is typically $> 99\%$ similar to its pre-encounter value after reaching two LD away from the Earth.

These particles were then integrated forward in time until they were at least three LD away from the Earth again. Any particles which came within 200 km of the Earth's surface were removed from the simulation, effectively removing impacts and grazing events. In total, 2.3 million particles were integrated to estimate the close encounter flux. This flux was then normalised using the estimated enhancement factor for each event.

In this model, we explicitly assume that each particle in the simulation represents a group of meteoroids. This is done to make the simulation feasible, as there are expected to be hundreds of billions of close encounters within this size-range annually. The size of the base dataset used (581 fireballs) is very small compared to the number of objects having close encounters with the Earth, however, the general trends observed by the model are likely representative.

In order to estimate the close encounter flux of the Earth, we derived the following equation to calculate the cumulative flux distribution:

$$Flux(r) = \left(\frac{r^3}{r_{\oplus}^3} \right) \times N_{H_F} \times \nu_T \quad (4.2)$$

$$where \quad N_{H_F} = \left[1 + (H_F - 1) \left(\frac{r_{\oplus}^3}{r^3} \right) \right] \quad (4.3)$$

N_{H_F} is the scaling factor included to account for the effect of gravitational enhancement at smaller geocentric distances, r is the distance from the Earth's centre, r_{\oplus} is the radius of the Earth, H_F is the enhancement factor, and ν_T is the total terrestrial flux estimated for the top of the atmosphere by Bland and Artemieva (2006). As $r \rightarrow r_{\oplus}$ the scaling factor $N_{H_F} \rightarrow H_F$, whereas as $r \rightarrow \infty$ then $N_{H_F} \rightarrow 1.0$ (i.e., no enhancement when encounters are more distant).

We then calculated the cumulative flux for each particle's MOID, and took the difference between each cumulative flux value to determine the number of objects represented by each particle. The mass and mass errors were determined using the pre-atmospheric masses and errors calculated by the DFN in combination with the terrestrial mass flux estimate for the given size range (0.01 – 100 kg) (Sansom et al., 2015; Bland and Artemieva, 2006).

4.3 Results and Discussion

4.3.1 Orbital Changes

Using global flux estimates from Bland and Artemieva (2006) along with DFN data to extrapolate, we were able to characterise the $\sim 10^{11}$ predicted close encounters that occur annually within 1.5 LD ranging from 0.01 – 100 kg. A vast majority of the objects that encounter the Earth do not have appreciable changes to their orbits. As seen in Fig. 4.3, the change in orbital elements are centred on zero with greater magnitude alterations occurring at smaller MOID values ($1/r^2$ relationship). Every object gains or loses energy, but usually a negligible amount. For example, for all objects coming within 1.5 LD, the median changes found in the semi-major axis, eccentricity, and inclination were 0.019 AU, 0.0022, and 0.11° respectively. However, for encounters within 0.1 LD, the median changes were 0.27 AU, 0.033, and 1.6° respectively.

The two factors controlling this process are the MOID of the encounter and the pre-encounter velocity of the meteoroid, as seen in Fig. 4.4. This change in the orbital parameters, as shown in Fig. 4.5, diffuses the objects along the lines of equal perihelion or aphelion. As the black ‘clouds’ of particles generated in the model encounter the Earth, they diffuse outward (grey) where they could be inserted into a resonance or the path of another planet (Fig. 4.5b). If these alterations are significant, the meteoroid’s T_J value could change enough to dynamically reclassify the orbit (Fig. 4.6). This crossover is especially prevalent within the size-range we investigate since many of the objects seen impacting the atmosphere by the DFN have T_J values around ~ 3 , which is approximately the boundary typically used to separate asteroids and JFCs.

Within this study, we were particularly interested in assessing the sub-population of Earth-scattered objects that are redirected from asteroid-like orbits ($T_J > 3$) to JFC-like orbits ($2 \geq T_J \leq 3$). Fig. 4.6 shows there are quite a significant fraction of close encounters that undergo this transformation in region A. In total, we calculate the net annual object flux for this population is about 2.5×10^8 objects per year. This number also takes into account objects coming from JFC-like orbits

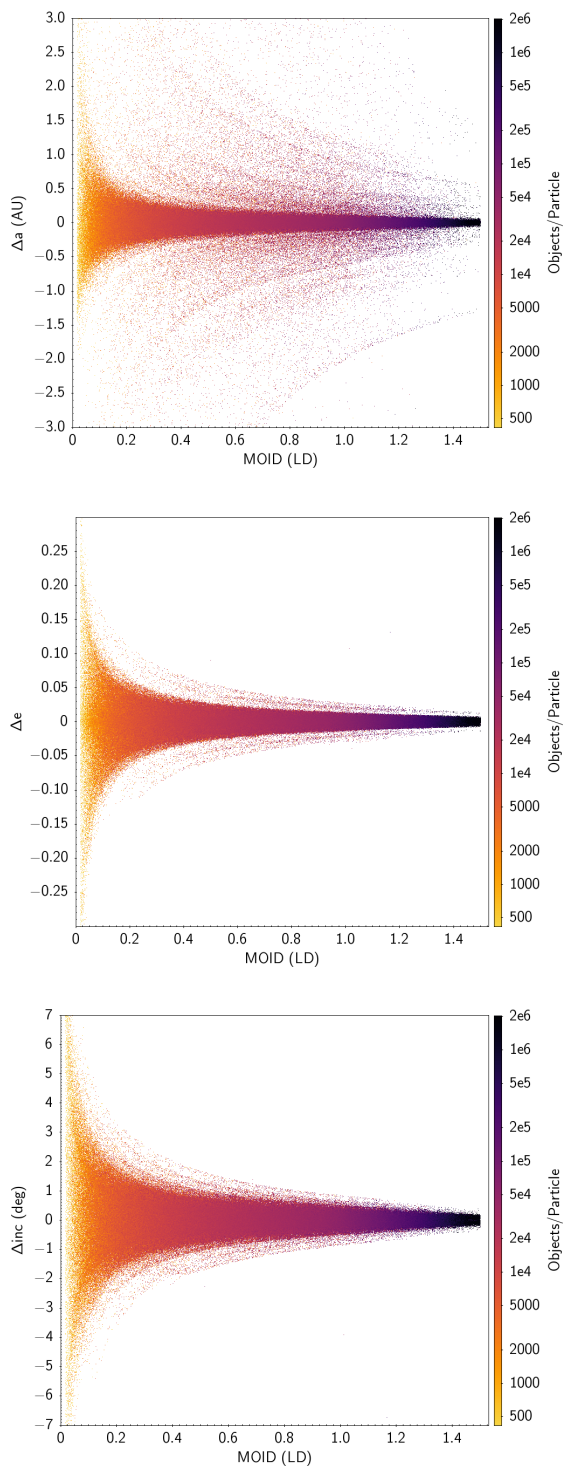


Figure 4.3: Change in semi-major axis (a), eccentricity (e), and inclination (inc) for every particle in our simulation as a function of the minimum orbital intersection distance (MOID) in Lunar Distances (LD). The color bar indicates the number of objects each particle represents annually.

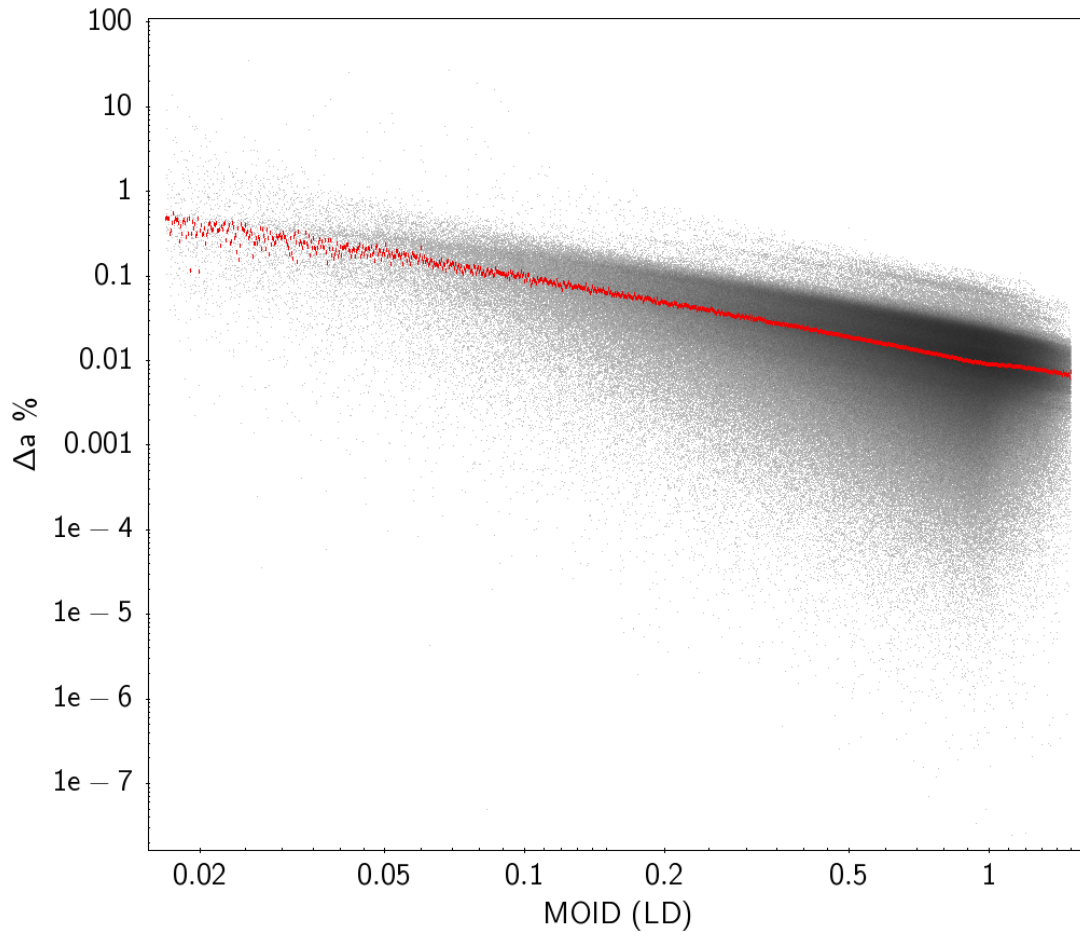
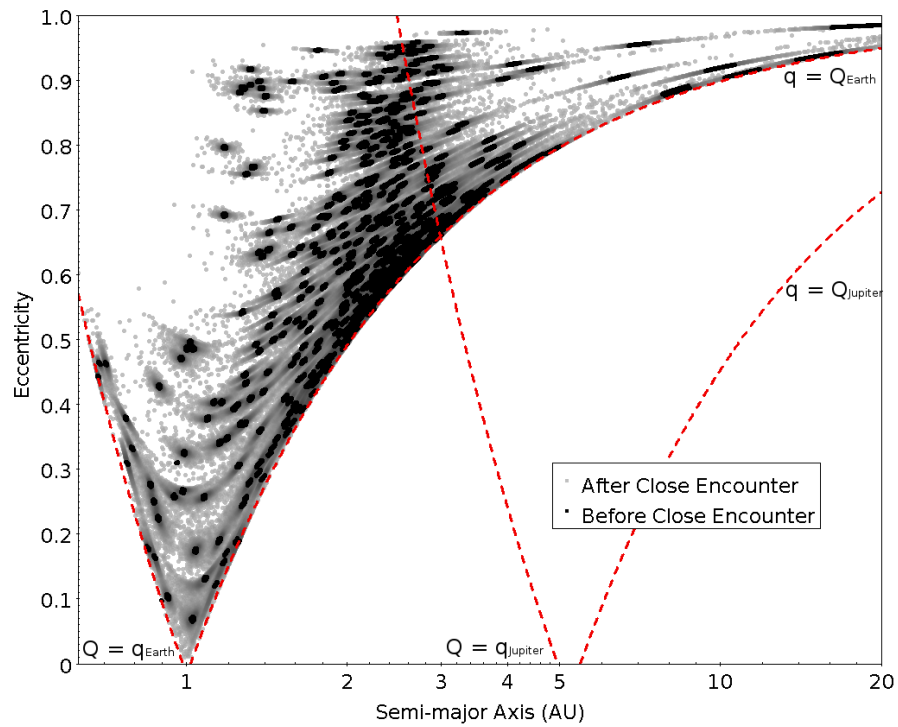


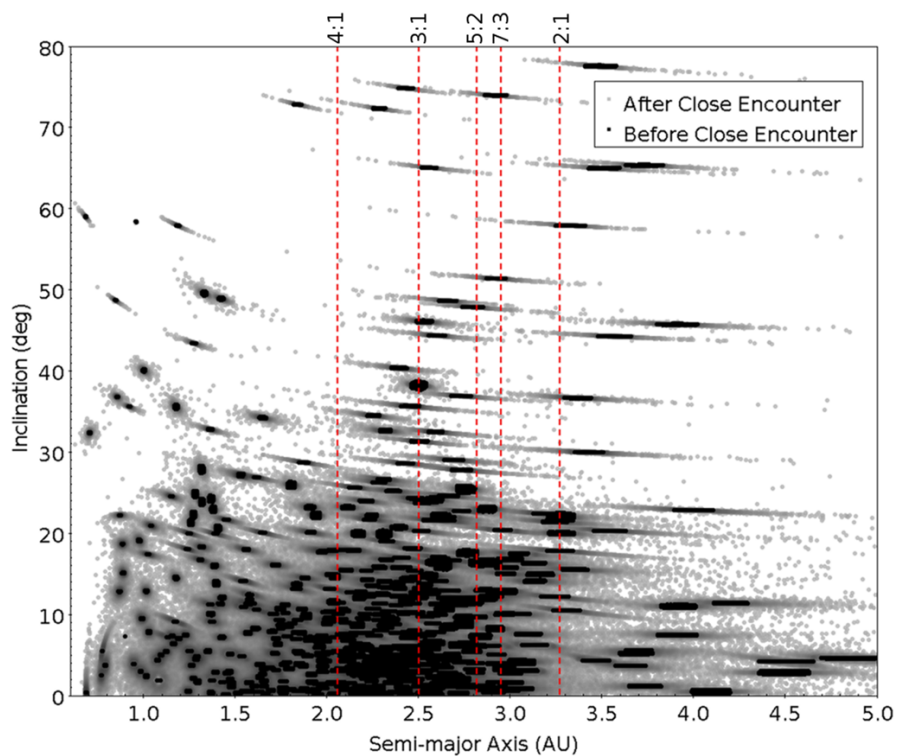
Figure 4.4: Percentage change in the particles' semi-major axis (a) varying according to the minimum orbital intersection distance (MOID). The red points indicate the median change. The largest change in orbital energy is logically experienced by objects with the closest encounters.

onto asteroidal ones (region B in Fig. 4.6). This flux is net positive onto JFC-like orbits because the most likely objects to have a close encounter with the Earth are objects with orbits most similar to the orbit of the Earth. As shown in Carusi and Dotto (1996), since orbits of near-Earth asteroids are more stable than JFCs and have orbits more like the Earth's, they are likely to encounter the Earth more regularly.

For a more useful interpretation of the same data shown in Fig. 4.6, please refer to the Appendix where there are three tables describing the mass and object flux.



(a)



(b)

Figure 4.5: 4.5a and 4.5b show the semi-major axis vs. eccentricity and inclination respectively for all the test particles in the model (2.3 million particles) before and after having a close encounter with the Earth. The grouping of black particles tend to get dispersed along lines of equal aphelion/perihelion after having a close encounter (grey particles). There is typically minimal change in the inclination, however, as $a \sim 1$ the changes in inclination becomes more significant.

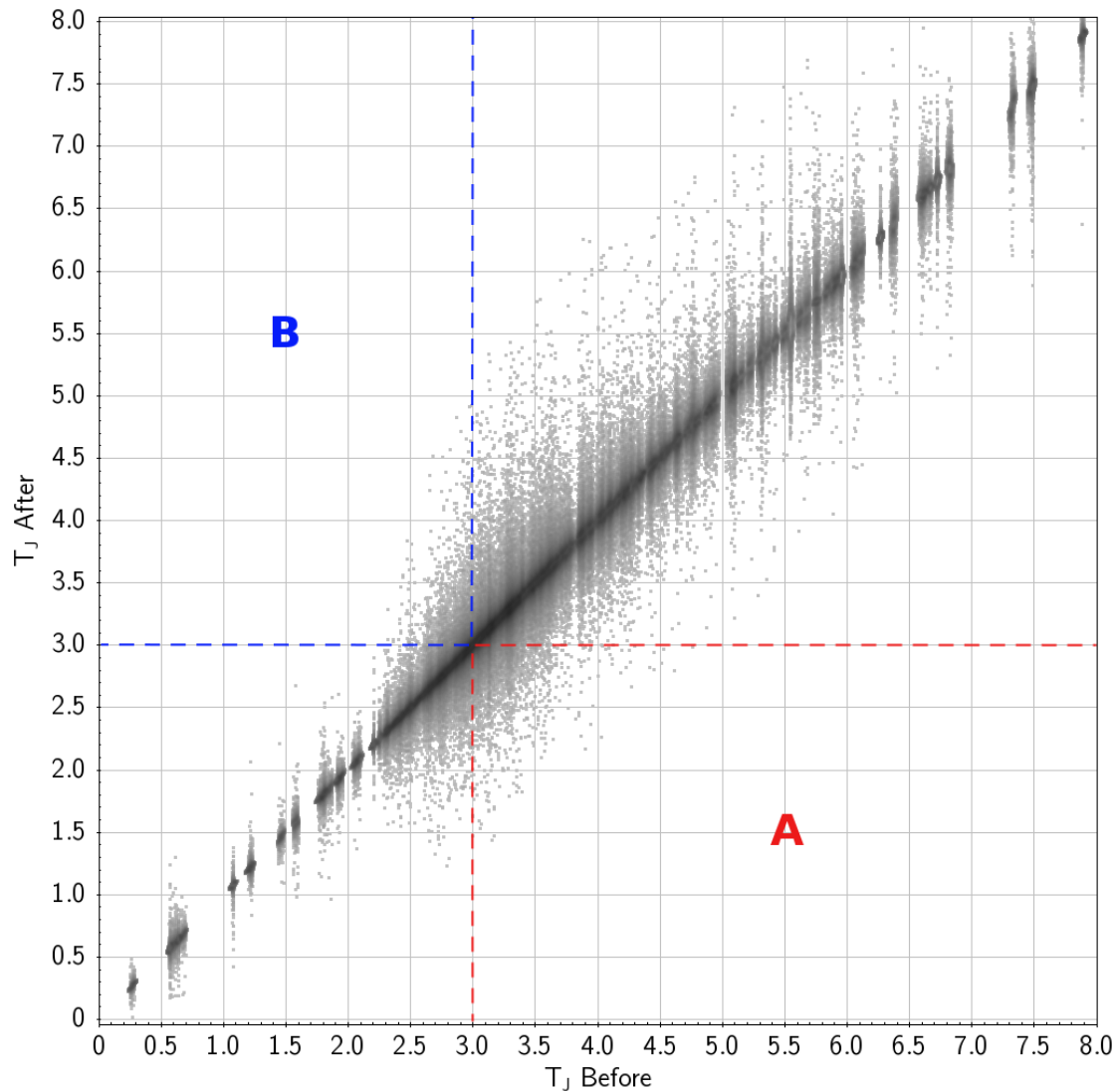


Figure 4.6: Close encounter simulation particles energy change in terms of Tisserand's parameter (T_J). The T_J value before and after encountering the Earth are the x and y axis respectively. Region A denotes contains particles that were transferred from a asteroid-like orbit to a JFC-like one, whereas region B contains particles that underwent the reverse transfer.

4.3.2 Cumulative Size-Frequency Distributions

From our model, we were able to estimate the cumulative size-frequency distribution (CSD) for the terrestrial close encounter population along with its sub-populations of interest. Annually, we have found that within 1.5, 0.5, and 0.1 LD the average largest encounter predicted respectively are > 100 m, ~ 50 m, and $10 - 20$ m in diameter. A more thorough analysis concerning the entire DFN's CSD will be addressed in a separate study (Sansom et al. in prep.). For the remainder of this study, we have focused on understanding the redirected smaller sub-population modelled.

Similar to Bland and Artemieva (2006), when characterizing the resulting CSDs from the close encounter model, the range was split into appropriate branches. These branches each have distinct slopes, and these are indicative of some underlying change in the production or physical evolution of objects within that size range. As seen in Fig. 4.7, we have split the CSD for objects going from asteroidal to JFC orbits into two branches. These branches, labeled A and B, have slopes of -1.21 ± 0.01 and -7.22 ± 1.30 , respectively. This trend, a shallower slope and then a sudden increase in slope at ~ 3 kg, is very similar to the top of the atmosphere flux found in Bland and Artemieva (2006) within the given size-range. However, the estimated slopes for the asteroidal to JFC-like flux are different than those in Bland and Artemieva (2006), indicating some size-dependence. The slope for branch A (< 0.1 m in diameter), is slightly shallower for the scattered asteroidal to JFC population, -0.410 ± 0.001 vs. -0.480 with $\log(\text{mass})$ as the x-axis. Whereas branch B (> 0.1 m in diameter) is exceptionally steep compared to the same size range in Bland and Artemieva (2006), -2.277 ± 0.103 vs. -0.926 with $\log(\text{mass})$ as the x-axis. This increase in the discrepancy between branches A and B is indicative that this sub-population (compared to all close encounters) is proportionally more weighted towards larger masses. This size sorting likely is caused by the increase in average mass for meteoroids from asteroidal sources compared to cometary ones. Moreover, these meteoroids are dispersed on a multitude of orbits, some of which may be indistinguishable from actual JFCs (Fig. 4.8) as they are likely to have multiple close encounters with Jupiter in their lifetime (Tancredi,

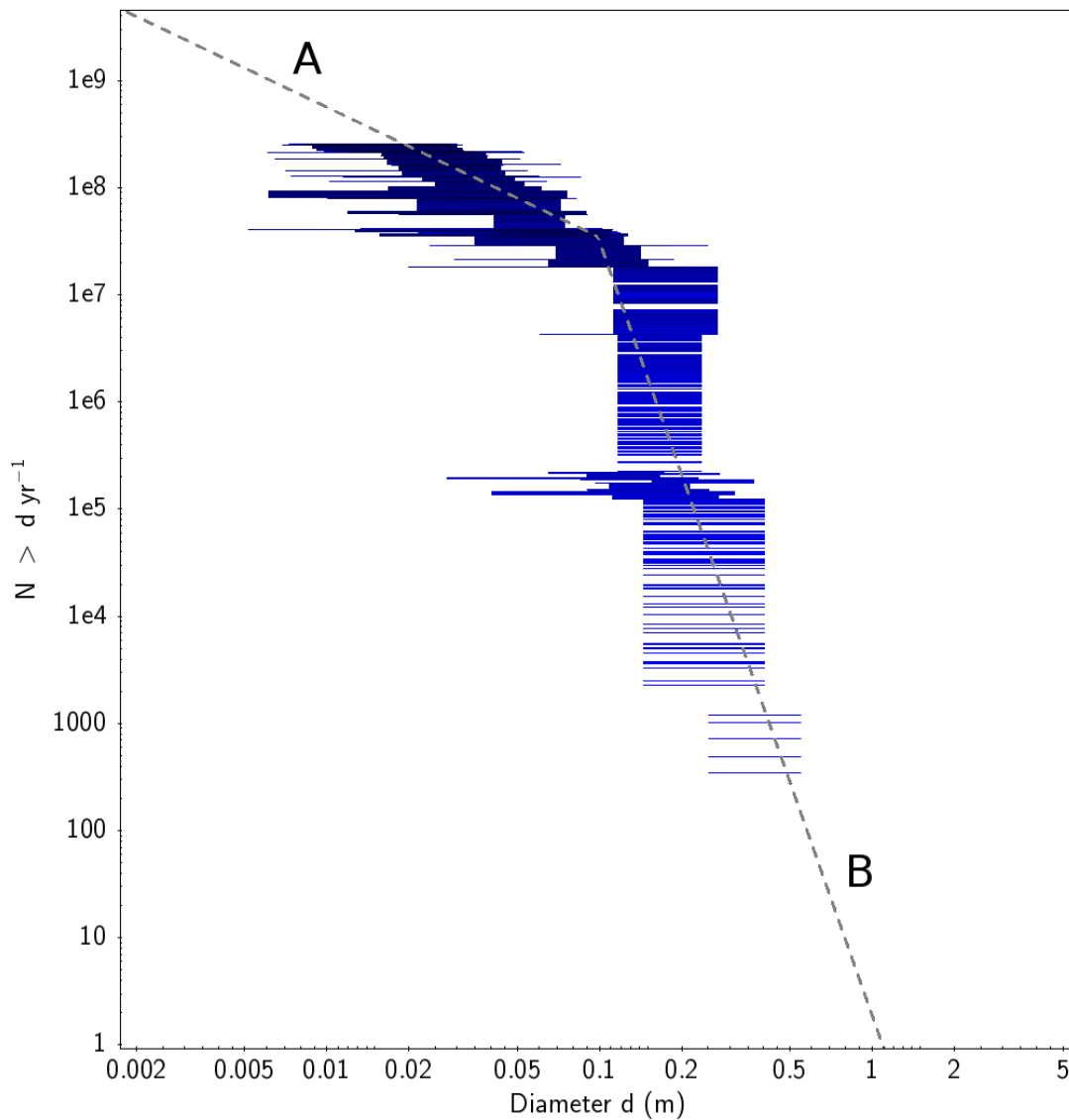


Figure 4.7: Cumulative size frequency distribution of annual close encounters < 1.5 LD redirected from asteroidal to JFC-like orbits. Horizontal lines are indicative of uncertainty in the diameter. This sub-population only represents $\sim 0.1\%$ of the close encounters given the maximum MOID. The slopes of branches A and B are -1.21 ± 0.01 and -7.22 ± 1.30 respectively. Compared to the entire close encounter flux, the B branch is steeper and the A branch is shallower. There are proportionally more higher mass meteoroids.

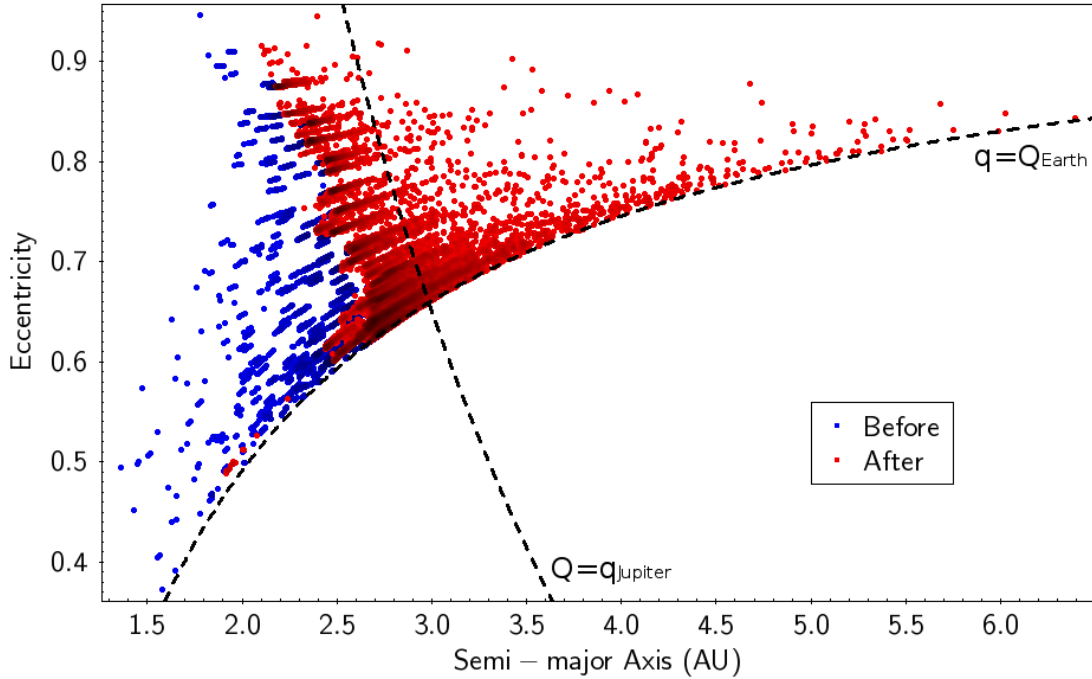


Figure 4.8: Semi-major axis vs. eccentricity for particles that were transferred from asteroidal like orbits ($T_J > 3$) to JFC-like orbits ($2 < T_J < 3$). As shown by the particles lying on or past the perihelion of Jupiter, close encounters transfer objects onto orbits indistinguishable at times from native JFCs.

2014).

In the metre size-range, there is no consistent mechanism to produce meteoroids from comets besides catastrophic breakup (Jenniskens, 2004; Jenniskens and Lyytinen, 2005). Furthermore, even if there exist centimetre-metre sized objects from breakup events, the physical lifetimes are predicted to be extremely short (Levison and Duncan, 1997; Beech and Nikolova, 2001; Boehnhardt, 2004). Whereas, this group of predominantly genetically ‘asteroidal’ material now on JFC-like orbits could survive much longer than any cometary meteoroids. Assuming the physical lifetime of these objects is much longer than the dynamic lifetime, these scattered meteoroids should exist on JFC-like orbits for about $10^5 - 10^6$ years based on previous dynamical models (Nugent et al., 2012; Vokrouhlický et al., 2015; Granvik et al., 2018). This would result in a steady-state population of scattered asteroidal meteoroids on JFC-like orbits of about $10^{13} - 10^{14}$ objects annually with perihelia near the Earth. Considering the uncertainty of the CSD slope of this population, if extrapolated, the most massive steady-state object is

predicted to be $10^0 - 10^2$ m in diameter based on our model.

Multiple studies have also found that there exists high-albedo ($p_v > 0.1$) asteroids on JFC-like orbits in near-Earth space (perihelion distance, $q < 1.3$ au) with diameters < 3 km (Kim et al., 2014; Licandro et al., 2016). These authors argued that these objects could have migrated into this region via non-gravitational effects (such as the Yarkovsky effect) due to their smaller size, higher reflectance, and smaller perihelion distance. These objects can also be transferred to JFC-like orbits directly via MMRs in the outer MB (like the 2:1 and 9:4 MMRs) (Fernández et al., 2002, 2014; Fernández and Sosa, 2015; Hsieh et al., 2020). While most outer-MB objects are dark with low-albedos ($p_v < 0.1$), some higher-albedo objects have also been observed to exist (Masiero et al., 2014). It is uncertain whether this population is large/efficient enough to account for the high-albedo objects on JFC-like orbits near the Earth. The high-albedo objects analysed in Kim et al. (2014) also only seem to be present for bodies with $q < 1.3$ au - an observation not due to detection bias as high-albedo objects with larger perihelia would have been detected. Alternatively, these high-albedo near-Earth objects in JFC-like orbits could result from close encounters with the Earth. In Hsieh et al. (2020), they found that close encounters with the terrestrial planets or non-gravitational forces were capable of generating a reasonable number of objects from the Themis family to go onto JFC-like orbits. This would not be entirely unprecedented; encounters with the Earth at the same scales have also been linked with refreshing the surfaces of some asteroids (Binzel et al., 2010). In Bland and Artemieva (2006), they found that the slope of the CSD for impactors of the upper atmosphere decreased significantly as the objects grew to 1.7×10^{10} kg (~ 88 m assuming a 3500 kg m^{-3} spheroid). Therefore, if this trend persists within the population scattered onto JFC orbits, it is possible that this population could provide an explanation for the asteroids observed by Kim et al. (2014). However, given the uncertainty in slope B (Fig. 4.7), this cannot be shown in this study.

4.3.3 Impact Frequency

Finally, we wanted to estimate the impact frequency of the population of objects scattered from asteroid to JFC-like orbits. The impact frequency is crucial as it determines whether this meteoroid population is observable by fireball networks. Thus, it could partially explain the durable JFC fireballs that have been observed. We employed the methodology described in Greenberg (1982) and Bottke et al. (1994), where the impact and close encounter probabilities were determined for Earth and Jupiter geometrically assuming uniform precession of nodes and apsides. For a concise explanation of this methodology, please refer to Appendix A found in Le Feuvre and Wieczorek (2008). To estimate the impact frequency, we calculated the 3 Hill radii close encounter frequency with Jupiter for all the test particles and the impact frequency with the Earth. Particles with close encounters with Jupiter were assumed to be removed from the Earth-crossing population during the encounter. In contrast, particles that avoid having close encounters with Jupiter were assumed to have Earth-crossing lifetimes of $10^5 - 10^6$ years according to published outer-MB NEO dynamical lifetimes (Nugent et al., 2012; Vokrouhlický et al., 2015; Granvik et al., 2018).

Upon investigation, we found that only $\sim 30\%$ of the asteroidal to JFC scattered population were capable of having close encounters with Jupiter. Thus, despite all the particles being within the range $2 < T_J < 3$, most of the objects likely still evolve on very predictable asteroid-like orbits like described in Tancredi (2014). The 30% that do experience close encounters do so every 10-200 years, with the median time being 50 years. These objects will likely evolve in a way indistinguishable from a comet from the scattered-disk, similar to the grazing meteoroid observed by the DFN in 2017 (Shober et al., 2020). However, given the shorter residence times, this unstable portion of the scattered population makes up minor fraction of the steady-state population.

Given the annual flux onto cometary orbits along with the estimated residence times from encounter and impact frequencies, we find that there are approximately $10^3 - 10^4$ impacts annually originating from this population. At a minimum, this means that the DFN should observe (taking into account daylight hours,

weather, and station malfunctions) 1 – 10 events per year. Based on our model, this minimum value indicates that this population is likely observed regularly by meteor and fireball networks. The test particles with the highest probabilities of impacting the Earth after being scattered were on orbits with low-inclinations ($< 5^\circ$), lower eccentricity, and perihelia near 1 au. Therefore, we predict that fireball networks should observe meteoroids that were previously scattered; however, all will be dynamically very consistent with asteroidal debris.

4.3.4 Additional Results

In addition to flux onto JFC-like orbits, we also found a net-positive annual flux onto Aten-type orbits. For similar reasons to the net flux onto JFC orbits, the model suggests it is slightly more favourable to go from an Apollo-type to an Aten-type orbit than the reverse. In total, we estimate about 10^7 objects are annually transferred to Aten-type orbits via a close encounter, but due to the low number statistics this value is tenuous. Unfortunately, we were unable to further explore this sub-population in detail as the uncertainties for the CSD were considerable. However, it is possible that some of these may eventually evolve onto Atira-type orbits via some combination of planetary perturbations or close encounters. The objects could also evolve periodically between classes if in a Kozai resonance (Greenstreet et al., 2012).

Small debris in the Solar System always eventually impacts a planet, impacts the Sun, or is ejected from the Solar System. Most of the material that is ejected is typically through close encounters with Jupiter, but our model also predicts a modest ejection rate of 10^4 objects annually resulting from close encounters with the Earth. This value is very tentative due to the small sample size of such objects in the model input data.

4.4 Future Work

We have also studied the dynamical and physical characteristics of > 0.01 kg meteoroids from the DFN dataset with JFC-like orbits (Shober et al. in prep.),

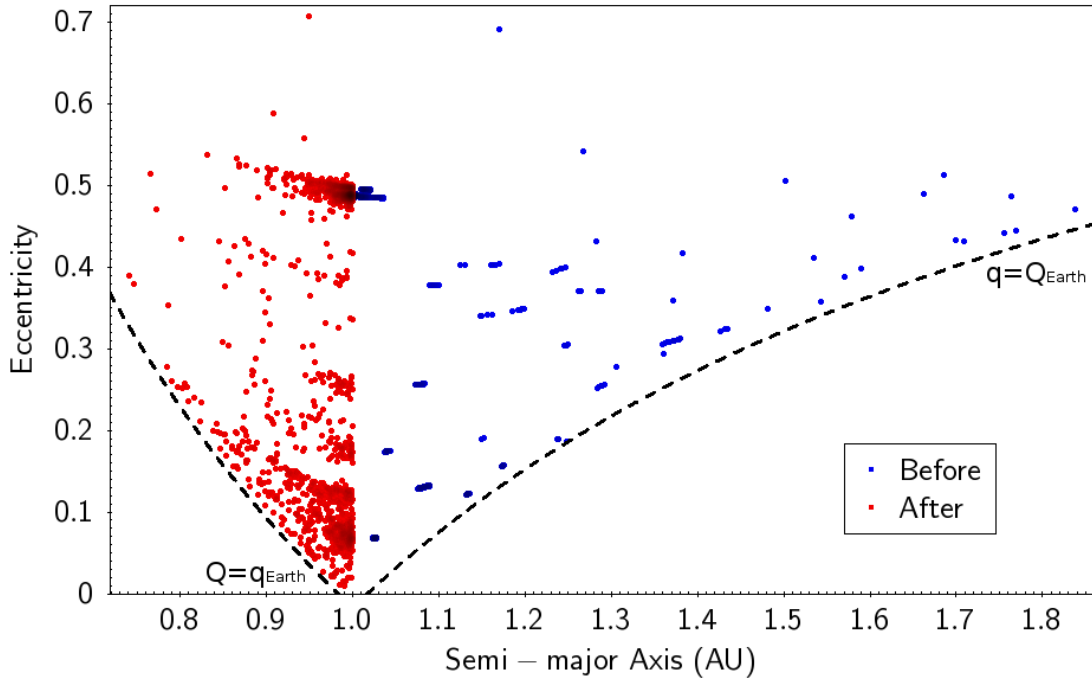


Figure 4.9: Semi-major axis vs. eccentricity for particles in model that were transferred onto Aten-type orbits as a result of the close encounter with the Earth. Meteoroids with similar orbits to the Earth ($a \sim 1 - 2$ au), are the most likely to undergo this process.

In this other study, we compared the results from the close encounter model to DFN observations, and tested our hypothesis that asteroidal material is dominant for orbits with $2 < T_J < 3$. In the future, we would also like to check our model by using steady-state NEO models (such as Granvik et al. (2018)) to characterise the close encounter flux at the Earth.

4.5 Conclusions

In this study, we produced a model of close terrestrial encounters within the 0.01 – 100 kg size-range by using DFN data along with global flux studies (Bland and Artemieva, 2006). Close encounters within the model were limited to < 1.5 LD, as farther encounters are less likely to have significant orbital alterations. The primary results include:

- there are approximately 1.6×10^{11} objects 0.01 – 100 kg that have encounters within 1.5 LD of the Earth every year based on extrapolating top of the

atmosphere flux rates found in Bland and Artemieva (2006).

- 2.5×10^8 objects annually are estimated to be transferred from asteroidal orbits ($T_J > 3$) to JFC-like orbits ($2 < T_J < 3$) (0.1% of total flux).
 - given a dynamic lifetime of $10^5 - 10^6$ years (Nugent et al., 2012; Vokrouhlický et al., 2015; Granvik et al., 2018), then there exists a steady-state population of $10^{13} - 10^{14}$ objects.
 - using the methodologies described by Greenberg (1982) and Bottke et al. (1994), we calculated the 3 Hill-radii encounter for Jupiter and impact frequencies for the Earth for all particles transferred from $T_J > 3$ to $2 < T_J < 3$. Using these values along with the predicted population size from the model, we found that $\sim 30\%$ of objects regularly encounter Jupiter and likely evolve chaotically on short-timescales. The remaining $\sim 70\%$ of objects avoid close encounters and persist on more stable orbits, evolving in a characteristically asteroidal manner.
 - approximately $10^3 - 10^4$ impacts occur from this population annually. Thus, the DFN should observe 1 – 10 fireballs every year with $2 < T_J < 3$ transferred from the MB.
 - extrapolating our CSD slope to larger sizes, the largest steady-state object is $10^0 - 10^2$ m in diameter given the slope uncertainty (-7.22 ± 1.30).
- The model predicts that $\sim 10^7$ objects are annually transferred onto Aten-type orbits, where some may evolve to Atira-type orbits.
- $\sim 10^4$ meteoroids are predicted to be directly ejected from the Solar System annually via a close encounter with the Earth, but this value is questionable due to small number statistics.

Observations of fireballs can be used to understand the sources of meteorites, and connect them to the observed asteroidal (or possibly cometary) parent body that they originate from. The speculation over whether or not cometary meteorites exist or can exist has been discussed for decades. However, in this study we have

found there should be many genetically asteroidal meteoroids on JFC-like orbits due to close encounters with the Earth that likely impact the Earth regularly. Compounded with material diffusing out from the MB (Fernández and Sosa, 2015; Hsieh et al., 2020), it may be expected that meteorites from JFC-like orbits ($2 < T_J < 3$) would be quite ordinary.

Acknowledgements

We are thankful for the reviewer M. Campbell-Brown and her valuable comments on the original manuscript which improved the paper. The authors would also like to thank P. Brown for his assistance and advice during the early stages of this study. This work was funded by the Australian Research Council as part of the Australian Discovery Project scheme (DP170102529). SSTC authors acknowledge institutional support from Curtin University. This work was supported by resources provided by the Pawsey Supercomputing Centre with funding from the Australian Government and the Government of Western Australia. This research made use of TOPCAT for visualisation and figures (Taylor, 2005). This research also made use of Astropy, a community-developed core Python package for Astronomy (Robitaille et al., 2013). Simulations in this paper made use of the REBOUND code which is freely available at <http://github.com/hannorein/rebound> (Rein and Liu, 2012).

4.6 Data availability

The data underlying this article were accessed from Desert Fireball Network (<https://dfn.gfo.rocks/>). The derived data generated in this research will be shared on reasonable request to the corresponding author.

4.7 Close Encounter Flux Tables

Bibliography

- M. Beech and S. Nikolova. The endurance lifetime of ice fragments in cometary streams. *Planetary and Space Science*, 49(1):23–29, 2001.
- R. P. Binzel, A. Morbidelli, S. Merouane, F. E. DeMeo, M. Birlan, P. Vernazza, C. A. Thomas, A. S. Rivkin, S. J. Bus, and A. T. Tokunaga. Earth encounters as the origin of fresh surfaces on near-earth asteroids. *Nature*, 463(7279):331–334, 2010.
- P. Bland, P. Spurný, A. Bevan, K. Howard, M. Towner, G. Benedix, R. Greenwood, L. Shrubený, I. Franchi, G. Deacon, et al. The australian desert fireball network: a new era for planetary science. *Australian Journal of Earth Sciences*, 59(2):177–187, 2012.
- P. A. Bland and N. A. Artemieva. The rate of small impacts on earth. *Meteoritics & Planetary Science*, 41(4):607–631, 2006.
- H. Boehnhardt. Split comets. *Comets II*, 745:301–316, 2004.
- W. F. Bottke, M. C. Nolan, R. Greenberg, and R. A. Kolvoord. Velocity distributions among colliding asteroids. *ICARUS-NEW YORK-*, 107:255–255, 1994.
- P. Brown, P. Wiegert, D. Clark, and E. Tagliaferri. Orbital and physical characteristics of meter-scale impactors from airburst observations. *Icarus*, 266:96–111, 2016.
- H. Campins and T. D. Swindle. Expected characteristics of cometary meteorites. *Meteoritics & Planetary Science*, 33(6):1201–1211, 1998.

- A. Carusi and E. Dotto. Close encounters of minor bodies with the earth. *Icarus*, 124(2):392–398, 1996.
- R. P. Di Sisto, J. A. Fernández, and A. Brunini. On the population, physical decay and orbital distribution of jupiter family comets: Numerical simulations. *Icarus*, 203(1):140–154, 2009.
- M. J. Duncan and H. F. Levison. A disk of scattered icy objects and the origin of jupiter-family comets. *Science*, 276(5319):1670–1672, 1997.
- J. Fernández, G. Tancredi, H. Rickman, and J. Licandro. The population, magnitudes, and sizes of jupiter family comets. *Astronomy and Astrophysics*, 352:327–340, 1999.
- J. A. Fernández and A. Sosa. Jupiter family comets in near-earth orbits: Are some of them interlopers from the asteroid belt? *Planetary and Space Science*, 118:14–24, 2015.
- J. A. Fernández, T. Gallardo, and A. Brunini. Are there many inactive jupiter-family comets among the near-earth asteroid population? *Icarus*, 159(2):358–368, 2002.
- J. A. Fernández, A. Sosa, T. Gallardo, and J. N. Gutiérrez. Assessing the physical nature of near-earth asteroids through their dynamical histories. *Icarus*, 238:1–12, 2014.
- Y. Fernández, M. Kelley, P. Lamy, I. Toth, O. Groussin, C. Lisse, M. F. A’Hearn, J. Bauer, H. Campins, A. Fitzsimmons, et al. Thermal properties, sizes, and size distribution of jupiter-family cometary nuclei. *Icarus*, 226(1):1138–1170, 2013.
- G. J. Flynn, G. J. Consolmagno, P. Brown, and R. J. Macke. Physical properties of the stone meteorites: Implications for the properties of their parent bodies. *Geochemistry*, 78(3):269–298, 2018.

- R. S. Gomes, J. A. Fernández, T. Gallardo, and A. Brunini. The scattered disk: Origins, dynamics, and end states. *The Solar System Beyond Neptune*, pages 259–273, 2008.
- M. Gounelle, A. Morbidelli, P. A. Bland, P. Spurny, E. D. Young, and M. Sephton. Meteorites from the outer solar system. *The solar system beyond Neptune*, pages 525–541, 2008.
- M. Granvik and P. Brown. Identification of meteorite source regions in the solar system. *Icarus*, 311:271–287, 2018.
- M. Granvik, A. Morbidelli, R. Jedicke, B. Bolin, W. F. Bottke, E. Beshore, D. Vokrouhlický, D. Nesvorný, and P. Michel. Debaised orbit and absolute-magnitude distributions for near-earth objects. *Icarus*, 312:181–207, 2018.
- R. Greenberg. Orbital interactions—a new geometrical formalism. *The Astronomical Journal*, 87:184–195, 1982.
- S. Greenstreet, H. Ngo, and B. Gladman. The orbital distribution of near-earth objects inside earth’s orbit. *Icarus*, 217(1):355–366, 2012.
- I. Halliday and A. A. Griffin. A study of the relative rates of meteorite falls on the earth’s surface. *Meteoritics*, 17(1):31–46, 1982.
- R. M. Howie, J. Paxman, P. A. Bland, M. C. Towner, M. Cupak, E. K. Sansom, and H. A. Devillepoix. How to build a continental scale fireball camera network. *Experimental Astronomy*, 43(3):237–266, 2017a.
- R. M. Howie, J. Paxman, P. A. Bland, M. C. Towner, E. K. Sansom, and H. A. Devillepoix. Submillisecond fireball timing using de bruijn timecodes. *Meteoritics & Planetary Science*, 52(8):1669–1682, 2017b.
- H. H. Hsieh and N. Haghhighipour. Potential jupiter-family comet contamination of the main asteroid belt. *Icarus*, 277:19–38, 2016.
- H. H. Hsieh, B. Novaković, K. J. Walsh, and N. Schörghofer. Potential themis-family asteroid contribution to the jupiter-family comet population. *The Astronomical Journal*, 159(4):179, 2020.

- D. W. Hughes. The variation of short-period comet size and decay rate with perihelion distance. *Monthly Notices of the Royal Astronomical Society*, 346(2): 584–592, 2003.
- T. Jansen-Sturgeon, E. K. Sansom, and P. A. Bland. Comparing analytical and numerical approaches to meteoroid orbit determination using hayabusa telemetry. *Meteoritics & Planetary Science*, 54(9):2149–2162, 2019.
- P. Jenniskens. 2003 eh1 is the quadrantid shower parent comet. *The Astronomical Journal*, 127(5):3018, 2004.
- P. Jenniskens and P. M. M. Jenniskens. *Meteor showers and their parent comets*. Cambridge University Press, 2006.
- P. Jenniskens and E. Lyytinen. Meteor showers from the debris of broken comets: D/1819 w1 (blanpain), 2003 wy25, and the phoenicids. *The Astronomical Journal*, 130(3):1286, 2005.
- Y. Kim, M. Ishiguro, and F. Usui. Physical properties of asteroids in comet-like orbits in infrared asteroid survey catalogs. *The Astrophysical Journal*, 789(2): 151, 2014.
- L. Kresák. The lifetimes and disappearance of periodic comets. *Bulletin of the Astronomical Institutes of Czechoslovakia*, 32:321–339, 1981.
- L. Kresák and M. Kresáková. Secular brightness decrease of periodic comets. *Icarus*, 86(1):82–92, 1990.
- M. Le Feuvre and M. A. Wieczorek. Nonuniform cratering of the terrestrial planets. *Icarus*, 197(1):291–306, 2008.
- H. F. Levison and M. J. Duncan. From the kuiper belt to jupiter-family comets: The spatial distribution of ecliptic comets. *Icarus*, 127(1):13–32, 1997.
- J. Licandro, V. Alí-Lagoa, G. Tancredi, and Y. Fernández. Size and albedo distributions of asteroids in cometary orbits using wise data. *Astronomy & Astrophysics*, 585:A9, 2016.

- J. M. Madiedo, J. M. Trigo-Rodríguez, J. Zamorano, L. Ana-Hernández, J. Izquierdo, J. L. Ortiz, A. J. Castro-Tirado, A. S. de Miguel, F. Ocaña, S. Pastor, et al. Trajectory, orbit, and spectroscopic analysis of a bright fireball observed over Spain on April 13, 2013. *Astronomy & Astrophysics*, 569:A104, 2014.
- J. R. Masiero, T. Grav, A. Mainzer, C. Nugent, J. Bauer, R. Stevenson, and S. Sonnett. Main-belt asteroids with wise/neowise: Near-infrared albedos. *The Astrophysical Journal*, 791(2):121, 2014.
- K. Meech, O. Hainaut, and B. Marsden. Comet nucleus size distributions from HST and Keck telescopes. *Icarus*, 170(2):463–491, 2004.
- D. Nesvorný, P. Jenniskens, H. F. Levison, W. F. Bottke, D. Vokrouhlický, and M. Gounelle. Cometary origin of the zodiacal cloud and carbonaceous micrometeorites. implications for hot debris disks. *The Astrophysical Journal*, 713(2):816, 2010.
- C. Nugent, J. Margot, S. Chesley, and D. Vokrouhlický. Detection of semimajor axis drifts in 54 near-earth asteroids: New measurements of the Yarkovsky effect. *The Astronomical Journal*, 144(2):60, 2012.
- E. J. Öpik. Collision probabilities with the planets and the distribution of interplanetary matter. *Proceedings of the Royal Irish Academy. Section A: Mathematical and Physical Sciences*, 54:165–199, 1951. ISSN 00358975. URL <http://www.jstor.org/stable/20488532>.
- H. Rein and S. F. Liu. REBOUND: an open-source multi-purpose N-body code for collisional dynamics. *Astronomy and Astrophysics*, 537:A128, Jan. 2012. doi: 10.1051/0004-6361/201118085.
- H. Rein and D. S. Spiegel. IAS15: a fast, adaptive, high-order integrator for gravitational dynamics, accurate to machine precision over a billion orbits. *Monthly Notices of the Royal Astronomical Society*, 446(2):1424–1437, Jan. 2015. doi: 10.1093/mnras/stu2164.

- T. P. Robitaille, E. J. Tollerud, P. Greenfield, M. Droettboom, E. Bray, T. Aldcroft, M. Davis, A. Ginsburg, A. M. Price-Whelan, W. E. Kerzendorf, et al. Astropy: A community python package for astronomy. *Astronomy & Astrophysics*, 558:A33, 2013.
- E. K. Sansom, P. Bland, J. Paxman, and M. Towner. A novel approach to fireball modeling: The observable and the calculated. *Meteoritics & Planetary Science*, 50(8):1423–1435, 2015.
- E. K. Sansom, M. Gritsevich, H. A. Devillepoix, T. Jansen-Sturgeon, P. Shober, P. A. Bland, M. C. Towner, M. Cupák, R. M. Howie, and B. A. Hartig. Determining fireball fates using the α - β criterion. *The Astrophysical Journal*, 885(2):115, 2019a.
- E. K. Sansom, T. Jansen-Sturgeon, M. G. Rutten, H. A. Devillepoix, P. A. Bland, R. M. Howie, M. A. Cox, M. C. Towner, M. Cupák, and B. A. Hartig. 3d meteoroid trajectories. *Icarus*, 321:388–406, 2019b.
- P. M. Shober, T. Jansen-Sturgeon, E. K. Sansom, H. A. Devillepoix, M. C. Towner, P. A. Bland, M. Cupák, R. M. Howie, and B. A. Hartig. Where did they come from, where did they go: Grazing fireballs. *The Astronomical Journal*, 159(5):191, 2020.
- A. Sosa, J. Fernández, and P. Pais. On the asymmetric evolution of the perihelion distances of near-earth jupiter family comets around the discovery time. *Astronomy & Astrophysics*, 548:A64, 2012.
- G. Tancredi. A criterion to classify asteroids and comets based on the orbital parameters. *Icarus*, 234:66–80, 2014.
- M. B. Taylor. TOPCAT & STILTS: starlink table/VOTable processing software. In *Astronomical Data Analysis Software and Systems XIV*, volume 347, page 29, 2005.
- M. C. Towner, M. Cupak, J. Deshayes, R. M. Howie, B. A. D. Hartig, J. Paxman, E. K. Sansom, H. A. R. Devillepoix, T. Jansen-Sturgeon, P. A. Bland,

- and et al. Fireball streak detection with minimal cpu processing requirements for the desert fireball network data processing pipeline. *Publications of the Astronomical Society of Australia*, 37:e008, 2020. doi: 10.1017/pasa.2019.48.
- D. Vida, P. G. Brown, and M. Campbell-Brown. Modelling the measurement accuracy of pre-atmosphere velocities of meteoroids. *Monthly Notices of the Royal Astronomical Society*, 479(4):4307–4319, 07 2018. ISSN 0035-8711. doi: 10.1093/mnras/sty1841. URL <https://doi.org/10.1093/mnras/sty1841>.
- D. Vokrouhlický, W. Bottke, S. Chesley, D. Scheeres, and T. Statler. The yarkovsky and yorp effects. *Asteroids IV*, pages 509–531, 2015.

CHAPTER 5

The main asteroid belt: the primary source of debris on comet-like orbits

Patrick M. Shober^a, Eleanor K. Sansom^a, Phil A. Bland^a, Hadrien A.R. Devillepoix^a, Martin C. Towner^a, Martin Cupák^a, Robert M. Howie^a, Benjamin A.D. Hartig^a, Seamus L. Anderson^a

^aSpace Science and Technology Centre (SSTC), School of Earth and Planetary Sciences, Curtin University, GPO Box U1987, Perth, Western Australia 6845, Australia

This article is published in The Planetary Science Journal, accepted 19 January 2021, published 13 May 2021

Abstract

Jupiter family comets contribute a significant amount of debris to near-Earth space. However, telescopic observations of these objects seem to suggest they have short physical lifetimes. If this is true, the material generated will also be short-lived, but fireball observation networks still detect material on cometary orbits. This study examines centimeter-meter scale sporadic meteoroids detected by the Desert Fireball Network from 2014-2020 originating from Jupiter family comet-like orbits. Analyzing each event's dynamic history and physical characteristics, we confidently determined whether they originated from the main asteroid belt or the trans-Neptunian region. Our results indicate that $< 4\%$ of sporadic meteoroids on JFC-like orbits are genetically cometary. This observation is statistically significant and shows that cometary material is too friable to survive in near-Earth space. Even when considering shower contributions, meteoroids on JFC-like orbits are primarily from the main-belt. Thus, the presence of genuine cometary meteorites in terrestrial collections is highly unlikely.

5.1 Introduction

Jupiter family comets (JFCs) are short-period comets near the ecliptic plane that are strongly influenced by Jupiter. They originate from the outer solar system in the scattered disk (Duncan and Levison, 1997) and are comprised of primitive volatile-rich material. They are conventionally defined by their Tisserand's parameter ($2 < T_J < 3$), which is an approximately conserved value in the circular restricted three-body problem (object - Jupiter - Sun). This is a better way to classify the orbits of small planetary bodies compared to the traditionally used orbital periods (Levison and Duncan, 1994). The physical properties of JFCs have been explored in numerous studies based on meteor/fireball analysis (Jenniskens and Jenniskens, 2006; Borovička et al., 2007; Madiedo et al., 2014), telescopic observations (Fernández et al., 2005, 2013), dynamical modeling (Duncan et al., 2004; Di Sisto et al., 2009; Nesvorný et al., 2010; Tancredi, 2014), and by space

missions (Brownlee et al., 2004; A'Hearn et al., 2005; Sunshine et al., 2006; Fornasier et al., 2015). Each method provides information about different size-ranges of objects on JFC-like orbits.

When observing meteors streak across the night sky, we are typically witnessing the size-range of the smallest objects in the near-Earth space (dust-sized; $\ll 10^{-3}$ kg). Conversely, telescopic observations are instrumental in characterizing the most massive objects (hundreds of meters to kilometers in diameter). This gap between the meteor and telescopic observations is the primary range for the progenitors of meteorites. Usually spanning centimeters to meters in scale, this size-range has been interpreted from fireballs and the meteorites they produce on the ground (Borovička et al., 2015; Granvik and Brown, 2018).

Based on telescopic observations and dynamical studies, many researchers believe there is a paucity of JFCs at sub-kilometer scales (Meech et al., 2004; Fernández and Morbidelli, 2006; Nesvorný et al., 2017). This lack of objects at smaller sizes is thought to be related to the inferred brief physical lifetimes ($10^3 - 10^4$ yrs) of JFCs in the inner solar system (Levison and Duncan, 1997; Fernández et al., 2002; Di Sisto et al., 2009). Due to their low-bulk density and high volatile content, JFCs should fade away relatively quickly when within ~ 3 au.

Nevertheless, despite the predicted sub-kilometer paucity, fireball observation networks have many accounts of durable centimeter to meter-sized meteoroids originating from JFC-like orbits (Brown et al., 2000; Borovička et al., 2013; Spurný et al., 2013; Spurný et al., 2017). By examining meter-size terrestrial impactors, it was found that about 5–10% had JFC-like orbits, relatively consistent with the flux estimates based on larger kilometer-scale near-Earth objects (NEOs) (Brown et al., 2016). Yet, they only found half of these displayed weaker than average structures based on their atmospheric ablation characteristics. Two of the five JFC-like events discussed were calibrated meteorite falls (Maribo and Sutter's Mill) likely to be from the main asteroid belt. Meanwhile, the remaining three events all came from US Government sensor (USG) data, two with a semi-major axis of ~ 2.9 au, i.e., well within the bounds of the outer main-belt. Also, it has since been demonstrated that the orbital information collected by USG events is

generally unreliable (Devillepoix et al., 2019).

Additionally, another study recalculated the orbits for 25 meteorite falls and identified their likely source regions using an advanced NEO model (Granvik and Brown, 2018; Granvik et al., 2018). The only meteorite that had a mean JFC probability $\geq 50\%$ was an H5/6 ordinary chondrite, Ejby. Furthermore, the fall with the second-highest JFC source region probability was another H5, Košice. However, both of these falls have relatively significant initial velocity uncertainties, increasing the uncertainty for the source region analysis. Carbonaceous-chondrites Maribo and Sutter's Mill (both CM2), also had probabilities of coming from the JFCs above 20%. Nevertheless, no precisely observed meteorite falls have yet come from an unambiguously cometary orbit.

The Taurid complex has also been discussed as being capable of larger, possibly meteorite-dropping, meteoroids (Brown et al., 2013). These meteoroids can be hundreds of kilograms in size, an order of magnitude higher than other showers. Although other studies have found that while the Taurids can produce very large meteoroids, the Taurids are still very weak and were unlikely to produce meteorites (Borovička et al., 2017). Given the highly evolved orbit of comet 2P/Encke and the other non-cometary possible parent bodies in similar orbits, this subset of Taurids observed also does not likely reflect the vast majority of JFC meteoroids (Asher et al., 1993).

Based on debiased NEO orbital and absolute-magnitude distributions, it is expected that the contribution from the JFC region is a few percent on average (Bottke Jr et al., 2002; Granvik et al., 2018). The contribution seems to increase at smaller sizes, reaching $\sim 10\%$ of the NEO population below diameters of 100 m (Granvik et al., 2018). However, this estimate assumes that JFCs are more likely to become dormant than disintegrate as JFC disruptions are less commonly observed compared to long-period comets. If this assumption breaks down at smaller sizes, then the JFC contribution to the NEO meteoroid flux may be negligible.

If the hypothesis that the physical lifetimes of sub-kilometer comets are very short is accurate, why do fireball networks still observe centimeter-meter debris originating from comet-like orbits? Does the larger cometary debris we observe impacting

the Earth originate from comets?

The massive orbital dataset collected by the Desert Fireball Network (DFN) was utilized to answer these questions. The DFN is the largest single photographic fireball network in the world, covering over 2.5 million km² of Australia. This massive project is part of a worldwide collaboration, the Global Fireball Observatory (<https://gfo.rocks/>) (GFO), currently consisting of 18 partner institutions (Devillepoix et al., 2020). The GFO has a semi-automated data processing pipeline which sorts images, detects fireball events, and triangulates these events (Howie et al., 2017; Jansen-Sturgeon et al., 2019; Towner et al., 2020; Sansom et al., 2019b,a).

5.2 Materials and Methods

5.2.1 Experimental Design

The dataset used for this study was collected by the Desert Fireball Network (DFN). Covering over one third of Australian outback, the DFN is the largest photographic fireball network globally. The observations made by the DFN are invaluable, and provide key insights into the debris impacting the Earth daily.

When parsing through the dataset for this study, all events that originated from an orbit with a JFC-like Tisserand's parameter ($2 < T_J < 3$) and had a significant initial mass (≥ 0.01 kg) were gathered. The Tisserand's parameter is an approximately conserved value in the three-body problem and is regularly used to distinguish between different kinds of small planetary bodies (Levison and Duncan, 1994). Typically this three body problem includes the sun, Jupiter, and the asteroid or comet; since Jupiter is seen as the primary perturber the parameter is written as T_J .

5.2.1.1 Trajectory Analysis & Orbit Determination

The fireball events detected by the DFN have atmospheric trajectories fitted using a modified straight-line least-squares (SLLS) and an extended Kalman smoother for the velocity profile (Sansom et al., 2015). The uncertainties associated with

the fitted fireball trajectories are propagated from the residuals of the fit itself along with the timing and positional uncertainties of the events' observations. The observational uncertainties are handled and incorporated by the Kalman filter. The initial masses and corresponding uncertainties were also determined using a dynamic model in a reverse extended Kalman filter (Sansom et al., 2015). The pre-atmospheric orbits are then determined numerically including any relevant perturbations by integrating the meteoroid's state until it was outside the Earth's sphere of influence (Jansen-Sturgeon et al., 2019). The orbital uncertainties are then obtained with a Monte Carlo approach, by numerically integrating samples randomly drawn from within the initial state uncertainties at the top of the atmosphere.

5.2.1.2 Addressing Observational Biases

The DFN uses photographic observations of fireballs to help better understand the debris in the inner solar system. However, to obtain meaningful results from this dataset, we must first address any observational biases.

The first bias we address is that the DFN is optimized for meteorite-dropping fireball events (~ 0.5 limiting magnitude) (Howie et al., 2017). In this study, we limit the meteoroids considered to a minimum initial mass of 10 grams. This bias does not affect the results as both asteroidal and cometary populations are known to produce material within this size-range (Boehnhardt, 2004; Fernández, 2009). Secondly, we must ensure that the DFN observations do not bias against either observing asteroidal or cometary debris due to the orbits they exist. The primary bias to be concerned with is due gravitational focusing. Since meteoroids with a lower relative velocity are more gravitationally focused, the terrestrial impact population contains a larger proportion of asteroidal impactors from orbits with smaller semi-major axis values. However, this study is concerned with meteoroids all originating from similar orbits, thus they are all weighted nearly equally. Other observational biases are associated with photographic fireball observations, however, none of these would have any affect on the results of this study. For a more exhaustive list and discussion of DFN observational biases please reference Shober

et al. (2020a).

5.2.1.3 Data Selection

A manual check of all the fireball observations and triangulations, any events with poor data were removed (e.g. fireball was very far from cameras, convergence angles for triangulations were too small, etc.). The orbital uncertainties of the meteoroids must be sufficiently low to obtain meaningful statistics from the Monte Carlo numerical integrations. If the uncertainties are too large, the number of samples required to get statistically reasonable results may be computationally unfeasible. Additionally, meteoroids with T_J values within three standard deviations of $T_J = 3.0$ or $T_J = 2.0$ were excluded to remove ambiguous events.

In this study, only fireballs with no shower-associations were considered, i.e., sporadic. Therefore, any events with distinctly cometary physical and dynamical characteristics could indicate a process to preserve cometary material in this range for longer periods. Using primarily the D_J similarity criterion, we sorted through associations with a limiting value of $D_J < 0.15$ (Jopek, 1993). A more inclusive limiting value was used to eliminate any potential shower events. We verified associations from this subset by comparing orbital elements, shower dates, right ascensions and declinations, initial velocities, nodal directions, arguments of perihelion, along with other similarity criteria (Southworth and Hawkins, 1963; Drummond, 1981). The meteor shower data used was taken from all showers listed by the IAU Meteor Data Center ¹, with a higher weight placed on established showers.

The fireball data used within this study, including uncertainties, are available in the Appendix.

We characterized the physical and dynamical characteristics of the sporadic meteoroids on JFC-like orbits using fireball data from the DFN with the following goals:

1. Determine proportion of genetically cometary material in excess of 10 g on sporadic JFC-like orbits
2. Assess whether or not the physical lifetimes of JFC meteoroids in the

¹<https://www.ta3.sk/IAUC22DB/MDC2007/>

meteorite-dropping size range are shorter than the disassociation lifetimes of cometary streams

3. Find out if it is possible to get a meteorite from a JFC-orbit, and what it would look like.

5.2.2 Dynamic Analysis

As shown in previous studies, genuine JFCs originating from the outer solar system tend to move on chaotic orbits over thousands of years, encountering Jupiter frequently over their lifetime (Tancredi, 1995; Levison and Duncan, 1997). In this work, we have adopted a similar search strategy to past studies by numerically integrating the fireball trajectories backward 10 kyrs, identifying fireballs originating from ‘stable’ and ‘unstable’ orbits (Tancredi, 2014; Fernández et al., 2014; Fernández and Sosa, 2015). For each event, a Monte Carlo simulation was undertaken where ten simulations with 100 particles were integrated -10 kyrs. These simulations were conducted using the IAS15 integrator, taking into account all planetary perturbations and close encounters considering all of the planets and the Moon (Rein and Liu, 2012; Rein and Spiegel, 2015). The particles were initialized within the formal triangulation uncertainties assuming a Gaussian distribution. The particles’ histories were then each assessed and labeled as either ‘stable’ or ‘unstable’ over the previous 10 kyrs. Those with frequent unpredictable jumps in their orbital elements were considered unstable (Fig. 5.1a), whereas those in resonances and followed smooth trajectories with little changes in perihelion distance were considered stable (Fig. 5.1b). The final instability probabilities and associated uncertainties were then obtained by taking the mean and standard deviation of the sample means.

5.2.3 Physical Analysis

In order to characterize the physical properties, we determined the PE value for each fireball. The PE criterion was first introduced as a way to discriminate between different meteoroid compositions based on the ability to penetrate the

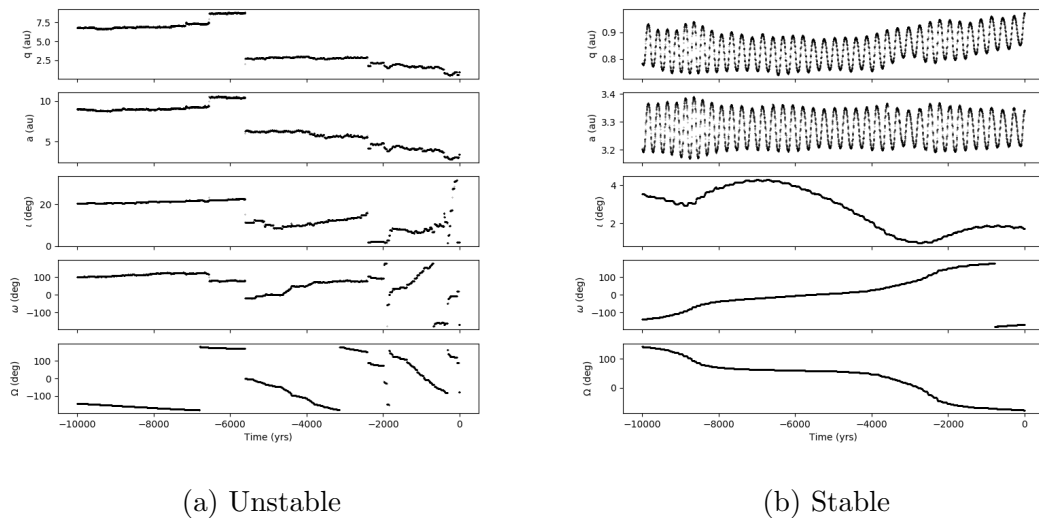


Figure 5.1: Backward integrations -10 kyrs of two particles generated within the triangulated trajectory uncertainties of event DN200104_01 where q is perihelion, a is semi-major axis, i is inclination, ω is argument of perihelion, and Ω is longitude of ascending node. On the left, a particle on a chaotic unstable orbit typical of a comet with numerous Jupiter close encounters. On the right, another particle provides an example of a stable orbit following a predictable path with no close encounters with Jupiter. This specific fireball event lasted over 5 sec and was recorded by 4 DFN stations, providing an excellent trajectory fit with very minimal uncertainties. Thus, this demonstrates the difficulty associated with backward propagation of meteoroids coming from orbits on the edge of two source regions (JFC and main-belt in this case).

atmosphere (Ceplecha and McCrosky, 1976). It has since been used in numerous studies to assess the physical nature of impacting meteoroids (Ceplecha, 1994; Brown et al., 2013; Borovička et al., 2015; Brown et al., 2016). The PE value is given by:

$$PE = \log(\rho_E) - 0.42 \log(m_\infty) + 1.49 \log(V_\infty) - 1.29 \log(\cos Z_R) \quad (5.1)$$

where ρ_E is the density of the atmosphere at the end the luminous trajectory (and the reason for the acronym ‘PE’), m_∞ is the initial mass of the meteoroid in grams, V_∞ is the initial velocity of the meteoroid in km/s , and Z_R is the local entry angle measured from the zenith.

The PE values are divided into four types: ordinary chondrite-like (type I), carbonaceous (type II), short-period cometary (type IIIa), and weak cometary (type IIIb) (Ceplecha et al., 1998). The boundaries for these groups are denoted in Table 5.1. The PE criterion is an extremely useful metric to evaluate the physical properties of meteoroids, however, the types are not strictly correct. While providing generally accurate results of relative strength, the physical composition of any individual meteoroid is uncertain due to the other factors that affect the durability while transiting the atmosphere (e.g. macro-scale fractures) (Popova et al., 2011; Borovička et al., 2020).

We additionally computed the ballistic coefficient (α) and the mass-loss parameter (β) based on the fireball observations (Gritsevich and Stulov, 2006; Gritsevich, 2007; Lyytinen and Gritsevich, 2016). Using these parameters one can quickly identify potential meteorite-dropping events (Sansom et al., 2019a). They can be calculated for any event showing some level of deceleration by using the velocity and height data (https://github.com/desertfireballnetwork/alpha_beta_modules).

In Fig. 5.4, we determined potential meteorite dropping fireballs using the α - β values. Assuming a 50 g final mass is the minimum meteorite dropping mass, the meteorite dropping lines were calculated with the following equations:

$$\ln \beta = \ln[13.2 - 3 \ln(\alpha \sin \gamma)], \quad \mu = 0 \quad (5.2)$$

$$\ln \beta = \ln[4.4 - \ln(\alpha \sin \gamma)], \quad \mu = \frac{2}{3} \quad (5.3)$$

when assuming $\rho_m = 3500 \text{ kg m}^{-3}$ (meteoroid density) and $c_d A = 1.5$ (product of drag coefficient and initial shape coefficient). Considering that the contribution from the outer main-belt may be significant, where many objects have low-albedos (Takir et al., 2015; DeMeo and Carry, 2014; DeMeo et al., 2015) (e.g., C- and D-types), we also plotted the equivalent lines for a CM-like density (Consolmagno et al., 2008) ($\rho_m = 2240 \text{ kg m}^{-3}$) using the following equations:

$$\ln \beta = \ln[14.09 - 3 \ln(\alpha \sin \gamma)], \quad \mu = 0 \quad (5.4)$$

$$\ln \beta = \ln[4.7 - \ln(\alpha \sin \gamma)], \quad \mu = \frac{2}{3} \quad (5.5)$$

Together, the dynamic simulations and analysis of the material properties can better elucidate what types of material regularly impact the Earth from JFC-like orbits in the considered size-range.

5.2.4 Statistical Analysis

Based on the dynamical and physical analysis, the source populations can be inferred for each meteoroid in this study. However, given the sample size, what does this tell us about the entire population of small JFC-like meteoroids?

In order to answer this question, we utilize a Markov Chain Monte Carlo (MCMC) to sample from the posterior probability distribution. The Bayesian model was created with the Python PyMC3 probabilistic programming package using the No-UTurn Sampler (Salvatier et al., 2016). A beta distribution was used as a prior with the hyperparameters (α) based on a study that examined the dynamical characteristics of 58 near-Earth JFCs ($q < 1.3 \text{ au}$) (Fernández and Sosa, 2015). This corresponded to hyperparameters $\alpha = [1.38, 8.62]$ and an observation vector $c = [48, 2]$; the hyperparameters were weighted less as they were based on kilometer-scale objects. Additionally, as a comparison, an uninformed uniform prior of $\alpha = [1.0, 1.0]$ was included. In total, fifteen thousand samples from the posterior were taken to estimate the posterior. To be counted as genetically JFC

in origin in the model, the meteoroids would need to have a $> 50\%$ probability of originating from an unstable orbit and be of PE types II or III. We considered a PE type II as plausibly cometary due to previous arguments that meteorites from JFCs could possibly be represented by primitive carbonaceous chondrites (Gounelle et al., 2008).

5.3 Results

In this study, we examined fireballs not associated with meteor showers detected by the DFN during four years of observations. All the fireballs considered were generated by meteoroids that originated from JFC-like orbits ($2 < T_J < 3$). The source region of these meteoroids, main-belt or JFC, was determined by analyzing the orbital stability and physical durability during atmospheric transit. It takes only ~ 1000 yrs to become orbitally disassociated from a JFC shower. Therefore, the identification of sporadic JFC material would indicate a minimum physical lifetime equal to the disassociation time (Tancredi, 1995). However, a lack of sporadic cometary debris in fireball observations would be clear evidence that the physical lifetimes are less than one thousand years.

5.3.1 Orbital characteristics of sporadic JFC-like meteoroids

JFCs move on chaotic orbits compared to main-belt asteroids; on the order of thousands of years (Tancredi, 1995). During their lifetimes, their orbital evolution is controlled by the numerous close encounters they have with Jupiter. Of the 50 sporadic JFC-like fireball events analyzed in this study, nearly all the meteoroids come from stable orbits over the previous 10 kyrs (see Appendix). This is inconsistent with the dynamics diagnostic of JFCs.

Only three events have a high probabilities of originating from an unstable orbits. However, one of these comes from within 3 au and crosses one of the major mean-motion resonances (MMRs). Events DN150817_01 and DN161028.02 have the highest probability of originating from unstable cometary orbits, with $86.1 \pm 5.5\%$

and $90.8 \pm 3.0\%$ of the particles integrated being chaotic respectively. As seen in Fig. 5.2, event DN150816_04 overlaps the 7:3 MMR when considering triangulation uncertainties, whereas, events DN150817_01 and DN161028_02 both lie outside the normal range of the main-belt with a semi-major axis of ~ 3.6 au. Several meteoroids have inconclusive dynamical histories; these include six events where several of the particles integrated evolved chaotically over thousands of years. On the other hand, nearly all of these inconclusive events come from orbits near MMRs, thus indicating that orbital uncertainty is very likely the cause of the inconclusive results. Otherwise, $> 80\%$ of the events originate from extremely stable orbits nearby one of the primary MMRs (Fig. 5.2).

A large majority of the fireballs examined in this study do not fall within the range consistent with observed kilometer-scale JFCs. As seen in Fig. 5.2, a majority of the near-Earth JFCs exist near ~ 3.1 au, where only a handful of events originate. However, only one of the four events in this range comes from an unstable orbit. This is in line with a previous model, where they found that main-belt material can contaminate the JFC population but would primarily be contained to the original bounds of the main-belt (Hsieh and Haghhighipour, 2016). Albeit, four of the 50 events examined fall beyond the 2:1 MMR, and of these, only two have higher probabilities of originating from unstable orbits (Fig. 5.2). Additionally, the inclinations of the fireballs examined tend to be relatively diffuse, but are most concentrated towards low-values within the $0 - 25^\circ$ range. This is more reconcilable with the main-belt inclination distribution than the JFC distribution, which is more highly concentrated around $\sim 12^\circ$ (see Appendix).

5.3.2 Physical characteristics of sporadic JFC-like meteoroids

The PE criterion characterizes the composition of meteoroids based on their ability to penetrate the atmosphere (Ceplecha and McCrosky, 1976). This metric is empirically determined based on the terminal height of the fireball, the entry mass, the velocity at the top of the atmosphere, and the impact angle. The PE criterion has been used for decades to understand the physical properties of meteoroids

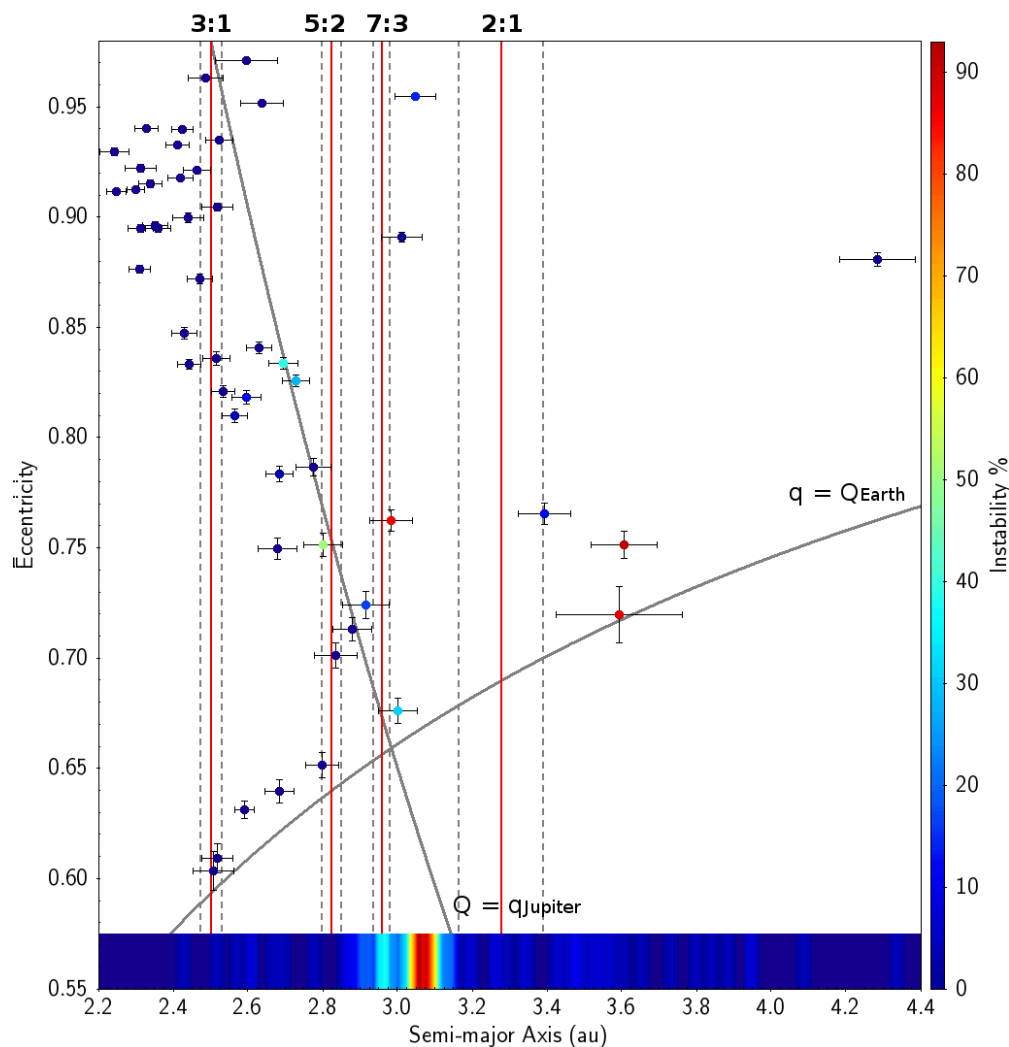


Figure 5.2: Triangulated semi-major axis vs. eccentricity for 50 non-shower JFC-like fireballs observed by the DFN that have predicted initial masses greater than 10 g. Error bars denote the formal 1σ orbital uncertainties associated with each meteoroid, and coloration is indicative of the orbital stability determined through numerical integrations -10 kyrs. The vertical red lines indicate the major MMRs with the dashed gray lines marking the maximum libration in semi-major axis (Tancredi, 2014). Most of the events originate from stable orbits near the MMRs. The densogram (<http://www.star.bris.ac.uk/~mbt/stilts/sun256/layer-densogram.html>) at the bottom of the plot represents the semi-major axis density for near-Earth ($q < 1.3$ au) JFCs within according to the NASA HORIZONS system (<http://ssd.jpl.nasa.gov/horizons.cgi>).

based on their atmospheric ablation characteristics (Borovička et al., 2015; Brown et al., 2016). The values are traditionally split accordingly (Ceplecha et al., 1998):

type I	$PE > -4.60$	Ordinary chondrite-like
type II	$-5.25 < PE \leq -4.60$	Carbonaceous chondrite
type IIIa	$-5.70 < PE \leq -5.25$	Short-period cometary
type IIIb	$PE \leq -5.70$	Weak cometary material

Table 5.1: Traditional PE classifications based on the atmospheric density at terminal height (Ceplecha and McCrosky, 1976).

The use of the PE criterion can be quite valuable when analyzing many fireballs; however, the types are not strictly exclusive and should not be taken as absolute truth. Other properties beyond physical composition can blur the lines between the types, such as macro-scale cracks (Popova et al., 2011; Borovička et al., 2020). As expected, considering the dynamic analysis, many of the JFC-like fireballs in this study are quite durable and strong (Fig.5.3). We only see meteoroids of types I or II, i.e., none fall into the standard categories associated with cometary material. Out of the 50 fireballs, 28 would be classified as type I and 22 as type II. Some short-period showers actually can produce more durable debris with similar strengths (Brown et al., 2013). Therefore, the PE criterion alone is not a sure way to distinguish between different materials for an individual fireball. In general, the PE types can give a sense of how strong the initial meteoroid was, but when combined with the dynamic analysis, the source population of a meteoroid can be more confidently obtained (main-belt or JFC).

5.3.2.1 Meteorite production from JFC-like meteoroids

Traditionally, the empirical criteria to predict whether a fireball has produced a meteorite on the ground (“a fall”) is height and velocity below 35 km and 10 kms⁻¹ respectively at the end of the luminous portion of the atmospheric trajectory (Wetherill and ReVelle, 1981). This gives us an easy way to identify possible recoverable falls quickly. A more rigorous way to determine which fireballs result in meteorites has since been demonstrated, where the ballistic coefficient (α) and the mass-loss parameter (β) are fit to the fireball observations (Sansom et al.,

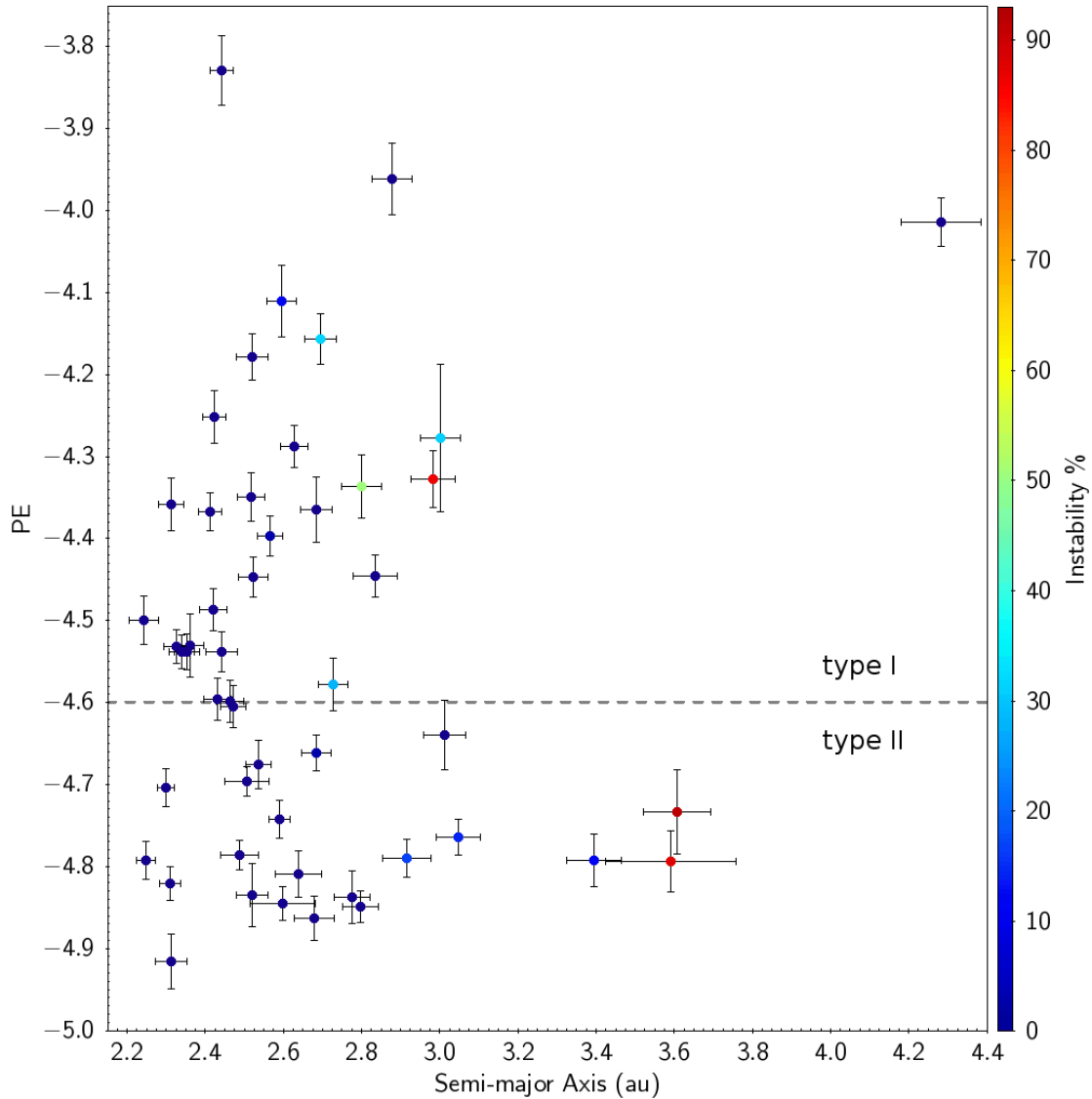


Figure 5.3: Sporadic JFC-like fireballs observed by the DFN with a minimum initial mass of 10g. The end heights of meteors can be used to ascertain the physical-nature of meteoroids using the PE criterion (Ceplecha and McCrosky, 1976). The PE values for the 50 fireballs examined are overwhelmingly stronger than the traditional comet types (Types IIIa and IIIb). The error bars associated with each meteoroid's semi-major axis and PE value are due to triangulation uncertainties.

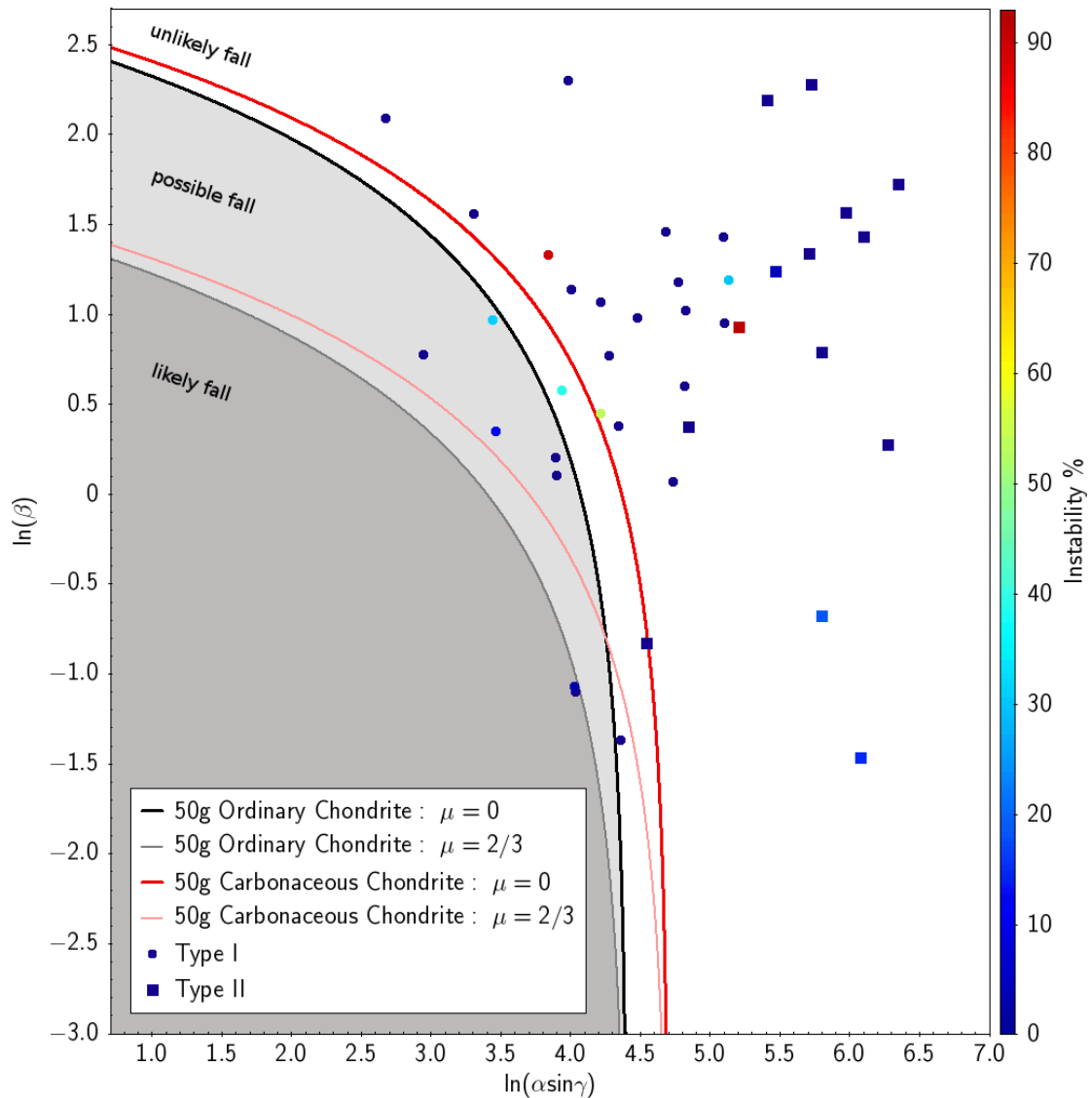


Figure 5.4: Distribution of non-shower JFC fireballs with enough deceleration to determine $\alpha - \beta$ values (at least $\sim 20\%$ deceleration). γ is the trajectory slope relative to the horizontal. If a macroscopic event is considered to have a final mass of ≥ 50 g, assuming $\rho_m = [2240, 3500]$ kg m^{-3} (carbonaceous and ordinary chondrite respectively) and $c_{dA} = 1.5$, meteorite dropping events can easily be identified given the range of possible shape change coefficients (μ).

2019a).

In Fig. 5.4, we see that several of the JFC-like fireballs examined in this study are quite durable. At least some events are likely to have meteorites on the ground > 50 g (DN150905_01 and DN191020_02). However, these events are likely asteroidal in origin based on their dynamic stability over the previous 10 kyrs and their PE classification. No events with high instabilities over the previous 10 kyrs or of type II drop meteorites in this study. Thus, meteorites from JFC-like orbits do occur, but they are all representative of main-belt material.

5.4 Discussion

Based on dynamical and physical analysis of sporadic JFC-like ($2 < T_J < 3$) fireballs with initial masses > 10 g, we find a clear abundance of stronger dynamically stable meteoroids (Fig. 5.3). As seen in Fig. 5.2, most meteoroids evolve in a deterministic way over the previous 10 kyrs, and have proximity to major MMRs. Dynamic instability is a diagnostic feature of JFCs originating from the outer solar system, as they suffer frequent close encounters with Jupiter (Tancredi, 1995, 2014). The predictable evolution of nearly all the meteoroids in this study is therefore indicative of their likely origin in the main belt. Additionally, events with indeterminate histories, where a non-negligible subset of particles evolved chaotically, also mostly lie near the primary MMRs. As does one of the three events with $> 80\%$ instability (Fig. 5.3). This proximity to MMRs could indicate possible main belt origins. Moreover, JFCs' arguments of perihelia tend to concentrate near 0° and 180° (Quinn et al., 1990), and there is no such correlation for the sporadic JFC-like fireballs in this study (see supplementary material). This further supports a dominantly main belt, asteroidal source.

Based on the calculated PE values, most of the events are also very durable and are classified as type I chondritic material. In fact, all of the fireballs in this sample are either classified as chondritic or carbonaceous chondritic material (type I or II; Fig. 5.3). No events have PE types traditionally associated with cometary material (type III). However, it has been previously argued that primitive carbonaceous chondrites may have come from cometary sources (Gounelle et al., 2008). Thus,

any DFN events that likely evolved chaotically over the previous 10 kyrs ($> 50\%$) and are of type II were also considered as cometary. At most only 2 meteoroids studied here are likely to originate from a short-period comet (DN150817_01 and DN161028_02). However, this would require centimeter to meter cometary debris to be stronger than expected. The subset of weaker type II meteoroids in our data are also generally smaller ($< 50 g$), perhaps debris released by dark carbonaceous asteroids in the outer main-belt (Takir et al., 2015; DeMeo and Carry, 2014; DeMeo et al., 2015). A novel process has been recently observed to release centimeter-sized particles on carbonaceous asteroid Bennu during the OSIRIS-REx mission (Lauretta et al., 2019).

Albeit, caution should be used with such a criterion to characterize meteoroids; a wide range of meteorite types have been recovered from type II/III events. For example, Almahatta Sitta (2008 TC3), Košice, and Sutter's Mill had PE values near the II/IIIa boundary, despite all being of different meteorite types on asteroidal orbits (polymict breccia, H5, and CM2 respectively) (Borovička et al., 2015; Brown et al., 2016). This is indicative that other physical factors, such as macroscopic cracks or porosity, can significantly affect the apparent strengths of impactors, and that there is still much unknown about the physical nature of meter-scale NEOs (Borovička et al., 2017, 2020). The PE criterion is useful to characterize the relative strength of meteoroids, but how much the meteorite type influences the strength is debatable.

5.4.1 Meteoroids beyond the 2:1 resonance

Previous studies have shown that a minor component of main-belt material can be transferred to JFC-like orbits, even in some circumstances, onto dynamically unstable orbits via close encounters with the terrestrial planets (Fernández et al., 2002, 2014; Hsieh and Haghhighipour, 2016; Shober et al., 2020b,a). Nevertheless, these objects' semi-major axes are predicted to be primarily constrained to the original range of the main-belt (Hsieh and Haghhighipour, 2016). Here we see that of the four events beyond 3.27 au, two are likely asteroidal in origin based on their PE classifications and stability (Fig. 5.3). The two most probable events

to originate from unstable comet-like orbits are DN150817_01 and DN161028_02, with $86.1 \pm 5.5\%$ and $90.8 \pm 3.0\%$ probabilities of having chaotic histories based on Monte Carlo simulations along with orbits beyond the 2:1 MMR (each around $a \sim 3.6$ au). The meteoroids from events DN150817_01 and DN161028_02 both fall into the type II, nominally carbonaceous and equally or more durable than many of the main-belt debris (Fig. 5.3). Even if both events are genuinely cometary in origin, they only comprise 4% of the sample.

5.4.2 Statistical Significance

Let's consider the null hypothesis to be that the source regions of sporadic meteoroids on JFC orbits match those of kilometer-scale JFCs. A P-test was used to determine if our results were significant enough to reject the null hypothesis. The P-value reflects the probability of observing an as or more extreme result. We considered a P-value of 0.01 to be significant enough to reject the null hypothesis. At most, two events are genetically cometary within the dataset (DN150817_01 and DN161028_02). Both of these events meet the criteria of being relatively weaker (type II) and likely originating from unstable orbits over the previous 10 kyrs ($> 50\%$). We assume the probability of observing a meteoroid from the main-belt within our sample matches the maximum value found from a dynamical study based on telescopic observations (19 out of 58 JFCs from the main-belt) (Fernández and Sosa, 2015). From these results, we find the P-value to be equal to 3.1×10^{-21} . This extraordinarily low probability clearly indicates we can reject the null hypothesis. Thus, the source region for centimeter-scale meteoroids on JFC-like orbits does not match the cometary kilometer-sized bodies.

We additionally utilized Bayesian inference to estimate the proportion of main-belt material on JFC-like orbits (Salvatier et al., 2016). The informed prior used is a beta distribution with hyperparameters $\alpha = [1.38, 8.62]$ and an observation vector $c = [48, 2]$. The hyperparameters are derived from observational data, but the weight of these prior observations on our expected values was slightly reduced as they corresponded to kilometer-scale objects (Fernández and Sosa, 2015). Using a Markov-Chain Monte Carlo to draw samples from the posterior

distribution, we found that sporadic JFC-like meteoroids in NEO space are $82.1 \pm 4.9\%$ from the main-belt and $17.9 \pm 4.9\%$ from the trans-Neptunian region with our reasonably informed prior. Whereas when an uninformed prior is used (i.e., the prior probability of observing a JFC or main-belt meteoroid is equal), the relative components are $94.2 \pm 3.2\%$ from the main-belt and $5.8 \pm 3.2\%$ from JFCs.

Furthermore, while processing the data in this study, we found that of the meteoroids originating from JFC-like orbits with initial masses greater than 10 g, about $78 \pm 3\%$ were sporadic and $22 \pm 3\%$ were associated with showers. Thus, even when considering showers along with the sporadic population, it is likely that main-belt material makes up the majority of near-Earth material on orbits with $2 < T_J < 3$ within this size range. Evidently the Tisserand's parameter is not a very informative metric when analyzing meteoroids in the inner solar system.

5.4.3 Why are there no sporadic cometary meteoroids?

5.4.3.1 Alternative explanations

A possible explanation for the lack of dynamically unstable meteoroids in our sample could be that non-gravitational forces are decoupling the material from Jupiter. Previous work has found that sporadic micron-sized meteoroids of the zodiacal cloud are not able to decouple from Jupiter via planetary perturbations along with solar radiation pressure before having another close encounter removing them from Earth-crossing orbits (Nesvorný et al., 2010). However, the meteoroids studied by Nesvorný et al. (2010) are in a completely different size range compared to those discussed here, and the effects on these meteoroids are very different.

Nevertheless, non-gravitational forces are highly unlikely to be responsible for the meteoroids with asteroidal dynamics in our data set. Non-gravitational forces, such as the Yarkovsky effect, would not be efficient enough to decouple these meteoroids before having another close encounter with Jupiter ($< 10^3$ yrs).

Alternatively, one could argue that we may not expect to see many JFC meteoroids on these low-perihelion orbits or within the examined size range (10 grams to a few kilograms). Firstly, there have been multiple studies on Earth-crossing JFCs with the current number known to be ~ 140 objects (<http://ssd.jpl.nasa.gov/>

[horizons.cgi](#)). A previous study investigated the dynamic stability of 58 JFCs in orbits with $q < 1.3$ au, and they found that most of the objects (over two thirds) move on unstable orbits over ± 10 kyrs (Fernández and Sosa, 2015). Thus, showing at the kilometer scale objects on these orbits are dominated by genetically cometary material. Secondly, larger meteoroids (centimeter or larger) are capable of being produced by comets through a few mechanisms such as cometary splitting or gas drag (Boehnhardt, 2004; Fernández, 2009). Thus, we should expect to observe cometary meteoroids within the range detected by the DFN.

5.4.3.2 Short physical-lifetimes

Given the numerous JFCs on Earth-crossing orbits and their ability to produce meteoroids within the range considered in this study, it is surprising that we observe nearly no meteoroids clearly sourced from the JFC population (Fernández and Morbidelli, 2006). According to debiased NEO models, as much as 10% of the NEO population at the smallest sizes considered (~ 100 m), should be sourced from the JFC population (Granvik et al., 2018). Yet, in this sample, we see no distinctly cometary meteoroids.

This lack of cometary debris within the sporadic population strongly supports the hypothesis that sub-kilometer JFCs have limited physical lifetimes in the inner solar system (Meech et al., 2004; Fernández et al., 2002; Fernández and Morbidelli, 2006; Nesvorný et al., 2017). The physical lifetimes of centimeter-meter debris must be less than ~ 1000 years (the decoherence time). This physical breakdown is consistent with the observations that there are less high-volatile asteroids at low-perihelion distances (Granvik et al., 2016). Planetary debris seems to break down in the inner solar system closer to the sun, depending on the object's size and volatile content. At large sizes ($> 10^{3-4}$ m), material from the trans-Neptunian region is dominant on JFC-like orbits. However, as the diameters decrease to typical meteorite-producing objects, the physical lifetimes are likely so short that main-belt material becomes a more viable source. Conversely, according to Nesvorný et al. (2010), micron-sized meteoroid impacts on Earth are dominated by JFC particles ($\sim 85\%$ of the mass influx). If accurate, these results suggest that dust-sized

and kilometer-sized objects on JFC-like orbits are genetically cometary, however, intermediate sizes are sourced from the main asteroid belt. This is consistent with the prediction by Nesvorný et al. (2010) that cm-sized particles ejected from comets likely quickly disrupt (< 10 kyrs) and form the robust micron-sized population observed within the zodiacal cloud.

5.4.4 Meteorites from Jupiter-family comets

A couple of the fireballs likely resulted in surviving meteorites > 50 g (Fig. 5.4), however, all of these are stable dynamically over the previous 10 kyrs and only have PE values of type I. Thus, even in the occasion where we do have some genetically cometary material impact the Earth, according to our sample, it is unlikely to survive. It has been argued that primitive carbonaceous chondrites may be the best candidates to originate from cometary bodies, however, given our results, this may be only possible if the meteoroid was recently released from the parent body (within a thousand years) (Gounelle et al., 2008). While the cosmic ray exposure ages are significantly shorter for some carbonaceous chondrites (< 1 Myr), they are still usually much longer than the $\sim 10^3$ yrs expected from our results (Eugster et al., 2006). Therefore, meteorites from $2 < T_J < 3$ orbits are expected, but they will not be cometary.

5.4.5 Limitations

This study is constrained by the amount of data collected by the DFN. However, given that the DFN is the largest fireball network in the world, this cannot be improved upon. Additionally, the PE value methodology is a very limited metric of meteoroid strength as macroscopic features of the meteoroids can significantly affect the strengths. However, the PE value was utilized liberally in this study to determine potentially cometary meteoroids. Any meteoroid with a slightly weaker strength was considered as potentially cometary. Even with this very inclusive criterion, we found nearly no meteoroids that fulfilled our physical and orbital requirements to be considered cometary. The results clearly demonstrate that cometary debris larger than dust-sized is too friable to survive in near-Earth

space for longer periods.

5.5 Summary

Sporadic fireball data collected by the DFN demonstrates there is a lack of cometary material on JFC-like orbits for meteoroids in the gram to kilogram size range. This supports the short physical lifetime hypothesis for JFC material (Meech et al., 2004; Fernández et al., 2002; Fernández and Morbidelli, 2006; Nesvorný et al., 2017). Additionally, it indicates that the primary source region for Earth-crossing material on JFC-like orbits ($2 < T_J < 3$) is size-dependent. A majority of the objects at dust-sizes and on kilometer-scales are likely sourced from the trans-Neptunian region of the outer solar system (Nesvorný et al., 2010; Fernández and Sosa, 2015). However, objects centimeters to meters in size are dominated by asteroidal material diffused out from the main-belt. This diffusion process likely occurs via some combination of orbital resonances, Kozai resonances, non-gravitational forces, and close encounters with terrestrial planets (Bottke Jr et al., 2002; Fernández et al., 2014; Hsieh and Haghhighipour, 2016; Shober et al., 2020b,a). In this study, we found a minor fraction of unstable possibly cometary objects, but the number of fireballs observed to originate from stable orbits from the main-belt over the previous 10kyrs is statistically significant. We estimate that as much as $94.2 \pm 3.2\%$ of Earth-crossing centimeter-sized debris on these orbits is sourced from the main-belt. Furthermore, considering that $22 \pm 3\%$ of the JFC-like fireballs observed by the DFN over the previous five years are associated with showers, our results suggest that the majority of centimeter material on JFC-like orbits in near-Earth space is main-belt in origin. Thus, we should expect to see ordinary types of meteorite falls coming from Jupiter-crossing orbits.

5.6 Acknowledgments

This work was funded by the Australian Research Council as part of the Australian Discovery Project scheme (DP170102529). SSTC authors acknowledge institutional support from Curtin University. This work was also supported by resources

provided by the Pawsey Supercomputing Centre with funding from the Australian Government and the Government of Western Australia. This research made use of TOPCAT for visualization and figures (Taylor, 2005). This research also made use of Astropy, a community-developed core Python package for Astronomy (Robitaille et al., 2013). Simulations in this paper made use of the REBOUND code which can be downloaded freely at <http://github.com/hannorein/REBOUND> (Rein and Liu, 2012). The authors declare no competing interests. All data needed to evaluate the conclusions in the paper are present in the paper and/or the Appendix.

Bibliography

- M. F. A'Hearn, M. Belton, W. Delamere, J. Kissel, K. Klaasen, L. McFadden, K. Meech, H. Melosh, P. Schultz, J. Sunshine, et al. Deep impact: excavating comet tempel 1. *science*, 310(5746):258–264, 2005.
- D. Asher, S. Clube, and D. Steel. Asteroids in the taurid complex. *Monthly Notices of the Royal Astronomical Society*, 264(1):93–105, 1993.
- H. Boehnhardt. Split comets. *Comets II*, 745:301–316, 2004.
- J. Borovička, P. Spurný, and P. Koten. Atmospheric deceleration and light curves of draconid meteors and implications for the structure of cometary dust. *Astronomy & Astrophysics*, 473(2):661–672, 2007.
- J. Borovička, J. Tóth, A. Igaz, P. Spurný, P. Kalenda, J. Haloda, J. Svoreň, L. Kornoš, E. Silber, P. Brown, et al. The košice meteorite fall: Atmospheric trajectory, fragmentation, and orbit. *Meteoritics & Planetary Science*, 48(10):1757–1779, 2013.
- J. Borovička, P. Spurný, and P. Brown. Small near-earth asteroids as a source of meteorites. *Asteroids IV*, 257, 2015.
- J. Borovička, P. Spurný, V. I. Grigore, and J. Svoreň. The january 7, 2015, superbolide over romania and structural diversity of meter-sized asteroids. *Planetary and Space Science*, 143:147–158, 2017.
- J. Borovička, P. Spurný, and L. Shrubný. Two strengths of ordinary chondritic

- meteoroids as derived from their atmospheric fragmentation modeling. *arXiv preprint arXiv:2006.07080*, 2020.
- W. F. Bottke Jr, A. Morbidelli, R. Jedicke, J.-M. Petit, H. F. Levison, P. Michel, and T. S. Metcalfe. Debaised orbital and absolute magnitude distribution of the near-earth objects. *Icarus*, 156(2):399–433, 2002.
- P. Brown, V. Marchenko, D. E. Moser, R. Weryk, and W. Cooke. Meteorites from meteor showers: A case study of the taurids. *Meteoritics & Planetary Science*, 48(2):270–288, 2013.
- P. Brown, P. Wiegert, D. Clark, and E. Tagliaferri. Orbital and physical characteristics of meter-scale impactors from airburst observations. *Icarus*, 266:96–111, 2016.
- P. G. Brown, A. R. Hildebrand, M. E. Zolensky, M. Grady, R. N. Clayton, T. K. Mayeda, E. Tagliaferri, R. Spalding, N. D. MacRae, E. L. Hoffman, et al. The fall, recovery, orbit, and composition of the tagish lake meteorite: A new type of carbonaceous chondrite. *Science*, 290(5490):320–325, 2000.
- D. E. Brownlee, F. Horz, R. L. Newburn, M. Zolensky, T. C. Duxbury, S. Sandford, Z. Sekanina, P. Tsou, M. S. Hanner, B. C. Clark, et al. Surface of young jupiter family comet 81p/wild 2: View from the stardust spacecraft. *Science*, 304(5678):1764–1769, 2004.
- Z. Ceplecha. Impacts of meteoroids larger than 1 m into the earth’s atmosphere. *Astronomy and Astrophysics*, 286:967–970, 1994.
- Z. Ceplecha and R. McCrosky. Fireball end heights: A diagnostic for the structure of meteoric material. *Journal of Geophysical Research*, 81(35):6257–6275, 1976.
- Z. Ceplecha, J. Borovička, W. G. Elford, D. O. ReVelle, R. L. Hawkes, V. Porubčan, and M. Šimek. Meteor phenomena and bodies. *Space Science Reviews*, 84(3-4):327–471, 1998.
- G. Consolmagno, D. Britt, and R. Macke. The significance of meteorite density and porosity. *Chemie der Erde-Geochemistry*, 68(1):1–29, 2008.

- F. DeMeo, C. Alexander, K. Walsh, C. Chapman, and R. Binzel. The compositional structure of the asteroid belt. *Asteroids IV*, 1:13, 2015.
- F. E. DeMeo and B. Carry. Solar system evolution from compositional mapping of the asteroid belt. *Nature*, 505(7485):629–634, 2014.
- H. A. Devillepoix, P. A. Bland, E. K. Sansom, M. C. Towner, M. Cupák, R. M. Howie, B. A. Hartig, T. Jansen-Sturgeon, and M. A. Cox. Observation of metre-scale impactors by the desert fireball network. *Monthly Notices of the Royal Astronomical Society*, 483(4):5166–5178, 2019.
- H. A. R. Devillepoix, M. Cupák, P. A. Bland, E. K. Sansom, M. C. Towner, R. M. Howie, B. A. D. Hartig, T. Jansen-Sturgeon, P. M. Shober, S. L. Anderson, G. K. Benedix, D. Busan, R. Sayers, P. Jenniskens, J. Albers, C. D. K. Herd, P. Carlson, P. J. A. Hill, P. G. Brown, Z. Krzeminski, G. R. Osinski, H. C. Aoudjehane, T. Shisseh, Z. Benkhaldoun, A. Jabiri, M. Guennoun, A. Barka, H. Darhmaoui, L. Daly, G. S. Collins, S. McMullan, M. D. Suttle, C. Shaw, J. S. Young, M. Alexander, A. D. Mardon, T. Ireland, G. Bonning, L. Baeza, T. Y. Arefay, J. Horner, T. D. Swindle, C. W. Hergenrother, M. D. Fries, A. Tomkins, A. Langendam, T. A. Rushmer, C. O’Neill, D. Janches, and J. L. Hormaechea. A global fireball observatory, 2020.
- R. P. Di Sisto, J. A. Fernández, and A. Brunini. On the population, physical decay and orbital distribution of jupiter family comets: Numerical simulations. *Icarus*, 203(1):140–154, 2009.
- J. D. Drummond. A test of comet and meteor shower associations. *Icarus*, 45(3):545–553, 1981.
- M. Duncan, H. Levison, and L. Dones. Dynamical evolution of ecliptic comets. *Comets II*, 193:204, 2004.
- M. J. Duncan and H. F. Levison. A disk of scattered icy objects and the origin of jupiter-family comets. *Science*, 276(5319):1670–1672, 1997.

- O. Eugster, G. Herzog, K. Marti, and M. Caffee. Irradiation records, cosmic-ray exposure ages, and transfer times of meteorites. *Meteorites and the early solar system II*, pages 829–851, 2006.
- J. A. Fernández and A. Morbidelli. The population of faint jupiter family comets near the earth. *Icarus*, 185(1):211–222, 2006.
- J. A. Fernández and A. Sosa. Jupiter family comets in near-earth orbits: Are some of them interlopers from the asteroid belt? *Planetary and Space Science*, 118:14–24, 2015.
- J. A. Fernández, T. Gallardo, and A. Brunini. Are there many inactive jupiter-family comets among the near-earth asteroid population? *Icarus*, 159(2):358–368, 2002.
- J. A. Fernández, A. Sosa, T. Gallardo, and J. N. Gutiérrez. Assessing the physical nature of near-earth asteroids through their dynamical histories. *Icarus*, 238:1–12, 2014.
- Y. Fernández, M. Kelley, P. Lamy, I. Toth, O. Groussin, C. Lisse, M. F. A’Hearn, J. Bauer, H. Campins, A. Fitzsimmons, et al. Thermal properties, sizes, and size distribution of jupiter-family cometary nuclei. *Icarus*, 226(1):1138–1170, 2013.
- Y. R. Fernández. That’s the way the comet crumbles: Splitting jupiter-family comets. *Planetary and Space Science*, 57(10):1218–1227, 2009.
- Y. R. Fernández, D. C. Jewitt, and S. S. Sheppard. Albedos of asteroids in comet-like orbits. *The Astronomical Journal*, 130(1):308, 2005.
- S. Fornasier, P. Hasselmann, M. Barucci, C. Feller, S. Besse, C. Leyrat, L. Lara, P. J. Gutierrez, N. Oklay, C. Tubiana, et al. Spectrophotometric properties of the nucleus of comet 67p/churyumov-gerasimenko from the osiris instrument onboard the rosetta spacecraft. *Astronomy & Astrophysics*, 583:A30, 2015.

- M. Gounelle, A. Morbidelli, P. A. Bland, P. Spurny, E. D. Young, and M. Sephton. Meteorites from the outer solar system. *The solar system beyond Neptune*, pages 525–541, 2008.
- M. Granvik and P. Brown. Identification of meteorite source regions in the solar system. *Icarus*, 311:271–287, 2018.
- M. Granvik, A. Morbidelli, R. Jedicke, B. Bolin, W. F. Bottke, E. Beshore, D. Vokrouhlický, M. Delbò, and P. Michel. Super-catastrophic disruption of asteroids at small perihelion distances. *Nature*, 530(7590):303–306, 2016.
- M. Granvik, A. Morbidelli, R. Jedicke, B. Bolin, W. F. Bottke, E. Beshore, D. Vokrouhlický, D. Nesvorný, and P. Michel. Debaised orbit and absolute-magnitude distributions for near-earth objects. *Icarus*, 312:181–207, 2018.
- M. Gritsevich and V. Stulov. Extra-atmospheric masses of the canadian network bolides. *Solar System Research*, 40(6):477–484, 2006.
- M. I. Gritsevich. Approximation of the observed motion of bolides by the analytical solution of the equations of meteor physics. *Solar System Research*, 41(6):509–514, Dec. 2007. doi: 10.1134/S003809460706007X.
- R. M. Howie, J. Paxman, P. A. Bland, M. C. Towner, M. Cupak, E. K. Sansom, and H. A. Devillepoix. How to build a continental scale fireball camera network. *Experimental Astronomy*, 43(3):237–266, 2017.
- H. H. Hsieh and N. Haghhighipour. Potential jupiter-family comet contamination of the main asteroid belt. *Icarus*, 277:19–38, 2016.
- T. Jansen-Sturgeon, E. K. Sansom, and P. A. Bland. Comparing analytical and numerical approaches to meteoroid orbit determination using hayabusa telemetry. *Meteoritics & Planetary Science*, 54(9):2149–2162, 2019.
- P. Jenniskens and P. M. M. Jenniskens. *Meteor showers and their parent comets*. Cambridge University Press, 2006.
- T. J. Jopek. Remarks on the meteor orbital similarity d-criterion. *Icarus*, 106(2): 603–607, 1993.

- D. Lauretta, C. Hergenrother, S. Chesley, J. Leonard, J. Pelgrift, C. Adam, M. Al Asad, P. Antreasian, R.-L. Ballouz, K. Becker, et al. Episodes of particle ejection from the surface of the active asteroid (101955) bennu. *Science*, 366(6470), 2019.
- H. F. Levison and M. J. Duncan. The long-term dynamical behavior of short-period comets. *Icarus*, 108(1):18–36, 1994.
- H. F. Levison and M. J. Duncan. From the kuiper belt to jupiter-family comets: The spatial distribution of ecliptic comets. *Icarus*, 127(1):13–32, 1997.
- E. Lyytinen and M. Gritsevich. Implications of the atmospheric density profile in the processing of fireball observations. *Planetary and Space Science*, 120:35–42, 2016.
- J. M. Madiedo, J. M. Trigo-Rodríguez, J. Zamorano, L. Ana-Hernández, J. Izquierdo, J. L. Ortiz, A. J. Castro-Tirado, A. S. de Miguel, F. Ocaña, S. Pastor, et al. Trajectory, orbit, and spectroscopic analysis of a bright fireball observed over spain on april 13, 2013. *Astronomy & Astrophysics*, 569:A104, 2014.
- K. Meech, O. Hainaut, and B. Marsden. Comet nucleus size distributions from hst and keck telescopes. *Icarus*, 170(2):463–491, 2004.
- D. Nesvorný, P. Jenniskens, H. F. Levison, W. F. Bottke, D. Vokrouhlický, and M. Gounelle. Cometary origin of the zodiacal cloud and carbonaceous micrometeorites. implications for hot debris disks. *The Astrophysical Journal*, 713(2):816, 2010.
- D. Nesvorný, D. Vokrouhlický, L. Dones, H. F. Levison, N. Kaib, and A. Morbidelli. Origin and evolution of short-period comets. *The Astrophysical Journal*, 845(1):27, 2017.
- O. Popova, J. Borovička, W. K. Hartmann, P. Spurný, E. Gnos, I. Nemtchinov, and J. M. Trigo-Rodríguez. Very low strengths of interplanetary meteoroids and small asteroids. *Meteoritics & Planetary Science*, 46(10):1525–1550, 2011.

- T. Quinn, S. Tremaine, and M. Duncan. Planetary perturbations and the origins of short-period comets. *The Astrophysical Journal*, 355:667–679, 1990.
- H. Rein and S. F. Liu. REBOUND: an open-source multi-purpose N-body code for collisional dynamics. *Astronomy and Astrophysics*, 537:A128, Jan. 2012. doi: 10.1051/0004-6361/201118085.
- H. Rein and D. S. Spiegel. IAS15: a fast, adaptive, high-order integrator for gravitational dynamics, accurate to machine precision over a billion orbits. *Monthly Notices of the Royal Astronomical Society*, 446(2):1424–1437, Jan. 2015. doi: 10.1093/mnras/stu2164.
- T. P. Robitaille, E. J. Tollerud, P. Greenfield, M. Droettboom, E. Bray, T. Aldcroft, M. Davis, A. Ginsburg, A. M. Price-Whelan, W. E. Kerzendorf, et al. Astropy: A community python package for astronomy. *Astronomy & Astrophysics*, 558:A33, 2013.
- J. Salvatier, T. V. Wiecki, and C. Fonnesbeck. Probabilistic programming in python using pymc3. *PeerJ Computer Science*, 2:e55, 2016.
- E. K. Sansom, P. Bland, J. Paxman, and M. Towner. A novel approach to fireball modeling: The observable and the calculated. *Meteoritics & Planetary Science*, 50(8):1423–1435, 2015.
- E. K. Sansom, M. Gritsevich, H. A. Devillepoix, T. Jansen-Sturgeon, P. Shober, P. A. Bland, M. C. Towner, M. Cupák, R. M. Howie, and B. A. Hartig. Determining fireball fates using the α - β criterion. *The Astrophysical Journal*, 885(2):115, 2019a.
- E. K. Sansom, T. Jansen-Sturgeon, M. G. Rutten, H. A. Devillepoix, P. A. Bland, R. M. Howie, M. A. Cox, M. C. Towner, M. Cupák, and B. A. Hartig. 3d meteoroid trajectories. *Icarus*, 321:388–406, 2019b.
- P. M. Shober, T. Jansen-Sturgeon, P. Bland, H. Devillepoix, E. Sansom, M. Towner, M. Cupák, R. Howie, and B. Hartig. Using atmospheric impact

- data to model meteoroid close encounters. *Monthly Notices of the Royal Astronomical Society*, 498(4):5240–5250, 2020a.
- P. M. Shober, T. Jansen-Sturgeon, E. K. Sansom, H. A. Devillepoix, M. C. Towner, P. A. Bland, M. Cupák, R. M. Howie, and B. A. Hartig. Where did they come from, where did they go: Grazing fireballs. *The Astronomical Journal*, 159(5):191, 2020b.
- R. Southworth and G. Hawkins. Statistics of meteor streams. *Smithsonian Contributions to Astrophysics*, 7:261–285, 1963.
- P. Spurný, J. Borovicka, H. Haack, W. Singer, D. Keuer, and K. Jobse. Trajectory and orbit of the maribo cm2 meteorite from optical, photoelectric and radar records. In *Meteoroids 2013 conference, Poznan, Poland, 2013*.
- P. Spurný, J. Borovička, G. Baumgarten, H. Haack, D. Heinlein, and A. N. Sørensen. Atmospheric trajectory and heliocentric orbit of the ejby meteorite fall in denmark on february 6, 2016. *Planetary and Space Science*, 143:192–198, 2017.
- J. Sunshine, M. A’hearn, O. Groussin, J.-Y. Li, M. Belton, W. Delamere, J. Kissel, K. Klaasen, L. McFadden, K. Meech, et al. Exposed water ice deposits on the surface of comet 9p/tempel 1. *Science*, 311(5766):1453–1455, 2006.
- D. Takir, J. P. Emery, and H. Y. McSween Jr. Toward an understanding of phyllosilicate mineralogy in the outer main asteroid belt. *Icarus*, 257:185–193, 2015.
- G. Tancredi. The dynamical memory of jupiter family comets. *Astronomy and Astrophysics*, 299:288, 1995.
- G. Tancredi. A criterion to classify asteroids and comets based on the orbital parameters. *Icarus*, 234:66–80, 2014.
- M. B. Taylor. TOPCAT & STILTS: starlink table/VOTable processing software. In *Astronomical Data Analysis Software and Systems XIV*, volume 347, page 29, 2005.

-
- M. C. Towner, M. Cupak, J. Deshayes, R. M. Howie, B. A. D. Hartig, J. Paxman, E. K. Sansom, H. A. R. Devillepoix, T. Jansen-Sturgeon, P. A. Bland, and et al. Fireball streak detection with minimal cpu processing requirements for the desert fireball network data processing pipeline. *Publications of the Astronomical Society of Australia*, 37:e008, 2020. doi: 10.1017/pasa.2019.48.
- G. Wetherill and D. ReVelle. Which fireballs are meteorites? a study of the prairie network photographic meteor data. *Icarus*, 48(2):308–328, 1981.

CHAPTER 6

Thesis Conclusions and Future Work

The small bodies in our solar system hold the clues necessary to understand its origin and evolution. They are the remnants left over from our solar system's formation and contain the primitive materials from which all the planets were built. Additionally, their distribution in orbital space can help us understand the planets' past motion and how they arrived at the current configuration.

Furthermore, as human interplanetary exploration increases, we need to understand better the complex foreign environment we are attempting to venture into. This necessitates that we better understand the dynamic and physical properties of small bodies that pose a significant threat as well as a great opportunity to missions. The potential impact risk from asteroids, comets and the debris they produce has inspired decades of observational surveys of near-Earth space. Meanwhile, the extraction of valuable resources from these bodies is gaining interest as humanity attempts to send people further into space than ever before.

Within planetary science, several approaches exist to gain insights about these objects. Asteroid and comets can be observed telescopically, providing orbital and spectral information of the objects. This method can provide some sense of physical characteristics. However, due to the unconstrained nature of the problem,

several assumptions usually are required. The asteroids are typically classified based on their spectral signature, which is assumed to correspond to surface composition variations. Nevertheless, due to other unknown factors about the surface properties, the compositions are not well calibrated.

Another obvious method to circumvent the assumptions made during telescopic observations is to send a sample-return mission to the asteroid or comet directly. This method is very effective at characterising small bodies, but it is too expensive and slow to employ as a general method to understand the variety of small bodies in the solar system.

For over a hundred years, geologists have also analysed the debris produced by small bodies that have impacted the Earth and survived as meteorites. The tens of thousands of meteorites in the world's collections have given us the most valuable information about small bodies' physical composition and history. These extraterrestrial samples have helped constrain the formation and evolution timeline of the solar system. Planetary geologists have spent a century categorising them based on their chemical, petrological, mineralogical, and isotopic properties. Yet, unlike telescopic or probe data, we have no orbital information associated with meteorites. Thus, how they relate to asteroid spectral types is still dubious. Sample-return missions can slowly provide linkages to different meteorite types. However, there is a faster and cheaper way. Photographic fireball networks solve this problem by continuously observing the night-sky for impacts of large pieces of debris called 'fireballs'. These fireball observations can then be used to predict the fall locations of meteorites produced along with the pre-impact orbital elements. This orbital information along with recovered meteorite samples can cheaply and effectively start to fill in gaps between meteorites and their parent bodies.

The Desert Fireball Network (DFN) has been the largest photographic fireball network in the world since its full deployment in 2015. Covering over one-third of Australian skies, the DFN has collected a massive fireball dataset during its operation. This fireball dataset contains an abundance of information about the debris in the inner solar system and meteorites' source populations. Within this thesis, meteoroids' dynamic and physical properties are explored, and what these

results imply about meteorites and their parent bodies is discussed.

One of the most intriguing sub-populations in near-Earth space is that of temporarily captured objects. When a meteoroid or asteroid approaches the Earth at sufficiently low-enough relative velocity and favourable geometry, they can be gravitationally captured by the Earth. These objects are of great interest because as they orbit the Earth, they are the easiest planetary bodies to reach in the solar system (lowest Δv). Thus, they would be the best candidates to test emerging space technologies related to in-situ resource utilisation and asteroid impact mitigation. In Chapter 2), I discuss the exhaustive search for ‘minimoons’ within the DFN dataset. One event within the fireball dataset (event DN160822_03), consistent with previous models, was found to have a very high probability of originating from a geocentric orbit ($>90\%$). This was determined based on the statistical analysis of comprehensive N-body numerical Monte Carlo simulations performed on the Magnus supercomputing cluster. It was found that due to likely multiple close encounters with the Moon during the meteoroid’s capture, the orbit is chaotic on the timescales of days. Numerical modelling of the meteoroid demonstrated that although the exact path was uncertain, the object was likely captured through either the L1 or L2 Lagrange points. There is a low probability that a close encounter with the Moon could have initiated the capture; however, this is less likely. Furthermore, the meteoroid simulations found an annual variation in the likely capture time, capture velocity, capture semi-major axis, capture NEO group, and capture mechanism. This annual variability in the meteoroid’s probable history provides a unique insight into possible variations and patterns that could occur in the general minimoon population. The best way to investigate these models in the future is to use advanced survey telescopes (e.g. Large Synoptic Survey Telescope) to gather more observations of captured objects while they are orbiting the Earth.

While some objects pass close to the Earth with low enough relative velocity to be captured gravitationally, many orders of magnitude more meteoroids have close encounters. In Chapter 3, I analysed the DFN observations of one particular meteoroid that had such a close encounter with the Earth that it grazed

the atmosphere. This grazing fireball last for 90 s, reached a minimum height of 58.5 km, and travelled over 1300 km through the atmosphere before returning to interplanetary space. This grazing fireball is one of the longest-lasting fireballs ever observed. Numerical integrations of the meteoroid prior to and after the encounter showed that the object gained orbital energy, similar to how probes use gravitational assists to save fuel. The meteoroid originated from an Apollo-type NEO orbit and was sent onto a JFC-like orbit ($2 < T_J < 3$). Interestingly, the object is likely to experience several close encounters with Jupiter in the future, a dynamic signature diagnostic of cometary material.

The observations of the grazing fireball in 2017 by the DFN and subsequent analysis led me to question the significance of close encounters as a mechanism to mix meteoroids from cometary and asteroidal populations. These encounters occur all the time, yet very few are detected telescopically. The telescopically detected objects are larger (hundreds of metres to kilometres) and usually do not have close enough encounters to have their orbits significantly effected. Meanwhile, centimetre to metre debris has numerous extremely close encounters all the time. In Chapter 4, I describe a model of meteoroid close encounters I constructed using the large fireball dataset collected by the DFN. The results showed that of the 1.6×10^{11} predicted annual close encounters < 1.5 LD within the 0.01 – 100 kg size-range, about 2.5×10^8 objects annually are estimated to be transferred from asteroidal orbits ($T_J > 3$) to JFC-like orbits ($2 < T_J < 3$) (0.1% of total flux). This net-flux results from the difference in the encounter frequencies of the two populations concerned. A vast majority of meteoroids have negligible changes to their orbits, however, given that these objects will stay on their new orbits for typically $10^5 - 10^6$ years, the steady-state population is significant ($10^{13} - 10^{14}$ objects). Of this asteroidal to cometary population, we also found that $\sim 70\%$ of the objects will avoid future close encounters with Jupiter and evolve in a manner consistent with asteroidal debris. Since the remaining $\sim 30\%$ of meteoroids behave chaotically over short-timescales, they are rapidly removed from near-Earth space. Thus, the predicted $10^3 - 10^4$ annual impacts from this population will all likely come from meteoroids with a stable dynamically asteroidal orbits. The model also predicts

$\sim 10^7$ meteoroids are annually transferred onto Aten-type NEO orbits, where they could eventually enter the Atira-type group.

The close encounter model described in Chapter 4 provides at least one pathway for main-belt debris to be transferred onto comet-like orbits. Moreover, it predicts that the population produced is significant enough for fireball networks to have many observations. Over the previous century, many studies have looked at meteorites and fireball data, waiting to find a cometary meteorite. Many have speculated what they would look like or if they even exist at all. Several previous studies reference bright fireballs observed to originate from comet-like orbits that were likely to have produced a meteorite. However, based on the close encounter model, there should be meteorite-producing material on these orbits, but not cometary.

In Chapter 5, I analysed the dynamic and physical properties of sporadic JFC-like fireballs within the DFN fireball dataset. Numerical N-body integrations were conducted to characterise each meteoroid's orbit's stability over the previous 10^4 years. Meanwhile, the PE criterion, a physical strength metric based on meteor end heights, was used to determine the meteoroids' relative strengths. Combining both of these analysis methodologies, I found that nearly all of the sporadic comet-like meteoroids observed by the DFN between 2014-2020 were consistent dynamically and physically with main-belt debris. This lack of cometary material within the sample is statistically significant and indicates some process is removing cometary debris within the centimetre to metre size-range. Based on telescopic observations of JFCs, it has been known for decades that there is a paucity of JFCs at the sub-kilometre scale. This paucity has been inferred by many authors to be caused by the friable nature of comets. Small cometary bodies are predicted to have short physical lifetimes in the inner solar system. Thus, according to my analysis, centimetre to metre cometary debris also have very short physical lifetimes in the inner solar system. The physical lifetimes must be less than the disassociation lifetimes of cometary streams, providing a maximum physical lifetime of $\sim 10^3$ years. Using a Markov chain Monte Carlo, I estimate that as much as $94.2 \pm 3.2\%$ of near-Earth centimetre-sized debris on comet-like orbits is actu-

ally sourced from the main asteroid belt. Even when considering showers within the same size-range, most material on comet-like orbits is asteroidal in origin.

The research conducted within this thesis has contributed significantly to the body of knowledge about debris in the inner solar system. Future research could be done by incorporating more data acquired from the meteorites themselves, such as cosmic-ray exposure ages (CRE). The CRE ages signify the amount of time spent by the meteoroid between being ejected by the parent body and impacting the Earth. Thus, this information could provide an additional constraint on the dynamic modelling of fireball orbits. Additionally, more work needs to be done comparing meteorites acquired by fireball networks and the spectra of potential parent bodies. If meteorite types can be better linked to asteroid spectral types, an overwhelming amount of knowledge of our solar system origin and evolution will be gained.

Appendices

First Author Journal Publication

Reprints

Paper 1 - Identification of a Minimoon Fireball

The Astronomical Journal (2019), Volume 158, Issue 5, p. 183-194.

Patrick M. Shober, Trent Jansen-Sturgeon, Eleanor K. Sansom, Hadrien A.R. Devillepoix, Phil A. Bland, Martin Cupák, Martin C. Towner, Robert M. Howie, Benjamin A.D. Hartig

REPRINTED WITH PERMISSION OF IOP PUBLISHING: *The authors have the right to use all or part of the Article in future works and derivative works of their own of any type, and to make copies of all or part of the Article for the authors' use for educational or research purposes.*

STATEMENT OF AUTHORSHIP

TITLE OF PAPER: Identification of a Minimoon Fireball

PUBLICATION STATUS: Published in The Astronomical Journal
(October 14, 2019).

AUTHOR CONTRIBUTIONS

By signing the Statement of Authorship, each author certifies that their stated contribution to the publication is accurate and that permission is granted for the publication to be included in the candidate's thesis.

Name of Principal Author: Patrick M. Shober

Contribution to the Paper: Led data analysis. Conducted the trajectory and orbital analysis. Wrote the manuscript.

Overall Percentage: 85 %

Signature:

Date:

Name of Co-Author: Trent Jansen-Sturgeon

Contribution to the Paper: Assisted with triangulation of the fireball.

Overall Percentage: 5 %

Signature:

Date:

Name of Co-Author: Eleanor K. Sansom

Contribution to the Paper: Assisted with triangulation of the fireball and initial mass determination.

Overall Percentage: 3 %

Signature:

Date:

Name of Co-Author: Hadrien A.R. Devillepoix

Contribution to the Paper: Assisted with data analysis and collection.

Overall Percentage: 3 %

Signature:

Date:

Name of Co-Author: Phil A. Bland

Contribution to the Paper: Assisted with writing manuscript.

Overall Percentage: 1 %

Signature:

Date:

Name of Co-Author: Martin Cupák

Contribution to the Paper: Data collection and helped review manuscript.

Overall Percentage: 1 %

Signature:

Date:

Name of Co-Author: Martin Towner

Contribution to the Paper: Data collection and helped review manuscript.

Overall Percentage: 1 %

Signature:

Date:

Name of Co-Author: Robert M. Howie

Contribution to the Paper: Data collection and built equipment.

Overall Percentage: 0.5 %

Signature:

Date:

Name of Co-Author: Benjamin A.D. Hartig

Contribution to the Paper: Data collection and built equipment.

Overall Percentage: 0.5 %

Signature:

Date:



Identification of a Minimoon Fireball

P. M. Shober , T. Jansen-Sturgeon , E. K. Sansom , H. A. R. Devillepoix , P. A. Bland , Martin Cupák, Martin C. Towner, Robert M. Howie , and Benjamin A. D. Hartig
 Space Science and Technology Centre (SSTC), School of Earth and Planetary Sciences, Curtin University, GPO Box U1987, Perth, Western Australia 6845, Australia
patrick.shober@postgrad.curtin.edu.au

Received 2019 May 20; revised 2019 August 23; accepted 2019 August 27; published 2019 October 14

Abstract

Objects gravitationally captured by the Earth–Moon system are commonly called temporarily captured orbiters (TCOs), natural Earth satellites, or minimoons. TCOs are a crucially important subpopulation of near-Earth objects (NEOs) to understand because they are the easiest targets for future sample-return, redirection, or asteroid mining missions. Only one TCO has ever been observed telescopically, 2006 *RH*₁₂₀, and it orbited Earth for about 11 months. Additionally, only one TCO fireball has ever been observed prior to this study. We present our observations of an extremely slow fireball (codename DN160822_03) with an initial velocity of around 11.0 km s^{−1} that was detected by six of the high-resolution digital fireball observatories located in the South Australian region of the Desert Fireball Network. Due to the inherent dynamics of the system, the probability of the meteoroid being temporarily captured before impact is extremely sensitive to its initial velocity. We examine the sensitivity of the fireball’s orbital history to the chosen triangulation method. We use the numerical integrator REBOUND to assess particle histories and assess the statistical origin of DN160822_03. From our integrations we have found that the most probable capture time, velocity, semimajor axis, NEO group, and capture mechanism vary annually for this event. Most particles show that there is an increased capture probability during Earth’s aphelion and perihelion. In the future, events like these may be detected ahead of time using telescopes like the Large Synoptic Survey Telescope, and the pre-atmospheric trajectory can be verified.

Key words: meteorites, meteors, meteoroids – planets and satellites: general

1. Introduction

Occasionally when an object gets close to the Earth–Moon system, it is captured by Earth’s gravity. These objects are commonly called temporarily captured orbiters (TCOs), natural Earth satellites, or minimoons (Granvik et al. 2012). The first mention of TCOs was by Chant (1913) and then Denning (1916) in a description of an extraordinarily long fireball that was witnessed over North America. Since the event lasted so long, according to witnesses, the source was speculated to be orbiting Earth before entering the atmosphere. Besides this brief hypothesis, the study of TCOs was mostly left unexplored for the rest of the twentieth century. During the space race, when artificial satellites began to be launched into orbit, there was speculation on whether or not natural Earth satellites would exist side by side with the artificial satellites (Baker & Robert 1958).

For the last half-century, there have been many studies of captured objects by the large gas giants in the solar system, particularly Jupiter (Heppenheimer & Porco 1977; Pollack et al. 1979; Kary & Dones 1996; Nesvorný et al. 2003, 2007). There have also been several papers discussing the capture mechanisms and dynamics in the circular restricted three-body problem (CRTBP) and whether or not individual planets are even capable of sustaining a TCO population. Originally the models were simple and showed that only the large gas giants were capable of capturing satellites (Yegorov 1959). Eventually, Bailey (1972) extended this methodology to any planet in the solar system. He showed that TCOs are possible for any planet when considering each in the limiting framework of the elliptic restricted three-body problem, instead of assuming circular orbits.

Following this study, Cline (1979) was the first to explore the viability of a lunar assisted capture as a way to check for viable ballistic trajectories to the outer solar system’s planets. Since then, there have been a handful of studies interested in the feasibility of Moon-assisted captures along with using moons for decreasing the delta-V required for space missions to outer solar system objects (Tsui 2000, 2002; Lynam et al. 2011; Gong & Li 2015; Luo & Topputo 2017).

While studying the capture dynamics of Jupiter, several papers found that the capture duration was highly unpredictable (Murison 1989; Brunini 1996; Kary & Dones 1996). This unpredictability was due to the fractal nature of the orbital phase space from which the objects originate. Furthermore, Murison (1989) stated that temporarily captured objects may have to have some chaotic origin, being on the boundary of two adjacent sinks (i.e., they can either evolve toward a heliocentric orbit or a planetocentric orbit). Thus, small perturbations in the initial conditions can radically change the evolutionary behavior of objects, i.e., whether or not it is captured and for how long the object is captured. Astakhov et al. (2003) also showed that whether an orbit displayed prograde or retrograde behavior was intrinsically tied to the initial energy along with the size and distribution of regular satellites in the Hill sphere. This chaotic nature associated with the dynamics of natural satellites will make it much more difficult to predict where the meteoroid observed by the Desert Fireball Network (DFN) originated from in the solar system.

It was not until 2006 that the first Earth TCO was observed. Asteroid 2006 *RH*₁₂₀ orbited Earth from 2006 to 2007 July before escaping the Earth–Moon system (Kwiatkowski et al. 2009). This asteroid is still the only observed TCO, but this will undoubtedly change once the Large Synoptic Survey Telescope (LSST) starts making regular survey observations in 2022

THE ASTRONOMICAL JOURNAL, 158:183 (11pp), 2019 November

Shober et al.

(Ivezić et al. 2019; Fedorets et al. 2015). Granvik et al. (2012) were the first to model TCOs that considered capture probability as a function of orbital element space for the near-Earth object (NEO) population. The model also calculated the size–frequency distribution and orbital distribution for TCOs. Fedorets et al. (2017) expanded on this work by focusing on objects that approached Earth and were captured but escaped before they could complete one orbit, also known as temporarily captured flybys (TCFs). Based upon these models, they predict that the largest object in orbit around Earth at any given time is about 1 m in diameter and that these objects are typically captured through Earth’s co-linear L1 and L2 regions. Additionally, they predicted that 0.1% of all meteors were previously TCOs before they impacted Earth. Given this information, we expect to find about one TCO within the DFN’s data set.

Clark et al. (2016) searched for fireballs that were natural satellites of Earth before they impacted the atmosphere. They found one fireball detected by the European Fireball Network (EFN) that had a 92%–98% chance of being captured by Earth before detection according to their model. Although, the capture duration for this meteoroid varied from 48 days up to over 5 yr. Clark et al. (2016) also looked at data from the Prairie Network in the United States along with data collected by United States government sensors. None of the low-speed objects could be confidently said to be captured before impact due to the unknown or high uncertainty in the pre-atmospheric velocity for the measurements. To date, the event recorded by the EFN and described by Clark et al. (2016) is the only fireball observed with a very high probability of originating from a TCO orbit.

Granvik et al. (2012) assumed the orbit–density distribution is independent of the size–frequency distribution for their TCO model. While this is accurate for more substantial objects, it is unlikely true for smaller NEOs. The DFN and other fireball networks like it are particularly ideal for characterizing this portion of the meteoroid population. Using TCO fireball data collected from these types of networks, we can ascertain how likely the Granvik model is accurate for smaller size ranges.

Generating an accurate orbital model for TCOs and TCFs is vital because these bodies are the most accessible in the solar system. They are the ideal targets for future sample-return, in situ resource utilization, and asteroid impact mitigation technology testing (Chodas 2014; Brelsford et al. 2016). Additionally, since the average TCO orbits multiple times before escaping, this allows for multiple observations within a small time frame. These observations of TCOs can be used to understand the smallest members of the NEO population (Bolin et al. 2014). TCOs have the potential to have far-reaching effects on our understanding of asteroids and the history of the solar system along with many other future space-based technology applications. Thus, if we can better predict the orbital paths of these bodies based on observations and models, finding TCOs and TCFs will become easier.

The DFN is a continental scale facility that observes fireballs in our atmosphere, calculates their pre-entry orbit, and determines where any possible meteorite material may land (Howie et al. 2017a). There are currently 1300+ fully triangulated events detected by the DFN. Previous models of the natural Earth satellite population (Granvik et al. 2012; Fedorets et al. 2017) predicted that about 0.1% of all meteors impacting Earth should have been temporarily captured prior to

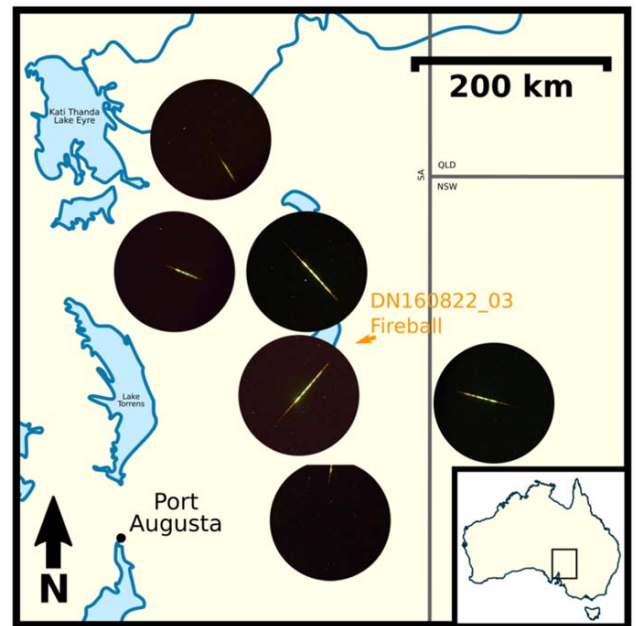


Figure 1. Map of camera observations for event DN160822_03 in Southern Australia by the DFN. The orange arrow indicates the ground track of the fireball’s luminous trajectory. This path is extremely small due to the nearly vertical slope of the trajectory ($\approx 86^\circ 6'$). Six camera observations were collected during the 5.32 s duration.

impact. Based on these models, assuming the orbit–density distribution is independent of the size–frequency distribution, there should be one or two events in the DFN data set that were captured objects before impacting the atmosphere.

The questions to be addressed within this study as follows.

- (i) Is the number of TCOs in the DFN data set consistent with previous models?
- (ii) How would such meteoroids get captured by the Earth–Moon system and is this different than expected from past models?
- (iii) How long might any TCOs have been captured before they hit Earth?
- (iv) How much does the presence of the Moon affect the capturability?

2. Event DN160822_03 Observations

Within the orbital data set of the DFN, one event was indeed flagged as a possible TCO: DN160822_03. Here we will detail the event from initial observations to triangulation and will discuss in the following sections its’ nature as a TCO.

Event Detection. DN160822_03 was observed by six of the DFN’s high-resolution fireball cameras in South Australia just before 11 PM local time on 2016 August 22 (Figure 1). All but one of the cameras were able to image nearly the entire trajectory (Table 1). The event lasted over five seconds and had a nearly vertical atmospheric trajectory ($\sim 87^\circ$). This high-angle impact argues against an artificial origin and pre-atmospheric trajectory integrations eliminate the possibility of standard satellite debris. Although, however unlikely, this does not eliminate the possibility of debris from Apollo or other past lunar/interplanetary missions. Table 2 summarizes the

Table 1

Locations and Observation Details for DFN Observatories that Detected Event DN160822_03

Observatory	Range (km) ^a	Start Time (s) ^b	End Time (s) ^b
Moolawatana	117	0.10	5.32
Wertaloona	117	0.20	5.12
Fowlers Gap	157	0.00	5.06
Weekeroo	203	0.20	2.66
Wilpoorinna	221	0.50	4.96
Etadunna	270	1.10	4.16

Notes. Start and end times are given relative to the event start/end (the first event to detect the fireball has a relative start time of 0.00).

^a Line-of-sight distance to the start of the trajectory.

^b Relative to 12:17:10.826 UTC on 2016 August 22.

Table 2

Atmospheric Trajectory of Event DN160822_03

	Beginning	Terminal
Time (isot)	2016-08-22T12:17:10.826	2016-08-22T12:17:16.146
Height (km)	74.1	24.1
Mass (kg)	11.8	0.3
Latitude (deg)	-30.53009	-30.53960
Longitude (deg)	140.38927	140.36020
SLLS TOPS velocity (km s ⁻¹)	10.95 ± 0.07	3.90 ± 0.18
DTF TOPS velocity (km s ⁻¹)	11.07 ± 0.14	3.77 ± 0.07
R.A. (deg)	-63.06557 ± 0.00831	
Decl. (deg)	-29.35007 ± 0.00726	
Slope (deg)	86.55081 ± 0.00725	
Duration (sec)	5.32	
Best convergence angle (deg)	87.8	
Number of observations	6	
Number of data points	506	

atmospheric trajectory, mass, and velocities determined for event DN160822_03.

The camera systems used to observe the event are described fully in Howie et al. (2017a). The absolute timing for the event was recorded using a de-Bruijn sequence that is encoded into the fireball image using a liquid crystal shutter in addition to the built-in shutter (Howie et al. 2017b). The liquid crystal is synchronized with a global navigation satellite system module using a microcontroller, which produces absolute times accurate to ±0.4 ms.

Astrometric calibration. Astrometric calibration is performed using background stars, as described by Devillepoix et al. (2018). This results in astrometric measurements that are generally accurate (1 σ) down to \simeq 1.5 minutes of arc (as shown by the errors bars in Figure 2), limited by astrometric noise in this case.

Triangulation. During the analysis of the event detected by the DFN, two separate triangulation methods were used. We did this to check the sensitivity of the orbital history for this meteoroid to the triangulation method based on the work of previous studies (Vida et al. 2018). Our primary method is a straight-line least-squares (SLLS) algorithm, modified from Borovicka (1990), with an extended Kalman smoother (EKS)

for velocity determination (Sansom et al. 2015). Additionally, the dynamic trajectory fit (DTF) of T. Jansen-Sturgeon et al. (2019, in preparation) was utilized alongside the traditional triangulation methods for comparison. The SLLS algorithm determines the straight-line trajectory by minimizing the angular distance between it and the observed lines of sight from every camera. The DTF algorithm is similar, however, it fits the observation rays to a trajectory based on meteor equations of motion, therefore dropping the straight-line assumption. One might say the SLLS is a purely geometric and simplifying fit, while the DTF is more based in reality. However, the initial velocity at the top of the luminous path (v_0) errors produced when using this DTF method cannot account for model error. The SLLS with an EKS velocity analysis can include this factor, therefore producing more reliable errors. Moreover, the event in question has a nearly vertical slope (87°8), and the luminous path deviates negligibly from linear (Figure 2). Thus, the backward integrations initiated after using the SLLS method in this paper are more statistically robust than those produced by the DTF method. We use both methods to demonstrate the highly sensitive pre-atmospheric orbit of event DN160822_03 to the calculated v_0 .

3. Methods

Summary of Definitions and Abbreviations. Within this study we followed the notation of Granvik et al. (2012) and Fedorets et al. (2017) for consistency (see the Appendix for a full list of symbols). Consistent with Granvik et al. (2012) and Kary & Dones (1996), to be considered temporarily captured the particle has to be within at least 3 Hill radii of Earth and have a planetocentric Keplerian energy of $E < 0$. Additionally, to be classified as a TCO, the particle must have orbited Earth at least once. Unlike previous studies (Granvik et al. 2012; Clark et al. 2016; Fedorets et al. 2017), instead of determining TCO membership by measuring the change in ecliptic longitudinal angle in the synodic frame, the TCO membership was determined by measuring the proportion of an orbital period each particle was captured. This reduces some of the ambiguity between TCFs and TCOs as demonstrated by Urrutxua & Bombardelli (2017).

Orbital Integrator. Simulations in this paper made use of the publicly available REBOUND code.¹ The 15th order IAS15 integrator of REBOUND was used for this study because of its resolution of close encounters, its adaptive time step, and the ability to incorporate nongravitational forces along with other perturbations like the nonsphericity of Earth (Rein & Liu 2012; Rein & Spiegel 2015). The IAS15 integrator is based on the RADAU-15 developed in Everhart (1985) and used by Clark et al. (2016) to model a captured-object impact detected by the EFN. IAS15 improves upon the RADAU-15 by suppressing the systematic error generated by the algorithm to well-below machine precision, implementing an adaptive time step, and adding the ability to include nonconservative forces easily while ensuring that the round-off errors are symmetric and at machine precision (Rein & Spiegel 2015).

Atmosphere Model. The publicly available additional forces of REBOUNDx² were used as a way to add other forces to our model. We split up the regression model into two scripts: one that integrates back through the top of the atmosphere, and one

¹ <http://github.com/hannorein/REBOUND>

² <https://github.com/dtamayo/REBOUNDx>

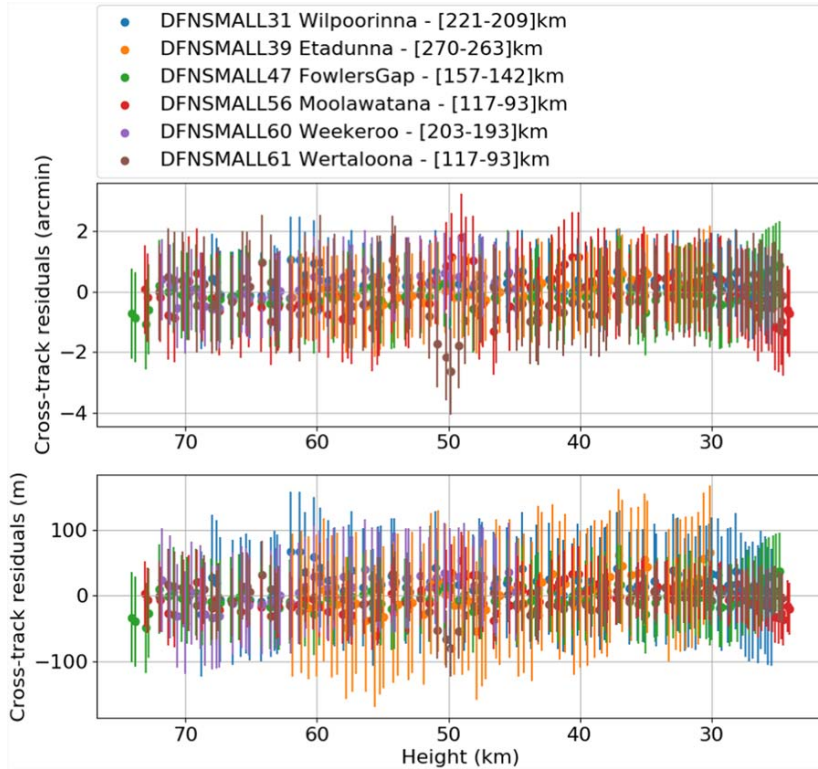


Figure 2. Cross-track residuals to the straight-line trajectory fit (SLLS) of the event DN160822_03. The dots correspond to the perpendicular distance between the observed lines of sight and the predicted straight-line trajectory. The error bars represent the 1σ formal astrometric uncertainties, however, these uncertainties are likely overestimated due to not well-constrained point-picking uncertainties (nominally 0.5 pixel error). The observation range from each DFN station is given in the legend (highest point–lowest point).

that integrates back until the particles are out of the Earth–Moon system. The first integration code uses the `whfast` integrator provided by `REBOUND` along with the `NRLMSISE-00` model 2001³ to take into account atmospheric drag that took place before the meteoroid started to ablate significantly in the upper atmosphere (Rein & Spiegel 2015). The model produces a multivariate normal distribution of 10,000 particles given by our triangulation of the event. The particles vary in shape factor from a sphere to a brick (1.21–1.55) and are either chondritic or metallic in density (3500 or 7500 kg m⁻³). These particles are then integrated backward in time until all the particles are above 200 km. At this point, the simulation is handed off to the next integration script.

Integration Method. The long-term integration script takes the distribution of particles from the results of the atmosphere script and generates particles from this distribution to be integrated out of the Earth–Moon system. The Sun, Moon, and Jupiter are directly added to the simulation from the JPL Horizons solar system data⁴ and ephemeris computation service. Only these bodies were added to reduce the computational load and because they are the primary gravitational perturbers. `REBOUNDx` was used to incorporate orbital variations due to Earth’s oblateness, and J2 and J4 gravitational harmonic coefficients were applied to the particles. We additionally accounted for radiation pressure using the

`REBOUNDx` module. The model automatically adjusts the time steps based on the nonlinearity at that point in time. The integration itself is also split up into thousands of sections in order to save the appropriate outputs at regular time intervals. At the end of each integration section, the algorithm checks and records the particle’s positions, orbital elements, and capture status, along with many other metrics.

In total, eight distinct orbit recursions were run. We varied the triangulation method, the meteoroid density, and the segment of the trajectory used to generate the orbits from the observations. In Table 3, we varied the density between high and low, corresponding to metallic (7500 kg m⁻³) and chondritic (3500 kg m⁻³) densities respectively (Consolmagno et al. 2008). Half of the orbital integrations were performed from triangulations using only the upper portion of the observed atmospheric trajectories. This top of trajectory (denoted as “tops” in Table 3) is defined by all observations triangulated above 65 km altitude. This was done to reduce the dependency on the chosen triangulation model where high sample rates can observe variations due to additional physical effects occurring lower in the atmosphere (i.e., gravity, atmosphere; Figure 3). If a similar event occurred where the sampling rate was lower, varying the triangulation method could lead to an erroneous analysis of the results as the models will likely converge on full trajectory solutions.

By reducing the amount of data, the uncertainties increase and the mean TCO probabilities converge. Therefore, any study that states that a TCO fireball was observed based on atmospheric observations by photographic networks should be accepted with a degree of skepticism. Events like these, that

³ Ported to python based off the Dominik Brodowski 20100516 version at <https://www.brodo.de/space/nrlmsise/index.html>.

⁴ <https://ssd.jpl.nasa.gov/>

Table 3

Summary of 5 yr Recursion Results for Event DN160822_03 in Which Over 16,000 Valid Particles Were Integrated, 10,000 for Each Run and 80,000 in Total

Triang. Method	Density	# Sputniks	%SC	% TCO	% TCF	% TC 3LH	% TC
SLLS full	Low	9728	98.1	93.3–99.9	0.1–6.2	92.9	99.5–100.0
SLLS full	High	9711	96.4	97.0–99.9	0.1–2.9	96.6	100.0
SLLS tops	Low	9060	95.3	88.5–99.5	0.4–8.5	87.8	97.0–99.9
SLLS tops	High	9173	95.5	90.6–99.6	0.3–6.8	90.0	97.4–99.9
DTF tops	Low	2974	36.5	23.3–51.3	8.4–13.3	22.5	36.6–59.7
DTF tops	High	2879	35.6	22.7–50.2	8.5–13.2	21.9	35.9–58.7

Note. TCs represent any captured particles, TCOs are captured and have orbited Earth at least once, TCFs are captured and have not yet completed 1 orbit of Earth, Sputniks are particles that originate from Earth, SC represents particles that are still captured after 5 yr, and TC 3LH is for TCs that go within 3 lunar Hill radii. The %TCO, %TCF, and %TC values are calculated after removing Sputniks. In all of the integrations initialized from the SLLS, the Sputniks account for >90% of the particles. Due to the highly irregular orbit originating from Earth, Sputnik particles are assumed to be invalid. There are no unbound particles that go within 3 lunar Hill radii recorded in the simulations, suggesting that the capture was facilitated by a close encounter with the Moon.

come from inherently chaotic dynamics, cannot have their orbital histories definitively known. Usually, the triangulation and velocity determination methods do not vary the results significantly. Although, event DN160822_03 is long lasting, has a significantly large observational data set (506 points; Table 2), and most importantly it is on the boundary of being geocentric and heliocentric, it is significantly more prone to model selection biases because slight variations in the starting conditions for this event drastically change the calculated orbital history. The particles were integrated back five years, enabling comparison with Clark et al. (2016).

4. Results and Discussion

Calculating Probabilities. The capture probabilities listed in Table 3 were calculated in a very similar way to Clark et al. (2016). If a particle was deemed to be gravitationally captured while integrating backward, it was classified as a TCF until completing one orbit around Earth and then it was reclassified as a TCO. The total number of temporarily captures (TCs) was determined by taking the sum of the TCO and TCF particles. If a particle appears to originate from Earth (i.e., impacts Earth in the backward integration), it would be removed from the TC, TCO, and TCF counts and classified as a Sputnik. Additionally, particles that were captured but never escaped from the Earth–Moon system within the 5 yr integration time were labeled as still captured (SC). If the particles were never captured by the Earth–Moon system, then they were marked as unbound (UB). Furthermore, if the particles passed within 3 or 1 lunar Hill spheres of the Moon, they were recorded as 3H or 1H, respectively.

Based on the pre-atmospheric orbit of event DN160822_03, the probability that the meteoroid originated from typical artificial satellite debris is unlikely. However, due to the lack of spectral data, the possibility of originating from some previous lunar or interplanetary mission cannot be eliminated. Subsequently, we have assumed based on the orbital characteristics that the event has a sufficiently small likelihood of coming from an artificial source. Thus, when calculating the capture probabilities, the Sputniks were removed from consideration due to their unlikelihood, producing the following general equation:

$$\text{Probability}_{\min} = \frac{\text{Subset}}{\text{TotalParticles} - \text{Sputniks}} \quad (1a)$$

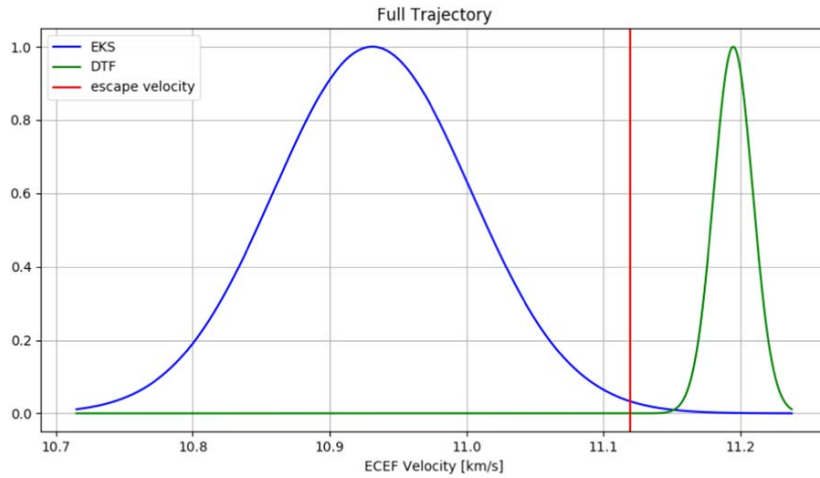
$$\text{Probability}_{\max} = \frac{\text{Subset}}{\text{TotalParticles} - \text{Sputniks} - \text{SC}}, \quad (1b)$$

where the subsets are either SCs, TCs, TCOs, or TCFs. The SCs were considered invalid when calculating the TCF, TCO, and TC minimum percentages and included when calculating the maximum percentages. This is done because they could either eventually evolve into Sputniks or they could just have TCO dynamic lifetimes longer than the 5 yr integration period. The 80,000 particles that describe this one event were integrated in groups of 1000 for computational purposes, and the results of each run were very consistent with each other. The %SC was calculated using Equation 1(a).

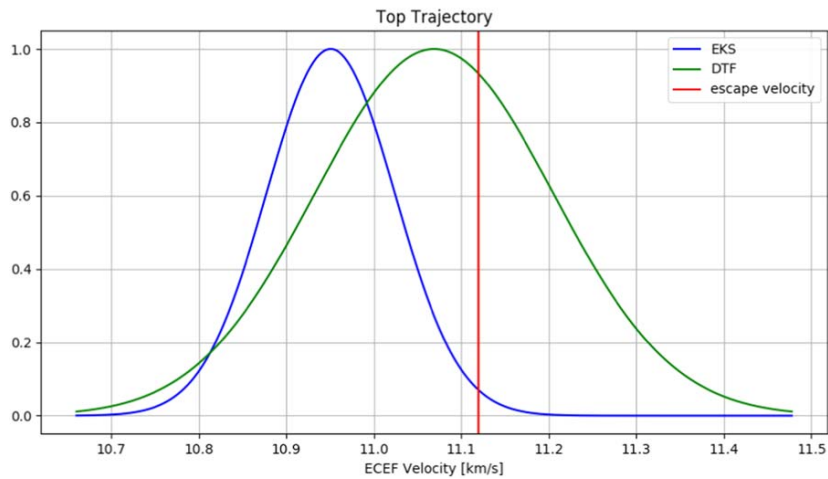
Capture Probability. Considering the large amount of data collected, the model choice affects the TC probability results more significantly when using the entire trajectory to determine v_0 . In order to reduce this dependency of the model choice, the integrations were also performed using just the top of the observed atmospheric trajectory (>65 km altitude). This reduces the effect of the assumptions you make when choosing a model. Predictably, the two models' results tend to converge more when only the top is used (Figure 3).

During the integrations using the top of the trajectory, the particles generated from the SLLS still are nearly all either gravitationally captured or seem to originate from Earth. On the other hand, about 30%–60% of the particles generated by the DTF method are TCs. The DTF produces nonconclusive probabilities for this event considering the v_0 distribution of the DTF is nearly centered (within 0.38σ) on the escape velocity for Earth at the corresponding altitude (Figure 3). In other words, the mean initial velocity (at the beginning of observations) predicted by the DTF method is very similar to the escape velocity. Therefore, the TCO probability for this event determined by the integrations initiated from DTF triangulation is predictably around 50%.

Given the results from the integrations (Table 3) using our most statistically robust triangulation method (SLLS with EKS), there is a >95% probability that the meteoroid observed was captured by the Earth–Moon system before atmospheric entry (i.e., only <5% chance it was heliocentric). Although, the pre-atmospheric path is impossible to exactly model due to the intrinsically chaotic nature of the system (as seen in Figure 4) and small variations in how the initial state of the fireball is determined have the potential to affect the resulting capture



(a) Full trajectory



(b) Top of trajectory

Figure 3. Comparison of the v_0 distribution generated by the EKS and the DTF methods using either (a) the full trajectory or (b) the top of the trajectory (observations >65 km altitude). Given the large amount of data collected for event DN160822_03, 506 data points, the v_0 is more dependent than usual on the choice of triangulation and velocity determination methods. When only the top of the observed atmospheric trajectory is used, the models' assumptions affect the results less and the v_0 distributions converge.

probability seriously. Due to the high probability that the meteoroid passed very close to the moon (possibly multiple times), the system is highly unpredictable as a result of the chaotic scattering.

Capture Mechanisms. In Figure 5, the capture distribution is clearly multimodal. Most of the TCs are captured through the first or second Lagrange points, with the remaining TCs captured through a close encounter with the Moon. The capture location probabilities for the L1, L2, and lunar captures are 23.8%, 67.1%, and 9.1%, respectively. The specific Lagrange point capture locations depend on the Jacobi value for that given particle; in other words, the spread of Lagrange capture locations is due to the variations in the orbital energy of the particles. These capture mechanisms are easily seen in Figure 5. The capture locations also do not significantly change when the triangulation method is changed, however the proportion of the captures at each location does very slightly because of differences in the v_0 estimate in each model.

As exhibited in Table 3, the captured particles have a significantly higher amount of close encounters with the Moon compared to unbound particles. This implies that the Moon likely played a significant role in the meteoroid's eventual impact with Earth. Considering that nearly all of the particles generated from the SLLS/EKS are still captured at the end of the integration, this may imply that the meteoroid was an extremely long-lived TCO like those described in Granvik et al. (2012). Granvik et al. (2012) found that the longest-lived TCO particles in their simulations were those that had multiple close encounters with the Moon, which lowered the apogee of the orbit below 1 LD. As seen in Figure 6, the temporarily captured particles within our simulations for the most extended times do indeed have numerous close encounters with the Moon throughout the integration. The presence of the Moon more often contributes to the length of the capture rather than the actual capture itself.

Orbital Evolution. As shown in Figure 7, there appears to be some trends over time for the geocentric orbital elements of

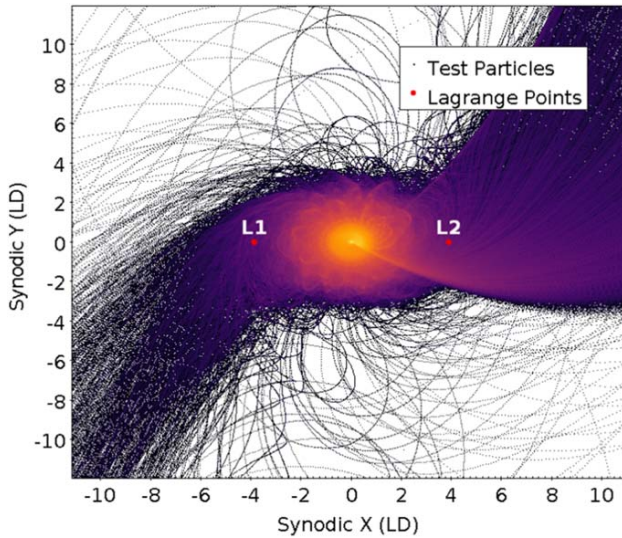
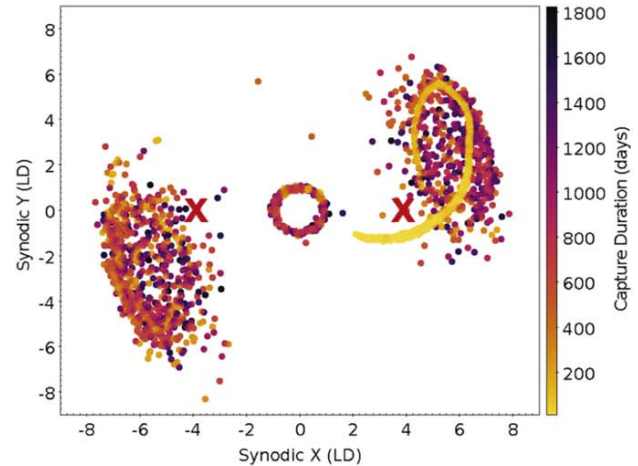


Figure 4. Particle orbits within the Sun–Earth–particle synodic reference frame centered on Earth’s center of mass and corotating with Earth so that the direction of the Sun is always at $(-1 \text{ au}, 0)$ in the x - y plane in this figure (not shown). The colors are indicative of the particles’ spatial density, yellow being the most dense and black/purple being the least. The axes are in units of lunar distances (LD). There appears to be a clear preference of entry into the Earth–Moon system through either the L1 or L2 Lagrange points (represented by red points), as shown by the prevalence of trajectories in the directions of the co-linear Lagrange points.

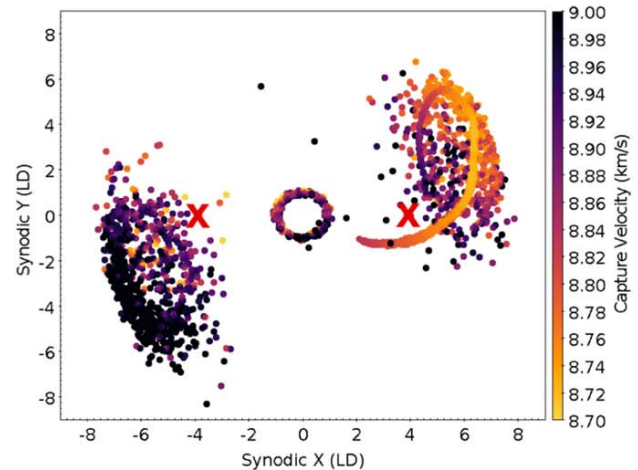
captured particles. In Figure 7(a), the captured particles that are integrated until they become heliocentric tend to approach higher semimajor axis and eccentricity values asymptotically. In Figure 7(b), TCs that are retrograde and do not have a low semimajor axis encounter the Moon more often, causing them to be less dynamically stable and have shorter capture durations. The longest-lived particles have an apogee value lower than 1 LD, thus reducing the number of close encounters with the Moon. This is consistent with the longest-lived TCOs in the simulations done by Granvik et al. (2012) in which particles with the longest dynamical lifetimes tended to have multiple close encounters with the Moon, which resulted in an orbit completely interior to the lunar orbit. Within this study, as shown in Figure 7, TCOs with low apogee values that had capture durations shorter than the integration period tended to evolve from highly eccentric retrograde orbits with larger semimajor axis values. This evolution from a retrograde, eccentric orbit to an orbit internal to the Moon was most likely due to a series of fortunate lunar close encounters like those described in Granvik et al. (2012).

Precapture Orbit. By studying the trajectories of the simulated particles before encountering the Earth–Moon system, we find the event DN160822_03 most likely to belong to the Apollo NEO group. Event DN160822_03 produced particles that were 88.4% Apollos, 6.2% Amors, 2.9% Atiras, and 2.5% Atens. Although, due to the chaotic nature of the event, the heliocentric orbit is impossible to determine accurately without more data, preferably pre-atmospheric observations (Murison 1989; Astakhov et al. 2003).

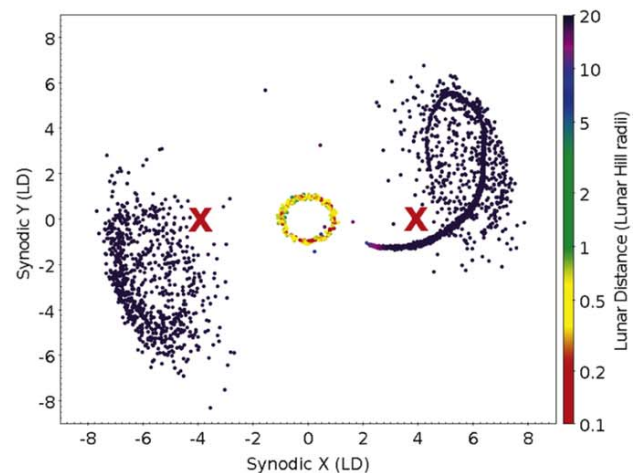
Comparison to Models. Finding this single TCO in the DFN data set is consistent with the models of Granvik et al. (2012) and Fedorets et al. (2017), although not statistically robust as



(a) Variation in capture duration.



(b) Variation in capture velocity.



(c) Variation in lunar distance.

Figure 5. Gravitational capture locations in the synodic reference frame with the L1 and L2 points marked by red crosses. The Sun–Earth synodic frame is centered on Earth’s center of mass and corotates with Earth so that the direction of the Sun in this case is always at $(-1 \text{ au}, 0)$ in the x - y plane. The figures above show three distinct capture regions: L1 capture, L2 capture, and close lunar encounter capture. The tail-like feature near the L2 point is caused by a large group of particles that were captured fairly quickly into the integration so they did not scatter as much.

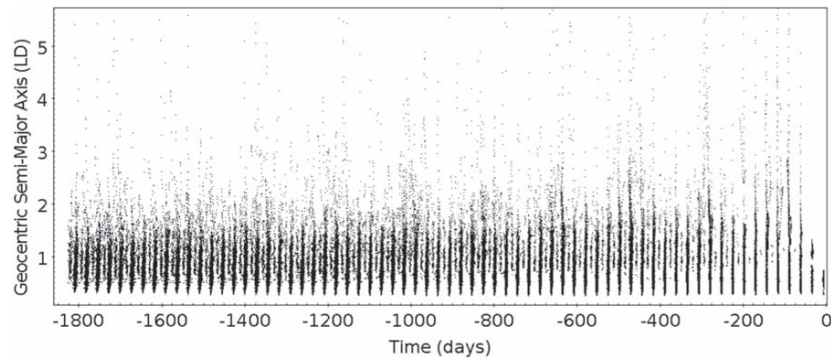
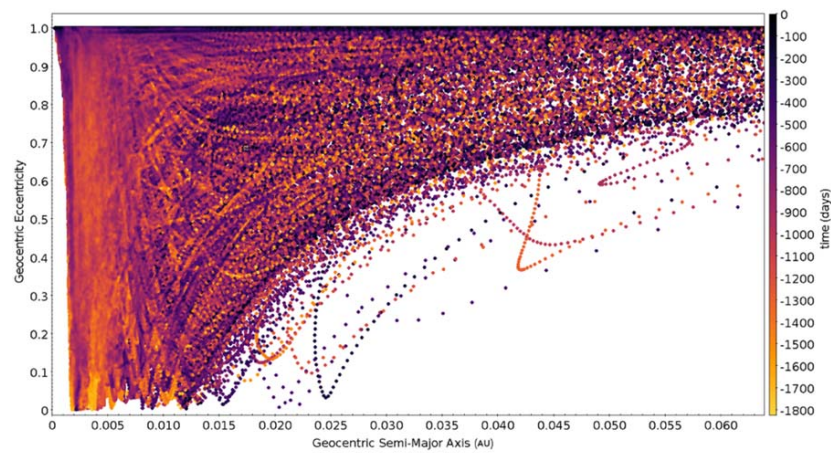
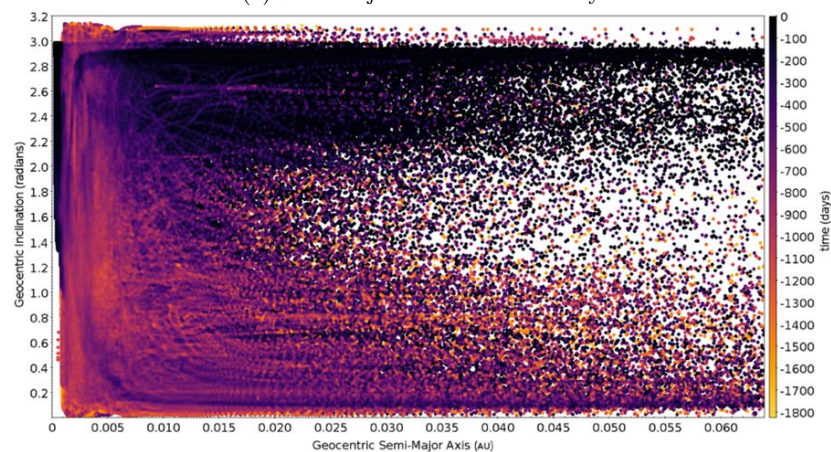


Figure 6. TCs that get within 3 Hill radii of the Moon (3H) produced by the SLLS and DTF. Each point represents one particle within 3H and the y-axis indicates the geocentric semimajor axis (LD) for that particle at that time. Most of the TCs in the simulations have close encounters with the Moon multiple times. The probability of an encounter increases once a month, due to the geometry of this specific event. This indicates that the Moon was likely critically important for the geocentric orbital evolution of the meteoroid and the impact of the meteoroid with Earth.



(a) Semi-major axis vs Eccentricity



(b) Semi-major axis vs Inclination

Figure 7. Geocentric semimajor axis vs. eccentricity and inclination for the temporarily captured particles. The color bar is indicative of gravitational capture duration during the simulation with yellow corresponding to a longer capture duration and black corresponding to a shorter capture duration. Particles that were captured the longest tended to have lower eccentricity, lower semimajor axis, and lower inclinations. This is generally true because the particles that had more close encounters with the Moon tended to be less dynamically stable. Also, particles that were not able to transition from the initially highly eccentric detected orbit to lower eccentricities typically had lower capture durations.

the numbers are small. We found the most probable capture locations were concentrated at Earth's aphelion and perihelion, as described in both Granvik et al. (2012) and Fedorets et al. (2017). Although, as shown in Figure 8, the particles captured

in proximity to the L1 and L2 points clearly display an annual variation in the probable magnitude of the capture velocity. Also, unlike general models of the entire TCO population, particles were captured through close encounters with the

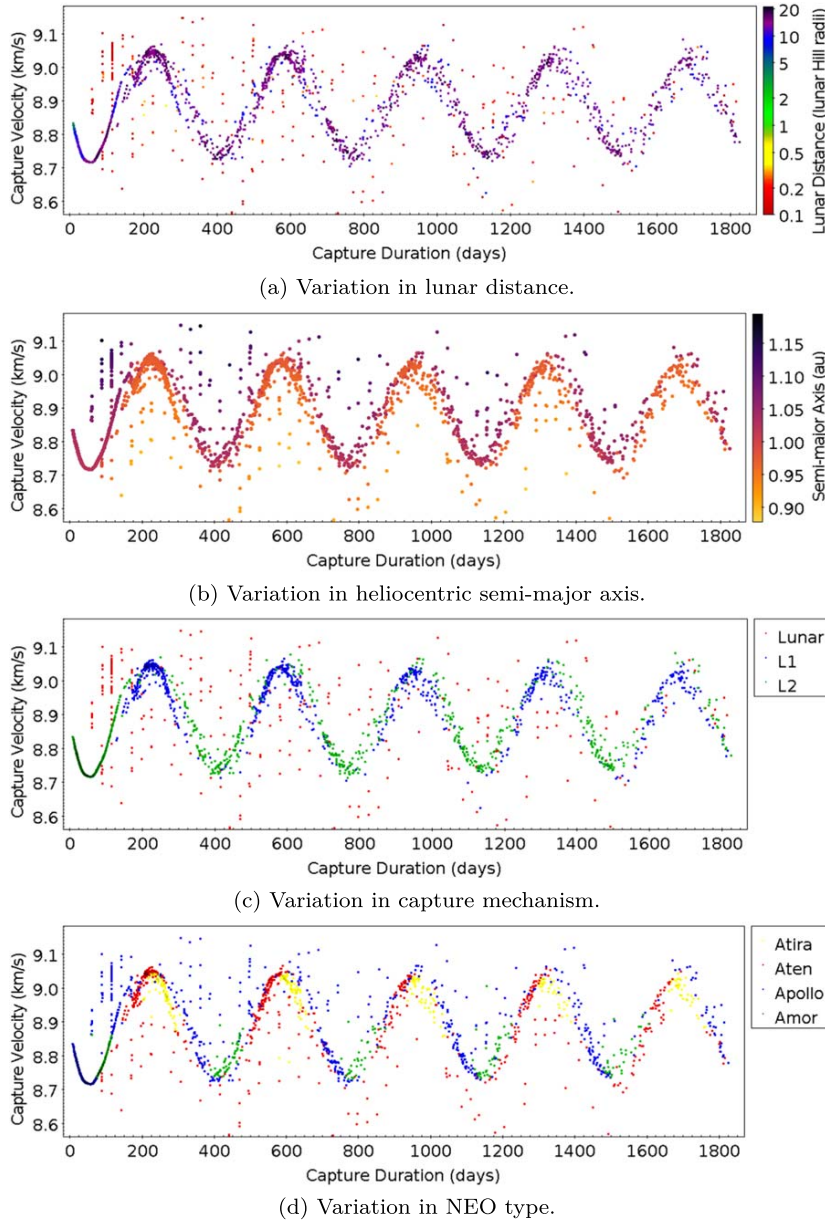


Figure 8. Total capture duration vs. velocity during capture for TC particles. The relatively large annual variation in probable capture velocity results from the eccentricity of Earth, as Earth moves closer or further from the Sun during the year, the capture velocity also varies. This annual variation in the probable capture velocity thus produces annual variations in the Lagrange point capture location and the source NEO group (panels (b) and (c)). Probably due to the geometry of the event (high eccentricity, low inclination, apogee $\approx 1LD$) there also exists vertical bands of close lunar encounter captures that occur every lunar month (panel (a)).

Moon (Figure 4(a)) and had only slightly lower capture durations compared to the Lagrange point captures.

Moreover, these close lunar encounter captures varied according to the lunar month for this event. This is seen in Figure 8(a), where the yellow/red points representing captures close to the Moon seem to make vertical stripes every 28 days. This lunar cycle is also seen in Figure 6, where the amount of lunar encounters seems to spike every month. Although, this cycle of close lunar encounters every lunar month is most likely specific to the geometry of this event. Due to the low geocentric inclination and very high geocentric eccentricity, the particles generated are consistently capable of making numerous close encounters with the Moon. The presence of a lunar influence was also identified by Clark et al. (2016), where the lunar

encounters tended to occur directly before the impact with Earth, implying that the Moon is highly influential on whether or not TCOs dynamically evolve into an Earth-impacting orbit.

Annual Variations. There is a relatively large annual variation in the expected capture velocity and capture semimajor axis, varying over 300 m s^{-1} and 0.15 au, respectively, for this particular event. This large annual variation in this event is due to the fact that Earth does not have a perfectly circular orbit around the Sun. This eccentricity causes the L1 and L2 Lagrange points in the simplified CRTBP to wobble in and out throughout the year by about 3.4%. As a result, the capture characteristics also wobble throughout the year. This implies that the source region for TCs also varies annually with Atras and Atens more likely to be gravitationally captured

during perihelion (January) and Amors and Apollos more likely to be gravitationally captured during aphelion (July) (Figure 8(d)). Atira and Aten orbits are more likely to be gravitationally captured during perihelion because the L1 and L2 points are closer to Earth and faster objects relative to Earth are capable of being captured, i.e., objects with orbits interior to that of Earth. Conversely, the Amor and Apollos are more likely during aphelion because they orbit relatively more slowly and have orbits more outward from Earth. As shown in Figure 8(d), interestingly the faster and slower lunar captures consistently come from Apollo and Aten type orbits respectively. Additionally, this annual variation in probable capture velocity also implies that the capture mechanism by L1 and L2 varies annually, as in Figure 8(c). The most probable gravitational capture time for this event is either during aphelion or perihelion, consistent with Granvik et al. (2012) and Fedorets et al. (2017).

Comparison to Clark et al. (2016). In the study by Clark et al. (2016), they detected an 8.1 s fireball over the Czech portion of the EFN with two high-resolution digital camera observatories. Given their observations, they determined that the detected event had a 92%–98% chance of being captured by Earth before impact detection. The DFN event described here was about 5.3 s in duration and was detected by six high-resolution digital camera stations in South Australia (Figure 1). Despite a large amount of data collected of our event (six cameras with >500 data points), the results varied significantly between model choices. Previous studies have demonstrated that the sensitivity initial orbits can have the choice of the initial velocity method (Vida et al. 2018). This is especially true for shallow events that penetrate deeper into the atmosphere where v_0 variations are more sensitive to model choice. The capture probabilities given for the EFN event are valid for the triangulation method that they used, but similar to our event, the use of a different triangulation method on their data may likewise find a reasonably high variation in the TC probability. Given that the event described in Clark et al. (2016) was longer and shallower than the one described here, the v_0 variation due to model choice may cause more discrepancy in their v_0 estimates if fitting to the entire trajectory. Despite this, the Clark et al. (2016) event has fewer observations, decreasing the sensitivity of model choice. This is because the v_0 distributions for multiple models have a higher chance of overlapping and possibly not causing as large of an issue with the discrepancy between models.

If an object likely has a geocentric orbit, we further need to prove it is of natural origin and not from a human-made object. The event observed by the EFN recorded spectral data of the fireball was able to conclude that the object was conclusively natural. The event described here, on the other hand, may still have originated from an artificial source; however, this is very improbable given the pre-atmospheric orbit of the event.

In the future, the best way to confirm TC impact events would be by collecting more data prior to atmospheric entry using telescopes, which may come to fruition with the beginning of observations in 2022 by the LSST (Ivezić et al. 2019; Fedorets et al. 2015). In addition, if TCs can be detected far enough in advance, future sample-return missions could target these objects as the Δv for the mission could be extremely low relative to other asteroid sample-return missions.

5. Conclusions

Based on our analysis, the event DN160822_03 detected by the DFN has a high pre-impact capture probability, as large as >95% captured with our most statistically robust model. We find that the probable capture time, capture velocity, capture semimajor axis, capture NEO group, and capture mechanism all vary annually, with most captures occurring during Earth's aphelion or perihelion. This has been noted to some extent previously (Granvik et al. 2012; Fedorets et al. 2017), but most of the annual probability variations associated with Earth's eccentricity found for this particular event have not been described before. We also discover that the probability of capture occurring as a result of a close lunar encounter varies according to the lunar month for this event. Although, this is probably due to the specific geometry of this event (i.e., low inclination, high eccentricity, geocentric apogee $\approx 1LD$). Despite the large amount of data collected by our six cameras of the event, we cannot say for certain that the pre-atmospheric orbit was due to the highly unpredictable nature of the system, and the chaotic scattering that occurs with every close encounter with the Moon and Earth. We caution future analysis of possible TCO events to explore the effects of small variations in the initial conditions and various triangulation methodologies. Despite these uncertainties and chaotic elements, we can determine the probable origins of this event statistically to be 88.4% Apollos, 6.2% Amors, 2.9% Atiras, and 2.5% Atens. In a couple of years, more fireball events like this may be able to be confirmed by additional telescopic observations like those from the LSST.

This work was funded by the Australian Research Council as part of the Australian Discovery Project scheme.

This research made use of Astropy, a community-developed core Python package for Astronomy (Robitaille et al. 2013). Simulations in this paper made use of the REBOUND code which can be downloaded freely at <https://github.com/hannorein/REBOUND>.

Appendix

Summary of Definitions and Abbreviations

Within this study we followed the notation of Granvik et al. (2012) and Fedorets et al. (2017) for consistency.

1. SLLS—straight-line least-squares triangulation method with extended Kalman filter for velocity and error determination
2. DTF—dynamic trajectory fit triangulation and dynamic modeling method
3. TC—temporarily captured. The sum of the total TCOs and TCFs
4. TCF—temporarily captured flyby; TC that has not orbited Earth once
5. TCO—temporarily captured orbiter; TC that has orbited Earth at least once
6. Sputnik—particle in integration that originates from Earth
7. NES—natural earth satellite
8. NEO—near-Earth object
9. UB—unbound (i.e., not gravitationally captured by Earth)
10. 1H—came within 1 lunar Hill sphere of the Moon
11. 3H—came within 3 lunar Hill spheres of the Moon

THE ASTRONOMICAL JOURNAL, 158:183 (11pp), 2019 November

Shober et al.

12. SC—particles that are still captured by the end of the integration
13. LD—distance from Earth to the Moon.

ORCID iDs

P. M. Shober  <https://orcid.org/0000-0003-4766-2098>
 T. Jansen-Sturgeon  <https://orcid.org/0000-0002-0363-0927>
 E. K. Sansom  <https://orcid.org/0000-0003-2702-673X>
 H. A. R. Devillepoix  <https://orcid.org/0000-0001-9226-1870>
 P. A. Bland  <https://orcid.org/0000-0002-4681-7898>
 Robert M. Howie  <https://orcid.org/0000-0002-5864-105X>
 Benjamin A. D. Hartig  <https://orcid.org/0000-0002-8646-0635>

References

- Astakhov, S. A., Burbanks, A. D., Wiggins, S., & Farrelly, D. 2003, *Natur*, **423**, 264
 Bailey, J. M. 1972, *AJ*, **77**, 177
 Baker, J., & Robert, M. L. 1958, *Sci*, **128**, 1211
 Bolin, B., Jedicke, R., Granvik, M., et al. 2014, *Icar*, **241**, 280
 Borovicka, J. 1990, *BAICz*, **41**, 391
 Brelsford, S., Chyba, M., Haberkorn, T., & Patterson, G. 2016, *P&SS*, **123**, 4
 Brunini, A. 1996, *CeMDA*, **64**, 79
 Chant, C. A. 1913, *JRASC*, **7**, 145
 Chodas, P. 2014, in *Asteroids Comets, Meteors 2014*, ed. K. Muinonen et al. (Helsinki: Univ. Helsinki), 94
 Clark, D., Spurný, P., Wiegert, P., et al. 2016, *AJ*, **151**, 135
 Cline, J. K. 1979, *CeMec*, **19**, 405
 Consolmagno, G., Britt, D., & Macke, R. 2008, *CHEG*, **68**, 1
 Denning, W. F. 1916, *JRASC*, **10**, 294
 Devillepoix, H. A. R., Sansom, E. K., Bland, P. A., et al. 2018, *M&PS*, **53**, 2212
 Everhart, E. 1985, in *IAU Coll. 83: Dynamics of Comets: Their Origin and Evolution 115*, ed. A. Carusi & G. B. Valsecchi (Cambridge: Cambridge Univ. Press), 185
 Fedorets, G., Granvik, M., & Jedicke, R. 2017, *Icar*, **285**, 83
 Fedorets, G., Granvik, M., Jones, L., & Jedicke, R. 2015, *IAUGA*, **29**, 2257052
 Gong, S., & Li, J. 2015, *Ap&SS*, **357**, 155
 Granvik, M., Vaubailon, J., & Jedicke, R. 2012, *Icar*, **218**, 262
 Heppenheimer, T. A., & Porco, C. 1977, *Icar*, **30**, 385
 Howie, R. M., Paxman, J., Bland, P. A., et al. 2017a, *ExA*, **43**, 237
 Howie, R. M., Paxman, J., Bland, P. A., et al. 2017b, *M&PS*, **52**, 1669
 Ivezić, Ž., Kahn, S. M., Tyson, J. A., et al. 2019, *ApJ*, **873**, 111
 Kary, D. M., & Dones, L. 1996, *Icar*, **121**, 207
 Kwiatkowski, T., Kryszczyńska, A., Polińska, M., et al. 2009, *A&A*, **495**, 967
 Luo, Z. F., & Toppoto, F. 2017, *CNSNS*, **48**, 211
 Lynam, A. E., Kloster, K. W., & Longuski, J. M. 2011, *CeMDA*, **109**, 59
 Murison, M. A. 1989, *AJ*, **98**, 2346
 Nesvorný, D., Alvarellos, J. L. A., Dones, L., & Levison, H. F. 2003, *AJ*, **126**, 398
 Nesvorný, D., Vokrouhlický, D., & Morbidelli, A. 2007, *AJ*, **133**, 1962
 Pollack, J. B., Burns, J. A., & Tauber, M. E. 1979, *Icar*, **37**, 587
 Rein, H., & Liu, S. F. 2012, *A&A*, **537**, A128
 Rein, H., & Spiegel, D. S. 2015, *MNRAS*, **446**, 1424
 Robitaille, T. P., Tollerud, E. J., Greenfield, P., et al. 2013, *A&A*, **558**, A33
 Sansom, E. K., Bland, P., Paxman, J., & Towner, M. 2015, *M&PS*, **50**, 1423
 Tsui, K. H. 2000, *Icar*, **148**, 139
 Tsui, K. H. 2002, *P&SS*, **50**, 269
 Urrutxua, H., & Bombardelli, C. 2017, in *26th Int. Symp. Space Flight Dynamics Number ISSFD-2017*, 74 (Cologne: Deutsches Zentrum fuer Luft- und Raumfahrt), 1
 Vida, D., Brown, P. G., & Campbell-Brown, M. 2018, *MNRAS*, **479**, 4307
 Yegorov, V. A. 1959, *Artificial Earth Satellites*, **3**, 17

Paper 2 - Where Did They Come From, Where Did They Go: Grazing Fireballs

The Astronomical Journal (2020), Volume 159, Issue 5, p. 191-206.

Patrick M. Shober, Trent Jansen-Sturgeon, Eleanor K. Sansom, Hadrien A.R. Devillepoix, Martin C. Towner, Phil A. Bland, Martin Cupák, Robert M. Howie, Benjamin A.D. Hartig

REPRINTED WITH PERMISSION OF IOP PUBLISHING: *The authors have the right to use all or part of the Article in future works and derivative works of their own of any type, and to make copies of all or part of the Article for the authors' use for educational or research purposes.*

STATEMENT OF AUTHORSHIP

TITLE OF PAPER: Where Did They Come From, Where Did They Go: Grazing Fireballs

PUBLICATION STATUS: Published in The Astronomical Journal (April 7, 2020).

AUTHOR CONTRIBUTIONS

By signing the Statement of Authorship, each author certifies that their stated contribution to the publication is accurate and that permission is granted for the publication to be included in the candidate's thesis.

Name of Principal Author: Patrick M. Shober

Contribution to the Paper: Led data analysis. Conducted the trajectory and orbital analysis. Wrote the manuscript.

Overall Percentage: 87 %

Signature:

Date:

Name of Co-Author: Trent Jansen-Sturgeon

Contribution to the Paper: Assisted with triangulation of the fireball.

Overall Percentage: 5 %

Signature:

Date:

Name of Co-Author: Eleanor K. Sansom

Contribution to the Paper: Assisted with triangulation of the fireball and initial mass determination.

Overall Percentage: 2 %

Signature:

Date:

Name of Co-Author: Hadrien A.R. Devillepoix

Contribution to the Paper: Assisted with data analysis and collection.

Overall Percentage: 2 %

Signature:

Date:

Name of Co-Author: Martin Towner

Contribution to the Paper: Data collection and helped review manuscript.

Overall Percentage: 1 %

Signature:**Date:****Name of Co-Author:** Phil A. Bland**Contribution to the Paper:** Assisted with writing manuscript.**Overall Percentage:** 1 %**Signature:****Date:****Name of Co-Author:** Martin Cupák**Contribution to the Paper:** Data collection and helped review manuscript.**Overall Percentage:** 1 %**Signature:****Date:****Name of Co-Author:** Robert M. Howie**Contribution to the Paper:** Data collection and built equipment.**Overall Percentage:** 0.5 %**Signature:****Date:**

Name of Co-Author: Benjamin A.D. Hartig

Contribution to the Paper: Data collection and built equipment.

Overall Percentage: 0.5 %

Signature:

Date:



Where Did They Come From, Where Did They Go: Grazing Fireballs

Patrick M. Shober , Trent Jansen-Sturgeon , Eleanor K. Sansom , Hadrien A. R. Devillepoix , Martin C. Towner, Phil A. Bland , Martin Cupák, Robert M. Howie , and Benjamin A. D. Hartig 
 Space Science & Technology Centre (SSTC), School of Earth and Planetary Sciences, Curtin University, GPO Box U1987, Perth, Western Australia 6845, Australia
patrick.shober@postgrad.curtin.edu.au

Received 2019 November 6; revised 2020 March 9; accepted 2020 March 14; published 2020 April 7

Abstract

For centuries extremely long grazing fireball displays have fascinated observers and inspired people to ponder about their origins. The Desert Fireball Network is the largest single fireball network in the world, covering about one third of Australian skies. This expansive size has enabled us to capture a majority of the atmospheric trajectory of a spectacular grazing event that lasted over 90 s, penetrated as deep as ~ 58.5 km, and traveled over 1300 km through the atmosphere before exiting back into interplanetary space. Based on our triangulation and dynamic analyses of the event, we have estimated the initial mass to be at least 60 kg, which would correspond to a 30 cm object given a chondritic density (3500 kg m^{-3}). However, this initial mass estimate is likely a lower bound, considering the minimal deceleration observed in the luminous phase. The most intriguing quality of this close encounter is that the meteoroid originated from an Apollo-type orbit and was inserted into a Jupiter-family comet (JFC) orbit due to the net energy gained during the close encounter with Earth. Based on numerical simulations, the meteoroid will likely spend ~ 200 kyr on a JFC orbit and have numerous encounters with Jupiter, the first of which will occur in 2025 January–March. Eventually the meteoroid will likely be ejected from the solar system or be flung into a trans-Neptunian orbit.

Unified Astronomy Thesaurus concepts: [Meteoroids \(1040\)](#); [Meteors \(1041\)](#); [Solar system \(1528\)](#); [Near-Earth objects \(1092\)](#); [Short period comets \(1452\)](#); [Close encounters \(255\)](#); [Fireballs \(538\)](#)

1. Introduction

1.1. Reports of Grazing Fireballs

People have reported witnessing brilliantly long-lasting and bright meteor processions for at least hundreds of years. The 1783 “Great Meteor” was estimated to have traveled >1600 km through the atmosphere over western Europe (Cavallo 1784). The “Great Comet of 1860,” which was most likely an Earth-grazing fireball over the eastern United States, was accounted for in a painting by American landscape artist Frederic Church entitled “The Meteor of 1860” and by American poet Walt Whitman in his poem “Year of Meteors” (Olson et al. 2010). Additionally, the “1913 Great Meteor Procession” reported sightings across Canada, the north-eastern United States, Bermuda, and many ships in the Atlantic as far south as Brazil. The event was initially hypothesized to have been formed by a natural Earth satellite that had a grazing encounter with the atmosphere (Chant 1913; Denning 1916).

A grazing event is considered to be when a meteoroid impacts the atmosphere at an extremely low angle relative to the horizon, and there are generally three possible outcomes. It can either escape back to interplanetary space after passing through the atmosphere, fully ablate, or slow down enough to fall to Earth. The first scientifically observed and triangulated grazing event was not until 1972 over Canada and the northwestern United States (Ceplecha 1979, 1994). The 1972 fireball lasted ~ 100 s, covering over 1500 km, and reached a minimum height of 58 km. Ceplecha (1979) estimated the mass to be between 10^5 and 10^6 kg with the most likely diameter of about 5 m. The original analysis done by Rawcliffe et al. (1974) and Jacchia (1974) is known to contain mistakes, and the values given should not be relied upon (Ceplecha 1979).

Since the 1972 fireball, there have been several atmospheric grazing events reported within scientific literature:

1. In 1990, Borovicka & Ceplecha (1992) published an analysis of the first Earth-grazing fireball observed by a photographic fireball network in which the meteoroid was estimated to be 44 kg with the closest approach of 98 km detected by two Czech stations of the European Fireball Network.
2. In 1992 October, a bright fireball endured for over 700 km over the eastern United States before dropping a meteorite in Peekskill, New York (Brown et al. 1994; Beech et al. 1995; Ceplecha et al. 1996).
3. In 1996 a fireball was observed to hit the western United States and only briefly escape for one orbit before allegedly impacting Earth (Revelle et al. 1997).
4. On 2006 March 29, a ~ 40 s grazing fireball was observed over Japan (Abe et al. 2006). The meteoroid traveled over 700 km through the atmosphere and reached a minimum height of 71.4 km. It appeared to come from a JFC-like orbit and the spectra collected was consistent with a chondritic composition.
5. On 2007 August 7, a grazing fireball was observed by the European Fireball Network originating from a Aten-type orbit (Spurný et al. 2008).
6. In 2012 June, the first grazing meteoroid associated with a meteor shower in the scientific literature was recorded by 13 stations with a 98 km minimum altitude over Spain and Portugal and belonged to the daytime ζ -Perseid shower (Madiedo et al. 2016).
7. In 2003, another grazing meteor, mass loss $\approx 5 \times 10^{-3}$ g, was detected over Ukraine before exiting back into interplanetary space (Kozak & Watanabe 2017).
8. In 2014 December, a 1200 km long grazing event occurred over Algeria, Spain, and Portugal and lasted approximately 60 s, reaching a minimum height of 75 km (Moreno et al. 2016).

9. On 2014 March 31, a ~ 34 s fireball over Germany and Austria originating from an Apollo-type orbit was observed. The meteoroid was estimated to have an initial mass of about 200 kg, but no material is believed to have exited back into interplanetary space (Oberst et al. 2014). Many meteorites may have survived to the ground, however, the uncertainty on the fall ellipse is very large due to the extremely shallow entry angle.

For some of these grazing meteoroids mentioned above, the object was able to survive its passage through the atmosphere. The rock then re-entered interplanetary space on an altered orbit, sending material from one part of the inner solar system to another. This is could be significant since various parts of the inner solar system are thought to be dynamically and physically distinct from one another.

1.2. Small Inner Solar System Bodies

The classical view of the solar system says that the Sun formed with a debris disk around it that was originally compositionally heterogeneous within bands of constant radial distance from the Sun. The snow line denoted the boundary between the planetesimals in which water ice and other volatiles would be retained and the bodies which were unable to hold ice, thus remaining dry. This classically separated the small bodies within the solar system into two main groups: comets and asteroids respectively.

Although, we have seen that this classical ideology does not usually fit our observations of the small bodies within the solar system. The solar system is complicated and dynamic. In the last 4.5 billion years, small bodies have been jumbled around and altered. The layout and distribution of the solar system is much more complicated than the idealized stratified one we tend to imagine.

Within the inner solar system there are short-period comets, main-belt objects (MBOs), and near-Earth objects (NEOs). Traditionally, the MBOs were considered asteroidal and inner solar system in origin, and NEOs primarily evolved from the MBO space after entering an orbital resonance (Bottke et al. 2002; Granvik et al. 2018). However, with the identifications of main-belt comets (MBCs; Hsieh & Jewitt 2006) and dry asteroidal material in the Kuiper belt (Meech et al. 2016), we have realized that the material in the solar system is more mixed than previously believed (Fernández & Sosa 2015). Additionally, the starkly drawn lines between asteroidal and cometary material have since faded with the identification of active asteroids, extinct comets, and mixing between populations (Fernández et al. 2001, 2002, 2005; Jewitt 2012; Kim et al. 2014). In reality, the physical properties of small bodies in the solar system most likely exist in a spectrum from primitive volatile-rich (comet-like) to dry volatile-poor (asteroid-like). We are still trying to determine the most probable mechanism by which this mixing could have occurred, but several models such as the “Nice Model” and the “Grand Tack” have begun to elucidate some of these mysteries (Walsh et al. 2011; Tsiganis et al. 2005).

Jupiter-family comets (JFCs) are a class of short-period comets, believed to have evolved from scattered disk and Kuiper belt orbits (Fernández 1980; Duncan & Levison 1997; Levison & Duncan 1997; Binzel et al. 2004). JFCs are primitive and contain a large amount of hydrated minerals and volatile ices (Kelley & Wooden 2009; Jenniskens et al. 2012).

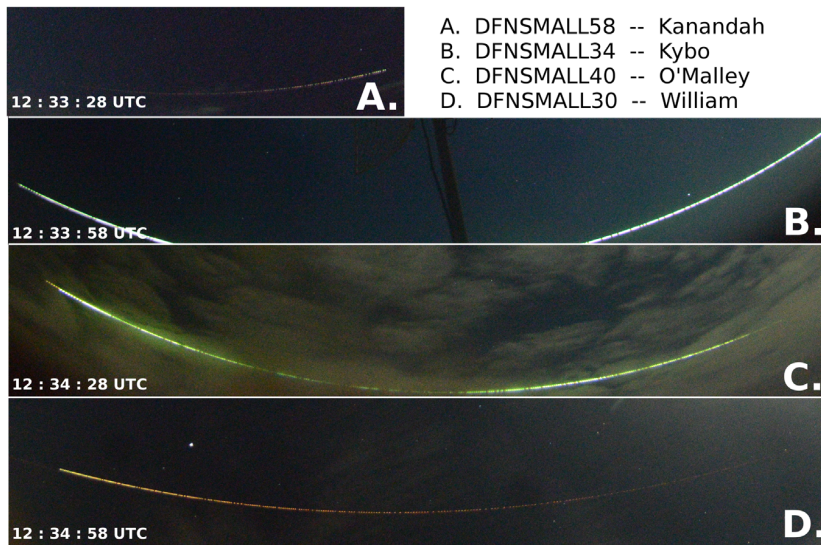
They are also characterized by their orbits being strongly linked to the orbit of Jupiter, typically defined by their Tisserand’s parameter to be $2 < T_J < 3$ (Carusi & Valsecchi 1987; Levison & Duncan 1994). JFCs usually have multiple low-velocity encounters with the gas giant over their lifetime (Duncan & Levison 1997; Levison & Duncan 1997; Duncan et al. 2004). These encounters with Jupiter make the orbits of JFCs more unpredictable compared to other small bodies, where the median dynamic lifetime of a JFC is ~ 325 kyr (Duncan et al. 2004). However, as described by Fernández & Sosa (2015), JFCs that display cometary features frequently encounter Jupiter at distances of ≤ 0.1 au making them highly unstable compared to a small subset of near-Earth asteroidal JFCs that typically exist on more stable orbits comparatively. A tiny fraction of JFCs are also thought to decouple from Jupiter and become Encke-like comets through either nongravitational perturbations or close planetary encounters (Steel & Asher 1996; Levison et al. 2006).

1.3. The Desert Fireball Network

Since 2003, the Desert Fireball Network (DFN) has been operating observatories across southwestern Australia to capture images of fireball events (Bland 2004). The network has since grown from 4 observatories by 2007 to over 50 observatories in western Australia and southern Australia by 2015 (Bland et al. 2012; Howie et al. 2017a). No other fireball camera network in the world is this expansive. Furthermore, we have expanded this effort worldwide with the start of Global Fireball Observatory (GFO) collaboration (H. A. R. Devillepoix et al. 2020, in preparation) with a coverage area expected to increase to 2% of Earth’s entire surface. This coverage area makes the GFO particularly well suited to characterize grazing meteoroids and other more rare fireball events (Shober et al. 2019).

2. DFN Observations

On 2017 July 7, a 90 s extremely shallow fireball was observed to graze the atmosphere above western Australia and southern Australia, entering the atmosphere at a slope of $\sim 4^\circ 6'$ (Figure 1). Ten DFN observatories made observations of the fireball as it traveled over 1300 km through the atmosphere. The luminous phase started at about 85 km and penetrated as deep as 58 km before ceasing to be visibly ablating at 86 km. This event is only equaled by the “Great Daylight Fireball of 1972,” which reached a similar depth and lasted ~ 9 s longer than our witnessed event (Ceplecha 1979). However, unlike the 1972 event, the DFN was able to photographically image the majority of the atmospheric trajectory of the fireball (including the beginning and the end), with observations from many of our fireball observatories spread across western Australia and southern Australia. Thus, providing us with a substantial amount of data to accurately fit a trajectory to our observations (2541 astrometric data points). A summary of the observations made of event DN170707_01 and the fitted trajectory are provided in Table 1. The number of observations refers to the number of 30 s exposures. Whereas, “without timing” denotes when observations of the fireball were collected, however, either the angular velocity of the meteoroid was too slow or the fireball was too bright to distinguish the encoded de Bruijn sequence (Howie et al. 2017b). Unfortunately, due to the DFN’s viewing geometry at the beginning of the observed luminous trajectory, the initial observation convergence angle



A. DFNSMALL58 -- Kanandah
 B. DFNSMALL34 -- Kybo
 C. DFNSMALL40 -- O'Malley
 D. DFNSMALL30 -- William

Figure 1. Long exposure images of event DN170707_01. The event lasted over 90 s and spanned four 30 s exposures (A, B, C, D). The fireball was first observed at 85 km altitude, reached as low as 58 km, and then was visible until 86 km before escaping Earth's atmosphere. The initial velocity was 16.1 km s^{-1} , and the exit velocity after passing through the atmosphere was about 14.6 km s^{-1} . The images are all oriented so that the fireball travels from left to right (west to east).

Table 1

Observations and Triangulated Trajectory for Event DN170707_01, Recorded over Western Australia and Southern Australia on 2017 July 7

	Entry Conditions	Exit Conditions
Time (UTC) after 2017 Jul 7	12:33:45.900	12:35:16.050
Height (km)	85.66 ± 0.03	86.04 ± 0.02
Mass range (depending on density; kg)	14–92	9–62
Latitude (deg)	-28.6933 ± 0.0003	-28.4144 ± 0.0002
Longitude (deg)	122.7161 ± 0.0010	136.3318 ± 0.0002
Velocity (km s^{-1})	15.71 ± 0.13	14.24 ± 0.10
Slope (deg)	4.6	7.8
Duration (s)		90.15
Minimum height (km)		58.5
Best convergence angle (deg)		45.9
Number of observations (with timing)		13
Number of observations (without timing)		7
Number of data points		2541

Note. The mass range was determined by varying the density between 2800 and 7300 kg m^{-3} and includes formal uncertainties. The timing uncertainty is nominally 10^{-4} – 10^{-5} s, considerably less than other sources of uncertainty for the trajectory (Howie et al. 2017b).

is only a few degrees (1° – 2°). Therefore, the uncertainty associated with the initial velocity is higher than usual, however, still sufficient to determine what part of the solar system the meteoroid originated.

At the meteoroid's closest approach, a fragmentation event occurred in which a smaller piece of the primary object broke off (Figure 2). DFN observatories captured the fragmentation event on video, and an uncalibrated light curve was able to be extracted (Figure 3). There are no other instances of fragmentation observed during the trajectory. This fragmentation event was taken into account when triangulating the path of the primary and determining the mass of the meteoroid.

3. Methods

3.1. Triangulation

In the past, fireball and meteor observation networks estimated the trajectories they witnessed using a simplified straight-line fit approach (Ceplecha 1987; Borovicka 1990). These simplified straight-line fit techniques are sufficient enough to obtain meaningful results when the trajectory is shorter than 100 km. However, recent studies have shown that more satisfactory results can be obtained with the use of more rigorous methodologies (Sansom et al. 2015, 2019; Jansen-Sturgeon et al. 2019a). This is particularly true for a grazing fireball where the meteoroid is traveling hundreds to thousands of kilometers through the atmosphere. In previous grazing fireball studies, this nonlinearity was accounted for in several different ways. Ceplecha (1979) was the first to recognize that a grazing trajectory should fit a hyperbola when neglecting the atmosphere, but is otherwise slightly more curved due to the atmospheric drag experienced. Thus, Ceplecha (1979) fit osculating circles to the trajectory of the 1972 grazing daylight fireball to account for this added curvature with reasonable accuracy. Borovicka & Ceplecha (1992) utilized the fact that one of the observation stations was nearly directly below the fireball (passed nearly through zenith) and saw the entire trajectory. They took their observations and performed a least-squares fit to an osculating circle at the point of pericenter, neglecting drag in this case based on fireball type. Similar methodologies using osculating circular trajectory fits have been utilized by other studies as well (Abe et al. 2006). Kozak & Watanabe (2017) triangulated a small, fast grazing, high-altitude meteor detected by video observatories in Ukraine by assuming minimal drag and fitting the observations to a hyperbolic orbit in the geocentric frame. Meanwhile, Madiedo et al. (2016) determined the atmospheric trajectory of a meteor belonging to the daytime ζ -Perseid shower using a segmented method-of-planes approach adapted from Ceplecha (1987).

For standard DFN events, we implement a modified straight-line least-squares (SLLS) method with an extended Kalman smoother (EKS) for velocity determination (Sansom et al. 2015).

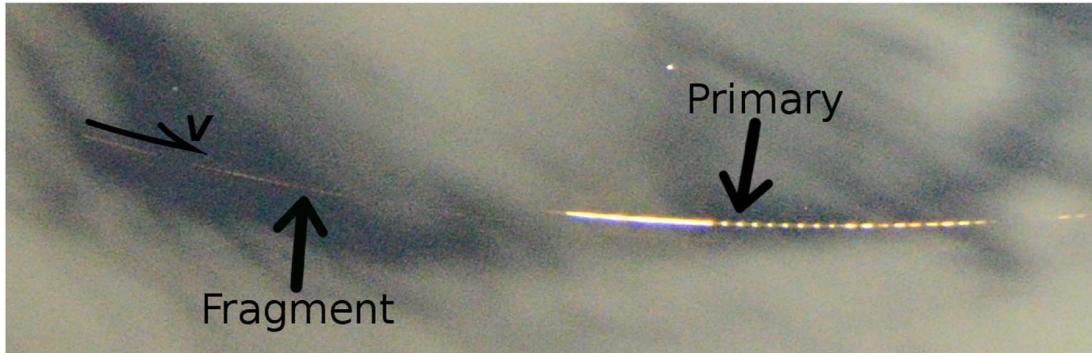


Figure 2. Fragmentation event captured for event DN170707_01 near the closest approach of its trajectory. The image shows two distinct paths offset from each other. The brighter path on the right side of the image belongs to the primary piece, whereas on the left the trail of a smaller fainter fragment can be seen. The decrease in velocity due to the observed fragmentation was not significant relative to the velocity scatter, and thus was not included during the trajectory fit. Additionally, only one camera observed the fragment due to cloud coverage and geometry, and therefore a trajectory for the fragment was unable to be determined. No other fragmentation events were detected along the path.

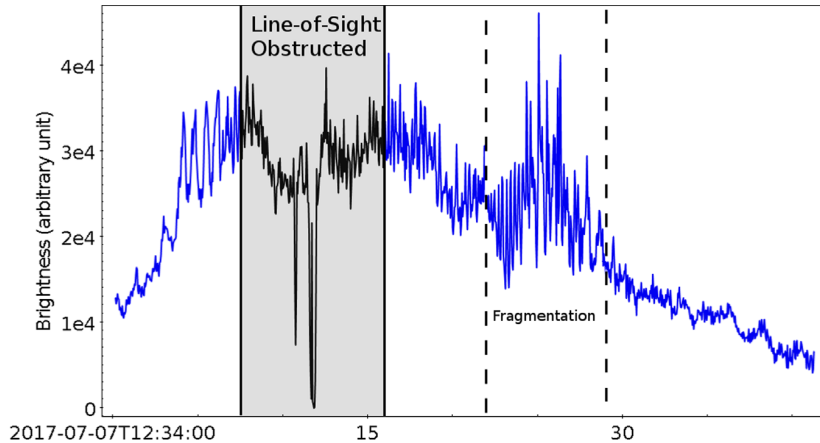


Figure 3. Light curve based on video from observatory DFNSMALL34-Kybo in the Nullarbor Plain in western Australia during the fragmentation of event DN170707_01. The fragmentation occurs about 25 s into this exposure (enclosed by dashed vertical lines), forming one detectable fragment. The y-axis is brightness in arbitrary units due to the photometry data lacking calibration. The ram pressure on the meteoroid just prior to the fragmentation was ~ 0.08 MPa. The line of sight was briefly obstructed by a telephone pole, reducing the brightness.

We then numerically determine the meteoroid’s orbit by including all relevant perturbations. Numerical methods are a slightly more accurate way to handle the orbit determination, especially for meteoroids that were slow or closely approached the Moon (Clark & Wiegert 2011; Dmitriev et al. 2015; Jansen-Sturgeon et al. 2019a). For longer and/or shallower fireball events, where the meteoroid trajectory can have noticeable curvature, the SLLS method cannot account for the nonlinear motion. Within this study, we implemented a dynamic trajectory fit (DTF) triangulation method that fits the observation rays directly to the equations of motion for fireballs (Jansen-Sturgeon et al. 2019b). This non-straight-line approach to the event triangulation represents the physical system more veraciously. Consequently, the DTF method produces a much better fit to the observations compared to the SLLS for both positions and velocities (Figures 4 and 5). We then use this trajectory (Figure 6) to numerically estimate the pre- and post-grazing orbits. Although, currently the DTF method does not provide adequate formal velocity errors, thus an EKS was utilized to determine the velocity uncertainties for this study.

3.2. Mass Determination

During the DTF procedure, the meteoroid’s ballistic parameter and ablation coefficient are determined alongside its dynamic parameters, based directly on the line-of-sight observations. By assuming the meteoroid’s shape and density, a mass estimation can be deduced from the meteoroid’s fitted ballistic parameter.

3.3. Orbital Integration

After triangulating the grazing event, we initialized several orbital integrations using the publicly available REBOUND code¹ (Rein & Liu 2012). We utilized the 15th order nonsymplectic IAS15 integrator for our simulations of the event (Rein & Spiegel 2015). This integrator is based upon the RADau-15 integrator developed by Everhart (1985). It improves upon its predecessor by minimizing the systematic error generated by the algorithm to well below machine precision, implementing an adaptive time step, and adding the

¹ <http://github.com/hannorein/REBOUND>

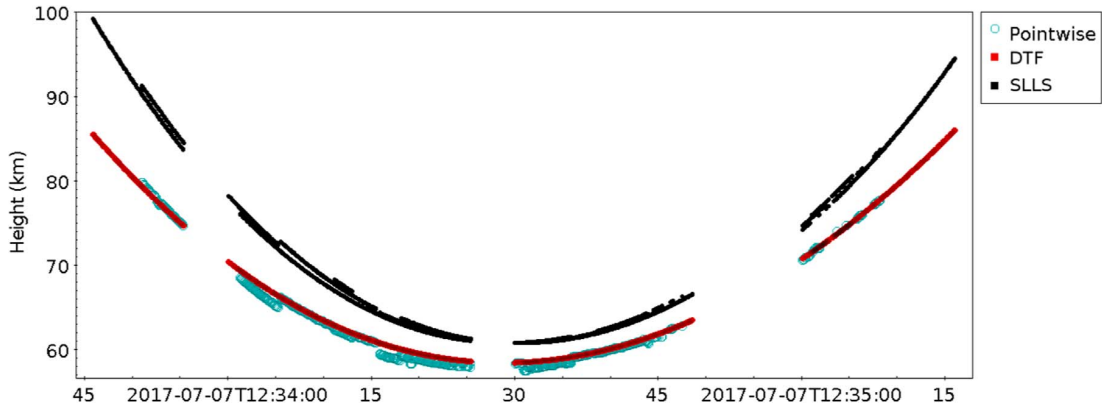


Figure 4. Height variation as a function of time determined by the straight-line least-squares (SLLS) and the dynamic trajectory fit (DTF) methods. The pointwise heights represent the points that minimize all the angular distances between the simultaneous lines of sight (given >2), the respective observatory, and the point itself. The DTF fits much better to the pointwise than the SLLS due to its incorporation of gravity, drag, and ablation. This non-straight-line fit produces a much more useful model to understand these grazing fireball events. The shape of the trajectory is somewhat misleading, as the trajectory would be concave with respect to a global, inertial reference frame instead of convex, as shown here. The three distinct gaps in the trajectory are due to latency between observation periods (Howie et al. 2017a). This lapse in observations occurs once every 30 s and is only typically noticeable for the longest fireball trajectories observed by the DFN. Toward the end of the trajectory, the largest lapse in observations was also due to the cloud coverage at the time.

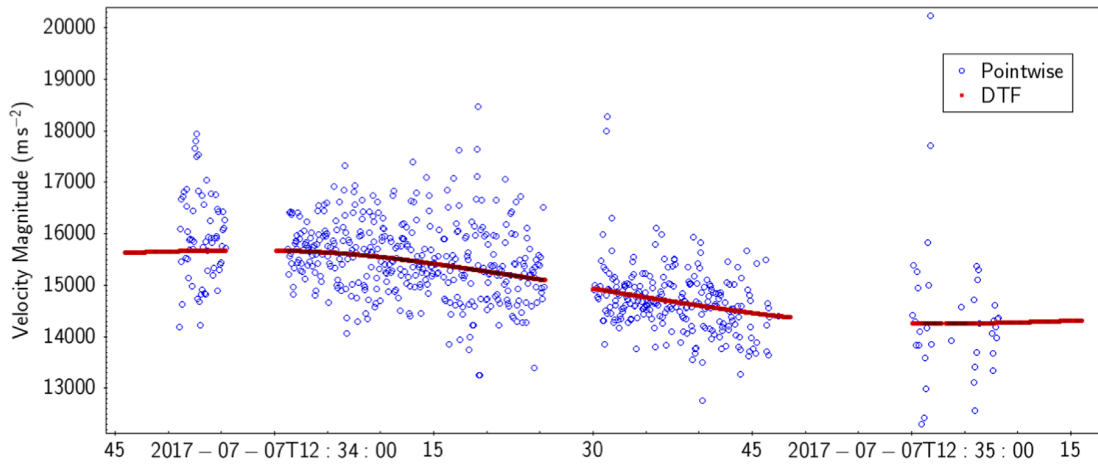


Figure 5. Velocity of the DN170707_01 meteoroid event as determined using both the dynamic trajectory fit (DTF) model (red) and a pointwise triangulation fit (blue). The DTF method fits the line-of-sight observations directly to the dynamic equations of motion that describe the motion of fireballs. Pointwise scattered instantaneous speeds correspond to the center difference between adjacent data points seen by >2 observatories. These points in 3D space are calculated by minimizing all the angular distances between the simultaneous lines of sight, the respective observatory, and the point itself.

ability to include in nonconservative forces easily while ensuring that the round-off errors are symmetric and at machine precision.

Initialization. From the trajectory determined by the DTF method, the pre- and post-atmospheric state vectors for the meteoroid can be used to initialize orbital simulations. These simulations contain N number of particles within the meteoroid state's uncertainties produced by the triangulation. Currently, the DTF methodology does not provide formal uncertainties as model errors are not accounted for (Jansen-Sturgeon et al. 2019b). Subsequently, for this event, we determined the velocity uncertainties using the EKS method in conjunction with the DTF trajectory fit. Additionally, we assume a Gaussian distribution for the errors, although this may not be strictly true. However, the results from the integration should not deviate significantly due to this assumption. The particles' positions are generated from the initial and final latitude, longitude, and height determined from the DTF triangulation. The speed of the particles and their R.A. and decl. are given in the Earth-

centered Earth-fixed frame and then converted to the Earth-centered inertial frame in order to generate the particles in the simulations.

Integration. Initial simulations were run within ± 100 yr of the grazing event in order to accurately characterize the short-term evolution of the meteoroid. The number of outputs recorded was increased so that any close encounters with Jupiter or Earth would be well resolved. Afterward, a series of long-term integrations were done in a similar manner. The primary goal of these more extended integrations was to determine what were the lasting effects of the meteoroid's grazing encounter with Earth. Does it stay on a JFC orbit as long as any typical JFC, and where does it evolve to after? Each integration recorded the positions, velocities, and osculating orbital elements for the meteoroid particles for a total period of 500,000 yr forward relative to the event epoch. Close encounters with other planets were also considered and inspected, particularly with Jupiter.

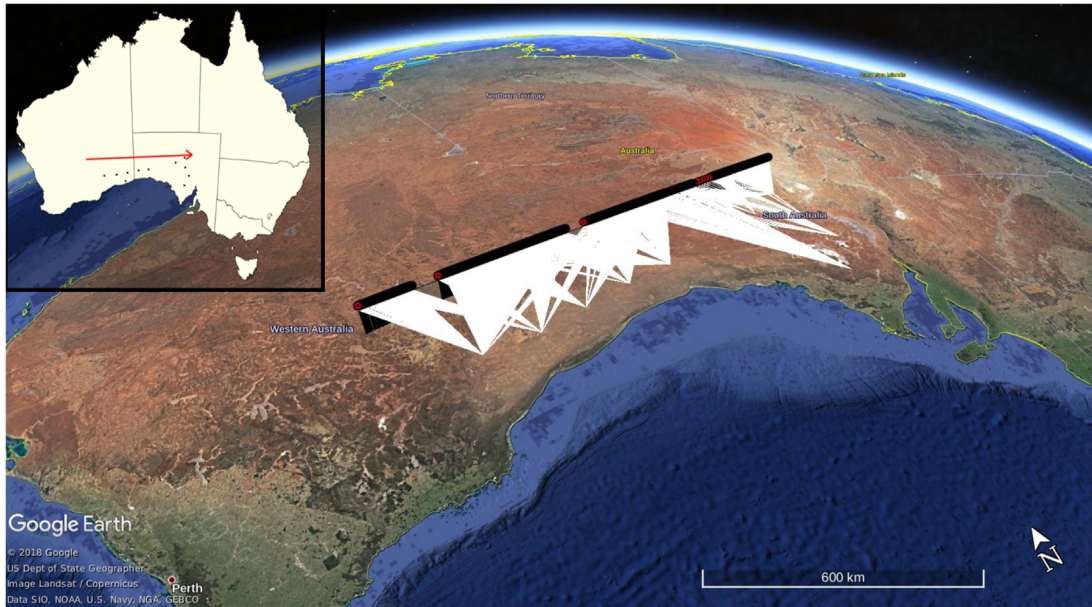


Figure 6. Triangulated luminous atmospheric trajectory for event DN170707_01, as seen over western Australia and southern Australia. The triangulation method used involves fitting the line-of-sight observations directly to the meteoroid’s dynamic equations of motion, thereby dropping any straight-line assumptions (Jansen-Sturgeon et al. 2019b). The event lasted 90 s, initially hitting the atmosphere at 47° and covering over 1300 km through the atmosphere. The white rays indicate the line-of-sight measurements from each DFN observatory, whereas the black path marks the triangulated trajectory based on the observations of the fireball.

4. Results and Discussion

4.1. Atmospheric Trajectory

As seen in Figure 4, the DTF methods fit the pointwise observations much better than the SLLS method for an event that is thousands of kilometers in length. The pointwise heights are given by minimizing the angular distance between the lines of sight when at least two observations are made. If a center difference is taken between all these points, a velocity scatter can be generated (Figure 5). The velocity scatter for event DN170707_01 is very large in some circumstances considering the low convergence angles, especially for the beginning of the trajectory. A majority of the fireball’s trajectory was north of the DFN observatories (Figure 6), thus reducing the accuracy of each measurement. However, since we gathered over 2500 data points from 10 DFN observatories, a reasonably good trajectory was able to be extracted. There are also three distinct gaps in the observations of event DN170707_01 primarily due to the latency between the 30 s observation periods. These lapses in observations are typically only noticeable for the longest enduring fireballs observed by the DFN. The longest gap, toward the end of the trajectory, is compounded by the poor visibility for the DFN observatories in that area of the network due to the cloud coverage at the time.

During the DTF procedure, the ballistic parameter was determined throughout the trajectory based directly on the line-of-sight measurements, and hinges on the deceleration profile of the observed meteoroid. The meteoroid’s mass was estimated by assuming its shape and density, as seen in Figure 7. For instance, assuming a spheroid of chondritic density (3500 kg m^{-3}), the DN170707_01 meteoroid was estimated to have a 60 kg initial mass and a 40 kg outbound mass. A majority of the mass loss is predicted to have occurred during the fragmentation observed near the closest approach of the object. However, as minimal deceleration was observed during the luminous atmospheric

encounter (Figure 5), this mass estimate would be more accurately viewed as a lower bound.

The loading ram pressure for the meteoroid at the time of fragmentation was also calculated using

$$p = \rho_h v_h^2, \quad (1)$$

where ρ_h is the atmospheric density at the height h of the fragmentation and v_h is the speed of the meteoroid at that instant. For event DN170707_01, we determined the fragmentation height based on the time of fragmentation observed in the light curve from video observations. We estimated the meteoroid to have fragmented at $58.49 \pm 0.01 \text{ km}$, just before the minimum height was reached, with a velocity of $15.5 \pm 0.1 \text{ km s}^{-1}$. We then used the NRLMSISE-00 global atmospheric model to determine the density of the atmosphere at the fragmentation height (Picone et al. 2002). The ram pressure experienced by the meteoroid just before fragmentation was calculated to be $0.084 \pm 0.01 \text{ MPa}$. This very low value is consistent with the results of Popova et al. (2011), in which it was found that bulk strengths determined by initial fragmentation are consistently much lower than the strength of recovered meteorites. Thus, this value likely reflects macro-scale fractures in the object and not the intrinsic material strength. For example, the Dingle Dell ordinary chondrite meteorite recovered by the DFN in 2016 also experienced similar low-pressure fragmentations (0.03–0.11 MPa) early in its bright flight, despite having a recovered bulk density of 3450 kg m^{-3} (Devillepoix et al. 2018).

4.2. Short-term Simulations

As shown in Table 2, the meteoroid that skipped off the atmosphere over western Australia and southern Australia in 2017 July originally came from an orbit in the inner main-belt, between the 4:1 and the 3:1 mean-motion resonances with

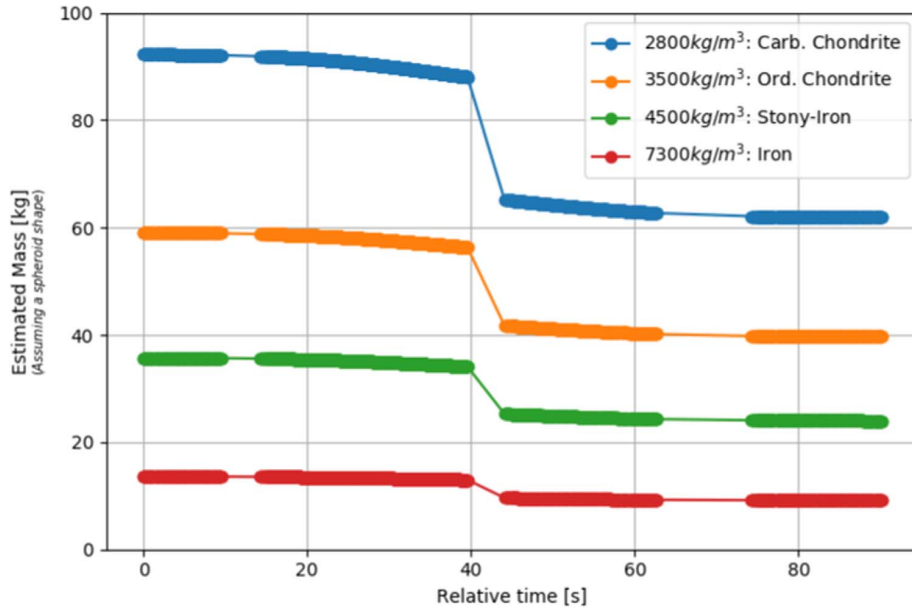


Figure 7. Mass estimation based on DTF triangulation fit to the DFN’s observations. The fragmentation event was taken into account, as seen by the sudden mass loss experienced at ~ 40 s into the luminous phase. Each line represents a different density estimate for the object, given the DTF ballistic parameter.

Table 2

Heliocentric Orbital Elements for the Meteoroid Associated with Event DN170707_01 Just before and after its Grazing Encounter with Earth

	Before	After
a (au)	2.23 ± 0.06	3.26 ± 0.12
e	0.59 ± 0.01	0.69 ± 0.01
i (deg)	2.79 ± 0.04	3.30 ± 0.04
Ω (deg)	286.46 ± 6.03	285.29 ± 0.01
ω (deg)	316.43 ± 3.56	350.91 ± 0.29
q (au)	0.9104 ± 0.0003	1.007 ± 0.0004
Q (au)	3.458 ± 0.114	5.36 ± 0.2300
T_J	3.41 ± 0.05	2.75 ± 0.05

Note. The uncertainties of the orbital elements were determined by a short Monte Carlo simulation consisting of 5000 particles randomly generated within triangulation errors and numerically integrated forward and backward relative to the grazing event. The immediate effect of the encounter on the orbit is apparent; the semimajor axis, eccentricity, and argument of perihelion of the meteoroid were all significantly increased. The grazing encounter changed the orbit of the meteoroid from an Apollo-type NEO to a JFC orbit. The resulting orbit is comparatively unstable due to its aphelion being very similar to the semimajor axis of Jupiter, increasing the chance of a close encounter with the gas giant.

Jupiter (Figure 8). It most likely evolved into an Earth-crossing orbit after passing through either the 3:1 or the ν_6 complex, which are the two most significant entry routes into the NEO region (Bottke et al. 2002; Granvik et al. 2018). As a result of the grazing encounter with Earth, the meteoroid was flung into an orbit with a higher energy (Figure 9). The geometry of the encounter enabled the meteoroid to gain angular momentum around the Sun (Figure 10). As a result, the semimajor axis and eccentricity both increased due to the increase in energy, and the object was inserted into a JFC orbit. Hereon, the object’s future is strongly governed by its interactions with the gas

giant. Figure 8 shows the evolution of the orbital elements for the meteoroid ± 100 yr relative to the grazing encounter.

With an post-encounter aphelion near Jupiter’s orbit, the meteoroid is likely to have multiple close encounters with the planet in the future. Thus, the object is unpredictable on relatively short timescales compared to other small bodies in the solar system. This is to be expected for an object on a JFC-like orbit that originated from the trans-Neptunian region (Fernández & Sosa 2015). As seen in Figure 8, the object will tend to decrease in eccentricity and slightly increase in semimajor axis over time. This will occur slowly for a majority of particles over about 10–100 kyr, as Jupiter perturbs them. If the orbit of the meteoroid evolves into an orbit with a similar semimajor axis to Jupiter, the close encounters with the gas giant will begin to increase the eccentricity of the meteoroid again and throw the body toward the outer solar system. The meteoroid is also nearly centered on the 2:1 mean-motion resonance (Figure 8), however, this resonance is not as destabilizing as the other prominent resonances on such short timescales (Morbidelli et al. 2002).

The first of these close encounters will most likely occur between 2025 January and March (~ 7.52 yr after encountering Earth) in which the meteoroid will very likely come within 3 Jupiter Hill radii (JHR) of the planet. A series of short-term highly resolved integrations were performed with 5000 test particles to analyze this first close encounter with Jupiter. As shown in Figure 11(a), the meteoroid is likely to get close to Jupiter (blue path) just 1.5 orbits after our observations of the fireball. Figure 11(b) shows the minimum distances reached by every particle in the integration, many of which (40%) approaching within 1 JHR with the mean approach of all particles being 0.7 JHR. After this close encounter, the test particles disperse relatively quickly, and precisely predicting the future orbit of the meteoroid becomes unrealistic.

As seen in Figure 12, the well-constrained orbit prior to the close encounter with Jupiter rapidly spreads out in the orbital

THE ASTRONOMICAL JOURNAL, 159:191 (15pp), 2020 May

Shober et al.

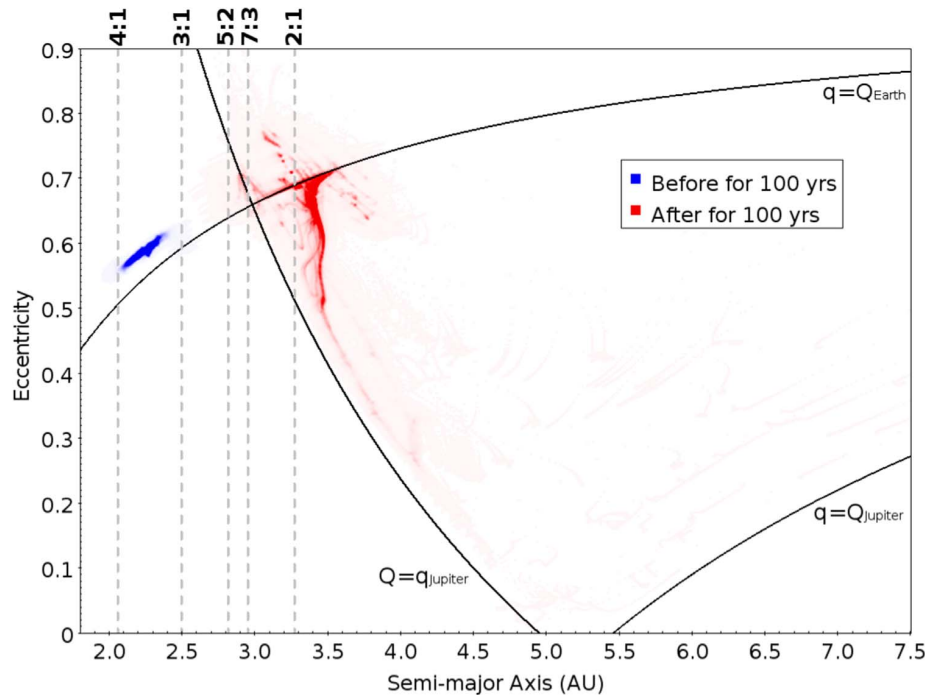


Figure 8. Semimajor axis vs. eccentricity during ± 100 yr of integrations involving 10,000 test particles. Particle density over time is indicated by opacity. A majority of the particles remain close together after the grazing encounter, with a small number of particles being scattered by Jupiter very quickly. The significant mean-motion resonances are also plotted as vertical dotted lines. The object came from an eccentric orbit between the 4:1 and 3:1 mean-motion resonances. After the grazing encounter with Earth, the object gained energy and was transferred onto a JFC orbit near the 2:1 resonance with Jupiter. In this orbit, the future of the meteoroid is strongly influenced by the gas giant. Over time, the meteoroid will tend to follow the aphelion and perihelion lines for Jupiter.

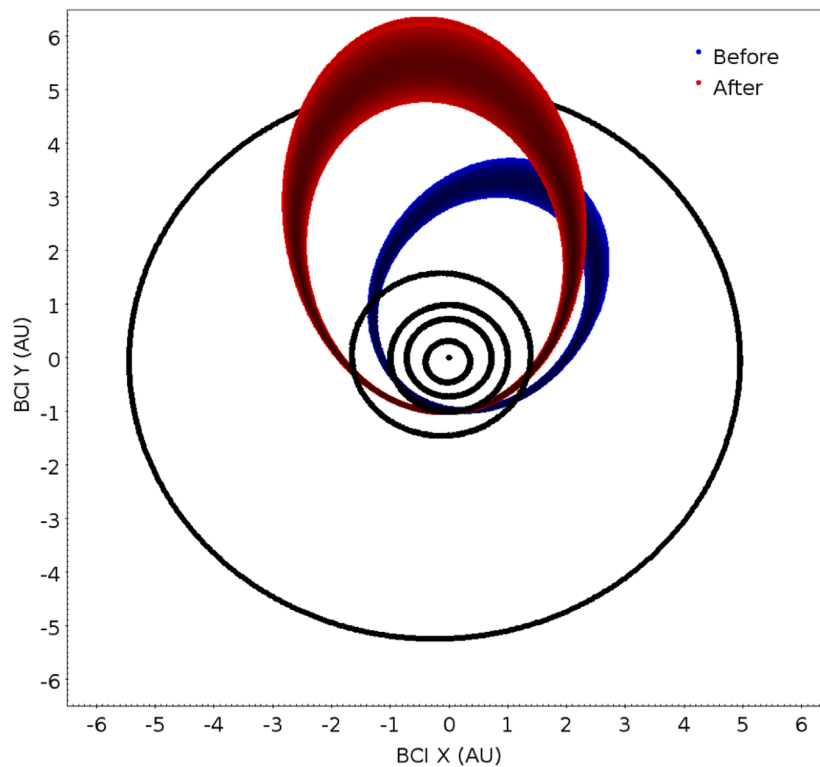


Figure 9. The meteoroid's orbit before and after the grazing encounter with Earth. The meteoroid originated from an Apollo-type asteroidal orbit and was inserted into a JFC orbit. Once in this JFC orbit, the object's path rapidly becomes less certain due to multiple close encounters with Jupiter.

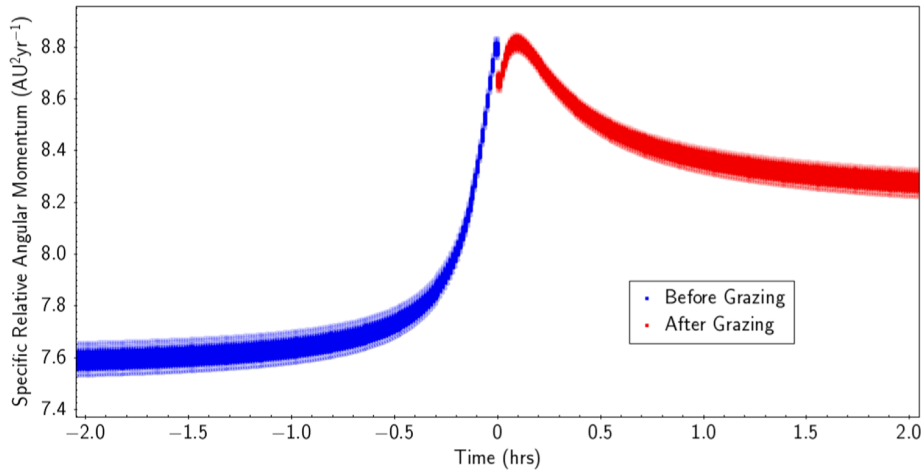


Figure 10. Specific relative angular momentum of the meteoroid ± 12 hours relative to the grazing event. The meteoroid gains energy after its encounter with Earth despite losing some energy during the atmospheric passage. At time $=0$, the discontinuity is due to the exclusion of the time when the meteoroid was passing through the atmosphere. The “instant” drop in energy here corresponds to the energy lost due to atmospheric drag. The object continues to gain angular momentum briefly after leaving the atmosphere before losing some energy as it travels away from Earth. This net gain in angular momentum effectively increased the semimajor axis and eccentricity of the body.

space. Following the likely meteoroid–Jupiter close encounter of 2025, the orbit of the meteoroid can only be treated statistically. The density plots in Figure 12 show the evolution of the semimajor axis, eccentricity, and inclination of 10,000 test particles forward in time only 100 yr. Most of the particles stay together, indicated by the darker portions of the plot. However, as seen by the multiple jumps in values over time, the meteoroid is likely to have a plethora of close encounters with Jupiter over its lifetime in a JFC orbit, and every one of these encounters obscures the future of the object.

Close Encounters with Earth. In order to determine the likelihood of future or previous close encounters with Earth, two simulations with 5000 particles were integrated both backward and forward 20 yr relative to the event (Figure 13). During these simulations, outputs were collected at a higher frequency in order to accurately characterize all possible close encounters. The probability that there was an encounter with Earth within three and one Hill radii within 20 yr prior to the grazing event was 2.4% and 0.7%, respectively. Additionally, the probability that a future close encounter with Earth will occur within the preceding 20 yr after the grazing event is 1.4% and 0.5%, respectively. Therefore, the probability of having the opportunity to telescopically observe this object as it re-approaches Earth is very slim. The most likely time for this to occur is in 2023 mid-July, but there is still only a 1.1% chance that it will get within 3 Hill radii of the planet.

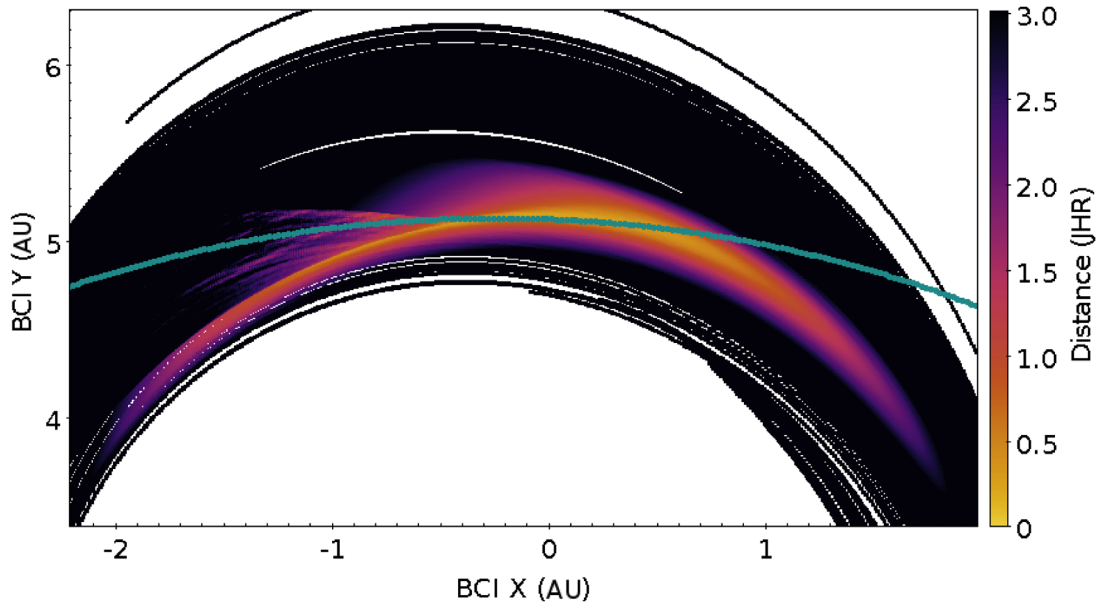
4.3. Long-term Simulations

Further analysis using substantially longer integrations of test particles was performed in order to statistically characterize the meteoroid’s future. The longest of these simulations was a forward integration of 1000 test particles for 500 kyr. Over the course of the 500 kyr forward integration, most of the particles (60.1%) are eventually ejected from the solar system, as expected (Figure 14). The vast majority of the particles that remain in the solar system (heliocentric orbits) stay in JFC

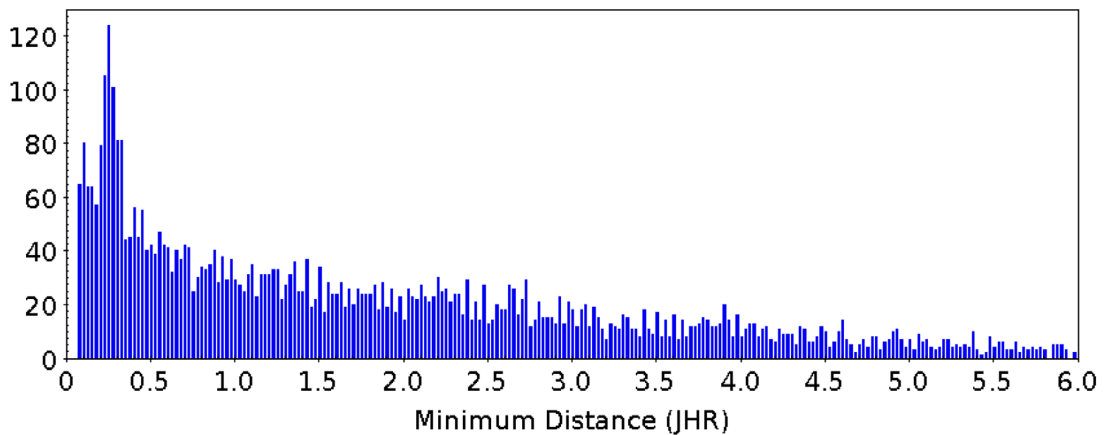
orbits (as defined by the Tisserand’s parameter) for the entire integration (Figure 15).

As seen in Figure 14, there is an exponential decay in the number of particles in heliocentric and JFC orbits. The average dynamical lifetime for the particles in JFC orbits is approximately 200 kyr, which is shorter than the ~ 325 kyr dynamical lifetime estimate for JFCs (Levison & Duncan 1997; Duncan et al. 2004). This is likely due to the initial post-grazing orbit, which has an aphelion very near the orbit of Jupiter. However, bodies in JFC orbits that display cometary features are more likely to have multiple ≤ 0.1 au encounters with Jupiter, reducing the orbital stability compared to asteroidal interlopers within the population (Fernández & Sosa 2015). Therefore, the JFC-orbit dynamical lifetime for the meteoroid is indistinguishable from a JFC from a more traditional source region. In Figure 14, the JFC, asteroidal, and LPC categories are solely determined by the particles’ Tisserand parameter. Whereas, the Centaur and trans-Neptunian objects are defined as having orbits between Jupiter and Neptune, and beyond the orbit of Neptune, respectively. This classification does lend itself to including some Centaurs and trans-Neptunian objects when counting the number of JFCs.

A smaller fraction (31.6%) of the test particles evolve onto asteroidal or long-period cometary orbits as defined by their Tisserand parameter values (Figure 16). The majority of asteroidal particles are determined to be in the outer solar system. These are particles that originated from JFC space that were decoupled from Jupiter over time due to planetary perturbations and are now on Centaur or trans-Neptunian orbits. This portrays a similar mechanism alluded to in the concluding statements in Meech et al. (2004), where they estimate that there should be ~ 20 objects of kilometer-size from the main-belt being scattered by Jupiter every million years in today’s solar system. The object discussed in this study differs in that it was gravitationally scattered by Earth and then by Jupiter, resulting in the possible transfer of volatile-depleted inner solar system material to the outer solar system.



(a) Close encounter of meteoroid with Jupiter (blue path).



(b) Histogram of the minimum distances between the particles and Jupiter.

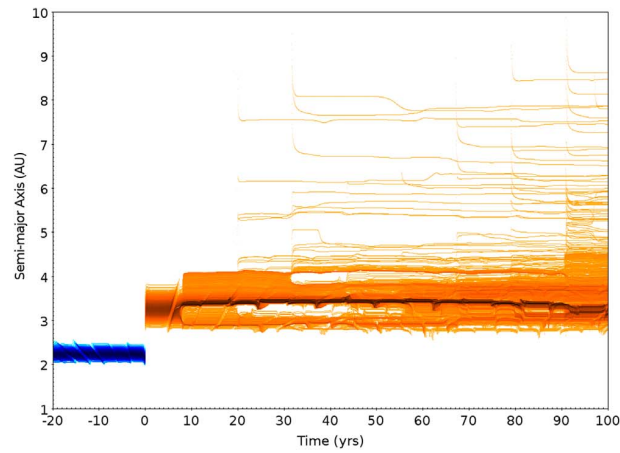
Figure 11. After grazing Earth’s atmosphere, the meteoroid will complete 1.5 orbits around the Sun before likely having its first close encounter with Jupiter. Both plots provide the distance from Jupiter in terms of Jupiter Hill Radii (JHR). Of the 5000 particles in this integration, nearly 40% come within 1 JHR and 80% are within 3 JHR. The mean approach is about 0.7 JHR. Consequently, the orbit of the meteoroid is highly uncertain after this point, approximately 7.52 yr after its grazing encounter with Earth (2025 January–March).

4.4. Analysis of Other Grazing Meteors/Fireballs

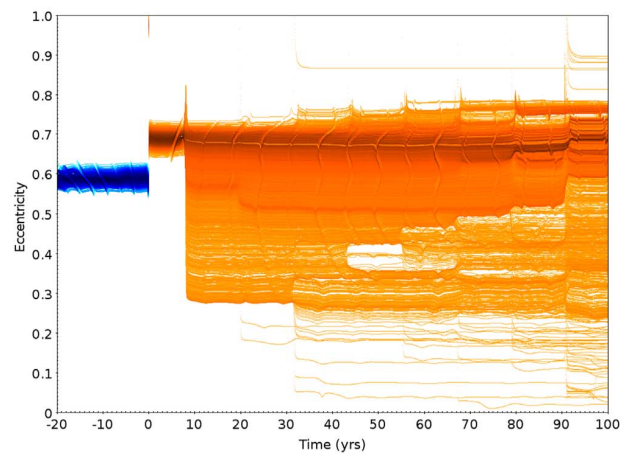
Within the current scientific literature, there have been in total 10 grazing fireballs observed. However, in only six of these cases did the meteoroid survive the atmospheric passage and return to interplanetary space (Table 3). These grazing events demonstrate the orbital changes experienced by meteoroids that come very close to Earth. In most of these occurrences, the objects experience a significant change to their orbits. Although, this does not necessarily change them enough to be orbitally reclassified. For the first photographically observed grazing fireball, in 1990 October, a 10^5 – 10^6 kg meteoroid in a higher inclination Apollo-type orbit with a JFC-like Tisserand parameter was inserted into a lower-energy orbit with a $T_J > 3$. Thus, not only has a meteoroid with a more asteroid-like T_J become more cometary due to close encounters, but the reverse has also been observed. It has been shown

that using Tisserand’s parameter is a better metric to classify small solar system bodies compared to the traditional arbitrary classification based on the orbital period (Carusi & Valsecchi 1987; Levison & Duncan 1997). Nevertheless, as shown in this study, small meter-sized objects occasionally experience close encounters with Earth and have a sufficient orbital energy change to be reclassified even under this scheme.

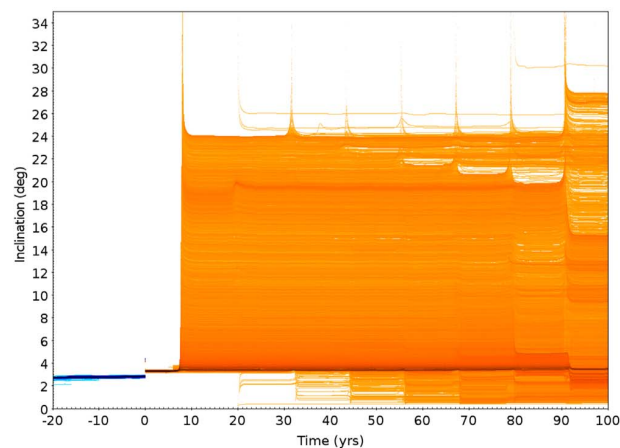
Other Grazing DFN Events. If we consider an fireball event to be grazing simply when the initial slope of the trajectory is $< 5^\circ$ and traveled > 100 km through the atmosphere, in the four years since the DFN has been fully operational, we have observed $\sim 1.2\%$ of the DFN data set to be grazing events. Indicating that although somewhat uncommon, grazing events are not extremely rare. However, in most of the events detected, the meteoroid either does not survive the atmospheric passage or loses enough velocity to be incapable of re-entering interplanetary space.



(a) Semi-major axis variation.



(b) Eccentricity variation.



(c) Inclination variation.

Figure 12. Due to the grazing encounter with Earth, the meteoroid from event DN170707_01 was sent into a Jupiter intersecting orbit. On this new trajectory, the object will likely experience many close encounters with Jupiter over its lifetime. In these density plots, the blue and orange particles represent the meteoroid before and after the grazing encounter, respectively. The darker coloration is indicative of a higher particle density. The many possible close encounters with Jupiter manifest as discrete “jumps” in the semimajor axis, eccentricity, or inclination. Over time the orbits tend to spread out due to numerous close encounters with Jupiter. Thus, the orbit of the meteoroid becomes less clear over a relatively short period of time.

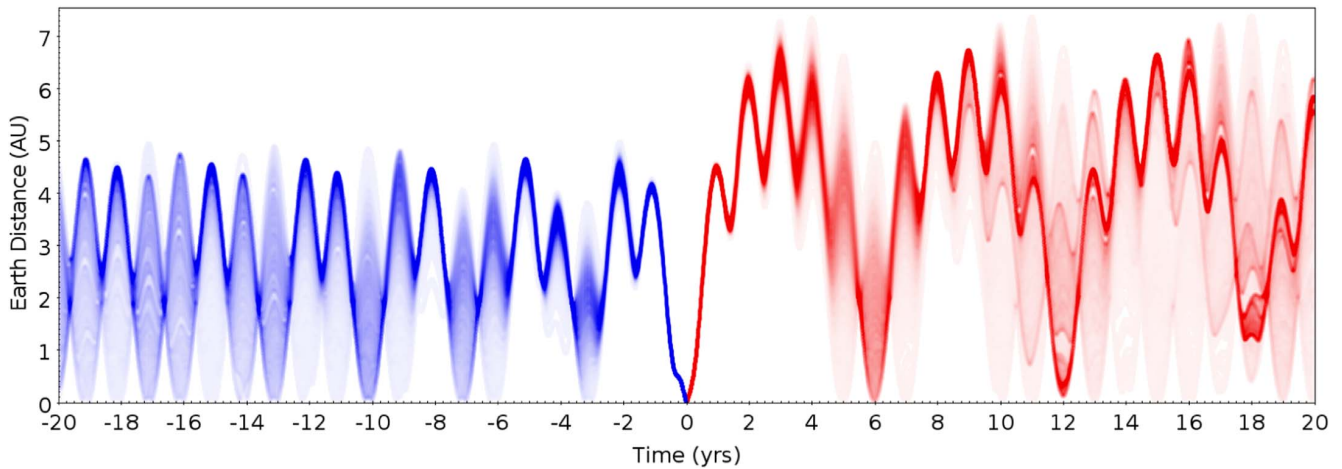


Figure 13. Plot of distance relative to Earth over time. These two simulations were conducted with 5000 particles and lasted 20 yr (forward and backward). The time on the x -axis is relative to the event epoch. The probability of an encounter with Earth for the 20 yr before and after the fireball observation is extremely low. There is a 2.4% probability of coming within 3 Hill radii and a 0.7% probability having a 1 Hill radii encounter with Earth within 20 yr before the grazing encounter. Meanwhile, there is a 1.4% and a 0.5% probability of the meteoroid encountering Earth again within one and three Hill radii in the next 20 yr respectively. There is 1.1% that the object will approach within 3 Hill radii in 2023 July.

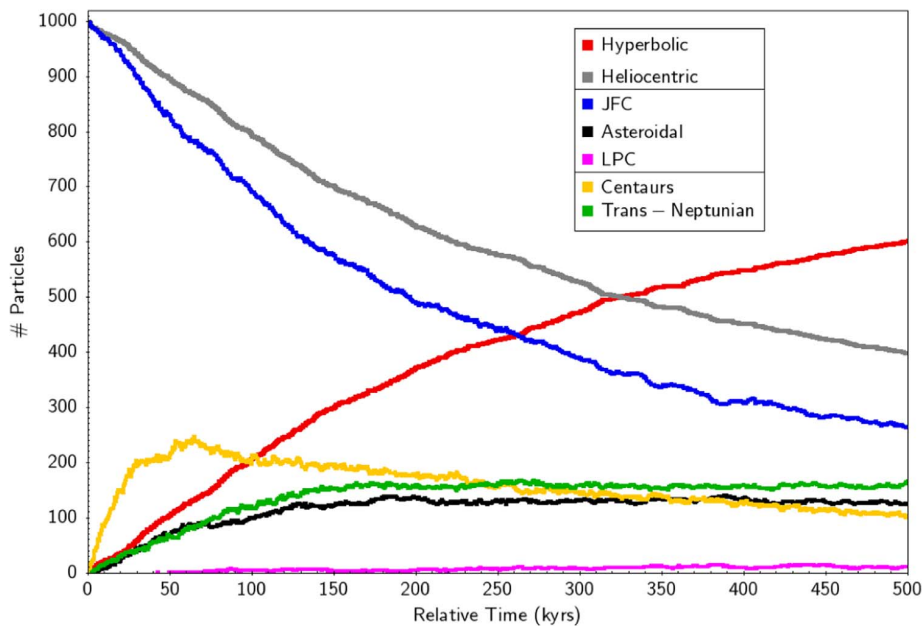


Figure 14. Plot showing the change in the orbital classification of the 1000 particles in the forward integration of event DN170707_01 for 500 kyr. The lines separating the labels in the legend group classifications together that are mutually exclusive (e.g., particles cannot be simultaneously hyperbolic and heliocentric). Over time, the likelihood that the meteoroid will have a close enough encounter to eject it from the solar system increases. By the end of the simulation, 60.1% of the particles are ejected, 27.3% are still on JFC orbits, and 12.6% have remained in the solar system but have either gone onto long-period cometary or asteroid-like orbits. Many of the particles (~20%) evolve onto Centaur and then trans-Neptunian orbits due to close encounters with Jupiter.

4.5. Implications and Further Research

Grazing fireballs indicate that meter-scale NEOs are occasionally inserted into categorically new orbits due to close encounters with Earth, or indeed other planets. How effective this mechanism is for mixing material in the inner solar system for small objects is still to be determined. Current work is being done to produce an artificial data set of close encounters undetected by telescopes based upon the entire orbital data set of the DFN (P. M. Shober et al. 2020, in preparation). This analysis will be extremely valuable to conclusively determine how significant this process is

for small objects in the inner solar system. If it is non-negligible, what populations in the near-Earth space may be more or less contaminated by genetically unrelated material, how significant are the orbit alterations, and what may this imply about where meteorites come from?

5. Conclusions

On 2017 July 7, the DFN observed a >1300 km long grazing fireball by 10 of its high-resolution digital fireball observatories. The meteoroid transited the atmosphere for over 90 s and

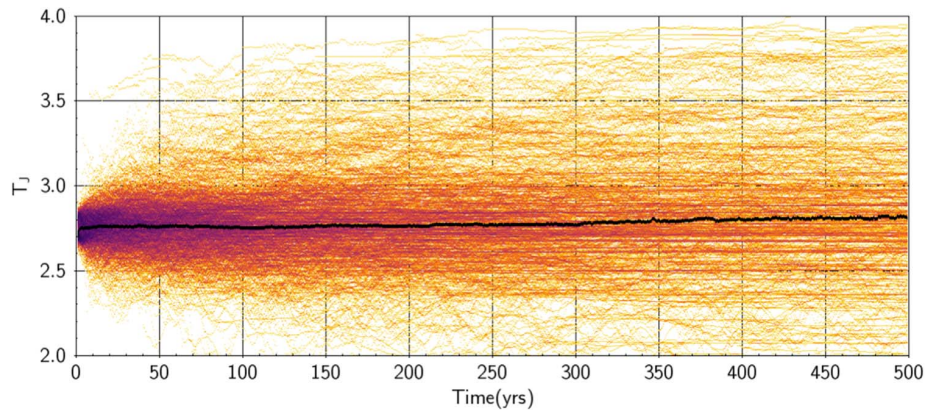


Figure 15. Tisserand’s parameter variation of 1000 particles integrated for 500 kyr post-grazing event for DN170707_01. Particles that are ejected from the solar system are removed. The meteoroid is likely to stay in a JFC orbit for an amount of time normal for a natural JFC object. The colorization in the plot is indicative of density—darker in areas of higher particle density and lighter in areas of lower particle density.

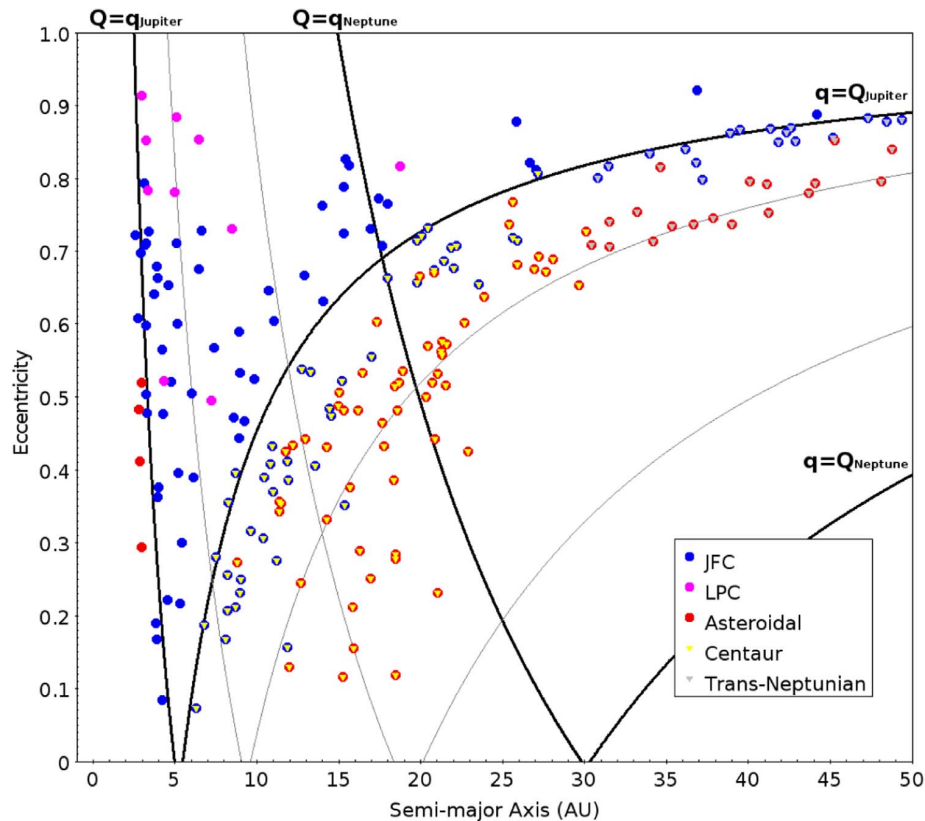


Figure 16. Semimajor axis vs. eccentricity for the particles that are still gravitationally bound to the Sun after the forward integration of 1000 particles for 500 kyr. The lines of equal perihelion and aphelion are plotted for Jupiter and Neptune in black, and in gray for Saturn and Uranus. Most of the remaining heliocentric particles (68.4%) are in JFC-like orbits (blue) according to their Tisserand parameter. However, a considerable number of particles (29.1%) are considered asteroidal, according to their Tisserand parameter with respect to Jupiter (red). Only a very small number of these are in the inner solar system. A vast majority appear to be former JFC particles that have completely decoupled from Jupiter and have drifted onto Centaur and trans-Neptunian orbits due to planetary perturbations over time. The Centaur and trans-Neptunian particles can have either JFC or asteroidal-like Tisserand parameters ($T_J > 2$), as shown by the colorization in this plot. Also, about 2.5% of the particles are categorized as long-period comets despite their low semimajor axis because they are orbiting in retrograde orbits.

reached a minimum height of 58.5 km before returning to interplanetary space. This fireball is only matched by the notorious “Great Daylight Fireball of 1972,” which penetrated to a very similar depth in the atmosphere but lasted ~ 9 s longer. As a result of the grazing encounter with Earth, the meteoroid observed by the DFN underwent a natural slingshot

maneuver in which it was transferred from an asteroidal Apollo-type orbit to a JFC orbit. Additionally, numerical integration of the object forward 500 kyr indicated that it will most likely stay in a JFC orbit for ~ 200 kyr—indistinguishable from any other JFC. Considering there are likely many small objects that go telescopically undetected that have close

Table 3
Summary of Six of the Ten Previous Earth-grazing Meteors within Scientific Literature in Which the Meteoroid Survived the Passage through the Atmosphere

Event Date	Event Location	Detection Method	Initial Mass	Orbit Before	Orbit After	T_J Before	T_J After	References
1972 Aug 10	Western US and Canada	Satellite infrared radiometer	10^3 – 10^6 kg	Amor	Apollo	4.14	4.52	Ceplecha (1979)
1990 Oct 13	Czechoslovakia and Poland	Photographic	~44 kg	Apollo	Apollo	2.27	3.07	Borovicka (1990)
2003 Sep 23	Ukraine	Video		Apollo	Apollo	0.66	0.79	Kozak & Watanabe (2017)
2006 Mar 29	Japan	Video, photographic, telescope	~100 kg	JFC		2.85		Abe et al. (2006)
2012 Jun 10	Spain	Video	1.5–115 kg	Daytime ζ -Perseid	Daytime ζ -Perseid	3.31	4.04	Madiedo et al. (2016)
2014 Dec 24	Spain	Video		Apollo		5.3		Moreno et al. (2016)

Note. Information omitted in the table was not included in the corresponding study.

encounters with Earth, there may be a non-negligible amount of meter-sized objects in modified orbits within the inner solar system.

This work was funded by the Australian Research Council as part of the Australian Discovery Project scheme (DP170102529). SSTC authors acknowledge institutional support from Curtin University.

This research made use of Astropy, a community-developed core Python package for Astronomy (Robitaille et al. 2013;?). Simulations in this paper made use of the REBOUND code which can be downloaded freely at <http://github.com/hannorein/REBOUND> (Rein & Liu 2012).

The authors would also like to thank David Clark for his assistance in creating animations of event DN170707_01 and searching telescope surveys for images of the meteoroid before and after DFN observations. Additionally, we would like to thank professor Jürgen Oberst for being being extremely helpful and providing additional information about the grazing fireball observed over central-Europe in 2014.

Software: Astropy (Robitaille et al. 2013; Astropy Collaboration et al. 2018), REBOUND (Rein & Liu 2012).

ORCID iDs

Patrick M. Shober  <https://orcid.org/0000-0003-4766-2098>
 Trent Jansen-Sturgeon  <https://orcid.org/0000-0002-0363-0927>
 Eleanor K. Sansom  <https://orcid.org/0000-0003-2702-673X>
 Hadrien A. R. Devillepoix  <https://orcid.org/0000-0001-9226-1870>
 Phil A. Bland  <https://orcid.org/0000-0002-4681-7898>
 Robert M. Howie  <https://orcid.org/0000-0002-5864-105X>
 Benjamin A. D. Hartig  <https://orcid.org/0000-0002-8646-0635>

References

- Abe, S., Borovicka, J., Spurný, P., et al. 2006, in European Planetary Science Congress 2006 (Paris: ESA), 486
- Astropy Collaboration, Price-Whelan, A. M., Sipőcz, B. M., et al. 2018, *AJ*, 156, 123
- Beech, M., Brown, P., Hawkes, R., et al. 1995, *EM&P*, 68, 189
- Binzel, R. P., Rivkin, A. S., Stuart, J. S., et al. 2004, *Icar*, 170, 259
- Bland, P., Spurný, P., Bevan, A., et al. 2012, *AuJES*, 59, 177
- Bland, P. A. 2004, *A&G*, 45, 5.20
- Borovicka, J. 1990, *BAICz*, 41, 391
- Borovicka, J., & Ceplecha, Z. 1992, *A&A*, 257, 323
- Bottke, W. F., Jr, Morbidelli, A., Jedicke, R., et al. 2002, *Icar*, 156, 399
- Brown, P., Ceplecha, Z., Hawkes, R., et al. 1994, *Natur*, 367, 624
- Carusi, A., & Valsecchi, G. 1987, *PAICz*, 67, 21
- Cavallo, T. 1784, *Philos. Trans. R. Soc. London*, 74, 108
- Ceplecha, Z. 1979, *BAICz*, 30, 349
- Ceplecha, Z. 1987, *BAICz*, 38, 222
- Ceplecha, Z. 1994, *A&A*, 283, 287
- Ceplecha, Z., Brown, P., Hawkes, R., et al. 1996, *EM&P*, 72, 395
- Chant, C. A. 1913, *JRASC*, 7, 145
- Clark, D. L., & Wiegert, P. A. 2011, *M&PS*, 46, 1217
- Denning, W. F. 1916, *JRASC*, 10, 294
- Devillepoix, H. A., Sansom, E. K., Bland, P. A., et al. 2018, *M&PS*, 53, 2212
- Dmitriev, V., Lupovka, V., & Gritsevich, M. 2015, *P&SS*, 117, 223
- Duncan, M., Levison, H., & Dones, L. 2004, in *Comets II*, ed. M. C. Festou, H. U. Keller, & H. A. Weaver (Tucson, AZ: Univ. Arizona Press), 193
- Duncan, M. J., & Levison, H. F. 1997, *Sci*, 276, 1670
- Everhart, E. 1985, in *IAU Coll. 83, Dynamics of Comets: Their Origin and Evolution*, ed. A. Carusi & G. B. Valsecchi (Dordrecht: Reidel), 185
- Fernández, J. A. 1980, *MNRAS*, 192, 481
- Fernández, J. A., Gallardo, T., & Brunini, A. 2002, *Icar*, 159, 358
- Fernández, J. A., & Sosa, A. 2015, *P&SS*, 118, 14
- Fernández, Y. R., Jewitt, D. C., & Sheppard, S. S. 2001, *ApJL*, 553, L197
- Fernández, Y. R., Jewitt, D. C., & Sheppard, S. S. 2005, *AJ*, 130, 308
- Granvik, M., Morbidelli, A., Jedicke, R., et al. 2018, *Icar*, 312, 181
- Howie, R. M., Paxman, J., Bland, P. A., et al. 2017a, *ExA*, 43, 237
- Howie, R. M., Paxman, J., Bland, P. A., et al. 2017b, *M&PS*, 52, 1669
- Hsieh, H. H., & Jewitt, D. 2006, *Sci*, 312, 561
- Jacchia, L. G. 1974, *S&T*, 48, 4
- Jansen-Sturgeon, T., Sansom, E. K., & Bland, P. A. 2019a, *M&PS*, 54, 2149
- Jansen-Sturgeon, T., Sansom, E. K., Devillepoix, H. A. R., et al. 2019b, arXiv:1911.00816
- Jenniskens, P., Fries, M. D., Yin, Q.-Z., et al. 2012, *Sci*, 338, 1583
- Jewitt, D. 2012, *AJ*, 143, 66
- Kelley, M. S., & Wooden, D. H. 2009, *P&SS*, 57, 1133
- Kim, Y., Ishiguro, M., & Usui, F. 2014, *ApJ*, 789, 151
- Kozak, P. M., & Watanabe, J. 2017, *MNRAS*, 467, 793
- Levison, H. F., & Duncan, M. J. 1994, *Icar*, 108, 18
- Levison, H. F., & Duncan, M. J. 1997, *Icar*, 127, 13
- Levison, H. F., Terrell, D., Wiegert, P. A., Dones, L., & Duncan, M. J. 2006, *Icar*, 182, 161
- Madiedo, J. M., Espartero, F., Castro-Tirado, A. J., Pastor, S., & de los Reyes, J. A. 2016, *MNRAS*, 460, 917
- Meech, K., Hainaut, O., & Marsden, B. 2004, *Icar*, 170, 463
- Meech, K. J., Yang, B., Kleyna, J., et al. 2016, *SciA*, 2, e1600038
- Morbidelli, A., Bottke, W., Froeschlé, C., Michel, P., et al. 2002, in *Asteroids III*, ed. W. F. Bottke, Jr et al. (Tucson, AZ: Univ. Arizona Press), 409
- Moreno, A., Madiedo, J., Zamorano, J., et al. 2016, *LPSC*, 47, 1088
- Oberst, J., Heinlein, D., Gritsevich, M., et al. 2014, *EPSC*, 9, EPSC2014-745
- Olson, D. W., Olson, M. S., Doescher, R. L., & Pope, A. G. 2010, *S&T*, 120, 28
- Picone, J. M., Hedin, A. E., Drob, D. P., & Aikin, A. C. 2002, *JGRA*, 107, A12
- Popova, O., Borovicka, J., Hartmann, W. K., et al. 2011, *M&PS*, 46, 1525
- Rawcliffe, R., Bartky, C., Li, F., Gordon, E., & Carta, D. 1974, *Natur*, 247, 449
- Rein, H., & Liu, S. F. 2012, *A&A*, 537, A128
- Rein, H., & Spiegel, D. S. 2015, *MNRAS*, 446, 1424
- Revelle, D. O., Whitaker, R. W., & Armstrong, W. T. 1997, *Proc. SPIE*, 3116, 156
- Robitaille, T. P., Tollerud, E. J., Greenfield, P., et al. 2013, *A&A*, 558, A33
- Sansom, E. K., Bland, P., Paxman, J., & Towner, M. 2015, *M&PS*, 50, 1423
- Sansom, E. K., Jansen-Sturgeon, T., Rutten, M. G., et al. 2019, *Icar*, 321, 388
- Shober, P., Jansen-Sturgeon, T., Sansom, E., et al. 2019, *AJ*, 158, 183
- Spurný, P., Borovicka, J., Ceplecha, Z., & Shrubny, L. 2008, *LPICo*, 1405, 8217
- Steel, D., & Asher, D. 1996, *MNRAS*, 281, 937
- Tsiganis, K., Gomes, R., Morbidelli, A., & Levison, H. 2005, *Natur*, 435, 459
- Walsh, K. J., Morbidelli, A., Raymond, S. N., O'Brien, D. P., & Mandell, A. M. 2011, *Natur*, 475, 206

Paper 3 - Using atmospheric impact data to model meteoroid close encounters

**Monthly Notices of the Royal Astronomical Society (2020),
Volume 498, Issue 4, p. 5240-5250.**

*Patrick M. Shober, Trent Jansen-Sturgeon, Phil A. Bland,
Hadrien A.R. Devillepoix, Eleanor K. Sansom, Martin C. Towner,
Martin Cupák, Robert M. Howie, Benjamin A.D. Hartig*

REPRINTED WITH PERMISSION: *As part of the copyright agreement with Oxford University Press, the authors have retained the right, after publication, to use all or part of the article and abstract, in the preparation of derivative works, extension of the article into a book length work, in a thesis/dissertation, or in another works collection, provided that a full acknowledgement is made to the original publication in the journal.*

STATEMENT OF AUTHORSHIP

TITLE OF PAPER: Using atmospheric impact data to model meteoroid close encounters

PUBLICATION STATUS: Published in Monthly Notices of the Royal Astronomical Society (August 27, 2020).

AUTHOR CONTRIBUTIONS

By signing the Statement of Authorship, each author certifies that their stated contribution to the publication is accurate and that permission is granted for the publication to be included in the candidate's thesis.

Name of Principal Author: Patrick M. Shober

Contribution to the Paper: Led data analysis. Conducted the trajectory and orbital analysis. Wrote the manuscript.

Overall Percentage: 93 %

Signature:

Date:

Name of Co-Author: Trent Jansen-Sturgeon

Contribution to the Paper: Assisted with triangulation of the fireball.

Overall Percentage: 2 %

Signature:

Date:

Name of Co-Author: Phil A. Bland

Contribution to the Paper: Assisted with writing manuscript.

Overall Percentage: 1 %

Signature:

Date:

Name of Co-Author: Hadrien A.R. Devillepoix

Contribution to the Paper: Assisted with data analysis and collection.

Overall Percentage: 1 %

8cmDate:

Name of Co-Author: Eleanor K. Sansom

Contribution to the Paper: Assisted with triangulation of the fireball and initial mass determination.

Overall Percentage: 1 %

Signature:

Date:

Name of Co-Author: Martin Towner

Contribution to the Paper: Data collection and helped review manuscript.

Overall Percentage: 0.5 %

Signature:

Date:

Name of Co-Author: Martin Cupák

Contribution to the Paper: Data collection and helped review manuscript.

Overall Percentage: 0.5 %

Signature:

Date:

Name of Co-Author: Robert M. Howie

Contribution to the Paper: Data collection and built equipment.

Overall Percentage: 0.5 %

Signature:

Date:

Name of Co-Author: Benjamin A.D. Hartig

Contribution to the Paper: Data collection and built equipment.

Overall Percentage: 0.5 %

Signature:

Date:



Using atmospheric impact data to model meteoroid close encounters

P. M. Shober ,  T. Jansen-Sturgeon, P. A. Bland, H. A. R. Devillepoix , E. K. Sansom, M. C. Towner, M. Cupák, R. M. Howie and B. A. D. Hartig

Space Science & Technology Centre, School of Earth and Planetary Sciences, Curtin University, GPO Box U1987, Perth, Western Australia 6845, Australia

Accepted 2020 August 17. Received 2020 August 11; in original form 2020 June 7

ABSTRACT

Based on telescopic observations of Jupiter-family comets (JFCs), there is predicted to be a paucity of objects at sub-kilometre sizes. However, several bright fireballs and some meteorites have been tenuously linked to the JFC population, showing metre-scale objects do exist in this region. In 2017, the Desert Fireball Network (DFN) observed a grazing fireball that redirected a meteoroid from an Apollo-type orbit to a JFC-like orbit. Using orbital data collected by the DFN, in this study, we have generated an artificial data set of close terrestrial encounters that come within 1.5 lunar distances (LD) of the Earth in the size-range of 0.01–100 kg. This range of objects is typically too small for telescopic surveys to detect, so using atmospheric impact flux data from fireball observations is currently one of the only ways to characterize these close encounters. Based on this model, we predict that within the considered size-range 2.5×10^8 objects (0.1 per cent of the total flux) from asteroidal orbits ($T_J > 3$) are annually sent on to JFC-like orbits ($2 < T_J < 3$), with a steady-state population of about 8×10^{13} objects. Close encounters with the Earth provide another way to transfer material to the JFC region. Additionally, using our model, we found that approximately 1.96×10^7 objects are sent on to Aten-type orbits and $\sim 10^4$ objects are ejected from the Solar system annually via a close encounter with the Earth.

Key words: meteorites, meteors, meteoroids – minor planets, asteroids: general.

1 INTRODUCTION

The diffusion of material out from the main-belt (MB) on to comet-like orbits has been discussed briefly in previous studies (Fernández, Gallardo & Brunini 2002; Fernández et al. 2014; Hsieh & Haghhighipour 2016; Shober et al. 2020). This mixing potentially can send many durable meteoroids from the MB on to comet-like orbits. Without a clear understanding of this process, meteoroids may be misidentified, leading to inaccurate conclusions about the comet population.

The possibility of already having cometary meteorites in the world's collections has been a topic of discussion for decades (Campins & Swindle 1998; Gounelle et al. 2008). Jupiter Family Comets (JFCs) are the most likely source region to supply cometary meteorites to the Earth, as the contribution from the nearly isotropic comet (NIC) population is negligible in comparison. However, whether JFCs are capable of producing genetically cometary material on Earth is dependent on the physical lifetimes of JFCs, the dynamic efficiency of JFCs evolving on to Earth-intersecting orbits, and the ability of the meteoroids to eventually survive the atmospheric passage intact as meteorites.

1.1 Jupiter family comets

Dynamical studies have shown that the scattered disc (SD) and the Kuiper Belt are the two primary sources for modern JFCs

(Duncan & Levison 1997; Levison & Duncan 1997). The SD is the most dominant, as the Kuiper Belt is slower at producing JFCs. The SD is cold, likely very primitive and volatile-rich, with larger eccentricities than the classical Kuiper Belt (Gomes et al. 2008). Other sources from within the MB have also been proposed to partially supply material to the JFCs (Fernández et al. 2002; Kim, Ishiguro & Usui 2014; Fernández & Sosa 2015; Hsieh et al. 2020). This can occur as a result of outward diffusion from the MB via mean-motion resonances (MMR), primarily the 2:1 MMR (3.27 au). Other outer-MB resonances such as the 9:4 and 11:5 MMRs have been suggested to be able to produce a modest amount of objects on JFC-like orbits (Fernández et al. 2014; Fernández & Sosa 2015; Hsieh et al. 2020). Studies have additionally found that terrestrial planets (particularly Earth and Venus) may play an important role by perturbing MB objects on to JFC-like orbits (Fernández et al. 2002; Hsieh et al. 2020).

Two primary factors are responsible for the observed JFC size distribution: the size distribution for the source regions of the JFCs and the physical evolution that bodies on JFC orbits underwent. Several studies have attempted to characterize the JFC cumulative size-frequency distribution (CSD; Meech, Hainaut & Marsden 2004; Fernández et al. 2013). The CSDs determined in these studies, based on telescopic observations, predict a break in the slope for sub-kilometre bodies. This break is due to the obvious sampling bias against telescopically observing these objects. However, Meech et al. (2004) argued that despite this sampling bias, there should still be more discovered sub-kilometre JFC objects according to their model. The most likely explanation for this paucity of sub-kilometre objects is the short physical lifetimes associated with these objects. While

* E-mail: patrick.shober@postgrad.curtin.edu.au

the average dynamical lifetime for JFCs is typically 10^5 yr, there is ample evidence that the physical lifetimes are $\sim 10^3$ yr for JFCs in the inner Solar system (Kresák 1981; Kresák & Kresáková 1990; Levison & Duncan 1997; Fernández et al. 1999; Hughes 2003; Di Sisto, Fernández & Brunini 2009; Sosa, Fernández & Pais 2012).

1.2 Meteors and fireballs

On the other end of the spectrum, ground-based meteor and fireball observation networks are able to characterize the smallest subset of objects on JFC-like orbits. There are several meteor showers observed to originate from JFCs (e.g. Draconids and Andromedids). These showers tend to have larger meteoroids than long-period comets (LPCs; $\sim 100 \mu\text{m}$) and lower impact speeds ($11\text{--}35 \text{ km s}^{-1}$; Jenniskens & Jenniskens 2006). In the study of the zodiacal cloud by Nesvorný et al. (2010), they concluded that particles from JFCs should represent 85 per cent of the total terrestrial mass influx. This result provides an explanation for the abundance of micrometeorites with primitive carbonaceous compositions found in Antarctica. Though, as the meteoroid sizes increase to centimetre and metre scales, the story becomes uncertain.

Despite the predicted paucity of sub-kilometre objects based on CSDs of the JFC population, there have been many bright fireballs observed to originate from JFC-like orbits. These meteoroids can be centimetres to metres in scale. However, the delivery mechanism and composition of these objects is still unclear. For example, Madiedo et al. (2014) reported observing a bright fireball originating from a JFC orbit with mass of 40 ± 5 kg. The meteoroid penetrated as deep as 68 km altitude and had a maximum luminosity of -13 ± 0.5 absolute magnitude. However, the object could not be associated with any known JFCs. If the object was genetically JFC material ($T_J = 2.3 \pm 0.2$), given its low perihelion distance, the meteoroid is predicted to have an extremely short physical lifetime. The physical lifetimes for kilometre-size JFCs is typically on the order of 10^3 yr; however, metre-sized fragments are estimated to only persist for a few revolutions (≤ 10 yr) (Beech & Nikolova 2001). Therefore, either it did not originate from the Jupiter family comet population or there is a mechanism capable of extending the physical lifetimes of JFC material in this size-range. Brown et al. (2016) also analysed 59 fireballs caused by meteoroids ≥ 1 m in diameter, and found 10–15 per cent have a possibly cometary origin, but only about half of these were observed to be weaker than average based on ablation behaviour. Additionally, in Flynn et al. (2018), they compared the connection between T_J and PE criterion for 600 fireball observations showing that fireballs with JFC-like T_J values display a similar spectrum of PE values to those of meteoroids from asteroidal orbits ($T_J > 3$). The catastrophic break-up or splitting of the parent body is currently the most favoured explanation to produce large fragments from a comet, as no other mechanism is capable of producing debris in this size range (Jenniskens 2004; Jenniskens & Lyttinen 2005).

1.3 Meteorite falls

There have been a handful of meteorite falls associated with JFC-like orbits. Nearly all of these have likely origins in the MB, given they all have $T_J \sim 3$. Granvik & Brown (2018) re-calculated the source region probabilities for 25 meteorite falls and found only one meteorite, Ejby, to have its most likely source be the JFCs. Curiously, Ejby and Košice, the two meteorites with the highest likelihoods of originating from the JFC source region, are both H-chondrites. Meanwhile, two CM-chondrites (Maribo and Sutter's Mill) both have non-negligible

chances of coming from the JFC population, but are most likely sourced from the MB via the 3:1 resonance.

1.4 Addressing the problem

Telescopic observations of JFCs display a paucity at sub-kilometre scales. When observing dust-sized objects, primitive CM-chondritic material is abundant and associated with JFCs (Nesvorný et al. 2010). Nevertheless, fireball networks report metre-scale objects on JFC orbits impacting the Earth. If asteroidal material from the MB is regularly transferred to the JFC population, given the extremely short physical lifetimes expected for cometary meteoroids, the fireballs from non-shower JFC-like orbits may be highly contaminated by asteroidal material.

Objects that are > 100 m in diameter regularly come close to the Earth. The Center for Near Earth Object Studies maintains a database¹ of these terrestrial close encounters managed by Paul Chodas. These bodies are much easier to identify telescopically. There are many more smaller objects that are not seen by telescopes that pass very close to the Earth. This smaller-size subset encompasses the size range of objects that typically generate meteorites. In a previous study, Shober et al. (2020) described a grazing fireball event that transferred a meteoroid from an Apollo-type orbit to a JFC-like orbit. Since there are many objects like this that go unnoticed by telescope surveys, there is likely a non-negligible amount of small objects that are quickly inserted into dynamically distinct orbits. Additionally, objects tend to evolve along the lines of equal perihelion or aphelion. Therefore, the probability of re-observing these gravitationally scattered objects may be worth consideration. Close encounters with the Earth could provide an additional way to transfer material from the MB to JFC-like orbits (Fernández & Sosa 2015; Hsieh et al. 2020).

Objectives for this study:

- (i) Simulate the close encounter population with the Earth based on the DFN data set.
- (ii) Identify how the orbits have changed as a result of the close encounters with the Earth.
- (iii) Characterize the sub-population of objects redirected on to JFC-like orbits ($2 < T_J < 3$) from asteroid-like orbits ($T_J > 3$).
- (iv) Estimate the impact frequency of objects redirected from asteroid-like ($T_J > 3$) to JFC-like orbits ($2 < T_J < 3$); i.e. determine whether this population impacts the Earth frequently enough to be observed by fireball networks.

2 METHODS

2.1 Desert Fireball Network data

The DFN is part of the Global Fireball Observatory (GFO), a multi-institutional collaboration of partner fireball networks around the Earth. The DFN, the largest single fireball network in the world, covers about one-third of Australian skies every night using automated high-resolution digital fireball observatories (Bland et al. 2012; Howie et al. 2017a). The DFN collects massive amounts of all-sky imagery that is automatically processed, producing a highly accurate orbital data set of fireballs (Sansom et al. 2015; Howie et al. 2017b; Jansen-Sturgeon, Sansom & Bland 2019; Towner et al. 2020; Sansom et al. 2019a, b).

¹<https://cneos.jpl.nasa.gov/ca/>

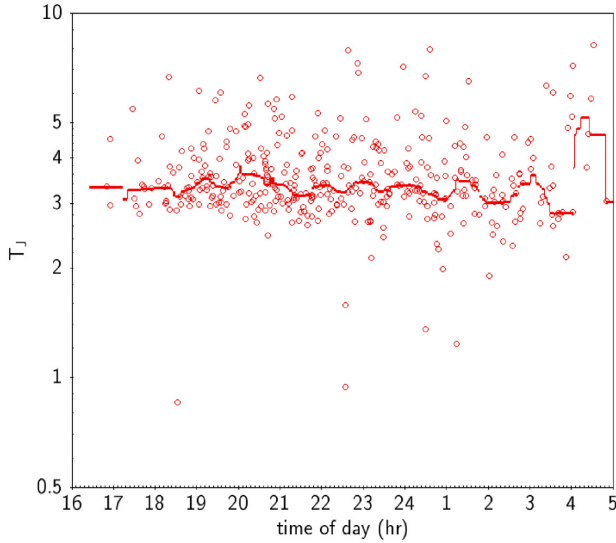
5242 *P. M. Shober et al.*

Figure 1. Tisserand's parameters (T_J) of the DFN events used in this study along with the time of day in which each fireball was observed. The red line represents the median T_J value.

2.2 Addressing observational biases

In this study, we will be producing an artificial data set of close encounters with the Earth of centimetre to metre-sized objects using data collected by the DFN. The flux of objects observed by the DFN for the previous 4 yr was employed to construct a model of the close encounter population. However, in order to adequately estimate this population, we must first address the intrinsic observational biases of the DFN. Biases are listed below along with how each were considered in this study:

(i) Observations are optimised for the size-range specific to meteorite dropping events.

(a) The DFN was designed to observe meteorite-dropping fireball events (fireball limiting magnitude ~ 0.5) (Howie et al. 2017a). Thus, our data set represents a subset of larger objects compared to other meteor networks. However, in this study, we are interested in the close encounters of centimetre to metre-sized objects, so this bias is what makes the DFN data set a good way of understanding these encounters.

(ii) The DFN exclusively observes at night; i.e. the antihelion direction.

(a) We anticipate that this bias will have a negligible effect on the observed population of objects, as it is primarily due to small changes in the orbital geometry at impact (Halliday & Griffin 1982). As seen in Fig. 1, the median Tisserand's parameter does not vary significantly over the course of the night. There is a single aberration, but this is due to low-statistics in this subset only around 4 am.

(iii) The DFN fireball data set contains some meteor showers in addition to sporadic events.

(a) The methodology used explicitly assumes there are meteoroids in similar nearby orbits. This assumption for the sporadic meteoroids may be an oversimplification. However, given we have the largest self-consistent fireball data set in the world

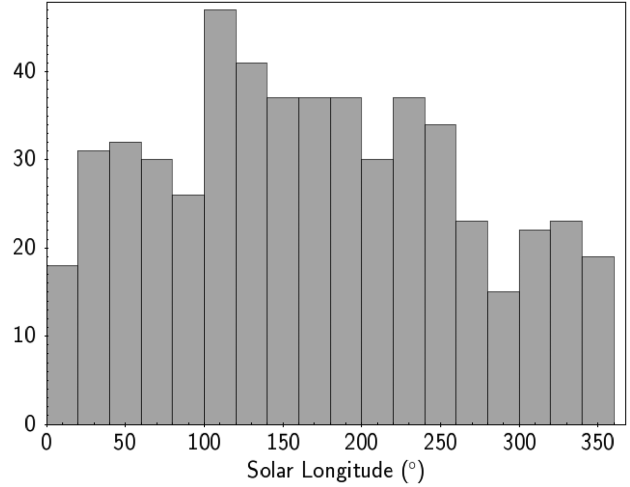


Figure 2. Solar longitude distribution for DFN events used to generate artificial close encounter population. There is a noticeable decrease in events detected during the summer months, as the duration of the night is shortest.

(most of which are sporadic), this should reduce the bias as much as possible.

(iv) The DFN observations vary annually with the seasons.

(a) Seasonal weather variation can also have a significant effect on observations, notably cloud cover. However, given the continental-scale and dry climate of Australia, the DFN's 4 yr of observations are negligibly affected. As seen in Fig. 2, even though the weather is more inclement during the winter months, there is no effect on the observations. There are, in fact, more observations during the winter, due to the longer nights. The amount of observable hours due to changes in daytime length varies about ± 25 per cent for DFN stations annually. This significantly decreases the total number of events observed during the summer; however, ~ 91 per cent of the events used in this study are sporadic. Thus, since the vast majority of the events are not affected by seasonal biases, we have decided to ignore it. This will cause only a minor underestimate in the summer shower contribution to the close encounter flux.

(v) The sensitivity of the DFN cameras varies due to whether the Moon is above or below the horizon.

(a) The DFN cameras have lower sensitivity when the Moon is above the horizon and higher sensitivity when it is below. The minimum-size cut-off in this study (0.01 kg) should eliminate these monthly variations, as we typically observe masses down to ~ 1 – 2 g on moonlit nights. However, there is expected to be a slight underestimate for objects that are tens of grams in mass.

(vi) Observed meteor velocities vary nightly due to changes in the viewing orientation relative to the Earth's motion around the Sun.

(a) This bias should not affect observations on an annual level.

(vii) The lower end of the observed size-range varies with impact speed.

(a) As noted by Vida, Brown & Campbell-Brown (2018), the minimum size object observed by meteor networks decreases as the velocity increases. Nevertheless, this observational bias can be mitigated by setting a minimum size limit when building

the artificial data set in this study (0.01 kg). This mass limit was chosen, as it is the limiting mass observed by the DFN. Events in the data set with nominal masses less than this are likely inaccurate.

(viii) Due to gravitational focusing, the Earth is hit by a higher proportion of slower objects.

(a) When objects approach the Earth at slower relative velocities, they tend to be more gravitationally focused towards the Earth, slightly increasing the ratio of slow impactors observed. Neglecting to account for gravitational focusing would lead to a slight overestimate of the proportion of slow close encounters. In this study, we used the formulation for the enhancement factor by Öpik (1951) to account for the gravitational focusing. The enhancement factor is thus defined as

$$H_F = \frac{A_G}{A_{NG}} = \left(1 + \frac{V_{\text{esc}}^2}{V_i^2}\right), \quad (1)$$

where A_G is the effective cross-sectional area of the Earth due to gravitational focusing, and A_{NG} is the physical cross-section of the Earth. This ratio can be estimated using the escape velocity at the surface of the Earth (V_{esc}) and the initial velocity of the meteoroid before the encounter (V_i). This enhancement factor was used to normalize the artificial close encounter flux generated, producing better relative abundances of certain kinds of encounters (i.e. not overestimating the number of slow approachers).

2.3 Creating the close encounter data set

The DFN is designed to observe and triangulate fireballs over Australia. Using the data collected over the last 4 yr, assuming that the flux is reasonably representative of the global flux, we can extrapolate outwards and try to characterize the close encounter flux for this size range. The events used to generate our model were limited to those with a predicted pre-atmospheric mass ranging from 0.01 to 100 kg. This size range was chosen to limit bias at small sizes, and it is the most well-measured range within the DFN data set. This results in a set of 581 fireball events with which to initiate our model. Of these events, 50 (~9 per cent) are associated with established and non-established showers.

For each event, the predicted state of the meteoroid at the beginning of the luminous phase was integrated back until it was at least three lunar distances (LD) away from the Earth. This procedure was chosen in order to primarily limit the close encounters to a minimum orbital intersection distance (MOID) of within about 1.5 LD, as the orbits will be decreasingly affected with larger MOID values. For the orbital integrations, we used the IAS15 integrator described in Rein & Spiegel (2015) including perturbations from all the planets in the Solar system as well as the Moon. At this point, a cloud of 4000 particles were generated uniformly by varying the position relative to the actual prediction of the meteoroid by ± 1.0 LD in each Cartesian direction in the heliocentric frame, without varying the velocity. A Hill radius for the Earth is ~ 3.89 LD; however, we decided to integrate slightly less to save on computation time. We justified this decision by finding that, for all DFN events, the Tisserand's parameter is typically > 99 per cent similar to its pre-encounter value after reaching two LD away from the Earth.

These particles were then integrated forwards in time until they were at least three LD away from the Earth again. Any particles which came within 200 km of the Earth's surface were removed from the simulation, effectively removing impacts and grazing events. In total,

2.3 million particles were integrated to estimate the close encounter flux. This flux was then normalized using the estimated enhancement factor for each event.

In this model, we explicitly assume that each particle in the simulation represents a group of meteoroids. This is done to make the simulation feasible, as there are expected to be hundreds of billions of close encounters within this size-range annually. The size of the base data set used (581 fireballs) is very small compared to the number of objects having close encounters with the Earth; however, the general trends observed by the model are likely representative.

In order to estimate the close encounter flux of the Earth, we derived the following equation to calculate the cumulative flux distribution:

$$\text{Flux}(r) = \left(\frac{r^3}{r_{\oplus}^3}\right) \times N_{H_F} \times \iota_T, \quad (2)$$

$$\text{where } N_{H_F} = \left[1 + (H_F - 1) \left(\frac{r_{\oplus}^3}{r^3}\right)\right]. \quad (3)$$

N_{H_F} is the scaling factor included to account for the effect of gravitational enhancement at smaller geocentric distances, r is the distance from the Earth's centre, r_{\oplus} is the radius of the Earth, H_F is the enhancement factor, and ι_T is the total terrestrial flux estimated for the top of the atmosphere by Bland & Artemieva (2006). As $r \rightarrow r_{\oplus}$ the scaling factor $N_{H_F} \rightarrow H_F$, whereas as $r \rightarrow \infty$ then $N_{H_F} \rightarrow 1.0$ (i.e. no enhancement when encounters are more distant).

We then calculated the cumulative flux for each particle's MOID and took the difference between each cumulative flux value to determine the number of objects represented by each particle. The mass and mass errors were determined using the pre-atmospheric masses and errors calculated by the DFN in combination with the terrestrial mass flux estimate for the given size range (0.01–100 kg) (Bland & Artemieva 2006; Sansom et al. 2015).

3 RESULTS AND DISCUSSION

3.1 Orbital changes

Using global flux estimates from Bland & Artemieva (2006) along with DFN data to extrapolate, we were able to characterize the $\sim 10^{11}$ predicted close encounters that occur annually within 1.5 LD ranging from 0.01 to 100 kg. A vast majority of the objects that encounter the Earth do not have appreciable changes to their orbits. As seen in Fig. 3, the change in orbital elements are centred on zero with greater magnitude alterations occurring at smaller MOID values ($1/r^2$ relationship). Every object gains or loses energy, but usually a negligible amount. For example, for all objects coming within 1.5 LD, the median changes found in the semimajor axis, eccentricity, and inclination were 0.019 au, 0.0022, and 0.11° , respectively. However, for encounters within 0.1 LD, the median changes were 0.27 au, 0.033, and 1.6° , respectively.

The two factors controlling this process are the MOID of the encounter and the pre-encounter velocity of the meteoroid, as seen in Fig. 4. This change in the orbital parameters, as shown in Fig. 5, diffuses the objects along the lines of equal perihelion or aphelion. As the black 'clouds' of particles generated in the model encounter the Earth, they diffuse outward (grey) where they could be inserted into a resonance or the path of another planet (Fig. 5b). If these alterations are significant, the meteoroid's T_J value could change enough to dynamically re-classify the orbit (Fig. 6). This crossover is especially prevalent within the size-range we investigate, since many of the objects seen impacting the atmosphere by the DFN have

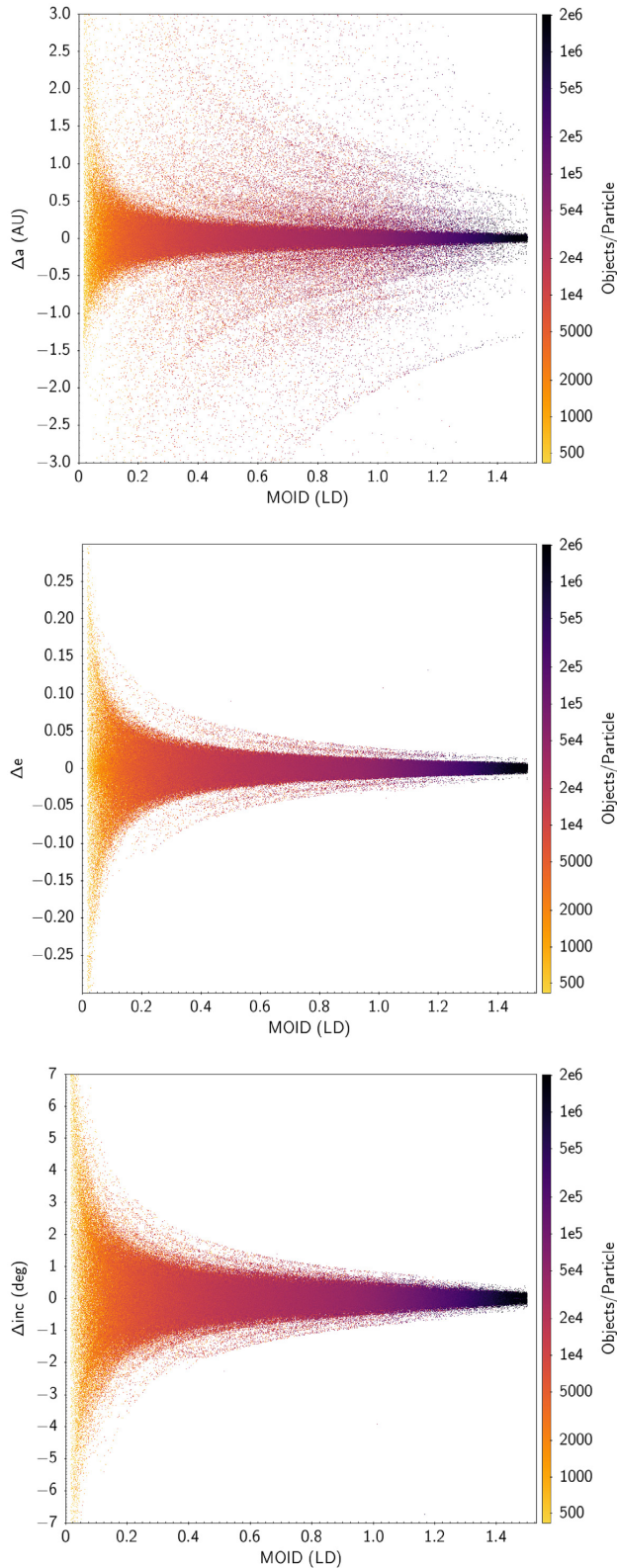
5244 *P. M. Shober et al.*

Figure 3. Change in semimajor axis (a), eccentricity (e), and inclination (inc) for every particle in our simulation as a function of the minimum orbital intersection distance (MOID) in Lunar Distances (LD). The colour bar indicates the number of objects each particle represents annually.

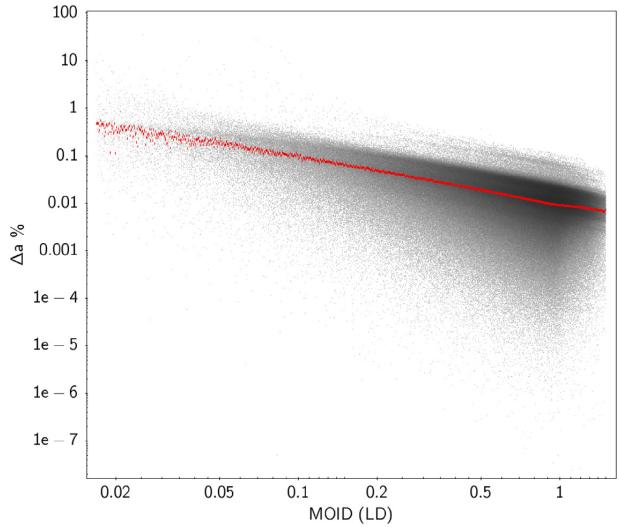


Figure 4. Percentage change in the particles' semimajor axis (a) varying according to the minimum orbital intersection distance (MOID). The red points indicate the median change. The largest change in orbital energy is logically experienced by objects with the closest encounters.

T_J values around ~ 3 , which is approximately the boundary typically used to separate asteroids and JFCs.

Within this study, we were particularly interested in assessing the sub-population of Earth-scattered objects that are redirected from asteroid-like orbits ($T_J > 3$) to JFC-like orbits ($2 \geq T_J \leq 3$). Fig. 6 shows there are quite a significant fraction of close encounters that undergo this transformation in region A. In total, we calculate the net annual object flux for this population is about 2.5×10^8 objects per year. This number also takes into account objects coming from JFC-like orbits on to asteroidal ones (region B in Fig. 6). This flux is net positive on to JFC-like orbits because the most likely objects to have a close encounter with the Earth are objects with orbits most similar to the orbit of the Earth. As shown in Carusi & Dotto (1996), since orbits of near-Earth asteroids are more stable than JFCs and have orbits more like the Earth's, they are likely to encounter the Earth more regularly.

For a more useful interpretation of the same data shown in Fig. 6, please refer to the Appendix where there are three tables describing the mass and object flux.

3.2 Cumulative size-frequency distributions

From our model, we were able to estimate the cumulative size-frequency distribution (CSD) for the terrestrial close encounter population along with its sub-populations of interest. Annually, we have found that within 1.5, 0.5, and 0.1 LD the average largest encounter predicted, respectively, are >100 , ~ 50 , and 10–20 m in diameter. A more thorough analysis concerning the entire DFN's CSD will be addressed in a separate study (Sansom et al. in preparation). For the remainder of this study, we have focused on understanding the redirected smaller sub-population modelled.

Similar to Bland & Artemieva (2006), when characterizing the resulting CSDs from the close encounter model, the range was split into appropriate branches. These branches each have distinct slopes, and these are indicative of some underlying change in the production or physical evolution of objects within that size range. As seen in Fig. 7, we have split the CSD for objects going from asteroidal to

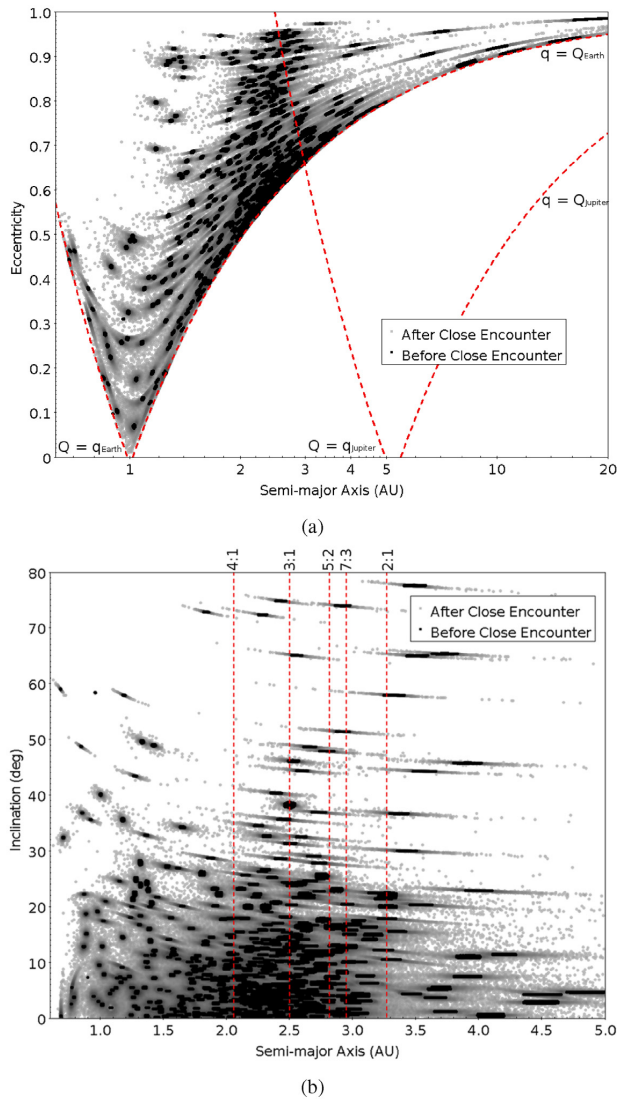


Figure 5. (a) and (b) show the semimajor axis versus eccentricity and inclination, respectively, for all the test particles in the model (2.3 million particles) before and after having a close encounter with the Earth. The grouping of black particles tend to get dispersed along lines of equal aphelion/perihelion after having a close encounter (grey particles). There is typically minimal change in the inclination, however, as $a \sim 1$ the changes in inclination becomes more significant.

JFC orbits into two branches. These branches, labelled A and B, have slopes of -1.21 ± 0.01 and -7.22 ± 1.30 , respectively. This trend, a shallower slope and then a sudden increase in slope at ~ 3 kg, is very similar to the top of the atmosphere flux found in Bland & Artemieva (2006) within the given size range. However, the estimated slopes for the asteroidal to JFC-like flux are different than those in Bland & Artemieva (2006), indicating some size dependence. The slope for branch A (< 0.1 m in diameter) is slightly shallower for the scattered asteroidal to JFC population, -0.410 ± 0.001 versus -0.480 with $\log(\text{mass})$ as the x -axis, whereas branch B (> 0.1 m in diameter) is exceptionally steep compared to the same size range in Bland & Artemieva (2006), -2.277 ± 0.103 versus -0.926 with $\log(\text{mass})$ as the x -axis. This increase in the discrepancy between branches A and B is indicative that this sub-population (compared to all close

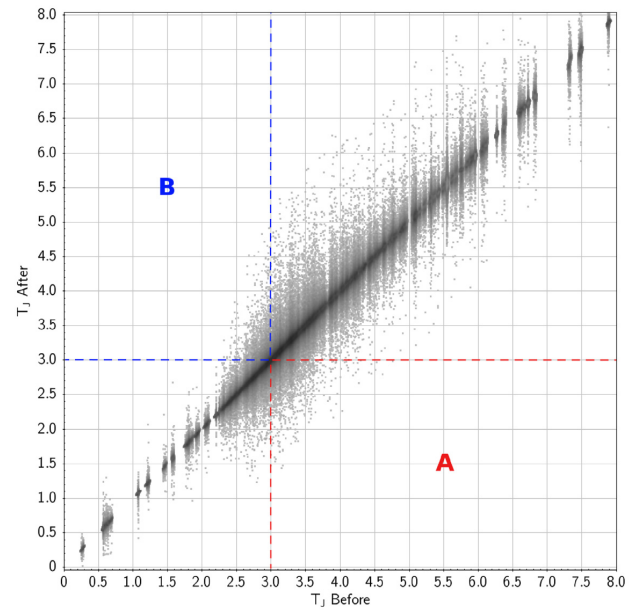


Figure 6. Close encounter simulation particles energy change in terms of Tisserand's parameter (T_J). The T_J value before and after encountering the Earth are the x -axis and y -axis, respectively. Region A contains particles that were transferred from an asteroid-like orbit to a JFC-like one, whereas region B contains particles that underwent the reverse transfer.

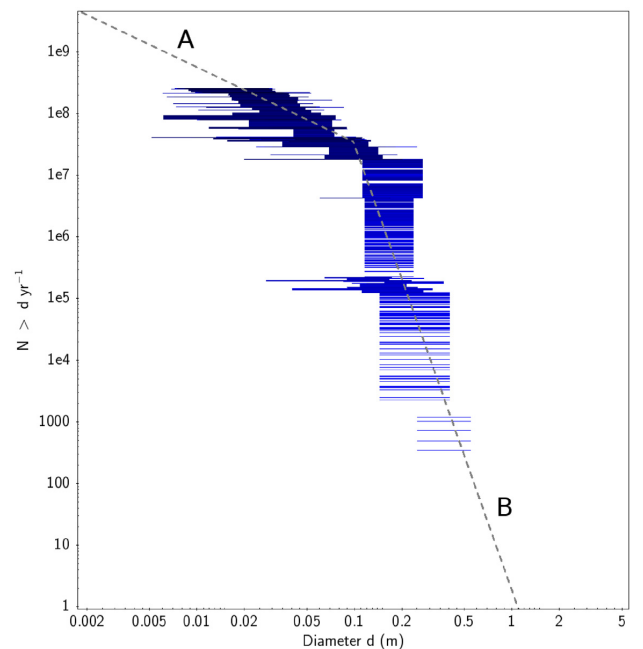


Figure 7. Cumulative size frequency distribution of annual close encounters < 1.5 LD redirected from asteroidal to JFC-like orbits. Horizontal lines are indicative of uncertainty in the diameter. This sub-population only represents ~ 0.1 per cent of the close encounters, given the maximum MOID. The slopes of branches A and B are -1.21 ± 0.01 and -7.22 ± 1.30 , respectively. Compared to the entire close encounter flux, the branch B is steeper and the branch A is shallower. There are proportionally more higher mass meteoroids.

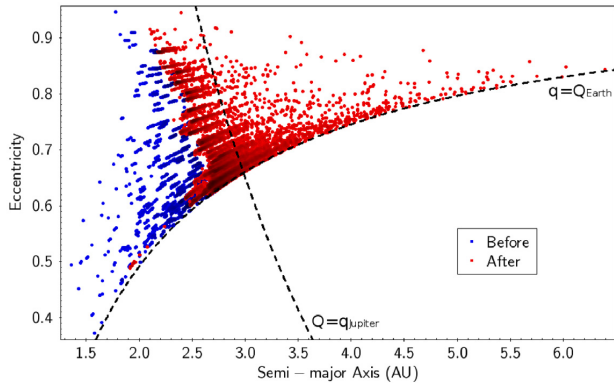
5246 *P. M. Shober et al.*

Figure 8. Semimajor axis versus eccentricity for particles that were transferred from asteroidal like orbits ($T_J > 3$) to JFC-like orbits ($2 < T_J < 3$). As shown by the particles lying on or past the perihelion of Jupiter, close encounters transfer objects on to orbits indistinguishable at times from native JFCs.

encounters) is proportionally more weighted towards larger masses. This size sorting likely is caused by the increase in average mass for meteoroids from asteroidal sources compared to cometary ones. Moreover, these meteoroids are dispersed on a multitude of orbits, some of which may be indistinguishable from actual JFCs (Fig. 8), as they are likely to have multiple close encounters with Jupiter in their lifetime (Tancredi 2014).

In the metre size-range, there is no consistent mechanism to produce meteoroids from comets besides catastrophic break-up (Jenniskens 2004; Jenniskens & Lyttinen 2005). Furthermore, even if there exist centimetre-metre-sized objects from break-up events, the physical lifetimes are predicted to be extremely short (Levison & Duncan 1997; Beech & Nikolova 2001; Boehnhardt 2004), whereas this group of pre-dominantly genetically ‘asteroidal’ material now on JFC-like orbits could survive much longer than any cometary meteoroids. Assuming the physical lifetime of these objects is much longer than the dynamic lifetime, these scattered meteoroids should exist on JFC-like orbits for about 10^5 – 10^6 yr based on previous dynamical models (Nugent et al. 2012; Vokrouhlický et al. 2015; Granvik et al. 2018). This would result in a steady-state population of scattered asteroidal meteoroids on JFC-like orbits of about 10^{13} – 10^{14} objects annually with perihelia near the Earth. Considering the uncertainty of the CSD slope of this population, if extrapolated, the most massive steady-state object is predicted to be 10^0 – 10^2 m in diameter based on our model.

Multiple studies have also found that there exists high-albedo ($p_v > 0.1$) asteroids on JFC-like orbits in near-Earth space (perihelion distance, $q < 1.3$ au) with diameters < 3 km (Kim et al. 2014; Licandro et al. 2016). These authors argued that these objects could have migrated into this region via non-gravitational effects (such as the Yarkovsky effect) due to their smaller size, higher reflectance, and smaller perihelion distance. These objects can also be transferred to JFC-like orbits directly via MMRs in the outer MB (like the 2:1 and 9:4 MMRs) (Fernández et al. 2002, 2014; Fernández & Sosa 2015; Hsieh et al. 2020). While most outer-MB objects are dark with low albedos ($p_v < 0.1$), some higher albedo objects have also been observed to exist (Masiero et al. 2014). It is uncertain whether this population is large/efficient enough to account for the high-albedo objects on JFC-like orbits near the Earth. The high-albedo objects analysed in Kim et al. (2014) also only seem to be present for bodies with $q < 1.3$ au – an observation not due to detection bias as

high-albedo objects with larger perihelia would have been detected. Alternatively, these high-albedo near-Earth objects in JFC-like orbits could result from close encounters with the Earth. In Hsieh et al. (2020), they found that close encounters with the terrestrial planets or non-gravitational forces were capable of generating a reasonable number of objects from the Themis family to go on to JFC-like orbits. This would not be entirely unprecedented; encounters with the Earth at the same scales have also been linked with refreshing the surfaces of some asteroids (Binzel et al. 2010). In Bland & Artemieva (2006), they found that the slope of the CSD for impactors of the upper atmosphere decreased significantly as the objects grew to 1.7×10^{10} kg (~ 88 m assuming a 3500 kg m^{-3} spheroid). Therefore, if this trend persists within the population scattered on to JFC orbits, it is possible that this population could provide an explanation for the asteroids observed by Kim et al. (2014). However, given the uncertainty in slope B (Fig. 7), this cannot be shown in this study.

3.3 Impact frequency

Finally, we wanted to estimate the impact frequency of the population of objects scattered from asteroid to JFC-like orbits. The impact frequency is crucial as it determines whether this meteoroid population is observable by fireball networks. Thus, it could partially explain the durable JFC fireballs that have been observed.

We employed the methodology described in Greenberg (1982) and Bottke et al. (1994), where the impact and close encounter probabilities were determined for Earth and Jupiter geometrically assuming uniform precession of nodes and apsides. For a concise explanation of this methodology, please refer to appendix A found in Le Feuvre & Wieczorek (2008). To estimate the impact frequency, we calculated the three Hill’s radii close encounter frequency with Jupiter for all the test particles and the impact frequency with the Earth. Particles with close encounters with Jupiter were assumed to be removed from the Earth-crossing population during the encounter. In contrast, particles that avoid having close encounters with Jupiter were assumed to have Earth-crossing lifetimes of 10^5 – 10^6 according to published outer-MB NEO dynamical lifetimes (Nugent et al. 2012; Vokrouhlický et al. 2015; Granvik et al. 2018).

Upon investigation, we found that only ~ 30 per cent of the asteroidal to JFC scattered population were capable of having close encounters with Jupiter. Thus, despite all the particles being within the range $2 < T_J < 3$, most of the objects likely still evolve on very predictable asteroid-like orbits like described in Tancredi (2014). The 30 per cent that do experience close encounters do so every 10–200 yr, with the median time being 50 yr. These objects will likely evolve in a way indistinguishable from a comet from the scattered disc, similar to the grazing meteoroid observed by the DFN in 2017 (Shober et al. 2020). However, given the shorter residence times, this unstable portion of the scattered population makes up minor fraction of the steady-state population.

Given the annual flux on to cometary orbits along with the estimated residence times from encounter and impact frequencies, we find that there are approximately 10^3 – 10^4 impacts annually originating from this population. At a minimum, this means that the DFN should observe (taking into account daylight hours, weather, and station malfunctions) 1–10 events per year. Based on our model, this minimum value indicates that this population is likely observed regularly by meteor and fireball networks. The test particles with the highest probabilities of impacting the Earth after being scattered were on orbits with low-inclinations ($< 5^\circ$), lower eccentricity, and perihelia near 1 au. Therefore, we predict that fireball networks

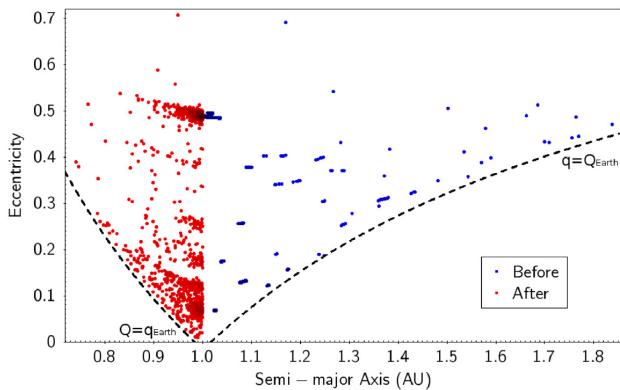


Figure 9. Semimajor axis versus eccentricity for particles in model that were transferred on to Aten-type orbits as a result of the close encounter with the Earth. Meteoroids with similar orbits to the Earth ($a \sim 1 - 2$ au) are the most likely to undergo this process.

should observe meteoroids that were previously scattered; however, all will be dynamically very consistent with asteroidal debris.

3.4 Additional results

In addition to flux on to JFC-like orbits, we also found a net-positive annual flux on to Aten-type orbits (Fig. 9). For similar reasons to the net flux on to JFC orbits, the model suggests it is slightly more favourable to go from an Apollo-type to an Aten-type orbit than the reverse. In total, we estimate about 10^7 objects are annually transferred to Aten-type orbits via a close encounter, but due to the low number statistics this value is tenuous. Unfortunately, we were unable to further explore this sub-population in detail as the uncertainties for the CSD were considerable. However, it is possible that some of these may eventually evolve on to Atira-type orbits via some combination of planetary perturbations or close encounters. The objects could also evolve periodically between classes if in a Kozai resonance (Greenstreet, Ngo & Gladman 2012).

Small debris in the Solar system always eventually impacts a planet, impacts the Sun, or is ejected from the Solar system. Most of the material that is ejected is typically through close encounters with Jupiter, but our model also predicts a modest ejection rate of 10^4 objects annually resulting from close encounters with the Earth. This value is very tentative due to the small sample size of such objects in the model input data.

4 FUTURE WORK

We have also studied the dynamical and physical characteristics of >0.01 kg meteoroids from the DFN data set with JFC-like orbits (Shober et al. in preparation). In this other study, we compared the results from the close encounter model to DFN observations, and tested our hypothesis that asteroidal material is dominant for orbits with $2 < T_J < 3$. In the future, we would also like to check our model by using steady-state NEO models (such as Granvik et al. 2018) to characterize the close encounter flux at the Earth.

5 CONCLUSIONS

In this study, we produced a model of close terrestrial encounters within the 0.01–100 kg size range by using DFN data along with global flux studies (Bland & Artemieva 2006). Close encounters

Meteoroid close encounters 5247

within the model were limited to <1.5 LD, as farther encounters are less likely to have significant orbital alterations. The primary results include the following:

(i) There are approximately 1.6×10^{11} objects 0.01–100 kg that have encounters within 1.5 LD of the Earth every year based on extrapolating top of the atmosphere flux rates found in Bland & Artemieva (2006).

(ii) 2.5×10^8 objects annually are estimated to be transferred from asteroidal orbits ($T_J > 3$) to JFC-like orbits ($2 < T_J < 3$) (0.1 per cent of total flux).

(a) Given a dynamic lifetime of 10^5 – 10^6 yr (Nugent et al. 2012; Vokrouhlický et al. 2015; Granvik et al. 2018), then there exists a steady-state population of 10^{13} – 10^{14} objects.

(b) Using the methodologies described by Greenberg (1982) and Bottke et al. (1994), we calculated the three Hill’s radii encounter for Jupiter and impact frequencies for the Earth for all particles transferred from $T_J > 3$ to $2 < T_J < 3$. Using these values along with the predicted population size from the model, we found that ~ 30 per cent of objects regularly encounter Jupiter and likely evolve chaotically on short time-scales. The remaining ~ 70 per cent of objects avoid close encounters and persist on more stable orbits, evolving in a characteristically asteroidal manner.

(c) Approximately, 10^3 – 10^4 impacts occur from this population annually. Thus, the DFN should observe 1–10 fireballs every year with $2 < T_J < 3$ transferred from the MB.

(d) Extrapolating our CSD slope to larger sizes, the largest steady-state object is 10^0 – 10^2 m in diameter given the slope uncertainty (-7.22 ± 1.30).

(iii) The model predicts that $\sim 10^7$ objects are annually transferred on to Aten-type orbits, where some may evolve to Atira-type orbits.

(iv) $\sim 10^4$ meteoroids are predicted to be directly ejected from the Solar system annually via a close encounter with the Earth, but this value is questionable due to small number statistics.

Observations of fireballs can be used to understand the sources of meteorites, and connect them to the observed asteroidal (or possibly cometary) parent body that they originate from. The speculation over whether or not cometary meteorites exist or can exist has been discussed for decades. However, in this study we have found there should be many genetically asteroidal meteoroids on JFC-like orbits due to close encounters with the Earth that likely impact the Earth regularly. Compounded with material diffusing out from the MB (Fernández & Sosa 2015; Hsieh et al. 2020), it may be expected that meteorites from JFC-like orbits ($2 < T_J < 3$) would be quite ordinary.

ACKNOWLEDGEMENTS

We are thankful for the reviewer M. Campbell-Brown and her valuable comments on the original manuscript that improved the paper. The authors would also like to thank P. Brown for his assistance and advice during the early stages of this study. This work was funded by the Australian Research Council as part of the Australian Discovery Project scheme (DP170102529). SSTC authors acknowledge institutional support from Curtin University. This work was supported by resources provided by the Pawsey Supercomputing Centre with funding from the Australian Government and the Government of Western Australia. This research made use of TOPCAT for visualization and figures (Taylor 2005). This research also made use of ASTROPY, a community-developed core PYTHON package for Astronomy (Robitaille et al. 2013). Simulations in this

5248 *P. M. Shober et al.*

paper made use of the REBOUND code which is freely available at <http://github.com/hannorein/rebound> (Rein & Liu 2012).

DATA AVAILABILITY

The data underlying this article were accessed from Desert Fireball Network (<https://dfn.gfo.rocks/>). The derived data generated in this research will be shared on reasonable request to the corresponding author.

REFERENCES

- Beech M., Nikolova S., 2001, *Planet. Space Sci.*, 49, 23
 Binzel R. P. et al., 2010, *Nature*, 463, 331
 Bland P. A., Artemieva N. A., 2006, *Meteorit. Planet. Sci.*, 41, 607
 Bland P. et al., 2012, *Aust. J. Earth Sci.*, 59, 177
 Boehnhardt H., 2004, *Comets II*, 745, 301
 Bottke W. F., Nolan M. C., Greenberg R., Kolvoord R. A., 1994, *ICARUS-NEW YORK*, 107, 255
 Brown P., Wiegert P., Clark D., Tagliaferri E., 2016, *Icarus*, 266, 96
 Campins H., Swindle T. D., 1998, *Meteorit. Planet. Sci.*, 33, 1201
 Carusi A., Dotto E., 1996, *Icarus*, 124, 392
 Di Sisto R. P., Fernández J. A., Brunini A., 2009, *Icarus*, 203, 140
 Duncan M. J., Levison H. F., 1997, *Science*, 276, 1670
 Fernández J. A., Sosa A., 2015, *Planet. Space Sci.*, 118, 14
 Fernández J., Tancredi G., Rickman H., Licandro J., 1999, *Astron. Astrophys.*, 352, 327
 Fernández J. A., Gallardo T., Brunini A., 2002, *Icarus*, 159, 358
 Fernández Y. et al., 2013, *Icarus*, 226, 1138
 Fernández J. A., Sosa A., Gallardo T., Gutiérrez J. N., 2014, *Icarus*, 238, 1
 Flynn G. J., Consolmagno G. J., Brown P., Macke R. J., 2018, *Geochem.*, 78, 269
 Gomes R. S., Fernández J. A., Gallardo T., Brunini A., 2008, *The Solar System Beyond Neptune*, University of Arizona Press, Tucson. p. 259
 Gounelle M., Morbidelli A., Bland P. A., Spurny P., Young E. D., Sephton M., 2008, *The Solar System Beyond Neptune*, University of Arizona Press, Tucson. p. 525
 Granvik M., Brown P., 2018, *Icarus*, 311, 271
 Granvik M. et al., 2018, *Icarus*, 312, 181
 Greenberg R., 1982, *ApJ*, 87, 184
 Greenstreet S., Ngo H., Gladman B., 2012, *Icarus*, 217, 355
 Halliday I., Griffin A. A., 1982, *Meteoritics*, 17, 31
 Howie R. M., Paxman J., Bland P. A., Towner M. C., Cupak M., Sansom E. K., Devillepoix H. A., 2017a, *Exp. Astron.*, 43, 237
 Howie R. M., Paxman J., Bland P. A., Towner M. C., Sansom E. K., Devillepoix H. A., 2017b, *Meteorit. Planet. Sci.*, 52, 1669
 Hsieh H. H., Haghighipour N., 2016, *Icarus*, 277, 19
 Hsieh H. H., Novaković B., Walsh K. J., Schörghofer N., 2020, *ApJ*, 159, 179
 Hughes D. W., 2003, *MNRAS*, 346, 584
 Jansen-Sturgeon T., Sansom E. K., Bland P. A., 2019, *Meteorit. Planet. Sci.*, 54, 2149
 Jenniskens P., 2004, *ApJ*, 127, 3018
 Jenniskens P., Jenniskens P. M. M., 2006, *Meteor Showers and their Parent Comets*. Cambridge Univ. Press, Cambridge
 Jenniskens P., Lyytinen E., 2005, *ApJ*, 130, 1286
 Kim Y., Ishiguro M., Usui F., 2014, *ApJ*, 789, 151
 Kresák L., 1981, *Bull. Astron. Inst. Czech.*, 32, 321
 Kresák L., Kresáková M., 1990, *Icarus*, 86, 82
 Levison H. F., Duncan M. J., 1997, *Icarus*, 127, 13
 Le Feuvre M., Wieczorek M. A., 2008, *Icarus*, 197, 291
 Licandro J., Alf-Lagoa V., Tancredi G., Fernández Y., 2016, *A&A*, 585, A9
 Madiedo J. M. et al., 2014, *A&A*, 569, A104
 Masiero J. R., Grav T., Mainzer A., Nugent C., Bauer J., Stevenson R., Sonnett S., 2014, *ApJ*, 791, 121
 Meech K., Hainaut O., Marsden B., 2004, *Icarus*, 170, 463
 Nesvorný D., Jenniskens P., Levison H. F., Bottke W. F., Vokrouhlický D., Gounelle M., 2010, *ApJ*, 713, 816
 Nugent C., Margot J., Chesley S., Vokrouhlický D., 2012, *ApJ*, 144, 60
 Öpik E. J., 1951, *Proc. R. Ir. Acad. A*, 54, 165
 Rein H., Liu S. F., 2012, *A&A*, 537, A128
 Rein H., Spiegel D. S., 2015, *MNRAS*, 446, 1424
 Robitaille T. P. et al., 2013, *A&A*, 558, A33
 Sansom E. K., Bland P., Paxman J., Towner M., 2015, *Meteorit. Planet. Sci.*, 50, 1423
 Sansom E. K. et al., 2019a, *Icarus*, 321, 388
 Sansom E. K. et al., 2019b, *ApJ*, 885, 115
 Shober P. M. et al., 2020, *ApJ*, 159, 191
 Sosa A., Fernández J., Pais P., 2012, *A&A*, 548, A64
 Tancredi G., 2014, *Icarus*, 234, 66
 Taylor M. B., 2005, *Astronomical Data Analysis Software and Systems XIV*, Astron. Soc. Pac., San Francisco. p. 29
 Towner M. C. et al., 2020, *Publ. Astron. Soc. Aust.*, 37, e008
 Vida D., Brown P. G., Campbell-Brown M., 2018, *MNRAS*, 479, 4307
 Vokrouhlický D., Bottke W., Chesley S., Scheeres D., Statler T., 2015, *Asteroids IV*, University of Arizona Press, Tucson, p. 509

APPENDIX: CLOSE ENCOUNTER FLUX TABLES

See the Tables A1–A3.

5250 *P. M. Shober et al.***Table A3.** Close encounter mass error flux table (kg). Columns represent the T_J value before, and the rows represent the T_J value after the close encounter.

	$T_J \leq -1$	$-1 - (-0.5)$	$-0.5 - 0$	$0 - 0.5$	$0.5 - 1.0$	$1.0 - 1.5$	$1.5 - 2.0$	$2.0 - 2.5$	$2.5 - 3.0$	$3.0 - 3.5$	$3.5 - 4.0$	$4.0 - 4.5$	$4.5 - 5.0$	$5.0 - 5.5$	$5.5 - 6.0$	$6.0 - 6.5$	$T_J \geq 6.5$
$T_J \leq -1$	7.57e6	-	-	-	-	-	-	-	-	-	-	-	-	-	-	-	-
$-1 - (-0.5)$	1.14e2	2.84e7	1.93e4	-	-	-	-	-	-	-	-	-	-	-	-	-	-
$-0.5 - 0$	-	1.10e6	4.37e8	1.44e2	-	-	-	-	-	-	-	-	-	-	-	-	-
$0 - 0.5$	-	-	2.38e1	1.40e7	3.69e4	2.77e1	-	-	-	-	-	-	-	-	-	-	-
$0.5 - 1.0$	-	-	-	6.88e7	1.20e4	1.89e2	-	-	-	-	-	-	-	-	-	-	-
$1.0 - 1.5$	-	-	-	1.29e2	5.68e8	1.59e5	3.46e2	3.93e3	1.35e0	-	-	-	-	-	-	-	-
$1.5 - 2.0$	-	-	-	-	1.50e7	1.98e8	1.62e5	1.51e4	1.46e3	-	-	-	-	-	-	-	-
$2.0 - 2.5$	-	-	-	-	5.89e2	2.61e4	3.52e9	7.03e6	3.26e4	9.60e2	1.29e1	-	-	-	-	-	-
$2.5 - 3.0$	-	-	-	-	-	5.21e3	1.54e7	1.10e10	5.50e8	1.95e4	1.67e3	2.19e1	-	-	-	-	-
$3.0 - 3.5$	-	-	-	-	-	-	8.82e3	1.28e8	1.88e10	1.04e8	6.87e4	9.41e1	2.63e2	-	-	-	-
$3.5 - 4.0$	-	-	-	-	-	-	1.61e1	1.05e5	3.95e7	3.89e9	1.71e8	2.43e5	4.51e2	2.06e0	-	-	-
$4.0 - 4.5$	-	-	-	-	-	-	-	3.33e3	4.24e4	6.09e7	3.04e9	1.22e7	1.81e5	5.94e2	6.87e2	-	-
$4.5 - 5.0$	-	-	-	-	-	-	-	6.46e2	7.72e3	9.29e4	1.07e7	6.95e9	1.81e8	1.23e5	7.96e1	-	-
$5.0 - 5.5$	-	-	-	-	-	-	-	-	7.41e2	5.77e3	4.36e4	1.85e7	1.42e9	6.91e6	6.64e4	-	-
$5.5 - 6.0$	-	-	-	-	-	-	-	-	-	4.74e2	3.42e3	1.63e5	2.99e6	1.12e9	2.22e7	-	-
$6.0 - 6.5$	-	-	-	-	-	-	-	-	-	3.97e1	1.44e3	1.50e4	8.06e4	7.13e7	1.68e9	-	-
$T_J \geq 6.5$	-	-	-	-	-	-	-	-	-	-	-	-	-	-	-	-	9.24e8

This paper has been typeset from a \LaTeX file prepared by the author.

Paper 4 - The main asteroid belt: the primary source of debris on comet-like orbits

The Planetary Science Journal (2021), Volume 2, Issue 3, p. 98.

Patrick M. Shober, Eleanor K. Sansom, Phil A. Bland, Hadrien A.R. Devillepoix, Martin C. Towner, Martin Cupák, Robert M. Howie, Benjamin A.D. Hartig, Seamus L. Anderson

REPRINTED WITH PERMISSION OF IOP PUBLISHING: *The authors have the right to use all or part of the Article in future works and derivative works of their own of any type, and to make copies of all or part of the Article for the authors' use for educational or research purposes.*

STATEMENT OF AUTHORSHIP

TITLE OF PAPER: The main asteroid belt: the primary source of debris on comet-like orbits

PUBLICATION STATUS: Published in The Planetary Science Journal (May 13, 2021).

AUTHOR CONTRIBUTIONS

By signing the Statement of Authorship, each author certifies that their stated contribution to the publication is accurate and that permission is granted for the publication to be included in the candidate's thesis.

Name of Principal Author: Patrick M. Shober

Contribution to the Paper: Led data analysis. Conducted the trajectory and orbital analysis. Wrote the manuscript.

Overall Percentage: 95 %

Signature:

Date:

Name of Co-Author: Eleanor K. Sansom

Contribution to the Paper: Assisted with triangulation of the fireball and initial mass determination.

Overall Percentage: 1 %

Signature:

Date:

Name of Co-Author: Phil A. Bland

Contribution to the Paper: Assisted with writing manuscript.

Overall Percentage: 1 %

Signature:

Date:

Name of Co-Author: Hadrien A.R. Devillepoix

Contribution to the Paper: Assisted with data analysis and collection.

Overall Percentage: 1 %

Signature:

Date:

Name of Co-Author: Martin Towner

Contribution to the Paper: Data collection and helped review manuscript.

Overall Percentage: 0.5 %

Signature:

Date:

Name of Co-Author: Martin Cupák

Contribution to the Paper: Data collection and helped review manuscript.

Overall Percentage: 0.5 %

Signature:

Date:

Name of Co-Author: Robert M. Howie

Contribution to the Paper: Data collection and built equipment.

Overall Percentage: 0.5 %

Signature:

Date:

Name of Co-Author: Benjamin A.D. Hartig

Contribution to the Paper: Data collection and built equipment.

Overall Percentage: 0.5 %

Signature:

Date:

Name of Co-Author: Seamus L. Anderson

Contribution to the Paper: Assisted with maintenance of the Desert Fireball Network and data collection.

Overall Percentage: 0.5 %

Signature:

Date:



The Main Asteroid Belt: The Primary Source of Debris on Comet-like Orbits

P. M. Shober , E. K. Sansom , P. A. Bland, H. A. R. Devillepoix , M. C. Towner , M. Cupák, R. M. Howie, B. A. D. Hartig, and S. L. Anderson

Space Science & Technology Centre, School of Earth and Planetary Sciences, Curtin University, GPO Box U1987, Perth, WA 6845, Australia
patrick.shober@postgrad.curtin.edu.au

Received 2020 December 12; revised 2021 January 17; accepted 2021 January 19; published 2021 May 13

Abstract

Jupiter-family comets (JFCs) contribute a significant amount of debris to near-Earth space. However, telescopic observations of these objects seem to suggest that they have short physical lifetimes. If this is true, the material generated will also be short-lived, but fireball observation networks still detect material on cometary orbits. This study examines centimeter-to-meter-scale sporadic meteoroids detected by the Desert Fireball Network from 2014 to 2020 originating from JFC-like orbits. Analyzing each event's dynamic history and physical characteristics, we confidently determined whether they originated from the main asteroid belt or the trans-Neptunian region. Our results indicate that $<4\%$ of sporadic meteoroids on JFC-like orbits are genetically cometary. This observation is statistically significant and shows that cometary material is too friable to survive in near-Earth space. Even when considering shower contributions, meteoroids on JFC-like orbits are primarily from the main belt. Thus, the presence of genuine cometary meteorites in terrestrial collections is highly unlikely.

Unified Astronomy Thesaurus concepts: [Meteoroids \(1040\)](#); [Solar system \(1528\)](#); [Meteorites \(1038\)](#); [Fireballs \(538\)](#); [Meteors \(1041\)](#); [Short period comets \(1452\)](#); [Near-Earth objects \(1092\)](#); [Small Solar System bodies \(1469\)](#); [Meteorite composition \(1037\)](#); [Orbital evolution \(1178\)](#); [Dynamical evolution \(421\)](#); [Orbits \(1184\)](#)

1. Introduction

Jupiter-family comets (JFCs) are short-period comets near the ecliptic plane that are strongly influenced by Jupiter. They originate from the outer solar system in the scattered disk (Duncan & Levison 1997) and are comprised of primitive volatile-rich material. They are conventionally defined by their Tisserand's parameter ($2 < T_J < 3$), which is an approximately conserved value in the circular restricted three-body problem (object—Jupiter—Sun). This is a better way to classify the orbits of small planetary bodies compared to the traditionally used orbital periods (Levison & Duncan 1994). The physical properties of JFCs have been explored in numerous studies based on meteor/fireball analysis (Jenniskens 2006; Borovička et al. 2007; Madiedo et al. 2014), telescopic observations (Fernández et al. 2005, 2013), dynamical modeling (Duncan et al. 2004; Di Sisto et al. 2009; Nesvorný et al. 2010; Tancredi 2014), and space missions (Brownlee et al. 2004; A'Hearn et al. 2005; Sunshine et al. 2006; Fornasier et al. 2015). Each method provides information about different size ranges of objects on JFC-like orbits.

When observing meteors streak across the night sky, we are typically witnessing the size range of the smallest objects in the near-Earth space (dust-sized; $\ll 10^{-3}$ kg). Conversely, telescopic observations are instrumental in characterizing the most massive objects (hundreds of meters to kilometers in diameter). This gap between the meteor and telescopic observations is the primary range for the progenitors of meteorites. Usually spanning centimeters to meters in scale, this size range has been interpreted from fireballs and the meteorites they produce on the ground (Borovička et al. 2015; Granvik & Brown 2018).

Based on telescopic observations and dynamical studies, many researchers believe there is a paucity of JFCs at subkilometer scales (Meech et al. 2004; Fernández & Morbidelli 2006; Nesvorný et al. 2017). This lack of objects at smaller sizes is thought to be related to the inferred brief physical lifetimes (10^3 – 10^4 yr) of JFCs in the inner solar system (Levison & Duncan 1997; Fernández et al. 2002; Di Sisto et al. 2009). Due to their low bulk density and high volatile content, JFCs should fade away relatively quickly when within ~ 3 au.

Nevertheless, despite the predicted subkilometer paucity, fireball observation networks have many accounts of durable centimeter-to-meter-sized meteoroids originating from JFC-like orbits (Brown et al. 2000; Borovička et al. 2013; Spurný et al. 2017; Borovička et al. 2019). By examining meter-sized terrestrial impactors, it was found that about 5%–10% had JFC-like orbits, relatively consistent with the flux estimates based on larger kilometer-scale near-Earth objects (NEOs; Brown et al. 2016). Yet they found that only half of these displayed weaker-than-average structures based on their atmospheric ablation characteristics. Two of the five JFC-like events discussed were calibrated meteorite falls (Maribo and Sutter's Mill) likely to be from the main asteroid belt. Meanwhile, the remaining three events all came from US Government sensor (USG) data; two of these had a semimajor axis of ~ 2.9 au, i.e., well within the bounds of the outer main belt. Also, it has since been demonstrated that the orbital information collected by USG events is generally unreliable (Devillepoix et al. 2019).

Additionally, another study recalculated the orbits for 25 meteorite falls and identified their likely source regions using an advanced NEO model (Granvik & Brown 2018; Granvik et al. 2018). The only meteorite that had a mean JFC probability $\geq 50\%$ was an H5/6 ordinary chondrite, Ejby. Furthermore, the fall with the second-highest JFC source region probability was another H5, Košice. However, both of these falls have relatively significant initial velocity uncertainties,

increasing the uncertainty for the source region analysis. Carbonaceous chondrites Maribo and Sutter's Mill (both CM2) also had probabilities of coming from the JFCs above 20%. Nevertheless, no precisely observed meteorite falls have yet come from an unambiguously cometary orbit.

The Taurid complex has also been discussed as being capable of larger, possibly meteorite-dropping, meteoroids (Brown et al. 2013). These meteoroids can be hundreds of kilograms in size, an order of magnitude higher than other showers. However, other studies have found that while the Taurids can produce very large meteoroids, they are still very weak and unlikely to produce meteorites (Borovička et al. 2017). Given the highly evolved orbit of comet 2P/Encke and the other noncometary possible parent bodies in similar orbits, this subset of observed Taurids also does not likely reflect the vast majority of JFC meteoroids (Asher et al. 1993).

Based on debiased NEO orbital and absolute-magnitude distributions, it is expected that the contribution from the JFC region is a few percent, on average (Bottke et al. 2002; Granvik et al. 2018). The contribution seems to increase at smaller sizes, reaching $\sim 10\%$ of the NEO population below diameters of 100 m (Granvik et al. 2018). However, this estimate assumes that JFCs are more likely to become dormant than disintegrate, as JFC disruptions are less commonly observed compared to long-period comets. If this assumption breaks down at smaller sizes, then the JFC contribution to the NEO meteoroid flux may be negligible.

If the hypothesis that the physical lifetimes of subkilometer comets are very short is accurate, why do fireball networks still observe centimeter–meter debris originating from comet-like orbits? Does the larger cometary debris we observe impacting the Earth originate from comets?

The massive orbital data set collected by the Desert Fireball Network (DFN) was utilized to answer these questions. The DFN is the largest single photographic fireball network in the world, covering over 2.5 million km^2 of Australia. This massive project is part of a worldwide collaboration, the Global Fireball Observatory (GFO; <https://gfo.rockets/>), currently consisting of 18 partner institutions (Devillepoix et al. 2020). The GFO has a semiautomated data processing pipeline that sorts images, detects fireball events, and triangulates these events (Howie et al. 2017; Jansen-Sturgeon et al. 2019; Sansom et al. 2019a, 2019b; Towner et al. 2020).

2. Materials and Methods

2.1. Experimental Design

The data set used for this study was collected by the DFN. Covering over one-third of the Australian outback, the DFN is the largest photographic fireball network globally. The observations made by the DFN are invaluable and provide key insights into the debris impacting the Earth daily.

When parsing through the data set for this study, all events that originated from an orbit with a JFC-like Tisserand's parameter ($2 < T_J < 3$) and had a significant initial mass (≥ 0.01 kg) were gathered. The Tisserand's parameter is an approximately conserved value in the three-body problem and is regularly used to distinguish between different kinds of small planetary bodies (Levison & Duncan 1994). Typically, this three-body problem includes the Sun, Jupiter, and the asteroid or comet; since Jupiter is seen as the primary perturber, the parameter is written as T_J .

2.1.1. Trajectory Analysis and Orbit Determination

The fireball events detected by the DFN have atmospheric trajectories fitted using a modified straight-line least-squares (SLLS) and an extended Kalman smoother for the velocity profile (Sansom et al. 2015). The uncertainties associated with the fitted fireball trajectories are propagated from the residuals of the fit itself, along with the timing and positional uncertainties of the events' observations. The observational uncertainties are handled and incorporated by the Kalman filter. The initial masses and corresponding uncertainties were also determined using a dynamic model in a reverse extended Kalman filter (Sansom et al. 2015). The preatmospheric orbits are then determined numerically including any relevant perturbations by integrating the meteoroid's state until it was outside the Earth's sphere of influence (Jansen-Sturgeon et al. 2019). The orbital uncertainties are then obtained with a Monte Carlo approach by numerically integrating samples randomly drawn from within the initial state uncertainties at the top of the atmosphere.

2.1.2. Addressing Observational Biases

The DFN uses photographic observations of fireballs to help better understand the debris in the inner solar system. However, to obtain meaningful results from this data set, we must first address any observational biases.

The first bias we address is that the DFN is optimized for meteorite-dropping fireball events (~ 0.5 limiting magnitude; Howie et al. 2017). In this study, we limit the meteoroids considered to a minimum initial mass of 10 g. This bias does not affect the results, as both asteroidal and cometary populations are known to produce material within this size range (Boehnhardt 2004; Fernández 2009).

Second, we must ensure that the DFN observations are not biased against observing either asteroidal or cometary debris due to the orbits in which they exist. The primary bias to be concerned with is due to gravitational focusing. Since meteoroids with a lower relative velocity are more gravitationally focused, the terrestrial impact population contains a larger proportion of asteroidal impactors from orbits with smaller semimajor axis values. However, this study is concerned with meteoroids originating from similar orbits; thus, they are all weighted nearly equally. Other observational biases are associated with photographic fireball observations; however, none of these would have any affect on the results of this study. For a more exhaustive list and discussion of DFN observational biases, please reference Shober et al. (2020a).

2.1.3. Data Selection

In a manual check of all of the fireball observations and triangulations, any events with poor data were removed (e.g., the fireball was very far from the cameras, the convergence angles for triangulations were too small, etc.). The orbital uncertainties of the meteoroids must be sufficiently low to obtain meaningful statistics from the Monte Carlo numerical integrations. If the uncertainties are too large, the number of samples required to get statistically reasonable results may be computationally unfeasible. Additionally, meteoroids with T_J values within three standard deviations of $T_J = 3.0$ or 2.0 were excluded to remove ambiguous events.

In this study, only fireballs with no shower associations were considered, i.e., sporadic. Therefore, any events with distinctly

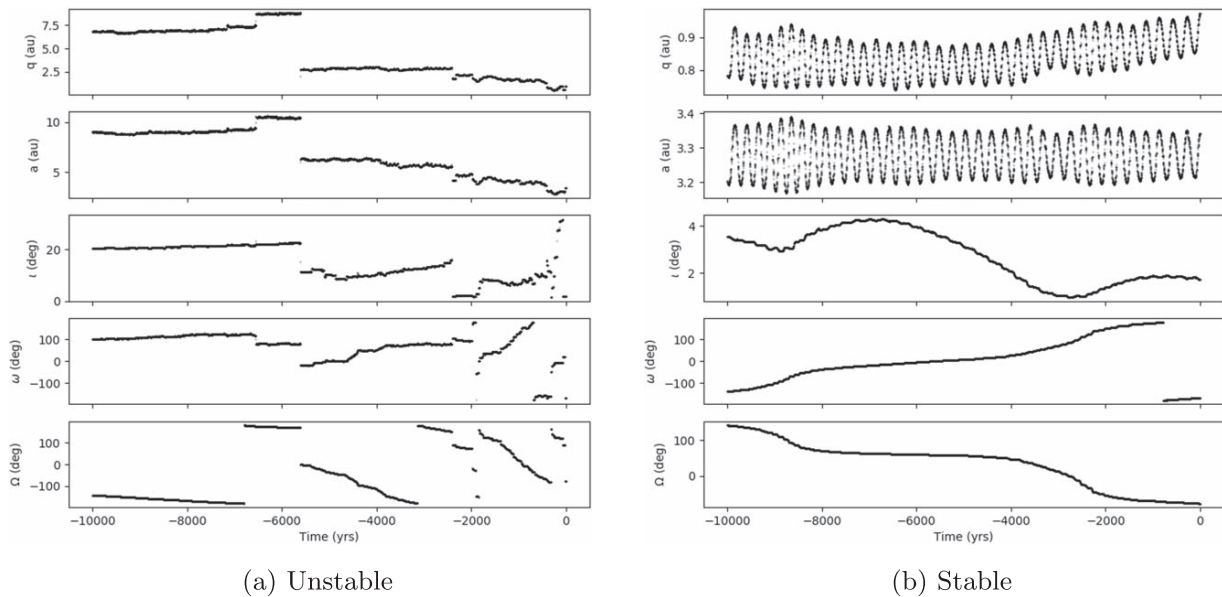


Figure 1. Backward integrations over -10 kyr of two particles generated within the triangulated trajectory uncertainties of event DN200104_01 where q is the perihelion, a is the semimajor axis, i is the inclination, ω is the argument of perihelion, and Ω is the longitude of the ascending node. On the left, we show a particle on a chaotic unstable orbit typical of a comet with numerous Jupiter close encounters. This specific fireball event lasted over 5 s and was recorded by four DFN stations, providing an excellent trajectory fit with very minimal uncertainties. Thus, this demonstrates the difficulty associated with backward propagation of meteoroids coming from orbits on the edge of two source regions (JFC and main belt, in this case).

cometary physical and dynamical characteristics could indicate a process to preserve cometary material in this range for longer periods. Using primarily the D_J similarity criterion, we sorted through associations with a limiting value of $D_J < 0.15$ (Jopek 1993). A more inclusive limiting value was used to eliminate any potential shower events. We verified associations from this subset by comparing orbital elements, shower dates, right ascensions and declinations, initial velocities, nodal directions, and arguments of perihelion, along with other similarity criteria (Southworth & Hawkins 1963; Drummond 1981). The meteor shower data used were taken from all showers listed by the IAU Meteor Data Center,¹ with a higher weight placed on established showers.

The fireball data used within this study, including uncertainties, are available at [10.5281/zenodo.4710556](https://www.tau.ac.il/~shober/zenodo.4710556).

We characterized the physical and dynamical characteristics of the sporadic meteoroids on JFC-like orbits using fireball data from the DFN with the following goals:

1. determining the proportion of genetically cometary material in excess of 10 g on sporadic JFC-like orbits,
2. assessing whether or not the physical lifetimes of JFC meteoroids in the meteorite-dropping size range are shorter than the disassociation lifetimes of cometary streams, and
3. finding out if it is possible to get a meteorite from a JFC-orbit and what it would look like.

2.2. Dynamic Analysis

As shown in previous studies, genuine JFCs originating from the outer solar system tend to move on chaotic orbits over

thousands of years, encountering Jupiter frequently over their lifetime (Tancredi 1995; Levison & Duncan 1997). In this work, we have adopted a similar search strategy to past studies by numerically integrating the fireball trajectories backward 10 kyr and identifying fireballs originating from “stable” and “unstable” orbits (Fernández & Sosa 2015; Fernández et al. 2014; Tancredi 2014). For each event, a Monte Carlo simulation was undertaken where 10 simulations with 100 particles were integrated over -10 kyr. These simulations were conducted using the IAS15 integrator, taking into account all planetary perturbations and close encounters considering all of the planets and the Moon (Rein & Liu 2012; Rein & Spiegel 2015). The particles were initialized within the formal triangulation uncertainties assuming a Gaussian distribution. The particles’ histories were then each assessed and labeled as either “stable” or “unstable” over the previous 10 kyr. Those with frequent unpredictable jumps in their orbital elements were considered unstable (Figure 1(a)), whereas those in resonances and following smooth trajectories with little change in perihelion distance were considered stable (Figure 1(b)). The final instability probabilities and associated uncertainties were then obtained by taking the mean and standard deviation of the sample means.

2.3. Physical Analysis

In order to characterize the physical properties, we determined the PE value for each fireball. The PE criterion was first introduced as a way to discriminate between different meteoroid compositions based on the ability to penetrate the atmosphere (Ceplecha & McCrosky 1976). It has since been used in numerous studies to assess the physical nature of impacting meteoroids (Ceplecha 1994; Brown et al. 2013, 2016; Borovička et al. 2015).

¹ <https://www.ta3.sk/IAUC22DB/MDC2007/>

Table 1

Traditional PE Classifications Based on the Atmospheric Density at Terminal Height (Ceplecha & McCrosky 1976)

Type	PE Range	Material Type
Type I	$PE > -4.60$	Ordinary chondrite-like
Type II	$-5.25 < PE \leq -4.60$	Carbonaceous chondrite
Type IIIa	$-5.70 < PE \leq -5.25$	Short-period cometary
Type IIIb	$PE \leq -5.70$	Weak cometary material

The PE value is given by

$$PE = \log(\rho_E) - 0.42 \log(m_\infty) + 1.49 \log(V_\infty) - 1.29 \log(\cos Z_R), \quad (1)$$

where ρ_E is the density of the atmosphere at the end of the luminous trajectory (and the reason for the acronym ‘‘PE’’), m_∞ is the initial mass of the meteoroid in grams, V_∞ is the initial velocity of the meteoroid in kilometers per second, and Z_R is the local entry angle measured from the zenith.

The PE values are divided into four types: ordinary chondrite-like (type I), carbonaceous (type II), short-period cometary (type IIIa), and weak cometary (type IIIb; Ceplecha et al. 1998). The boundaries for these groups are denoted in Table 1. The PE criterion is an extremely useful metric to evaluate the physical properties of meteoroids; however, the types are not strictly correct. While providing generally accurate results of relative strength, the physical composition of any individual meteoroid is uncertain due to the other factors that affect the durability while transiting the atmosphere (e.g., macro-scale fractures; Popova et al. 2011; Borovička et al. 2020).

We additionally computed the ballistic coefficient (α) and mass-loss parameter (β) based on the fireball observations (Gritsevich & Stulov 2006; Gritsevich 2007; Lyytinen & Gritsevich 2016). Using these parameters, one can quickly identify potential meteorite-dropping events (Sansom et al. 2019a). They can be calculated for any event showing some level of deceleration by using the velocity and height data (https://github.com/desertfireballnetwork/alpha_beta_modules).

In Figure 4, we determined potential meteorite-dropping fireballs using the α - β values. Assuming that a 50 g final mass is the minimum meteorite-dropping mass, the meteorite-dropping lines were calculated with the following equations:

$$\ln \beta = \ln[13.2 - 3 \ln(\alpha \sin \gamma)], \quad \mu = 0, \quad (2)$$

$$\ln \beta = \ln[4.4 - \ln(\alpha \sin \gamma)], \quad \mu = \frac{2}{3}, \quad (3)$$

when assuming $\rho_m = 3500 \text{ kg m}^{-3}$ (meteoroid density) and $c_d A = 1.5$ (product of drag coefficient and initial shape coefficient). Considering that the contribution from the outer main belt may be significant, where many objects have low albedos (DeMeo & Carry 2014; DeMeo et al. 2015; Takir et al. 2015; e.g., C and D types), we also plotted the equivalent lines for a CM-like density (Consolmagno et al. 2008; $\rho_m = 2240 \text{ kg m}^{-3}$) using the following equations:

$$\ln \beta = \ln[14.09 - 3 \ln(\alpha \sin \gamma)], \quad \mu = 0, \quad (4)$$

$$\ln \beta = \ln[4.7 - \ln(\alpha \sin \gamma)], \quad \mu = \frac{2}{3}. \quad (5)$$

Together, the dynamic simulations and analysis of the material properties can better elucidate what types of material

regularly impact the Earth from JFC-like orbits in the considered size range.

2.4. Statistical Analysis

Based on the dynamical and physical analysis, the source populations can be inferred for each meteoroid in this study. However, given the sample size, what does this tell us about the entire population of small JFC-like meteoroids?

In order to answer this question, we utilize a Markov Chain Monte Carlo to sample from the posterior probability distribution. The Bayesian model was created with the Python PyMC3 probabilistic programming package using the No-UTurn Sampler (Salvatier et al. 2016). A beta distribution was used as a prior with the hyperparameters (α) based on a study that examined the dynamical characteristics of 58 near-Earth JFCs ($q < 1.3 \text{ au}$; Fernández & Sosa 2015). This corresponded to the hyperparameters $\alpha = [1.38, 8.62]$ and an observation vector $c = [48, 2]$; the hyperparameters were weighted less, as they were based on kilometer-scale objects. Additionally, as a comparison, an uninformed uniform prior of $\alpha = [1.0, 1.0]$ was included. In total, 15,000 samples from the posterior were taken to estimate the posterior. To be counted as genetically JFC in origin in the model, the meteoroids would need to have a $>50\%$ probability of originating from an unstable orbit and be of PE types II or III. We considered a PE type II as plausibly cometary due to previous arguments that meteorites from JFCs could possibly be represented by primitive carbonaceous chondrites (Gounelle et al. 2008).

3. Results

In this study, we examined fireballs not associated with meteor showers detected by the DFN during 4 yr of observations. All of the fireballs considered were generated by meteoroids that originated from JFC-like orbits ($2 < T_J < 3$). The source region of these meteoroids, the main belt or JFCs, was determined by analyzing the orbital stability and physical durability during atmospheric transit. It takes only $\sim 1000 \text{ yr}$ to become orbitally disassociated from a JFC shower. Therefore, the identification of sporadic JFC material would indicate a minimum physical lifetime equal to the disassociation time (Tancredi 1995). However, a lack of sporadic cometary debris in fireball observations would be clear evidence that the physical lifetimes are less than 1000 yr.

3.1. Orbital Characteristics of Sporadic JFC-like Meteoroids

The JFCs move on chaotic orbits compared to main-belt asteroids, on the order of thousands of years (Tancredi 1995). During their lifetimes, their orbital evolution is controlled by the numerous close encounters they have with Jupiter. Of the 50 sporadic JFC-like fireball events analyzed in this study, nearly all of the meteoroids come from stable orbits over the previous 10 kyr (see <https://doi.org/10.5281/zenodo.4710556>). This is inconsistent with the dynamics diagnostic of JFCs.

Only three events have a high probability of originating from an unstable orbit. However, one of these comes from within 3 au and crosses one of the major mean-motion resonances (MMRs). Events DN150817_01 and DN161028_02 have the highest probability of originating from unstable cometary orbits, with $86.1\% \pm 5.5\%$ and $90.8\% \pm 3.0\%$ of the particles integrated being chaotic, respectively. As seen in Figure 2, event DN150816_04 overlaps the 7:3 MMR when considering

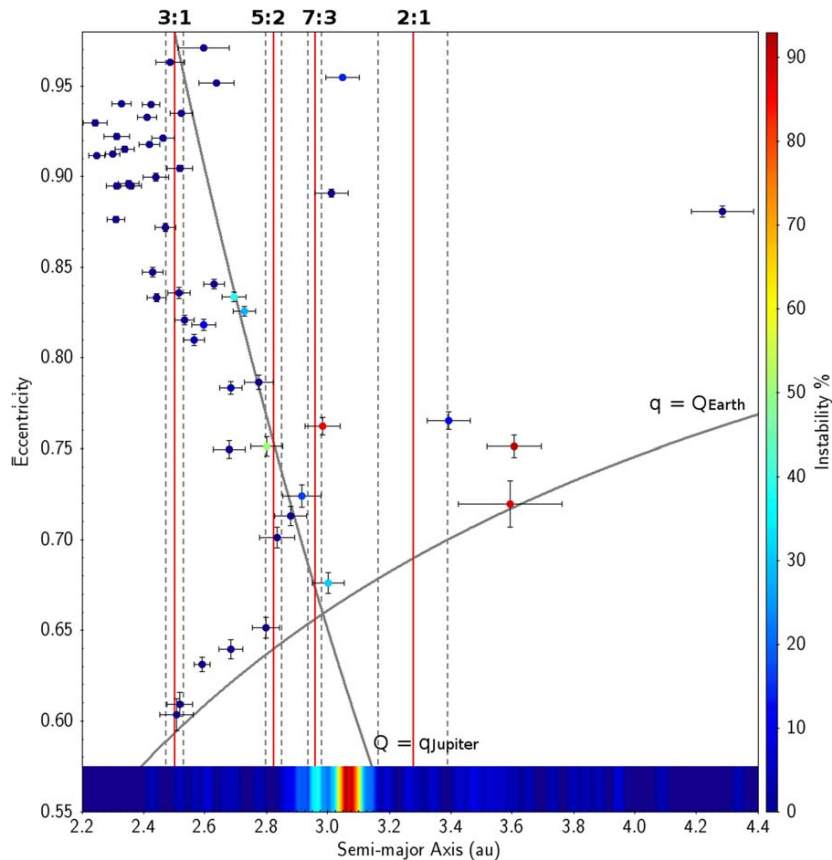


Figure 2. Triangulated semimajor axis vs. eccentricity for 50 nonshower JFC-like fireballs observed by the DFN that have predicted initial masses greater than 10 g. Error bars denote the formal 1σ orbital uncertainties associated with each meteoroid, and coloration is indicative of the orbital stability determined through numerical integrations of -10 kyr. The vertical red lines indicate the major MMRs, with the dashed gray lines marking the maximum libration in semimajor axis (Tancredi 2014). Most of the events originate from stable orbits near the MMRs. The densogram (<http://www.star.bris.ac.uk/mbt/stilts/sun256/layer-densogram.html>) at the bottom of the plot represents the semimajor axis density for all near-Earth ($q < 1.3$ au) JFCs according to the NASA HORIZONS system (<http://ssd.jpl.nasa.gov/horizons.cgi>).

triangulation uncertainties, whereas events DN150817_01 and DN161028_02 both lie outside the normal range of the main belt with a semimajor axis of ~ 3.6 au. Several meteoroids have inconclusive dynamical histories; these include six events where several of the particles integrated evolved chaotically over thousands of years. On the other hand, nearly all of these inconclusive events come from orbits near MMRs, thus indicating that orbital uncertainty is very likely the cause of the inconclusive results. Otherwise, $>80\%$ of the events originate from extremely stable orbits near one of the primary MMRs (Figure 2).

A large majority of the fireballs examined in this study do not fall within the range consistent with observed kilometer-scale JFCs. As seen in Figure 2, a majority of the near-Earth JFCs exist near ~ 3.1 au, where only a handful of events originate. However, only one of the four events in this range comes from an unstable orbit. This is in line with a previous model, where they found that main-belt material can contaminate the JFC population but would primarily be contained to the original bounds of the main belt (Hsieh & Haghighipour 2016). However, four of the 50 events examined fall beyond the 2:1 MMR, and of these, only two have higher probabilities of originating from unstable orbits (Figure 2). Additionally, the inclinations of the fireballs examined tend to be relatively diffuse, but are most concentrated toward low values within the

0° – 25° range. This is more reconcilable with the main-belt inclination distribution than the JFC distribution, which is more highly concentrated around $\sim 12^\circ$ (see <https://doi.org/10.5281/zenodo.4710556>).

3.2. Physical Characteristics of Sporadic JFC-like Meteoroids

The PE criterion characterizes the composition of meteoroids based on their ability to penetrate the atmosphere (Ceplecha & McCrosky 1976). This metric is empirically determined based on the terminal height of the fireball, the entry mass, the velocity at the top of the atmosphere, and the impact angle. The PE criterion has been used for decades to understand the physical properties of meteoroids based on their atmospheric ablation characteristics (Borovička et al. 2015; Brown et al. 2016). The values are traditionally split accordingly (Ceplecha et al. 1998).

The use of the PE criterion can be quite valuable when analyzing many fireballs; however, the types are not strictly exclusive and should not be taken as absolute truth. Other properties beyond physical composition can blur the lines between the types, such as macro-scale cracks (Popova et al. 2011; Borovička et al. 2020). As expected, considering the dynamic analysis, many of the JFC-like fireballs in this study are quite durable and strong (Figure 3). We only see meteoroids of types I or II; i.e., none fall into the standard categories

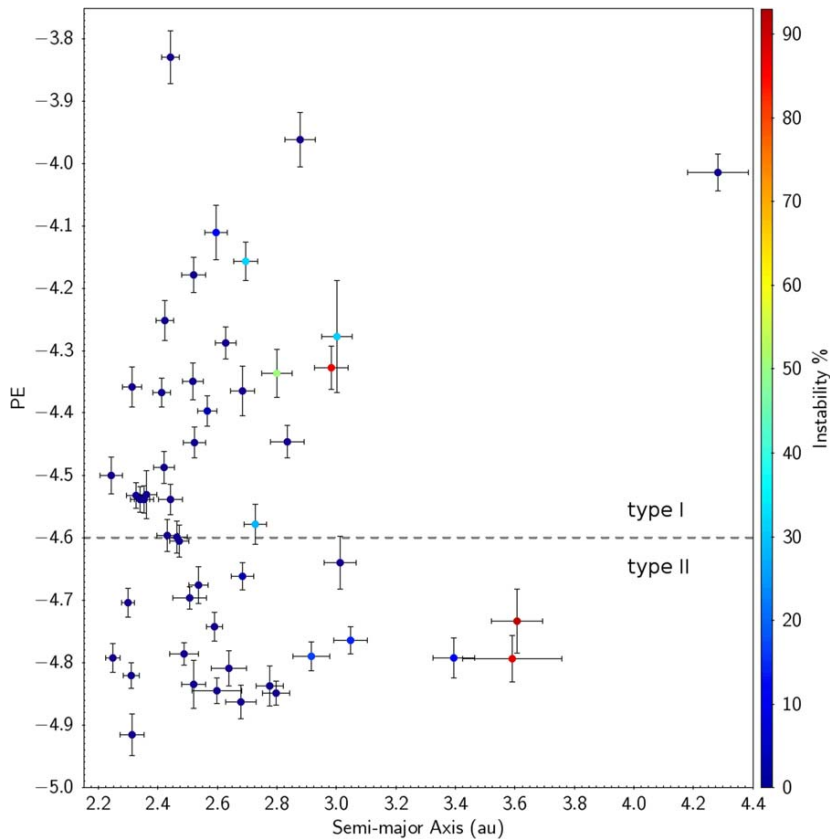


Figure 3. Sporadic JFC-like fireballs observed by the DFN with a minimum initial mass of 10 g. The end heights of meteors can be used to ascertain the physical nature of meteoroids using the PE criterion (Ceplecha & McCrosky 1976). The PE values for the 50 fireballs examined are overwhelmingly stronger than the traditional comet types (types IIIa and IIIb). The error bars associated with each meteoroid’s semimajor axis and PE value are due to triangulation uncertainties.

associated with cometary material. Out of the 50 fireballs, 28 would be classified as type I and 22 as type II. Some short-period showers actually can produce more durable debris with similar strengths (Brown et al. 2013). Therefore, the PE criterion alone is not a sure way to distinguish between different materials for an individual fireball. In general, the PE types can give a sense of how strong the initial meteoroid was, but when combined with the dynamic analysis, the source population of a meteoroid can be more confidently obtained (main belt or JFC).

3.2.1. Meteorite Production from JFC-like Meteoroids

Traditionally, the empirical criteria to predict whether a fireball has produced a meteorite on the ground (a “fall”) are height and velocity below 35 km and 10 km s^{-1} , respectively, at the end of the luminous portion of the atmospheric trajectory (Wetherill & ReVelle 1981). This gives us an easy way to identify possible recoverable falls quickly. A more rigorous way to determine which fireballs result in meteorites has since been demonstrated, where the ballistic coefficient (α) and the mass-loss parameter (β) are fit to the fireball observations (Sansom et al. 2019a).

In Figure 4, we see that several of the JFC-like fireballs examined in this study are quite durable. At least some events are likely to have meteorites on the ground that are $>50 \text{ g}$ (DN150905_01 and DN191020_02). However, these events are likely asteroidal in origin based on their dynamic stability over the previous 10 kyr and their PE classification. No events

with high instabilities over the previous 10 kyr or of type II drop meteorites in this study. Thus, meteorites from JFC-like orbits do occur, but they are all representative of main-belt material.

4. Discussion

Based on a dynamical and physical analysis of sporadic JFC-like ($2 < T_J < 3$) fireballs with initial masses $>10 \text{ g}$, we find a clear abundance of stronger, dynamically stable meteoroids (Figure 3). As seen in Figure 2, most meteoroids evolve in a deterministic way over the previous 10 kyr and have proximity to major MMRs. Dynamic instability is a diagnostic feature of JFCs originating from the outer solar system, as they suffer frequent close encounters with Jupiter (Tancredi 1995, 2014). The predictable evolution of nearly all of the meteoroids in this study is therefore indicative of their likely origin in the main belt. Additionally, events with indeterminate histories, where a nonnegligible subset of particles evolved chaotically, also mostly lie near the primary MMRs, as does one of the three events with $>80\%$ instability (Figure 3). This proximity to MMRs could indicate possible main-belt origins. Moreover, JFCs’ arguments of perihelia tend to concentrate near 0° and 180° (Quinn et al. 1990), and there is no such correlation for the sporadic JFC-like fireballs in this study (see supplementary material). This further supports a dominantly main-belt, asteroidal source.

Based on the calculated PE values, most of the events are also very durable and classified as type I chondritic material. In

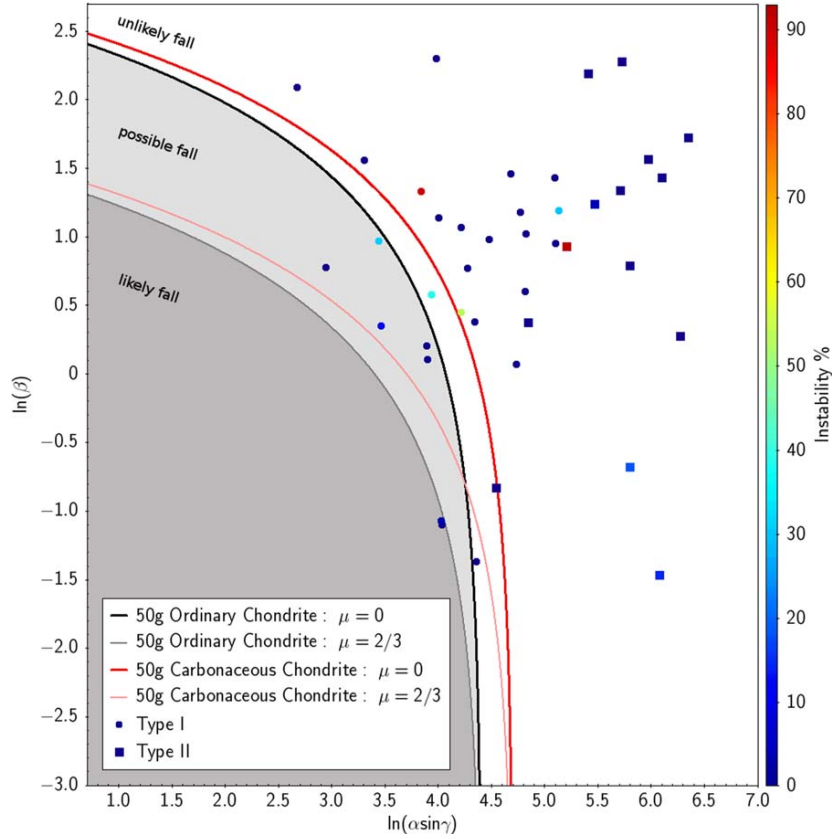


Figure 4. Distribution of nonshower JFC fireballs with enough deceleration to determine α - β values (at least $\sim 20\%$ deceleration). Here γ is the trajectory slope relative to the horizontal. If a macroscopic event is considered to have a final mass of ≥ 50 g, assuming $\rho_m = [2240, 3500] \text{ kg m}^{-3}$ (carbonaceous and ordinary chondrite, respectively) and $c_{dA} = 1.5$, meteorite-dropping events can easily be identified given the range of possible shape change coefficients (μ).

fact, all of the fireballs in this sample are classified as either chondritic or carbonaceous chondritic material (type I or II; Figure 3). No events have PE types traditionally associated with cometary material (type III). However, it has been previously argued that primitive carbonaceous chondrites may have come from cometary sources (Gounelle et al. 2008). Thus, any DFN events that likely evolved chaotically over the previous 10 kyr ($>50\%$) and are of type II were also considered cometary. At most, only two of the meteoroids studied here are likely to originate from a short-period comet (DN150817_01 and DN161028_02). However, this would require centimeter-to-meter cometary debris to be stronger than expected. The subset of weaker type II meteoroids in our data is also generally smaller (<50 g), perhaps debris released by dark carbonaceous asteroids in the outer main belt (DeMeo & Carry 2014; DeMeo et al. 2015; Takir et al. 2015). A novel process has been recently observed to release centimeter-sized particles on carbonaceous asteroid Bennu during the OSIRIS-REx mission (Lauretta et al. 2019).

However, caution should be used with such a criterion to characterize meteoroids; a wide range of meteorite types have been recovered from type II/III events. For example, Almahatta Sitta (2008 TC3), Košice, and Sutter’s Mill had PE values near the II/IIIa boundary, despite all being of different meteorite types on asteroidal orbits (polymict breccia, H5, and CM2, respectively; Borovička et al. 2015; Brown et al. 2016). This is indicative that other physical factors, such as macroscopic cracks or porosity, can significantly affect the

apparent strengths of impactors, and that there is still much unknown about the physical nature of meter-scale NEOs (Borovička et al. 2017, 2020). The PE criterion is useful to characterize the relative strength of meteoroids, but how much the meteorite type influences the strength is debatable.

4.1. Meteoroids Beyond the 2:1 Resonance

Previous studies have shown that a minor component of main-belt material can be transferred to JFC-like orbits and, in some circumstances, even onto dynamically unstable orbits via close encounters with the terrestrial planets (Fernández et al. 2002, 2014; Hsieh & Haghighipour 2016; Shober et al. 2020a, 2020b). Nevertheless, these objects’ semimajor axes are predicted to be primarily constrained to the original range of the main belt (Hsieh & Haghighipour 2016). Here we see that of the four events beyond 3.27 au, two are likely asteroidal in origin based on their PE classifications and stability (Figure 3). The two most probable events to originate from unstable comet-like orbits are DN150817_01 and DN161028_02, with $86.1\% \pm 5.5\%$ and $90.8\% \pm 3.0\%$ probabilities of having chaotic histories based on Monte Carlo simulations along with orbits beyond the 2:1 MMR (each around $a \sim 3.6$ au). The meteoroids from events DN150817_01 and DN161028_02 both fall into type II, nominally carbonaceous and equally as or more durable than much of the main-belt debris (Figure 3). Even if both events are genuinely cometary in origin, they only comprise 4% of the sample.

4.2. Statistical Significance

Let us consider the null hypothesis to be that the source regions of sporadic meteoroids on JFC orbits match those of kilometer-scale JFCs. A P -test was used to determine if our results were significant enough to reject the null hypothesis. The P -value reflects the probability of observing a result at least as extreme as the one measured. We considered a P -value of 0.01 to be significant enough to reject the null hypothesis. At most, two events are genetically cometary within the data set (DN150817_01 and DN161028_02). Both of these events meet the criteria of being relatively weaker (type II) and likely originating from unstable orbits over the previous 10 kyr (>50%). We assume that the probability of observing a meteoroid from the main belt within our sample matches the maximum value found from a dynamical study based on telescopic observations (19 out of 58 JFCs from the main belt; Fernández & Sosa 2015). From these results, we find the P -value to be equal to 3.1×10^{-21} . This extraordinarily low probability clearly indicates that we can reject the null hypothesis. Thus, the source region for centimeter-scale meteoroids on JFC-like orbits does not match the cometary kilometer-sized bodies.

We additionally utilized Bayesian inference to estimate the proportion of main-belt material on JFC-like orbits (Salvatier et al. 2016). The informed prior used is a beta distribution with hyperparameters $\alpha = [1.38, 8.62]$ and an observation vector $c = [48, 2]$. The hyperparameters are derived from observational data, but the weight of these prior observations on our expected values was slightly reduced, as they corresponded to kilometer-scale objects (Fernández & Sosa 2015). Using a Markov Chain Monte Carlo to draw samples from the posterior distribution, we found that sporadic JFC-like meteoroids in NEO space are $82.1\% \pm 4.9\%$ from the main belt and $17.9\% \pm 4.9\%$ from the trans-Neptunian region with our reasonably informed prior. When an uninformed prior is used (i.e., the prior probability of observing a JFC or main-belt meteoroid is equal), the relative components are $94.2\% \pm 3.2\%$ from the main belt and $5.8\% \pm 3.2\%$ from JFCs.

Furthermore, while processing the data in this study, we found that of the meteoroids originating from JFC-like orbits with initial masses greater than 10 g, about $78\% \pm 3\%$ were sporadic and $22\% \pm 3\%$ were associated with showers. Thus, even when considering showers along with the sporadic population, it is likely that main-belt material makes up the majority of near-Earth material on orbits with $2 < T_J < 3$ within this size range. Evidently, the Tisserand's parameter is not a very informative metric when analyzing meteoroids in the inner solar system.

4.3. Why Are There No Sporadic Cometary Meteoroids?

4.3.1. Alternative Explanations

A possible explanation for the lack of dynamically unstable meteoroids in our sample could be that nongravitational forces are decoupling the material from Jupiter. Previous work has found that sporadic micron-sized meteoroids of the zodiacal cloud are not able to decouple from Jupiter via planetary perturbations along with solar radiation pressure before having another close encounter removing them from Earth-crossing orbits (Nesvorný et al. 2010). However, the meteoroids studied by Nesvorný et al. (2010) are in a completely different size

range compared to those discussed here, and the effects on these meteoroids are very different.

Nevertheless, nongravitational forces are highly unlikely to be responsible for the meteoroids with asteroidal dynamics in our data set. Nongravitational forces, such as the Yarkovsky effect, would not be efficient enough to decouple these meteoroids before having another close encounter with Jupiter ($< 10^3$ yr).

Alternatively, one could argue that we may not expect to see many JFC meteoroids on these low-perihelion orbits or within the examined size range (10 g to a few kilograms). First, there have been multiple studies of Earth-crossing JFCs, with the current number known to be ~ 140 objects (<http://ssd.jpl.nasa.gov/horizons.cgi>). A previous study investigated the dynamic stability of 58 JFCs in orbits with $q < 1.3$ au, and they found that most of the objects (over two-thirds) move on unstable orbits over ± 10 kyr (Fernández & Sosa 2015). Thus, showing at the kilometer scale, objects on these orbits are dominated by weak genetically cometary material. Second, larger meteoroids (centimeter or larger) are capable of being produced by comets through a few mechanisms, such as cometary splitting or gas drag (Boehnhardt 2004; Fernández 2009). Thus, we should expect to observe cometary meteoroids within the range detected by the DFN.

4.3.2. Short Physical Lifetimes

Given the numerous JFCs on Earth-crossing orbits and their ability to produce meteoroids within the range considered in this study, it is surprising that we observe almost no meteoroids clearly sourced from the JFC population (Fernández & Morbidelli 2006). According to debiased NEO models, as much as 10% of the NEO population at the smallest sizes considered (~ 100 m) should be sourced from the JFC population (Granvik et al. 2018). Yet in this sample, we see no distinctly cometary meteoroids.

This lack of cometary debris within the sporadic population strongly supports the hypothesis that subkilometer JFCs have limited physical lifetimes in the inner solar system (Fernández et al. 2002; Meech et al. 2004; Fernández & Morbidelli 2006; Nesvorný et al. 2017). The physical lifetimes of centimeter-meter debris must be less than ~ 1000 yr (the decoherence time). This physical breakdown is consistent with the observations that there are less highly volatile asteroids at low perihelion distances (Granvik et al. 2016). Planetary debris seems to break down in the inner solar system closer to the Sun, depending on the object's size and volatile content. At large sizes ($> 10^{3-4}$ m), material from the trans-Neptunian region is dominant on JFC-like orbits. However, as the diameters decrease to typical meteorite-producing objects, the physical lifetimes are likely so short that main-belt material becomes a more viable source. Conversely, according to Nesvorný et al. (2010), micron-sized meteoroid impacts on Earth are dominated by JFC particles ($\sim 85\%$ of the mass influx). If accurate, these results suggest that dust- and kilometer-sized objects on JFC-like orbits are genetically cometary; however, intermediate sizes are sourced from the main asteroid belt. This is consistent with the prediction by Nesvorný et al. (2010) that centimeter-sized particles ejected from comets likely quickly disrupt (< 10 kyr) and form the robust micron-sized population observed within the zodiacal cloud.

4.4. Meteorites from JFCs

A couple of the fireballs likely resulted in surviving meteorites >50 g (Figure 4); however, all of these are dynamically stable over the previous 10 kyr and only have PE values of type I. Thus, even on the occasion where we do have some genetically cometary material impact the Earth, according to our sample, it is unlikely to survive. It has been argued that primitive carbonaceous chondrites may be the best candidates to originate from cometary bodies; however, given our results, this may be only possible if the meteoroid was recently released from the parent body (within 1000 yr; Gounelle et al. 2008). While the cosmic-ray exposure ages are significantly shorter for some carbonaceous chondrites (<1 Myr), they are still usually much longer than the $\sim 10^3$ yr expected from our results (Eugster et al. 2006). Therefore, meteorites from $2 < T_J < 3$ orbits are expected, but they will not be cometary.

4.5. Limitations

This study is constrained by the amount of data collected by the DFN. However, given that the DFN is the largest fireball network in the world, this cannot be improved upon. Additionally, the PE value methodology is a very limited metric of meteoroid strength, as macroscopic features of the meteoroids can significantly affect the strengths. However, the PE value was utilized liberally in this study to determine potentially cometary meteoroids. Any meteoroid with a slightly weaker strength was considered as potentially cometary. Even with this very inclusive criterion, we found almost no meteoroids that fulfilled our physical and orbital requirements to be considered cometary. The results clearly demonstrate that cometary debris larger than dust-sized is too friable to survive in near-Earth space for longer periods.

5. Summary

Sporadic fireball data collected by the DFN demonstrates that there is a lack of cometary material on JFC-like orbits for meteoroids in the gram-to-kilogram size range. This supports the short physical lifetime hypothesis for JFC material (Fernández et al. 2002; Meech et al. 2004; Fernández & Morbidelli 2006; Nesvorný et al. 2017). Additionally, it indicates that the primary source region for Earth-crossing material on JFC-like orbits ($2 < T_J < 3$) is size-dependent. A majority of the objects at dust sizes and on kilometer scales are likely sourced from the trans-Neptunian region of the outer solar system (Nesvorný et al. 2010; Fernández & Sosa 2015). However, objects centimeters to meters in size are dominated by asteroidal material diffused out from the main belt. This diffusion process likely occurs via some combination of orbital resonances, Kozai resonances, nongravitational forces, and close encounters with terrestrial planets (Bottke et al. 2002; Fernández et al. 2014; Hsieh & Haghhighipour 2016; Shober et al. 2020a, 2020b). In this study, we found a minor fraction of unstable, possibly cometary objects, but the number of fireballs observed to originate from stable orbits from the main belt over the previous 10 kyr is statistically significant. We estimate that as much as $94.2\% \pm 3.2\%$ of Earth-crossing centimeter-sized debris on these orbits is sourced from the main belt. Furthermore, considering that $22\% \pm 3\%$ of the JFC-like fireballs observed by the DFN over the previous 5 yr are associated with showers, our results suggest that the majority of centimeter material on

JFC-like orbits in near-Earth space is main belt in origin. Thus, we should expect to see ordinary types of meteorite falls coming from Jupiter-crossing orbits.

This work was funded by the Australian Research Council as part of the Australian Discovery Project scheme (DP170102529). The SSTC authors acknowledge institutional support from Curtin University. This work was also supported by resources provided by the Pawsey Supercomputing Centre with funding from the Australian Government and the Government of Western Australia. This research made use of TOPCAT for visualization and figures (Taylor 2005). This research also made use of Astropy, a community-developed core Python package for astronomy (Robitaille et al. 2013). Simulations in this paper made use of the REBOUND code, which can be downloaded freely at <http://github.com/hannorein/REBOUND> (Rein & Liu 2012). The authors declare no competing interests. All data needed to evaluate the conclusions in the paper are present in the paper and/or at <https://doi.org/10.5281/zenodo.4710556>.

ORCID iDs

P. M. Shober  <https://orcid.org/0000-0003-4766-2098>
 E. K. Sansom  <https://orcid.org/0000-0003-2702-673X>
 H. A. R. Devillepoix  <https://orcid.org/0000-0001-9226-1870>
 M. C. Towner  <https://orcid.org/0000-0002-8240-4150>

References

- A'Hearn, M. F., Belton, M., Delamere, W., et al. 2005, *Sci*, **310**, 258
 Asher, D., Clube, S., & Steel, D. 1993, *MNRAS*, **264**, 93
 Boehnhardt, H. 2004, in *Comets II*, ed. M. C. Festou, H. U. Keller, & H. A. Weaver (Tucson, AZ: Univ. Arizona Press), 301
 Borovička, J., Popova, O., & Spurný, P. 2019, *M&PS*, **54**, 1024
 Borovička, J., Spurný, P., & Brown, P. 2015, *Asteroids IV*, Vol. 257
 Borovička, J., Spurný, P., Grigore, V. I., & Svoreň, J. 2017, *P&SS*, **143**, 147
 Borovička, J., Spurný, P., & Koten, P. 2007, *A&A*, **473**, 661
 Borovička, J., Spurný, P., & Šrbený, L. 2020, *AJ*, **160**, 42
 Borovička, J., Tóth, J., Igaz, A., et al. 2013, *M&PS*, **48**, 1757
 Bottke, W. F., Jr., Morbidelli, A., Jedicke, R., et al. 2002, *Icar*, **156**, 399
 Brown, P., Marchenko, V., Moser, D. E., Weryk, R., & Cooke, W. 2013, *M&PS*, **48**, 270
 Brown, P., Wiegert, P., Clark, D., & Tagliaferri, E. 2016, *Icar*, **266**, 96
 Brown, P. G., Hildebrand, A. R., Zolensky, M. E., et al. 2000, *Sci*, **290**, 320
 Brownlee, D. E., Horz, F., Newburn, R. L., et al. 2004, *Sci*, **304**, 1764
 Ceplecha, Z. 1994, *A&A*, **286**, 967
 Ceplecha, Z., Borovička, J., Elford, W. G., et al. 1998, *SSRv*, **84**, 327
 Ceplecha, Z., & McCrosky, R. 1976, *JGR*, **81**, 6257
 Consolmagno, G., Britt, D., & Macke, R. 2008, *Geoch*, **68**, 1
 DeMeo, F., Alexander, C., Walsh, K., Chapman, C., & Binzel, R. 2015, in *Asteroids IV*, ed. P. Michel, F. E. DeMeo, & W. F. Bottke (Tucson, AZ: Univ. Arizona Press), 13
 DeMeo, F. E., & Carry, B. 2014, *Natur*, **505**, 629
 Devillepoix, H. A., Bland, P. A., Sansom, E. K., et al. 2019, *MNRAS*, **483**, 5166
 Devillepoix, H. A. R., Cupák, M., Bland, P. A., et al. 2020, *P&SS*, **191**, 105036
 Di Sisto, R. P., Fernández, J. A., & Brunini, A. 2009, *Icar*, **203**, 140
 Drummond, J. D. 1981, *Icar*, **45**, 545
 Duncan, M., Levison, H., & Dones, L. 2004, *Comets II* (Tucson, AZ: Univ. Arizona Press), 193
 Duncan, M. J., & Levison, H. F. 1997, *Sci*, **276**, 1670
 Eugster, O., Herzog, G., Marti, K., & Caffee, M. 2006, in *Meteorites and the Early Solar System II*, ed. D. S. Lauretta & H. Y. McSween, Jr. (Tucson, AZ: Univ. Arizona Press), 829
 Fernández, J. A., Gallardo, T., & Brunini, A. 2002, *Icar*, **159**, 358
 Fernández, J. A., & Morbidelli, A. 2006, *Icar*, **185**, 211
 Fernández, J. A., & Sosa, A. 2015, *P&SS*, **118**, 14

THE PLANETARY SCIENCE JOURNAL, 2:98 (10pp), 2021 June

Shober et al.

- Fernández, J. A., Sosa, A., Gallardo, T., & Gutiérrez, J. N. 2014, *Icar*, **238**, 1
- Fernández, Y., Kelley, M., Lamy, P., et al. 2013, *Icar*, **226**, 1138
- Fernández, Y. R. 2009, *P&SS*, **57**, 1218
- Fernández, Y. R., Jewitt, D. C., & Sheppard, S. S. 2005, *AJ*, **130**, 308
- Fornasier, S., Hasselmann, P., Barucci, M., et al. 2015, *A&A*, **583**, A30
- Gounelle, M., Morbidelli, A., Bland, P. A., et al. 2008, in *The Solar System Beyond Neptune*, ed. M. A. Barucci, D. P. Cruikshank, & A. Morbidelli (Tucson, AZ: Univ. Arizona Press), 525
- Granvik, M., & Brown, P. 2018, *Icar*, **311**, 271
- Granvik, M., Morbidelli, A., Jedicke, R., et al. 2016, *Natur*, **530**, 303
- Granvik, M., Morbidelli, A., Jedicke, R., et al. 2018, *Icar*, **312**, 181
- Gritsevich, M., & Stulov, V. 2006, *SoSyR*, **40**, 477
- Gritsevich, M. I. 2007, *SoSyR*, **41**, 509
- Howie, R. M., Paxman, J., Bland, P. A., et al. 2017, *ExA*, **43**, 237
- Hsieh, H. H., & Haghhighipour, N. 2016, *Icar*, **277**, 19
- Jansen-Sturgeon, T., Sansom, E. K., & Bland, P. A. 2019, *M&PS*, **54**, 2149
- Jenniskens, P. 2006, *Meteor Showers and Their Parent Comets* (Cambridge: Cambridge Univ. Press)
- Joepe, T. J. 1993, *Icar*, **106**, 603
- Lauretta, D., Hergenrother, C., Chesley, S., et al. 2019, *Sci*, **366**, 6470
- Levison, H. F., & Duncan, M. J. 1994, *Icar*, **108**, 18
- Levison, H. F., & Duncan, M. J. 1997, *Icar*, **127**, 13
- Lyytinen, E., & Gritsevich, M. 2016, *P&SS*, **120**, 35
- Madiedo, J. M., Trigo-Rodríguez, J. M., Zamorano, J., et al. 2014, *A&A*, **569**, A104
- Meech, K., Hainaut, O., & Marsden, B. 2004, *Icar*, **170**, 463
- Nesvorný, D., Jenniskens, P., Levison, H. F., et al. 2010, *ApJ*, **713**, 816
- Nesvorný, D., Vokrouhlický, D., Dones, L., et al. 2017, *ApJ*, **845**, 27
- Popova, O., Borovička, J., Hartmann, W. K., et al. 2011, *M&PS*, **46**, 1525
- Quinn, T., Tremaine, S., & Duncan, M. 1990, *ApJ*, **355**, 667
- Rein, H., & Liu, S. F. 2012, *A&A*, **537**, A128
- Rein, H., & Spiegel, D. S. 2015, *MNRAS*, **446**, 1424
- Robitaille, T. P., Tollerud, E. J., Greenfield, P., et al. 2013, *A&A*, **558**, A33
- Salvatier, J., Wiecki, T. V., & Fonnesbeck, C. 2016, *PeerJ Computer Science*, **2**, e55
- Sansom, E. K., Bland, P., Paxman, J., & Towner, M. 2015, *M&PS*, **50**, 1423
- Sansom, E. K., Gritsevich, M., Devillepoix, H. A., et al. 2019a, *ApJ*, **885**, 115
- Sansom, E. K., Jansen-Sturgeon, T., Rutten, M. G., et al. 2019b, *Icar*, **321**, 388
- Shober, P. M., Jansen-Sturgeon, T., Bland, P., et al. 2020a, *MNRAS*, **498**, 5240
- Shober, P. M., Jansen-Sturgeon, T., Sansom, E. K., et al. 2020b, *AJ*, **159**, 191
- Southworth, R., & Hawkins, G. 1963, *SCoA*, **7**, 261
- Spurný, P., Borovička, J., Baumgarten, G., et al. 2017, *P&SS*, **143**, 192
- Sunshine, J., A'hearn, M., Groussin, O., et al. 2006, *Sci*, **311**, 1453
- Takir, D., Emery, J. P., & McSween, H. Y., Jr. 2015, *Icar*, **257**, 185
- Tancredi, G. 1995, *A&A*, **299**, 288
- Tancredi, G. 2014, *Icar*, **234**, 66
- Taylor, M. B. 2005, *adass XIV*, **347**, 29
- Towner, M. C., Cupák, M., Deshayes, J., et al. 2020, *PASA*, **37**, e008
- Wetherill, G., & ReVelle, D. 1981, *Icar*, **48**, 308

**First Author Conference
Publication Reprints**

Coauthored Journal Publication

Reprints

Coauthored Paper 1 – Determining fireball fates using the α - β criterion

The Astrophysical Journal (2019), Volume 885, Issue 2, p. 115-122.

*Eleanor K. Sansom, Maria Gritsevich, Hadrien A. R. Devillepoix, Trent Jansen-Sturgeon, **Patrick M. Shober**, Phil A. Bland, Martin C. Towner, Martin Cupák, Robert M. Howie, Benjamin A. D. Hartig*

REPRODUCED BY PERMISSION OF THE AAS: *Permission to reproduce this article as part of this thesis has been granted by American Astronomical Society, under license number 4675800498723.*

Statement of Authorship

TITLE OF PAPER: DETERMINING FIREBALL FATES USING THE α - β CRITERION

.

PUBLICATION STATUS: Published.

Author Contributions

I, Patrick M. Shober, as a coauthor, contributed to the reduction of the fireball observations and the revisions of the manuscript. These efforts made a 5% contribution to the total work of this paper.

I, Eleanor K. Sansom, as first author, endorse that the level of contribution indicated above is accurate.



Determining Fireball Fates Using the α - β Criterion

Eleanor K. Sansom¹, Maria Gritsevich^{2,3,4}, Hadrien A. R. Devillepoix¹, Trent Jansen-Sturgeon¹, Patrick Shober¹, Phil A. Bland¹,
 Martin C. Towner¹, Martin Cupák¹, Robert M. Howie¹, and Benjamin A. D. Hartig¹

¹Space Science and Technology Centre, Curtin University, GPO Box U1987, Perth, WA 6845, Australia

²Department of Physics, Helsinki University, Finland

³Finnish Geospatial Research Institute (FGI), Masala, Finland

⁴Institute of Physics and Technology, Ural Federal University, Ekaterinburg, Russia

Received 2019 June 26; revised 2019 August 23; accepted 2019 September 5; published 2019 November 6

Abstract

As fireball networks grow, the number of events observed becomes unfeasible to manage by manual efforts. Reducing and analyzing big data requires automated data pipelines. Triangulation of a fireball trajectory can swiftly provide information on positions and, with timing information, velocities. However, extending this pipeline to determine the terminal mass estimate of a meteoroid is a complex next step. Established methods typically require assumptions to be made of the physical meteoroid characteristics (such as shape and bulk density). To determine which meteoroids may have survived entry there are empirical criteria that use a fireball's final height and velocity—low and slow final parameters are likely the best candidates. We review the more elegant approach of the dimensionless coefficient method. Two parameters, α (ballistic coefficient) and β (mass loss), can be calculated for any event with some degree of deceleration, given only velocity and height information. α and β can be used to analytically describe a trajectory with the advantage that they are not mere fitting coefficients; they also represent the physical meteoroid properties. This approach can be applied to any fireball network as an initial identification of key events and determine on which to concentrate resources for more in-depth analyses. We used a set of 278 events observed by the Desert Fireball Network to show how visualization in an α - β diagram can quickly identify which fireballs are likely meteorite candidates.

Unified Astronomy Thesaurus concepts: [Fireballs \(538\)](#); [Meteors \(1041\)](#); [Bolides \(172\)](#); [Meteoroids \(1040\)](#)

1. Introduction

Meteorites are examples of planetesimal building blocks and hold invaluable information on early solar system processes. Less than 0.1% have known preimpact origins. When extraterrestrial material encounters the Earth's atmosphere, a bright phenomenon can be observed as the meteoroid ablates and ionizes the atmosphere. If observed from different locations with high precision, these phenomena can be triangulated and their trajectories determined. Dedicated observation networks, such as the Desert Fireball Network in Australia, record the timing along the luminous trajectory to acquire velocity information (Howie et al. 2017).

The goal of such networks is to determine heliocentric orbits for these bodies as well as establish if any mass survived atmospheric ablation to impact the Earth's surface. Recovering a fresh meteorite minimizes terrestrial contamination, and the ability to associate an orbit with this material is of exceptional value. Despite the knowledge obtainable from meteorite samples on solar system formation and evolution, very few have orbits to provide location context information (<0.1%). Fireball networks are bridging the gap between asteroidal observations and meteoritic analyses by providing this context.

Whipple (1938) details the first multistation photographic meteor program from the mid 1930s, designed to determine trajectories and velocities of meteors. Larger fireball networks have been observing the skies since the 1960s (Ceplecha & McCrosky 1997) and have accumulated large data sets, though those deemed “unspectacular” were classed as low priority for data reduction (Halliday et al. 1996). There were not enough resources to measure and reduce all observed meteors, and it was an identified bias in flux surveys. Interesting events were assessed to determine if they were candidates for meteorite

searches (Halliday et al. 1996). Common practice for identifying which meteoroids may have survived entry is by assessing a fireball's final height and velocity—low and slow final parameters are likely the best candidates. Brown et al. (2013) discuss how this was empirically determined by early studies of meteorite-producing fireballs of the Meteor Observation and Recovery Project (MORP; Halliday et al. 1989) and the Prairie Network (PN; McCrosky et al. 1971). The set of empirically determined conditions for a fireball to produce a meteorite is an end height below 35 km and a terminal velocity below 10 km s^{-1} (Wetherill & ReVelle 1981; Halliday et al. 1989; Brown et al. 2013). This has been used to direct resource focus to the most likely meteorite-dropping events.

1.1. Established Methods of Identifying Meteorite-dropping Events

Despite advances, reducing fireball data to determine terminal mass estimates is still a nontrivial task. Established methods, such as those of Sansom et al. (2016, 2017), Egal et al. (2017), and Ceplecha & ReVelle (2005), are based on a set of single body aerodynamic equations that require assumptions to be made about the physical properties of the meteoroid, or in some way statistically estimate their values. These unobservable values, such as shape, density, and even ablation efficiencies, introduce many degrees of freedom to modeling scenarios. More complex Monte Carlo and particle filter techniques can intelligently assess the parameter space to give statistical likelihood of parameter sets (i.e., Sansom et al. 2017). However, these methods still require a multivariate solution and require supercomputing resources to run.

One concise way of assessing the trajectory without assuming any parameters is the dimensionless coefficient

method first described by Gritsevich (2007). The method is based on dimensionless equations describing the trajectory introduced by Stulov et al. (1995). Gritsevich & Stulov (2006) describe the simplified (asymptotic) solution of the method, and the latest, more advanced realization of the algorithm (including the incorporation of an arbitrary atmospheric model) is well outlined in Lyytinen & Gritsevich (2016). The ballistic coefficient α , and mass-loss parameter β can be calculated for any event with some degree of deceleration, given only velocity and height information. For meteors showing no deceleration these parameters may be linked to the terminal height of luminous flight (Moreno-Ibáñez et al. 2015). These two parameters can be used to analytically describe a trajectory, given an entry velocity (V_0). This is similar to the mathematical curve fitting performed by Jacchia & Whipple (1956), subsequently improved by Egal et al. (2017), with the added advantage that there is a link to the physical meteoroid parameters through using α and β rather than mere fitting coefficients. This link allows more robust conclusions to be made on the incoming body by assessing the groupings of specific α - β values. This is also a fast and easy method to implement and run on a large data set, such as that which has been done by Gritsevich (2009) for both the PN and MORP data. It has also been applied to well-documented meteorite falls including Prábram, Lost City, Innisfree, Neuschwanstein (Gritsevich 2008b), Bunburra Rockhole (Sansom et al. 2015), Annama (Lyytinen & Gritsevich 2016), Park Forest (Meier et al. 2017), and Košice (Gritsevich et al. 2017).

1.2. Applying the α - β Criterion to DFN Events

Here we calculate the α and β parameters for 278 fireballs observed by the Desert Fireball Network (Section 2). This is a subset of some 1300+ fireball trajectories triangulated by the DFN, where noticeable deceleration has occurred ($V_f/V_0 < 80\%$). We then plot these data in a similar fashion to PN and MORP data in Gritsevich et al. (2012).⁵ The location of events on this plot instantly allows us to identify key events, such as those likely to drop meteorites. This is an under-utilized tool by fireball networks with large data sets to determine such events to concentrate resources for data reduction. Often, identification of good meteorite-dropping candidates is done by assessing how low and slow a fireball was observed in our atmosphere using the empirical criteria (end height < 35 km and final velocity < 10 km s⁻¹; Wetherill & ReVelle 1981; Halliday et al. 1989; Brown et al. 2013). However, such a classification scheme is highly dependent on the equipment used to record a fireball, and the range at which it was observed. This is also not a rigorous assessment of the event where slope, mass, and shape dependencies all come into play. The α - β approach may seem oversimplified, but led to the fast recovery of both the Annama meteorite (Gritsevich et al. 2014; Dmitriev et al. 2015; Trigo-Rodríguez et al. 2015; Kohout et al. 2017) and the Ozerki⁶ meteorite.

With the statistically large data set of the DFN, along with PN and MORP data, we aim to establish an α - β criterion for classifying the possible outcomes of meteoroid atmospheric entry (Section 3). We are ultimately looking to establish crude

criteria for whether further analyses and meteorite searches are worth prioritizing.

2. The α - β Diagram—Desert Fireball Network Data

Values of α and β are calculated using a least squares minimization of the analytical function (see Section 3 of Lyytinen & Gritsevich 2016, after Gritsevich & Stulov 2007)

$$y = \ln \alpha + \beta - \ln \frac{\Delta}{2}, \quad (1)$$

where y is the height of the meteoroid normalized to the atmospheric scale height ($h_0 = 7160$ m), Δ is a function of the exponential integral ($\bar{E}i$) as follows:

$$\Delta = \bar{E}i(\beta) - \bar{E}i(\beta v^2),$$

and v the meteoroid velocity normalized by V_0 . An example of the fit of this function to observational data is shown in Figure 1. The code used to generate such figures, and determine α and β values for decelerating meteoroids is provided at https://github.com/desertfireballnetwork/alpha_beta_modules.

α is related to the initial mass of the meteoroid (M_0 , Equation (2)) and the entry angle (γ), while β is related to the instantaneous mass (M_f , Equation (3)) and the shape change coefficient (μ) (Lyytinen & Gritsevich 2016):

$$M_0 = \frac{1}{2} \frac{c_d \rho_0 h_0 S_0}{\alpha \sin \gamma} = \left(\frac{1}{2} \frac{c_d A_0 \rho_0 h_0}{\alpha \rho_m^{2/3} \sin \gamma} \right)^3 \quad (2)$$

$$M = M_0 \exp \left\{ -\frac{\beta}{1 - \mu} \left(1 - \left(\frac{V}{V_0} \right)^2 \right) \right\}. \quad (3)$$

If quantitative values of these masses are required then assumptions must be made for the drag coefficient (c_d), initial cross-sectional area (S_0), or initial shape coefficient (A_0) and meteoroid bulk density (ρ_m); the atmospheric surface density (ρ_0) is typically set to 1.21 kg m⁻³. Applying such assumptions is similar to other methods, albeit the parameters that are needed to assume in this case have a limited range of values (meteoroid densities are well documented, as are shape, shape change, and drag coefficients). β here entirely replaces the need to assume an ablation parameter and subsequently a luminous efficiency—the two most highly uncertain parameters usually required. The advantage of this method, however, lies not in extracting individual parameters, but in assessing the relationship between α and β values directly. With such a large data set, we wish to determine if any deductions can be made from groupings in these parameter spaces. By rearranging Equation (2) for α , we can see that a body of different entry masses, slopes, and volumes are able to produce the same α values. The inclusiveness of these two parameters makes them more appropriate than the typical suite of parameters for predicting the outcomes of meteoroid atmospheric entry.

We extracted all fireballs within the current DFN data set where there is noticeable deceleration ($V_f/V_0 < 80\%$), and have calculated α and β value for the resulting 278 events (see the supplementary material for reduced data). We plot the results in a similar fashion to Gritsevich et al. (2012), taking the natural logarithm of the α and β values (Figure 2). Although

⁵ Note that fireballs from the PN and MORP surveys were not subject to any deceleration thresholding.

⁶ <https://www.lpi.usra.edu/meteor/metbull.php?code=67709>

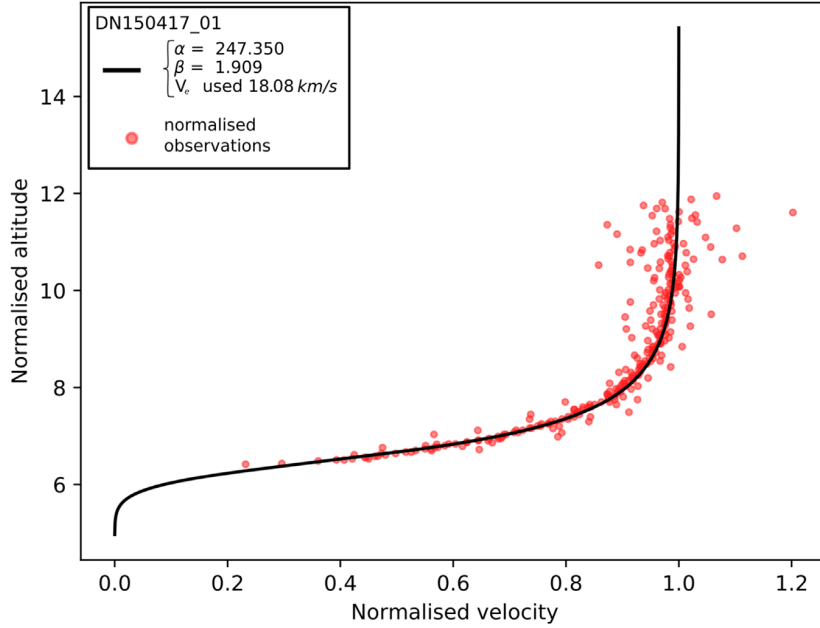


Figure 1. Plot of observational data with velocity normalized to entry velocity V_0 and height normalized to the atmospheric scale height ($h_0 = 7160$ m). The fit is good despite significant scatter in the data.

not a direct input parameter of either Equation (2) or (3), the final observed height of the fireball (where the observation limit of the hardware can no longer observe ablation) shows a clear horizontal trend with little relationship to β . Points with lower $\ln \alpha$ values will also have higher initial masses, as given by Equation (2).

3. Determining the Meteorite Fall Region

As previously stated, if we were to assume values for, say, density and shape in Equation (2), it would be possible to then calculate the entry mass of a meteoroid using α . Further assuming the shape change coefficient of the body can give a final mass using the β value and Equation (3) (with luminosity values, μ can be determined following Bouquet et al. 2014). Here we plot a series of bounding curves for a given set of assumptions on the α - β diagram. This is an ideal visual tool for quickly assessing which fireballs from a large network might be meteorite droppers.

As discussed in Gritsevich et al. (2012) the interpretation of the events is biased to the trajectory slope, individual for each event. Here we look at removing the effect of trajectory slope from the α - β diagram. If we plot instead $\ln(\alpha \sin \gamma)$ as the x -axis, this effect is removed (Figure 3). The clear horizontal trend in end heights, discussed in the previous section, now falls apart; there is no longer a distinct relationship. This is where the modified α - β diagram in Figure 3 is a more inclusive classification tool for fireballs. We no longer need to rely on final velocity and final end height requirements to classify a meteorite-dropping event.

How are we then able to identify such a meteorite-dropping region in these plots? If we would like to assess the relationship between α , β , and mass, we can extract α from Equation (2) to give a parameter M_0^* which is no longer dependent on α or the

slope of the trajectory (Equation (4)):

$$M_0 = \frac{1}{\alpha^3 \sin^3 \gamma} M_0^*, \quad \text{where } M_0^* = \left(\frac{1}{2} \frac{c_d \rho_0 h_0 A_0}{\rho_m^{2/3}} \right)^3. \quad (4)$$

To assess the final mass of a fireball, we look at Equation (3) in the case where the velocity becomes insignificant compared to the entry velocity (where $(V/V_0)^2 \rightarrow 0$):

$$M_f = \frac{1}{\alpha^3 \sin^3 \gamma} M_0^* \exp \left\{ -\frac{\beta}{1 - \mu} \right\}. \quad (5)$$

To define a region on the modified α - β diagram where a certain minimum final mass is obtainable, we can rearrange Equation (5) for β :

$$\beta = (\mu - 1) \left(\ln \left(\frac{M_f}{M_0^*} \right) + 3 \ln(\alpha \sin \gamma) \right). \quad (6)$$

To solve Equation (6) for a final mass of $M_f = 1$ kg, we use a density, $\rho_m = 3500 \text{ kg m}^{-3}$ and a typical shape-drag coefficient, $c_{dA} = 1.5$ (Gritsevich 2008a), to get a value of $\ln(M_f/M_0^*) = -10.21$. We can plot this boundary line given the two extreme values of the shape change coefficient—when $\mu = 0$, there is no spin of the meteoroid, and when $\mu = 2/3$, there is sufficient spin to allow equal ablation over the entire meteoroid surface and no shape change is expected to occur, giving:

$$\mu = 0, \quad \ln \beta = \ln \{ 10.21 - 3 \ln(\alpha \sin \gamma) \} \quad (7)$$

$$\mu = \frac{2}{3}, \quad \ln \beta = \ln \{ 3.4 - \ln(\alpha \sin \gamma) \}. \quad (8)$$

These boundary curves are plotted on the modified α - β diagram in Figure 3 for such a 1 kg mass. Many similar

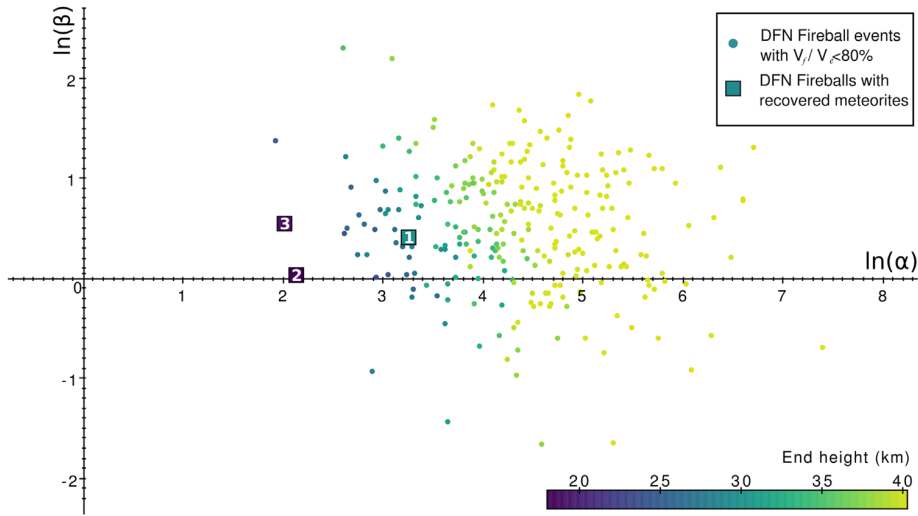


Figure 2. Distribution of α and β parameters for Desert Fireball Network fireballs. Recovered meteorite falls plotted: (1) Bunburra Rockhole (DN200707B); (2) Murrili (DN151127_01); Dingle Dell (DN 161031_01)

scenarios can be actualized for various shapes, densities, and minimum terminal mass values.⁷ Such an example plotted in Figure 3 includes using $c_{dA} = 1.21$ for a perfectly spherical meteoroid body.

As mentioned previously, there is a general rule of thumb that crudely uses a fireball end height of <35 km and terminal velocity <10 km s^{-1} to determine which meteoroids may have survived entry. If we define a macroscopic meteorite-dropping event as having a final mass of >50 g (following Halliday et al. 1996 and Gritsevich et al. 2011), Equations (7)–(8) become:

$$\mu = 0, \quad \ln \beta = \ln \{13.20 - 3 \ln(\alpha \sin \gamma)\} \quad (9)$$

$$\mu = \frac{2}{3}, \quad \ln \beta = \ln \{4.4 - \ln(\alpha \sin \gamma)\}, \quad (10)$$

given a $\rho_m = 3500$ kg m^{-3} and a $c_{dA} = 1.5$.

In Figure 4 we plot these boundary curves with the fireball data from the DFN and these previous studies (MORP and PN). Note that PN and MORP data were not subject to the same deceleration thresholding applied to DFN data here, and any differences in α – β values for these other studies to Gritsevich et al. (2012) are due to the slope dependence being addressed here. As the boundary lines are given for the two extremes of the shape change coefficient μ , events falling beyond the $\mu = 0$ line are unlikely to have produced a 50 g meteorite. Fireballs associated with known meteor shower events are all plot in this area, with high $\ln(\beta)$ and $\ln(\alpha \sin(\gamma))$ values. Fireballs below the $\mu = 2/3$ line are strong meteorite-producing candidates. The significant area between these two curves illustrates the sensitivity of the dynamic flight equations to meteoroid rotation. As a subsequent step, the shape change coefficient can be calculated for individual events from luminosity values following Bouquet et al. (2014).

Events that meet the empirical criteria ($V_f < 10$ km s^{-1} and $H_f < 35$ km) are highlighted in Figure 4. Within the “likely fall” area, nearly all events meet this criteria. All highlighted events fall within the $\mu = 0$ bounding line. These bounding lines are highly compatible with the empirical fall criteria and

present a physical basis for the classification of such events. We propose that these bounding lines be used in the future for more rigorously determining a meteoroid’s potential to survive entry. We will further discuss the advantages and limitations of using the α – β diagram, and the cases in particular of “likely fall” events that do not meet the empirical criteria.

4. Discussion

Figure 4 clearly demonstrates the suitability of Equations (9)–(10) to determine the likelihood of a macroscopic terminal mass. Although the general rule of thumb is consistent, there are multiple events in both the “possible fall” region and the “likely fall” region that do not satisfy the simplified empirical criteria. Could these missed events really be falls? Let us first discuss the possible limitations of this method before addressing these events.

Once an event is located on this modified α – β diagram, if it falls in either of the gray regions in Figure 4 it is worth further investigation. Following this α – β approach, there are several advancements on this basic implementation that can be performed. Despite using the simplified exponential atmosphere as a generic model, the actual atmospheric conditions for individual cases can be accounted for, given the time and location of the fireball as described in Lyytinen & Gritsevich (2016). There is also a strong sensitivity of this method to the initial velocity, as the normalization of velocity values uses V_0 . Although a first order V_0 can be used initially, for possible fall events, it is best to recalculate velocities using a robust method (such as discussed in Sansom et al. 2015 and Vida et al. 2018). Differences in V_0 calculation methods by MORP and PN could be a possible explanation for many of the light gray events falling in the “likely fall” region. Using more realistic atmospheric conditions (Lyytinen & Gritsevich 2016), and with recalculated V_0 values, the resulting α and β values become more representative.

The position of an event on the α – β diagram within the gray region indicates that there may be a macroscopic mass at the last observation point. This may not, in some cases, correspond to the terminal bright flight mass, or to an equivalent meteorite mass on the ground. For example when the last observed point

⁷ The interactive tool available at https://github.com/desertfireballnetwork/alpha_beta_modules provides a means to investigate these scenarios.

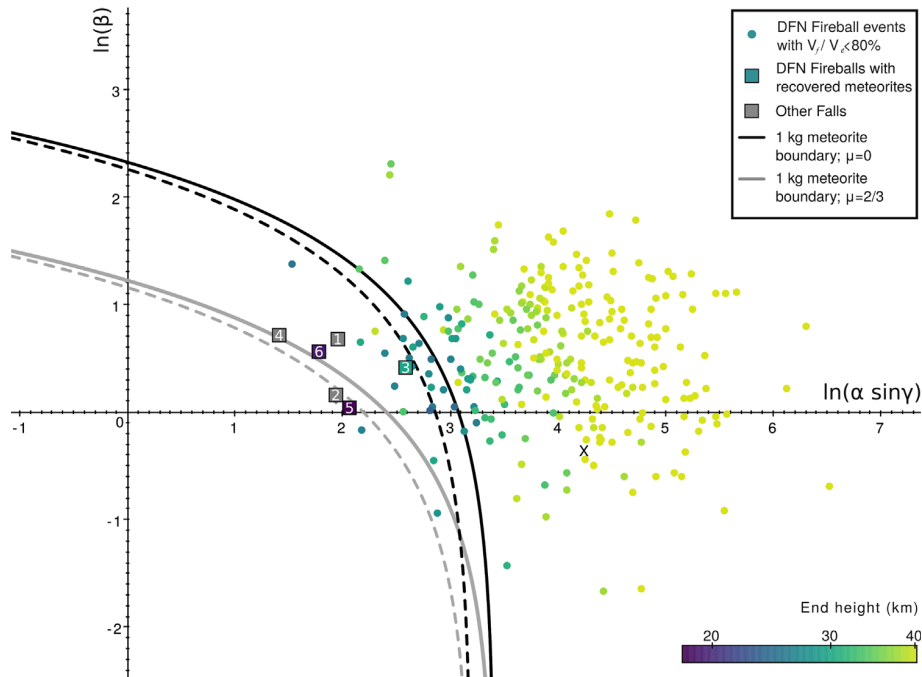


Figure 3. Distribution of fireballs from the Desert Fireball Network (DFN) with trajectory slope dependence removed (x -axis is now a function of γ). This changes the relationship between α and end height seen in Figure 2. The bounding line for a 1 kg meteorite is shown in black for the case where there is no spin ($\mu = 0$) and in gray where spin allows uniform ablation over the entire surface ($\mu = 2/3$). Solid lines are for likely values of $c_d A = 1.5$ and are dashed if $c_d A = 1.21$. Meteorite falls plotted: (1) Innisfree (MORP285, 2.07 kg+); (2) Lost City (PN40590, 9.83 kg+); (3) Bunburra Rockhole (DN200707B, 174 g+); (4) Annama (FFN, 120 g); (5) Murrili (DN151127_01, 1.68 kg); (6) Dingle Dell (DN161031_01, 1.15 kg), where masses are given for largest recovered fragment and “+” indicates other fragments were found. Also note that the α - β values for Annama (4) were calculated using the method of Lyytinen & Gritsevich (2016) where a realistic atmosphere model is used rather than the exponential atmosphere as for other falls.

is not the end of the bright flight trajectory, due to missing observations, or distance of the trajectory end to the observer. Distant fireballs may continue to ablate beyond the limiting magnitude of imaging systems. MORP and PN studies used large format film systems recording a single image per night, with fireball segments recorded at a frequency of 4 Hz (Halliday et al. 1978) and 20 Hz (McCrosky & Boeschenstein 1965) respectively. PN systems identify typical projected limiting magnitudes of -3 at the center of their frames (with -5 toward the edges; McCrosky & Boeschenstein 1965). These systems may not have been sensitive enough to reliably image the end of bright flight. Such missing information could account for why terminal masses may appear overestimated in the α - β diagram. Fragmentation within the bright flight is to some extent accounted for by the nature of fitting the deceleration profile with Equation (1). Where fragmentation occurs at the end of the bright flight; however, the terminal mass expected will no longer be a single main mass. Modeling of fragments through darkflight may still be valuable if the end mass is significant enough. An estimate of this terminal mass can be calculated using Equation (3). This does require assumptions to be made for density, shape, and of course μ . For a more in-depth analysis/assessment of specific meteoroid trajectories, more involved modeling techniques, such as those of Sansom et al. (2019) and Egal et al. (2017), can now be applied with confident use of resources.

Let us return to the gray DFN events in Figure 4 that are within the “likely fall” region (we include the two on the $\mu = 2/3$ line). Of the five, the most eye catching is at [2.88, -0.936] in Figure 4 and from video data shows significant flaring, including a final late flare. The mass at this point is still

significant (1 kg) and a search for fragments will be conducted in the future. The event at [2.30, 0.75] in Figure 4 is a great example of hardware limitations interfering with expected results. DFN observatories are designed to take a 25 s long-exposure image every 30 s. This 5 s down time allows images to be saved and systems to be reset. This event likely continued to ablate beyond the end of the exposure and was unfortunately not captured in the subsequent image. The remaining three are triangulated from observatories at significant ranges; the closest camera to DN151105_15 (Figure 4 [3.08, 0.27]) was 430 km. These are therefore still possible fall candidates that were missed by the empirical criteria, simply because the end of bright flight was not observed. These were modeled using Sansom et al. (2015) and masses at this last observed point are all >100 g. This method is therefore able to identify likely fall events that might previously have been missed if using the empirical criteria for a typical meteorite-dropping event.

5. Conclusions

Here we demonstrate an α - β diagram as a simple, yet powerful, tool to visualize which fireball events are likely to have macroscopic terminal masses. We plot 278 fireballs from the Desert Fireball Network on a modified α - β diagram, accounting for the differences in trajectory slopes (Figure 3). Boundary lines can be plotted to define a region of events having a given minimum terminal mass. The shape change coefficient, μ , is capable of enhancing mass loss and its influence should be considered. Equations (9)–(10) define the boundary curves for a terminal 50 g chondritic mass, given the two extremes of meteoroid rotation ($0 < \mu < 2/3$; Figure 4).

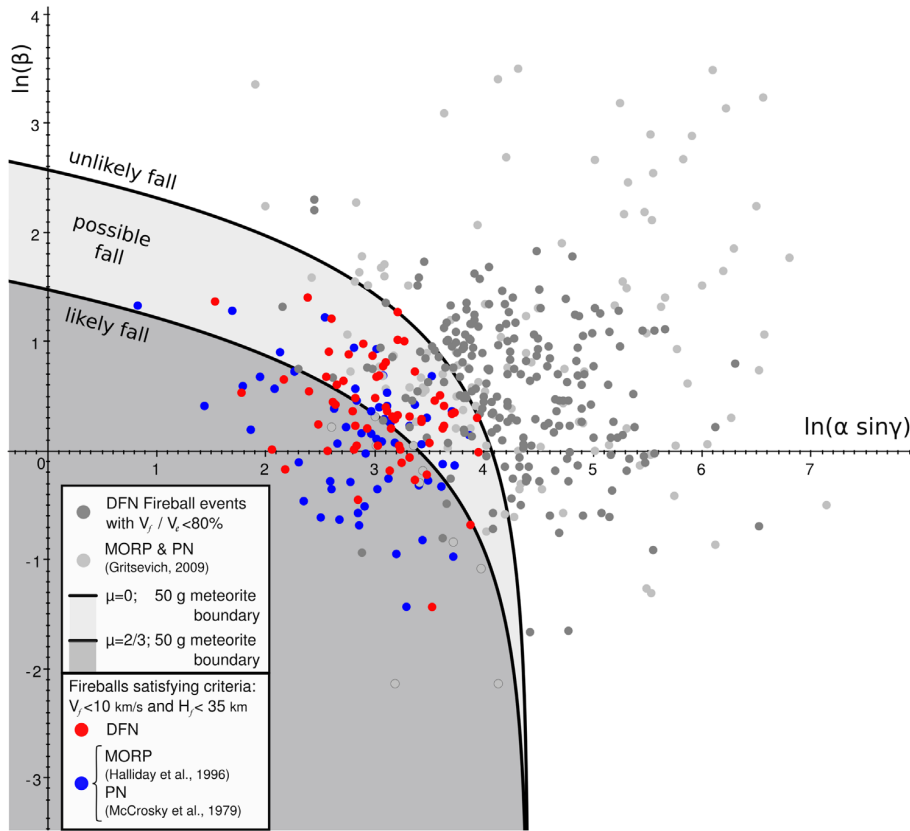


Figure 4. Distribution of fireballs from both the Desert Fireball Network (DFN) and previous studies (Meteor Observation and Recovery Project, Halliday et al. 1996; Prairie Network, McCrosky et al. 1979). Fireball events that meet the criteria $V_f < 10 \text{ km s}^{-1}$ and $H_f < 35 \text{ km}$ are considered likely meteorite droppers (after Brown et al. 2013) and are shown in red (DFN) and blue (previous studies). Boundary lines for a 50 g meteorite are given for the two extremes of the shape change coefficient μ using Equations (9)–(10). The area beyond both these lines will be unlikely to drop a $>50 \text{ g}$ meteorite, while those within the dark gray “likely fall” region will be strong meteorite-producing candidates.

Events beyond both these lines are unlikely to have survived atmospheric entry, while those below both lines are likely to have dropped a macroscopic meteorite. Depending on the meteoroid rotation, events in the region between these lines should also be considered as possible falls. Events from previous studies (MORP and PN) are also shown for comparison.

Events that meet the current empirical fall criteria ($V_f < 10 \text{ km s}^{-1}$ and $H_f < 35 \text{ km}$) all lie within the proposed fall regions of the α – β diagram (Figure 4). Not only can this method locate all events identified by the empirical criteria, but it is able to provide the physical justification for highlighting such events. Additionally, the α – β method is able to detect likely fall events that do not meet these empirical criteria, identifying nontypical events. The use of the α – β criterion is a way to quickly and easily identify key events in large data sets. This method is easily automated and has previously been shown to scale to airburst and cratering events. With more data, this could become increasingly useful for identifying where hazardous material may be originating from in the solar system.

E.K.S. acknowledges the Australian Research Council for funding received as part of the Australian Discovery Project scheme (DP170102529).

STSC authors acknowledge institutional support from Curtin University.

M.G. acknowledges Academy of Finland project No. 325806 and the Russian Foundation for Basic Research, project Nos. 18-08-00074 and 19-05-00028. Research at the Ural Federal University is supported by the Act 211 of the Government of the Russian Federation, agreement No. 02.A03.21.0006.

This research made use of TOPCAT for visualization and figures (Taylor 2005).

The code used to determine the α and β parameters for a fireball data set (after Gritsevich 2009) is available on GitHub as an interactive Jupyter notebook (https://github.com/desertfireballnetwork/alpha_beta_modules).

Appendix

Summary of Definitions and Abbreviations

A_0 – Initial shape factor—a cross-sectional area to volume ratio $A = S \left(\frac{\rho_m}{m} \right)^{2/3}$.

c_d – Drag coefficient.

c_h – Heat-transfer coefficient.

$\bar{E}i$ – Exponential integral, $\bar{E}i(x) = \int_{-\infty}^x \frac{e^z}{z} dz$.

\mathbf{g} – Vector of local gravitational acceleration ($m \text{ s}^{-2}$).

h_0 – Scale height of the homogeneous atmosphere ($h_0 = 7160 \text{ m}$).

H^* – Enthalpy of sublimation (J kg^{-1}).

m – Normalized meteoroid mass, $m = \frac{M}{M_0}$ (dimensionless).

THE ASTROPHYSICAL JOURNAL, 885:115 (7pp), 2019 November 10

Sansom et al.

M – Meteoroid mass (kg).
 M_0 – Initial entry mass of meteoroid at the beginning of the observed, luminous trajectory (kg).
 M_0 – An intermediate variable defined by Equation (4) (dimensionless).
 M_f – Terminal mass of the main meteoroid body at the end of the luminous trajectory (kg).
 S – Cross-sectional area of the body (m^2).
 S_0 – Initial cross-sectional area of the body (m^2).
 v – Normalized meteoroid velocity, $v = \frac{V}{V_0}$ (dimensionless).
 V – Meteoroid velocity (m s^{-1}).
 V_0 – Initial entry velocity of the meteoroid at the beginning of the observed, luminous trajectory (m s^{-1}).
 V_f – Terminal velocity of the main meteoroid body at the end of the luminous trajectory (m s^{-1}).
 y – Normalized meteoroid height, $y = \frac{\text{altitude}}{h_0}$ (dimensionless).
 α – Ballistic Coefficient.
 β – Mass loss parameter.
 γ – Angle of the meteoroid flight to the horizontal.
 μ – Shape change coefficient representing the rotation of a meteoroid body ($0 < \mu < 2/3$).
 ρ_a – Atmospheric density (kg m^{-3}).
 ρ_m – Meteoroid bulk density (kg m^{-3}).

References

- Bouquet, A., Baratoux, D., Vaubaillon, J., et al. 2014, *P&SS*, **103**, 238
 Brown, P., Marchenko, V., Moser, D. E., Weryk, R., & Cooke, W. 2013, *M&PSA*, **48**, 270
 Ceplecha, Z., & McCrosky, R. E. 1997, *M&PSA*, **32**, A157
 Ceplecha, Z., & Revelle, D. O. 2005, *M&PS*, **40**, 35
 Dmitriev, V., Lupovka, V., & Gritsevich, M. 2015, *P&SS*, **117**, 223
 Egal, A., Gural, P., Vaubaillon, J., Colas, F., & Thuillot, W. 2017, *Icar*, **294**, 43
 Gritsevich, M. 2007, *SoSyR*, **41**, 509
 Gritsevich, M., Dmitriev, V., Vinnikov, V., et al. 2017, Assessment and Mitigation of Asteroid Impact Hazards (Berlin: Springer), 153
 Gritsevich, M., Lyytinen, E., Moilanen, J., et al. 2014, in Proc. Int. Meteor Conf. (*Giron, France*) ed. J.-L. Rault & P. Roggemans, 162
 Gritsevich, M., & Stulov, V. 2006, *SoSyR*, **40**, 477
 Gritsevich, M. I. 2008a, *DokPh*, **53**, 97
 Gritsevich, M. I. 2008b, *SoSyR*, **42**, 372
 Gritsevich, M. I. 2009, *AdSpR*, **44**, 323
 Gritsevich, M. I., & Stulov, V. P. 2007, *DokPh*, **52**, 219
 Gritsevich, M. I., Stulov, V. P., & Turchak, L. I. 2011, *DokPh*, **56**, 199
 Gritsevich, M. I., Stulov, V. P., & Turchak, L. I. 2012, *CosRe*, **50**, 56
 Halliday, I., Blackwell, A. T., & Griffin, A. A. 1978, *JRASC*, **72**, 15
 Halliday, I., Blackwell, A. T., & Griffin, A. A. 1989, *Metic*, **24**, 173
 Halliday, I., Griffin, A. A., & Blackwell, A. T. 1996, *M&PS*, **31**, 185
 Howie, R. M., Paxman, J., Bland, P. A., et al. 2017, *ExA*, **43**, 237
 Jachia, L. G., & Whipple, F. L. 1956, *VA*, **2**, 982
 Kohout, T., Haloda, J., Halodová, P., et al. 2017, *M&PS*, **52**, 1525
 Lyytinen, E., & Gritsevich, M. 2016, *P&SS*, **120**, 35
 McCrosky, R., Posen, A., Schwartz, G., & Shao, C.-Y. 1971, *JGR*, **76**, 4090
 McCrosky, R., Shao, C.-Y., & Posen, A. 1979, *Metic*, **38**, 106
 McCrosky, R. E., & Boeschenstein, J. H. 1965, *SAOSR*, 173
 Meier, M. M., Welten, K. C., Riebe, M. E., et al. 2017, *M&PS*, **52**, 1561
 Moreno-Ibáñez, M., Gritsevich, M., & Trigo-Rodríguez, J. M. 2015, *Icar*, **250**, 544
 Sansom, E., Rutten, M., & Bland, P. 2017, *AJ*, **153**, 87
 Sansom, E. K., Bland, P. A., Paxman, J., & Towner, M. C. 2015, *M&PS*, **50**, 1423
 Sansom, E. K., Bland, P. A., Rutten, M. G., Paxman, J., & Towner, M. C. 2016, *AJ*, **152**, 148
 Sansom, E. K., Jansen-Sturgeon, T., Rutten, M. G., et al. 2019, *Icar*, **321**, 388
 Stulov, V. P., Mirsky, V. N., & Visly, A. I. 1995, *Aerodynamics of Bolides* (Moscow: Nauka)
 Taylor, M. B. 2005, *adass XIV*, 347, 29
 Trigo-Rodríguez, J. M., Lyytinen, E., Gritsevich, M., et al. 2015, *MNRAS*, **449**, 2119
 Vida, D., Brown, P. G., & Campbell-Brown, M. 2018, *MNRAS*, **479**, 4307
 Wetherill, G., & ReVelle, D. 1981, *Icar*, **48**, 308
 Whipple, F. L. 1938, *PAPHS*, **79**, 499

Coauthored Paper 2 – A Global Fireball Observatory

Planetary and Space Science (2020), Volume 191, p. 105036.

*H.A.R. Devillepoix, M. Cupák, P.A. Bland, E.K. Sansom, M.C. Towner, R.M. Howie, B.A.D. Hartig, T. Jansen-Sturgeon, **P.M. Shober**, S.L. Anderson, G.K. Benedix, D. Busan, R. Sayers, P. Jenniskens, J. Albers, C.D.K. Herd, P.J.A. Hill, P.G. Brown, Z. Krzeminski, G.R. Osinski, H. Chennaoui Aoudjehane, Z. Benkhal-doun, A. Jabiri, M. Guennoun, A. Barka, H. Darhmaoui, L. Daly, G.S. Collins, S. McMullan, M.D. Suttle, T. Ireland, G. Bonning, L. Baeza, T.Y. Alrefay, J. Horner, T.D. Swindle, C.W. Hergenrother, M.D. Fries, A. Tomkins, A. Langendam, T. Rushmer, C. O'Neill, D. Janches, J.L. Hormaechea, C. Shaw, J.S. Young, M. Alexander, A.D. Mardon, J.R. Tate*

REPRODUCED WITH PERMISSION FROM ELSEVIER: *Permission to reproduce this article as part of this thesis has been granted by Elsevier.*

Statement of Authorship

TITLE OF PAPER: A GLOBAL FIREBALL OBSERVATORY

PUBLICATION STATUS: Published.

Author Contributions

I, Patrick M. Shober, as a coauthor, contributed to the reduction of the fireball observations collected, analysis of fireball orbits, maintenance of the Australian node of the Global Fireball Observatory and the revisions of the manuscript. These efforts made a 1% contribution to the total work of this paper.

I, Hadrien A.R. Devillepoix, as first author, endorse that the level of contribution indicated above is accurate.



Contents lists available at ScienceDirect

Planetary and Space Science

journal homepage: www.elsevier.com/locate/pss

A Global Fireball Observatory



H.A.R. Devillepoix^{a,*}, M. Cupák^a, P.A. Bland^a, E.K. Sansom^a, M.C. Towner^a, R.M. Howie^a, B.A.D. Hartig^a, T. Jansen-Sturgeon^a, P.M. Shober^a, S.L. Anderson^a, G.K. Benedix^a, D. Busan^a, R. Sayers^a, P. Jenniskens^{b,c}, J. Albers^b, C.D.K. Herd^d, P.J.A. Hill^d, P.G. Brown^{e,f}, Z. Krzeminski^e, G.R. Osinski^g, H. Chennaoui Aoudjehane^h, Z. Benkhaldounⁱ, A. Jabiriⁱ, M. Guennounⁱ, A. Barkaⁱ, H. Darhmaoui^j, L. Daly^{k,a,1}, G.S. Collins^m, S. McMullan^m, M.D. Suttleⁿ, T. Ireland^o, G. Bonning^p, L. Baeza^p, T.Y. Alrefay^q, J. Horner^r, T.D. Swindle^s, C.W. Hergenrother^s, M.D. Fries^t, A. Tomkins^u, A. Langendam^u, T. Rushmer^v, C. O'Neill^v, D. Janches^w, J.L. Hormaechea^x, C. Shaw^y, J.S. Young^z, M. Alexander^{aa}, A.D. Mardon^{ab}, J.R. Tate^{ac}

^a Space Science and Technology Centre, School of Earth and Planetary Sciences, Curtin University, GPO Box U1987, Perth, WA, 6845, Australia

^c NASA Ames Research Center, Moffett Field, California, 94035, USA

^b SETI Institute, Carl Sagan Center, Mountain View, CA, 94043, USA

^d Dept. of Earth and Atmospheric Sciences, 1-26 Earth Sciences Building, University of Alberta, Edmonton, Alberta, T6G 2EG, UK, Canada

^e Dept. of Physics and Astronomy, University of Western Ontario, London, ON, N6 A 3K7, Canada

^f Dept. Earth Sciences, University of Western Ontario, London, ON, N6 A 3K7, Canada

^g Institute for Earth and Space Exploration, University of Western Ontario, London, ON, N6 A 3K7, Canada

^h GAIA Laboratory, Hassan II University of Casablanca, Faculty of Sciences Ain Chock, Km 8 Route d'El Jadida, 20150, Casablanca, Morocco

ⁱ Oukaimeden Observatory, LPHEA, Cadi Ayyad University, Marrakech, Morocco

^j School of Science and Engineering, Al Akhawayn University in Ifrane, 53000, Morocco

^k School of Geographical and Earth Sciences, University of Glasgow, Glasgow, G12 8QQ, United Kingdom

¹ Australian Centre for Microscopy and Microanalysis, University of Sydney, Sydney, 2006, NSW, Australia

^m Dept. Earth Science and Engineering, Imperial College, London, SW7 2AZ, United Kingdom

ⁿ Dipartimento di Scienze della Terra, Università di Pisa, 56126, Pisa, Italy

^o Planetary Science Institute, The Australian National University, Canberra, ACT, 2611, Australia

^p Research School of Earth Sciences, The Australian National University, Canberra, ACT, 2611, Australia

^q National Center for Astronomy, KACST, Riyadh, Saudi Arabia

^r Centre for Astrophysics, University of Southern Queensland, Toowoomba, Queensland, 4350, Australia

^s Lunar and Planetary Laboratory, University of Arizona, 1629 E University Boulevard Tucson, Arizona, 85721, USA

^t Astromaterials Research and Exploration Science, NASA Johnson Space Center, Houston, TX, 77058, USA

^u School of Earth, Atmosphere and Environment, Melbourne, Victoria, Australia

^v Department of Earth and Planetary Sciences, Macquarie University, North Ryde, Sydney, NSW, 2109, Australia

^w ITM Physics Laboratory, Heliophysics Science Division, GSFC/NASA, Greenbelt, MD, 20771, USA

^x Facultad de Ciencias Astronómicas y Geofísicas, Universidad Nacional de La Plata, Argentina; Estacion Astronomica Rio Grande, Rio Grande, Tierra del Fuego, Argentina

^y Mullard Radio Astronomy Observatory, University of Cambridge, Lord's Bridge, Barton, Cambridge, CB3 7EX, United Kingdom

^z Cavendish Laboratory, University of Cambridge, Cambridge, CB3 0HE, United Kingdom

^{aa} Galloway Astronomy Centre, Glasserton, Nr Whithorn, Scotland, DG8 8NE, United Kingdom

^{ab} Newby Hall and Gardens, Ripon, Yorkshire, HG4 5AE, United Kingdom

^{ac} The Spaceguard Centre, Llanshay Lane, Knighton, Powys, LD7 1LW, United Kingdom

ARTICLE INFO

Keywords:

Meteoroids

Meteors

Asteroids: general

ABSTRACT

The world's meteorite collections contain a very rich picture of what the early Solar System would have been made of, however the lack of spatial context with respect to their parent population for these samples is an issue. The asteroid population is equally as rich in surface mineralogies, and mapping these two populations (meteorites and asteroids) together is a major challenge for planetary science. Directly probing asteroids achieves this at

* Corresponding author.

E-mail address: hadrien.devillepoix@curtin.edu.au (H.A.R. Devillepoix).

<https://doi.org/10.1016/j.pss.2020.105036>

Received 15 November 2019; Received in revised form 28 April 2020; Accepted 11 June 2020

Available online 23 July 2020

0032-0633/© 2020 Elsevier Ltd. All rights reserved.

high cost. Observing meteorite falls and calculating their pre-atmospheric orbit on the other hand, is a cheaper way to approach the problem. The Global Fireball Observatory (GFO) collaboration was established in 2017 and brings together multiple institutions (from Australia, USA, Canada, Morocco, Saudi Arabia, the UK, and Argentina) to maximise the area for fireball observation time and therefore meteorite recoveries. The members have a choice to operate independently, but they can also choose to work in a fully collaborative manner with other GFO partners. This efficient approach leverages the experience gained from the Desert Fireball Network (DFN) pathfinder project in Australia. The state-of-the-art technology (DFN camera systems and data reduction) and experience of the support teams is shared between all partners, freeing up time for science investigations and meteorite searching. With all networks combined together, the GFO collaboration already covers 0.6% of the Earth's surface for meteorite recovery as of mid-2019, and aims to reach 2% in the early 2020s. We estimate that after 5 years of operation, the GFO will have observed a fireball from virtually every meteorite type. This combined effort will bring new, fresh, extra-terrestrial material to the labs, yielding new insights about the formation of the Solar System.

1. Introduction

Our view of the early solar system is provided by the variety of meteorites that fall to Earth each year. These meteorites tell of diverse processes affecting the building of planetesimals and planets in the earliest stages of our solar system. Our interpretation of the messages provided is clouded by a lack of constraint in where and when these processes are occurring. Meteorites are sourced primarily from bodies which are in Earth crossing orbits and from the Main Asteroid Belt. Spectral analysis of asteroids shows diverse surface compositions that can be related to the mineralogies of meteorites. Still, relating meteorites to potential source bodies is difficult because of space weathering of asteroids, and the close relationships of many meteorites. Direct mapping of meteorites to a particular asteroid is being achieved through remote analysis and sample-return missions, which achieve the goals at extremely high cost (e.g. JAXA's *Hayabusa-1* and *Hayabusa-2*, NASA's *OSIRIS-REx* and *Stardust* missions). A more complete overview of the relationships between meteorites and asteroids is a major challenge for planetary science (Reddy et al., 2015).

A cheaper approximation is to observe meteorite falls with enough accuracy to calculate their pre-atmospheric orbit and the location of the meteorites on the ground for recovery. This has been done for over 50 years, but at a low success rate given the frequency of meteorite dropping events within the deployed camera coverage (Halliday et al., 1989; Oberst et al., 1998). Although the number of successful meteorite recoveries has increased significantly in the last 10–15 years (Borovička et al., 2015), there is still a significant deficit of meteorites found compared to the number of meteorite producing fireballs that are observed. Systematic issues in the way observation data are analysed may contribute to this discrepancy (Spurný et al., 2014), but locating meteorites outside of populated areas is a non-trivial task and is likely the main limiting factor. The recovery rate could be increased by improving search techniques, which generally involve small teams conducting visual searches on foot (for the most part). Another solution to increase the global number of meteorites recovered is making the collecting area larger, in order to observe more falls (Howie et al., 2017).

Conversely, in some parts of the world visually observed meteorites falls are routinely recovered without the help of specific fireball observing equipment. Over the last 20 years, a number of meteorites falls have been recovered in Morocco thanks to the considerable local interest and awareness in meteorites, relying on intuitive searching methodology (Chennaoui Aoudjehane et al., 2012; Chennaoui Aoudjehane and Agee, 2019), effectively making this part of the world the area where the largest number of falls are recovered per unit of surface area (Chennaoui Aoudjehane, 2016). In the USA, a number of falls have been recovered in recent years without the aid of detailed fireball observations, using Doppler radar signatures of the falling meteorites (more on this in Sec. 3.3.1). For these specific areas, deploying fireball observation hardware is merely an easy way of adding value (orbital context) to the samples that are already being recovered.

From the 30–40 meteorite cases for which an orbit has been derived,

some clues about where the most common types of meteorites come from are already starting to emerge. Orbits of LL chondrites seem to point to a source in the inner edge of the inner main belt. Combined with Cosmic-Ray Exposure (CRE) ages, the dynamical history of recovered H and L chondrites indicate that there might be multiple sources for these groups. CM chondrites likely come from a source that can efficiently feed material into the 3:1 mean-motion resonance with Jupiter. The reader is referred to Jenniskens (2014, 2020) and references therein for a more in-depth review.

In this benchmark paper we describe how a global collaborative approach to fireball observation and meteorite recovery will help build a geological map of the inner Solar System as well as a better understanding of the flux of centimetre to metre scale impactors on Earth.

2. The Global Fireball Observatory collaboration

The Global Fireball Observatory (GFO) collaboration was established in 2017 thanks to support from the Australian Research Council Linkage Infrastructure, Equipment and Facilities (LIEF) program. The goal is to deploy fireball observatories all around the world to maximise fireball observation area and therefore meteorite recoveries, using common hardware and data reduction, and facilitate collaboration amongst a range of planetary science partner institutions. The project brings together over 19 institutions within Australia, USA, Canada, Morocco, Saudi Arabia, UK, and Argentina (Table 1). A key aspect of the project is that partners have independence. Each partner has a discrete network which is operated entirely independently as a distinct regional or national network. The GFO itself can be thought of as an emergent “network-of-networks”, akin to a large-scale astronomy facility, allowing datasets from partner networks to be consolidated and analysed with common processing. The project builds upon the engineering heritage from the Desert Fireball Network (DFN) pathfinder project in Australia in order to roll out operational partner networks as quickly as possible.

A few systems were installed in California prior to the full scale global deployment and establishment of the GFO collaboration. This effort soon paid off with the first GFO success—the recovery of the Creston meteorite in California in 2015 (Jenniskens et al., 2019). The one-design approach for the camera hardware (see Sec. 3.1) brings economies of scale on hardware design and building costs, and makes it easier to develop and maintain an automated data reduction pipeline. This approach also allows research groups that are not necessarily involved with fireball studies to broaden their range of expertise quickly and at a relatively low cost.

Current partner networks are listed in Table 1. Ground coverage for the GFO is plotted on maps for each part of the world in Fig. 1-2-3-4-5. To define coverage of a given area, we distinguish two criteria. One for *meteorite recovery*: based on the published details of previous falls in the literature (Borovička et al. (2015) and references therein) and limits on precision of astrometric measurements close to horizon. We estimate that at least one camera needs to be closer than 130 km to the meteoroid ground track, and a second viewpoint within 300 km, in order to reliably

Table 1
Partner networks within the Global Fireball Observatory collaboration.

Network name	Region/Country	Managing institutions
Desert Fireball Network (DFN)	Western and South Australia - Fig. 1	Curtin University
NASA Meteorite Tracking and Recovery Network	California and Nevada, USA - Fig. 2	SETI Institute, NASA Ames Research Center
Moroccan Observatory for Fireball Detections (MOFID)	Morocco - Fig. 3	Hassan II University of Casablanca, Oukaïmeden Observatory
Meteorite Observation and Recovery Project 2.0 (MORP 2.0)	Alberta and Saskatchewan, Canada - Fig. 2	University of Alberta
Southern Ontario Meteor Network (SOMN)	South-Western Ontario, Canada - Fig. 2	University of Western Ontario
UK Fireball Network (UKFN)	United Kingdom - Fig. 4	Imperial College London, University of Glasgow, University of Cambridge
TBD	Australian Capital Territory, New South Wales - Fig. 1	Australian National University
TBD	Victoria, Australia	Macquarie University, Australia
Kingdom of Saudi Arabia Fireball Network (KSAFN)	Kingdom of Saudi Arabia - Fig. 5	Monash University National Center for Astronomy, King Abdulaziz City for Science and Technology
Arizona Fireball Network (AZFN)	Arizona, USA - Fig. 2	University of Arizona
TBD	Texas, USA	NASA Johnson Space Center
TBD	Queensland, Australia - Fig. 1	University of Southern Queensland
TBD	Tierra del Fuego, Argentina	NASA Goddard Space Flight Center, Estacion Astronomica Rio Grande

calculate meteorite fall positions. We also distinguish the sampling area of *fireball orbits*, for which we relax the previous criterion to having two viewpoints within 300 km.

With all networks combined, the Global Fireball Observatory

collaboration covers 0.6% of the Earth's surface for meteorite recovery (dark purple in Figs. 1 and 2), and 1% of Earth for orbital coverage (light purple). In the early 2020s, the aim will be to cover 2% of Earth for meteorite recovery, and 3% for orbital sampling.

3. Methods

3.1. Observatory hardware

The observatories employed in the GFO are built upon the engineering heritage of the observatories used by the Desert Fireball Network in Australia. The DFN observatories were designed with a strong focus on reliability and autonomy, with the first digital prototypes assembled in 2013, iterating to a design that was eventually mass-produced in 2014–2015 and rolled out to cover about a third of Australia using approximately 50 stations (Howie et al., 2017). To move beyond a network operated by the DFN and make a global expansion via a “network-of-networks” possible, changes to the design were required. The motivation for the update was to improve the manufacturability of the design (as a large number of observatories were required in a short period of time) and to improve the maintainability and usability of the observatories (Howie, 2019). The update notably aimed to improve cooling and add in the capability to heat the observatory for cold weather operation, allowing the system to operate from over 50°C on hot days in the Australian outback down to nearly –50°C in the Canadian winter. The standard definition analogue video camera was replaced by a higher resolution (2.3 MP) digital model capable of capturing periodic long exposure calibration frames as well as detect bright daytime bolides. Finally, weatherproof external connections were added to improve observatory connectivity and allow plug-and-play auxiliary instruments such as a radiometer (Buchan et al., 2019).

Along with the hardware improvements, software improvements were also made including a move to a new pulse frequency encoding, resulting in improved fireball velocity data and the addition of periodic calibration frames unobscured by the operation of the liquid crystal shutter for improved astrometry. The software and firmware of the improvements are backwards compatible with the previous observatories,

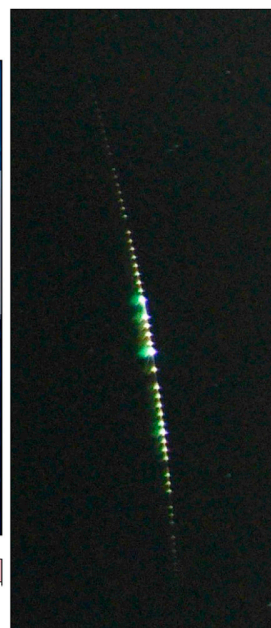
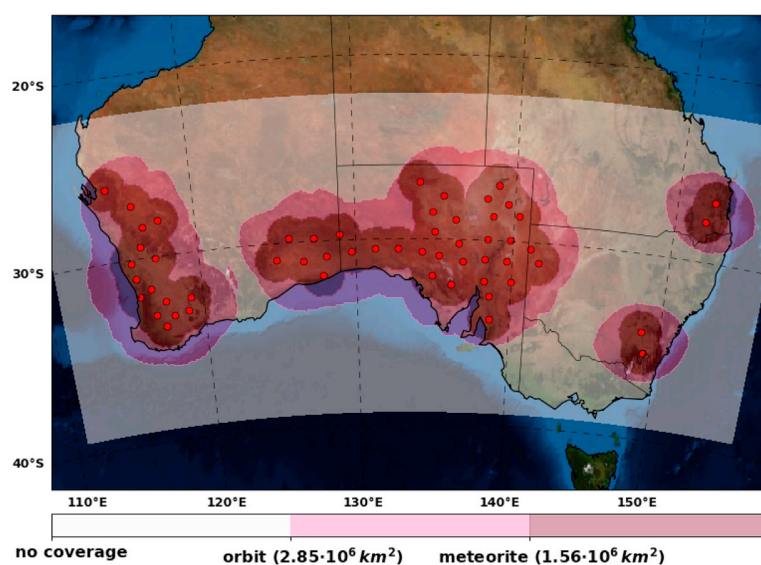


Fig. 1. GFO networks in Australia: Desert Fireball Network (Western and South Australia), South-Eastern Australian Fireball Network, and Queensland Fireball Network. left: Fireball observation coverage in Australia as of January 2020. Each red dot corresponds to an observatory site. See Sec. 2 for explanation on coverage area. right: Fireball observed from Mount Stromlo observatory near Canberra on Sept 9, 2019. (For interpretation of the references to colour in this figure legend, the reader is referred to the Web version of this article.)

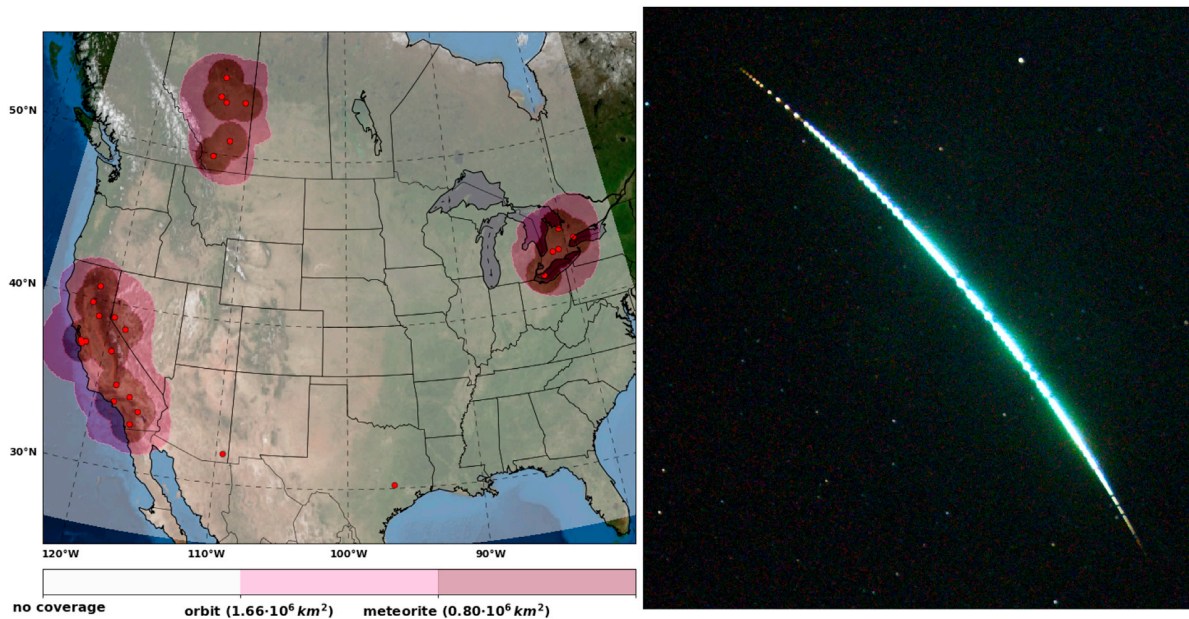


Fig. 2. The GFO networks in North America: NASA Meteorite Tracking and Recovery Network (California and Nevada), Meteorite Observation and Recovery Project 2.0 (Alberta), Southern Ontario Meteor Network (SOMN), Arizona Fireball Network. left: Fireball observation coverage in North America as of January 2020. Each red dot corresponds to an observatory site. See Sec. 2 for explanation on coverage area. right: Fireball observed from the Allen Telescope Array station in California on Jul 1, 2019. (For interpretation of the references to colour in this figure legend, the reader is referred to the Web version of this article.)

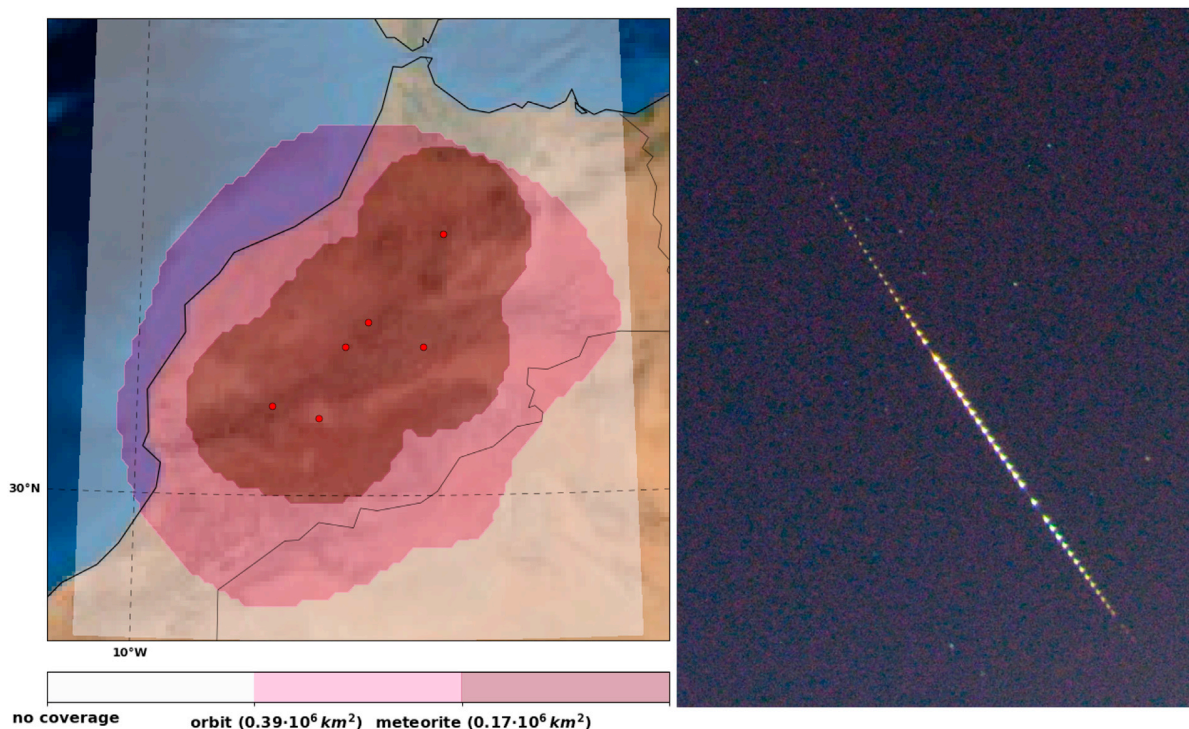


Fig. 3. The Moroccan Observatory for Fireball Detections (MOFID). left: Fireball observation coverage in Morocco as of January 2020. Each red dot corresponds to an observatory site. See Sec. 2 for explanation on coverage area. right: Fireball observed from Oukaïmeden Observatory in Morocco on Dec 25, 2018. (For interpretation of the references to colour in this figure legend, the reader is referred to the Web version of this article.)

which allows improvements made to be easily ported to older observatory models. In addition, the new observatories also run a customised version of Freeture (the software designed to run the Fireball Recovery and Interplanetary Observation Network cameras (Audureau et al., 2014)) to handle the digital video observations. The new revision of the

observatory is shown in Fig. 6 (cf. Howie et al. (2017) Fig. 6).

3.2. Data reduction

With the current number of cameras installed (~ 100), over 6 TB of

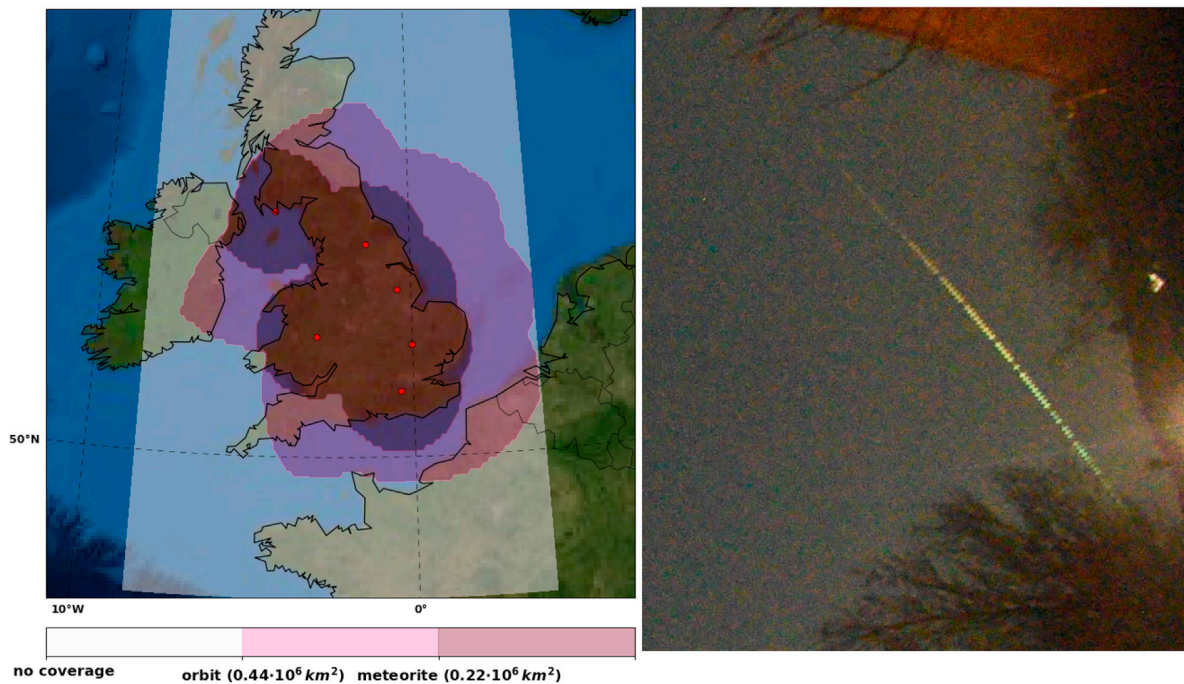


Fig. 4. The UK Fireball Network (UKFN). left: Fireball observation coverage in the UK as of January 2020. Each red dot corresponds to an observatory site. See Sec. 2 for explanation on coverage area. right: Fireball observed from Welwyn station in the South-East of the UK on Feb 15, 2019. (For interpretation of the references to colour in this figure legend, the reader is referred to the Web version of this article.)

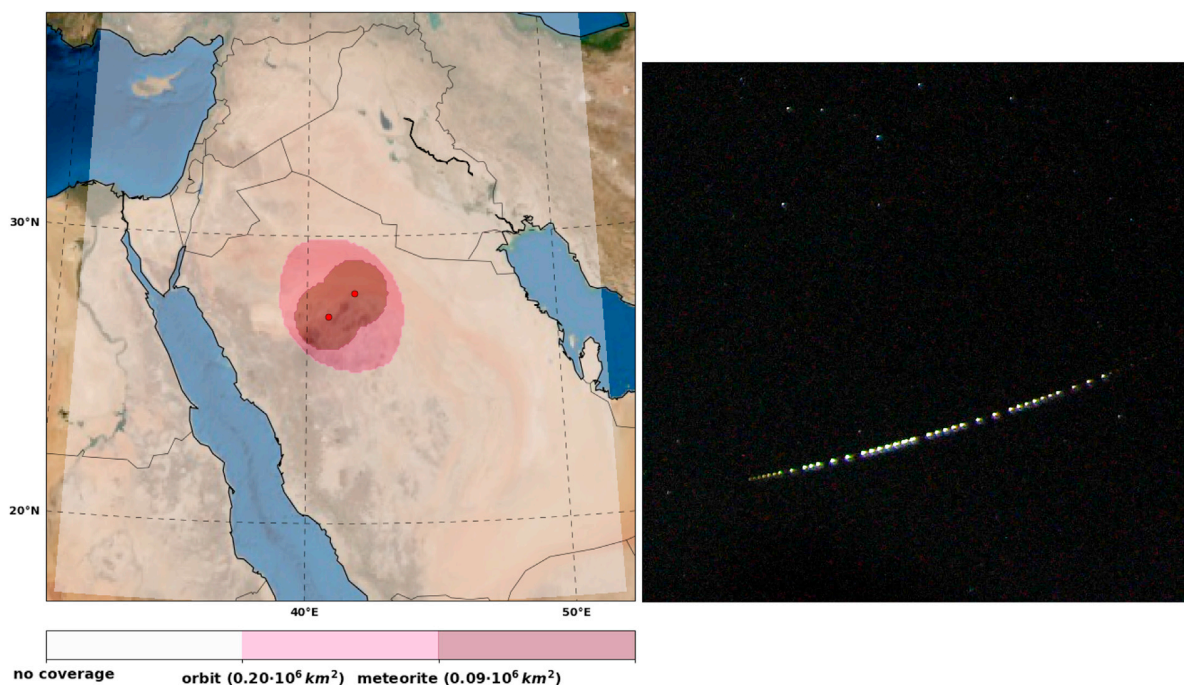


Fig. 5. The Kingdom of Saudi Arabia Fireball Network (KSAFN). left: Fireball observation coverage in the Arabian peninsula as of January 2020. Each red dot corresponds to an observatory site. See Sec. 2 for explanation on coverage area. right: Fireball observed from Alshaiq station in the Ha'il region on Jan 31, 2020. (For interpretation of the references to colour in this figure legend, the reader is referred to the Web version of this article.)

raw imagery is collected every night by the GFO. An automated data reduction pipeline has been developed to quickly determine which images contain fireballs, and process these events to determine meteorite fall locations, as well as calculate the meteoroids' dynamical origins (orbits).

Fireball event detection and corroboration between cameras are detailed by [Towner et al. \(2020\)](#), this part is mostly done on the embedded PCs on-board the observatories, while other steps of the pipeline are run on a central server. These include astrometric calibration of observational data, triangulation and analysis of fireball trajectories,



Fig. 6. GFO fireball observatory showing (clockwise from bottom left) embedded PC, video camera, DSLR photographic camera, hard disc drives, observatory electronics board and 4G data modem, from (Howie, 2019).

orbit determination and darkflight modelling for meteorite recoveries.

Minute of arc astrometric precision is achieved with the method of Devillepoix (2018), allowing reliable astrometric measurements of observed fireballs down to $\sim 5^\circ$ elevations for clear horizons, and $\sim 10^\circ$ in the case of more light polluted and/or partly obstructed skies.

The triangulation and trajectory analysis are performed using a variety of methods, as no single technique exists that can reliably determine the state vector of a large meteoroid throughout the trajectory with full uncertainty propagation. We notably use the straight line trajectory determination method of Borovička (1990), run in combination with various dynamical analysis techniques (Sansom et al., 2015, 2017, 2019b). Some more modern approaches aim to derive the state vectors and physical parameters concurrently (Sansom et al., 2019a; Jansen-Sturgeon et al., 2019a).

The pre-encounter orbit of a meteoroid is determined by numerical integration, as described by Jansen-Sturgeon et al. (2019b). On a typical fireball observed with our camera hardware, processed using the above methods, we get a pre-atmospheric speed formal uncertainty of $\sim 60 \text{ m s}^{-1}$. According to Granvik and Brown (2018), this precision on the meteoroid entry speed is generally sufficient to get accurate source region information when using Near-Earth Objects (NEO) population models like the one described by Granvik et al. (2018). The authors say that better precision would evidently lead to better results, but the difference is minor unless the speed and radiant measurements improve by orders of magnitude.

The meteorite search region is determined from the final conditions given by the triangulation and dynamic modelling stage, and an atmospheric model. The atmospheric model is calculated following the methodology described by Devillepoix et al. (2018).

From this model, the darkflight integrator interpolates wind speed, wind direction, pressure, temperature and relative humidity, at whatever position and time is required (available heights range up to $\sim 30 \text{ km}$). A number of virtual particles of varying mass, density, and shape are generated within the modelled uncertainty surrounding the meteoroid's final position and velocity along the observed trajectory. These particles are then numerically integrated through their ballistic descent, under the influence of meteoroid ablation and atmospheric winds. The numerical integration uses the 3D equations of the meteoroid's motion to realistically model the cosmic material until it reaches Earth's surface, producing a distribution of possible meteorite impact sites. This Monte Carlo

approach aims to encompass all uncertainties associated with the meteoroid state vector and physical properties, to derive probabilistic maps on the ground of where the meteorites likely landed (for an example see Fig. 10 of Devillepoix et al. (2018)).

3.3. 21st century meteorite searching techniques

Based on the knowledge gained during the meteoroid's initial bright flight phase (see Sec. 3.2), the position of the meteoroid must be numerically integrated through the last tens of kilometres of the atmosphere (the dark flight phase), carrying forward all the uncertainty on the state vector, physical characteristics (shape, mass, density, inner structure), and atmospheric conditions. This process typically constrains the meteorite's fall location to an area on the order of a square kilometre for a favourable case, but up to several tens of square kilometres. These large areas, combined with sometimes unfavourable searching terrains, can significantly inhibit meteorite recoveries. Here we present some recent techniques that can help refine search areas.

3.3.1. Weather Doppler radars

In some regions of the world, tight grids of weather Doppler radars have been set up to detect precipitation. These can also be used to detect falling meteorites (Fries et al., 2014). As the radars scan very low on the horizon (down to 0.5°), the altitudes at which the meteorites are detected are relatively low (sometimes down to a kilometre above the ground). This can lead to tightly constrained fall positions on the ground without necessarily taking the winds into account.

The detailed analysis of radar data have notably helped with some meteorite recoveries: Grimsby (Brown et al., 2011), Sutter's Mill (Jenniskens et al., 2012), Creston (Jenniskens et al., 2019), Dishchii'bikoh (Palotai et al., 2019), and Hamburg (Brown et al., 2019). Although optical data were still used to determine the trajectory and orbit in these cases, the radar signatures were crucial to quickly locate the whereabouts of the meteorites on the ground, with a precision that exceeds what the observatory data alone would have been capable of achieving.

In areas with good radar coverage (mainly North America), we expect these data to simplify the recovery of GFO meteorites. Also, with the GFO observatories now having daylight bolide detection capability (24h video capture), for these cases, we anticipate traditional meteorite recovery after darkflight integration to be even more difficult because of larger uncertainties; radar data will constitute important clues to help the recovery process.

3.3.2. Use of small Uncrewed Aerial Vehicles (UAVs)

With the hope that the ground search area has been reduced as much as possible, the recovery still depends on human vision and attention over long periods of time. The deterioration of an individual's ability to identify signals or events over time has been documented as "vigilance decrement", it often becomes apparent after less than 1 h of engaging in repetitive a task (Parasuraman, 1986; See et al., 1995). When considering that a typical search lasts for 8 h per day, for sometimes more than 10 consecutive days, vigilance decrement becomes a serious problem.

To counter these issues, a dedicated team is working on automated meteorite searching techniques using a combination of *robotic surveying* with small Uncrewed Aerial Vehicles (UAVs, also known as drones), and *object recognition* using deep learning algorithms (Citron et al., 2017; Anderson et al., 2019).

From a technology standpoint, the surveying part is relatively easy and is becoming cheap, thanks to the large commercial off-the-shelf development of small UAVs that come with easy to use control and surveying software. Field tests show that one drone operator can reduce the total searching time by a factor of 10 compared to foot searching.

The real challenge lies with machine vision software. The automated detection of objects in images using deep learning is a very active field of research (Szegeedy et al., 2013). These deep learning approaches typically require a lot of training data. Acquiring a meteorite training dataset is a

non-trivial problem, as meteorites vary significantly in size, shape, colour etc. Nonetheless, initial tests show that, using state of the art deep learning technology, 95% of the meteorites used for validation can be found. In addition, it is equally important to minimise the number of false positive identifications which otherwise require manual evaluation by human researchers.

We expect the first live UAV searching tests on a real meteorite fall to be conducted in 2020 in Australia. Once optimised, this technique will be used on several DFN fall sites that have not yet been searched because of a lack of person time, and eventually become a general tool for meteorite searching around the world.

3.4. Other international efforts

The Czech/European Fireball Network are covering a large fraction of central Europe, and have a long track record for recovering meteorites (Borovička et al., 2015). Their expertise in high-resolution long exposure camera systems contributed to shaping the DFN pathfinder project (Bland et al., 2012).

The Fireball Recovery and Interplanetary Observation Network (FRIPON) (Colas et al., 2015) and their partners in Europe are well under way to covering a significant part of Western Europe. They have chosen a radically different approach to observation hardware, with lower resolution observatories but on a much tighter grid, adding a level of reliability when poor weather conditions are present. They developed reduction methods suitable for this different strategy (Jeanne et al., 2019).

Along with other smaller groups (see Kotten et al. (2019) for a review), the global combined effort of fireball observation networks is going to create an unprecedented large web collecting centimetre to metre-scale objects impacting our planet.

4. Likely GFO outcomes in the early 2020s

4.1. Meteorites

There are 10^4 sizeable meteorites (> 0.1 kg) reaching the Earth's surface every year (Bland and Artemieva, 2006). With 2% of the Earth monitored by fireball observatories, assuming a conservative average of 75% downtime because of daylight and cloudy conditions, the full GFO will observe ~ 50 falls per year. From basic statistics on the falls subset recorded in the Meteoritical Bulletin Database,¹ the main meteorite groups fall in these proportions:

- Ordinary Chondrites: 70% (8% LL, 33% L, 28% H)
- Howardites, Eucrites, & Diogenites (5%)
- Carbonaceous chondrites (3.5%)
- Irons (3.5%)

The GFO will regularly observe many of these types of meteorites falling. Better still, it is statistically likely that representatives of almost every meteorite group will have been observed to fall over the course of 5 years of observation, including a Martian meteorite ($\sim 1\%$ of falls).

Regardless of the type of material detected by the GFO, the advanced data reduction and concomitant potential for rapid recovery of freshly fallen meteorites from GFO data provide new opportunities to reduce the amount of time that meteorite specimens spend in the field, thus minimising terrestrial contamination and weathering (McCubbin et al., 2019). Such events enable the application of best methods of curation in support of sample return, and build on lessons learned from previous falls (e.g. the organic-rich Tagish Lake meteorite (Herd et al., 2016)). In this way, meteorites recovered as a result of the GFO can be collected and transferred to curation facilities in such a manner as to preserve them

against the oxidative, organic- and moisture-rich environment of the Earth's surface, and maximise their scientific return (McCubbin et al., 2019).

Here we present a selection of highlights of what questions the GFO might be able to answer over the next few years, given the recovery of a full suite of meteorite types.

Ordinary chondrites H chondrites are the group that has the most sample with orbits recovered, however there is still no consensus on what the parent body is (Brown et al., 2019). We hope that a large number of orbits for these objects can help pinpoint the various sources for this class of objects. Although the sources for LL chondrites (broadly associated with the Flora family) and most of the shocked L chondrites (Gefion) are a little bit clearer, there are still some questions (see Jenniskens (2020) for a review).

Iron meteorites. Irons make up about 3.5% of meteorite falls. It would be fascinating to recover an iron meteorite with a well-defined orbit. Long Cosmic-Ray Exposure (CRE) ages are the norm for magmatic iron meteorites (Eugster et al., 2006). Defined peaks in CRE ages are clear in several groups, indicating discrete break-up events. Group III irons show a peak at around 650 Myr, and group IVs at around 400 Myr. On the other hand some irons have CRE ages exceeding 1 Gyr. These extreme ages are certainly due in part to the strength and preferential survival of iron meteorites, but the fact that we see defined CRE age peaks indicates that their extreme ages may also be a product of an unusual orbital history. The suggestion that the parent bodies for magmatic irons formed in the terrestrial planet region rather than at asteroidal distances, and that they were scattered into the main belt following interactions with planetary embryos (Bottke et al., 2006), may offer an explanation. It is possible that this could be resolved with high quality orbital data, allowing source region determination.

Carbonaceous chondrites Although carbonaceous chondrites with well-defined orbits have been recovered (C2-ungrouped *Tagish Lake* (Brown et al., 2000); CM2 *Maribo* (Borovička et al., 2019; Haack et al., 2012) and *Sutter's Mill* (Jenniskens et al., 2012)), the dataset is currently too small to draw firm conclusions about the Solar System history of different groups, and how orbits relate to source regions and CRE ages. Expanding this dataset is a headline priority for the GFO collaboration. The distribution of CRE ages varies widely between groups. The majority of CK and CV chondrites have ages in the range 8–30 Myr. CO chondrites show a diffuse peak at around 30 Myr. But CM and CI chondrites are completely different. These meteorites have very short exposure ages. CMs have a peak at 0.2 Myr, but some have ages of < 0.05 Myr (Nishiizumi and Caffee, 2009). The differences here likely reflect very different source regions for these groups. It may be that CK/CV/CO chondrites are delivered from the main belt, while CI/CM come from a parent body on an Earth-crossing orbit. A larger dataset of meteorites with orbits will allow us to determine their provenance.

From a comet Comets are the most pristine material in the Solar System, containing a high-fidelity record of early Solar System processes, including the variety of stellar sources that contributed to our protoplanetary disk, and the earliest chemical processes that occurred within it (Davidsson et al., 2016). They may have supplied Earth's water and organics. The Stardust mission to recover 10^{-6} kg of Comet 81P/Wild 2 (Brownlee et al., 2006) is testimony to the value placed on comets as witnesses of early Solar System processes. The DFN recently observed a meteorite dropping fireball on a peculiar orbit (Fig. 7). This meteoroid is clearly dynamically de-coupled from the main belt. Although more work is required to determine its origin, it could be a fragment of a Jupiter family comet and maybe even be part of a meteor shower. Unfortunately the estimated ~ 0.1 kg surviving mass fell into the ocean, annihilating chances of recovery, but at the same time proving that the endeavour of collecting meteorite samples goes well beyond a simple sampling of main belt material.

From meteor showers So far no meteorite has conclusively been associated with a meteor shower, but we know that this is possible, notably from the Geminids and Taurids streams (Brown et al., 2013a). There have

¹ <https://www.lpi.usra.edu/meteor/metbull.php>.

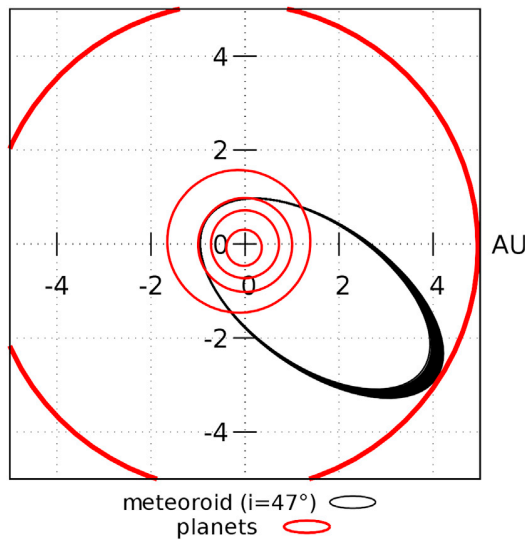


Fig. 7. Ecliptic plot of the orbit of DFN meteorite dropping event *DNI90221_03*. Its large inclination (47°) and its Tisserand criterion with Jupiter of 2.53 make this meteoroid well into the Jupiter Family comet region, beyond any connection with the main asteroid belt.

been cases reported of Geminid meteoroids entering the atmosphere and convincingly leaving a non-zero mass (Spurný and Borovička, 2013; Madioed et al., 2013), a very large network such as the GFO should be able to observe these exceptional events on a more regular basis.

4.2. Large dataset

Not every fireball observed leads to a meteorite, but the collation of all observed events contains precious clues about the near-Earth environment. The distribution of orbits, strengths, and sizes all help build a picture of NEOs at the centimetre to metre-scale sizes. So far the reference dataset remains the legacy work of Halliday et al. (1996) on the MORP survey.

The DFN pathfinder project has already collected $575 > 0.1\text{kg}$ events over its initial 4 year survey, consistent with its 0.4% Earth surveying area (using the size-frequency work of $10^5 > 0.1\text{ kg}$ impactors year^{-1} Earth^{-1} of Bland and Artemieva (2006)). While we wait for the meteorites with orbits to grow to statistically significant numbers, this large dataset of observed meteoroids is going to help refine the size-frequency distribution numbers of meteoroids at the centimetre to metre size ranges. This meteoroid orbit dataset could yield important insights on what might be happening at slightly larger asteroid sizes: there are still some questions about the size of the population of 10–50 m impactors (Brown et al., 2013b). This size range has the potential to do damage on the ground, yet is poorly studied because of the lack of observations: the impacts on Earth are too infrequent, while the bodies are too small to be significantly observed by telescopes in sun-reflected light (Devillepoix et al., 2019). Constraining the impact flux on Earth can also help with the study of Mars, both for dating small areas/young surfaces, which have only accumulated small craters, and also for assessing the hazard to future human space exploration. This scale of impactors is difficult to detect on Mars because of the limits on resolution and coverage of current Mars imagery – impact splotches can occasionally be detected in surface images taken by Mars orbiters, but only in some (dusty) regions of Mars and these features quickly fade. One goal of the current InSight mission is to detect small impacts using seismology to help address the observational bias and lack of good flux estimates (Daubar et al., 2018).

Having a representative survey of the origin of asteroid material will also let us investigate further the lack of low perihelion NEOs proposed by Granvik et al. (2016), and how this effect scales for small objects

(Granvik et al., 2018). Furthermore, a statistically significant number of orbits from suspected meteorite falls is going to help answer important questions. Notably, can we reconcile the statistics on the number of meteorite falls and their classifications with the proportions of falls originating from various parts of the main asteroid belt?

4.3. Probing the meteorite/asteroid link, synergy with NEO hunters

A major goal in the study of small Solar System bodies is reconciling telescopic observations of asteroids and the study of their surface composition through reflectance spectra, with the meteorites analysed in the lab. Other than through expensive sample return missions, the only way to get an irrefutable link between a spectral type of asteroid and a meteorite class is to have observed the meteorite progenitor before atmospheric impact.

Up to mid-2019, four asteroids have been detected before their confirmed impact on Earth: 2008 TC3 (Jenniskens et al., 2009; Farnocchia et al., 2017), 2014 AA (Farnocchia et al., 2016), and more recently 2018 LA and 2019 MO. The two that impacted over land have led to the recovery of meteorites (Farnocchia et al., 2019). These asteroids were detected by telescope facilities such as the Catalina Sky Survey (CSS), the Panoramic Survey Telescope and Rapid Response System (Pan-STARRS), and the Asteroid Terrestrial-impact Last Alert System (ATLAS). Each have different and complementary NEO hunting strategies, with ATLAS covering the entire visible sky very rapidly at shallow depths, Pan-STARRS with a strong focus on a deep survey at opposition, and CSS somewhere in the middle (Tonry et al., 2018).

With the Large Synoptic Survey Telescope (LSST) coming online in 2022 (Ivezić et al., 2019), the number of known asteroids is going to significantly increase, as is the number of NEOs and the number of imminent impactors. The meteorite dropping objects observed by the GFO are typically decimetre to metre-scale, a size that will be detectable by LSST in the hours/days leading up to the impact, if the solar elongation approach is favourable.

To get a better idea of what we can expect LSST to observe, we have carried out a small study, taking the 20 largest objects seen by the DFN pathfinder project during the first 4 years of science operations, and assuming LSST was online carrying its so-called “Wide Fast Deep” survey. It is not clear at present what the observing strategy is exactly going to be, and the details of this strategy will have large implications for linking tracklets from fast moving objects together. For simplicity here, the definition for a successful observation by LSST is if the telescope was to get a single picture of a specific object. We also assume that LSST images the Southern sky at $> 90^\circ$ solar elongations once every 3 days. We integrated backwards the positions of the meteoroid from the impact time, and generated ephemerides projected into (solar elongation, declination) coordinates, as these coordinates are easily relatable with the LSST survey. Along with the ephemerides, we calculated the illumination of the targets and their brightness over time, assuming an S-type albedo (0.15) for all objects. Most of our large objects are only visible in the last 10–20 h before impact (Fig. 8), and most have relatively large solar elongations (Fig. 9). This skew towards large solar elongations likely comes from the fact that the objects impacted at night time. Also, most of the objects seem to spend their last hours in Southern declinations (Fig. 9). This observation bias is caused by the mostly Southern location of the DFN pathfinder project, it is not expected to scale with a Global Fireball Observatory. We note that *DNI70630_01*, a 1.3 m object observed in South Australia (Devillepoix et al., 2019), would have remained visible to LSST for over 4 days before impact, and therefore would have had a very high chance of being detected.

Statistically speaking, when we convolve the observability of these 20 objects with the Wide-Fast-Deep survey of LSST, we get 3.6 objects detected by LSST. We estimate the coverage of the Earth to have been $\sim 0.4\%$ for the DFN pathfinder project over these 4 years. Scaling this to the Global Fireball Observatory (2% Earth) would give us ~ 2 GFO meteoroids pre-detected every year by LSST. It is not exactly clear how many of these

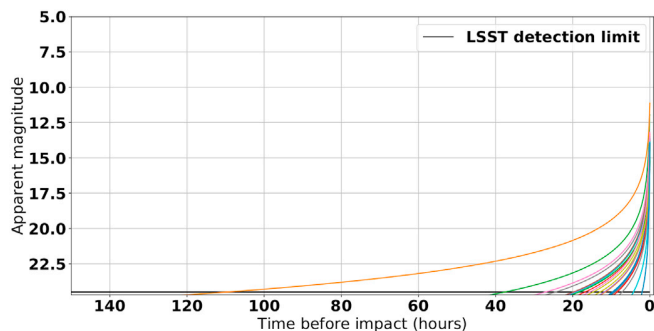


Fig. 8. Estimated pre-impact apparent magnitude of the 20 biggest objects observed by the DFN. The lower cut-off is set to the announced LSST point source limiting magnitude in a single visit (24.5 in V band). The meteoroid plotted in orange, visible for over 100 h, is DN170630_01, described by Devillepoix et al. (2019). (For interpretation of the references to colour in this figure legend, the reader is referred to the Web version of this article.)

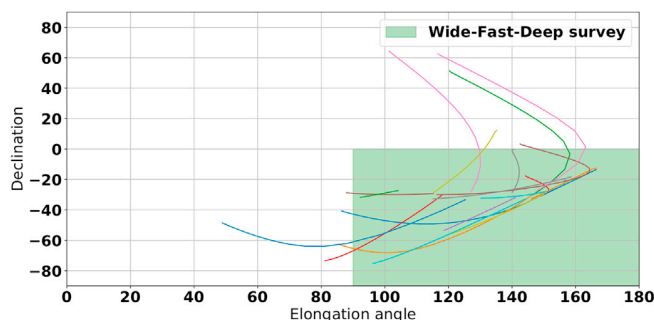


Fig. 9. Pre-entry sky positions for the 20 biggest objects observed by the DFN. The paths are cut off once when the objects go fainter than apparent magnitude 24.5 (LSST limit). The green area corresponds to the so-called “Wide Fast Deep” survey of the LSST, with revisits expected every 3 days. (For interpretation of the references to colour in this figure legend, the reader is referred to the Web version of this article.)

would actually be flagged as new objects and sent as alerts by the LSST processing pipeline (see Chesley and Veres (2017) for a review). This alert process would be helpful to enable follow-up observations before impact, as was the case for 2008 TC3.

In all cases, the GFO/LSST synergy will not only give strong astrometric constraints to refine calculated orbits, but also help constrain other characteristic properties such as colours, rotations, and albedos, providing further insights into asteroids/meteorites links.

4.4. Other uses of the data

The GFO’s ability to constantly monitor large areas of the sky can also be applied to transient astronomy. Although rare, the brightest transient events are also the most interesting because they are easy to follow up spectroscopically.

These transients include optical counterparts of Gamma-Ray Bursts. In 2008, GRB 080319B achieved a brightness of $V = 5.3$ (Racusin et al., 2008), well within the magnitude range reachable by a single GFO exposure.

In the era of multi-messenger astronomy, quickly determining the location of gravitational waves is also an area where the GFO can contribute. Albeit not sensitive enough for this particular event, the DFN pathfinder project was notably the first optical observatory on-sky for the neutron star merger GW170817 (LIGO Scientific Collaboration et al., 2017; Andreoni et al., 2017).

The fact that GFO observatories are already recording imagery before

the events happen is useful because some transients cannot be followed up by traditional methods. For example, fast radio bursts experience a frequency-dependent time shift, which would make any emission in the optical arrive before any radio signals are detected (Macquart et al., 2019; Bannister et al., 2019).

Declaration of competing interest

The authors declare that they have no known competing financial interests or personal relationships that could have appeared to influence the work reported in this paper.

Acknowledgements

This research is supported by the Australian Research Council through the Linkage Infrastructure, Equipment and Facilities program (LE170100106). The DFN receives institutional support from Curtin University, and uses the computing facilities of the Pawsey supercomputing center. The team would like to thank the people hosting the observatories.

The NASA Tracking and Recovery Network is funded by NASA grant 80 NSSC18K08. PJ acknowledges logistic support from NASA’s SERVII program.

The UKFN would like to thank a number of people helping with the project: Ian McMullan, Adam Suttle, Pierre-Etienne Martin, Cameron Floyd, Áine O’ Brien, Sammy Griffin, Charlotte Slaymark, Annemarie E. Pickersgill, Peter Chung, Joshua F. Einsle, Mohammad Ali Salik.

The data reduction pipeline makes intensive use of Astropy, a community-developed core Python package for Astronomy (Astropy Collaboration et al., 2013).

Appendix A. Supplementary data

Supplementary data to this article can be found online at <https://doi.org/10.1016/j.pss.2020.105036>.

References

- Anderson, S.L., Bland, P.A., Towner, M.C., Paxman, J.P., 2019. In: Lunar and Planetary Science Conference. Lunar and Planetary Science Conference, p. 2426.
- Andreoni, I., et al., 2017. Publications of the Astronomical Society of Australia 34, e069.
- Astropy Collaboration, et al., 2013. A&A 558, A33.
- Audureau, Y., et al., 2014. In: Rault, J.-L., Roggemans, P. (Eds.), Proceedings of the International Meteor Conference, pp. 39–41. Giron, France, 18–21 September 2014.
- Bannister, K.W., et al., 2019. Science 365, 565.
- Bland, P.A., Artemieva, N.A., 2006. Meteoritics Planet Sci. 41, 607.
- Bland, P.A., et al., 2012. Aust. J. Earth Sci. 59, 177.
- Borovička, J., 1990. Bull. Astron. Inst. Czech. 41, 391.
- Borovička, J., Spurný, P., Brown, P., 2015. Small Near-Earth Asteroids as a Source of Meteorites. University of Arizona Press, pp. 257–280. https://doi.org/10.2458/azu_uapress_9780816532131-ch014.
- Borovička, J., Popova, O., Spurný, P., 2019. Meteoritics Planet Sci. 54, 1024.
- Botke, W.F., Nesvorný, D., Grimm, R.E., Morbidelli, A., O’Brien, D.P., 2006. Nature 439, 821.
- Brown, P.G., et al., 2000. Science 290, 320.
- Brown, P., et al., 2011. Meteoritics Planet Sci. 46, 339.
- Brown, P., Marchenko, V., Moser, D.E., Weryk, R., Cooke, W., 2013a. Meteoritics Planet Sci. 48, 270.
- Brown, P.G., et al., 2013b. Nature 503, 238.
- Brown, P.G., et al., 2019. Meteoritics Planet Sci. 54, 2027.
- Brownlee, D., et al., 2006. Science 314, 1711.
- Buchan S. R. G., Howie R. M., Paxman J., Devillepoix H. A. R., 2019, arXiv e-prints, p. arXiv:1907.12807.
- Chennaoui Aoudjehane, H., 2016. In: 79th Annual Meeting of the Meteoritical Society, p. 6119.
- Chennaoui Aoudjehane, H., Agee, C.B., 2019. LPI Contrib. 2157, 6297.
- Chennaoui Aoudjehane, H., et al., 2012. Science 338, 785.
- Chesley S. R., Veres P., 2017, arXiv e-prints, p. arXiv:1705.06209.
- Citron, R.I., Shah, A., Sinha, S., Watkins, C., Jenniskens, P., 2017. In: Lunar and Planetary Science Conference, p. 2528.
- Colas, F., et al., 2015. In: Rault, J.-L., Roggemans, P. (Eds.), International Meteor Conference Mistelbach, pp. 37–40. Austria.
- Daubar, I., et al., 2018. Space Sci. Rev. 214, 132.
- Davidsson, B.J.R., et al., 2016. A&A 592, A63.

H.A.R. Devillepoix et al.

Planetary and Space Science 191 (2020) 105036

- Devillepoix, H.A.R., 2018. PhD thesis, school of Earth and planetary sciences. Curtin University. <https://espace.curtin.edu.au/handle/20.500.11937/76001>.
- Devillepoix, H.A.R., et al., 2018. *Meteoritics Planet Sci.* 53, 2212.
- Devillepoix, H.A.R., et al., 2019. *MNRAS* 483, 5166.
- Eugster, O., Herzog, G.F., Marti, K., Caffee, M.W., 2006. *Irradiation Records, Cosmic-Ray Exposure Ages, and Transfer Times of Meteorites*, p. 829.
- Farnocchia, D., Chesley, S.R., Brown, P.G., Chodas, P.W., 2016. *Icarus* 274, 327.
- Farnocchia, D., Jenniskens, P., Robertson, D.K., Chesley, S.R., Dimare, L., Chodas, P.W., 2017. *Icarus* 294, 218.
- Farnocchia, D., Chesley, S.R., Chodas, P.W., Christensen, E., Kowalski, R.A., Brown, P.G., Jenniskens, P., 2019. In: *AAS/Division of Dynamical Astronomy Meeting*, 200.04.
- Fries, M., Le Corre, L., Hankey, M., Fries, J., Matson, R., Schaefer, J., Reddy, V., 2014. *Meteoritics Planet Sci.* 49, 1989.
- Granvik, M., Brown, P., 2018. *Icarus* 311, 271.
- Granvik, M., et al., 2016. *Nature* 530, 303.
- Granvik, M., et al., 2018. *Icarus* 312, 181.
- Haack, H., et al., 2012. *Meteoritics Planet Sci.* 47, 30.
- Halliday, I., Blackwell, A.T., Griffin, A.A., 1989. *Meteoritics* 24, 65.
- Halliday, I., Griffin, A.A., Blackwell, A.T., 1996. *Meteoritics Planet Sci.* 31, 185.
- Herd, C.D.K., Hiltz, R.W., Skelhorne, A.W., Simkus, D.N., 2016. *Meteoritics Planet Sci.* 51, 499.
- Howie, R.M., 2019. Mechanical engineering. PhD thesis. Curtin University. <http://hdl.handle.net/20.500.11937/75046>.
- Howie, R.M., Paxman, J., Bland, P.A., Towner, M.C., Cupák, M., Sansom, E.K., Devillepoix, H.A.R., 2017. *Experimental Astronomy*.
- Ivezić, Z., et al., 2019. *APJ (Acta Pathol. Jpn.)* 873, 111.
- Jansen-Sturgeon T., Sansom E. K., Devillepoix H. A. R., Bland P. A., Towner M. C., Howie R. M., Hartig B. A. D., 2019a, arXiv e-prints, p. arXiv:1911.00816.
- Jansen-Sturgeon, T., Sansom, E.K., Bland, P.A., 2019b. *Meteoritics Planet Sci.* 54, 2149.
- Jeanne, S., et al., 2019. *A&A* 627, A78.
- Jenniskens, P., 2014. In: *Jopek, T.J., Rietmeijer, F.J.M., Watanabe, J., Williams, I.P. (Eds.), The Meteoroids 2013, Proceedings of the Astronomical Conference held at A.M. University, Poznań, Poland, Aug. 26-30, 2013. A.M. University Press*, pp. 57–68.
- Jenniskens, P., 2020. In: *IAU General Assembly*, pp. 9–12. <https://doi.org/10.1017/S1743921319003235>.
- Jenniskens, P., et al., 2009. *Nature* 458, 485.
- Jenniskens, P., et al., 2012. *Science* 338, 1583.
- Jenniskens, P., et al., 2019. *Meteoritics Planet Sci.* 54, 699.
- Koten, P., Rendtel, J., Shrubny, L., Gural, P., Borovička, J., Kozak, P., Here, D.O.I., 2019. *Meteors and Meteor Showers as Observed by Optical Techniques*, p. 90.
- Ligo Scientific Collaboration, et al., 2017. *APJ (Acta Pathol. Jpn.)* 848, L12.
- Macquart, J.P., Shannon, R.M., Bannister, K.W., James, C.W., Ekers, R.D., Bunton, J.D., 2019. *APJ (Acta Pathol. Jpn.)* 872, L19.
- Madiedo, J.M., Trigo-Rodríguez, J.M., Castro-Tirado, A.J., Ortiz, J.L., 2013. *Cabrera-Caño J.* 436, 2818. *MNRAS*.
- McCubbin, F.M., et al., 2019. *Space Sci. Rev.* 215, 48.
- Nishiizumi, K., Caffee, M.W., 2009. *Meteoritics and Planetary Science Supplement* 72, 5358.
- Oberst, J., et al., 1998. *Meteoritics Planet Sci.* 33.
- Palotai, C., Sankar, R., Free, D.L., Howell, J.A., Botella, E., Batcheldor, D., 2019. *MNRAS* 487, 2307.
- Parasuraman, R., 1986. *Vigilance, monitoring, and search*. In: *Boff, K.R., Kaufman, L., Thomas, J.P. (Eds.), Handbook of perception and human performance, Vol. 2. Cognitive processes and performance (p. 1–39)*. John Wiley & Sons.
- Racusin, J.L., et al., 2008. *Nature* 455, 183.
- Reddy, V., Dunn, T.L., Thomas, C.A., Moskovitz, N.A., Burbine, T.H., 2015. *Mineralogy and Surface Composition of Asteroids*. University of Arizona Press, pp. 43–63. https://doi.org/10.2458/azu_uapress.9780816532131-ch003.
- Sansom, E.K., Bland, P., Paxman, J., Towner, M., 2015. *Meteoritics Planet Sci.* 50, 1423.
- Sansom, E.K., Rutten, M.G., Bland, P.A., 2017. *AJNR* 153, 87.
- Sansom, E.K., et al., 2019a. *Icarus* 321, 388.
- Sansom, E.K., et al., 2019b. *APJ (Acta Pathol. Jpn.)* 885, 115.
- See, J.E., Howe, S.R., Warm, J.S., Dember, W.N., 1995. *Psychol. Bull.* 117, 230.
- Spurný, P., Borovička, J., 2013. In: *Masiero, J. (Ed.), Meteoroids Conference*. http://www.astro.amu.edu.pl/Meteoroids2013/main_content/data/abstracts.pdf.
- Spurný, P., Haloda, J., Borovička, J., Shrubny, L., Halodová, P., 2014. *A&A* 570, A39.
- Szegedy, C., Toshev, A., Erhan, D., 2013. In: *Burges, C.J.C., Bottou, L., Welling, M., Ghahramani, Z., Weinberger, K.Q. (Eds.), Advances in Neural Information Processing Systems, vol. 26. Curran Associates, Inc.*, pp. 2553–2561. <http://papers.nips.cc/paper/5207-deep-neural-networks-for-object-detection.pdf>
- Tonry, J.L., et al., 2018. *PASP* 130, 064505.
- Towner, M.C., et al., 2020. *Publications of the Astronomical Society of Australia* 37, e008.

Coauthored Paper 3 – Machine learning for semi-automated meteorite recovery

Meteoritics & Planetary Science (2020), Volume 55, Issue 11 p. 2461-2471.

*Seamus Anderson, Martin Towner, Phil Bland, Christopher Haikings, William Volante, Eleanor Sansom, Hadrien Devillepoix, **Patrick Shober**, Benjamin Hartig, Martin Cupak, Trent Jansen-Sturgeon, Robert Howie, Gretchen Benedix, Geoff Deacon*

REPRINTED WITH PERMISSION OF JOHN WILEY AND SONS:

Permission to reproduce this article as part of this thesis has been granted by John Wiley and Sons.

Statement of Authorship

TITLE OF PAPER: MACHINE LEARNING FOR SEMI-AUTOMATED METEORITE RECOVERY

PUBLICATION STATUS: Published.

Author Contributions

I, Patrick M. Shober, as a coauthor, contributed to the reduction of the fireball observations collected, analysis of fireball trajectories and the revisions of the manuscript. These efforts made a 0.5% contribution to the total work of this paper.

I, Seamus L. Anderson, as first author, endorse that the level of contribution indicated above is accurate.



Meteoritics & Planetary Science 1–11 (2020)
doi: 10.1111/maps.13593

Machine learning for semi-automated meteorite recovery

Seamus ANDERSON *¹, Martin TOWNER¹, Phil BLAND¹, Christopher HAIKINGS^{2,3}, William VOLANTE⁴, Eleanor SANSON ¹, Hadrien DEVILLEPOIX ¹, Patrick SHOBER¹, Benjamin HARTIG¹, Martin CUPAK¹, Trent JANSEN-STURGEON ¹, Robert HOWIE ¹, Gretchen BENEDIX¹, and Geoff DEACON⁵

¹Space Science and Technology Center, Curtin University, GPO Box U1987, Perth, Western Australia 6845, Australia

²Spectre UAV Concepts, 191 St Georges Terrace, Perth, Western Australia 6000, Australia

³Amotus Pty Ltd, Level 25/71 Eagle St, Brisbane City, Queensland 4000, Australia

⁴Department of Psychology, Clemson University, 418 Brackett Hall, Clemson, South Carolina 29634, USA

⁵Western Australian Museum, 49 Kew St, Welshpool, Western Australia 6106, Australia

*Corresponding author. E-mail: seamus.anderson@postgrad.curtin.edu.au

(Received 14 July 2020; revision accepted 13 October 2020)

Abstract—We present a novel methodology for recovering meteorite falls observed and constrained by fireball networks, using drones and machine learning algorithms. This approach uses images of the local terrain for a given fall site to train an artificial neural network, designed to detect meteorite candidates. We have field tested our methodology to show a meteorite detection rate between 75% and 97%, while also providing an efficient mechanism to eliminate false positives. Our tests at a number of locations within Western Australia also showcase the ability for this training scheme to generalize a model to learn localized terrain features. Our model training approach was also able to correctly identify three meteorites in their native fall sites that were found using traditional searching techniques. Our methodology will be used to recover meteorite falls in a wide range of locations within globe-spanning fireball networks.

INTRODUCTION

Fireballs and meteors have been observed since antiquity by Chinese, Korean, Babylonian, and Roman astronomers (Bjorkman 1973), while meteorites and their unique metallurgical properties have also been known and used by various cultures around the world from Inuit tools (Rickard 1941) to Egyptian ceremonial daggers (Comelli et al. 2016), their connection to each other and to asteroids as source bodies was not proposed until the 19th century, with the fall of the l'Aigle meteorite (Biot 1803; Gounelle 2006). Since this link was established, meteorites have and continue to offer unique insights into the history of the solar system, as well as the contemporary characteristics, both physical and chemical, of asteroids, the Moon, and Mars. Unfortunately, the overwhelming majority of these ~60,000 samples have no spatial context since their falls were not observed, leaving their prior orbits uncharacterized. Less than 0.1% of meteorites in the

global collection was observed well enough during their atmospheric entry to properly constrain their orbits (Borovička et al. 2015; Meier 2017; Jenniskens 2020). This ultra-rare subset of meteorites affords some of the most valuable information pertaining to extraterrestrial geology, since their physical and geochemical properties along with their orbital histories can be combined to characterize the nature of asteroid families, and therefore possible parent bodies, that inhabit the same orbital space.

The best methodology for recovering meteorites with corresponding orbits utilizes fireball camera networks, which use automated all sky camera stations in an overlapping arrangement such that a potential fireball can be imaged by two or more stations. From these observations, scientists can triangulate an atmospheric trajectory, from which a pre-entry orbit and a fall area can also be calculated. The first success of such a system was demonstrated in Czechoslovakia in 1959, with the Příbram meteorite fall (Ceplecha

1961). This event spurred the establishment of the Czech fireball network (Spurný et al. 2006), along with multiple networks across the globe (McCorsky and Boeschstein 1965; Halliday et al. 1996; Oberst et al. 1998; Bland 2004; Brown et al. 2010; Colas et al. 2014; Gardiol et al. 2016; Devillepoix et al. 2020).

The Desert Fireball Network

An ideal location for one of these networks was determined to be the Nullarbor region in Western and South Australia, due to its low humidity, sparse vegetation, and typically clear skies (Bevan and Binns 1989); thus, the Desert Fireball Network (DFN) was born (Bland et al. 2012). Since its inception, the DFN has been responsible for the recovery of four confirmed meteorite falls: Bunburra Rockhole, Mason Gully, Murrili, and Dingle Dell (Towner et al. 2011; Spurný et al. 2012; Bland et al. 2016; Devillepoix et al. 2018), all of which have well-constrained orbits. To date, the network covers approximately 30% of the land mass of Australia, with more than 50 camera stations (Howie et al. 2017). On average, it observes 300 fireballs per year, typically five of which result in a meteorite fall.

For every fireball event observed by multiple camera stations, the bright flight trajectory is triangulated. If a terminal mass (meteorite fall) is predicted, we incorporate wind models into Monte Carlo simulations in order to estimate the likely fall area (Sansom et al. 2015; Howie et al. 2017; Jansen-Sturgeon et al. 2019). Since the fireball appears only as a streak of light, crucial attributes pertaining to the object such as size, mass, and shape are all co-dependent variables. This means that the predicted fall location results in a line, along which all of these parameters vary (Sansom et al. 2019). Inherent uncertainties and gaps in reported wind conditions at altitudes all along the flight lead to a variation of ~250 m on either side of this fall line. Each predicted fall zone is entirely dependent on the conditions of the fireball, though typical events can result in a fall zone 2–4 km² in area. The decision to search for a particular meteorite is dependent on many factors, from the geometry and confidence of the trajectory triangulation to local terrain features and geographic accessibility. Once the team has determined the fidelity of the triangulation and conditions of the fall area itself, a searching trip is commissioned to look for the fallen meteorite.

Meteorite Recovery

Traditional methods for meteorite recovery include two main strategies, petal searching and line searching.

Petal searching involves sending individuals out from a central point, walking alone or in small groups in a loop, typically a few kilometers long, looking for and collecting meteorites along the way. This method generally covers a larger area but comes with a higher risk of missing meteorites in the area covered. Since this method is usually implemented in strewn fields or in areas with older surface ages and higher meteorite density, such as the Nullarbor (Bevan 2006), where the objective is to recover older meteorite finds, missing some meteorites is less detrimental.

Alternatively, line searching is more useful when trying to recover a meteorite fall with a well-constrained fall line, like those observed through a fireball network. The DFN implements this strategy by assembling searchers in a line, spaced 5–10 m apart, then sweeping the area ~250 m on either side of the fall line on foot. This approach is usually able to cover 1–2 km² for each trip, assuming six people search 8 h per day, for 10 days. The Antarctic Search for Meteorites (ANSMET) uses a similar method, only they are not restricted by a fall line, and instead cover the area with greater spacing while mounted on snowmobiles (Eppler 2011). The benefit of the line method is higher fidelity on the area covered, due to overlapping fields of view by the searchers, although generally, less area is covered with this method.

When considering both the number of meteorites found by the DFN, and the number of searching trips it has commissioned (4 and ~20, respectively), the success rate remains at ~20%. This relatively low rate combined with the cost (~20,000 AUD) of sending six people on trips for 2 weeks at a time necessitates an improvement in the meteorite recovery rate, particularly due to the establishment and expansion of the Global Fireball Observatory (Devillepoix et al. 2020).

Previous Drone-Meteorite Recovery Methods

The gargantuan strides that have been made in the last 10 years in the manufacture of high-resolution DSLR cameras and commercial drones capable of carrying them have opened the possibility of using both to aid in the recovery of meteorites. Previous attempts have been met with mixed to promising results. Moorhouse (2014) in his honors thesis explored the possibility of using a hyperspectral camera mounted to a drone to look for the possibly unique spectral signature of meteorites. This approach is unfeasible in our framework since the best hyperspectral cameras are prohibitively expensive (>100,000 AUD), and more importantly, would limit our area coverage rate to little more than 0.1 km² per day, due to low spatial resolution in the camera. Further complications arise

from the fact that Moorhouse used a spectral library of meteorite interiors, rather than meteoritic fusion crust, which is what would appear on the surface of fresh meteorite falls. Although meteorite fusion crusts could have a unique spectra compared to typical terrestrial environments, this is not explored in his work. Su (2017) focused on the feasibility of using magnetic sensors suspended from a drone, but this method would preclude us from finding non-magnetic meteorites, and also limit our area coverage to less than 0.1 km² per day. This approach would also be the most susceptible to obstacles on the ground and changes in local elevation, since they prescribe flying at a 2 m altitude.

Citron et al. (2017) relied on an RGB camera to survey an area, and used a machine learning algorithm to identify likely meteorites in the images. Their tests resulted in a meteorite detection rate of 50% and encountered a false-positive rate of ~4 per 100 m². These results are very promising and seem to be limited mainly by the performance of the drone and camera hardware. The other limitation is false positives, and more importantly, how to separate them from promising meteorite candidates. This is a crucial detail when considering that a typical fall line (>2 km²), analyzed with their model, could have over 100,000 detections, all of which must be examined by a human in one way or another.

The work of Zender et al. (2018) also employed an RGB camera to image meteorites in native backgrounds. They showed the unique reflectance signature of meteorites in each color channel and created an algorithm to detect these signatures. This approach was able to detect half of their test meteorites, though it did suffer from a high rate of false positives.

AlOwais et al. (2019) also used an RGB camera, while additionally investigating the utility of a thermal imaging system. They also trained a number of neural networks to detect meteorites within images. One of their chief priorities was to create such an image processing system that would fit onboard their surveying drone. With this in mind, they elected to use transfer learning (Pan and Yang 2009) from a handful of smaller pretrained neural networks, to detect meteorites. Their training resulted in a high model accuracy using images taken from the internet, as well as photoshopping cropped meteorite images onto terrain backgrounds. These results are promising and await validation in the form of field tests.

Our previous work on drone-meteorite recovery is described in Anderson et al. (2019). In this previous iteration, we trained a machine learning model on a synthetic data set. We created it by taking survey images from a drone, splitting them into tiles, and then overlaying the tiles with cropped meteorite images.

Although training on these tiles yielded a high training accuracy, it was unable to consistently identify real test meteorites placed on the ground, most likely because the training data lacked the native lighting conditions and shadows seen in the real test-meteorite images.

Here, we report on updated methods to achieve a practical system for recovering meteorites using drones and machine learning. Such a system must fulfill the following six requirements to be effective (1) survey at least 1 km²/day, (2) meteorite recovery chance (success rate) greater than 50%, (3) portable to different terrains/locations, (4) deployable by three people or less (1 vehicle), (5) total cost <40,000 AUD (two traditional searching trips), and (6) data processing rate equal to data surveying rate (including model prediction and false-positive sorting).

METHODS

Drone and Camera Hardware

In recent years, the number of options for consumer and commercial drones has grown dramatically, with many options including fixed-wing, multi-copter, vertical takeoff/landing, and even blimps. The designs with the most flight-proven heritage, at our price range, are fixed-wing and multi-copters. Our previous experience has shown that fixed-wing models produce too much image blur and are unable to achieve a meaningful image resolution due to lower limits on most models' cruising altitude. Given these constraints, we chose a DJI M600 drone to perform full-scale tests as well as surveys of our fall sites. This drone was able to carry our camera and gimbal payload with mass to spare for possible later upgrades. It was also able to perform preplanned survey flights, with meter-scale GPS precision, for more than 15 min at a time.

We also decided to use an RGB camera, since these systems are both scalable and widespread, as opposed to thermal or hyperspectral cameras that are more expensive, specialized, and are only capable of smaller spatial resolutions. We specifically chose a Sony A7R Mk. 3 (42 MPixel), with a 35 mm lens, set to take images with a 1/4000 s exposure, at f/4.5, and an ISO of 320. The total cost of the camera, drone, batteries, and accessories was 30,000 AUD, well below the 40,000 AUD limit we self-imposed in Criteria (5).

We used the DJI GO 4 app to control the drone manually during training data collection flights, while the survey flights were planned and executed using the DJI GS Pro app. With this equipment, we conducted tests at varying altitudes and determined that an image resolution of 1.8 mm/pixel (15 m altitude) would be sufficient to detect most of our typical meteorite falls

4

S. Anderson et al.

(0.3–4 kg). This would allow meteorites to appear in the image between a size of 18 and 60 pixels in diameter. Using this fixed resolution value, we found that this system could survey approximately 1.3 km²/day, when we flew nearly continuously for 7 h per day, easily fulfilling Criteria (1). Although we had 12 h of daylight at the time of our full-scale test, we found that surveying less than 2.5 h after sunrise or before sunset produced long shadows that resulted in an unacceptably high rate of false positives.

Machine Learning Software

Since a meteorite would appear to be small (18–60 pixels) relative to the total size of the image (42 MPixel), we decided to split each image into 125 × 125 pixel tiles with a stride of 70. This allowed a meteorite to fully appear in at least one tile, to maximize the chance of detection, and minimize false positives. These tiles were then fed to a binary image classifier, a type of deep convolutional neural network, to separate uninteresting terrain (0) from meteorite suspects (1). We considered any prediction over 0.9 confidence to be a detection or a possible meteorite.

We implemented our neural network by constructing a model in Python using TensorFlow (Abadi et al. 2015) and Keras (Chollet 2015), the architecture of which is shown in Table 1. Although a sufficiently deep architecture is important when training a neural network, the training data itself is the most important factor, especially in our case where we trained the model from randomized initial weights (from scratch), rather than using a pretrained network. This means that for a given fall site we needed numerous, diverse examples of both True (meteorite) and False (non-meteorite) tiles. The False tiles were relatively easy to assemble. We simply took a survey of an area without any meteorites, and made all of the images into False tiles.

The True tiles required a bit more effort. Since all the meteorites we would be searching for would have fallen within the last 10 years, they would all have intact, dark fusion crusts covering their surface. Fresh meteorites such as these also tend to be minimally altered, making them more analytically valuable to the meteorite community. This consideration limited the number of real meteorites that were available to us to use in data sets. To artificially bolster the number of True tiles we could generate, we also used stones with desert varnish surfaces, a dark, slightly shiny exterior that develops on some rocks in hot deserts (Engel and Sharp 1958), as “synthetic” meteorites. At each site, we also found stones that had a plausible meteoritic shape (non-jagged and without a noticeable elongated axis)

Table 1. Our neural network architecture.

Layer type	Filters/ neurons	Kernel size	Stride size	Activation function
Convolutional 2D	30	3	1	Rectified linear unit
Batch normalization				
Max pooling		2	2	
Convolutional 2D	60	3	1	Rectified linear unit
Batch normalization				
Max pooling		2	2	
Convolutional 2D	120	2	2	Rectified linear unit
Batch normalization				
Max pooling		2	1	
Convolutional 2D	240	3	1	Rectified linear unit
Batch normalization				
Max pooling		2	1	
Flatten				
Dense	100			Rectified linear unit
Dropout	30%			
Dense	50			Rectified linear unit
Dense	25			Rectified linear unit
Dense	5			Rectified linear unit
Dropout	30%			
Dense	5			Rectified linear unit
Dense	1			Sigmoid

and painted them black. Using this combination of fusion-crusted meteorites, desert varnish stones, and painted stones, we always had enough samples to make a substantial number of True tiles.

Our procedure for making these tiles is illustrated in Fig. 1. Step 1 consisted of laying out the stones in a line at the fall site, spaced more than 1 m apart, and then imaging them with the drone. This line could be either in the fall zone or just outside of it, in order to train the model on similar backgrounds. We gave a 1 m separation to ensure that two stones would not appear in the same tile, when we augmented the data later on. We found the best way to accomplish this stone imaging was for one person to walk ~3 m parallel to the line of black stones, and point to each one, while another person manually flew the drone at the prescribed survey altitude, following the first person. Physically pointing out each individual stone allowed us to annotate each stone only once, avoiding a possible

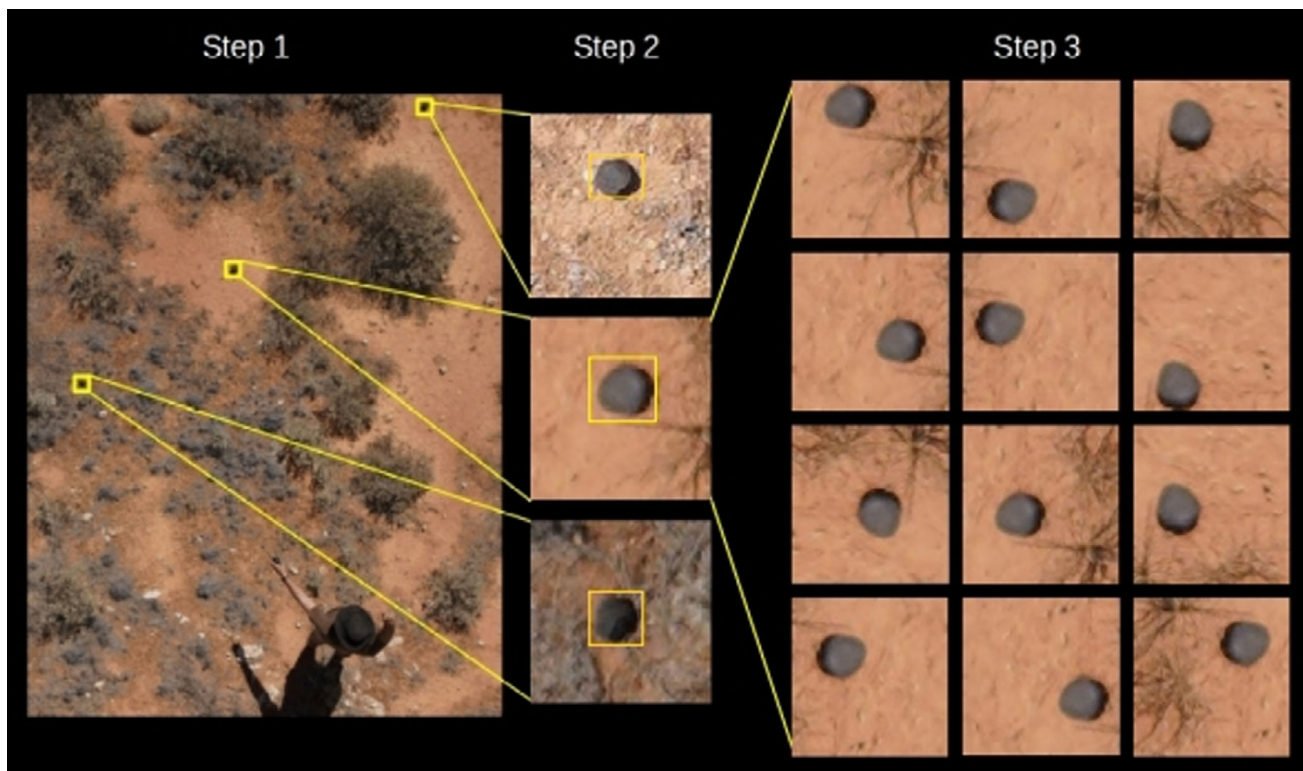


Fig. 1. Our workflow for obtaining meteorite training data. Step 1 consists of laying out the stones on the ground >1 m apart, and imaging them at a 1.8 mm per pixel resolution. Step 2 shows how we record the position, height, and width of each rock in the full-sized image, by drawing a bounding box. Step 3 is where we generate the tiles to be used for training and validation.

double appearance of a particular stone in both the training and validation sets. For Step 2, we drew a tight bounding box around each stone and recorded the box's height, width, and position in the image. These annotations were completed using ImageJ (Schneider et al. 2012). We typically laid out ~ 100 stones at a time; 15% of these stones and their resultant tiles are set aside for validation, not used in training. This ensured that the validation set only consisted of stones that the model had never seen, as opposed to unseen permutations of stones that the model was already familiar with.

At Step 3, we took each annotation, in both the training and validation sets, and strode by 15 pixels in both axes over each meteorite, creating a new tile at each stride, while keeping the stone fully in the tile frame. Each of those tiles was then rotated in intervals of 90° and saved for each permutation. These strides and rotations force each rock to appear in nearly every position of a tile, without any preference in local directionality, that is, shadows and windblown vegetation. We repeat this data collection process at different times of the day, at different sections of the

fall line, to include as much variety as possible. Details like these are crucial when making a widely generalized training set.

This process ideally generates $\sim 50,000$ True tiles for the training set. To assemble the False tiles, we flew the drone 350 m, parallel to the fall line, taking images all along the way. By splitting the images into tiles, we generated $\sim 2,500,000$ False samples. The process of laying out stones, imaging everything, and making the annotations typically took an hour.

Since dramatically unbalanced data sets can negatively affect training (Miroslav and Matwin 1997), we could only train with as many False tiles as we had True tiles, to keep a 1:1 ratio. A simplified example of unbalanced data sets is a training set containing 1 True and 99 False samples. Mathematically speaking, the shortest path to the model achieving a high accuracy would be for it to label everything false, resulting in an accuracy of 99%. Obviously, this kind of solution is useless, which is why we must maintain a ratio as close to 1:1 as possible. We did this by randomly selecting 50,000 False tiles from the pool of 2.5 million, and combining them with the 50,000 True tiles, to form the

whole training set. We also included ~8000 False tiles from the 2.5 million into the validation set, ensuring they did not also appear in the training set.

We trained on our data set for 150 epochs (rounds of training), using a batch size of 250, with 400 steps per epoch, which ensured that each tile is seen by the model once per epoch. The validation set was evaluated at the end of each epoch, also using a batch size of 250 with 64 steps. For smaller data sets, we adjusted our batch size and steps per epoch such that the product of these two values equaled the size of the training set.

Once the model completed training, we judged its utility based on its meteorite detection chance, and rate of false positives. The meteorite detection chance was determined by predicting on each of the True tiles in the validation set, and dividing the number of predictions over 0.9 confidence by the total number of tiles. This provided a metric for how well the model could correctly identify new black rocks that it had never seen. For the false-positive rate, we wanted to obtain a more widespread and representative value that would reflect model performance across the whole fall zone. So we randomly selected 50 images from the survey of the fall line and predicted on them with the model, recording the average number of detections across all the images.

False Positive Sorting Interface

An issue we anticipated with any model we would train was the processing of false positives. Even in best-case scenarios, where we assume a model accuracy of 99.999%, with ~8500 tiles per image and ~650 images per flight, a model would return approximately 5500 detections per flight, and more than 150,000 per fall line. Thus, we required a tool to help searchers efficiently examine each of these model detections, and determine which of these were obvious false positives and which ones required further investigation. We created a graphical user interface in Python using the Tkinter module to accomplish this task (Fig. 2).

The program displays nine detections at a time, in a 3×3 grid pattern. Each grid space is mapped to numbers 1–9 on a standard keyboard's keypad (1 for lower left, 5 for middle-center, 9 for upper right). Each detection is displayed such that the frame is centered on the detection tile, outlined in a yellow box (~25 cm on one side), and extends 70 pixels beyond the target tile, to give the user context of the larger area. Below the grid, three images of meteorites are displayed, scaled from the smallest to the largest meteorite possible for that fall site (lowest mass with iron density, to highest mass with chondritic density, respectively). This allows users to easily reference how big a meteorite should

appear in the tiles. If the user decides that the tile likely contains a meteorite, they press the number on the keypad corresponding to that grid space, before advancing to the next set. The program also allows the user to remove their responses from the current set of nine tiles, as well as go back to the previous set.

Through testing trials, we determined that the average user could sort through ~120 tiles per minute. Assuming 150,000 detections per fall line, the task of sorting through these data would take over 20 labor hours. This problem of staying focused over long periods of time is known as “vigilance” by human factors psychologists, who have observed decrements in user performance over extended task sessions (See et al. 1995). To mitigate such decrements in vigilance, we ensured that each user would only sort for 20 min increments. This was chosen as a conservative time limit according to Teichner (1974), who found the vigilance decrement to be fully observed 20–35 min into a task. Additionally, to reduce the consequence of individual errors, each tile was inspected by two separate users. We also anticipated that the overwhelming majority of detections would be false positives, thereby counterproductively enticing the users to speed through the tiles, without properly inspecting each one. The resulting consequence of such task parameters has been shown in signal detection literature to result in the missed detection of such rare signals (Stanislaw and Todorov 1999), in our case the user detection of a meteorite. To combat this, we added a test function to the program, whereby each set of nine tiles had a uniform probability of containing 0, 1, or 2 test tiles, taken from the training set. This forced the user to slow down and select, on average, one tile per set, thus reducing the rarity of a “hit.”

A final failsafe was included in this sorting task, such that once the user missed two test tiles during a sorting session, the program would shut down, forcing the user to take a break. The user's score of successfully completed tests, along with the number of meteorite candidates identified, is shown at the top of the display. Both of these strategies, increasing the “hit” rate and providing performance feedback, have been shown to combat the vigilance decrement (Hancock et al. 2016).

Once two users sorted through the detections for a flight, we overlaid the original images with bounding boxes around meteorite candidates. We also set aside the false positives, so that we may use them for retraining if needed.

RESULTS

We conducted small-scale tests of our methodology by visiting four sites in Western Australia and training a

Semi-automated meteorite recovery

7

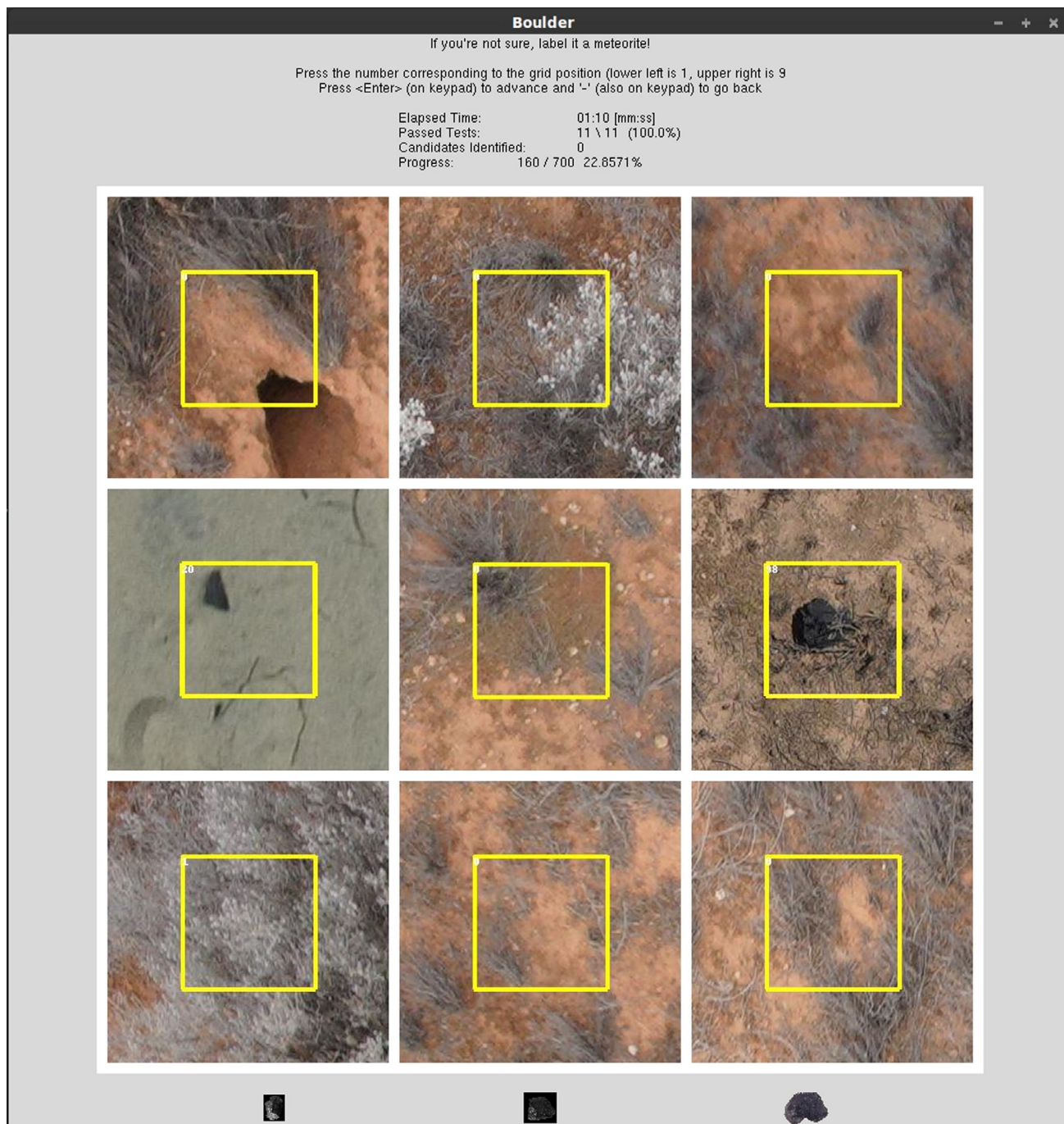


Fig. 2. Our sorting user interface we designed to aid in the separation of candidates from false positives. Test tiles (True tiles from the model training set) for this set appear in the center-left and center-right positions. Users press the corresponding number on the keypad to mark the tile(s) as a likely meteorite.

model at each location. Although they were not at real meteorite fall sites, they were all located within the DFN's operational area, and could conceivably be representative of future fall sites. These sites and the results from the models we trained for them are listed in

Table 2. For these smaller tests, we only obtained training data for ~30 synthetic and real meteorites and surveyed less than 0.1 km² at each site.

We also conducted a full test of our methodology by visiting one of our fall sites, DN150413_01,

Table 2. Distinct models at various locations within the DFN. Model performance is dependent on the size of the training data set.

Location	(Lat, long)	Total number of training tiles	Training accuracy (%)	Meteorite detection (%)	False-positive rate (per image)
Ledge Point	(−31.151, 115.395)	16,352	92.58	68.50	21.7
Dalgaranga	(−27.635, 177.289)	30,874	97.03	85.60	6.5
Lake Kondinin	(−32.496, 118.192)	32,348	96.85	86.70	5.1
Balladonia	(−32.370, 124.790)	98,470	98.73	93.20	1.3

northeast of Forrest Airport, Western Australia (30.764 S, 128.184 E). We obtained training data for this fall site at different times during the day (morning, cloudy mid-morning, midday, early afternoon, and late afternoon). Over the course of 2 days, we also surveyed 2 km² of the fall zone, so that we could identify meteorite candidates for secondary inspection in an upcoming expedition. We also placed four painted rocks, unseen by the model, within the survey area and recorded their GPS coordinates. This served as a test of our ability to use the model to correctly identify a meteorite candidate, correctly sort it with the user interface, and accurately correlate the image’s GPS coordinates to those recorded by our handheld unit. During the survey, each of three team members was assigned a distinct role during flight operations. The first team member’s job was to fly the drone and calibrate the camera, the second oversaw data collection and backups on the computer, and the third was responsible for cooling and charging the batteries.

When we returned from the field, we trained a model on our RTX 2080 Ti (11 GB RAM) GPU, with an Intel i9-9000 CPU for approximately 3 h (150 epochs). This resulted in a final training accuracy of 99.07% and a validation accuracy of 98.65%. Furthermore, we achieved a meteorite detection chance of 98.71%, and a false-positive rate of 2.5 per image. Using the trained model, the detection algorithm was able to process 1 day’s images in 22 h. The model returned a combined total of 92,595 detections for the 2 days of survey, which we were able to sort through in 12 h, excluding breaks. Sorting through all of our detections yielded 752 meteorite candidates. Of the four test rocks we laid out, we successfully located three of them (by comparing GPS coordinates) using our prescribed searching methods, meaning that we successfully met fulfilled Criteria (2).

Four months after this initial trip, when the COVID-19 travel restrictions were lifted in Western Australia, we revisited the same site northeast of Forrest Airport. We began by inspecting ~20 of the 749 candidates in-person and noticed that they generally belonged to one of two populations: dark stones (most likely iron-rich siliceous

rock) and small holes in the ground (<7 cm in diameter) most likely made by small animals. The small hole population was far more numerous than the dark stone group and was easy to distinguish in the images, once we knew which features to look for. We then sorted through the remaining ~700 candidate images and narrowed the list to 32 candidates that did not appear to be holes in the ground. Unfortunately after inspecting these remaining candidates, we found that none of them were meteorites.

On this same follow-up trip, we also visited a second, separate fall site located northwest of Forrest Airport. For this site, we employed the traditional line searching technique and found the meteorite on the afternoon of the first day. Using our Mavic Pro drone, we took ~100 images of this meteorite (Fig. 3, left) from a top-down view, with heights ranging from 1 to 30 m. We also generated training data at this site, trained a model, and used it to predict on 86 of these images (those in which the meteorite was between 10 and 80 pixels in diameter). The model was able to correctly identify the meteorite in 84 of the 86 images, or 97%.

During a separate trip, whereby two members of our research group were scouting a third fall site south of Madura, Western Australia, for an upcoming six-person searching trip, they discovered the meteorite in question (Fig. 3, right), on the dirt road which roughly bisected the predicted fall line. They also used the Mavic Pro to take images of the meteorite from altitudes of 2 to 30 m, and created training data on-site. When they returned from the trip, we trained a model and predicted on the 27 meteorite images, finding that the model correctly identified the meteorite in 24 of the images (88% success rate). At the writing of this article, these two meteorites have not yet been registered with the Meteoritical Bulletin, as their classifications are forthcoming.

An additional and final test of our approach involved using our Forrest-NE model to predict on a drone image of an older meteorite find, shared with us by a volunteer meteorite hunter who regularly searches in the Nullarbor. We found that the model correctly identified the old chondrite with a prediction value of 1.0: a perfect match.



Fig. 3. The meteorites recovered northwest of Forrest Airport (left) and South of Madura (right). Although these two were not recovered using the full surveying methodology, they serve as valuable demonstrations for the feasibility of our approach.

DISCUSSION AND FUTURE WORK

Our smaller tests (Table 2) show that more training data makes for a more robust model in terms of both meteorite detection and false positives, reinforcing the notion that more training data makes for a better model. These tests also showcase the portability of our methodology, accounting for variations in available training data, which successfully satisfies Criteria (3).

The results of the full test, while not a total success, are a promising prospect for the future of meteorite recovery. Not only is this methodology capable of locating test meteorite analogs, it is able to cover a fall zone nearly six times faster than a traditional line search, when accounting for invested labor. If we assume that in the future we would predict on images and sorting through detections in the field, this rate of data processing can keep pace with data collection through a combination of switching sorting users and simply taking breaks, satisfying the final outstanding Criteria (6).

There are two possibilities as to why the full test did not result in a complete success of recovering the meteorite. The first explanation is that our methodology failed at some stage of the searching, whether the model failed to detect the meteorite, or we failed to label the detection as a candidate. The second possibility was that we did not cover enough of the fall line. Since the initial surveying trip was limited to 2 days, we were only able to cover 2 km² of the entire 5 km² fall zone. Our other successes with the models correctly identifying two fresh falls and one old find, all in situ, lead us to believe that the second explanation is more likely. For this reason, we

plan on returning to the Forrest-NE fall site and surveying the remainder of the fall zone.

We will also embark on an extensive surveying campaign of all of our meteorite fall sites. We initially plan on training a new model for each fall site, using randomly initialized weights. Although as we gain more training data from a range of diverse fall sites, we will investigate the possibility of combining data sets and training a “base model” whose final weights will then be used as the initial weights for each new model we train. This future approach may improve the generalizability of our models and reduce training time on-site.

The Python software that we have created, as well as our trained model weights, will be made available to collaborators upon request, so that the entire meteoritics community can benefit from this new method of semi-automated meteorite recovery.

Acknowledgments—We thank Robert Tower for providing us with additional drone survey images. We also thank L. Folco and our anonymous reviewer for their valuable inputs, which improved the quality of this manuscript. This work was funded by the Australian Research Council (Grant DP200102073).

Editorial Handling—Dr. Akira Yamaguchi

REFERENCES

- Abadi M., Agarwal A., Barham P., Brevdo E., Chen Z., Citro C., Corrado G. S., Davis A., Dean J., Devin M., Ghemawat S., Goodfellow I., Harp A., Irving G., Isard M., Jozefowicz R., Jia Y., Kaiser L., Kudlur M., Levenberg J., Mané D., Schuster M., Monga R., Moore

- S., Murray D., Olah C., Shlens J., Steiner B., Sutskever I., Talwar K., Tucker P., Vanhoucke V., Vasudevan V., Viégas F., Vinyals O., Warden P., Wattenberg M., Wicke M., Yu Y., and Zheng X. 2015. TensorFlow: Large-scale machine learning on heterogeneous systems. <http://tensorflow.org>. Accessed September 21, 2020.
- AlOwais A., Naseem S., Dawdi T., Abdisalam M., Elkalyoubi Y., Adwan A., Hassan K., and Fernini I. 2019. Meteorite hunting using deep learning and UAVs. 2nd International Conference on Signal Processing and Information Security (ICSPIS). pp. 1–4.
- Anderson S. L., Bland P. A., Towner M. C., and Paxman J. P. 2019. Utilizing drones and machine learning for meteorite searching and recovery (abstract #2426). 49th Lunar and Planetary Science Conference. CD-ROM.
- Bevan A. W. R. 2006. Desert meteorites: A history. *Geological Society, London, Special Publications* 256:325–343.
- Bevan A. W. R. and Binns R. A. 1989. Meteorites from the Nullarbor Region, Western Australia: II. Recovery and classification of 34 new meteorite finds from the Mundrabilla, Forrest, Reid and Deakin areas. *Meteoritics* 24:135–141.
- Biot J. B. 1803. Relation d'un voyage fait dans le department de l'Orne, pour constater la realite d'un meteore observe a l'Aigle le 26 floreal an 11. Baudouin, Imprimeur de L'Institut National, Paris.
- Bjorkman J. K. 1973. Meteors and meteorites in the ancient near east. *Meteoritics* 8:91–132.
- Bland P. A. 2004. The Desert Fireball Network. *Astronomy and Geophysics* 45:520–523.
- Bland P. A., Spurny P., Bevan A. W. R., Howard K. T., Towner M. C., Benedix G. K., Greenwood R. C., Shrubeny L., Franchi I., Deacon G., Borovička J., Ceplecha Z., Vaughan D., and Hough R. M. 2012. The Australian Desert Fireball Network: A new era for planetary science. *Australian Journal of Earth Sciences* 59:177–187.
- Bland P. A., Towner M. C., Sansom E. K., Devillepoix H., Howie R. M., Paxman J. P., Cupak M., Benedix G. K., Cox M. A., Jansen-Sturgeon T., and Stuart D. 2016. Fall and recovery of the Murrilli meteorite, and an update on the Desert Fireball Network (abstract #6265). 79th Annual Meeting of the Meteoritical Society.
- Borovička J., Spurný P., and Brown P. 2015. Small near-Earth asteroids as a source of meteorites. In *Asteroids IV*, edited by Michel P., DeMeo F. E., and Bottke W. F. Tucson, Arizona: University of Arizona Press. pp. 257–280.
- Brown P., Weryk R. J., Kohut S., Edwards W. N., and Krzeminski Z. 2010. Development of an all-sky video meteor network in Southern Ontario, Canada The ASGARD System. *WGN, Journal of the International Meteor Organization* 38:25–30.
- Ceplecha Z. 1961. Multiple fall of Pribram meteorites photographed. 1. Double-station photographs of the fireball and their relations to the found meteorites. *Bulletin of the Astronomical Institutes of Czechoslovakia* 12:21.
- Chollet F. 2015. Keras. keras.io. Accessed September 21, 2020.
- Citron R. I., Shah A., Sinha S., Watkins C., and Jenniskens P. 2017. Meteorite recovery using an autonomous drone and machine learning (abstract #2528). 48th Lunar and Planetary Science Conference. CD-ROM.
- Colas F., Zanda B., Bouley S., Vaubaillon J., Vernazza P., Gattacceca J., Marmo C., Audureau Y., Kwon M. K., Maquet L., and Rault J. L. 2014. The FRIPON and Vigié-Ciel networks. 33rd International Meteor Conference, September. pp. 18–21.
- Comelli D., Dorazio M., Folco L., El-Halwagy M., Frizzi T., Alberti R., Capogrosso V., Elnaggar A., Hassan H., Nevin A., and Porcelli F. 2016. The meteoritic origin of Tutankhamun's iron dagger blade. *Meteoritics & Planetary Science* 51:1301–1309.
- Devillepoix H. A. R., Sansom E. K., Bland P. A., Towner M. C., Cupak M., Howie R. M., Jansen-Sturgeon T., Cox M. A., Hartig B. A., Benedix G. K., and Paxman J. P. 2018. The Dingle Dell meteorite: A Halloween treat from the Main Belt. *Meteoritics & Planetary Science* 53:2212–2227.
- Devillepoix H. A. R., Cupak M., Bland P. A., Sansom E. K., Towner M. C., Howie R. M., Hartig B. A. D., Jansen-Sturgeon T., Shober P. M., Anderson S. L., Benedix G. K., Busan D., Sayers R., Jenniskens P., Albers J., Herd C. D. K., Carlson P., Hill P. J. A., Brown P. G., Krzeminski Z., Osinski G. R., Chennaoui Aoudjehane H., Shissh T., Benkhaldoun Z., Jabiri A., Guennoun M., Barka A., Darhmaoui H., Daly L., Colline G. S., McMullan S., Suttle M. D., Shaw C., Young J. S., Alexander M., Mardon A. D., Ireland T., Bonning G., Baeza L., Alrefay T. Y., Horner J., Swindle T. D., Hergenrother C. W., Fries M. D., Tomkins A., Langendam A., Rushmer T. A., O'Neill C., Janches D., and Hormaechea J. L. 2020. A global fireball observatory. *arXiv preprint arXiv:2004.01069*.
- Engel C. G. and Sharp R. P. 1958. Chemical data on desert varnish. *Geological Society of America Bulletin* 69:487–518.
- Eppler D. B. 2011. Analysis of Antarctic logistics and operations data: Results from the Antarctic Search for Meteorites (ANSMET), austral summer season, 2002–2003, with implications for planetary surface operations. *Geological Society of America Special Papers* 483:75–84.
- Gardiol D., Cellino A., and Di Martino M. 2016. PRISMA Italian network for meteors and atmospheric studies. Proceedings of the International Meteor Conference 2016, Egmond, Netherlands, pp. 76–79.
- Gounelle M. 2006. The meteorite fall at L'Aigle and the biot report: Exploring the cradle of meteoritics. *Geological Society London Special Publications* 256:73–89.
- Halliday I., Griffin A. A., and Blackwell A. T. 1996. Detailed data for 259 fireballs from the Canadian camera network and inferences concerning the influx of large meteoroids. *Meteoritics & Planetary Science* 31:185–217.
- Hancock P. A., Volante W. G., and Szalma J. L. 2016. Defeating the vigilance decrement. *IIE Transactions on Occupational Ergonomics and Human Factors* 4:151–163.
- Howie R. M., Paxman J., Bland P. A., Towner M. C., Cupak M., Sansom E. K., and Devillepoix H. A. 2017. How to build a continental scale fireball camera network. *Experimental Astronomy* 43:237–266.
- Jansen-Sturgeon T., Sansom E. K., and Bland P. A. 2019. Comparing analytical and numerical approaches to meteoroid orbit determination using Hayabusa telemetry. *Meteoritics & Planetary Science* 54:2149–2162.
- Jenniskens P. 2020. Review of asteroid-family and meteorite-type links. *Proceedings of the International Astronomical Union* 14:9–12.
- McCorsky R. E. and Boeschstein H. 1965. The prairie meteorite network. *Optical Engineering* 3:304127.
- Meier M. M. M. 2017. Meteoriteorbits.info—Tracking all known meteorites with photographic orbits (abstract

- #1178). 49th Lunar and Planetary Science Conference. CD-ROM.
- Miroslav K. and Matwin S. 1997. Addressing the curse of imbalanced training sets: One sided selection. *International Conference on Machine Learning* 97:179–186.
- Moorhouse D. 2014. Hyper-spectral imaging for airborne meteorite detection. Honors bachelor thesis. University of Southern Queensland, Toowoomba, Australia.
- Oberst J., Molau S., Heinlein D., Gritzner C., Schindler M., Spurný P., Ceplecha Z., Rendtel J., and Betlem H. 1998. The European Fireball Network: Current status and future prospects. *Meteoritics & Planetary Science* 33:49–56.
- Pan S. J. and Yang Q. 2009. A survey on transfer learning. *IEEE Transactions on Knowledge and Data Engineering* 22:1345–1359.
- Rickard T. A. 1941. The use of meteoric iron. *The Journal of the Royal Anthropological Institute of Great Britain and Ireland* 71:55–56.
- Sansom E. K., Bland P., Paxman J., and Towner M. 2015. A novel approach to fireball modeling: The observable and the calculated. *Meteoritics & Planetary Science* 50:1423–1435.
- Sansom E. K., Jansen-Sturgeon T., Rutten M. G., Devillepoix H. A., Bland P. A., Howie R. M., Cox M. A., Towner M. C., Cupák M., and Hartig B. A. 2019. 3D meteoroid trajectories. *Icarus* 321:388–406.
- Schneider C. A., Rasband W. S., and Eliceiri K. W. 2012. NIH Image to ImageJ: 25 years of image analysis. *Nature Methods* 9:671–675.
- See J. E., Howe S. R., Warm J. S., and Dember W. N. 1995. Meta-analysis of the sensitivity decrement in vigilance. *Psychological Bulletin* 117:230–249.
- Spurný P., Borovička J., and Shrubný L. 2006. Automation of the Czech part of the European Fireball Network: Equipment, methods and the first results. *Proceedings of the International Astronomical Union* 2:121–130.
- Spurný P., Bland P. A., Shrubný L., Borovička J., Ceplecha Z., Singelton A., Bevan A. W., Vaughan D., Towner M. C., McClafferty T. P., and Toumi R. 2012. The Bunburra Rockhole meteorite fall in SW Australia: Fireball trajectory, luminosity, dynamics, orbit, and impact position from photographic and photoelectric records. *Meteoritics & Planetary Science* 47:163–185.
- Stanislaw H. and Todorov N. 1999. Calculation of signal detection theory measures. *Behavior Research Methods, Instruments, & Computers* 31:137–149.
- Su D. 2017. Drag-line sensor for drone assisted meteorite detection. Honors bachelor thesis. Macquarie University, Sydney, Australia.
- Teichner W. H. 1974. The detection of a simple visual signal as a function of time of watch. *Human Factors* 16:339–352.
- Towner M. C., Bland P. A., Spurný P., Benedix G. K., Dyl K., Greenwood R. C., Gibson J., Franchi I. A., Shrubný L., Bevan A. W. R., and Vaughan D. 2011. Mason gully: The second meteorite recovered by the Desert Fireball Network. *Meteoritics & Planetary Science Supplement* 74:5124.
- Zender J., Rudawska R., Koschny D., Drolshagen G., Netjes G. J., Bosch M., Bijl R., Crevecoeur R., and Bettonvil F. 2018. Meteorite detection with airborne support—A study case. *Proceedings of the International Meteor Conference, Pezinok-Modra, Slovakia*. pp. 145–152.

Coauthored Paper 4 – The proposed Silicate-Sulfuric Acid Process: Mineral processing for In Situ Resource Utilization (ISRU)

Acta Astronautica (2021), Volume 188, p. 57-63.

*Seamus Anderson, Eleanor Sansom, **Patrick Shober**, Benjamin Hartig, Hadrien Devillepoix, Martin Towner*

REPRODUCED BY PERMISSION OF ELSEVIER: *As the author of this*

Elsevier article, I retain the right to include it in a thesis or dissertation

Statement of Authorship

TITLE OF PAPER: THE PROPOSED SILICATE-SULFURIC ACID PROCESS: MINERAL PROCESSING FOR IN SITU RESOURCE UTILIZATION (ISRU)

PUBLICATION STATUS: Published.

Author Contributions

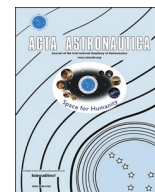
I, Patrick M. Shober, as a coauthor, contributed to the discussions of the novel ISRU mechanism proposed and the revisions of the manuscript. These efforts made a 1 % contribution to the total work of this paper.

I, Seamus L. Anderson, as first author, endorse that the level of contribution indicated above is accurate.



Contents lists available at ScienceDirect

Acta Astronautica

journal homepage: www.elsevier.com/locate/actaastro

The proposed Silicate-Sulfuric Acid Process: Mineral processing for In Situ Resource Utilization (ISRU)

Seamus L. Anderson^{*}, Eleanor K. Sansom, Patrick M. Shober, Benjamin A.D. Hartig, Hadrien A.R. Devillepoix, Martin C. Towner

Space Science and Technology Center, Curtin University, GPO Box U1987, Perth, WA, 6845, Australia

ARTICLE INFO

Keywords:

Space resources
ISRU
Asteroids
Lunar surface
Mineral processing
Space mining

ABSTRACT

Volatile elements and compounds found in extra-terrestrial environments are often the target of In Situ Resource Utilization (ISRU) studies. Although water and hydroxide are most commonly the focus of these studies as they can be used for propellant and human consumption; we instead focus on the possible exploitation of sulfur and how it could be utilized to produce building materials on the Moon, Mars and Asteroids. We describe the physical and chemical pathways for extracting sulfur from native sulfide minerals, manufacturing sulfuric acid in situ, and using the produced acid to dissolve native silicate minerals. The final products of this process, which we call the Silicate-Sulfuric Acid Process (SSAP), include iron metal, silica, oxygen and metal oxides, all of which are crucial in the scope of a sustainable, space-based economy. Although our proposed methodology requires an initial investment of water, oxygen, and carbon dioxide, we show that all of these volatiles are recovered and reused in order to repeat the process. We calculate the product yield from this process if it were enacted on the lunar highlands, lunar mare, Mars, as well as an array of asteroid types.

1. Introduction

Humanity's renewed interest in deep-space exploration will bring to bear countless challenges we as a species have not yet faced. As humans plan to depart from Earth for longer durations and further distances than ever before, they must be equipped with an increasingly large stockpile of resources in order to survive and thrive on their voyages. An alternative to this 'bring everything' approach, is to instead make use of the resources present at the various destinations, such as the Moon and Mars. This concept is known as in situ resource utilization (ISRU), and although the basic principle is not a novel idea [1], its numerous demonstrations and theoretical implementations are emerging at a faster rate than ever before [2–5].

Previous ISRU studies have investigated a wide range of possibilities for extracting and utilizing materials from celestial bodies across the solar system, from rare earth elements on certain asteroids [6], to the constructional uses of regolith for radiation shielding on the Moon and Mars [7]. Much of this current literature regarding ISRU focuses on extracting volatile elements, chiefly oxygen and hydrogen, which are often locked away in the form of non-volatile minerals. The importance of these two resources cannot be understated, since they can be used not only as breathable air and potable water for human consumption but could also serve as propellant for rocket engines [5,8,9]. To that end, carbon also plays an important role in martian ISRU, since it can be

combined with hydrogen to make fuel for methane-based rocket engines [10–12]. Extracting volatile elements and refining propellants on the surfaces of the Moon and Mars will significantly reduce the mass required to launch from Earth, and therefore the cost of spacecraft for interplanetary missions. That being said, we focus on an often overlooked volatile element that is present on the Moon, Mars and numerous asteroids: sulfur.

A study by Vaniman et al. [13] illustrated possible uses for lunar sulfur, from sealants to electricity generation and storage. A series of experiments have also evaluated the mechanical properties and durability of concrete made from lunar soil simulant and elemental sulfur [14,15]. Unfortunately the deterioration of such concretes due to simulated lunar thermal cycling and degassing under vacuum has reduced the interest in this application in recent years.

Here, we will instead explore the physical and chemical pathways for manufacturing sulfuric acid (H_2SO_4) from native sulfur in order to dissolve silicate minerals, also native to these bodies. Doing so would produce considerable amounts of iron metal, silica, oxygen as well as other useful building materials for permanent human settlement in space. We call this methodology: The Silicate-Sulfuric Acid Process (SSAP). Although mineral processing for ISRU using sulfuric acid has been examined in the past [16, 17], harvesting oxygen from the less abundant mineral ilmenite ($FeTiO_3$) was the main focus. In this paper, a variety of highly-abundant silicate minerals are the principle focus for refinement into building materials.

^{*} Corresponding author.

E-mail addresses: seamus.anderson@postgrad.curtin.edu.au, seamus.L.anderson@gmail.com (S.L. Anderson).

Using a relatively small investment of other volatile elements including carbon, oxygen, and hydrogen, this process could be carried out on the Moon, Mars, and many Asteroids. Although this initial investment could be costly, many of these elements can be found in situ especially for mission profiles where the primary goal is to extract water, such as on C-type asteroids, the lunar poles, and high-latitude locations on Mars. The other main invested volatile, carbon, is also found on C-type asteroids, as well as on the surface and atmosphere of Mars. Furthermore, we will show that the SSAP allows for inherent recycling of the invested volatile elements, for continuous reuse.

1.1. Sulfur availability

In the ordinary and carbonaceous chondrite meteorite groups, which originated from S and C-type asteroids, respectively [18–20], sulfur is fairly abundant (~2.5 wt%). In ordinary chondrites it is almost entirely contained in the mineral troilite (FeS) [21], while carbonaceous chondrites usually contain pyrrhotite (Fe_{1-0.8}S) and pentlandite ((Fe, Ni)₉S₈) instead [22]. Martian dust can contain 2.5 wt% sulfur [23], while sulfates (e.g. MgSO₄, FeSO₄) are regularly detected in martian soils [24,25]. On the Moon, troilite exists across most of the surface, although in comparatively low abundance (<0.5 wt%) [26]. In the permanently shadowed crater regions near the poles, the sulfur content could be as high as 1 wt% in the form of SO₂ ice [27]. Although sulfur may not be one of the most abundant elements on these bodies, its presence as a minor element still offers an opportunity to utilize it.

1.2. Silicate-bound resources

Silicate minerals are an obvious target for acid-driven dissolution, since they are abundant on essentially all terrestrial bodies. They usually exist in

the general formula: $\alpha_1\text{Si}_j\text{O}_k$, where α can represent Mg, Fe, Ca, Al, Na, K, or other metals present within the crystal lattice. On the Moon, silicate minerals mostly consist of plagioclase (CaAl₂Si₂O₈), pyroxene ([Mg,Fe]₂Si₂O₆) and some olivine ([Mg,Fe]₂SiO₄), totaling more than 70 vol% of the regolith [28]. Similarly, most soils on Mars have a total silicate abundance near 80 wt%, where it is also mostly composed of plagioclase, pyroxene and olivine [29]. On C-type asteroids, with similar mineralogies to CM and CI meteorites, silicates in the form of olivine and water-bearing phyllosilicates, collectively account for between 75 and 95% of the total weight [22]. Meanwhile S-type asteroids contain mostly olivine and pyroxene with some plagioclase, totaling between 75 and 90 wt% of these bodies [19,30]. Once the metal components in these minerals are liberated they would be extremely valuable and useful for building large structures and other essential hardware off-world.

Iron is a prime example since it is already widely used for building large structures here on Earth, particularly when it is combined with other elements to form steel. Currently, the only way to obtain steel off-world is to launch it into orbit from Earth, a very expensive means of construction. Alternatively, producing iron metal at the desired destination could significantly reduce mission costs when the goal is to make large, permanent structures and equipment in space.

Silica (SiO₂), another main product of the SSAP, can serve as the precursor for fused quartz, which has been used as spacecraft windows on the Space Shuttle orbiters and the International Space Station [31]. Fused quartz is made by melting silica grains (~1650 °C) either under vacuum or in an inert atmosphere. Due to this high melting temperature, fused quartz can be used in some high temperature environments. This additionally makes it a possible candidate for constructing some of the equipment required for the processes we describe below.

As previously discussed, oxygen has obvious applications for human space exploration, since it can be used as breathable air. When carefully

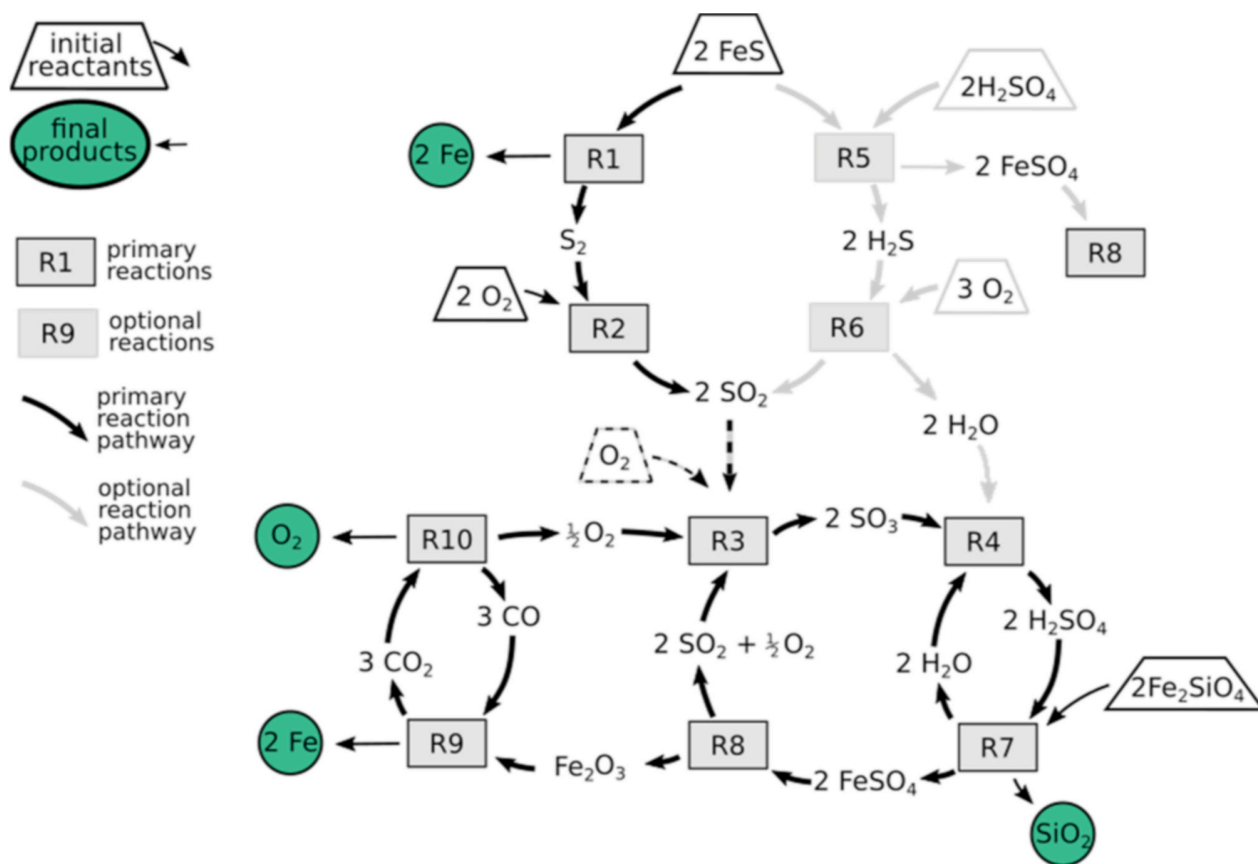


Fig. 1. This flowchart illustrates the chemical reaction pathways for the SSAP, while also highlighting the recycling of oxygen, sulfur dioxide, carbon monoxide and water. For simplicity, this shows only the processing of fayalite (Fe₂SiO₄). Final products are signified by a green circle, input reactants are outlined by trapezoids, and named reactions steps (see text) appear in rectangles. The upper half of this figure shows two pathways for processing troilite, either through thermal decomposition (left) or acid-dissociation (right) when sulfuric acid is available. (For interpretation of the references to colour in this figure legend, the reader is referred to the Web version of this article.)

S.L. Anderson et al.

Acta Astronautica 188 (2021) 57–63

combined with hydrogen it can also be used as rocket propellant; otherwise it forms pure water for both human consumption and industrial processes.

The various oxides formed by the SSAP have an extensive variety of niche uses, possibly the most useful of which is the molten electrolysis of aluminum oxide to form pure metal. Although this refinement is not a focus of this paper, aluminum metal could feed into the fabrication of lightweight, high-strength alloys.

2. Physical and chemical pathways of the SSAP

The proposed Silicate-Sulfuric Acid Process consists of four main stages. The first stage contains optional pre-processing steps so that the SSAP can be compatible with other resource extraction methods such as water harvesting. The second stage entails the synthesis of sulfuric acid, either from indigenous minerals or from recycled sulfur, water and oxygen. The third stage then uses this sulfuric acid to dissociate the silicate minerals into silica and sulfate minerals; the former of which is a final product and is removed from further processing. The sulfates are then thermally decomposed, and some of their products reduced to form metal and simple oxides in the fourth and final stage. Each of these stages is discussed below in further detail. Fig. 1 provides an overview of the SSAP in the form of a flow diagram.

For each of the reaction steps, we calculate the change in Gibbs free energy (ΔG), at 20 °C and 1 bar, from reported values in the NIST Standard Reference Database [32]. Eq. (1) shows this relation to enthalpy (H), entropy (S) and temperature (T). For the minerals that did not appear in this database, we compiled their thermodynamic properties from individual sources (listed in supplementary materials). Although this approach of combining multiple databases for comparison and calculation is not ideal, it does provide an estimate for the energy requirements at each step.

$$\Delta G = \Delta H - T\Delta S \quad (1)$$

We also calculate Gibbs free energy at pressures of 10^{-2} , 10^{-5} , and 10^{-8} bar (G_p) for each compound we assess, using Eq. (2), where R is the ideal gas constant, n is number of moles of gas, and P is pressure. From these G_p values, we also calculate the temperature-dependent equilibrium constant (K_{eq}) at those pressures via Eq. (3). This enables us to predict the equilibrium composition of each reaction using Eqs. (4) and (5), where a compound's concentration is signified by square brackets (e.g. [A]). This is especially important for reactions that involve thermal decomposition, as we will show that performing these steps under vacuum can significantly reduce the temperatures required for the reaction to proceed.

$$G_p = G + nRT \ln(P) \quad (2)$$

$$K_{eq} = e^{\left(\frac{-\Delta G_p}{RT}\right)} \quad (3)$$

$$K_{eq} = \frac{[X]^x [Y]^y}{[A]^a [B]^b} \quad (4)$$

$$aA + bB = xX + yY \quad (5)$$

2.1. Pre-processing

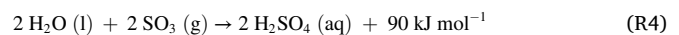
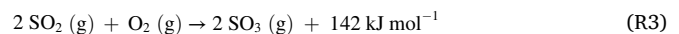
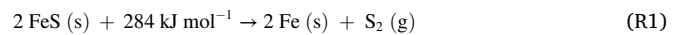
Ideally the first step in the SSAP consists of mechanically crushing larger silicate rocks to reduce the average particle size, which would allow for a quicker reaction with the sulfuric acid. This can be bypassed if regolith is used instead of large boulders or rocks. The bulk material should also be magnetically separated to extract native Fe–Ni metal grains present on the Moon and some asteroids [21,28]. Although these metal grains could be processed along with the silicates, doing so would be redundant as iron metal is an end product of the SSAP. Magnetic separation on the Moon could also separate the weakly magnetic mineral ilmenite from the silicates, which can separately be reduced into iron metal, titanium oxide and oxygen [33–35].

As we discussed earlier, water is possibly the most valuable resource to be harvested off-world. To avoid further complicating its extraction, water-bearing minerals and regoliths can be heated, and their evolved vapors collected in a cold trap, prior to the rest of the material being subjected to the SSAP. On the Moon, this means that water-ice rich regoliths [36] should be

heated to 150 °C in order to sublimate the ice into vapor [37]. For C-type asteroids, the phyllosilicates should be heated to liberate the lattice-bound OH^- molecules [38], which will also recrystallize much of the phyllosilicates into olivine [39]. Alternatively, if sulfuric acid were applied to water-bearing ores prior to heating, the silicates would still dissociate but the aqueous solution will be more dilute, which would likely slow the reaction rate.

2.2. Sulfuric acid synthesis

The sulfuric acid synthesis stage of the SSAP consists of thermal decomposition of sulfide minerals, followed by the industry-proven wet sulfuric acid process (WSA) [40], which creates sulfuric acid from sulfur-bearing gases. The main ore for sulfur on the Moon and S-type asteroids comes in the form of troilite (FeS), where as for C-type asteroids, the slightly more sulfur-rich pyrrhotite ($\text{Fe}_{(1-0.8)}\text{S}$) is the dominant sulfide mineral [22]. For simplicity in our description we assume that the sulfides appear in their stoichiometric form troilite (FeS). For Mars, the main sulfur-ore consists of sulfates (e.g. MgSO_4 , FeSO_4) which can be heated to release SO_2 gas and form solid oxides (discussed later in Reaction 8).



Reaction 1 shows the thermal decomposition of troilite and yields both iron metal and sulfur gas by heating to approximately 1250 °C in vacuum. More sulfur-rich minerals such as pyrrhotite and pyrite will begin releasing their sulfur component before this temperature [41]. This decomposition has been explored in meteorite heating experiments [38] which show that CM chondrites undergo a minor sulfur volatilization event around 550 °C, followed by a major outgassing event at 1200 °C. In these experiments, the sulfide minerals were not separated from the rest of the meteorite sample when they were heated and formed SO_2 gas rather than pure S_2 . It is unclear how much, if any of the iron in the sulfides was oxidized into Fe_2O_3 or Fe_3O_4 in this more oxygen-available environment. If the sulfide minerals were instead isolated from the rest of the bulk material before they were heated, the resultant gas would more likely be comprised of pure sulfur, while the iron within the sulfides would not likely be oxidized, resulting in pure iron metal. This iron metal is the first product harvested from the SSAP.

If pure sulfur gas is produced in Reaction 1, it must be exothermically combined with oxygen to yield sulfur dioxide (Reaction 2). If the thermal decomposition of the sulfide minerals results instead in sulfur dioxide, then Reaction 2 can be bypassed. The sulfur dioxide is then subjected to the WSA process (Reactions 3–4), whereby the gas is oxidized in the presence of a vanadium oxide catalyst between 400 and 620 °C (Reaction 3), in order to form sulfur trioxide. It is important to note that this catalyst is not depleted during the reaction and can be reused. The resulting sulfur trioxide is then exothermically hydrated before being condensed to form highly concentrated sulfuric acid in Reaction 4. Although Reactions 2–4 require an investment of oxygen and hydrogen, we will show in later stages that they will be recovered and can be reused, such that no volatiles are lost or wasted.

Alternatively, pre-existing sulfuric acid either brought to location or created in earlier processing, can be reacted with troilite to produce iron sulfate and hydrogen sulfide gas (Reaction 5). The resulting gas can then be burned with oxygen to form water and sulfur dioxide (Reaction 6), both of which are used in the above reactions to produce sulfuric acid. The processing of the iron sulfate in Reaction 5, will be elaborated on further in the next subsection. This alternative approach may be more logistically feasible since the sulfide and silicate minerals would not need to be separated prior to their reaction with the acid. This approach would also be ideal on the martian surface, as the main sulfuric ores are various sulfates [29] that should dissolve in sulfuric acid.

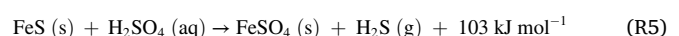


Table 1

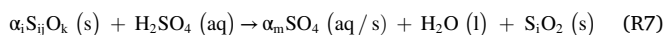
The generalized reactions between sulfuric acid and the end-members of each silicate mineral. Change in Gibbs free energy was calculated at 20 °C and 1 bar. The silica and sulfate products will both precipitate and be dissolved in solution depending the conditions of the reaction chamber. The negative values for ΔG in this table indicate that each reaction is exothermic and will proceed under standard temperature and pressure.

Reactants					Products			
Silicates (s)			Sulfuric Acid (aq)		Water (l)	Silica (s/aq)	Sulfates (s/aq)	ΔG° [kJ mol ⁻¹] (20 °C, 1 bar)
Mineral	Endmember	Formula						
Olivine	Fayalite	Fe ₂ SiO ₄	2 H ₂ SO ₄	→	2 H ₂ O	SiO ₂	2 FeSO ₄	-292
	Forsterite	Mg ₂ SiO ₄	2 H ₂ SO ₄		2 H ₂ O	SiO ₂	2 MgSO ₄	-258
Pyroxene	Ferrosilite	Fe ₂ Si ₂ O ₆	2 H ₂ SO ₄		2 H ₂ O	2 SiO ₂	2 FeSO ₄	-1220
	Enstatite	Mg ₂ Si ₂ O ₆	2 H ₂ SO ₄		2 H ₂ O	2 SiO ₂	2 MgSO ₄	-270
	Wollastonite	Ca ₂ Si ₂ O ₆	2 H ₂ SO ₄		2 H ₂ O	2 SiO ₂	2 CaSO ₄	-2080
Plagioclase	Anorthite	CaAl ₂ Si ₂ O ₈	4 H ₂ SO ₄		4 H ₂ O	2 SiO ₂	CaSO ₄ , Al ₂ (SO ₄) ₃	-2250



2.3. Silicate dissolution and Silica extraction

Once the sulfuric acid is synthesized, the SSAP proceeds to the next stage: silicate dissolution. By combining the acid with the silicate minerals (Reaction 7), this stage produces silica, water, and sulfate minerals; the last of which will be broken down further in final stage of the SSAP. The reactions between the silicates and the acid are listed in Table 1.



Although we list the pure end-members of these minerals, nearly every silicate grain native to terrestrial bodies is actually a solid solution, with a varying proportion of the appropriate metal cation coexisting in the same crystal lattice. It is for simplicity that we examine the reactions of the pure end members with sulfuric acid.

A suite of previous experiments describe in detail, the acid-silicate reactions listed in Table 1 [42–46]. The results of these experiments show the general trend that the silicate minerals are broken down into a hydrated amorphous silica gel, while the cations (Fe, Mg, etc.) are released into the water-acid solution and eventually precipitate into their hydrated sulfate counterparts. Minor amounts of iron oxides also form from olivine when the initial aqueous sulfuric acid solution is less concentrated [43]. The mixture should be mechanically perturbed or mixed to prevent a nonreactive product layer to form on the surface of unreacted silicate grains. Since previous experiments did not mix or perturb the rock-acid mixtures, it is unclear exactly how quickly this step will progress.

Once all of the initial silicates have reacted with the acid, the fluid can be evaporated such that any excess water or acid can be collected for later use. The evaporation will cause the ions in the solution to precipitate into the

sulfates listed in Table 1. At this point most of the solid products will still likely contain water and can be dehydrated by heating to 100 °C under vacuum. This released water can be immediately reused in Reaction 4. This step of separating water and unreacted acid from dissolved components is one of the key factors that will determine the overall efficiency of the entire SSAP in terms of energy. Adding more acid-water solution at the beginning of Reaction 7 will cause it to progress more quickly; however this also requires more energy to evaporate the remaining liquid. In later sections we estimate discuss efficiency bottlenecks for the SSAP.

2.4. Metal and oxide production

The final stage of the SSAP produces iron metal, oxygen, as well as metal oxides, via thermal decomposition and carbothermal reduction. The sulfates previously produced in Reaction 7 (Table 1) can be intermixed for this next step, since calcium, aluminum, magnesium and iron(II) sulfate each have distinct thermal decomposition temperatures. Heating the sulfates will decompose the iron(II) sulfate into iron(III) oxide (Fe₂O₃), sulfur dioxide, and oxygen, as shown in Reaction 8 (Table 2). Simultaneously, the aluminum sulfates will decompose into aluminum oxide, sulfur dioxide and oxygen. Since iron(III) oxide is ferromagnetic, while aluminum oxide, calcium and magnesium sulfate are diamagnetically susceptible, the iron(III) oxide can be magnetically separated before further heating. The remaining magnesium and calcium sulfates will thermally decompose into their corresponding metal oxides at higher temperatures. The equilibrium compositions for each of these reactions is shown in Fig. 2. Further refining these oxides into pure metals (Al, Mg, Ca) is not addressed in this work; we will only describe the extraction of iron metal from iron(III) oxide.



The gases produced in Table 2 can be collected and reused in Reactions 2

Table 2

Generalized thermal decomposition reactions for produced sulfates. The Oxides described here are in their simple form (MgO:Magnesia, Al₂O₃:Alumina). The positive values attained for ΔG° indicate that heat-energy is required for the reaction to proceed (see Fig. 2). These reactions are collectively referred to as Reaction 8.

Reactants			Products			
Sulfate (s)			Sulfur Dioxide (g)	Oxygen (g)	Oxide (s)	ΔG° [kJ mol ⁻¹] (20 °C, 1 bar)
2 FeSO ₄	→	2 SO ₂	½ O ₂	Fe ₂ O ₃	306	
2 MgSO ₄		2 SO ₂	O ₂	MgO	557	
2 CaSO ₄		2 SO ₂	O ₂	CaO	868	
Al ₂ (SO ₄) ₃		3 SO ₂	¾ O ₂	Al ₂ O ₃	621	

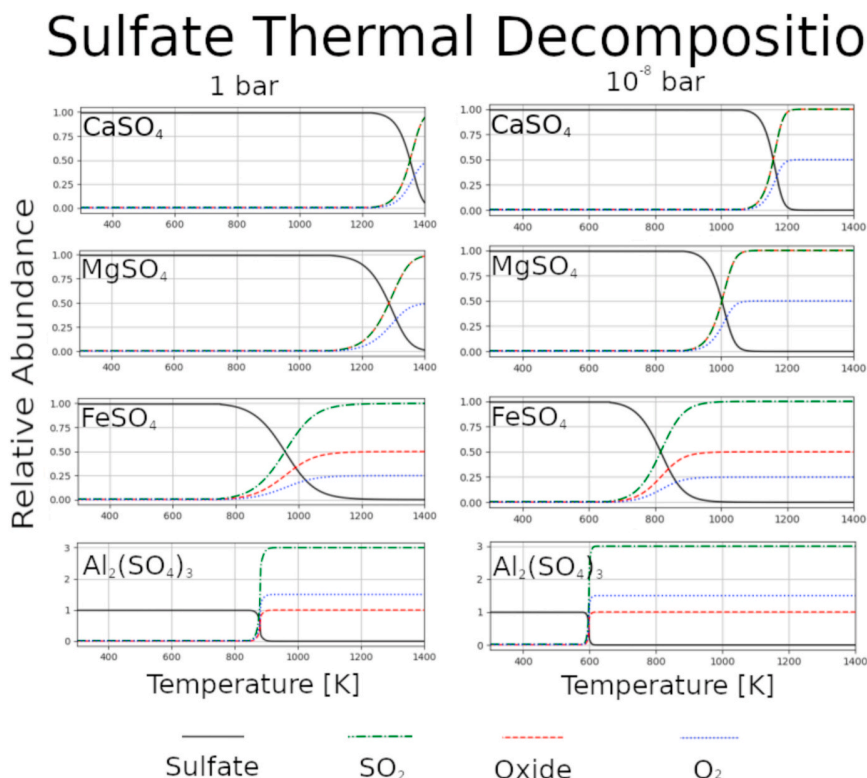
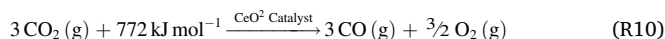
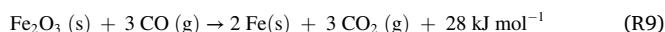


Fig. 2. The calculated equilibrium compositions for each major sulfate species at 1 bar (left column) and 10⁻⁸ bar (right column). This shows the general trend that reducing the ambient pressure lowers the temperatures required for the reactions to proceed. Note the legend at the bottom of the figure. The Y axes represent molar abundance of each compound.

and 3 to produce more sulfuric acid. Although not all the invested oxygen is recovered from iron(III) oxide the final steps will net a 1 mol surplus of O₂.

Iron metal is produced by reducing iron(III) oxide using carbon monoxide in Reaction 9. Although Chen et al. [47] show that this process consists of multiple steps: Fe₂O₃ → Fe₃O₄ → FeO → Fe, oxidizing the ambient CO atmosphere all along the way, we forgo these intermediates and represent the reaction more concisely.



The final step of the SSAP is to recover the oxygen locked away in the carbon dioxide at the end of Reaction 9, while also replenishing the supply of carbon monoxide for repeating the very same reaction. This is done by electrolyzing CO₂ with a cerium oxide catalyst near 500 °C [48], shown in Reaction 10. We would like to note that the energy required that we list in Reaction 10 is likely an overestimate since we do not consider the effects of the catalyst in our calculations. Now that the CO gas has been replenished for

repeat use, 1 mol of O₂ has also been created for every 2 mol of iron metal produced, and the SSAP is complete.

3. Results and discussion

We have calculated the theoretical yield of the SSAP for each terrestrial body listed in Table 3. We assume an initial silicate mass of one ton, with mineral chemistry and abundance representative of each particular body. By taking the product of each mineral's abundance and its end member molar percentage, we calculated the total number of moles of each silicate end member. With this, we use Reactions 7–10 to calculate how many moles, and by extension kilograms, of each resource could be produced from the SSAP. For H, L, and LL chondrites (S-type asteroids) we obtained average mineral abundances from Ref. [30], and mineral compositions from Refs. [49–51]. For C-type asteroids we used mineral data reported by Ref. [22] for the meteorites: Murchison, Orgueil and Allende (CM, CI, CV chondrites-respectively). The C and S-type asteroid calculations include contributions from native sulfides. For the lunar highlands and mare calculations, we averaged the bulk chemical compositions reported in Ref. [28] including the ilmenite

Table 3

Theoretical yield for various solar system bodies, assuming 100% efficient processing of 1000 kg of native silicates. The Oxides described here are in their simple form (e.g. MgO:Magnesia, Al₂O₃:Alumina, etc.).

Body	Recoverable Resource [kg]								Reference
	Fe (metal)	O ₂	SiO ₂	Al ₂ O ₃	MgO	CaO	H ₂ O	TiO ₂	
Luna Mare	143	31	492	143	100	123	–	46	[28]
Luna Highlands	53	13	475	237	85	142	–	8	[28]
Mars	121	35	514	124	77	96	–	–	[29]
Asteroids									
C-type (CI-Orgueil mineralogy)	65	3	430	–	436	–	118	–	[22]
C-type (CM-Murchison mineralogy)	375	125	260	–	174	–	87	–	[22]
C-type (CV-Allende mineralogy)	267	53	393	4	359	2	–	–	[22]
S-type (H Chondrite mineralogy)	132	27	509	25	323	20	–	–	[30,49–51]
S-type (L Chondrite mineralogy)	170	35	490	22	308	20	–	–	[30,49–51]
S-type (LL Chondrite mineralogy)	164	40	473	21	304	18	–	–	[30,49–51]

and sulfide contributions. This calculation assumes that the ilmenite cannot be separated by pre-processing and is included in the silicate dissolution step (Reaction 7). For the martian calculations we averaged the values reported in Ref. [29] across both models and localities (Gusev and Meridiani), but we did not include contributions from native sulfates, which would increase the total yield of iron metal and oxygen.

3.1. Products and uses

Our calculations show that a significant quantity of building material can be obtained on the Moon, Mars, and asteroids. Table 3 shows that CM-like C-type asteroids are the most fruitful candidate for the SSAP, as it would produce the most iron metal and oxygen, with harvested water being an added benefit. Resource utilization on S-type asteroids would particularly benefit from the SSAP, as they would be otherwise considered relatively resource-poor, due to their lack of native water, while also hosting a relatively high abundance of sulfur. For some C-type asteroids, we list water as a SSAP-product only because their silicates contain significant native water that is incidentally released, otherwise water is not a product of the SSAP. For lunar operations, the lunar mare would be preferable to the lunar highlands in terms of a more useful product yield, since it is more highly concentrated in iron which can be used in 3D printing (discussed below). As for the longevity of SSAP operations at a destination, Mars may be the best candidate since it has abundant water ice as well as the highest relative abundances of carbon and sulfur. This would allow for higher tolerances in volatile loss.

On the lunar surface, the SSAP could considerably contribute to the Artemis program's goals of establishing a sustainable presence on the surface on the Moon, by providing some building materials in situ. The produced iron metal will likely take the form of small particles, which can be used as the feedstock for direct metal laser sintering to 3D print components or structures including landing pads, radiation shields, or electrical wire. The silica produced here will also likely be in granular form, which can be melted in a cast to produce windows for future habitats. Alumina is a natural insulator of electricity, making it ideal for encasing power cables for extra-terrestrial solar power plants. As we mentioned earlier, alumina could be further reduced into aluminum metal, although this pathway is beyond the scope of the SSAP.

We envision a logistical framework, whereby a cargo spacecraft could deliver to a planetary surface: a metal 3D printer, a casting furnace, and a SSAP-refinery including some initial sulfuric acid, water, and carbon dioxide. The refinery could begin producing silica for the furnace and iron for the printer, to construct the hull or main body of a habitat in situ. Later cargo missions can deliver robotic workers and more specialized components such as airlock doors or life support systems to be installed. Although the mission architecture for the Artemis program prescribes an Earth-fabricated habitat, any attempts at permanent human settlement will likely require a process to create infrastructure in situ.

3.2. Engineering and logistical considerations

Although most of the steps within our proposed process are supported by a suite of previous experiments including some industry-proven methodologies, its effectiveness should be validated by performing these techniques on lunar, martian, and asteroid regolith simulants. These experiments will help to determine reaction rates and will characterize some of the engineering challenges that will inevitably become apparent.

The first experimental validation should be focused on the feasibility of processing the bulk material, not solely the silicates, for a given locale. For instance, the magnetic force required for collecting native iron metal and iron oxide must be determined. This is especially important for martian regolith, which contains considerable iron oxide. Once the separation is complete, the remaining non-magnetic material should be dissolved in acid (Reaction 7) to determine what problems, if any, might arise from insoluble impurities while also characterizing the reaction rate. Previous experiments [46] also indicate that Reaction 7 progresses more quickly if the temperature is slightly elevated. Keeping Reaction 7 in thermal contact with Reaction 8 (thermal decomposition) may be an efficient way to conserve energy.

The overall efficiency of the SSAP will be heavily influenced by the efficiency of Reaction 7. The less water and mechanical perturbations required

to fully react the silicates (or non-magnetic material) will reduce the overall energy requirements for this step. Unfortunately we cannot accurately calculate the total energy required to enact the SSAP from start to finish, as it is unclear which hydrated sulfates would form (monohydrate, pentahydrate, etc.) in Reaction 7. Additionally, an accurate calculation would require knowledge of the power and duration needed to operate the vacuum systems in Reaction 8. These reasons underline the need for experimental investigation in the future.

As we briefly mentioned in the previous subsection, the long term viability of the SSAP will also depend on how much of the volatile compounds can be retained, especially when trapping evolved gases in Reaction 8. Having the ability to replenish volatile elements (sulfur, oxygen, carbon, hydrogen) in situ will alleviate strict leak tolerances for the processing equipment. This makes Mars and C-type asteroids more forgiving in terms of volatile loss, while the Moon and S-type asteroids are relatively volatile poor and therefore less forgiving. Striking a balance between chamber pressure and heating in Reaction 8 will also influence energy efficiency and volatile loss. As Fig. 2 shows, decreasing overbearing pressure during sulfate decomposition will also decrease the temperatures required to drive off the sulfur-bearing gases, but will also require a more robust and energy intensive vacuum system. Validation experiments should explore this balance to determine which pressure and temperature profiles are most efficient to fully decompose the sulfates.

3.3. Comparison to other ISRU methodologies

Although we cannot accurately calculate the energy requirements of the SSAP, we can qualitatively compare its inherent strengths and weaknesses to a collection of other ISRU techniques: molten salt electrolysis (modified FCC Cambridge Process), vapor phase pyrolysis, and hydrogen reduction. An inherent advantage that all of these methods have over the SSAP, is their experimental characterization.

Molten salt electrolysis [52,53], specifically one modified for lunar surface operations [54] can essentially reduce all oxides and silicates into metallic alloys, while also releasing nearly all the oxygen present. This benefit comes at the cost of the required operating temperature. While the SSAP will need to reach similar operating temperatures as this approach (~950 °C), this is only the peak temperature required, while salt electrolysis will need to maintain this temperature for the duration of the process. Special consideration will also need to be taken when choosing which salt and anode to use such that they are not depleted or corroded respectively, though this concern is relatively minor.

Like salt electrolysis, vapor phase pyrolysis [55–57] can also reduce the native minerals into metals while also liberating all the oxygen. A major benefit of pyrolysis is its relative simplicity: heating up the rocks they vaporize. This heating however is also the major drawback, since the temperatures required are in excess of 2000 °C.

Another approach for reducing minerals into metals, while also harvesting oxygen involves using hydrogen [34] on the bulk material. This process works mostly on ilmenite, reducing it into titanium oxide and iron metal, while releasing some oxygen (~5 wt% [58]) at the same time. Unfortunately this approach has a lesser effect on silicates. This approach also requires operating temperatures which are slightly higher than the SSAP's peak temperature. An advantage to this approach is its simplicity compared to the SSAP and could conceivably be performed as a pre-processing step for the SSAP.

4. Conclusions

In this paper, we have presented the physical and chemical pathways for the proposed Silicate-Sulfuric Acid Process, which aims to manufacture building materials from abundant resources found in situ on major planetary bodies such as the Moon, Mars and asteroids. Although this approach has not yet been tested, it allows for inherent recycling of volatile elements, such that little to no material must be supplied after the initial investment. This proposed ISRU approach could provide substantial building materials including iron metal for 3D printing, silica for window construction, as well as modest amounts of oxygen gas. The next step for further investigating the utility of the SSAP lies in experimental validation.

S.L. Anderson et al.

Acta Astronautica 188 (2021) 57–63

Declaration of competing interest

The authors declare that they have no known competing financial interests or personal relationships that could have appeared to influence the work reported in this paper.

5 Acknowledgments

We would like to thank our anonymous reviewers for their insightful suggestions that considerably improved the scope and quality of this manuscript. This work was funded by the Commonwealth Scientific and Industrial Research Organisation's Top Up Scholarship (No. 50077118).

Appendix A. Supplementary data

Supplementary data to this article can be found online at <https://doi.org/10.1016/j.actaastro.2021.07.016>.

References

- [1] B. O'Leary, Mining the apollo and amor asteroids, *Science* 197 (1997) 363–366.
- [2] F.E. Meyen, M.H. Hecht, J.A. Hoffman, MOXIE Team, Thermodynamic model of Mars ISRU experiment (MOXIE), *Acta Astronaut.* 129 (2016) 82–87.
- [3] M. Anand, I.A. Crawford, M. Balat-Pichelin, S. Abanades, W. Van Westrenen, G. Péraudeau, R. Jaumann, W. Seboldt, A brief review of chemical and mineralogical resources on the Moon and likely initial in situ resource utilization (ISRU) applications, *Planet. Space Sci.* 74 (2012) 42–48.
- [4] P.T. Metzger, A. Muscatello, R.P. Mueller, J. Mantovani, Affordable, Rapid bootstrapping of the space industry and solar system civilization, *J. Aero. Eng.* 26 (2013) 18–29.
- [5] D. Kornuta, A. Abbud-Madrid, J. Atkinson, J. Barr, G. Barnhard, D. Bienhoff, B. Blair, V. Clark, J. Cyrus, B. DeWitt, C. Dreyer, Commercial lunar propellant architecture: a collaborative study of lunar propellant production, *Reach. Out.* 13 (2019) 100026.
- [6] A.M. Hein, M. Saidani, H. Tollu, Exploring potential environmental benefits of asteroid mining, 2018 arXiv preprint arXiv:1810.04749.
- [7] N.J. Lindsey, Lunar station protection: lunar regolith shielding, *Sci. Technol.* 108 (2004) 143–148.
- [8] S.D. Rosenberg, R.L. Beegle, G.A. Guter, F.E. Miller, M. Rothenberg, The onsite manufacture of propellant oxygen from lunar resources, *NASA Johnson Space Center, Space Resources* 3 (1992) Materials.
- [9] F. Chandler, D. Bienhoff, J. Cronick, G. Grayson, Propellant depots for earth orbit and lunar exploration, in: *AIAA SPACE 2007 Conference & Exposition*, 2007.
- [10] R.L. Ash, W.L. Dowler, G. Varsi, Feasibility of rocket propellant production on Mars, *Acta Astronaut.* 5 (1978) 705–724.
- [11] A. Muscatello, R. Devor, J. Captain, Atmospheric processing module for Mars propellant productions, *Earth Space* (2018) 444–454.
- [12] J.E. Kleinhenz, A. Paz, An ISRU propellant production system for a fully fueled Mars Ascent Vehicle, in: *10th Symposium on Space Resource Utilization*, 2017, p. 423.
- [13] D. Vaniman, D. Pettit, G. Heiken, Uses of Lunar Sulfur, *Lunar Bases and Space Activities of the 21st Century*, 1998.
- [14] R.N. Grugel, H. Toutanji, Sulfur “concrete” for lunar applications—Sublimation concerns, *Adv. Space Res.* 41 (2008) 103–112.
- [15] H.A. Toutanji, S. Evans, R.N. Grugel, Performance of lunar sulfur concrete in lunar environments, *Construct. Build. Mater.* 29 (2012) 444–448.
- [16] L.A. Taylor, W.D. Carrier III, Production of oxygen on the Moon: which processes are best and why, *AIAA J.* 30 (12) (1992) 2858–2863.
- [17] C. Schwandt, J.A. Hamilton, D.J. Fray, I.A. Crawford, The production of oxygen and metal from lunar regolith, *Planet. Space Sci.* 74 (1) (2012) 49–56.
- [18] M.J. Gaffey, Rotational spectral variations of asteroid (8) Flora: implications for the nature of the S-type asteroids and for the parent bodies of the ordinary chondrites, *Icarus* 60 (1984) 83–114.
- [19] T. Nakamura, T. Noguchi, M. Tanaka, M.E. Zolensky, M. Kimura, A. Tsuchiyama, A. Nakato, T. Ogami, H. Ishida, M. Uesugi, T. Yada, Itokawa dust particles: a direct link between S-type asteroids and ordinary chondrites, *Science* 333 (6046) (2011) 1113–1116.
- [20] T. Hiroi, M.E. Zolensky, C.M. Pieters, M.E. Lipschutz, Thermal metamorphism of the C, G, B, and F asteroids seen from the 0.7 μm , 3 μm , and UV absorption strengths in comparison with carbonaceous chondrites, *Meteoritics Planet. Sci.* 31 (3) (1996) 321–327.
- [21] O.N. Menzies, P.A. Bland, F.J. Berry, G. Cressey, A Mössbauer spectroscopy and X-ray diffraction study of ordinary chondrites: quantification of modal mineralogy and implications for redox conditions during metamorphism, *Meteoritics Planet. Sci.* 40 (7) (2005) 1023–1042.
- [22] P.A. Bland, G. Cressey, O.N. Menzies, Modal mineralogy of carbonaceous chondrites by X-ray diffraction and Mössbauer spectroscopy, *Meteoritics Planet. Sci.* 39 (1) (2004) 3–16.
- [23] S.R. Taylor, S. McLennan, *Planetary Crusts: Their Composition, Origin and Evolution* vol. 10, Cambridge University Press, 2009.
- [24] D.L. Blaney, T.B. McCord, Indications of sulfate minerals in the Martian soil from Earth-based spectroscopy, *J. Geophys. Res.: Plan* 100 (E7) (1995) 14433–14441.
- [25] M.D. Lane, M.D. Dyar, J.L. Bishop, Spectroscopic evidence for hydrous iron sulfate in the Martian soil, *Geophys. Res. Lett.* 31 (19) (2004).
- [26] E.K. Gibson, G.W. Moore, Sulfur abundances and distributions in the valley of Taurus-Littrow, *Lunar and Planetary Science Conference Proceedings* 5 (1974) 1823–1837.
- [27] A.A. Berezhnoy, N. Hasebe, T. Hiramoto, B.A. Klumov, Possibility of the presence of S, SO₂, and CO₂ at the poles of the Moon, *Publications of the Astronomical Society of Japan* 55 (4) (2003) 859–870.
- [28] L. Haskin, P. Warren, 8. Lunar chemistry, in: G.H. Heiken, D.T. Vaniman, B. M. French (Eds.), *Lunar Sourcebook, a User's Guide to the Moon*, Cambridge University Press, New York, 1991, pp. 357–475.
- [29] H.Y. McSween, I.O. McGlynn, A.D. Rogers, Determining the modal mineralogy of Martian soils, *J. Geophys. Res.: Plan* 115 (E7) (2010).
- [30] T.L. Dunn, T.J. McCoy, J.M. Sunshine, H.Y. McSween, A coordinated spectral, mineralogical, and compositional study of ordinary chondrites, *Icarus* 208 (2) (2010) 789–797.
- [31] J.A. Salem, Transparent armor ceramics as spacecraft windows, *J. Am. Ceram. Soc.* 96 (1) (2013) 281–289. [32] Thermodynamics Research Center, ‘Thermodynamics Source Database’ in NIST Chemistry WebBook, NIST Standard Reference Database Number 69, Eds P.J. Linstrom, W.G. Mallard, National Institute of Standards and Technology, Gaithersburg MD, 20899 <https://doi.org/10.18434/T4D303>.
- [33] A.H. Cutler, P. Krag, A carbothermal scheme for lunar oxygen production, *Lunar bases and space activities of the 21st century*, 1985, p. 559.
- [34] M.A. Gibson, C.W. Knudsen, Lunar oxygen production from ilmenite, *Lunar bases and space activities of the 21st century*, 1985, p. 543.
- [35] J. Pesl, R.H. Eric, High temperature carbothermic reduction of Fe₂O₃-TiO₂-MxOy oxide mixtures, *Miner. Eng.* 15 (11) (2002) 971–984.
- [36] C.I. Honniball, P.G. Lucey, S. Li, S. Shenoy, T.M. Orlando, C.A. Hibbitts, D. M. Hurley, W.M. Farrell, Molecular water detected on the sunlit Moon by SOFIA, *Nature Astronomy* (2020) 1–7.
- [37] U. Hegde, R. Balasubramanian, S. Gokoglu, Analysis of water extraction from lunar regolith, in: *50th AIAA Aerospace Sciences Meeting Including the New Horizons Forum and Aerospace Exposition*, 2012, p. 634.
- [38] A.B. Verchovsky, M. Anand, S.J. Barber, S. Sheridan, G.H. Morgan, A quantitative evolved gas analysis for extra-terrestrial samples, *Planet. Space Sci.* 181 (2020) 104830.
- [39] N.H. Brett, K.J.D. MacKenzie, J.H. Sharp, The thermal decomposition of hydrous layer silicates and their related hydroxides, *Q. Rev. Chem. Soc.* 24 (2) (1970) 185–207.
- [40] J.K. Laursen, *The process principles, Hydrocarb. Eng.*, 12 (8) 47–50.
- [41] M. Thompson, J.J. Fortney, M. Telus, D. Lederman, T. Joshi, Meteorite Outgassing Experiments to Inform Chemical Abundances of Super-earth Atmospheres, *AGUFM*, 2019, pp. P23B–P3487.
- [42] J. Van Herk, H.S. Pietersen, R.D. Schuiling, Neutralization of industrial waste acids with olivine—the dissolution of forsteritic olivine at 40–70 C, *Chem. Geol.* 76 (3–4) (1989) 341–352.
- [43] R.C.L. Jonckbloedt, Olivine dissolution in sulphuric acid at elevated temperatures—implications for the olivine process, an alternative waste acid neutralizing process, *J. Geochem. Explor.* 62 (1–3) (1998) 337–346.
- [44] H.E. King, O. Plümpfer, T. Geisler, A. Putnis, Experimental investigations into the silicification of olivine: implications for the reaction mechanism and acid neutralization, *Am. Mineral.* 96 (10) (2011) 1503–1511.
- [45] A. Lazaro, H.J.H. Brouwers, G. Quercia, J.W. Geus, The properties of amorphous nano-silica synthesized by the dissolution of olivine, *Chem. Eng. J.* 211 (2012) 112–121.
- [46] E.C. Marcucci, B.M. Hynek, Laboratory simulations of acid-sulfate weathering under volcanic hydrothermal conditions: implications for early Mars, *J. Geophys. Res.: Plan* 119 (3) (2014) 679–703.
- [47] H. Chen, Z. Zheng, Z. Chen, X.T. Bi, Reduction of hematite (Fe₂O₃) to metallic iron (Fe) by CO in a micro fluidized bed reaction analyzer: a multistep kinetics study, *Powder Technol.* 316 (2017) 410–420.
- [48] T.L. Skafte, Z. Guan, M.L. Machala, C.B. Gopal, M. Monti, L. Martinez, E. Stamate, S. Sanna, J.A.G. Torres, E.J. Crumlin, M. Garcia-Melchor, Selective high-temperature CO₂ electrolysis enabled by oxidized carbon intermediates, *Nature Energy* 4 (10) (2019) 846–855.
- [49] A.E. Rubin, Kamacite and olivine in ordinary chondrites: intergroup and intragroup relationships, *Geochim. Cosmochim. Acta* 54 (5) (1990) 1217–1232.
- [50] R.T. Dodd, W.R. Van Schmus, D.M. Koffman, A survey of the unequilibrated ordinary chondrites, *Geochim. Cosmochim. Acta* 31 (6) (1967) 921–951.
- [51] R. Kessel, J.R. Beckett, E.M. Stolper, The thermal history of equilibrated ordinary chondrites and the relationship between textural maturity and temperature, *Geochim. Cosmochim. Acta* 71 (7) (2007) 1855–1881.
- [52] D.J. Fray, G.Z. Chen, Reduction of titanium and other metal oxides using electrodeoxidation, *Mater. Sci. Technol.* 20 (3) (2004) 295–300.
- [53] G.Z. Chen, D.J. Fray, T.W. Farthing, Direct electrochemical reduction of titanium dioxide to titanium in molten calcium chloride, *Nature* 407 (6802) (2000) 361–364.
- [54] B.A. Lomax, M. Conti, N. Khan, N.S. Bennett, A.Y. Ganin, M.D. Symes, Proving the viability of an electrochemical process for the simultaneous extraction of oxygen and production of metal alloys from lunar regolith, *Planet. Space Sci.* 180 (2020) 104748.
- [55] W. Steurer, Vapor phase pyrolysis, *Space Resources* 3 (1992) 210–213.
- [56] C. Senior, Lunar oxygen production by pyrolysis, in: *Space Programs and Technologies Conference*, 1993, p. 1663.
- [57] J.P. Matchett, B.R. Pomeroy, E.H. Cardiff, An oxygen production plant in the lunar environment: a vacuum pyrolysis approach, in: *Space Resources Roundtable VII: LEAG Conference on Lunar Exploration* vol. 1287, 2005.
- [58] H.M. Sargeant, F.A. J. Abernathy, S.J. Barber, I.P. Wright, M. Anand, S. Sheridan, A. Morse, Hydrogen reduction of ilmenite: towards an in situ resource utilization demonstration on the surface of the Moon, *Planet. Space Sci.* 180 (2020) 104751.

Coauthored Paper 5 – Taurid meteoroid stream 628: a reservoir of large impactors

The Planetary Science Journal (2021), Volume 55, Issue 11
p. 2461-2471.

*Hadrien Devillepoix, Peter Jenniskens, Phil Bland, Eleanor Sansom,
Martin Towner, **Patrick Shober**, Martin Cupak, Robert Howie,
Benjamin Hartig, Seamus Anderson, Trent Jansen-Sturgeon, Jim
Albers*

REPRODUCED BY PERMISSION OF THE AAS: *Permission to repro-
duce this article as part of this thesis has been granted by American Astronomical Society,
under license number 4675800498723.*

Statement of Authorship

TITLE OF PAPER: TAURID METEOROID STREAM 628: A RESERVOIR OF LARGE IMPACTORS

PUBLICATION STATUS: Published.

Author Contributions

I, Patrick M. Shober, as a coauthor, contributed to the reduction of the fireball observations collected, analysis of orbital modelling results, and the revisions of the manuscript. These efforts made a 0.5% contribution to the total work of this paper.

I, Hadrien A.R. Devillepoix, as first author, endorse that the level of contribution indicated above is accurate.

DRAFT VERSION AUGUST 20, 2021

Typeset using L^AT_EX preprint style in AASTeX631

Taurid stream #628: a reservoir of large cometary impactors

HADRIEN A. R. DEVILLEPOIX ¹ PETER JENNISKENS ^{2,3} PHILIP A. BLAND ¹
 ELEANOR K. SANSOM ¹ MARTIN C. TOWNER ¹ PATRICK SHOBER ¹ MARTIN CUPÁK,¹
 ROBERT M. HOWIE ¹ BENJAMIN A. D. HARTIG ¹ SEAMUS ANDERSON ¹
 TRENT JANSEN-STURGEON ¹ AND JIM ALBERS²

¹*School of Earth and Planetary Sciences, Curtin University, Perth WA 6845, Australia*

²*SETI Institute, 189 Bernardo Avenue, Mountain View, CA 94043, USA*

³*NASA Ames Research Center, Mail Stop 241-11, Moffett Field, CA 94035, USA*

(Received June 30, 2021; Accepted August 18, 2021)

Submitted to PSJ

ABSTRACT

The Desert Fireball Network observed a significant outburst of fireballs belonging to the Southern Taurid Complex of meteor showers between October 27 and November 17, 2015. At the same time, the Cameras for Allsky Meteor Surveillance project detected a distinct population of smaller meteors belonging to the irregular IAU shower #628, the s-Taurids. While this returning outburst was predicted and observed in previous work, the reason for this stream is not yet understood. 2015 was the first year that the stream was precisely observed, providing an opportunity to better understand its nature. We analyse the orbital elements of stream members, and establish a size frequency distribution from millimetre to metre size range.

The stream is highly stratified with a large change of entry speed along Earth's orbit. We confirm that the meteoroids have orbital periods near the 7:2 mean-motion resonance with Jupiter. The mass distribution of this population is dominated by larger meteoroids, unlike that for the regular Southern Taurid shower. The distribution index is consistent with a gentle collisional fragmentation of weak material.

A population of metre-sized objects is identified from satellite observations at a rate consistent with a continuation of the size-frequency distribution established at centimetre size. The observed change of longitude of perihelion among the s-Taurids points to recent (a few centuries ago) activity from fragmentation involving surviving asteroid 2015TX24. This supports a model for the Taurid Complex showers that involves an ongoing fragmentation cascade of comet 2P/Encke siblings following a breakup some 20,000 years ago.

Corresponding author: Hadrien A. R. Devillepoix
hadrien.devillepoix@curtin.edu.au

Keywords: Meteoroids — Meteor Shower: Taurids, s-Taurids — Comet: 2P/Encke

1. INTRODUCTION

The Southern and Northern Taurid showers are part of a Taurid Complex of meteor showers with daytime and nighttime components, the night-time showers of which spread from September to December along Earth's path (Jenniskens 2006; Brown et al. 2013). Whipple (1940) first identified comet 2P/Encke as the likely parent body. The comet now has evolved to a phase in the rotation of the nodal line that keeps its nodes far from Earth. However, this Jupiter family comet moves in a short 3.3-year orbit that is decoupled from Jupiter, which makes both the comet and meteoroid orbits relatively stable for long periods of time. The wide dispersion of the showers' longitude of perihelion requires a formation age at least 20,000 years ago, the minimum time it takes to disperse the longitude of perihelion of the orbits as wide as observed.

Clube & Napier (1984) first suggested that the a large number of potential other parent body asteroids were part of a Taurid Complex that originated from a giant comet breakup 20,000 years ago. However, Jenniskens (2006) pointed out that these early proposed parent bodies appeared to be S- or O-class stony asteroids, instead, which evolved into Encke-like orbits from a source in the asteroid belt via the ν_6 resonance. The same conclusion was also reached more recently by Popescu et al. (2014) and Tubiana et al. (2015).

Jenniskens (2006) and Jenniskens et al. (2016a) also noticed that there was no mirror image between Taurid shower component nodes in northern and southern branches, suggesting that meteoroids did not survive long enough to fully disperse their nodes around the original orbit. A full precession of the nodal line takes about 5,000 years, hence individual shower components in the South and North branches are likely younger than 5000 years. Instead, Jenniskens (2006) proposed that a more restrictive set of possible parent bodies with semi-major axis close to the 2.22 AU of comet 2P/Encke was responsible and the 20,000 year old stream now reflects the current dispersion of these smaller parent bodies that continue to generate Taurid meteoroids in the recent past. One possible parent was identified as asteroid 2004 TG10, now known to be a 1.3 km large object ($H = 19.4$) with low 0.018 albedo.

This idea that the Taurid complex is active as a whole, and is not just the remnant of a single 20,000+ years old break up, is supported by the orbital analysis done by Whipple & El-Din Hamid (1952). Long before modern orbital integrators and the introduction of orbital similarity criteria D (Southworth & Hawkins 1963; Drummond 1981), they were able to identify a group of Southern Taurids that dynamically converged 1400 years in the past. To explain why Encke did not match the orbit of the group, they suggested that the stream of material could have come from a companion, which could have itself separated from Encke earlier. More recently, Olech et al. (2016) reported two large bolides entering the skies of Poland on October 31, 2015. The meteoroids have very similar orbits ($D_D = 0.011$), and the authors identify two asteroids (2005 UR and 2005 TF50) as potential members of the stream. Using a backward integration, they show that these 4 objects (two meteoroids and two NEOs) have their orbital elements converge 1500 years ago, in good agreement with Whipple & El-Din Hamid (1952). That does not exclude that the bolides originated from one of the two asteroids in more recent times.

Year	Δ_M	Observations
1995	+29°	Spurný (1997)
1998	-13°	Beech et al. (2004)
2005	+11°	Dubietis & Arlt (2007); Shrbený & Spurný (2012); Olech et al. (2017)
2008	-30°	SonotaCo (2009)
2012	+35°	Madiedo et al. (2014)
2015	-07°	this work; Spurný et al. (2017) Olech et al. (2017)
2022	+17°	upcoming return

Table 1. Predicted returns of the Taurid Swarm. Updates for recent years are published at the website <https://www.cantab.net/users/davidasher/taurid/swarmyears.html>, accessed May 16, 2017.

The 2015 bolides were part of an outburst of fireballs that is a repeating phenomenon for the Southern Taurid complex in late October and early November. Every 3+ years, there is a significant uptick of Taurid fireballs (Table 1). There is no clear link to the times when comet Encke returns to perihelion. Instead, it appears that a cloud of meteoroids remains concentrated around a certain position (range of mean anomaly) along the orbit. Olech et al. (2017) reported on Taurids observed in the Polish Fireball Network in 2005 and 2015 and found that over 100 fireballs moved in similar orbits as asteroid 2015 TX24. Similarly, Spurný et al. (2017) found that 113 out of 144 Taurid fireballs observed by the European Network (EN) in 2015 had similar orbital elements and suggested that both asteroids 2015 TX24 and 2005 UR were associated with this stream, and possibly 2005 TF50, arguing that these several hundred metre diameter bodies represented an extension of the population of bodies seen among the observed fireballs.

Froeschle & Scholl (1986) first suggested that meteoroids can be trapped by strong mean motion resonances (MMR) with Jupiter. Material trapped in a MMR is prevented from undergoing full nodal precession, explaining concentrations of dust in mean anomaly over long periods of time. Asher et al. (1993) suggested that this occurred to some Taurids trapped in 7:2 MMR with Jupiter. The expected periodic signature of outbursts was later verified by Asher & Izumi (1998). Their model is successful at explaining enhanced activity in years when the Earth comes within $\Delta_M \in \pm 30/40^\circ$ of the resonance centre in mean anomaly (Table 1). Asher & Izumi (1998) also published future and past year outburst predictions by his model.

Jenniskens et al. (2016b) have identified this shower in 2010 - 2013 CAMS data as #628 in the IAU Working List of Meteor Showers, and called it the s-Taurids (IAU code *STS*). We note that the "new stream" of Spurný et al. (2017) corresponds to the same IAU #628. Hereafter meteor showers IAU #2 (codenamed STA) refers to the "regular" Southern Taurids, IAU #628 (codenamed STS) designates the resonant Southern Taurid branch (s-Taurids), and the Southern Taurid Complex encompass members from both sub-streams.

Spurný et al. (2017) outlined a correlation between size and strength: larger bodies among the 2015 Taurids tend to be more fragile. If so, that would imply that metre-sized objects would break at such high altitudes in the Earth's atmosphere that they might be recognised in satellite observations. More recently, Borovička & Spurný (2020) found from a sample of 16 studied Taurid fireballs that the meteoroids > 10 cm in size had low tensile strength, less than 0.01 MPa, and a density less than 1 g cm^{-3} . Smaller meteoroids contain a higher fraction of materials up to 0.3 MPa in strength.

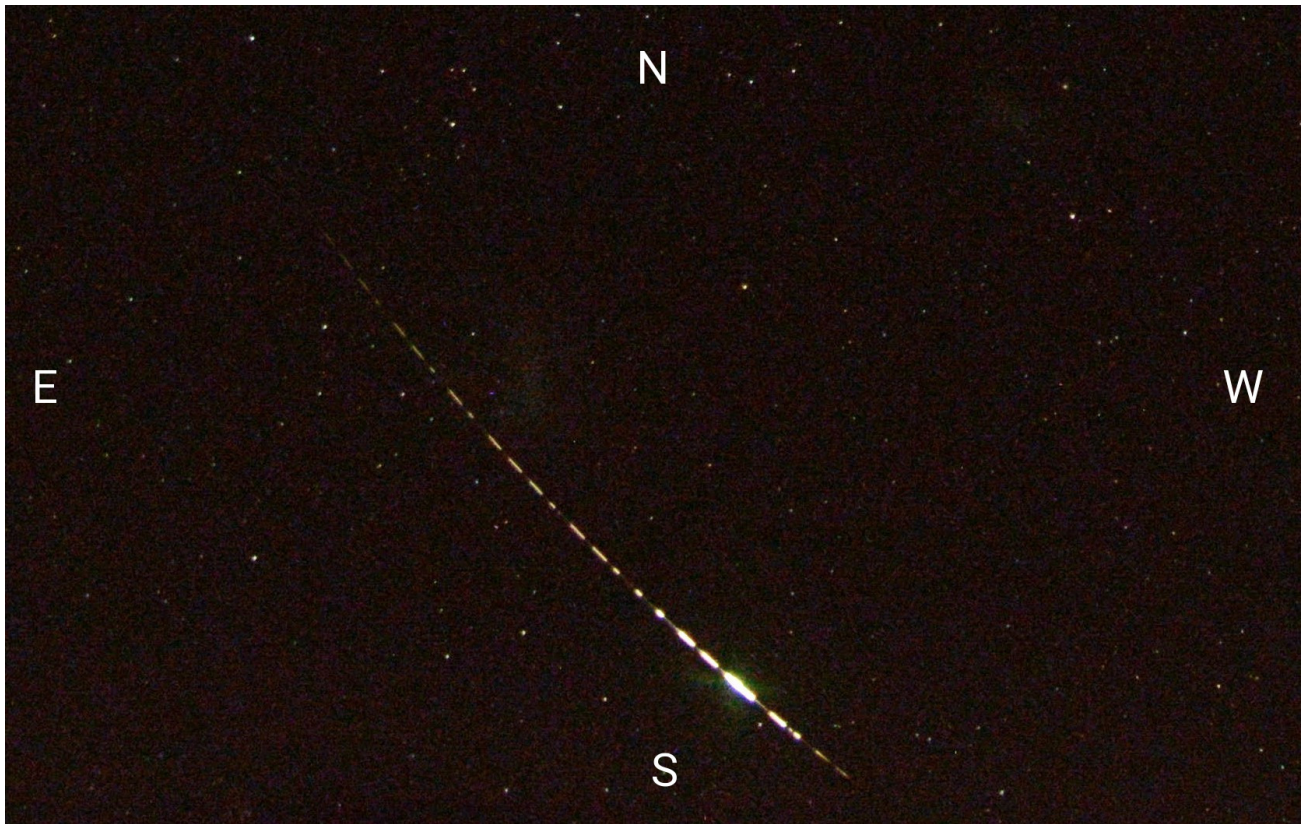


Figure 1. DN151104.01: a 2.6s s-Taurid observed at Hughes siding in the Nullarbor plain, near the Magellanic clouds. This is a crop of the original all-sky picture. The meteoroid experiences a catastrophic fragmentation at 74 km altitude, shortly before the meteor faded.

With an eye on the upcoming 2022 return of the s-Taurids, we present in this paper observations of the enhanced 2015 Taurid fireball activity as observed by the Desert Fireball Network (DFN) in Australia and by the Cameras for Allsky Meteor Surveillance (CAMS) network in California. We investigate changes in the orbital elements along Earth’s path, the stream’s semi-major axis distribution and the particle size distribution of the stream in order to better understand its relationship to comet 2P/Encke and other Taurid Complex parent bodies.

2. DATA AND METHODS

DFN and CAMS survey meteoroid impacts at different sizes ranges: CAMS has the sensitivity to detect large numbers of small millimetre to centimetre size grains, while the DFN takes advantage of a large collecting area to catch centimetre to decimetre scale meteoroids, at the cost of lower sensitivity. When it comes to observing a bright meteor shower like the Taurids, the two systems complement each other well.

2.1. DFN

In 2015, the Australian Desert Fireball Network covered 1.5 million km^2 of sky viewing area, established around 30° S latitude (Howie et al. 2017a). Each DFN observatory comprises of a high-resolution still imaging system: a 36 Mpixels digital camera (Nikon D800, D800E, or D810),

associated with a Samyang 8 mm f/3.5 fish-eye lens, taking 25 seconds exposures at 6400 ISO. In 2015 all observatories operated with these settings. The field of view of the cameras is all-sky, except for a crop of 10 degrees on the horizons of long sides of the sensor (usually North and South). The pixel size is 119 seconds of arc in the center, decreasing towards the edges (87 seconds of arc at 5° elevation). The cameras are sensitive to stellar magnitude 0.5 for meteors (7.5 for stars), and reliably detect meteors that are brighter than apparent magnitude -1.5 for > 0.9 second.

Meteor events are automatically detected in the images by the software procedures described by Towner & et al. (2019). Astrometric measurements are performed in the same manner as described by Devillepoix et al. (2018), resulting in measurements precise down to 1-2 minutes of arc. The triangulation of meteor trajectories are performed using a weighted straight line least squares approach, similar to the one described in Borovička (1990). In order to get an appropriate entry velocity for the meteoroid, an extended Kalman smoother is applied to the positional data, throughout the visible bright flight (Sansom et al. 2015). This method also yields statistical uncertainties that encompass both model errors and measurement errors. These results are crucial for initialising orbit determination as orbital parameters, like the semi-major axis and eccentricity, are very sensitive to the errors in initial velocity. The heliocentric orbit of the meteoroids are determined using a backward integration from the start of the visible bright flight. The meteoroid is back-tracked through the upper layers of the atmosphere, and out of the sphere of influence of the Earth to a distance of one Hill sphere (Jansen-Sturgeon et al. 2019). Uncertainties on the orbital parameters are computed using a Monte Carlo method based on the uncertainties of the first velocity vector observed.

The DFN data reduction pipeline uses aperture photometry on the fireball track to calculate brightness. Doing photometry on the reference stars used for astrometry yield instrumental zero point of each camera, accounting for extinction and vignetting. The fireball brightness is converted into magnitudes by accounting for the different exposure times: the effective exposure time for stars is typically 11.2s (25s exposure modulated by the liquid crystal shutter), and 0.06s or 0.02s for a fireball shutter break (see Howie et al. (2017b) for details on the action of the liquid crystal shutter). Apparent magnitude is converted to absolute (for constant distance of 100 km) after triangulation, using the observation range. The main limitation on this technique is the saturation of the sensor, which typically happens when the fireball exceeds apparent magnitude -6. Blooming of the trail enables brightness measurements out to about -10 magnitude.

The main use of photometric measurement in the present study is to calculate meteoroid strength and to get a zero-order mass estimate. As detailed by Brown et al. (2016), the peak brightness instant of a fireball is a good indicator of catastrophic fragmentation, and therefore a reasonable proxy for calculating a bulk tensile strength for the entering body. This method is more robust to instrumental bias than the PE criterion introduced by Ceplecha & McCrosky (1976), and has the advantage of being inferred directly from observable parameters (no mass calculation involved). We therefore use the following relation from Bronshten (1981) to calculate tensile strength S : $S = \rho_{atm} v^2$, where ρ_{atm} is the density of the atmosphere estimated using the *NRLMSISE-00* atmospheric model (Picone et al. 2002). v is the velocity at that instant calculated by the Kalman smoother described by Sansom et al. (2015). The main limitation of the method comes from the uncertainty on the instant of peak brightness, dominated by the sampling rate (10 Hz), which translates into 2 km of altitude for the average Taurid, or a $\simeq 1.3$ factor in strength.

Thanks to the continental scale of the network, operational and weather biases are mitigated by the large collecting area and observation time. However a consequence of this is that precisely determining the surveying area probed by the instrument is difficult. While calculating probing area as a function of time may be done accurately and relatively easily when a small number of narrow angle optics are used, such as described in [Blaauw et al. \(2016\)](#). Even at a basic level, this kind of work with all-sky cameras spaced on a continent-scale network, is more tricky, and de-biasing the DFN dataset to get precise fluxes will be the subject of a future paper.

The DFN observatories, combined with the data reduction methods described above, have led already to multiple meteorite recoveries: Creston ([Jenniskens et al. 2019](#)), Murrili ([Sansom et al. 2020](#)), Dingle Dell ([Devillepoix et al. 2018](#)), as well as 3 more recent (not yet published) recoveries. These successes in precisely pinpointing the location of meteorites are good indications that the data reduction process is free of major systematic issues.

2.2. CAMS

The main goal of CAMS is to map the presence of meteor showers of +4 to -5 magnitude meteors throughout the year. In November 2015, CAMS networks had been established in California, Arizona, Florida, the BeNeLux, and New Zealand. Most CAMS networks are on the northern hemisphere, but they experienced a relatively small number of cloudy days that year. CAMS methods are described in detail in [Jenniskens et al. \(2011\)](#). In brief, CAMS utilises a network of analog low-light video cameras, mostly Watec Wat902H2 Ultimate cameras with $30^\circ \times 20^\circ$ field of view each and +5.4 stellar limiting magnitude. Customised software detects the meteors, calibrates the background star field to obtain astrometric positions, and then combines such data from two or more stations to triangulate the meteor trajectory. CAMS yields more than 100,000 meteoroid orbits per year, and has proven to be a very efficient tool for studying meteor showers and linking them to possible parent objects ([Jenniskens et al. 2016b,c,a](#)).

The high detection rate of meteors not assigned to showers by ([Jenniskens et al. 2016a](#)), with geocentric entry speed < 35 km/s from the antihelion source at the same time as the Taurid showers, provides a baseline of sporadic meteor shower activity that can be used to calculate the effective observing time due to weather. The CAMS flux data were de-biasing by assuming a constant sporadic flux during the s-Taurid activity period. The main CAMS networks are situated at a latitude of $\phi = +37$ deg, where the Southern Taurid radiant is up almost all night in early November and the mean altitude of the Southern Taurid radiant is $hR \simeq 40$ deg. This results in a correction factor of $1/\sin(hR) = 1.35$ to get the equivalent zenithal hourly rate. For scaling the distribution we use the flux density of [Grün et al. \(1985\)](#), $f_G = 6.85 \times 10^{-8} > 1$ g meteoroids $\text{m}^{-2} \text{year}^{-1}$, and the correction factor between interplanetary and top of the atmosphere $S = 0.67$ be of [Moorhead et al. \(2019\)](#). From this, we can calculate the influx of s-Taurid on the Earth as:

$$N(\#628 > 1 \text{ g impacts on Earth}) = \frac{n}{m} * \frac{1}{\sin(hR)} * f_G * S * 2 * \Delta\lambda_\odot * \text{X-section}_{\text{Earth}}$$

In this formulation $\Delta\lambda_\odot$ is the exposure time to the shower as observed by CAMS, and the factor 2 is there to compensate that a surface at top of the atmosphere is effectively twice the collecting area of the model randomly tumbling plate of [Moorhead et al. \(2019\)](#). In relation to a meteoroid stream, the Earth's exposure to the stream can be effectively represented as a cross-section area defined by its radius.

The reported flux values are limited to a 1 g threshold mass using the observed magnitude distribution. The count of all sporadic meteors with the 25-30 km/s entry speed of Taurids was assumed to be exponential in shape of this magnitude interval, from which a detection probability function was derived by fitting an exponential slope to the bright-end of the magnitude distribution and then dividing observed counts by the fit-predicted count. The fraction of completeness for magnitudes -1 and up was: $P(m) = 1.00, 0.80 \pm 0.02, 0.37 \pm 0.01, 0.093 \pm 0.003, 0.014 \pm 0.002, 0.0011 \pm 0.0002$, and $\sim 5e-6$. This probability function was then applied to the detected count of shower meteors to derive the magnitude size distribution of different Taurid Complex component showers.

3. RESULTS

The 73 measured DFN orbits from the Southern Taurid Complex in 2015 are provided as an appendix to this manuscript. The CAMS-derived Southern Taurid Complex orbits were released as part of the 2013 – 2016 CAMS data release and can be accessed via the project website (<http://cams.seti.org>) and via the Meteor Data Center. In 2015, CAMS detected $N = 10,942$ Southern Taurids ($N = 177 > 1$ g) between $\lambda_{\odot} \in [213.19-234.25]^{\circ}$. In the same period, 131,230 ($N_{\text{spo}} = 1193 > 1$ g) sporadic meteors were recorded.

3.1. Comparison of *s*-Taurids with regular Southern and Northern Taurids

The *s*-Taurid shower stands out well from other Southern Taurid complex meteors by their geocentric speed. Fig. 2 plots the geocentric speed and time (solar longitude) of all meteors associated with the Southern Taurid complex in both the CAMS (top) and DFN (bottom) datasets. Vertical white bands are due to cloudy weather with less than complete coverage. The data are split in two groups: the outburst years of 2012 and 2015 (Table 4), and the no-outburst years of 2010, 2011, 2013, 2014, and 2016. The 2012 encounter with the *s*-Taurids is $\Delta_M = 35^{\circ}$ from the centre of the resonance according to the model of Table 1. Hence, the weak detection of the *s*-Taurids in 2012 by CAMS implies an extend of this component until at least mean anomaly 35° , in agreement.

The outburst years show a component that produces a narrow range of geocentric entry speed at any given solar longitude, with a strong change in the speed as a function of time. This component is only weakly present in non-outburst years (Fig. 2). This component was earlier identified as shower #628, the *s*-Taurids (IAU code STS). The period of activity for this component is $\lambda_{\odot} \in [213, 234]^{\circ}$.

The presence of this STS component is also evident in the 2015 DFN data (Fig. 2), despite a lower number of orbits, as the STS stream largely dominates the Southern Taurid activity at fireball sizes. The change in velocity with solar longitude translates into a strong increase of perihelion distance with increasing solar longitude and a decreasing eccentricity. The semi-major axis and inclination of the orbits remain nearly constant, as does the longitude of perihelion.

Fig. 3 shows the de-biased STS rates for CAMS, along with that of the remaining STA and NTA streams. The rates are normalised to that of all sporadic meteors with speeds $< 35 \text{ km s}^{-1}$. This ensures that the total sporadic count reflects the observing conditions during that part of the night when the antihelion source is best observed. The sporadic apex and Toroidal sources have been removed from the count. The 2015 STS count was compared to the sporadic meteor rate in 2015 only. The multi-year de-biased distribution produced better defined shower activity profiles than early results in Jenniskens et al. (2016c). The shower components identified in Jenniskens et al. (2016a) are still present. The STA and NTA shower profiles are different, an indication that the nodal line of individual meteoroid orbits did not fully rotate, as earlier pointed out.

8

DEVILLEPOIX ET AL.

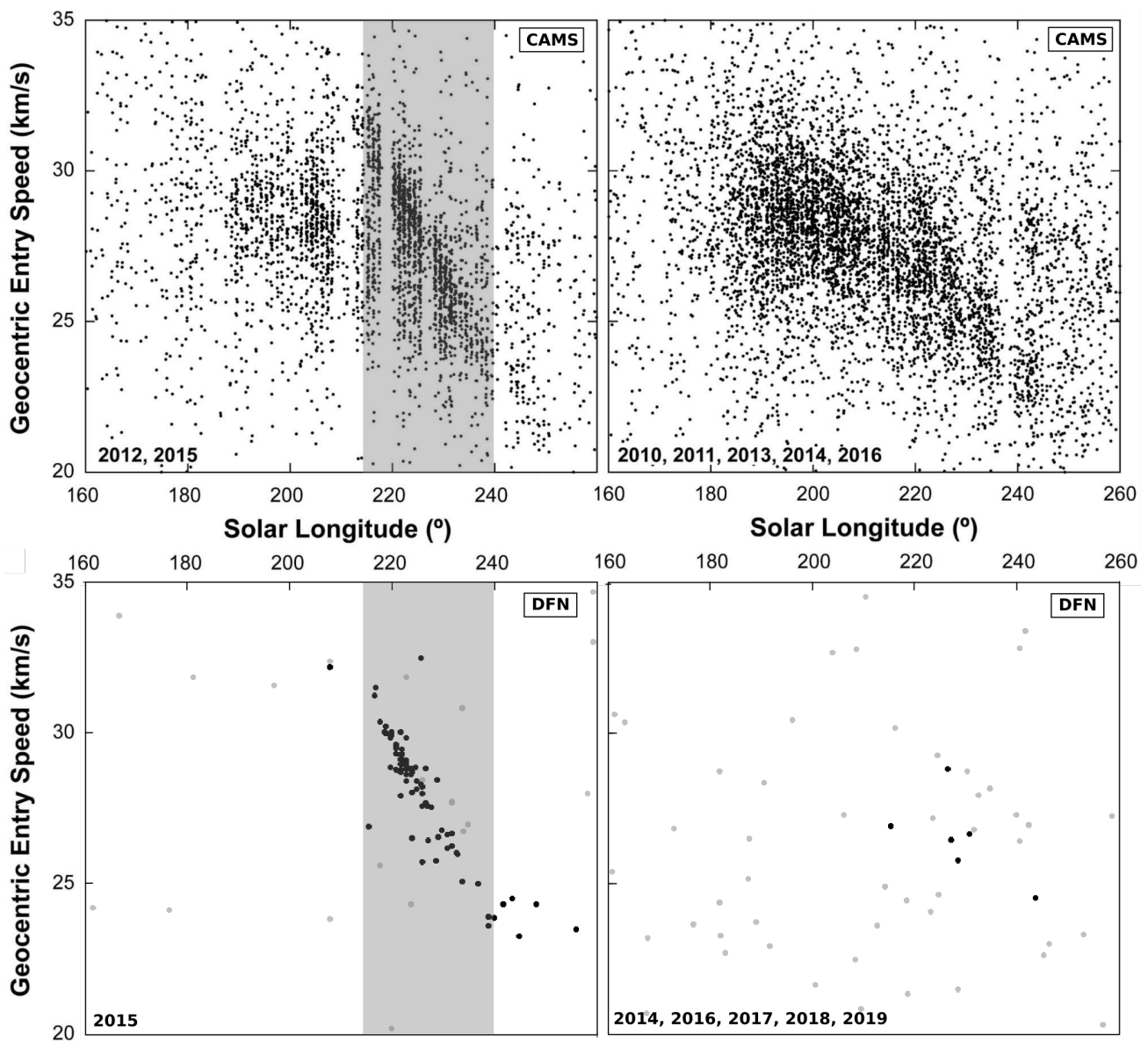


Figure 2. Detected meteors geocentric entry speed as a function of solar longitude. STS activity years (left) are separated from other observation years (right). In DFN data, fireballs identified as Southern Taurids are marked in black against grey background fireballs. While the STS component of the Southern Taurids, recognised by its strong date-speed linear relationship, is visible in the meteor data (CAMS, top left), it is even more obvious at fireball sizes (DFN, bottom left).

3.2. Size frequency distribution of the #628 STS stream

Fig. 4 shows the distribution of peak magnitudes in 0.5 magnitude intervals for CAMS-detected NTA, STA and STS meteors. The STS population is significantly more skewed towards brighter meteors. The cumulative mass-frequency distribution as observed by CAMS (Fig. 8) can be expressed as $N(> m) = am^{-b}$ with $a = 1.42 \times 10^5$ and $b = 0.94$ when expressed in grams. This is representative of the total influx of s-Taurids during the 2015 encounter.

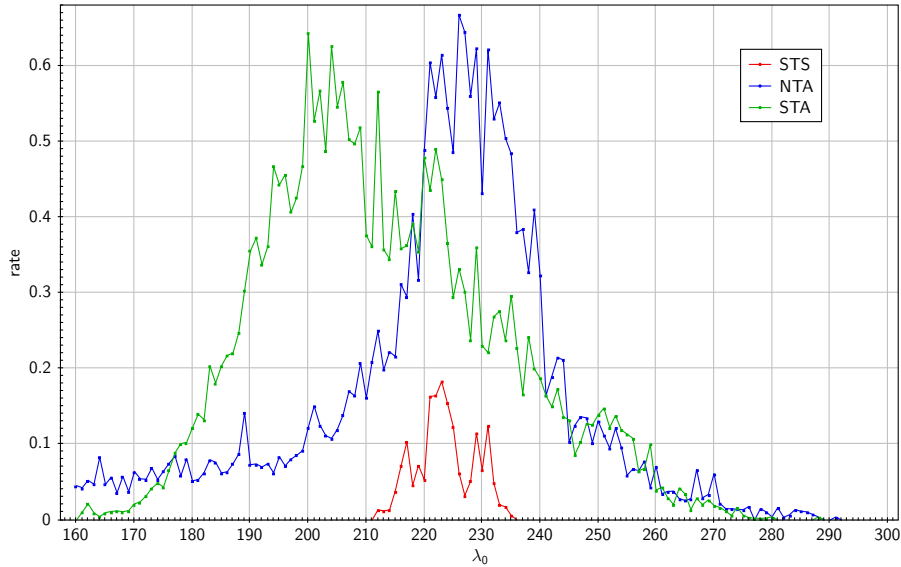


Figure 3. De-biased CAMS shower rates relative to that of sporadic meteors $< 35 \text{ km/s}$ for shower 628 (STS), the Southern Taurids (STA) and the Northern Taurids (NTA), as a function of solar longitude.

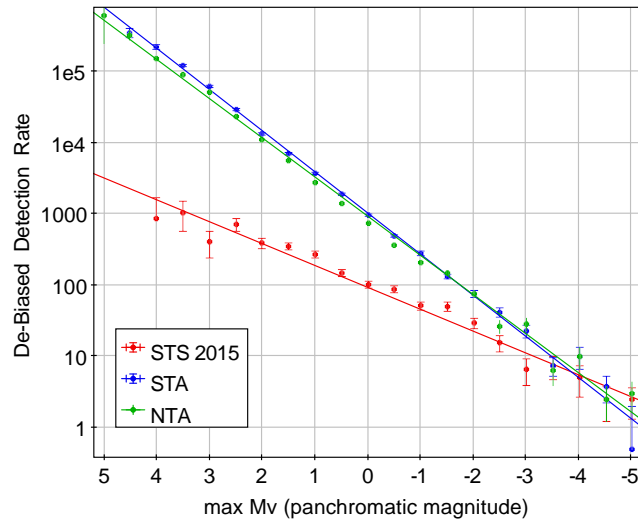


Figure 4. Peak magnitude frequency distribution for Southern Taurids substreams #2 STA, #17 NTA and #628 STS. Resonant Taurids (STS branch) are generally larger than regular Southern Taurids (STA).

The annual Southern and Northern Taurids have differential magnitude indices of $\chi \simeq 3.0$ (Fig. 3), this is close to the typical value for JFC material ($\chi = 3.29 \pm 0.09$, as determined by Jenniskens et al. (2016a)). On the other hand s-Taurids have a much shallower distribution with $\chi \simeq 2.0$ (assuming a sporadic $\chi = 3.4$). This gives a differential mass index for the observable stream of $s = 1.75$ ($s = 1 + 2.5 \log(\chi)$).

The observed size distribution confirms that the s-Taurids are relatively rich in large meteoroids. Indeed, a study by Soja et al. (2011) on radar meteor observed by the Canadian Meteor Orbit Radar (CMOR) in 2005 (typical observed mass of 10^{-7} kg , which roughly corresponds to optical magnitude

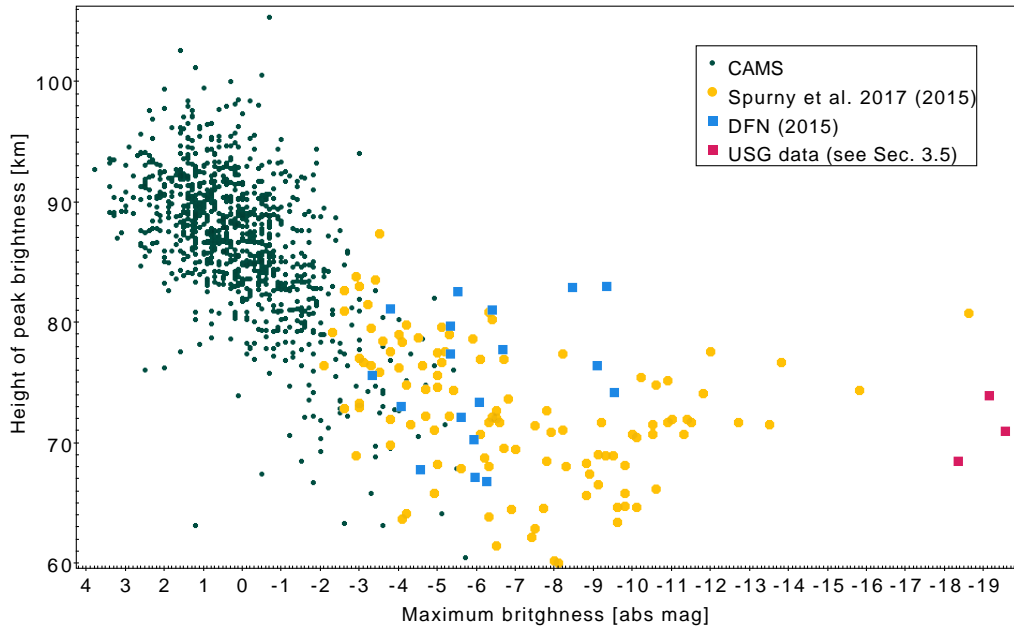


Figure 5. s-Taurids height of peak brightness as a function of brightness. DFN magnitudes may be slightly underestimated because of saturation issues.

+7), failed to identify the 7:2 resonance from regular Southern Taurids. They discuss that this is partly due to the poor constraints the radar observations put on the velocities (and therefore the semi-major axes), so it is not possible to distinguish STSs from STAs dynamically. Therefore unless the STS outburst is strong enough to significantly skew the overall Southern Taurids rates, it is not detectable. Soja et al. (2011) do not provide an upper constraint on the STS/STA activity, but even without hard numbers this analysis confirms the trend shown in Fig. 4: the STA branch dominates the STS branch at the low mass end ($Mv_{max} > -4$).

Beyond CAMS data, towards fireball sizes, flux density data for this stream becomes more scarce. The DFN and EN fireball networks do not yet have time-area de-biasing information to calculate flux densities. The masses reported by (Spurný et al. 2017) give an idea of the slope of the distribution at magnitudes below -9, where the EN sample appears to be complete (Figure 8). Although it is apparently more shallow than the slope calculated by CAMS, the numbers are so small that the extrapolated flux agrees within 2 error bars (2 sigma). Even at these bright magnitudes there may still be an effect of the brightness-dependent variation in effective covering/reporting: the brighter the bolide, the further it can get detected and studied.

3.3. Strength of the meteoroids in the #628 STS stream

Figure 5 shows the altitude of peak brightness as a function of peak meteor magnitude. The result shows that larger meteoroids penetrate deeper in Earth's atmosphere before reaching peak brightness, as expected. Among CAMS-detected visual meteors, that is a fairly continuous trend. However, at the larger fireball sizes, meteoroid penetration enters a strength dominated regime. The transition into the strength-dominated regime occurs at about -7 magnitude. In the strength-dominated regime, the altitude of peak brightness is independent of mass, although there is a weak trend that the largest meteoroids are weaker than the smaller meteoroids near this transition. All s-Taurids experience

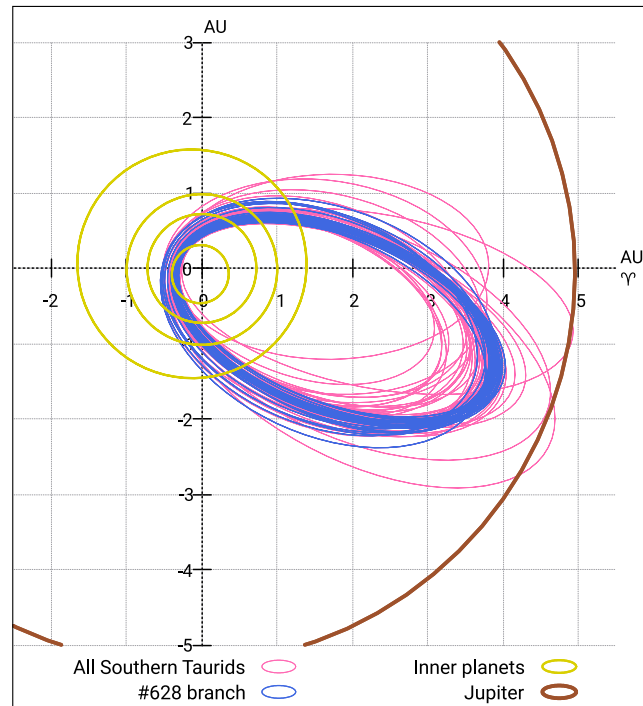


Figure 6. Ecliptic orbit plot of all Southern Taurids observed by the DFN in 2015 (pink), and the #628 branch (blue).

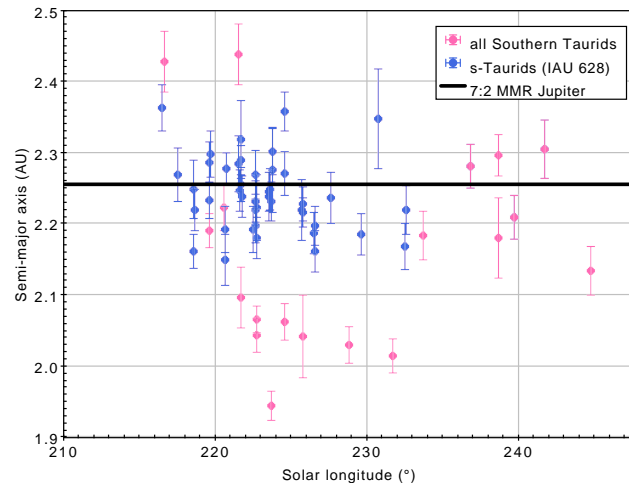


Figure 7. Semi-major axis measurements (with 1σ uncertainties error bars) of all Southern Taurid fireballs observed by the DFN 2015. Most are significantly higher than typical Southern Taurids, compatible with the a 7:2 mean-motion resonance with Jupiter (centered on 2.256 AU).

their peak brightness above 60 km altitude (Fig. 5), and do not survive below 50 km altitude. The deepest penetrating fireball had a minimum height of 54.5 km, while the average end height of the DFN fireballs was 67.2 km (see suppl. mat. table). This is consistent with the results of Spurný et al. (2017).

3.4. *Semi-major axis of the fireball orbits*

Figure 6 is an ecliptic orbit plot of all Southern Taurids observed by the DFN in 2015. The Figure shows that most observed Taurid fireballs clustered in a tight stream with constant longitude of perihelion (all ellipses pointed in the same direction). These s-Taurids are shown in blue. This stream is highly stratified: they form a series of more or less concentric ellipses for fireballs detected at different solar longitude along the Earth's orbit. Unlike most meteoroid streams, this stream appears to be more narrower at aphelion than at perihelion. The dispersion of perihelion distances (q) of the blue orbits is 8.9 percent (one standard deviation), while the aphelion distance (Q) is dispersed by only 2.4 percent, and the semi-major axis (a) by 2.1 percent. a and Q are tightly correlated, a and q are not. The stream approaches the orbit of Jupiter near aphelion, suggesting that the secular perturbations responsible for the observed dispersion are strongest near aphelion, not near perihelion.

Figure 7 plots the semi-major axis of the 2015 Taurid fireballs measured in the DFN network as a function of solar longitude (time in the year). The DFN-derived orbits during solar longitudes 217.5 and 227.5 show a clear concentration of semi-major axis values around the mean semi-major axis $a = 2.234 \pm 0.007$ AU with a standard dispersion of 0.041 AU. The mean calculated error in the semi-major axis values is 0.034 ± 0.014 AU, in good agreement with the observed dispersion if all these orbits have exactly the same semi-major axis of $a = 2.2563$ AU corresponding to the 7:2 mean-motion resonance with Jupiter (dashed line). This result confirms earlier conclusions from EN fireball observations reported by Spurný et al. (2017) that the meteoroids appear to be trapped in this resonance, and demonstrates the accuracy of the semi-major axis calculations. Most of the observed dispersion in semi-major axis is due to measurement error. However, there is a small systematic error of -0.022 ± 0.007 AU.

The fireballs shown in pink are outside the main dispersion. Most have slightly smaller semi-major axis, while three orbits just reach the orbit of Jupiter. 52 of the observed trajectories have a semi-major axis within 2 sigma from the resonant value. 21 have not. Surprisingly, the ones that have not scatter around the time of the outburst over 216.5 to 231.7 degrees solar longitude (CAMS has 212 to 235 degrees range, see below), while the ones that are within 2 sigma from the resonant value scatter over the whole observing interval of 207.7 to 255.9 solar longitude. Hence, whether or not the trajectories scatter around the resonant value is not a mark of the s-Taurids, it is a mark of the Southern Taurids as a whole.

Some of the pink orbits may represent measurement errors in the initial velocity determination. Or they are a more perturbed population of meteoroids that possibly already experienced some changes in semi-major axis due to encounters with the terrestrial planets. If so, they are likely part of the background Southern Taurids.

3.5. *The metre-size population*

Spurný et al. (2017) first pointed out that the stream contains metre-sized asteroids. Here, we will attempt to quantify this. The US government (USG) satellite sensors detect m-scale impactors in Earth's atmosphere over the entire planet as a collecting area, or if a meteoroid stream is involved approaching from a given direction that collection area is the projected Earth surface to that stream.

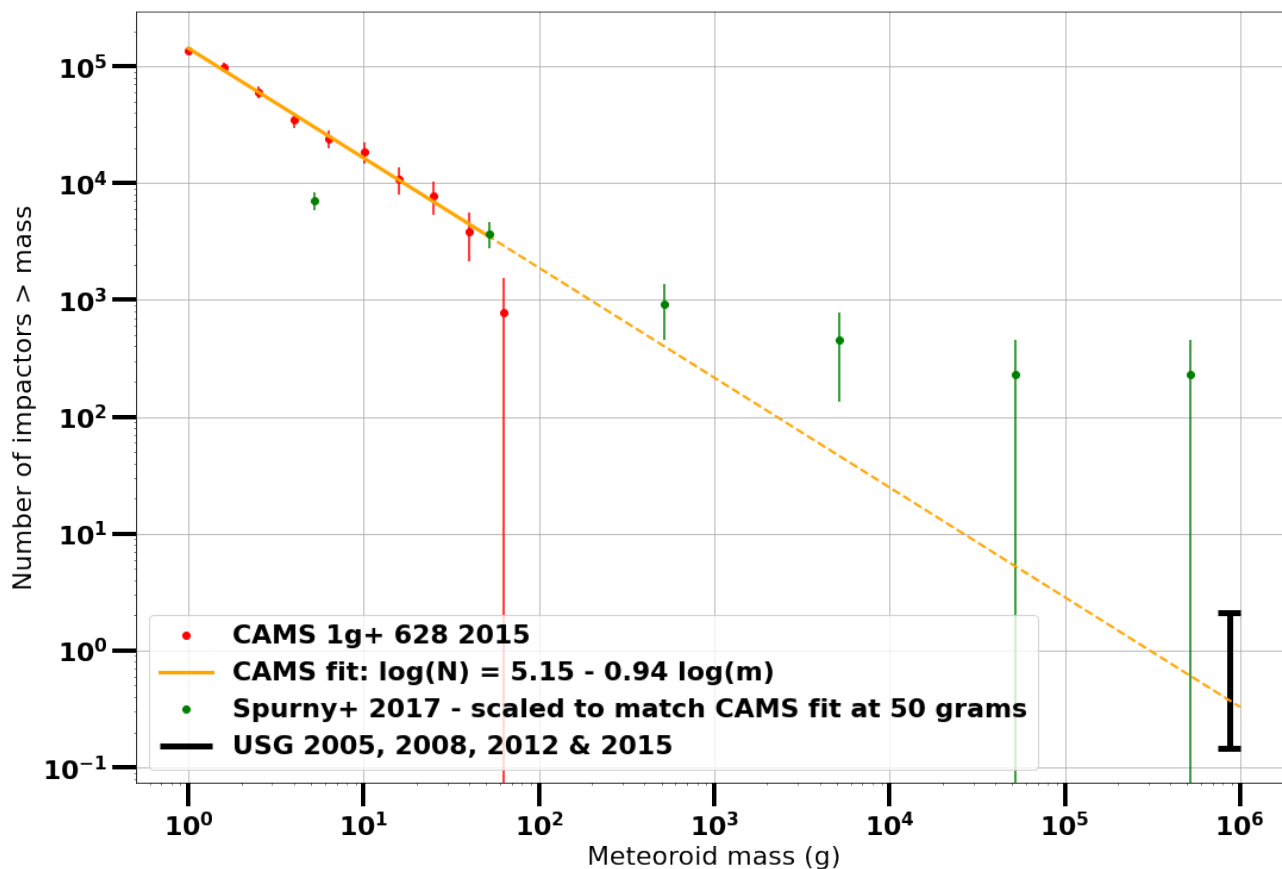


Figure 8. Cumulative mass-frequency distribution. CAMS > 1 g meteors left is fitted based on the 2015 data (see Sec. 3.2). The s-Taurid 2015 data of Spurný et al. (2017) is presented in green, with the event frequency scaled to match CAMS' at 50 grams. Note that the different slope for this data may not be real and could come from a brightness-dependent variation in effective covering area. The right-hand side estimate comes from 3 likely large s-Taurids observed by the USG sensors in 2005 and 2015.

These data are reported online on the NASA JPL fireball website¹. Even with this large a collection area, the chance of detecting impacts is small. Figure 8 shows the cumulative mass-frequency distribution from CAMS and DFN data. The USG detected bolides are about -18 magnitude and brighter (Tagliaferri 1994). That leaves a large gap without de-biased data.

Extrapolating the mass-frequency distribution established in Sec. 3.2, we predict 0.37 meteoroid > 940 kg impacting the Earth during the 2015 s-Taurid episode. Indeed, the USG satellites detected no unusual number of fireballs in late October and early November 2015. One bolide was detected on 2015-10-31, one on 2015-11-02 and one on 2015-11-13. No velocity components are reported, so we do not know the radiant or speed of these bolides.

However, there are data from multiple years of observation now. If any Taurids are among these impactors, we expect their penetration depth to be relatively shallow based on the size-dependence

¹ <https://cneos.jpl.nasa.gov/fireballs/>, accessed May 16, 2017

Table 2. 14 high altitude (≥ 60 km) meteoroid airbursts observed by the USGS. No velocity information was provided for the events presented here. Highlighted rows show events that fall within the STS activity period. The 4 events at the bottom are excluded for statistical significance reasons (see in the text). Size is calculated from the energy, assuming the velocity is equal to the mean STS velocity observed by the DFN at the same given solar longitude (see Suppl. Mat. Table), and the 1600 kg m^{-3} bulk density estimated by (Babadzhanov & Kokhirova 2009).

Peak brightness time ISO UTC	λ_{\odot} °	Latitude ° (N+)	Longitude ° (E+)	Altitude km	Total Impact Energy kilotons TNT	Size m
2015-10-31 11:34:30	217.51	9.0	-138.0	71.0	0.29	1.5
2015-06-10 17:43:03	79.32	-11.5	-161.9	61.1	1.0	
2013-08-12 18:08:02	140.00	-34.4	118.2	66.6	0.15	
2012-02-12 05:25:52	322.72	-31.7	54.9	61.0	0.41	
2011-01-21 15:11:43	301.07	18.9	-44.6	61.0	0.23	
2010-12-09 02:54:07	256.76	-54.5	-169.7	66.0	0.2	
2005-12-24 15:30:26	272.85	-54.0	17.3	66.0	0.51	
2005-11-02 07:04:32	219.89	33.9	-154.9	68.5	0.11	1.1
2005-11-02 05:16:47	219.81	22.9	-123.8	74.0	0.21	1.3
2005-04-06 01:30:24	16.28	-42.7	154.6	70.0	0.1	
*2011-08-04 07:25:57	131.44	-40.7	-86.7	63.0	0.098	
2004-01-02 04:27:59	281.05	-28.2	3.2	63.0	0.39	
1999-06-25 06:27:41	93.30	50.0	121.0	69.0	0.37	
1999-01-02 18:25:51	281.93	47.0	103.0	65.0	0.12	

shown in Figure 5. The observed cm-dm sized meteoroids by CAMS, DFN, and EN show no significant decrease in peak height as sizes get larger.

The USG data only include the altitude of peak brightness. We started by filtering the USG dataset by height of maximum brightness > 60 km as a first pass to identify weak cometary impacts, as STS observed by the DFN break up > 66 km (Fig. 5). We note that the stated peak brightness altitude from the sensors is generally reliable to about ± 4 km, as shown by Brown et al. (2016), and that these altitudes are reported for most events from the beginning of 2005 onwards. Detections are made at night, but also in daytime. As mentioned by Devillepoix et al. (2019), the typical energy report limit is 0.1 kT TNT, therefore we exclude event *2011-08-04 07:25:57* (0.098 kT reported yield) from our analysis for detection significance issues. We are left with 10 significant events that fit the height criterion (Table 2). However, there are no velocity vectors reported for these events, so there is no direct dynamic link between any of these and the Taurid complex.

Nevertheless, 3 out of these 10 very weak meteoroids fall in the STS activity period, and even more remarkable they happen in 2005 and 2015, two years during which strong STS activity has been reported and are predicted by the model of Asher & Izumi (1998) (Table 1). In 2005, two events occurred in short succession. All three events suggest the largest fragments in this stream are at solar longitude $[213, 234]^{\circ}$. This combined with data in Fig. 3, these USG bolides occurred during the STS activity period. We confirm that these 3 events happened while the Southern Taurid radiant was above the local horizon.

Table 3. Poisson test on the significance of the impact rate increase of metre-sized weak material (peak brightness > 60 km) hitting the Earth observed by the USGS during STS outburst episodes ($\lambda_{\odot} \in [213, 234]^{\circ}$). Ranges given are at 2σ confidence. The influx increase factor during an STS outburst is $[2.1, 46]\times$.

population	surveyed years	observed events	λ_{\odot} integrated ($^{\circ}$)	rate ($Earth^{-1}\lambda_{\odot}^{-1}$)
weak impactors population	[2005-2016]	10	3960	[0.001 - 0.005]
probable STS	2005, 2008, 2012, 2015	3	84	[0.007 - 0.1]

Can these bolides signify a detection of the s-Taurids? Considering the very low number of events observed, we need to build a statistical test to assess the significance of this apparent rate increase during a swarm episode. Let us test the hypothesis H_1 : "An airburst from weak material (main explosion > 60 km) is more likely to happen during a STS activity period" against the null hypothesis H_0 : "No increase in the rate of impacts from weak bodies can be observed during a STS activity episode". We define a STS swarm episode as a period that happens on a year predicted by the model of Asher & Izumi (1998), within the interval where the USG sensors have consistently observed airbursts heights (2005, 2008, 2012, 2015), and within the activity period observed by CAMS (solar longitude $\in [213, 234]^{\circ}$). We use the *rateratio.test R* package², that implements the methods described in Fay (2010) to carry out the statistical test. At 95% confidence, the background weak metre scale impact rate is $[0.001, 0.005]$, compared to $[0.007, 0.1] Earth^{-1}\lambda_{\odot}^{-1}$ when $\lambda_{\odot} \in [213, 234]^{\circ}$, which corresponds to a weak impactors influx increase of $[2.5, 55]\times$ (see Table. 3 for full test data and results). The small p - value = 0.004 shows strong evidence against the null hypothesis (at 95% confidence).

Although we cannot definitely link any individual events with the Taurids, the apparent rate increase in metre-scale weak impactors during the STS outburst activity is statistically significant, and we can say that during an STS outburst episode the Earth is more likely to get impacted by a metre-scale STS than a sporadic meteoroid of the same size. Over an s-Taurid episode, the number of > 0.1 kT TNT of s-Taurid impactor is $[0.15, 2.1]$ (Fig. 8).

Adding this detection rate to the overall picture shows that the meteoroid size distribution does not change down to metre size scale (Fig. 8). This result implies that the #628 STS stream contains some of the largest meteoroids known to any cometary meteor shower.

Finally, it is possible that the USG satellite detections do not represent all large bolides in Earth's atmosphere. The European Network detected one superbolide during the 2015 outburst called *EN311015_180520* (Spurný et al. 2017). The observation of this 1300 kg bolide over a superbolide coverage area of roughly 0.1% Earth is statistically unlikely, but not impossible (Fig. 8). The *EN311015_180520* superbolide (0.17 kT TNT total kinetic energy) should have been well within the detection range of the USG sensors, but this bolide was not reported. A single mis-match is not indicative of a particular issue as the USG sensors are known to have had as low as 70-80% Earth coverage in the past (Brown et al. 2002). The USG sensors s-Taurid flux could have been underestimated by a factor of 2 considering both 2008 and 2012 were taken into account for the USG clear-sky calculations (Sec. 3.5), as these 2 years were quite distant from the resonance centre. It could mean

² <https://cran.r-project.org/package=rateratio.test>

that the metre-scale s-Taurid is a factor of 2 larger than what we calculated here. That would still be consistent with a constant mass distribution index from cm to metre scale (Fig. 8).

4. DISCUSSION

4.1. *Nature and origin of the s-Taurids*

The low magnitude distribution index ($\chi = 2.0$) and small differential mass index ($s = 1.75$) is atypical of most JFC showers. Such values point to a collisionally relaxed population, with equal combined cross-section area in each magnitude bin ($s = 1.67$), or a collisional cascade where each meteoroid is broken by a mass just big enough to do so ($s = 1.83$). This points to a very gentle collision process such as would be experienced during a cometary breakup of relatively strong material with intrinsic low- s size distribution. High velocity collisions in the interstellar medium or other aging processes like grain charging and thermal cycling did not significantly affect the size distribution index of this population of meteoroids. That means that the stream is relatively young and was born from relatively strong cometary material. Weak cometary material breaks into very steep distributions towards small particles (Jenniskens 2006).

The unusual large number of shower fireballs detected by DFN and EN points to the presence of large meteoroids in this stream. Continuation of the particle size distribution to larger sizes implies a population of metre-sized objects in this stream that appears to have been detected in USG satellite observations. The presence of such large bodies in the stream is consistent with the material being relatively strong for cometary material in general. This stream is currently a major contributor to the overall population of large weak meteoroids. If the USG statistics are representative of larger cometary impact hazards, the s-Taurids dominate the flux when they are active, increasing the impact risk by $[2.5, 55] \times (2\sigma)$, and overall they represent a significant fraction of all large cometary impactors, even though their activity period is only a few weeks every couple of years!

Our measured DFN fireball mean semi-major axis of 2.234 ± 0.007 AU is 0.019 AU higher than the semi-major axis of 2P/Encke, but 0.022 AU lower than the $a = 2.2563$ AU corresponding to the 7:2 mean-motion resonance with Jupiter. It is also 0.031 AU lower than the current semi-major axis of 2015 TX24. Natural oscillations of semi-major axis are about 0.03 AU in this part of the asteroid belt (Nesvorný & Morbidelli 1998), so the motion of all objects will be affected by the mean-motion resonance. If the breakup happened in the resonance with small relative ejection velocities, it is likely the resonance prevented the dispersion of the dust by avoiding Jupiter's presence at aphelion when the dust was there.

Spurný et al. (2017) argued that the s-Taurids are the product of fragmentation event (of 2004 TG10?) at about 3.6 AU distance from the Sun, where the fireball orbits have lowest dispersion, with relatively high ejection speeds of 1.5 km/s. The observed asteroids 2005 TF50, 2015 TX24 and 2005 UR (and 2004 TG10) were created in that event and now have evolved along the rotation of the nodal line, now located 2000, 2300 and 2400 yr in rotation behind 2004 TG10. Material not trapped in the 7:2 mean-motion resonance has since been lost.

That high ejection speed of 1.5 km/s is contrary to the gentle breakup conditions implied by the particle size distribution we measured in this paper. It would also suggest that much of the material was ejected into orbits outside of the mean-motion resonance and material would still be dispersing rather quickly along mean anomaly over time. Instead, we see that dust is confined in a narrow range of mean anomaly. The best handle on age comes from the work by Whipple & El-Din Hamid

Table 4. Proposed parent bodies for the s-Taurids.

object	epoch TDB	a AU	e	q AU	i °	long. ascen. node °	arg. peri. °	long. peri. °
2P/Encke	2015-08-04.0	2.2152	0.8483	0.3360	11.781	334.568	186.547	161.115
2003 WP21	2020-12-17.0	2.2620	0.7849	0.4866	4.295	37.654	124.030	161.390
2004 TG10	2020-12-17.0	2.2334	0.8620	0.3083	4.183	205.073	317.381	162.454
2005 UR	2005-10-26.0	2.2492	0.8818	0.2660	6.935	20.030	140.477	160.507
2005 TF50	2020-12-17.0	2.2730	0.8692	0.2972	10.725	0.564	159.962	160.526
2015 TX24	2020-12-17.0	2.2647	0.8724	0.2890	6.049	32.827	127.151	159.978
s-Taurids (DFN)	2015-11-05.1	2.237	0.847	0.358	5.45	42.72	115.70	158.31

(1952) and Olech et al. (2016) who found that individual fireball orbits originated from a common orbit about 1,500 years ago. However, if the mean-motion resonance is involved, this age may be an upper limit only.

On closer inspection, we find that the change of argument of perihelion with node does not align all three bodies (Figure 9). As noticed before by Spurný et al. (2017), the longitude of perihelion is not quite constant in the s-Taurids stream. Instead, the trend of argument of perihelion points directly at asteroid 2015 TX24, which is only 3.5 degrees further in node than the range of DFN fireballs observed. A few EN fireballs cover the node of 2015 TX24. 2025 TX24 is also close in position to the nodal dependence seen with perihelion distance, eccentricity and inclination, but those parameters can scatter more easily and that difference may merely reflect the change in orbital elements needed to intersect Earth's orbit.

Asteroid 2005 UR and 2005 TF50 have similar longitude of perihelion as 2015 TX24, but don't fall along the trend line seen among the meteoroids. We conclude that these larger asteroids are not simply fragments of this stream as proposed by Spurný et al. (2017).

A likely scenario is that we are seeing recent activity from a breakup involving surviving asteroid 2015 TX24. 2015 TX24 now has a semi-major axis of 2.2647 AU (Epoch 2020-Dec-17.0 TDB). That puts it within the normal semi-major axis oscillation of ± 0.03 AU from the resonance. Solar radiation pressure will slightly increase the semi-major axis of the DFN meteoroids, but if the ejection conditions were slightly lowering the semi-major axis, this could have been compensated. It is possible that the change of longitude of perihelion away from the node of 2015 TX24 is due the influence of the 7:2 mean-motion resonance. Presumably, the further the meteoroid node now is from 2015 TX24, the stronger the influence of the resonance. The precision of the semi-major axis is not good enough to verify that. If so, that could mean that the breakup happened rather recently, perhaps as recently as a few centuries ago.

This supports a model for the Taurid Complex showers that involves an ongoing fragmentation cascade of comet 2P/Encke siblings that were created following a breakup some 20,000 years ago (Jenniskens, 2006). In this scenario, 2015 TX25 broke with 2005 UR and 2005 TF50 from a larger precursor body about 1,500 years ago, and in the past few centuries a further breakup of 2015 TX24 created the fragments observed as the s-Taurids today. Asteroid 2003 WP21 does not belong to this group and was created earlier.

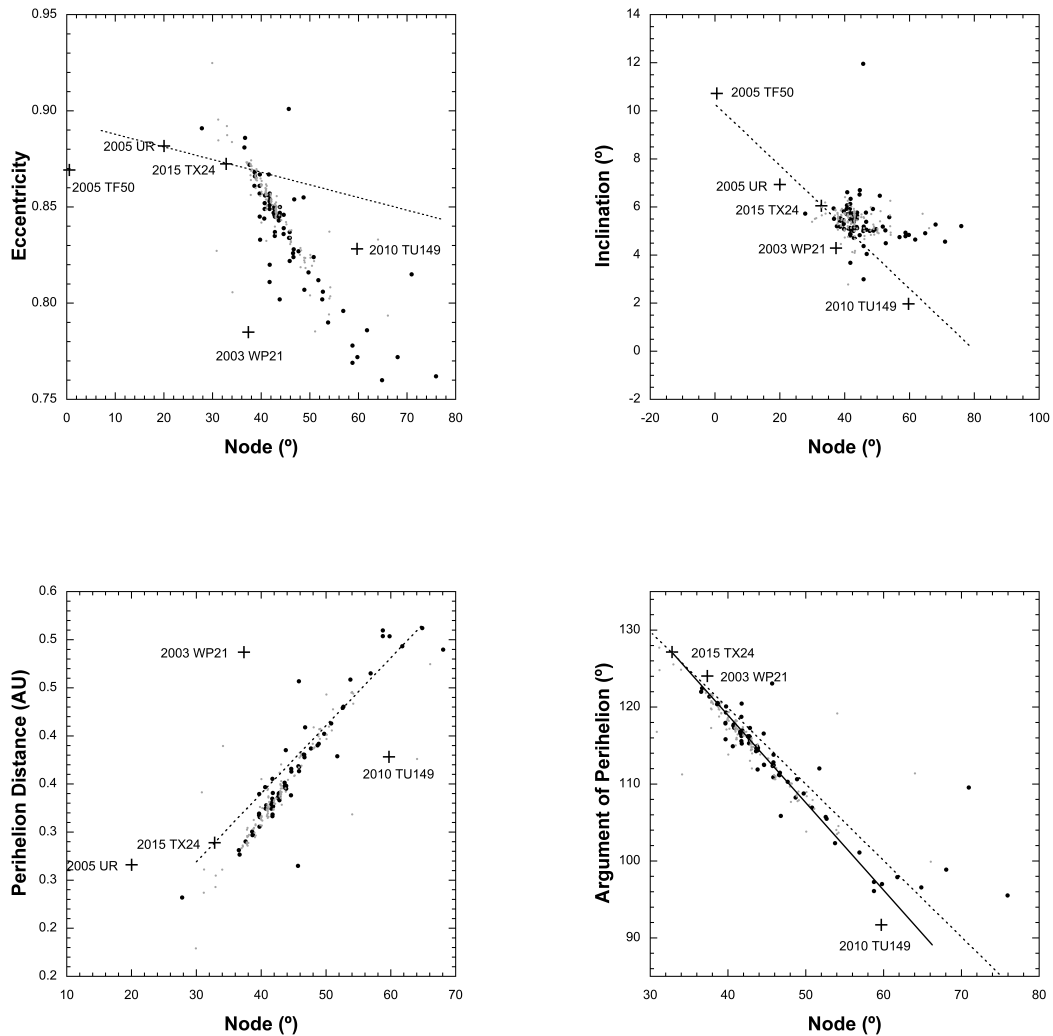


Figure 9. Orbital elements of #628 meteoroids observed by DFN (black dots) and EN (grey dots, Spurný et al. (2017)), put in context with the discussed possible parent bodies for the stream (Table 4).

It is more difficult to understand how we could be seeing activity from comet 2P/Encke. In that case, the resonance must have more dramatically changed the nodal line. Comet 2P/Encke would be expected to cause meteoroid activity centered on $\lambda_{\odot} = 224.6^{\circ}$, using method "H" of Hasegawa (1990), implemented by Neslusan et al. (1998). However, Encke now has nodes close to perihelion near Mercury and aphelion in the asteroid belt. Comet Encke's orbit has changed its longitude of perihelion significantly over the past two centuries. In 1769, the node was at 157.46° , $P_i = 159.19^{\circ}$. In 2020, the node is at 154.55° , $P_i = 161.11^{\circ}$. That rate of change is about the same as seen in the meteor stream. Around A.D. 1700, the longitude of perihelion of Encke was the same as that of the core of the s-Taurids. If we are seeing meteoroids ejected from 2P/Encke in the century around 1700 A.D., there must have been a subsequent dramatic change of the nodal line.

It is not clear whether or not the periodic nature of the s-Taurids is due to the 7:2 mean-motion resonance with Jupiter, other than preventing close encounters with Jupiter. The mean semi-major axis of the meteoroids appears to be related to that of its parent body. It is perhaps possible that the dust was released with very low relative ejection speeds and has remained concentrated in range of mean anomaly due to its young age. In particular, it is interesting that Spurný et al. (2017) noted that the 1995 detected Taurid fireballs did not quite have the orbital elements of the 2015 Taurids. They had larger semi-major axes and smaller perihelia that did not change so much with solar longitude. This could point to the presence of streams being more dispersed but narrow, which occasionally wander in Earth's path.

4.2. Meteorite dropping Taurids?

Brown et al. (2013) identified the Taurid showers as a potential source of macroscopic meteorite dropping events if a large enough meteoroid enters Earth's atmosphere. We have seen that the STS branch contains large members, do members of that population have a chance of surviving entry and falling as a meteorite? Large s-Taurids behave like weak matter (Fig. 5). They experience catastrophic disruption at very high altitudes (> 66 km, see suppl. mat. table). Their weak nature is not compensated by size, as Spurný et al. (2017) noted the larger s-Taurids tend to be the weaker ones. The deepest penetrating STS observed by the DFN (DN151114.04) is not visible below 52 km. According to the criteria of Brown et al. (2013), which states that a height of 35 km and velocity of 10 km s^{-1} are approximate terminal dynamical criteria for a given event to have a chance of producing a meteorite fall, this is unlikely to produce a recoverable meteorite on the ground. The two very bright STSs described by Olech et al. (2016); Spurný et al. (2017) also terminate at high altitudes of 57.86 and 60.20 km.

Is this weakness a feature of all Southern Taurids? The deepest penetrating Southern Taurid (MORP #715) described in the MORP dataset (Halliday et al. 1996), only penetrates to 54.8 km. As outlined by Brown et al. (2013), one of the EN fireballs in 1995 penetrated as deep as 30 km. Although this fireball was tentatively linked with the Taurid Complex, no definite association with either branch of the Taurids was reported, and the final velocity was not reported either. More generally, to our knowledge there is no report in the literature of a Southern Taurid that comes close to the terminal parameter of Brown et al. (2013).

On the other hand, we have examples of Northern Taurids that are able to penetrate much lower than the 50 km ceiling that Southern Taurids seem to hit. For example, on October 9th, 2016, the DFN observed a Northern Taurid penetrating as deep as 36.4 km, slowing down to 9.7 km s^{-1} : the terminal parameters for this NTA are much closer to the cut-off criteria of Brown et al. (2013), but still greater than required for a meteorite to survive. Are we seeing inhomogeneities here in the original composition of 2P/Encke? Or are the stronger materials representative for older meteoroids that survived the harsh conditions in the interplanetary medium?

5. CONCLUSIONS

The periodic outbursts of Taurid fireballs and visible meteors are from a stream called the s-Taurids (IAU shower 628, STS). The shower stands out well as a concentration of orbits in speed versus solar longitude diagram, with the shower members having a strongly changing entry speed with position along Earth's orbit.

We have established the size frequency distribution for the s-Taurid stream. Even at gram sizes, the stream shows a very shallow distribution with a magnitude distribution index of 2.0 (differential mass distribution index of $s = 1.75$), atypical of other JFC showers. The distribution appears to remain unchanged up to metre-sized fragments.

The highly stratified structure of this stream, and the shallow size-frequency distribution remaining constant over a large range in size, points to the stream being the product of a gentle and relatively recent break up.

Because the meteoroids initially move on different orbits than 2P/Encke, the breakup involved a different parent body. That body consisted of weak material. The distribution of longitude of perihelion along Earth's orbit points to the stream having originated from surviving asteroid *2015 TX24* a low albedo 0.07 , 0.25 ± 0.04 km sized ($H = 21.5$) asteroid that is a good candidate for a 2P/Encke sibling, together with *2014 TG10* and other such bodies identified earlier. *2015 TX24*, *2005 UR* and *2005 TF50* may have broken from a common body 1,500 years ago, with recent activity from *2015 TX24* now producing the meteoroids detected at Earth as the s-Taurids.

Large metre-sized bodies survive in the s-Taurids, possibly because they represent relatively strong cometary materials. During the s-Taurid #628 stream (STS) outburst years, the chance of the Earth being hit by a metre scale weak meteoroid is enhanced by a factor of at least [2.5, 55]. The Earth encounters the STS stream on average every 5 years, therefore the STS stream is responsible for as much as 20% of all weak (airburst > 60 km altitude) metre scale bodies.

From the analysis of terminal parameters (heights and speeds) of the large Taurid meteoroids observed by the DFN, a macroscopic meteorite from a Southern Taurid stream seems unlikely, on the other hand we have examples of Northern Taurids that approach the meteorite dropping terminal parameters discussed by (Brown et al. 2013). Given their shallow penetration depth, large meteoroids from the s-Taurids are unlikely to drop meteorites, but might generate dust that can be collected in the atmosphere.

When the cloud of meteoroids next returns close to the Earth in 2022, the Large Synoptic Survey Telescope (Ivezic et al. 2008) will be able up and running and should be able to better constraint on the hypothetical population of metre-sized s-Taurids. The recently commissioned Geostationary Lightning Mapper (Jenniskens et al. 2018) should also be able to fill the observation gap around the decimetre scale, and notably provide good estimate of the flux density of STS meteoroids in this range.

This research is supported by the Australian Research Council through the Australian Laureate Fellowships scheme, receives institutional support from Curtin University, and uses the computing facilities of the Pawsey supercomputing centre. The DFN data reduction pipeline makes intensive use of Astropy, a community-developed core Python package for Astronomy (Astropy Collaboration et al. 2013). PJ is supported by grant 80NSSC19K0513 of NASA's Emerging Worlds program and grant 80NSSC19K0563 of NASA's Solar System Workings program.

REFERENCES

- Asher, D. J., Clube, S. V. M., & Steel, D. I. 1993, MNRAS, 264, 93, doi: [10.1093/mnras/264.1.93](https://doi.org/10.1093/mnras/264.1.93)
- Asher, D. J., & Izumi, K. 1998, MNRAS, 297, 23, doi: [10.1046/j.1365-8711.1998.01395.x](https://doi.org/10.1046/j.1365-8711.1998.01395.x)

- Astropy Collaboration, Robitaille, T. P., Tollerud, E. J., et al. 2013, *A&A*, 558, A33, doi: [10.1051/0004-6361/201322068](https://doi.org/10.1051/0004-6361/201322068)
- Babadzhanov, P. B., & Kokhirova, G. I. 2009, *A&A*, 495, 353, doi: [10.1051/0004-6361:200810460](https://doi.org/10.1051/0004-6361:200810460)
- Beech, M., Hargrove, M., & Brown, P. 2004, *The Observatory*, 124, 277
- Blaauw, R. C., Campbell-Brown, M., & Kingery, A. 2016, *MNRAS*, 463, 441, doi: [10.1093/mnras/stw1979](https://doi.org/10.1093/mnras/stw1979)
- Borovička, J. 1990, *Bulletin of the Astronomical Institutes of Czechoslovakia*, 41, 391
- Borovička, J., & Spurný, P. 2020, *Planet. Space Sci.*, 182, 104849, doi: [10.1016/j.pss.2020.104849](https://doi.org/10.1016/j.pss.2020.104849)
- Bronshten, V. A. 1981, *Moscow Izdatel Nauka*
- Brown, P., Marchenko, V., Moser, D. E., Weryk, R., & Cooke, W. 2013, *Meteoritics and Planetary Science*, 48, 270, doi: [10.1111/maps.12055](https://doi.org/10.1111/maps.12055)
- Brown, P., Spalding, R. E., ReVelle, D. O., Tagliaferri, E., & Worden, S. P. 2002, *Nature*, 420, 294, doi: [10.1038/nature01238](https://doi.org/10.1038/nature01238)
- Brown, P., Wiegert, P., Clark, D., & Tagliaferri, E. 2016, *Icarus*, 266, 96, doi: [10.1016/j.icarus.2015.11.022](https://doi.org/10.1016/j.icarus.2015.11.022)
- Ceplecha, Z., & McCrosky, R. E. 1976, *J. Geophys. Res.*, 81, 6257, doi: [10.1029/JB081i035p06257](https://doi.org/10.1029/JB081i035p06257)
- Clube, S. V. M., & Napier, W. M. 1984, *MNRAS*, 211, 953, doi: [10.1093/mnras/211.4.953](https://doi.org/10.1093/mnras/211.4.953)
- Devillepoix, H. A. R., Sansom, E. K., Bland, P. A., et al. 2018, *Meteoritics and Planetary Science*, 53, 2212, doi: [10.1111/maps.13142](https://doi.org/10.1111/maps.13142)
- Devillepoix, H. A. R., Bland, P. A., Sansom, E. K., et al. 2019, *MNRAS*, 483, 5166, doi: [10.1093/mnras/sty3442](https://doi.org/10.1093/mnras/sty3442)
- Drummond, J. D. 1981, *Icarus*, 45, 545, doi: [10.1016/0019-1035\(81\)90020-8](https://doi.org/10.1016/0019-1035(81)90020-8)
- Dubietis, A., & Arlt, R. 2007, *MNRAS*, 376, 890, doi: [10.1111/j.1365-2966.2007.11488.x](https://doi.org/10.1111/j.1365-2966.2007.11488.x)
- Fay, M. P. 2010, *The R Journal*, 2, 53
- Froeschle, C., & Scholl, H. 1986, *A&A*, 158, 259
- Grün, E., Zook, H. A., Fechtig, H., & Giese, R. H. 1985, *Icarus*, 62, 244, doi: [10.1016/0019-1035\(85\)90121-6](https://doi.org/10.1016/0019-1035(85)90121-6)
- Halliday, I., Griffin, A. A., & Blackwell, A. T. 1996, *Meteoritics and Planetary Science*, 31, 185, doi: [10.1111/j.1945-5100.1996.tb02014.x](https://doi.org/10.1111/j.1945-5100.1996.tb02014.x)
- Hasegawa, I. 1990, *PASJ*, 42, 175
- Howie, R. M., Paxman, J., Bland, P. A., et al. 2017a, *Experimental Astronomy*, doi: [10.1007/s10686-017-9532-7](https://doi.org/10.1007/s10686-017-9532-7)
- . 2017b, *Meteoritics and Planetary Science*, 52, 1669, doi: [10.1111/maps.12878](https://doi.org/10.1111/maps.12878)
- Ivezic, Z., Axelrod, T., Brandt, W. N., et al. 2008, *Serbian Astronomical Journal*, 176, 1, doi: [10.2298/SAJ0876001I](https://doi.org/10.2298/SAJ0876001I)
- Jansen-Sturgeon, T., Sansom, E. K., & Bland, P. A. 2019, *Meteoritics and Planetary Science*, 54, 2149, doi: [10.1111/maps.13376](https://doi.org/10.1111/maps.13376)
- Jenniskens, P. 2006, *Meteor Showers and Their Parent Comets* (Cambridge University Press)
- Jenniskens, P., Gural, P. S., Dynneson, L., et al. 2011, *Icarus*, 216, 40, doi: [10.1016/j.icarus.2011.08.012](https://doi.org/10.1016/j.icarus.2011.08.012)
- Jenniskens, P., Nénon, Q., Gural, P. S., et al. 2016a, *Icarus*, 266, 384, doi: [10.1016/j.icarus.2015.11.009](https://doi.org/10.1016/j.icarus.2015.11.009)
- Jenniskens, P., Nénon, Q., Albers, J., et al. 2016b, *Icarus*, 266, 331, doi: [10.1016/j.icarus.2015.09.013](https://doi.org/10.1016/j.icarus.2015.09.013)
- Jenniskens, P., Nénon, Q., Gural, P. S., et al. 2016c, *Icarus*, 266, 355, doi: [10.1016/j.icarus.2015.08.014](https://doi.org/10.1016/j.icarus.2015.08.014)
- Jenniskens, P., Albers, J., Tillier, C. E., et al. 2018, *Meteoritics and Planetary Science*, 53, 2445, doi: [10.1111/maps.13137](https://doi.org/10.1111/maps.13137)
- Jenniskens, P., Utas, J., Yin, Q.-Z., et al. 2019, *Meteoritics and Planetary Science*, 54, 699, doi: [10.1111/maps.13235](https://doi.org/10.1111/maps.13235)
- Madiedo, J. M., Ortiz, J. L., Trigo-Rodríguez, J. M., et al. 2014, *Icarus*, 231, 356, doi: [10.1016/j.icarus.2013.12.025](https://doi.org/10.1016/j.icarus.2013.12.025)
- Moorhead, A. V., Egal, A., Brown, P. G., Moser, D. E., & Cooke, W. J. 2019, *Journal of Spacecraft and Rockets*, 56, 1531, doi: [10.2514/1.A34416](https://doi.org/10.2514/1.A34416)
- Neslusan, L., Svoren, J., & Porubcan, V. 1998, *A&A*, 331, 411
- Nesvorný, D., & Morbidelli, A. 1998, *AJ*, 116, 3029, doi: [10.1086/300632](https://doi.org/10.1086/300632)
- Olech, A., Żołądek, P., Wiśniewski, M., et al. 2016, *MNRAS*, 461, 674, doi: [10.1093/mnras/stw1261](https://doi.org/10.1093/mnras/stw1261)
- . 2017, *MNRAS*, 469, 2077, doi: [10.1093/mnras/stx716](https://doi.org/10.1093/mnras/stx716)

- Picone, J. M., Hedin, A. E., Drob, D. P., & Aikin, A. C. 2002, *Journal of Geophysical Research (Space Physics)*, 107, 1468, doi: [10.1029/2002JA009430](https://doi.org/10.1029/2002JA009430)
- Popescu, M., Birlan, M., Nedelcu, D. A., Vaubaillon, J., & Cristescu, C. P. 2014, *A&A*, 572, A106, doi: [10.1051/0004-6361/201424064](https://doi.org/10.1051/0004-6361/201424064)
- Sansom, E. K., Bland, P., Paxman, J., & Towner, M. 2015, *Meteoritics and Planetary Science*, 50, 1423, doi: [10.1111/maps.12478](https://doi.org/10.1111/maps.12478)
- Sansom, E. K., Bland, P. A., Towner, M. C., et al. 2020, *Meteoritics and Planetary Science*, 55, 2157, doi: [10.1111/maps.13566](https://doi.org/10.1111/maps.13566)
- Shrbený, L., & Spurný, P. 2012, in *LPI Contributions*, Vol. 1667, Asteroids, Comets, Meteors 2012, 6436
- Soja, R. H., Baggaley, W. J., Brown, P., & Hamilton, D. P. 2011, *MNRAS*, 414, 1059, doi: [10.1111/j.1365-2966.2011.18442.x](https://doi.org/10.1111/j.1365-2966.2011.18442.x)
- SonotaCo. 2009, *WGN, Journal of the International Meteor Organization*, 37, 55
- Southworth, R. B., & Hawkins, G. S. 1963, *Smithsonian Contributions to Astrophysics*, 7, 261
- Spurný, P. 1997, *Planet. Space Sci.*, 45, 541, doi: [10.1016/S0032-0633\(97\)00006-8](https://doi.org/10.1016/S0032-0633(97)00006-8)
- Spurný, P., Borovička, J., Mucke, H., & Svoreň, J. 2017, *A&A*, 605, A68, doi: [10.1051/0004-6361/201730787](https://doi.org/10.1051/0004-6361/201730787)
- Tagliaferri, E. 1994, In: *Hazards Due to Comets and Asteroids*, ed. T. Gehrels, M. S. Matthews, & A. Schumann (University of Arizona Press)
- Towner, M., & et al. 2019, *PASA*
- Tubiana, C., Snodgrass, C., Michelsen, R., et al. 2015, *A&A*, 584, A97, doi: [10.1051/0004-6361/201425512](https://doi.org/10.1051/0004-6361/201425512)
- Whipple, F. 1940, *Photographic Meteor Studies*, III. The Taurid Shower, Harvard reprint (Astronomical Observatory of Harvard College)
- Whipple, F. L., & El-Din Hamid, S. 1952, *Helwan Institute of Astronomy and Geophysics Bulletins*, 41, 3

Bibliography

- S. Abe, et al. (2006). ‘Earth-grazing fireball on March 29, 2006’. In *European Planetary Science Congress 2006*, p. 486.
- M. F. A’Hearn, et al. (2005). ‘Deep impact: excavating comet Tempel 1’. *science* **310**(5746):258–264.
- D. Asher, et al. (1993). ‘Asteroids in the Taurid complex’. *Monthly Notices of the Royal Astronomical Society* **264**(1):93–105.
- S. A. Astakhov, et al. (2003). ‘Chaos-assisted capture of irregular moons’. *Nature* **423**:264–267.
- P. Babadzhanov, et al. (2009). ‘Photographic observations of fireballs in Tajikistan’. *Solar System Research* **43**(4):353–363.
- J. M. Bailey (1972). ‘Studies on Planetary Sattelites. Satellite Capture in the Three-Body Elliptical Problem’. *The Astronomical Journal* **77**:177.
- J. Baker, Robert M. L. (1958). ‘Ephemeral Natural Satellites of the Earth’. *Science* **128**:1211–1213.
- M. Beech, et al. (1995). ‘The fall of the Peekskill meteorite: Video observations, atmospheric path, fragmentation record and orbit.’. *Earth, Moon, and Planets* **68**(1):189–197.
- M. Beech & S. Nikolova (2001). ‘The endurance lifetime of ice fragments in cometary streams’. *Planetary and Space Science* **49**(1):23–29.
- R. P. Binzel, et al. (2010). ‘Earth encounters as the origin of fresh surfaces on near-Earth asteroids’. *Nature* **463**(7279):331–334.

- R. P. Binzel, et al. (2015). ‘The near-Earth object population: Connections to comets, main-belt asteroids, and meteorites’. *Asteroids IV* **1**:243.
- R. P. Binzel, et al. (2004). ‘Observed spectral properties of near-Earth objects: results for population distribution, source regions, and space weathering processes’. *Icarus* **170**(2):259–294.
- P. Bland, et al. (2012). ‘The Australian Desert Fireball Network: a new era for planetary science’. *Australian Journal of Earth Sciences* **59**(2):177–187.
- P. A. Bland (2004). ‘The desert fireball network’. *Astronomy & Geophysics* **45**(5):5–20.
- P. A. Bland & N. A. Artemieva (2006). ‘The rate of small impacts on Earth’. *Meteoritics & Planetary Science* **41**(4):607–631.
- H. Boehnhardt (2004). ‘Split comets’. *Comets II* **745**:301–316.
- B. Bolin, et al. (2014). ‘Detecting Earth’s temporarily-captured natural satellites—Minimoons’. *Icarus* **241**:280–297.
- J. Borovička (1990). ‘The comparison of two methods of determining meteor trajectories from photographs’. *Bulletin of the Astronomical Institutes of Czechoslovakia* **41**:391–396.
- J. Borovička & Z. Ceplecha (1992). ‘Earth-grazing fireball of October 13, 1990’. *Astronomy and Astrophysics* **257**:323–328.
- J. Borovička, et al. (2015). ‘Small near-Earth asteroids as a source of meteorites’. *Asteroids IV* **257**.
- J. Borovička, et al. (2017). ‘The January 7, 2015, superbolide over Romania and structural diversity of meter-sized asteroids’. *Planetary and Space Science* **143**:147–158.
- J. Borovička, et al. (2007). ‘Atmospheric deceleration and light curves of Draconid meteors and implications for the structure of cometary dust’. *Astronomy & Astrophysics* **473**(2):661–672.
- J. Borovička, et al. (2020). ‘Two Strengths of Ordinary Chondritic Meteoroids as Derived from their Atmospheric Fragmentation Modeling’. *arXiv preprint arXiv:2006.07080* .

- J. Borovička, et al. (2013). ‘The Košice meteorite fall: Atmospheric trajectory, fragmentation, and orbit’. *Meteoritics & Planetary Science* **48**(10):1757–1779.
- W. F. Bottke, et al. (1994). ‘Velocity distributions among colliding asteroids’. *ICARUS-NEW YORK-* **107**:255–255.
- W. F. Bottke Jr, et al. (2002). ‘Debiased orbital and absolute magnitude distribution of the near-Earth objects’. *Icarus* **156**(2):399–433.
- S. Brelsford, et al. (2016). ‘Rendezvous missions to temporarily captured near Earth asteroids’. *Planetary and Space Science* **123**:4–15.
- P. Brown, et al. (1994). ‘The orbit and atmospheric trajectory of the Peekskill meteorite from video records’. *Nature* **367**(6464):624.
- P. Brown, et al. (2013). ‘Meteorites from meteor showers: A case study of the Taurids’. *Meteoritics & Planetary Science* **48**(2):270–288.
- P. Brown, et al. (2010). ‘Development of an all-sky video meteor network in Southern Ontario, Canada The ASGAR System’. *WGN, Journal of the International Meteor Organization* **38**:25–30.
- P. Brown, et al. (2016). ‘Orbital and physical characteristics of meter-scale impactors from airburst observations’. *Icarus* **266**:96–111.
- P. G. Brown, et al. (2000). ‘The fall, recovery, orbit, and composition of the Tagish Lake meteorite: A new type of carbonaceous chondrite’. *Science* **290**(5490):320–325.
- D. E. Brownlee, et al. (2004). ‘Surface of young Jupiter family comet 81P/Wild 2: View from the Stardust spacecraft’. *Science* **304**(5678):1764–1769.
- A. Brunini (1996). ‘On the Satellite Capture Problem Capture and stability regions for planetary satellites’. *Celestial Mechanics and Dynamical Astronomy* **64**:79–92.
- J. G. Burke (1991). *Cosmic debris: Meteorites in history*. Univ of California Press.
- H. Campins & T. D. Swindle (1998). ‘Expected characteristics of cometary meteorites’. *Meteoritics & Planetary Science* **33**(6):1201–1211.
- A. Carusi & E. Dotto (1996). ‘Close encounters of minor bodies with the Earth’. *Icarus* **124**(2):392–398.

- A. Carusi & G. Valsecchi (1987). 'Dynamical evolution of short-period comets'. *Publications of the Astronomical Institute of the Czechoslovak Academy of Sciences* **67**:21–28.
- T. Cavallo (1784). 'IX. Description of a meteor, observed Aug. 18, 1783'. *Philosophical Transactions of the Royal Society of London* **74**:108–111.
- Z. Ceplecha (1979). 'Earth-grazing fireballs/the daylight fireball of Aug. 10, 1972'. *Bulletin of the Astronomical Institutes of Czechoslovakia* **30**:349–356.
- Z. Ceplecha (1987). 'Geometric, dynamic, orbital and photometric data on meteoroids from photographic fireball networks'. *Bulletin of the Astronomical Institutes of Czechoslovakia* **38**:222–234.
- Z. Ceplecha (1994a). 'Earth-grazing daylight fireball of August 10, 1972'. *Astronomy and Astrophysics* **283**:287–288.
- Z. Ceplecha (1994b). 'Impacts of meteoroids larger than 1 m into the Earth's atmosphere'. *Astronomy and Astrophysics* **286**:967–970.
- Z. Ceplecha, et al. (1998). 'Meteor phenomena and bodies'. *Space Science Reviews* **84**(3-4):327–471.
- Z. Ceplecha, et al. (1973). 'Data on three significant fireballs photographed within the European Network in 1971'. *Bulletin of the Astronomical Institutes of Czechoslovakia* **24**:13.
- Z. Ceplecha & R. McCrosky (1976). 'Fireball end heights: A diagnostic for the structure of meteoric material'. *Journal of Geophysical Research* **81**(35):6257–6275.
- Z. Ceplecha & J. Rajchl (1965). 'Programme of fireball photography in Czechoslovakia'. *Bulletin of the Astronomical Institutes of Czechoslovakia* **16**:15.
- Z. Ceplecha, et al. (1996). 'Video observations, atmospheric path, orbit and fragmentation record of the Peekskill meteorite'. *Earth, Moon, and Planets* **72**(1-3):395–404.
- C. A. Chant (1913). 'An Extraordinary Meteoric Display'. *Journal of the Royal Astronomical Society of Canada* **7**:145.

- E. F. F. Chladni (1794). *Über den Ursprung der von Pallas gefundenen und anderer ihr ähnlicher Eisenmassen und über einige damit in Verbindung stehende Naturerscheinungen*. bey Johann Friedrich Hartknoch.
- P. Chodas (2014). ‘Finding and characterizing candidate targets for the Asteroid Redirect Mission (ARM)’. In K. Muinonen, A. Penttilä, M. Granvik, A. Virkki, G. Fedorets, O. Wilkman, & T. Kohout (eds.), *Asteroids, Comets, Meteors 2014*, p. 94.
- D. Clark, et al. (2016). ‘Impact detections of temporarily captured natural satellites’. In *AAS/Division for Planetary Sciences Meeting Abstracts #48*, AAS/Division for Planetary Sciences Meeting Abstracts, p. 311.06.
- D. L. Clark & P. A. Wiegert (2011). ‘A numerical comparison with the Ceplecha analytical meteoroid orbit determination method’. *Meteoritics & Planetary Science* **46**(8):1217–1225.
- J. K. Cline (1979). ‘Satellite Aided Capture’. *Celestial Mechanics* **19**:405–415.
- G. Consolmagno, et al. (2008). ‘The significance of meteorite density and porosity’. *Chemie der Erde-Geochemistry* **68**(1):1–29.
- F. DeMeo, et al. (2015). ‘The compositional structure of the asteroid belt’. *Asteroids IV* **1**:13.
- F. E. DeMeo & B. Carry (2014). ‘Solar System evolution from compositional mapping of the asteroid belt’. *Nature* **505**(7485):629–634.
- W. F. Denning (1916). ‘Great Meteoric Stream of February 9th, 1913’. *Journal of the Royal Astronomical Society of Canada* **10**:294.
- H. A. Devillepoix, et al. (2019). ‘Observation of metre-scale impactors by the Desert Fireball Network’. *Monthly Notices of the Royal Astronomical Society* **483**(4):5166–5178.
- H. A. Devillepoix, et al. (2018). ‘The Dingle Dell meteorite: A Halloween treat from the Main Belt’. *Meteoritics & Planetary Science* **53**(10):2212–2227.
- H. A. R. Devillepoix, et al. (2020). ‘A Global Fireball Observatory’. *Planetary and Space Science* **191**:105036.
- H. A. R. Devillepoix, et al. (2020). ‘A Global Fireball Observatory’.

- H. A. R. Devillepoix, et al. (2018). ‘The Dingle Dell meteorite: A Halloween treat from the Main Belt’. *Meteoritics and Planetary Science* **53**:2212–2227.
- R. P. Di Sisto, et al. (2009). ‘On the population, physical decay and orbital distribution of Jupiter family comets: Numerical simulations’. *Icarus* **203**(1):140–154.
- V. Dmitriev, et al. (2015). ‘Orbit determination based on meteor observations using numerical integration of equations of motion’. *Planetary and Space Science* **117**:223–235.
- J. D. Drummond (1981). ‘A test of comet and meteor shower associations’. *Icarus* **45**(3):545–553.
- M. Duncan, et al. (2004). ‘Dynamical evolution of ecliptic comets’. *Comets II* **193**:204.
- M. J. Duncan & H. F. Levison (1997). ‘A disk of scattered icy objects and the origin of Jupiter-family comets’. *Science* **276**(5319):1670–1672.
- O. Eugster, et al. (2006). ‘Irradiation records, cosmic-ray exposure ages, and transfer times of meteorites’. *Meteorites and the early solar system II* pp. 829–851.
- E. Everhart (1985). ‘An efficient integrator that uses Gauss-Radau spacings’. In A. Carusi & G. B. Valsecchi (eds.), *IAU Colloq. 83: Dynamics of Comets: Their Origin and Evolution*, vol. 115, p. 185.
- G. Fedorets, et al. (2017). ‘Orbit and size distributions for asteroids temporarily captured by the Earth-Moon system’. *Icarus* **285**:83–94.
- G. Fedorets, et al. (2015). ‘Discovering asteroids temporarily captured by the Earth with LSST’. In *IAU General Assembly*, vol. 29, p. 2257052.
- J. Fernández, et al. (1999). ‘The population, magnitudes, and sizes of Jupiter family comets’. *Astronomy and Astrophysics* **352**:327–340.
- J. A. Fernández (1980). ‘On the existence of a comet belt beyond Neptune’. *Monthly Notices of the Royal Astronomical Society* **192**(3):481–491.
- J. A. Fernández, et al. (2002). ‘Are there many inactive Jupiter-family comets among the near-Earth asteroid population?’. *Icarus* **159**(2):358–368.

- J. A. Fernández & A. Morbidelli (2006). ‘The population of faint Jupiter family comets near the Earth’. *Icarus* **185**(1):211–222.
- J. A. Fernández & A. Sosa (2015). ‘Jupiter family comets in near-Earth orbits: Are some of them interlopers from the asteroid belt?’. *Planetary and Space Science* **118**:14–24.
- J. A. Fernández, et al. (2014). ‘Assessing the physical nature of near-Earth asteroids through their dynamical histories’. *Icarus* **238**:1–12.
- Y. Fernández, et al. (2013). ‘Thermal properties, sizes, and size distribution of Jupiter-family cometary nuclei’. *Icarus* **226**(1):1138–1170.
- Y. R. Fernández (2009). ‘That’s the way the comet crumbles: Splitting Jupiter-family comets’. *Planetary and Space Science* **57**(10):1218–1227.
- Y. R. Fernández, et al. (2001). ‘Low albedos among extinct comet candidates’. *The Astrophysical Journal Letters* **553**(2):L197.
- Y. R. Fernández, et al. (2005). ‘Albedos of asteroids in comet-like orbits’. *The Astronomical Journal* **130**(1):308.
- G. J. Flynn, et al. (2018). ‘Physical properties of the stone meteorites: Implications for the properties of their parent bodies’. *Geochemistry* **78**(3):269–298.
- E. G. Forbes (1971). ‘Gauss and the Discovery of Ceres’. *Journal for the History of Astronomy* **2**(3):195–199.
- S. Fornasier, et al. (2015). ‘Spectrophotometric properties of the nucleus of comet 67P/Churyumov-Gerasimenko from the OSIRIS instrument onboard the ROSETTA spacecraft’. *Astronomy & Astrophysics* **583**:A30.
- A. Fujiwara, et al. (2006). ‘The rubble-pile asteroid Itokawa as observed by Hayabusa’. *Science* **312**(5778):1330–1334.
- R. S. Gomes, et al. (2008). ‘The scattered disk: Origins, dynamics, and end states’. *The Solar System Beyond Neptune* pp. 259–273.
- S. Gong & J. Li (2015). ‘Planetary capture and escape in the planar four-body problem’. *Astrophysics and Space Science* **357**:155.
- M. Gounelle, et al. (2008). ‘Meteorites from the outer solar system’. *The solar system beyond Neptune* pp. 525–541.

- M. Granvik & P. Brown (2018). ‘Identification of meteorite source regions in the Solar System’. *Icarus* **311**:271–287.
- M. Granvik, et al. (2016). ‘Super-catastrophic disruption of asteroids at small perihelion distances’. *Nature* **530**(7590):303–306.
- M. Granvik, et al. (2018). ‘Debiased orbit and absolute-magnitude distributions for near-Earth objects’. *Icarus* **312**:181–207.
- M. Granvik, et al. (2012). ‘The population of natural Earth satellites’. *Icarus* **218**:262–277.
- R. Greenberg (1982). ‘Orbital interactions-A new geometrical formalism’. *The Astronomical Journal* **87**:184–195.
- S. Greenstreet, et al. (2012). ‘The orbital distribution of near-Earth objects inside Earth’s orbit’. *Icarus* **217**(1):355–366.
- M. Gritsevich (2009). ‘Determination of parameters of meteor bodies based on flight observational data’. *Advances in Space Research* **44**(3):323–334.
- M. Gritsevich & V. Stulov (2006). ‘Extra-atmospheric masses of the Canadian Network bolides’. *Solar System Research* **40**(6):477–484.
- M. I. Gritsevich (2007). ‘Approximation of the observed motion of bolides by the analytical solution of the equations of meteor physics’. *Solar System Research* **41**(6):509–514.
- I. Halliday, et al. (1978). ‘The Innisfree meteorite and the Canadian camera network’. *Journal of the Royal Astronomical Society of Canada* **72**:15–39.
- I. Halliday & A. A. Griffin (1982). ‘A study of the relative rates of meteorite falls on the earth’s surface’. *Meteoritics* **17**(1):31–46.
- R. E. S. Heineman & L. F. Brady (1929). ‘The Winona meteorite’. *American Journal of Science* (108):477–486.
- T. A. Heppenheimer & C. Porco (1977). ‘New Contributions to the Problem of Capture’. *Icarus* **30**:385–401.
- R. M. Howie, et al. (2017a). ‘How to build a continental scale fireball camera network’. *Experimental Astronomy* **43**(3):237–266.

- R. M. Howie, et al. (2017b). ‘Submillisecond fireball timing using de Bruijn time-codes’. *Meteoritics & Planetary Science* **52**(8):1669–1682.
- H. H. Hsieh & N. Haghighipour (2016). ‘Potential Jupiter-Family comet contamination of the main asteroid belt’. *Icarus* **277**:19–38.
- H. H. Hsieh & D. Jewitt (2006). ‘A population of comets in the main asteroid belt’. *Science* **312**(5773):561–563.
- H. H. Hsieh, et al. (2020). ‘Potential Themis-family Asteroid Contribution to the Jupiter-family Comet Population’. *The Astronomical Journal* **159**(4):179.
- D. W. Hughes (2003). ‘The variation of short-period comet size and decay rate with perihelion distance’. *Monthly Notices of the Royal Astronomical Society* **346**(2):584–592.
- R. Hutchison (2006). *Meteorites: A petrologic, chemical and isotopic synthesis*, vol. 2. Cambridge University Press.
- Ž. Ivezić, et al. (2008). ‘LSST: from Science Drivers to Reference Design and Anticipated Data Products’. *ArXiv e-prints* p. arXiv:0805.2366.
- L. G. Jacchia (1974). ‘A meteorite that missed the Earth’. *Sky and Telescope* **48**.
- T. Jansen-Sturgeon, et al. (2019a). ‘Comparing analytical and numerical approaches to meteoroid orbit determination using Hayabusa telemetry’. *Meteoritics & Planetary Science* **54**(9):2149–2162.
- T. Jansen-Sturgeon, et al. (2019b). ‘Comparing analytical and numerical approaches to meteoroid orbit determination using Hayabusa telemetry’. *Meteoritics & Planetary Science* **54**(9):2149–2162.
- T. Jansen-Sturgeon, et al. (2019c). ‘A Dynamic Trajectory Fit to Multi-Sensor Fireball Observations’.
- P. Jenniskens (2004). ‘2003 EH1 is the Quadrantid shower parent comet’. *The Astronomical Journal* **127**(5):3018.
- P. Jenniskens, et al. (2012). ‘Radar-enabled recovery of the Sutter’s Mill meteorite, a carbonaceous chondrite regolith breccia’. *Science* **338**(6114):1583–1587.
- P. Jenniskens & P. M. M. Jenniskens (2006). *Meteor showers and their parent comets*. Cambridge University Press.

- P. Jenniskens & E. Lyytinen (2005). ‘Meteor showers from the debris of broken comets: D/1819 W1 (Blanpain), 2003 WY25, and the Phoenicids’. *The Astronomical Journal* **130**(3):1286.
- D. Jewitt (2012). ‘The active asteroids’. *The Astronomical Journal* **143**(3):66.
- T. J. Jopek (1993). ‘Remarks on the meteor orbital similarity D-criterion’. *Icarus* **106**(2):603–607.
- D. M. Kary & L. Dones (1996). ‘Capture Statistics of Short-Period Comets: Implications for Comet D /Shoemaker-Levy 9’. *Icarus* **121**:207–224.
- M. S. Kelley & D. H. Wooden (2009). ‘The composition of dust in Jupiter-family comets inferred from infrared spectroscopy’. *Planetary and Space Science* **57**(10):1133–1145.
- Y. Kim, et al. (2014). ‘Physical properties of asteroids in comet-like orbits in infrared asteroid survey catalogs’. *The Astrophysical Journal* **789**(2):151.
- P. M. Kozak & J. Watanabe (2017). ‘Upward-moving low-light meteor – I. Observation results’. *Monthly Notices of the Royal Astronomical Society* **467**(1):793–801.
- L. Kresák (1981). ‘The lifetimes and disappearance of periodic comets’. *Bulletin of the Astronomical Institutes of Czechoslovakia* **32**:321–339.
- L. Kresák & M. Kresáková (1990). ‘Secular brightness decrease of periodic comets’. *Icarus* **86**(1):82–92.
- T. Kwiatkowski, et al. (2009). ‘Photometry of 2006 RH120: an asteroid temporarily captured into a geocentric orbit’. *Astronomy & Astrophysics* **495**(3):967–974.
- D. Lauretta, et al. (2017). ‘OSIRIS-REx: sample return from asteroid (101955) Bennu’. *Space Science Reviews* **212**(1-2):925–984.
- D. Lauretta, et al. (2019). ‘Episodes of particle ejection from the surface of the active asteroid (101955) Bennu’. *Science* **366**(6470).
- D. S. Lauretta & H. Y. McSween (2006). *Meteorites and the early solar system II*. University of Arizona Press.
- M. Le Feuvre & M. A. Wieczorek (2008). ‘Nonuniform cratering of the terrestrial planets’. *Icarus* **197**(1):291–306.

- H. F. Levison & M. J. Duncan (1994). ‘The long-term dynamical behavior of short-period comets’. *Icarus* **108**(1):18–36.
- H. F. Levison & M. J. Duncan (1997a). ‘From the Kuiper belt to Jupiter-family comets: The spatial distribution of ecliptic comets’. *Icarus* **127**(1):13–32.
- H. F. Levison & M. J. Duncan (1997b). ‘From the Kuiper belt to Jupiter-family comets: The spatial distribution of ecliptic comets’. *Icarus* **127**(1):13–32.
- H. F. Levison, et al. (2006). ‘On the origin of the unusual orbit of Comet 2P/Encke’. *Icarus* **182**(1):161–168.
- J. Licandro, et al. (2016). ‘Size and albedo distributions of asteroids in cometary orbits using WISE data’. *Astronomy & Astrophysics* **585**:A9.
- Z. F. Luo & F. Topputo (2017). ‘Capability of satellite-aided ballistic capture’. *Communications in Nonlinear Science and Numerical Simulations* **48**:211–223.
- A. E. Lynam, et al. (2011). ‘Multiple-satellite-aided capture trajectories at Jupiter using the Laplace resonance’. *Celestial Mechanics and Dynamical Astronomy* **109**:59–84.
- E. Lyytinen & M. Gritsevich (2016). ‘Implications of the atmospheric density profile in the processing of fireball observations’. *Planetary and Space Science* **120**:35–42.
- J. M. Madiedo, et al. (2016). ‘An Earth-grazing fireball from the Daytime ζ -Perseid shower observed over Spain on 2012 June 10’. *Monthly Notices of the Royal Astronomical Society* **460**(1):917–922.
- J. M. Madiedo, et al. (2014a). ‘Trajectory, orbit, and spectroscopic analysis of a bright fireball observed over Spain on April 13, 2013’. *Astronomy & Astrophysics* **569**:A104.
- J. M. Madiedo, et al. (2014b). ‘Trajectory, orbit, and spectroscopic analysis of a bright fireball observed over Spain on April 13, 2013’. *Astronomy & Astrophysics* **569**:A104.
- J. R. Masiero, et al. (2014). ‘Main-belt asteroids with WISE/NEOWISE: Near-infrared albedos’. *The Astrophysical Journal* **791**(2):121.
- D. L. Mathias, et al. (2017). ‘A probabilistic asteroid impact risk model: assessment of sub-300 m impacts’. *Icarus* **289**:106–119.

- D. D. Mazanek, et al. (2015). ‘Asteroid redirect mission concept: a bold approach for utilizing space resources’. *Acta Astronautica* **117**:163–171.
- R. E. McCrosky & H. Boeschstein (1965). ‘The prairie meteorite network’. *Optical Engineering* **3**(4):304127.
- K. Meech, et al. (2004). ‘Comet nucleus size distributions from HST and Keck telescopes’. *Icarus* **170**(2):463–491.
- K. J. Meech, et al. (2016). ‘Inner solar system material discovered in the Oort cloud’. *Science Advances* **2**(4):e1600038.
- S. Molau & J. Rendtel (2009). ‘A comprehensive list of meteor showers obtained from 10 years of observations with the IMO Video Meteor Network’. *WGN, Journal of the International Meteor Organization* **37**:98–121.
- A. Morbidelli, et al. (2002). ‘Origin and evolution of near-Earth objects’. *Asteroids iii* **409**.
- A. Moreno, et al. (2016). ‘Preliminary Spectroscopic and Dynamical Analysis of an Earth-Grazer Fireball Observed on December 24, 2014’. In *Lunar and Planetary Science Conference*, vol. 47, p. 1088.
- M. Moreno-Ibáñez, et al. (2020). ‘Physically based alternative to the PE criterion for meteoroids’. *Monthly Notices of the Royal Astronomical Society* **494**(1):316–324.
- M. A. Murison (1989). ‘The fractal dynamics of satellite capture in the circular restricted three-body problem’. *The Astronomical Journal* **98**:2346–2359.
- D. Nesvorný, et al. (2003). ‘Orbital and Collisional Evolution of the Irregular Satellites’. *The Astronomical Journal* **126**:398–429.
- D. Nesvorný, et al. (2010). ‘Cometary origin of the zodiacal cloud and carbonaceous micrometeorites. Implications for hot debris disks’. *The Astrophysical Journal* **713**(2):816.
- D. Nesvorný, et al. (2017). ‘Origin and evolution of short-period comets’. *The Astrophysical Journal* **845**(1):27.
- D. Nesvorný, et al. (2007). ‘Capture of Irregular Satellites during Planetary Encounters’. *The Astronomical Journal* **133**:1962–1976.

- C. Nugent, et al. (2012). ‘Detection of semimajor axis drifts in 54 near-Earth asteroids: New measurements of the Yarkovsky effect’. *The Astronomical Journal* **144**(2):60.
- J. Oberst, et al. (2014). ‘The extraordinary grazing fireball over Central Europe on March 31, 2014’. In *Proceedings of the European Planetary Science Congress 2014. EPSC Abstracts*, vol. 9.
- J. Oberst, et al. (1998). ‘The “European Fireball Network”: current status and future prospects’. *Meteoritics & Planetary Science* **33**(1):49–56.
- D. W. Olson, et al. (2010). ‘Literary Mystery: Walt Whitman’s “Year of Meteors”’. *Sky and telescope* **120**(1):28–33.
- ΩÖpik
- E. J. Öpik (1951). ‘Collision Probabilities with the Planets and the Distribution of Interplanetary Matter’. *Proceedings of the Royal Irish Academy. Section A: Mathematical and Physical Sciences* **54**:165–199.
- J. M. Picone, et al. (2002). ‘NRLMSISE-00 empirical model of the atmosphere: Statistical comparisons and scientific issues’. *Journal of Geophysical Research: Space Physics* **107**(A12):SIA 15–1–SIA 15–16.
- J. B. Pollack, et al. (1979). ‘Gas drag in primordial circumplanetary envelopes: A mechanism for satellite capture’. *Icarus* **37**:587–611.
- O. Popova, et al. (2011). ‘Very low strengths of interplanetary meteoroids and small asteroids’. *Meteoritics & Planetary Science* **46**(10):1525–1550.
- T. Quinn, et al. (1990). ‘Planetary perturbations and the origins of short-period comets’. *The Astrophysical Journal* **355**:667–679.
- R. Rawcliffe, et al. (1974). ‘Meteor of August 10, 1972’. *Nature* **247**(5441):449.
- V. Reddy, et al. (2015). ‘Mineralogy and surface composition of asteroids’. *Asteroids IV* (2867).
- T. Rehren, et al. (2013). ‘5,000 years old Egyptian iron beads made from hammered meteoritic iron’. *Journal of Archaeological Science* **40**(12):4785–4792.
- H. Rein & S. F. Liu (2012). ‘REBOUND: an open-source multi-purpose N-body code for collisional dynamics’. *Astronomy and Astrophysics* **537**:A128.

- H. Rein & D. S. Spiegel (2015). ‘IAS15: a fast, adaptive, high-order integrator for gravitational dynamics, accurate to machine precision over a billion orbits’. *Monthly Notices of the Royal Astronomical Society* **446**(2):1424–1437.
- D. O. Revelle, et al. (1997). ‘Infrasonic observations of bolides on October 4, 1996’. In F. A. Allahdadi, E. K. Casani, & T. D. Maclay (eds.), *Small Spacecraft, Space Environments, and Instrumentation Technologies*, vol. 3116 of *Proceedings Volume 3116, Small Spacecraft, Space Environments, and Instrumentation Technologies*, pp. 156–167.
- T. P. Robitaille, et al. (2013). ‘Astropy: A community Python package for astronomy’. *Astronomy & Astrophysics* **558**:A33.
- J. Salvatier, et al. (2016). ‘Probabilistic programming in Python using PyMC3’. *PeerJ Computer Science* **2**:e55.
- E. K. Sansom, et al. (2015). ‘A novel approach to fireball modeling: The observable and the calculated’. *Meteoritics & Planetary Science* **50**(8):1423–1435.
- E. K. Sansom, et al. (2019a). ‘Determining Fireball Fates Using the α - β Criterion’. *The Astrophysical Journal* **885**(2):115.
- E. K. Sansom, et al. (2019b). ‘3D meteoroid trajectories’. *Icarus* **321**:388–406.
- P. M. Shober, et al. (2020a). ‘Using atmospheric impact data to model meteoroid close encounters’. *Monthly Notices of the Royal Astronomical Society* **498**(4):5240–5250.
- P. M. Shober, et al. (2019). ‘Identification of a Minimoons Fireball’. *The Astronomical Journal* **158**(5):183.
- P. M. Shober, et al. (2020b). ‘Where Did They Come From, Where Did They Go: Grazing Fireballs’. *The Astronomical Journal* **159**(5):191.
- P. M. Shober, et al. (2021). ‘The main asteroid belt: the primary source of debris on comet-like orbits’. *The Planetary Science Journal* **2**(3):98.
- A. Sosa, et al. (2012). ‘On the asymmetric evolution of the perihelion distances of near-Earth Jupiter family comets around the discovery time’. *Astronomy & Astrophysics* **548**:A64.
- R. Southworth & G. Hawkins (1963). ‘Statistics of meteor streams’. *Smithsonian Contributions to Astrophysics* **7**:261–285.

- P. Spurný, et al. (2017). ‘Atmospheric trajectory and heliocentric orbit of the Ejby meteorite fall in Denmark on February 6, 2016’. *Planetary and Space Science* **143**:192–198.
- P. Spurný, et al. (2008). ‘Precise Multi-Instrument Data on 45 Fireballs Recorded over Central Europe in the Period 2006-2008’. In *Asteroids, Comets, Meteors 2008*, vol. 1405.
- P. Spurný, et al. (2013). ‘Trajectory and orbit of the Maribo CM2 meteorite from optical, photoelectric and radar records’. In *Meteoroids 2013 conference, Poznan, Poland*.
- D. Steel & D. Asher (1996). ‘On the origin of Comet Encke’. *Monthly Notices of the Royal Astronomical Society* **281**(3):937–944.
- J. Sunshine, et al. (2006). ‘Exposed water ice deposits on the surface of comet 9P/Tempel 1’. *Science* **311**(5766):1453–1455.
- D. Takir, et al. (2015). ‘Toward an understanding of phyllosilicate mineralogy in the outer main asteroid belt’. *Icarus* **257**:185–193.
- G. Tancredi (1995). ‘The dynamical memory of Jupiter family comets.’. *Astronomy and Astrophysics* **299**:288.
- G. Tancredi (2014). ‘A criterion to classify asteroids and comets based on the orbital parameters’. *Icarus* **234**:66–80.
- M. B. Taylor (2005). ‘TOPCAT & STILTS: starlink table/VOTable processing software’. In *Astronomical Data Analysis Software and Systems XIV*, vol. 347, p. 29.
- M. C. Towner, et al. (2020). ‘Fireball streak detection with minimal CPU processing requirements for the Desert Fireball Network data processing pipeline’. *Publications of the Astronomical Society of Australia* **37**:e008.
- J. Trigo-Rodríguez, et al. (2005). ‘The development of the Spanish Fireball Network using a new all-sky CCD system’. In *Modern Meteor Science An Interdisciplinary View*, pp. 553–567. Springer.
- K. Tsiganis, et al. (2005). ‘Origin of the orbital architecture of the giant planets of the Solar System’. *Nature* **435**(7041):459.

- K. H. Tsui (2000). ‘Asteroid-Planet-Sun Interaction in the Presence of a Planetary Satellite’. *Icarus* **148**:139–146.
- K. H. Tsui (2002). ‘Satellite capture in a four-body system’. *Planetary and Space Science* **50**:269–276.
- H. Urrutxua & C. Bombardelli (2017). ‘A look at the capture mechanisms of the “temporarily captured asteroids” of the earth,’. In *26th International Symposium on Space Flight Dynamics, number ISSFD-2017*, vol. 74, pp. 1–7.
- D. Vida, et al. (2018). ‘Modelling the measurement accuracy of pre-atmosphere velocities of meteoroids’. *Monthly Notices of the Royal Astronomical Society* **479**(4):4307–4319.
- D. Vokrouhlický, et al. (2015). ‘The Yarkovsky and YORP Effects’. *Asteroids IV* pp. 509–531.
- K. J. Walsh, et al. (2011). ‘A low mass for Mars from Jupiter’s early gas-driven migration’. *Nature* **475**(7355):206.
- S.-i. Watanabe, et al. (2017). ‘Hayabusa2 mission overview’. *Space Science Reviews* **208**(1-4):3–16.
- G. Wetherill & D. ReVelle (1981). ‘Which fireballs are meteorites? A study of the Prairie Network photographic meteor data’. *Icarus* **48**(2):308–328.
- M. Wiśniewski, et al. (2017). ‘Current status of Polish fireball network’. *Planetary and Space Science* **143**:12–20.
- V. A. Yegorov (1959). ‘The capture problem in the three-body restricted orbital problem’. *Artificial Earth Satellites* **3**:17.

Every reasonable effort has been made to acknowledge the owners of copyright material. I would be pleased to hear from any copyright owner who has been omitted or incorrectly acknowledged.